A. Steiner · B. Pirscher
U. Foelsche · G. Kirchengast
(Eds.)

New Horizons in Occultation Research

Studies in Atmosphere and Climate

Springer

New Horizons in Occultation Research

Andrea Steiner · Barbara Pirscher ·
Ulrich Foelsche · Gottfried Kirchengast
Editors

New Horizons in Occultation Research

Studies in Atmosphere and Climate

Springer

Editors
Dr. Andrea Steiner
Wegener Center for Climate
and Global Change (WegCenter)
University of Graz
Leechgasse 25
8010 Graz
and
Institute for Geophysics, Astrophysics,
and Meteorology (IGAM)
University of Graz
Universitätsplatz 5
8010 Graz
Austria

Dr. Ulrich Foelsche
Wegener Center for Climate
and Global Change (WegCenter)
University of Graz
Leechgasse 25
8010 Graz
and
Institute for Geophysics, Astrophysics,
and Meteorology (IGAM)
University of Graz
Universitätsplatz 5
8010 Graz
Austria

Barbara Pirscher
Wegener Center for Climate
and Global Change (WegCenter)
University of Graz
Leechgasse 25
8010 Graz
and
Institute for Geophysics, Astrophysics,
and Meteorology (IGAM)
University of Graz
Universitätsplatz 5
8010 Graz
Austria

Prof. Dr. Gottfried Kirchengast
Wegener Center for Climate
and Global Change (WegCenter)
University of Graz
Leechgasse 25
8010 Graz
and
Institute for Geophysics, Astrophysics,
and Meteorology (IGAM)
University of Graz
Universitätsplatz 5
8010 Graz
Austria

ISBN 978-3-642-00320-2 e-ISBN 978-3-642-00321-9
DOI 10.1007/978-3-642-00321-9
Springer Heidelberg Dordrecht London New York

Library of Congress Control Number: 2009926953

Cover design: Bauer, Thomas

Printed on acid-free paper

Springer is part of Springer Science+Business Media (www.springer.com)

Preface

Building on its heritage in planetary science, remote sensing of the Earth's atmosphere and ionosphere with occultation methods has undergone remarkable developments since the first GPS/Met 'proof of concept' mission in 1995. Signals of Global Navigation Satellite Systems (GNSS) satellites are exploited by radio occultation while natural signal sources are used in solar, lunar, and stellar occultations. A range of atmospheric variables is provided reaching from fundamental atmospheric parameters such as density, pressure, and temperature to water vapor, ozone, and other trace gas species. The utility for atmosphere and climate arises from the unique properties of self-calibration, high accuracy and vertical resolution, global coverage, and (if using radio signals) all-weather capability. Occultations have become a valuable data source for atmospheric physics and chemistry, operational meteorology, climate research as well as for space weather and planetary science.

The 3rd International Workshop on Occultations for Probing Atmosphere and Climate (OPAC-3) was held September 17–21, 2007, in Graz, Austria. OPAC-3 aimed at providing a casual forum and stimulating atmosphere for scientific discussion, co-operation initiatives, and mutual learning and support amongst members of all different occultation communities. The workshop was attended by 40 participants from 14 different countries who actively contributed to a scientific programme of high quality and to an excellent workshop atmosphere.

The programme included 6 invited keynote presentations and 16 invited presentations, complemented by about 20 contributed ones including 8 posters. It covered occultation science from occultation methodology and analysis via results of recent occultation missions and application of occultation data in atmospheric and climate science to the presentation of future occultation missions. The detailed programme and all further workshop information will continue to be available online at the OPAC-3 website at http://www.uni-graz.at/opac3.

Key challenges, as defined by the workshop participants, are to establish occultation as a future climate monitoring system demanding the demonstration of traceability to the International System of Units (SI), which is a fundamental property of a climate benchmark data type. Enhancement and validation of processing chains for the quantification of uncertainty between different retrieval methods and processing systems are further important requirements. Of high importance in this respect is the continuation of GNSS radio occultation missions with a sufficient number of satellites as well as the conveyance of new mission concepts towards new horizons in occultation research.

This book was compiled based on selected papers presented at OPAC-3 and well represents in its five chapters the broad scope of the workshop. Occultation methodology and analysis with an overview on applications is given in chapter 1. The use of solar, lunar, and stellar occultations from SCIAMACHY and GOMOS onboard ENVISAT for atmospheric studies is described in chapter 2. Chapter 3 and chapter 4 present applications of GNSS occultation from the current missions CHAMP and Formosat-3/COSMIC for atmospheric and climate studies. The topics comprise the use of occultation data in numerical weather prediction and atmospheric wave analysis as well as in climate monitoring and change research. Upcoming occultation missions and new concepts are presented in Chapter 5.

We cordially thank all OPAC-3 colleagues, who contributed as authors and co-authors to the book, for their effort and work. All papers were subject to a peer review process, involving two independent expert reviewers per paper from the community of OPAC-3 participants and beyond. We very much thank these reviewers for their important service to ensure scientific correctness and high quality of the book. The reviewers, in alphabetical order, were S. P. Alexander, L. K. Amekudzi, C. O. Ao, G. Beyerle, C. Boone, K. Bramstedt, S. Cho, L. B. Cornman, M. Dominique, A. von Engeln, U. Foelsche, J. M. Fritzer, S. Healy, S.-P. Ho, K. Hocke, N. Jakowski, Y.-H. Kuo, B. C. Lackner, F. Ladstädter, K. B. Lauritsen, S. S. Leroy, A. Löscher, J.-P. Luntama, A. G. Pavelyev, M. Petitta, D. Pingel, B. Pirscher, P. Poli, T. M. Schrøder, S. Schweitzer, V. F. Sofieva, S. V. Sokolovskiy, A. K. Steiner, M. Stendel, S. Syndergaard, A. de la Torre, F. Vespe, J. Wickert, and J. J. W. Wilson.

Special thanks are due to Mrs. Helen Rachner and Mrs. Janet Sterritt-Brunner from Springer Verlag, Heidelberg, for the kind offer to issue this book as Springer publication and for the related technical support. Many thanks also to all others who provided support in one or another way, in representation of which we thank the sponsors of OPAC-3 (http://www.uni-graz.at/opac3). The Department of Science and Research of the Province of Styria is especially thanked for providing financial support enabling to cover the costs of the book.

We hope that, in the spirit of the OPAC-3 aims, the book will become a useful reference for the members of the occultation-related community but also for members of the science community at large interested in the present status and future promise of the field of occultations for probing atmosphere and climate.

Graz, Austria
July 2009

Andrea K. Steiner
Barbara Pirscher
Ulrich Foelsche
Gottfried Kirchengast

Contents

Part I GNSS Occultation: Methodology, Analysis, and Applications

Part II Solar, Lunar, and Stellar Occultation for Atmospheric Studies

Part III GNSS Occultation for Atmospheric Studies

Part IV GNSS Occultation for Climate Studies

Part V Future Occultation Missions

Contributors

S. Albanna Steward Observatory, University of Arizona, Tucson, AZ, USA

P. Alexander Departamento de Fisica (FCEN), Universidad de Buenos Aires, Argentina

S.P. Alexander Research Institute for Sustainable Humanosphere (RISH), Kyoto University, Kyoto, Japan

L.K. Amekudzi Institute of Environmental Physics and Remote Sensing (IUP/IFE), University of Bremen, Bremen, Germany and Department of Physics, Kwame Nkrumah University of Science and Technology (KNUST), Kumasi, Ghana

J.G. Anderson Harvard School of Engineering and Applied Sciences, Harvard University, Cambridge, MA, USA

C. Arras German Research Centre for Geosciences (GFZ), Potsdam, Germany

C. Benedetto Consorzio INNOVA, Matera, Italy

W. Bertiger Jet Propulsion Laboratory, California Institute of Technology, Pasadena, CA, USA

G. Beyerle German Research Centre for Geosciences (GFZ), Potsdam, Germany

M. Borsche Wegener Center for Climate and Global Change (WegCenter) and Institute for Geophysics, Astrophysics, and Meteorology (IGAM), University of Graz, Austria

H. Bovensmann Institute of Environmental Physics and Remote Sensing (IUP/IFE), University of Bremen, Bremen, Germany

K. Bramstedt Institute of Environmental Physics and Remote Sensing (IUP/IFE), University of Bremen, Bremen, Germany

J.P. Burrows Institute of Environmental Physics and Remote Sensing (IUP/IFE), University of Bremen, Bremen, Germany

S. Casotto CISAS-Universita’ di Padova, Padova, Italy

S. Cho Korea Astronomy and Space Science Institute, Daejeon, Korea

Y. Chun Korea Aerospace Research Institute, Daejeon, Korea

J. Chung Korea Astronomy and Space Science Institute, Daejeon, Korea

L.B. Cornman National Center for Atmospheric Research, Boulder, CO, USA

F. Dalaudier Service d'Aeronomie du CNRS, Verrieres-le-Buisson CEDEX, France

V. De Cosmo Agenzia Spaziale Italiana, Rome, Italy

A. de la Torre Departamento de Fisica (FCEN), Universidad de Buenos Aires, Argentina

H. Doleisch VRVis Research Center, Vienna, Austria

M. Dominique Royal Observatory of Belgium and Belgian Institute for Space Aeronomy, Brussels, Belgium

J.A. Dykema Harvard School of Engineering and Applied Sciences, Harvard University, Cambridge, MA, USA

C. Falck German Research Centre for Geosciences (GFZ), Potsdam, Germany

U. Foelsche COSMIC Project Office, University Corporation for Atmospheric Research (UCAR), Boulder, CO, USA; Wegener Center for Climate and Global Change (WegCenter) and Institute for Geophysics, Astrophysics, and Meteorology (IGAM), University of Graz, Austria

R. Frehlich CIRES, University of Colorado, Boulder, CO, USA

D. Fussen Belgian Institute for Space Aeronomy, Brussels, Belgium

P.J. Gero Harvard School of Engineering and Applied Sciences, Harvard University, Cambridge, MA, USA

D. Gillotay Belgian Institute for Space Aeronomy, Brussels, Belgium

The GOMOS Team Service d'Aeronomie, France; FMI, Finland; BIRA, Belgium; ACRI-ST, France; ESA/ESRIN, Italy; ESA/ESTEC, The Netherlands

R.K. Goodrich National Center for Atmospheric Research and University of Colorado, Boulder, CO, USA

M.E. Gorbunov Institute for Atmospheric Physics, Moscow, Russia

C. Groppi Steward Observatory, University of Arizona, Tucson, AZ, USA

V.N. Gubenko Institute of Radio Engineering and Electronics of the Russian Academy of Sciences (IRE RAS), Moscow, Russia

A. Hauchecorne Service d'Aeronomie du CNRS, Verrieres-le-Buisson CEDEX, France

W. He University Corporation for Atmospheric Research (UCAR), Boulder, CO, USA and Institute of Atmospheric Physics, Chinese Academy of Sciences, Beijing, China

S. Heise German Research Centre for Geosciences (GFZ), Potsdam, Germany

S.-P. Ho National Center for Atmospheric Research (NCAR) and University Corporation for Atmospheric Research (UCAR), Boulder, CO, USA

J.F. Hochedez Royal Observatory of Belgium, Brussels, Belgium

J. Kehrer VRVis Research Center, Vienna, Austria

G. Kirchengast Wegener Center for Climate and Global Change (WegCenter) and Institute for Geophysics, Astrophysics, and Meteorology (IGAM), University of Graz, Austria

R. König German Research Centre for Geosciences (GFZ), Potsdam, Germany

Y.-H. Kuo National Center for Atmospheric Research (NCAR) and University Corporation for Atmospheric Research (UCAR), Boulder, CO, USA

E.R. Kursinski Institute of Atmospheric Physics, University of Arizona, Tucson, AZ, USA

B.C. Lackner Wegener Center for Climate and Global Change (WegCenter) and Institute for Geophysics, Astrophysics, and Meteorology (IGAM), University of Graz, Austria

F. Ladstädter Wegener Center for Climate and Global Change (WegCenter) and Institute for Geophysics, Astrophysics, and Meteorology (IGAM), University of Graz, Austria

K.B. Lauritsen Danish Meteorological Institute (DMI), Copenhagen, Denmark

S. Lee Korea Aerospace Research Institute, Daejeon, Korea

S.S. Leroy Harvard School of Engineering and Applied Sciences, Harvard University, Cambridge, MA, USA

Y.A. Liou Center for Space and Remote Sensing Research, National Central University, Taiwan

P. Llamedo Departamento de Fisica (FCEN), Universidad de Buenos Aires, Argentina

A. Löscher European Space Agency (ESA), Noordwijk, The Netherlands

J.-P. Luntama Finnish Meteorological Institute, Helsinki, Finland

M. Materassi Istituto dei Sistemi Complessi (ISC/CNR), Firenze, Italy

S.S. Matyugov Institute of Radio Engineering and Electronics of the Russian Academy of Sciences (IRE RAS), Moscow, Russia

G. Michalak German Research Centre for Geosciences (GFZ), Potsdam, Germany

P. Muigg VRVis Research Center, Vienna, Austria

R. Notarpietro Politecnico di Torino, Torino, Italy

A. Otarola Institute of Atmospheric Physics, University of Arizona, Tucson, AZ, USA

J. Park Korea Astronomy and Space Science Institute, Daejeon, Korea

A.A. Pavelyev Institute of Radio Engineering and Electronics of the Russian Academy of Sciences (IRE RAS), Moscow, Russia

A.G. Pavelyev Institute of Radio Engineering and Electronics of the Russian Academy of Sciences (IRE RAS), Moscow, Russia

G. Perona Istituto Superiore Mario Boella (ISMB), Torino, Italy

M. Petitta Universita "La Sapienza", Rome, Italy

H. Pickett Jet Propulsion Laboratory, California Institute of Technology, Pasadena, CA, USA

D. Pingel Deutscher Wetterdienst (DWD), Offenbach, Germany

B. Pirscher Wegener Center for Climate and Global Change (WegCenter) and Institute for Geophysics, Astrophysics, and Meteorology (IGAM), University of Graz, Austria

A. Rhodin Deutscher Wetterdienst (DWD), Offenbach, Germany

C. Rocken COSMIC Project Office, University Corporation for Atmospheric Research (UCAR), Boulder, CO, USA

M. Ross The Aerospace Corporation, El Segundo, CA, USA

M. Rothacher German Research Centre for Geosciences (GFZ), Potsdam, Germany

A. Rozanov Institute of Environmental Physics and Remote sensing (IUP/IFE), University of Bremen, Bremen, Germany

T. Schmidt German Research Centre for Geosciences (GFZ), Potsdam, Germany

W. Schmutz PMOD/WRC, Davos, Switzerland

M. Shein Steward Observatory, University of Arizona, Tucson, AZ, USA

V.F. Sofieva Finnish Meteorological Institute, Earth Observation, Helsinki, Finland

M. Sørensen Danish Meteorological Institute (DMI), Copenhagen, Denmark

A. Speranza Universita' di Camerino, Camerino, Italy

A.K. Steiner Wegener Center for Climate and Global Change (WegCenter) and Institute for Geophysics, Astrophysics, and Meteorology (IGAM), University of Graz, Austria

A. Sutera Universita "La Sapienza", Rome, Italy

N. Tartaglione Universita' di Camerino, Camerino, Italy

T. Tsuda Research Institute for Sustainable Humanosphere (RISH), Kyoto University, Kyoto, Japan

F. Vanhellemont Belgian Institute for Space Aeronomy, Brussels, Belgium

F. Vespe Agenzia Spaziale Italiana-Centro di Geodesia Spaziale, Matera, Italy

J. Vira Finnish Meteorological Institute, Earth Observation, Helsinki, Finland

D. Ward Institute of Atmospheric Physics, University of Arizona, Tucson, AZ, USA

A. Weekley National Center for Atmospheric Research, Boulder, CO, USA

J. Wickert German Research Centre for Geosciences (GFZ), Potsdam, Germany

J.J.W. Wilson EUMETSAT, Darmstadt, Germany

J. Yoon Korea Aerospace Research Institute, Daejeon, Korea

A. Zin THALES-Alenia Spazio, Milano, Italy

Part I
GNSS Occultation: Methodology, Analysis, and Applications

GPS Radio Occultation with CHAMP, GRACE-A, SAC-C, TerraSAR-X, and FORMOSAT-3/COSMIC: Brief Review of Results from GFZ

J. Wickert, T. Schmidt, G. Michalak, S. Heise, C. Arras, G. Beyerle, C. Falck, R. König, D. Pingel, and M. Rothacher

Abstract Several GPS Radio Occultation (RO) missions (GRACE-A (GRavity And Climate Experiment), FORMOSAT-3/COSMIC (FORMOsa SATellite mission-3/Constellation Observing System for Meteorology, Ionosphere, and Climate), and MetOp) started data provision in 2006 and 2007. Together with the measurements from CHAMP (CHAllenging Minisatellite Payload, since 2001) and the recently launched (June 15, 2007) TerraSAR-X an operational multi-satellite constellation for precise GPS based atmospheric sounding became reality. The data base is supplemented by measurements from SAC-C (Satélite de Aplicaciones Científicas-C). Our contribution briefly reviews current GFZ activities regarding processing and application of GPS RO data from different satellites. These activities include precise satellite orbit determination and the provision of near-real time analysis results for weather forecast centers within 2 h after measurement. Available satellite data are used for climatological investigations of global gravity wave characteristics.

1 Introduction

During the last decade ground and space based GPS techniques for atmospheric and ionospheric remote sensing were established (see, e.g., Wickert et al. 2007). The currently increasing number of receiver platforms (e.g., extension of regional and global GPS ground networks and additional Low Earth Orbiting (LEO) satellites) together with future additional transmitters (GALILEO, reactivated GLONASS, new GPS satellite generations, and COMPASS) will extend the potential of these innovative sounding techniques during the next years. Here, we focus on GPS radio occultation for the derivation of vertical profiles of atmospheric parameters on a global scale (e.g., Kursinski et al. 1997). We present selected examples of

---

J. Wickert (✉)
German Research Centre for Geosciences (GFZ), Potsdam, Germany
e-mail: wickert@gfz-potsdam.de

A. Steiner et al. (eds.), *New Horizons in Occultation Research*,
DOI 10.1007/978-3-642-00321-9_1,

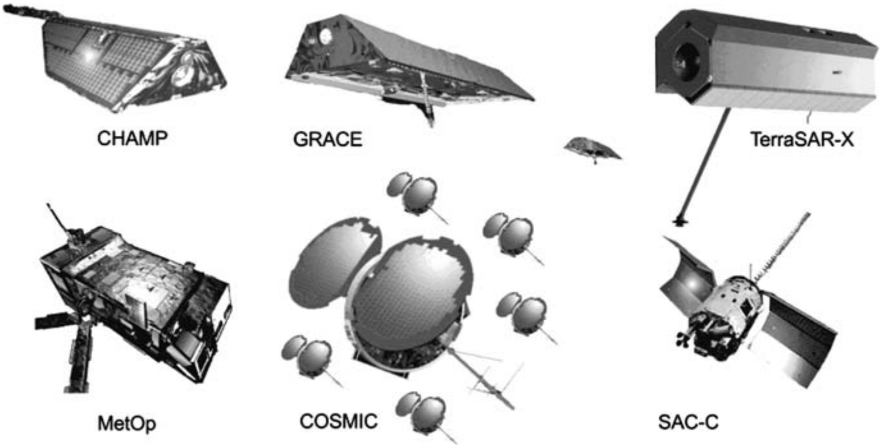

Fig. 1 Current GPS radio occultation missions: CHAMP (launch July 15, 2000), GRACE (March 17, 2002), TerraSAR-X (June 15, 2007), MetOp (October 19, 2006), FORMOSAT-3/COSMIC (April 15, 2006), and SAC-C (November 21, 2000)

recent GFZ activities. These include orbit, atmospheric, and ionospheric occultation data analysis for several satellite missions (CHAMP (Wickert et al. 2004), GRACE-A (Wickert et al. 2005), SAC-C (Hajj et al. 2004), TerraSAR-X, and FORMOSAT-3/COSMIC (Anthes et al. 2008); see Fig. 1) , but also scientific applications of the GPS radio occultation data.

2 Status of Radio Occultation with CHAMP and GRACE

CHAMP is in orbit already for more than seven years. Currently it is expected to get occultation data until 2009. CHAMP's observations form the first and unique long term set of GPS radio occultation data. The measurements are recorded with a consistent receiver firmware since March 2002. Continuous activation of GRACE-A occultations (settings only) began on May 22, 2006 (Fig. 2), after a longer temporarily measurement campaign in January/February 2006. The GRACE mission is currently expected to last at least until 2012/13. We note that setting GRACE-B occultations (except the initial measurements, (see, e.g., Beyerle et al. 2005; Wickert et al. 2005, 2006a) were activated only for a short period between September 23 (14:00 UTC) and 30 (12:00 UTC), 2005. During this time GRACE-B trailed GRACE-A and its occultation antenna pointed to anti-velocity direction. A validation study for occultation results within this period with ECMWF (European Centre for Medium-Range Weather Forecasts) showed nearly identical characteristics as those from GRACE-A (Wickert et al. 2006b). The major difference between the GRACE satellites is the better value for the long-term stability of the Ultra Stable Oscillator (USO) aboard GRACE-B (about 30 ns/s) compared to GRACE-A (about 230 ns/s). The current GRACE constellation would allow for the additional

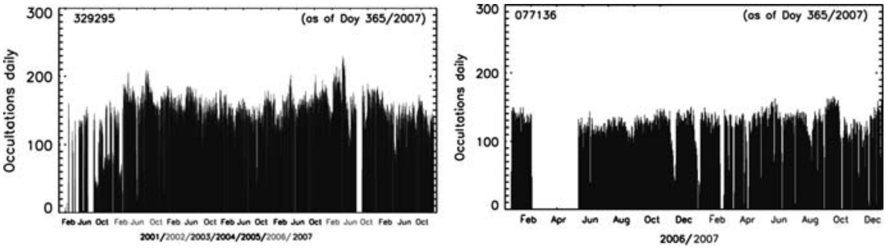

Fig. 2 Number of daily vertical atmospheric profiles, derived from CHAMP (*left*) and GRACE-A (*right*) GPS occultation measurements (GFZ processing). For the 2357 days of CHAMP RO activation 329 295 profiles have been collected (on average about 140 per day) as of December 31, 2007. The number of available profiles from GRACE-A for 618 days of RO activation is 77 136 as of the same day (on average about 120 daily)

activation of rising occultations aboard GRACE-B. Technical aspects of such activation are currently under evaluation. For more details see Wickert et al. (2009) and references therein.

3 Data Analysis and Validation

We briefly review current GFZ activities in RO data processing and validation (Sects. 3.1–3.4) and present new gravity wave results (Sect. 4). Other activities at GFZ, related to the application of GPS RO data as, e.g., global investigations of tropopause parameters and ionospheric disturbances, are treated by, e.g., Schmidt et al. (2005, 2006); Viehweg et al. (2007); Wickert et al. (2009).

3.1 Vertical Profiling of the Neutral Atmosphere

GPS RO data from CHAMP, GRACE (complete data set, see Fig. 2), and SAC-C (August 18–October 22, 2001 and March 11–November 16, 2002) have been processed by GFZ, including precise satellite orbit determination (GPS and LEO), atmospheric excess phase calibration, and inversion to get atmospheric parameters. The algorithms for the GFZ orbit and occultation processing are described in several publications (e.g., Wickert et al. 2004, 2006a, 2009; König et al. 2005a,b). The FORMOSAT-3/COSMIC temperature profiles for the gravity wave study, presented in Sect. 4, were provided by UCAR (University Corporation for Atmospheric Research, Boulder).

Current plans at GFZ related to the GPS RO data analysis are, e.g., a complete reprocessing of the CHAMP and GRACE data including the calibration files (level 2, PD, atmospheric Phase Delay) and the extension of the operational analysis software to process OpenLoop (OL, see, e.g., Sokolovskiy et al. (2006)) data from FORMOSAT-3/COSMIC, TerraSAR-X, or SAC-C (after 2003). Initial GFZ results of orbit and OL processing for selected examples of FORMOSAT-3/COSMIC data were presented by Michalak et al. (2007a) and Wickert et al. (2009). There are currently no plans for an operational FORMOSAT-3/COSMIC processing at GFZ.

3.2 Ionosphere Profiling: Initial Results

The GFZ processing system will be extended to operationally generate vertical electron density profiles. These data can be used for several applications in ionospheric research and space weather monitoring and forecast (e.g., Hajj et al. 2000; Jakowski et al. 2005).

Figure 3 shows the first vertical electron density profile, derived with GFZ software from CHAMP SST (Satellite-Satellite Tracking) GPS observation processing level. The data are compared with inversion results from UCAR (Schreiner et al. 1999), DLR (Jakowski 2005), and in-situ data, provided by the Planar Langmuir Probe (PLP) aboard CHAMP. We have used the differences of the excess phases $L_1 - L_2$ during the occultation (1 Hz data), which directly can be converted to a series of TEC values (Total Electron Content). Orbit and clock errors are automatically eliminated in the difference. The series of TEC data can be converted to a vertical electron density profile using the spherical symmetry assumption by Abel inversion. Details of this technique are given by Schreiner et al. (1999). In contrast to the authors, we apply an alternative technique for the absolute calibration of the TEC values before Abel inversion, described by Lei et al. (2007). This approach is used to estimate the exponential decrease of the electron density vs. height above the orbit altitude.

The initial GFZ results are in nearly perfect agreement with profiles from UCAR and DLR. Depending on the different scale heights used, 98 km and 182 km (right

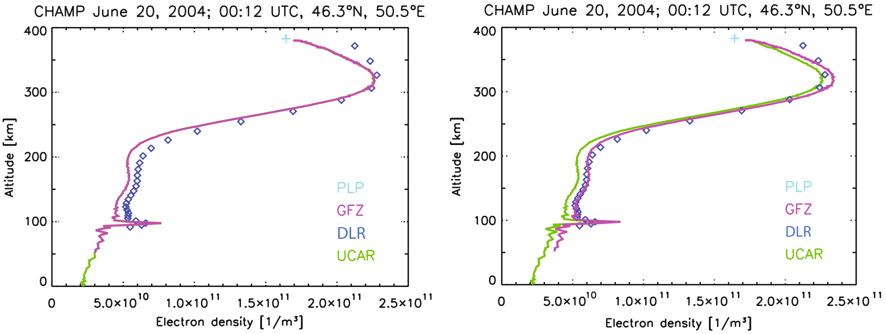

Fig. 3 First vertical profiles of electron density (*red*) from CHAMP, completely derived using GFZ analysis software. The data are compared with processing results from UCAR (*green*), DLR (*dark blue diamond*), and in-situ data from the PLP (Planar Langmuir Probe, *light blue cross*). A sporadic E-layer was observed at ∼100 km altitude. The GFZ profiles are derived using two different scale heights for the estimation of the TEC (Total Electron Content) above the orbit altitude (scale height for exponential decrease of the electron density 182 km, *left*; and 98 km, *right*)

and left plot in Fig. 3), the GFZ profile is more close to the UCAR or DLR solution. GFZ and UCAR profiles show remarkably good agreement with the completely independent PLP measurements. Future work will be related to the optimal choice for the TEC calibration and to the automatization of the ionosphere profiling.

3.3 Water Vapor Comparison with MOZAIC

Beside radiosonde observations and meteorological analyses, aircraft measurements of pressure, temperature, and humidity provide a valuable data source for GPS RO validation in the troposphere region. The MOZAIC (Measurement of OZone and wAter vapor by Airbus Inservice airCraft) program currently includes five aircrafts performing up to 2500 flights per year. These data are not assimilated to ECMWF analyses and consequently provide an opportunity to assess whether GPS RO data could provide significant additional water vapor information compared to ECMWF data without assimilating RO. In a first comparison study for GPS RO and MOZAIC data (Heise et al. 2008), about 320 coinciding profiles of CHAMP and MOZAIC (Fig. 4) were found from March 2001 until March 2006 (coincidence radius: 3 h, 300 km). Between about 650 hPa and 300 hPa (not shown here), this comparison reveals slightly better agreement of MOZAIC humidity with CHAMP than with ECMWF analyses. Figure 5 gives an example of CHAMP (1DVAR and DWVP, Direct Water Vapor Pressure, retrievals) specific humidity (left) and refractivity (right) vertical profiles in comparison to MOZAIC and ECMWF data. Here,

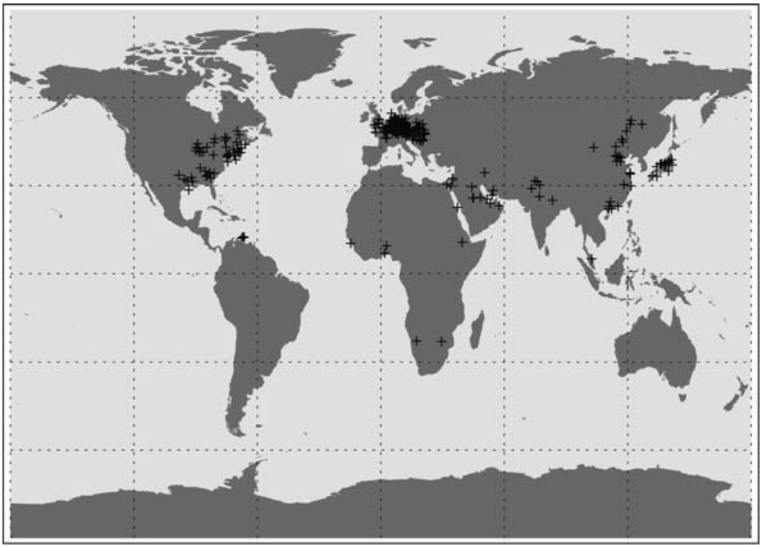

Fig. 4 Global distribution of coincidences of CHAMP and MOZAIC (during aircraft ascent and descent) vertical profiles from March 2001 until March 2006 (coincidence criteria: 3 h, 300 km)

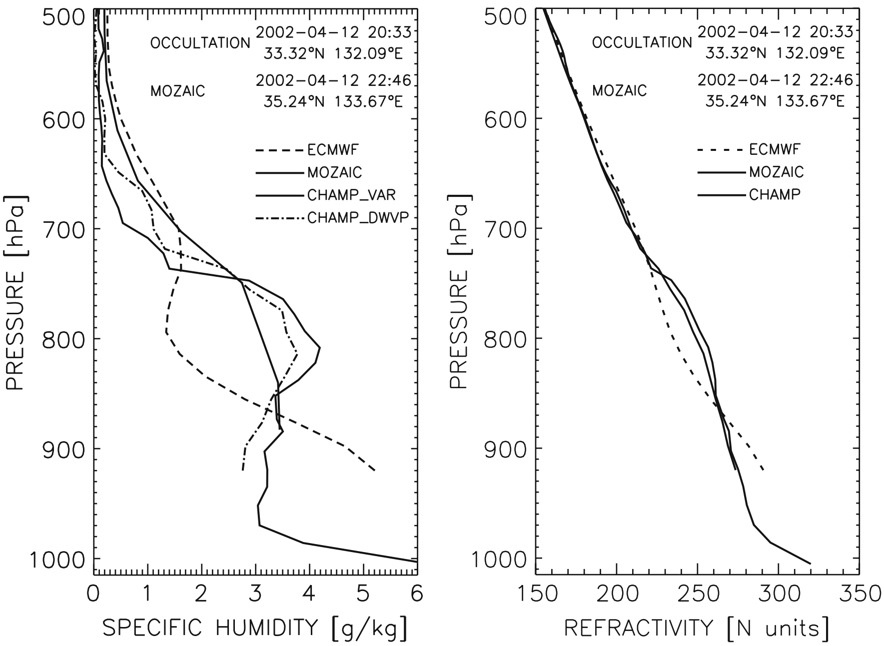

Fig. 5 Comparison of vertical specific humidity (*left*) and refractivity (*right*) profiles derived from CHAMP (1DVAR and DWVP) retrieval with MOZAIC and ECMWF data. Example for a CHAMP occultation on April 12, 2002, 20:33 UTC, 33.32°N, 132.09°E

both CHAMP humidity retrieval methods come to similar results revealing significant improvement over the ECMWF specific humidity in comparison to MOZAIC data. This is obviously due to better refractivity agreement between MOZAIC and CHAMP than between MOZAIC and ECMWF (Fig. 5, right).

3.4 Near-Real Time Data Processing

The Near-Real Time (NRT) processing is an essential key in ensuring that the GPS radio occultation data collected by CHAMP and GRACE are fully exploited and benefit the numerical weather prediction. Various weather forecast centers monitor and assimilate GPS RO bending angle and refractivity profiles from FORMOSAT-3/COSMIC, CHAMP, and GRACE since September 2006. These centers are ECMWF, Met Office, Japan Meteorological Agency (JMA), Meteo France, National Center for Environmental Prediction (NCEP, US), and Deutscher Wetterdienst. Results of a recent impact study with GPS RO data from CHAMP and GRACE-A NRT data were published by Healy et al. (2007).

The GFZ work on NRT data provision is supported by an international research project (NRT-RO, Near-Real Time Radio Occultation), funded by the German

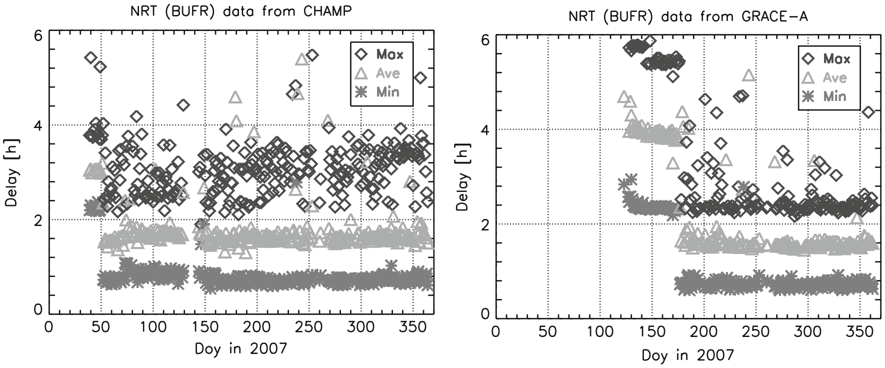

Fig. 6 Time delay between CHAMP (*left*) and GRACE-A (*right*) occultation measurements aboard the satellites and availability of corresponding bending angle and refractivity profiles (BUFR file format, Binary Universal Form of Representation of meteorological data) at the GFZ NRT ftp-server in 2007. *Light gray triangles* indicate the daily mean time delay for all occultation events. The significant reduction of the delay end February (CHAMP) and June (GRACE-A) is due to the activation of an improved NRT processing mode

Federal Ministry of Education and Research within the GEOTECHNOLOGIEN research program. The project is also supported by contributions from ECMWF and Met Office.

The main goals of this project are: 1. The development of appropriate analysis software for the precise and rapid derivation of GPS and LEO satellite orbits and globally distributed atmospheric profiles from GPS SST data; 2. The demonstration of a NRT provision of atmospheric data from CHAMP and GRACE-A with an average delay of less than 2 h; and 3. The corresponding assimilation in global weather models. Bending angles and refractivities are made available with average delay between the LEO measurements and provision of corresponding atmospheric data of less than 2 h since 2007 with the activation of the new NRT processing mode on February 21 (doy 52) for CHAMP and on June 26 (doy 177) for GRACE-A (see Fig. 6, Fig. 7). The monitoring of the GFZ data product latency at the Met Office (*http://monitoring.grassaf.org*) confirms that processing at GFZ delivers continuously data in a timely manner – some 50% of the data arrives in less than 2 h and almost all within 3 h (personal communication, Dave Offiler, Met Office, 2008). A crucial task of the NRT data analysis is the precise and rapid satellite orbit determination. More details on this task are given by Michalak et al. (2007b) and Wickert et al. (2009).

4 Selected RO Application: Global Gravity Wave Characteristics

Gravity waves (GW) play an important role for the general atmospheric circulation, as they transport energy and momentum between different regions of the atmosphere. Various satellite data sets enable a global view on major GW parameters, as

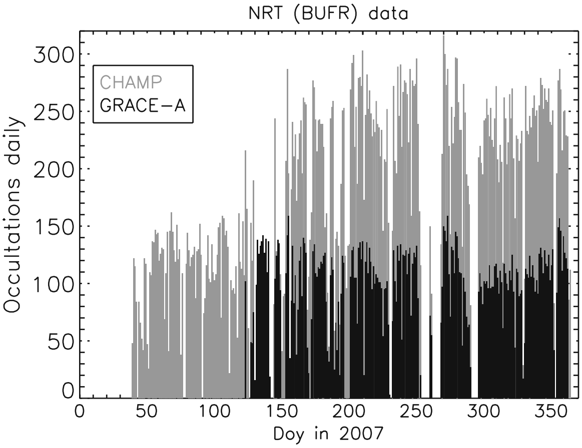

Fig. 7 Number of daily provided NRT profiles from CHAMP and GRACE-A in 2007. The data are provided since February 2007 in BUFR format and are currently distributed also via the Global Telecommunication Service (GTS)

e.g., temperature variances, momentum fluxes, or (potential) energy. But this view depends on the used measurement characteristics, which was described in more detail by Wu et al. (2006). According to the categorization of Wu et al. (2006) GPS RO belongs to the sensors, which observe the atmosphere through a long transparent LOS (Line of Sight) path centered at the tangent point where most of the signal comes from. Since such instruments normally have a narrow field of view (FOV), their vertical resolution is often excellent, while their horizontal resolution is coarse due to the LOS-smearing. Thus, GPS RO is mostly sensitive to GWs with small ratio of vertical to horizontal wavelengths λ_z/λ_h. Up to the present, GW analysis from GPS RO temperature measurements is restricted to vertical wavelengths mostly less than ~10 km to separate the GWs from the background and planetary waves (PW). The current restriction to provide only vertical GW information with GPS RO is caused by the sparse temporal and spatial measurement density provided by a single satellite only (e.g., CHAMP). Data from missions as FORMOSAT-3/COSMIC could also allow to derive information on horizontal GW properties.

In the past several GW studies based on GPS RO were mainly focussed on the lower stratosphere (Tsuda et al. 2000; Ratnam et al. 2004a,b; de la Torre et al. 2006a,b, 2009; Fröhlich et al. 2007). A study to Kelvin waves using the CHAMP data set from 2001 to 2003 was performed by Randel and Wu (2005).

De la Torre et al. (2006b) applied a Gaussian filter to investigate different vertical wavelength ranges (λ_z <10 km, λ_z < 4 km, and 4 km< λ_z <10 km). The authors used the specific potential energy E_p to describe the GW activity. Here we use also the potential energy derived for vertical wavelengths less than 10 km, expressed by db values, to describe the wave activity. Figure 8 (top) shows the global GW activity averaged over the northern hemispheric (NH) winter (DJF) and summer (JJA) months between 20 km and 25 km based on CHAMP data from 2001 to 2007. The maximum GW activity is clearly seen in the tropics with slightly higher values during NH winter. In the extra-tropics the maximum GW activity is also found during winter. Due to the sparse data density of the CHAMP measurements the horizontal

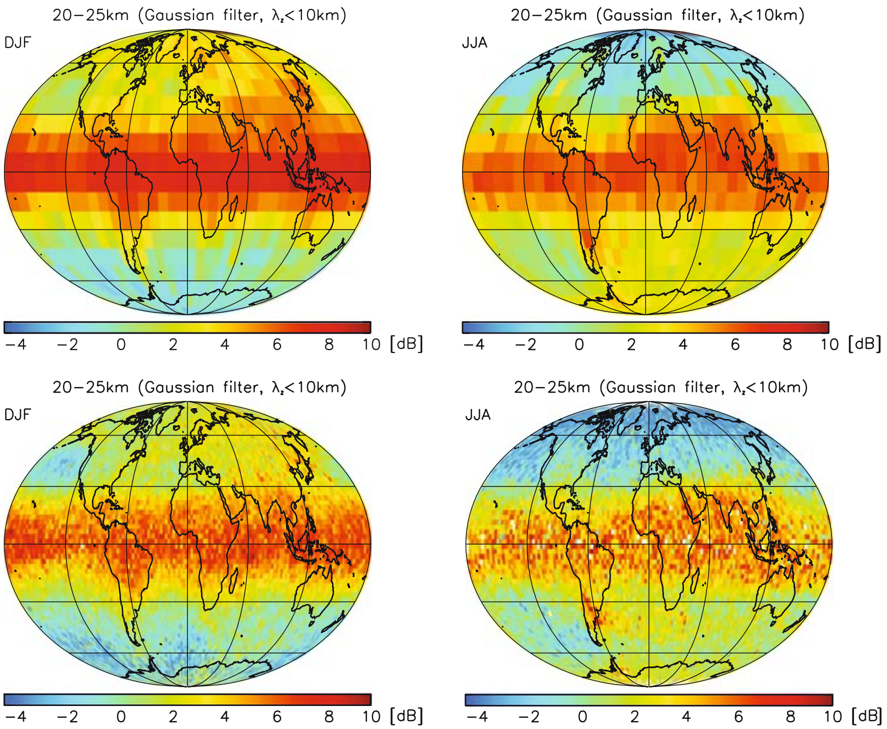

Fig. 8 *Above*: Global mean potential energy between 20 and 25 km altitude derived using a Gaussian filter for CHAMP/SAC-C/GRACE for northern hemispheric winter (DJF) and summer (JJA) based on the data from May 2001 to June 2007. The latitude/longitude resolution represent 10° × 10°. *Below*: same as above, but using FORMOSAT-3/COSMIC data from DJF 2006/2007 and JJA 2006/2007. The latitude/longitude resolution is 2.5° × 2.5°

resolution is only 10° × 10°. The FORMOSAT-3/COSMIC mission offers new possibilities because of the much better data density (about 10 times more temperature profiles daily than CHAMP). Figure 8 (bottom) demonstrates this showing only one NH winter and summer season, but with a horizontal resolution of 2.5° × 2.5°. These plots represent first GW related results with FORMOSAT-3/COSMIC data using the GFZ GW analysis software, which is described in more detail by de la Torre et al. (2006b) for the CHAMP data.

5 GPS Radio Occultation with TerraSAR-X

The German TerraSAR-X satellite (see Fig. 1) was launched on June 15, 2007 with a Dnepr-1 rocket from the Aerodrome Baikonur. The main science instrument aboard is a new generation X-band radar (9.65 GHz) for Earth observation with up to 1–2 m resolution (spotlight mode). GFZ (together with University Texas) is operating an IGOR (Integrated GNSS Occultation Receiver). The operational activation

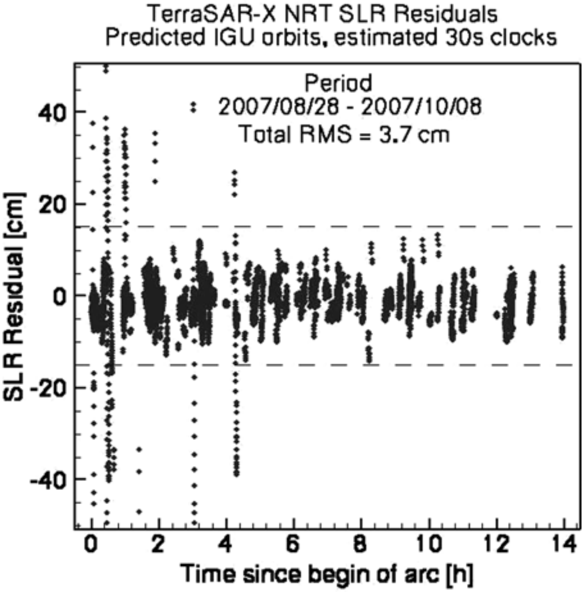

Fig. 9 Comparison of NRT orbits from TerraSAR-X with SLR measurements between August 28 and October 8, 2007. The mean RMS is 3.7 cm. The orbits were calculated during the test periods for the multi mission reception of GPS data from CHAMP, GRACE-A, and TerraSAR-X at the receiving station Ny Ålesund, Spitsbergen

of occultation measurements is planned for 2008. GFZ is planning a near-real time data provision similar to CHAMP and GRACE-A.

The multi mission reception of GPS data from CHAMP, GRACE-A, and TerraSAR-X at the GFZ receiving station Ny Ålesund, Spitsbergen, was already successfully demonstrated. Several test campaigns took place between July and October 2007 using both antennas for either redundant or parallel satellite reception. During these time periods also near-real time orbit processing was activated. Figure 9 shows results of a comparison of TerraSAR-X NRT orbit data with SLR (Satellite Laser Ranging) measurements between August 28 and October 8, 2007. The comparison yields an average RMS of 3.7 cm, which is in good agreement with the NRT orbit comparisons from CHAMP and GRACE-A with SLR (Michalak et al. 2007b). The operational NRT reception of IGOR data from TerraSAR-X was activated for a longer period from October 2007 until mid February 2008. The TerraSAR-X occultation data are recorded in OpenLoop (OL) mode (see, e.g., Beyerle et al. (2006); Sokolovskiy et al.(2006)). To analyze the OL data the navigation bit information from the respective occulting GPS satellite is required. For this purpose GFZ operates a dedicated global ground network (Beyerle et al. 2008), which currently (as of end 2008) consists of 6 stations.

6 Conclusions and Outlook

Several GFZ results from the current GPS RO multi-satellite constellation were presented. CHAMP is generating the first long-term set of GPS radio occultation data, which is expected to cover at least a period of 8 years. GRACE-A is expected to extend this data set until at least 2013. CHAMP and also GRACE-A data are provided to various international weather centers and stimulated the use of GPS RO data for numerical weather forecast. Currently these data are provided with average delay of less than 2 h.

Initial results of ionospheric occultation processing at GFZ were presented. The profiles are in good agreement with inversion results from other centers but also with PLP data from CHAMP. Further work is needed for an automatization of the processing. FORMOSAT-3/COSMIC orbit and occultation data are processed at GFZ for selected periods. Currently the OpenLoop analysis of the occultation data is not yet operational.

Results on validation of RO data with airplane measurements within the international MOZAIC research program were presented. It was shown, that these data are a valuable source for the evaluation and improvement of the GPS RO data quality.

Data from CHAMP, GRACE-A, SAC-C, and FORMOSAT-3/COSMIC are used to derive characteristics of vertical gravity waves on a global scale. It was shown, that especially the FORMOSAT-3/COSMIC data allow a significant enhancement of the spatial and temporal resolution of these investigations.

It is expected that TerraSAR-X will extend the current multi-satellite configuration for GPS RO with continuous occultation activation in 2008. Current activities are aimed to provide TerraSAR-X occultation data also in near-real time, similar to CHAMP and GRACE-A. Initial results on NRT orbit determination of TerraSAR-X were presented, indicating appropriate accuracy for precise occultation processing.

MetOp (EUMETSAT, launched October 2006) GPS occultation data are available since 2008. The Indian OCEANSAT-2 satellite is schedule for launch in 2009 and will carry an Italian GPS flight receiver with occultation capability (ROSA, Radio Occultation Sounder Antenna for the Atmosphere).

In general the described multi-satellite configuration significantly increases the potential of GPS RO for atmospheric sounding on a global scale with application in weather forecast, climate research, and for other atmospheric investigations.

Acknowledgements We thank the CHAMP, GRACE, SAC-C, FORMOSAT-3/COSMIC, and TerraSAR-X teams for their great work to guarantee the availability of GPS occultation data. The near-real time activities at GFZ and DWD are supported by the German Ministry for Education and Research within the GEOTECHNOLOGIEN program (Research project NRT-RO). This project is also aided by ECMWF and Met Office. We are grateful for this support. Last but not least, we also acknowledge the careful work of two anonymous reviewers to improve the paper.

References

Anthes R, et al. (2008) The COSMIC/FORMOSAT-3 Mission: Early Results. Bull Am Met Soc 89(3):313–333, doi:10.1175/BAMS-89-3-313

Beyerle G, Schmidt T, Michalak G, Heise S, Wickert J, Reigber C (2005) GPS radio occultation with GRACE: Atmospheric profiling utilizing the zero difference technique. Geophys Res Lett 32(L13806), doi:10.1029/2005GL023109

Beyerle G, Schmidt T, Wickert J, Heise S, Rothacher M, König-Langlo G, Lauritsen K (2006) Observations and simulations of receiver-induced refractivity biases in GPS radio occultation. J Geophys Res 111(D12101), doi:10.1029/2005JD006673

Beyerle G, Ramatschi M, Galas R, Schmidt T, Wickert J, Rothacher M (2008) A data archive of GPS navigation messages. GPS solutions, doi:10.1007/s10291-008-0095-y

Fröhlich K, Schmidt T, Ern M, Preusse P, de la Torre A, Wickert J, Jacobi C (2007) The global distribution of gravity wave energy in the lower stratosphere derived from GPS data and gravity wave modeling: Attempt and challenges. J Atmos Terr Phys 69(17):2238–2248, doi:10.1016/j.jastp.2007.07.005

Hajj GA, Lee LC, Pi X, Romans LJ, Schreiner WS, Straus PR, Wang C (2000) COSMIC GPS ionospheric sensing and space weather. Terr Atmos Ocean Sci 11:235–272

Hajj GA, et al. (2004) CHAMP and SAC-C atmospheric occultation results and intercomparisons. J Geophys Res 109(D06109), doi:10.1029/2003JD003909

Healy SB, Wickert J, Michalak G, Schmidt T, Beyerle G (2007) Combined forecast impact of GRACE-A and CHAMP GPS radio occultation bending angle profiles. Atmos Sci Lett 8(2): 43–50, doi:10.1002/asl.149

Heise S, Wickert J, Beyerle G, Schmidt T, Smit H, Cammas JP, Rothacher M (2008) Comparison of water vapour and temperature results from GPS radio occultation aboard CHAMP with MOZAIC aircraft measurements. IEEE TGARS, 46(11):3406–3411, 10.1109/TGRS. 2008.920268

Jakowski N (2005) Radio occultation techniques for probing the ionosphere. Radio Sci Bull (314):4–15

Jakowski N, Wilken V, Schlueter S, Stankov SM, Heise S (2005) Ionospheric space weather effects monitored by simultaneous ground and space based GNSS signals. J Atmos Terr Phys 67(12):1074–1084

König R, Michalak G, Neumayer K, Zhu S (2005a) Remarks on CHAMP Orbit Products. In: Flury J, Rummel R, Reigber C, Rothacher M, Boedecker G, Schreiber U (eds) Observation of the Earth System from Space, Springer Verlag, pp 17–26, doi:10.1007/3-540-29522-4_2

König R, et al. (2005b) Recent Developments in CHAMP Orbit Determination at GFZ. In: Reigber C, Lühr H, Schwintzer P, Wickert J (eds) Earth Observation with CHAMP: Results from Three Years in Orbit, Springer Verlag, pp 65–70, doi:10.1007/3-540-26800-6_10

Kursinski ER, Hajj GA, Schofield JT, Linfield RP, Hardy KR (1997) Observing the Earth's atmosphere with radio occultation measurements using Global Positioning System. J Geophys Res 102(D19):23429–23465

Lei J, et al. (2007) Comparison of COSMIC ionospheric measurements with ground-based observations and model predictions: Preliminary results. J Geophys Res 112(A07308), doi:10.1029/2006JA012240

Michalak G, Wickert J, König R, Rothacher M (2007a) Precise Orbit Determination of COSMIC/FORMOSAT-3 Satellites for Radio Occultations. EGU Vienna

Michalak G, Wickert J, König R, Rothacher M (2007b) Precise Satellite Orbit Determination for GPS Radio Occultation in Near-Real Time (NRT). EGU Vienna

Randel WJ, Wu F (2005) Kelvin wave variability near the equatorial tropopause observed in GPS radio occultation measurements. J Geophys Res 110(D03102), doi:10.1029/2004JD005006

Ratnam MV, Tetzlaff G, Jacobi C (2004a) Global and seasonal variations of stratospheric GW activity deduced from the CHAllenging Minisatellite Payload (CHAMP)-GPS satellite. J Atmos Sci 61(13):1610–1620

Ratnam MV, Tsuda T, Jacobi C, Aoyama Y (2004b) Enhancement of gravity wave activity observed during a major Southern Hemisphere stratospheric warming by CHAMP/GPS measurements. Geophys Res Lett 31(L16101), doi:10.1029/2004GL019789

Schmidt T, Heise S, Wickert J, Beyerle G, Reigber C (2005) GPS radio occultation with CHAMP and SAC-C: global monitoring of thermal tropopause parameters. Atmos Chem Phys 5: 1473–1488

Schmidt T, Beyerle G, Heise S, Wickert J, Rothacher M (2006) A climatology of multiple tropopauses derived from GPS radio occultations with CHAMP and SAC-C. Geophys Res Lett 33(L04808), doi:10.1029/2005GL024600

Schreiner WS, Sokolovskiy SV, Rocken C, Hunt DC (1999) Analysis and validation of GPS/MET radio occultation data in the ionosphere. Radio Sci 34(4):949–966

Sokolovskiy S, et al. (2006) GPS profiling of the lower troposphere from space: Inversion and demodulation of the open-loop radio occultation signals. Geophys Res Lett 33(L14816), doi:10.1029/2006GL026112

de la Torre A, Alexander P, Llamedo P, Menéndez C, Schmidt T, Wickert J (2006a) Gravity waves above the Andes detected from GPS radio occultation temperature profiles: Jet mechanism? Geophys Res Lett 33(L24810), doi:10.1029/2006GL027343

de la Torre A, Schmidt T, Wickert J (2006b) A global analysis of wave potential energy in the lower stratosphere derived from 5 years of GPS radio occultation data with CHAMP. Geophys Res Lett 33(L24809), doi:10.1029/2006GL027696

de la Torre A, Alexander P, Llamedo P, Schmidt T, Wickert J (2009) Recent advances in gravity wave analysis from long term global GPS radio occultation observations. In: Steiner A, Pirscher B, Foelsche U, Kirchengast G (eds) New Horizons in Occultation Research, Springer-Verlag, Berlin Heidelberg, doi:10.1007/978-3-642-00321-9_13

Tsuda T, Nishida M, Rocken C, Ware RH (2000) A global morphology of gravity wave activity in the stratosphere revealed by the GPS occultation data. J Geophys Res 105(D6):7257–7273

Viehweg C, et al. (2007) Global distribution of plasma irregularities in the lower ionosphere derived from GPS radio occultation data. EGU Vienna 2007, Geophysical Abstract EGU2007-A-07823

Wickert J, Schmidt T, Beyerle G, König R, Reigber C, Jakowski N (2004) The radio occultation experiment aboard CHAMP: Operational data analysis and validation of vertical atmospheric profiles. J Meteorol Soc Jpn 82(1B):381–395

Wickert J, Beyerle G, König R, Heise S, Grunwaldt L, Michalak G, Reigber C, Schmidt T (2005) GPS radio occultation with CHAMP and GRACE: A first look at a new and promising satellite configuration for global atmospheric sounding. Ann Geophysicae 23:653–658

Wickert J, Schmidt T, Beyerle G, Michalak G, König R, Heise S, Reigber C (2006a) GPS radio occultation with CHAMP and GRACE: Recent results. In: Foelsche U, Kirchengast G, Steiner AK (eds) Atmosphere and Climate, Springer Verlag, ISBN 3-540-34116-1, 3–16

Wickert J, et al. (2006b) GPS Based Atmospheric Sounding with CHAMP and GRACE: Preliminary Results of Comparative Data Analysis.Geophys Abstracts, EGU Vienna EGU06-A-03737

Wickert et al. (2007) Ground and space based GPS atmospheric sounding: Brief overview and examples. In: Anandan VK, Roettger J, Rao DN (eds), Proc. of the INTAR Colloquium-International Network of Atmosphere Radar, National Atmospheric Research Laboratory, Gadanki, pp 1–10

Wickert et al. (2009) GPS Radio Occultation: Results from CHAMP, GRACE and FORMOSAT-3/COSMIC. TAO 20(1): 35–50, doi:10.3319/TAO.2007.12.26.01 (F3C)

Wu D, Preuße P, Eckermann S, Jiang J, de la Torre Juarez M, Coy L, Wang D (2006) Remote sounding of atmospheric gravity waves with satellite limb and nadir techniques. Adv Space Res 37:2269–2277

Error Estimate of Bending Angles in the Presence of Strong Horizontal Gradients

M.E. Gorbunov and K.B. Lauritsen

Abstract The CT/FSI (Canonical Transform/Full-Spectrum Inversion) technique permits achieving a high accuracy and vertical resolution in the retrieval of bending angle from radio occultation data. This technique can be universally applied for the (hypothetical) spherically-symmetric atmosphere and any multipath situation can be unfolded. The reason is that the CT/FSI technique uses a Fourier Integral Operator that maps the measured wave field into the impact parameter representation, and for a spherically-symmetric medium each ray has a unique impact parameter. For the real atmosphere with horizontal gradients the situation is different. Horizontal gradients result in the variation of the impact parameter along a ray. In the presence of strong horizontal gradients, a bending angle profile can become a multi-valued function. In this case, the CT/FSI technique in its standard variant will fail to correctly retrieve the bending angle profile. It is, however, possible to estimate bending angle errors. For this purpose we apply the sliding spectral analysis of the CT-transformed wave field. The spectral width is used as a measure of the bending angle errors. We perform numerical simulations with global fields from re-analyses of the European Centre for Medium-Range Weather Forecasts and show that this radio holographic technique can be effectively used for error estimation in the areas of multi-valued bending angle profiles.

1 Introduction

The Canonical Transform (CT) (Gorbunov 2002; Gorbunov and Lauritsen 2004), Full-Spectrum Inversion (FSI) (Jensen et al. 2003), and Phase Matching (Jensen et al. 2004) methods were designed for the reconstruction of the ray manifold structure from the measurements of the complex wave. They are widely used for the retrieval of bending angle profiles from radio occultation (RO) data. The central concept of the CT method is the ray manifold in the phase space. The canonical

---

K.B. Lauritsen (✉)
GRAS SAF, Danish Meteorological Institute, Copenhagen, Denmark
e-mail: kbl@dmi.dk

A. Steiner et al. (eds.), *New Horizons in Occultation Research*,
DOI 10.1007/978-3-642-00321-9_2,

coordinates (coordinates and momenta) in phase space can be chosen in different ways. A particular choice is the physical coordinate and ray direction vector projection to the coordinate axis. This coordinate system is used for the description of the physical wave field. Multipath propagation corresponds to the multi-valued projection of the ray manifold to the coordinate axis. For the retrieval of the ray manifold structure it is however necessary to find another coordinate axis such that the ray manifold should have a single-valued projection upon it. For the rays in a spherically-symmetrical atmosphere the impact parameter is an invariant quantity that is constant for each ray. The impact parameter is, therefore, a unique coordinate along the ray manifold. Impact parameter and bending angle are conjugated coordinate and momentum. The canonical transform from the physical coordinate and ray direction vector projection to impact parameter and bending angle would then completely disentangle multipath structure. The impact parameter provides a universal coordinate choice for the case of the spherically symmetrical atmosphere.

The situation changes as we consider the atmosphere with horizontal gradients. In this case, it is possible to introduce the effective impact parameter, whose definition will depend on the horizontal gradients of refractivity. It turns out that the standard CT algorithm can work in most practical situations. However, numerical simulations with global fields from the European Centre for Medium-Range Weather Forecasts (ECMWF) do also reveal cases where atmospheric horizontal gradients are strong enough to make the bending angle a multi-valued function of the effective impact parameter. Because the structure of the ray manifold depends on the unknown horizontal gradients, it proves impossible to specify a universal coordinate choice that can unfold multipath. Therefore, it is necessary to estimate bending angle errors.

Two approaches were introduced for the dynamic estimate of bending angle errors, both based on the analysis of the CT/FSI-transformed wave field: (1) the sliding spectral analysis of the full complex wave fields in the transformed space (Gorbunov et al. 2005, 2006) and (2) the analysis of the fluctuation of the amplitude of the wave field in the transformed space (Lohmann 2006). The first approach is applied in the operational processing of RO data. The second approach was recently used to estimate the summary effect of receiver tracking errors and lower-tropospheric turbulence and to generate maps of convection and turbulence structures (Sokolovskiy et al. 2007).

Here, we estimate errors of the bending angle retrieval by using the sliding-spectral analysis of the CT-transformed wave field. We will present some atmosphere examples with horizontal gradients and obtain results for the corresponding bending angle error estimates.

2 Ray Manifold and its Description in the Phase Space

In a RO experiment rays are emitted by a GPS satellite, pass through the atmosphere, where they undergo refraction, and are received by a Low-Earth Orbiter (LEO). Each ray may be characterized by its impact parameter p. For a spherically symmetrical medium, Snell's law reads (Kravtsov and Orlov 1990):

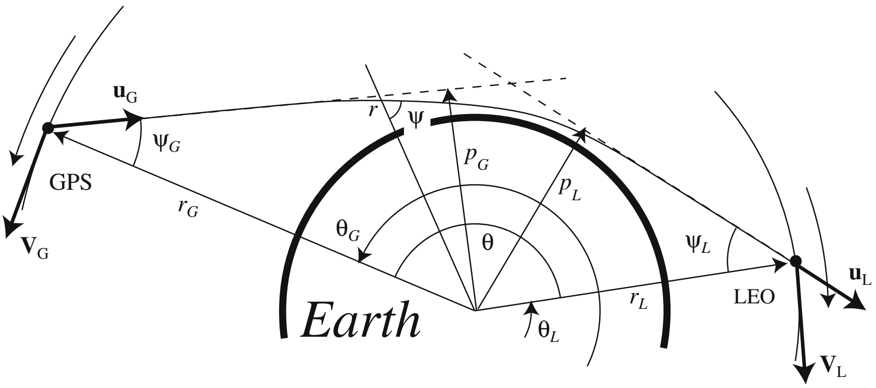

Fig. 1 Schematic drawing of the occultation geometry. The various quantities are discussed in the main text

$$nr \sin \psi = p = \text{const} \tag{1}$$

where ψ is the angle between the ray direction and the radius vector r (Fig. 1) and n is the refractive index. Since the GPS and LEO satellites are located outside of the atmosphere where $n = 1$ (here we neglect the ionosphere), it follows that $p = r_\mathrm{G} \sin \psi_\mathrm{G} = r_\mathrm{L} \sin \psi_\mathrm{L}$, which equals the leveling distance between the ray and the Earth's curvature center.

When considering an atmosphere with horizontal gradients, the situation changes. The complex wave field in the inhomogeneous medium can be written in the following form: $u(\mathbf{x}) = A(\mathbf{x}) \exp(ik\Psi(\mathbf{x}))$, where $\mathbf{x} = (x^i)$ is the coordinate vector, $k = 2\pi/\lambda$ is the wave number, λ is the wavelength, $A(\mathbf{x})$ is the amplitude, and $\Psi(\mathbf{x})$ is the eikonal. The geometrical optics of inhomogeneous media is based on the eikonal equation (Kravtsov and Orlov 1990):

$$(\nabla\Psi)^2 = n^2(\mathbf{x}) \tag{2}$$

Rays are described by the Hamilton system, where the Hamilton function follows from Eq. (2): $H(\mathbf{p}, \mathbf{x}) = 1/2 \cdot (\mathbf{p}^2 - n^2(\mathbf{x}))$, where $\mathbf{p} = \nabla\Psi$ is the momentum. The associated Hamilton equations for a ray take the following form:

$$\frac{\mathrm{d}\mathbf{x}}{\mathrm{d}\tau} = \mathbf{p}; \qquad \frac{\mathrm{d}\mathbf{p}}{\mathrm{d}\tau} = n\nabla n, \tag{3}$$

where τ is the trajectory parameter. Along the ray trajectories, $H(\mathbf{p}, \mathbf{x}) = 0$, therefore $|\mathrm{d}\mathbf{x}/\mathrm{d}\tau| = |\mathbf{p}| = n(\mathbf{x})$, which allows for the conclusion that $\mathrm{d}\tau = \mathrm{d}s/n$ (since $\mathrm{d}s = |\mathrm{d}\mathbf{x}|$). Consider now polar coordinates (r, θ) and the corresponding metrics $\mathrm{diag}(1, r^2)$. The equations for the angular component of the momentum p_θ take the following form:

$$\begin{aligned} p_\theta &= r^2\frac{\mathrm{d}\theta}{\mathrm{d}\tau} = nr\frac{r\mathrm{d}\theta}{\mathrm{d}s} = nr\sin\psi; \\ \frac{\mathrm{d}p_\theta}{\mathrm{d}\tau} &= n\frac{\partial n}{\partial\theta} \end{aligned} \tag{4}$$

From the first equation we see that in the polar coordinates the angular component of momentum equals the ray impact parameter as it is defined for a spherically symmetrical medium, i.e., $p = p_\theta$. The second equation generalizes Snell's law (Eq. 1) and indicates that p is only invariant in a spherically symmetrical medium ($\partial n/\partial\theta = 0$). When discussing the RO sounding of the atmosphere with horizontal gradients we must consider two impact parameters: $p_\mathrm{G} = r_\mathrm{G}\sin\psi_\mathrm{G}$ and $p_\mathrm{L} = r_\mathrm{L}\sin\psi_\mathrm{L}$. The relation between them follows from Eq. (4):

$$p_\mathrm{L} = p_\mathrm{G} + \int_\mathrm{GPS}^\mathrm{LEO}\frac{\partial n}{\partial\theta}\mathrm{d}s. \tag{5}$$

In processing radio occultation data it is not possible to directly determine the two impact parameters, at the receiver and at the transmitter. Instead, an effective impact parameter can be found. It is computed from σ, the time derivative of the optical path $\Psi(t)$ measured along the LEO observation trajectory as a function of time t, using the same formulas as for the unique impact parameter in a spherically symmetrical atmosphere. The general expression for σ is as follows:

$$\begin{aligned} \sigma &= \frac{\mathrm{d}\Psi}{\mathrm{d}t} = \mathbf{V}_\mathrm{L}\cdot\mathbf{u}_\mathrm{L} - \mathbf{V}_\mathrm{G}\cdot\mathbf{u}_\mathrm{G} \\ &= \dot{r}_\mathrm{G}\cos\psi_\mathrm{G} + r_\mathrm{G}\dot{\theta}_\mathrm{G}\sin\psi_\mathrm{G} + \dot{r}_\mathrm{L}\cos\psi_\mathrm{L} - r_\mathrm{L}\dot{\theta}_\mathrm{L}\sin\psi_\mathrm{L} \\ &= \frac{\dot{r}_\mathrm{G}}{r_\mathrm{G}}\sqrt{r_\mathrm{G}^2 - p_\mathrm{G}^2} + \frac{\dot{r}_\mathrm{L}}{r_\mathrm{L}}\sqrt{r_\mathrm{L}^2 - p_\mathrm{L}^2} + p_\mathrm{G}\dot{\theta}_\mathrm{G} - p_\mathrm{L}\dot{\theta}_\mathrm{L}. \end{aligned} \tag{6}$$

Here, in the final expression for σ we neglect horizontal gradients perpendicular to the occultation plane. For the effective impact parameter p we have the following implicit definition:

$$\sigma = p\dot{\theta} + \frac{\dot{r}_\mathrm{G}}{r_\mathrm{G}}\sqrt{r_\mathrm{G}^2 - p^2} + \frac{\dot{r}_\mathrm{L}}{r_\mathrm{L}}\sqrt{r_\mathrm{L}^2 - p^2}. \tag{7}$$

Using the following formula for the optical path:

$$\Psi = |\mathbf{r}_\mathrm{L} - \mathbf{r}_\mathrm{G}| + \Delta S, \tag{8}$$

where ΔS is the phase excess, we can obtain the effective impact parameter from orbit data and phase excess by numerically solving Eq. (7) in single ray areas, or by applying the Canonical Transform (CT) (Gorbunov 2002; Gorbunov and Lauritsen 2004), Full-Spectrum Inversion (FSI) (Jensen et al. 2003), or Phase Matching (Jensen et al. 2004) methods for unfolding multipath propagation. These techniques are based on the assumption that the effective impact parameter as defined by Eq. (7) is a unique coordinate of the ray manifold, in other words, that different rays have different p's. The (implicit) relation between p_G, p_L, and p is given by Eqs. (5), (6), and (7). It includes the horizontal gradient of refractivity $\partial n/\partial\theta$.

In the presence of strong horizontal gradients varying with height the effective impact parameter may no longer represent a unique coordinate of the ray manifold. One possible way of dealing with this situation would be to modify the CT method in such a way that the ray manifold is projected to a coordinate different than p. By itself, this might be straightforward except for the fact that this new unique coordinate is unknown, because it depends on the unknown horizontal gradients of refractivity. Here we will follow another prospect: instead of modifying the CT method, we will estimate bending angle errors due to strong horizontal gradients.

3 Radio Holographic Error Estimation

Radio holographic analysis of the wave signal can be performed both in t- and p-domains. The radio holographic (or sliding spectrum) analysis in the t-domain is widely used for the visual analysis of RO data in order to identify reflected rays, different sorts of problems etc. (Igarashi et al. 2000; Gorbunov et al. 2005). The radio holographic analysis in p-domain allows for the error estimate of retrieved bending angles (Gorbunov et al. 2005).

Here we will apply the method for the estimate of the bending angle error due to non-fully unfolded multipath structure (Fig. 2).

In the CT method, the wave field $u(t)$ is mapped to the impact parameter representation by the Fourier Integral Operator (FIO) $\hat{\Phi}$. The field in the transformed space, $\hat{\Phi}u(p) = A'(p)\exp(ik\Psi'(p))$ can be subjected to the sliding spectral analysis (Gorbunov et al. 2005):

$$\omega(p,\xi) = \int\limits_{p-\Delta p/2}^{p+\Delta p/2} \cos\frac{\pi(p'-p)}{\Delta p}\,\frac{\hat{\Phi}u(p')}{\exp\left(ik\overline{\Psi}'(p)\right)}\exp\left(-ik\xi p'\right)\mathrm{d}p', \tag{9}$$

where Δp is the window width, $\overline{\Psi}'(p)$ is the model of the phase variation in the p-domain, and ξ is the bending angle variation. $\omega(p,\xi)$ has a maximum near the true bending angle $\xi = \varepsilon(p) - \overline{\varepsilon}(p)$, where $\overline{\varepsilon}(p)$ is the smooth model of the bending angle corresponding to $\overline{\Psi}'(p)$.

We used $\Delta p = 250$ m and model $\overline{\Psi}'(p)$ was computed as $\Psi'(p)$ smoothed with window Δp. The bending angle error is then estimated as the spectral width (cf. the schematic widths indicated in the two left panels of Fig. 2) (Gorbunov et al. 2005):

$$\delta\varepsilon(p) = \left(\frac{\int|\omega(p,\xi)|^2\,\xi^2\mathrm{d}\xi}{\int|\omega(p,\xi)|^2\,\mathrm{d}\xi}\right)^{1/2}. \tag{10}$$

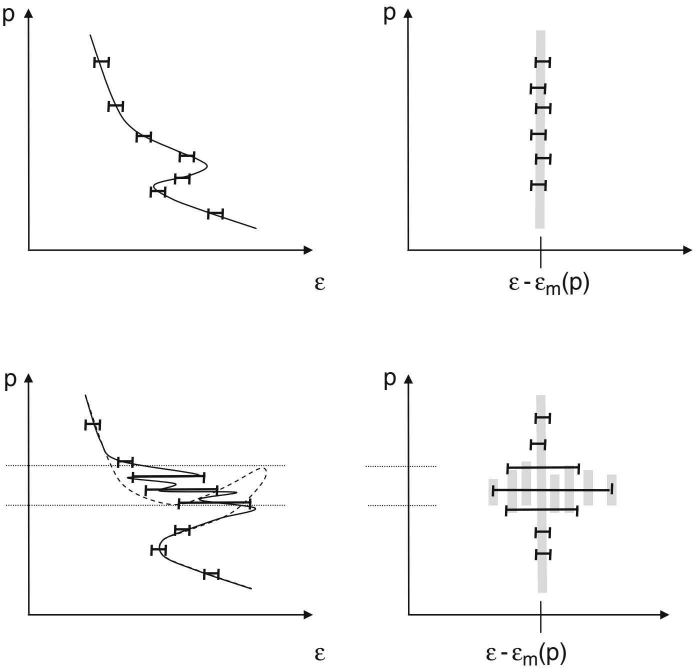

Fig. 2 The principle of the radio holographic (sliding spectrum) estimate of bending angle errors. *Top*: the situation where the impact parameter is a unique coordinate and where the spectrum is narrow; *bottom*: the situation where horizontal gradients result in p not being the unique coordinate of the ray manifold. The spectral width allows for the estimate of the bending angle errors

In non-unique ray regions the sliding spectrum will exhibit a broad structure, which eventually is mapped into a larger bending angle error than in the case where there is only one ray present for a given value of impact parameter.

4 Numerical Simulations

For the numerical simulations we choose an artificial occultation example, where the situation with a non-unique projection of the ray manifold to the impact parameter axis occurred. The simulated occultation was based on an ECMWF re-analysis field from February 5, 1997, UTC 00:00. We simulated soundings of the same region from different azimuths. Azimuths are characterized by the angle between the occultation plane and local north direction. We changed the azimuth from 0° to 330° with a step of 30°. The resulting 12 geometric optical profiles (the simulated “truth”) are shown in Fig. 3. These profiles were obtained by the geometric optical ray-tracing. Here bending angles ε are shown as functions of the ray impact heights defined as $p - r_E$, where r_E is the Earth’s curvature radius. The strongest effect of a

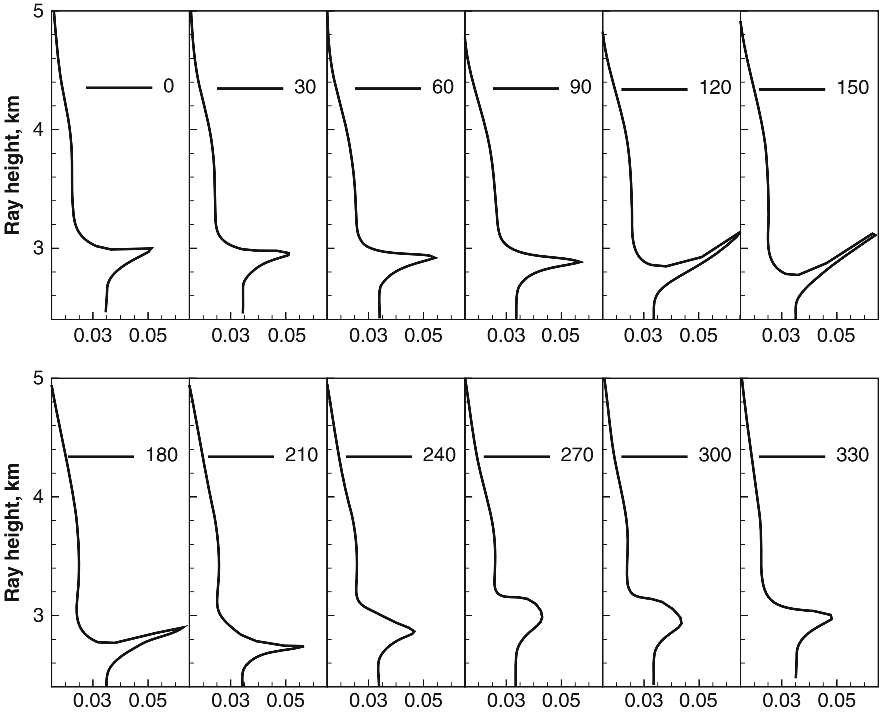

Fig. 3 True simulated bending angle profiles for sounding of the same location 12.4°N, 170.9°W from different azimuths (from 0° to 330°, with a step of 30°). Azimuths are characterized by the angle between the occultation plane and local north direction. The modeling was based on ECMWF fields February 5, 1997, UTC 00:00

multi-valued bending angle profile is observed for the azimuths of 120°, 150°, and 180°. A small area of the non-unique ray manifold projection can also be noticed for the azimuth of 0°.

Figure 4 presents the CT-retrieved bending angle profiles. These profiles were retrieved from the artificial RO data simulated by wave optics (Gorbunov 2002). Because the standard CT technique relies upon the impact parameter p being a unique coordinate for the ray manifold, it is incapable of reproducing the true multi-valued bending angle profiles for the azimuths of 120°, 150°, and 180°.

A small area of multi-valued bending angle profile can also be noticed for the azimuth of 0°. Single-valued profiles are retrieved instead. The azimuths, where the assumption of the uniqueness of the ray manifold parameterization with the impact parameter p is broken, are marked by the increased level of the estimated errors based on Eq. (10). In Fig. 5 we show the radio holographic running spectra in the p-domain. It is observed that for the three cases, the spectral width increases in areas of the multi-valued projection of the ray manifold, in accordance with the theoretical expectations. The error bars are, however, smaller than the difference between the

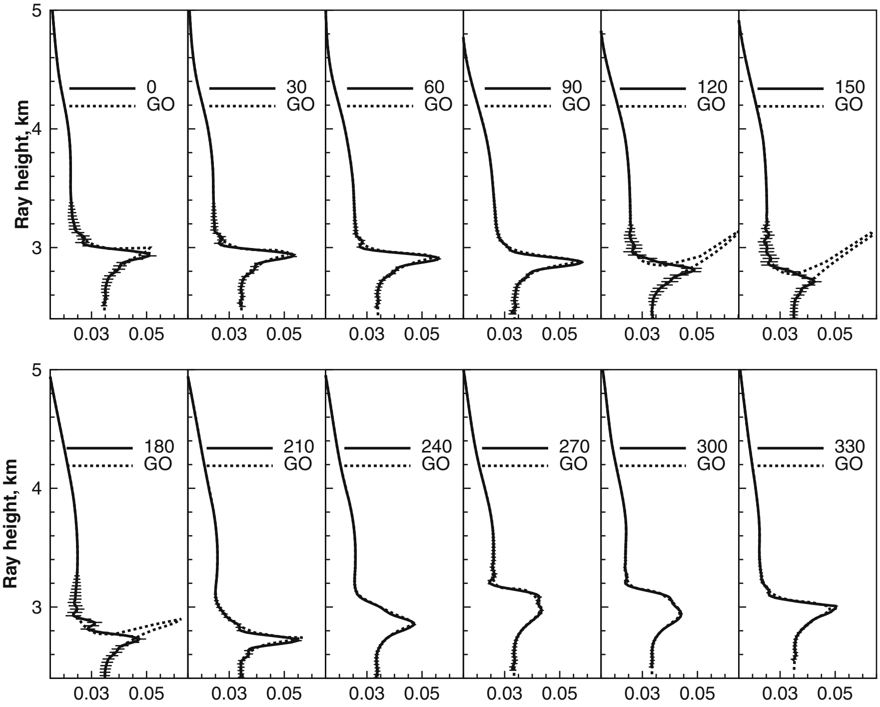

Fig. 4 True simulated bending angle profiles (GO, *dashed line*), retrieved simulated bending angle profiles (*solid lines*) and their error estimates for sounding at the same location 12.4°N, 170.9°W from different azimuths (from 0° to 330°, with a step of 30°). Azimuths are characterized by the angle between the occultation plane and local north direction. The modeling was based on ECMWF fields February 5, 1997, UTC 00:00

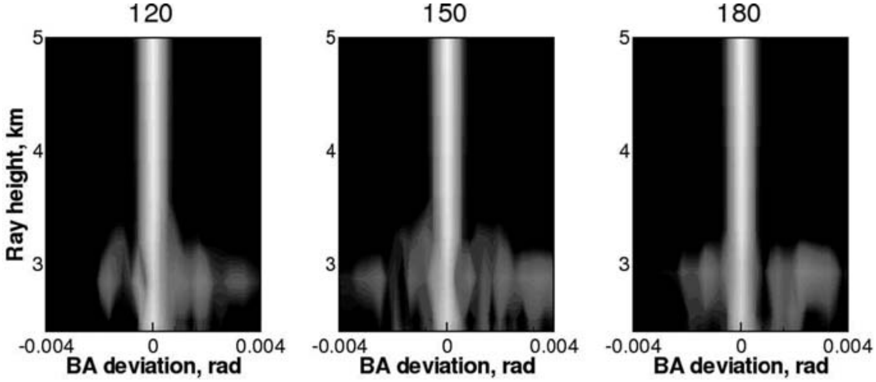

Fig. 5 Sliding spectra in the p-domain for three occultation plane directions, where the bending angle is a multi-valued function of the impact parameter (the text above the figures corresponds to the azimuth value). One observes the broadening of the spectra in the multi-valued multipath regions around 2.75–3.25 km (cf. Fig. 3)

true multi-valued and the CT-retrieved bending angle. This is because the spike of the bending angle contains a small portion of energy, which is distributed over a stretched fragment of the ray manifold.

5 Conclusions

The CT/FSI methods use the fact that the impact parameter p is the unique coordinate in the ray space. This condition is universally valid for a spherically symmetrical atmosphere. In an atmosphere with horizontal gradients of refractivity this is not always the case. Strong horizontal gradients result in the variation of the impact parameters along rays rather than being invariant. This is the reason why it is generally impossible to introduce the concept of impact parameter for the atmosphere with horizontal gradients. Instead, we introduce the so-called effective impact parameter using the same definition from the Doppler frequency as for the unique impact parameter for a spherically symmetric atmosphere. In the presence of strong horizontal gradients varying with height, perturbations of the effective impact parameter may result in the non-unique projection of the ray manifold to the impact parameter axis. In this case the bending angle can be a multi-valued function of the effective impact parameter. Because the CT/FSI methods rely upon the impact parameter being the unique coordinate along the ray manifold, it follows that in this situation this method will be incapable of correctly retrieving the bending angle profile.

In the general CT formalism it may be possible to introduce a new coordinate, other than impact parameter, such that the ray manifold should have a unique projection to the corresponding axis. Still, this definition of the new coordinate depends on the specific atmospheric fields and, therefore, it cannot be specified a priori. Another opportunity is the estimation of the errors of the retrieved bending angles by means of the radio holographic (sliding spectrum) analysis in the p-domain. Numerical simulations with realistic atmospheric fields from re-analyses of ECMWF show that the error estimate increases in the presence of strong horizontal gradients resulting in multi-valued geometric optical bending angle profiles. This makes the standard CT/FSI techniques complemented with radio holographic error estimates a valuable tool for the analysis of RO data in all situations.

References

Gorbunov ME (2002) Canonical transform method for processing radio occultation data in lower troposphere. Radio Sci 37(5), doi:10.1029/2000RS002592

Gorbunov ME, Lauritsen KB (2004) Analysis of wave fields by Fourier Integral Operators and its application for radio occultations. Radio Sci 39(4), doi:10.1029/2003RS002971

Gorbunov ME, Lauritsen KB, Rhodin A, Tomassini M, Kornblueh L (2005) Analysis of the CHAMP experimental data on radio-occultation sounding of the earth's atmosphere. Izv Atmos Ocean Phys 41(6):726–740

Gorbunov ME, Lauritsen KB, Rhodin A, Tomassini M, Kornblueh L (2006) Radio holographic filtering, error estimation, and quality control of radio occultation data. J Geophys Res 111(D10105), doi:10.1029/2005JD006427

Igarashi K, Pavelyev A, Hocke K, Pavelyev D, Kucherjavenkov IA, Matyugov S, Zakharov A, Yakovlev O (2000) Radio holographic principle for observing natural processes in the atmosphere and retrieving meteorological parameters from radio occultation data. Earth Planets Space 52(11):893–899

Jensen AS, Lohmann MS, Benzon HH, Nielsen AS (2003) Full spectrum inversion of radio occultation signals. Radio Sci 38, doi:10.1029/2002RS002763

Jensen AS, Lohmann MS, Nielsen AS, Benzon HH (2004) Geometrical optics phase matching of radio occultation signals. Radio Sci 39(3), doi:10.1029/2003RS002899

Kravtsov YA, Orlov YI (1990) Geometrical Optics of Inhomogeneous Media. Springer-Verlag, Berlin, Heidelberg, New York

Lohmann MS (2006) Dynamic error estimation for radio occultation bending angles retrieved by the full spectrum inversion technique. Radio Sci 41(RS5005), doi:10.1029/2005RS003396

Sokolovskiy SV, Rocken C, Lenschow DH, Kuo YH, Anthes RA, Schreiner WS, Hunt DC (2007) Observing the moist troposphere with radio occultation signals from COSMIC. Geophys Res Lett 34(L18802), doi:10.1029/2007GL030458

Phase Transform Algorithm for Radio Occultation Data Processing

J.J.W. Wilson and J.-P. Luntama

Abstract The phase transform algorithm is described and derived in the context of GRAS instrument data processing. This algorithm allows radio occultation neutral bending angles to be recovered in a locally spherically symmetrical atmosphere in the presence of multipath. The instrument operation and carrier phase reconstruction is described for both open loop mode and closed loop mode.

1 Introduction

The Global Navigation Satellite Systems (GNSS) Radio Occultation Receiver for Atmospheric Sounding (GRAS) instrument (Luntama 2006; Wilson and Luntama 2007) is one of the instruments carried by the ESA/EUMETSAT METOP satellites (METOP-A, METOP-B, and METOP-C). Data from GRAS, in conjunction with other data, is used to estimate atmospheric temperature, pressure, and humidity profiles (for numerical weather prediction) and also to investigate ionospheric total electron content (TEC). An advanced processing algorithm for estimating neutral bending angles from the GRAS data is described and discussed; this algorithm is the phase transform algorithm.

2 The GRAS Instrument and Signal Regeneration

The GRAS instrument consists of three antennas (the GVA, the GAVA, and the GZA), three RF Conditioning Units (RFCUs), one GRAS Electronics Unit (GEU), and harness items (Loiselet et al. 2000). Each antenna is connected to its RFCU and each RFCU is connected to the GEU. The GVA and GAVA view the Earth's limb in the satellite velocity direction and satellite anti-velocity direction, respectively.

J.J.W. Wilson (✉)
EUMETSAT, Postfach 10 05 55, 64205 Darmstadt, Germany
e-mail: julian.wilson@eumetsat.int

A. Steiner et al. (eds.), *New Horizons in Occultation Research*,
DOI 10.1007/978-3-642-00321-9_3,

These two antennas have 18 dual frequency receiving elements in a 3 by 6 array. The GZA is a wide beam, low gain antenna viewing the region of space above the satellite; this antenna has two receiving elements–one for each frequency. The GRAS receiver has 16 complex channels assigned to the GZA antenna, 4 complex channels assigned to the GVA antenna, and 4 complex channels assigned to the GAVA antenna. Thus the receiver can track up to 8 GPS satellites (on both L1 and L2) for navigation purposes with the GZA antenna and simultaneously observe 2 occultations with the GVA antenna (on both L1 and L2) and 2 occultations with GAVA antenna (on both L1 and L2). Each channel can be assigned to a frequency and a satellite.

The signal received at an antenna is subject to RF filtering, low noise amplification, and down conversion from RF to IF in the associated RFCU. It is then transmitted to the GEU where it is digitized, filtered, subjected to further digital down conversion, de-spread, and finally subjected to code and carrier phase tracking. The most important elements within the GEU are the A/D convertors, the DISC ASICs, the AGGA-2A ASICs, the Digital Signal Processor (DSP), the Frequency Generator (FG), and the Ultra Stable Oscillator (USO). The IF signals from the RFCUs are digitized by the A/D convertors and digitally filtered and down converted by the DISC ASICs. The AGGA-2A ASICs perform the required correlations and accumulations operations under the control of the DSP. The receiver measures, under suitable conditions, the following observable parameters for each GPS satellite tracked: (1) L1 C/A-code phase, (2) L1 P-code phase, (3) L1 carrier phase, (4) L1 signal amplitude, (5) L2 P-code phase, (6) L2 carrier phase, and (7) L2 signal amplitude. These measurements are time stamped with the GRAS Instrument Measurement Time (IMT). The carrier phases are tracked using a tracking loop to give a very narrow band output (50 Hz) except under poor phase noise conditions where the carrier phase is brought to base-band using a tracking law, based on expected behavior, which results in a wider bandwidth output (1000 Hz).

The GRAS instrument performs navigation, satellite prediction and selection, acquisition and tracking, and data handling. Navigation entails calculation of the METOP position and velocity from the data acquired by the GZA antenna. Satellite prediction and selection entails determination of which GPS satellites are to be tracked and when this is to be done for both navigation and for occultation. Satellite acquisition involves synchronizing the carrier frequency and code generators of the receiver to the received transmitted signal. C/A-code acquisition is based on a two dimensional search over defined ranges of code phase and carrier frequency using a maximum likelihood decision criteria; the search is simplified if a good navigation solution is available. When the C/A-code phase has been determined the C/A-code tracking and the L1 frequency tracking loops are started. Code tracking utilizes a normalized dot product discriminator operating on the in-phase and quadrature components of the early, late, and punctual outputs of correlators within the AGGA-2A ASIC to estimate code offset. Frequency tracking is done with a second order loop filter using the code offsets. Before starting the L1 carrier phase tracking loop a FFT based frequency estimator is employed to reduce the frequency error to an acceptable level. The carrier phase tracking is performed with an arctangent phase discriminator and a third order Costas loop. When L1 carrier tracking has been achieved the P-code on the L1 carrier and the L2 carrier can be searched; the search makes use of the hand over word from the navigation data from the tracked C/A-code. If the P-code is encrypted a code-less acquisition and tracking scheme must be used employing cross-correlation of the P-codes on the L1 and L2 channels. When the P-code on the L2 carrier is tracked, L2 carrier phase tracking can be started.

The first part of the GRAS data processing on-ground involves the reconstruction of the carrier phase received on a given channel at the antenna phase center (for that channel) from the data produced by the instrument. This involves adding back the signals removed by fixed down conversions and by the tracking loop or law-based final down conversion. This reconstruction is quite a complex and instrument specific process. The resulting signal is called the regenerated signal.

Let the set of N regenerated phase samples and their corresponding GRAS IMT for a given channel and a particular occultation be:

$$\left\{\left(\varphi_{\mathrm{REG}}(i), \tau_{\mathrm{RX}}^{\mathrm{IMT}}(i)\right); \quad i : 1 \rightarrow N\right\}. \tag{1}$$

These IMT times are times stamped at the ADC. The regenerated phase is given by the following equation:

$$\begin{aligned}
\varphi_{\mathrm{REG}}\left(\tau_{\mathrm{RX}}^{\mathrm{IMT}}\right) = {} & \frac{2\pi f_{\mathrm{GPS}(n)}\left|\mathbf{r}_{\mathrm{GRAS\text{-}ANT}(m)}^{\mathrm{ECI}}\left(t_{\mathrm{RX}}^{\mathrm{REF}}\right) - \mathbf{r}_{\mathrm{GPS}(n)-\mathrm{ANT}}^{\mathrm{ECI}}\left(t_{\mathrm{TX}}^{\mathrm{REF}}\right)\right|}{c} \\
& + 2\pi f_{\mathrm{GPS}(n)} \cdot \\
& \quad G_{\mathrm{GREL\text{-}TOF}}\left(\mathbf{r}_{\mathrm{GRAS\text{-}ANT}(m)}^{\mathrm{ECI}}\left(t_{\mathrm{RX}}^{\mathrm{REF}}\right), \mathbf{r}_{\mathrm{GPS}(n)-\mathrm{ANT}}^{\mathrm{ECI}}\left(t_{\mathrm{TX}}^{\mathrm{REF}}\right)\right) \\
& + 2\pi f_{\mathrm{GPS}(n)}\left(\Delta_{\mathrm{IMT}}\left(t_{\mathrm{RX}}^{\mathrm{REF}}\right) - \Delta_{\mathrm{GPS}(n)}\left(t_{\mathrm{TX}}^{\mathrm{REF}}\right)\right) \\
& + \varphi_{\mathrm{TROP}}\left(\tau_{\mathrm{RX}}^{\mathrm{IMT}}\right) \\
& - \varphi_{\mathrm{IONO}}\left(\tau_{\mathrm{RX}}^{\mathrm{IMT}}\right) \\
& + \varphi_{\mathrm{CH}(i)}\left(\theta\left(t_{\mathrm{RX}}^{\mathrm{REF}}\right), \phi\left(t_{\mathrm{RX}}^{\mathrm{REF}}\right), T_k\left(t_{\mathrm{RX}}^{\mathrm{REF}}\right)\right) \\
& + N_{\mathrm{CS}}\left(\tau_{\mathrm{RX}}^{\mathrm{IMT}}\right) \\
& + \varphi_{\mathrm{constant}}
\end{aligned} \tag{2}$$

In Eq. (2) for the regenerated phase the terms have the following significance. The first and second terms are associated with geometric delay between the transmitter and the receiver; the first term is the normal geometrical distance and the second term is a correction for general relativistic effects due to the Earth's gravitational field. The third term is associated with the clock offset of the transmitter and receiver with respect to the inertial reference time, t^{REF}. The fourth and fifth terms are the phases associated with the troposphere and the ionosphere, that it is desired to recover. The sixth term is an instrument characterization term. The seventh term is the cycle slip term; this term is ideally zero however cycle slips will occur if phase changes occur at a faster rate than the receiver can track during the occultation. The eighth and last term is a constant phase offset.

The measurement of the lowest part of the troposphere is difficult due to the low signal-to-noise ratio (SNR) of the GPS signal and strong atmospheric modulation. The receiver has problems in maintaining phase lock on the GPS carrier phase in a setting occultation and in acquiring the phase lock in a rising occultation. The GRAS receiver enters a “Raw Sampling” (RS) measurement mode (also called open loop mode) when the tracking of the L1 C/A-code is possible, but the phase lock on the carrier phase is not available. In the raw sampling mode the GRAS measurement data contain the output of the correlator unit of the receiver sampled at a 1000 Hz rate.

The GRAS receiver makes the switch between a phase locked tracking mode and an RS mode automatically. In a setting occultation the GRAS receiver switches normally into a single frequency tracking mode tracking the L1 code phase, carrier phase, and amplitude when the phase lock on the L2 signal is lost. At some point when the ray path tangent height is in the lower troposphere, the receiver may also lose the phase lock on the L1 carrier. The receiver software predicts this by monitoring the L1 signal and enters the RS mode if the instability of the L1 phase lock exceeds a predetermined level. This ensures the continuity of the observation data. The measurement of this particular setting occultation will end when the lock on the L1 code phase is lost.

A measurement of a rising occultation is slightly more complex as there is nothing for the receiver to track until the GPS signal becomes available from behind the limb of the Earth. The start time of a rising occultation is predicted by the receiver on-board software based on the propagated GPS and METOP orbits. The GPS orbits are calculated by using the GPS navigation message and the METOP orbit is determined by the on-board navigation solution. Normally the GRAS receiver should be able to acquire the L1 C/A-code phase very quickly after the signal becomes available. At this point phase lock on the L1 carrier is not possible and measurement of the rising occultation starts with the GRAS receiver in RS mode. The RS mode for a rising occultation continues until the receiver has acquired a stable phase lock on the L1 carrier phase. When the L1 carrier phase lock has been achieved, the receiver enters a single-frequency tracking mode. Eventually the L2 code phase signal will also become strong enough to be tracked by the receiver. After a stable lock on the L2 carrier phase has been acquired, the receiver will enter a two frequency tracking mode.

In RS mode the final down conversion is done by using a law whose parameters are given as part of the output data. This allows the carrier phase to be reconstructed in the ground processing.

There are two main differences between the carrier phase measurements provided in the RS mode and those provided when the tracking loop is locked. In raw sampling mode the sampling rate is 1000 Hz and the Navigation Signal Message (NSM) is not demodulated from the sampled data. This NSM signal is a binary signal modulated on the raw sampling mode carrier phase at 50 Hz. Where a 0 to 1 or a 1 to 0 transition occurs the carrier phase is shifted by π radians. In the ground processing the raw sampling mode data is combined with the closed loop data. The raw sampling mode data must agree with the closed loop data at the beginning of the overlapping region. To make this occur all the raw sampling mode data is rotated by 0 or π radians. The last part (or first part in the case of a rising occultation) of the single frequency tracking data is unreliable because the receiver is losing the phase lock. Thus, the overlapping closed loop data is discarded.

There are two ways to remove the NSM from the raw sampling mode data: the NSM is either removed automatically or the NSM is removed using knowledge of what it is from an alternative source. The automatic NSM removal is based on the possibility to locate one of the NSM π jumps in the region of the raw sampling mode data near to the closed loop data. Once the location of one carrier phase jump by π is found the positions of all other potential transitions are determined. The raw sampling mode carrier phase may therefore be averaged over regions (e.g., 20 samples) where the NSM is constant to reduce noise. In this way the NSM can be estimated and removed from the raw sampling mode carrier phase by rotating the phase by 0 or π according to the value of the NSM at that sample. Automatic removal will become more difficult the further one goes away from the closed loop data and will fail when the phase noise associated with the atmosphere approaches the π jumps associated with NSM bit transitions. Raw sampling mode data from which the NSM cannot be removed must be discarded. The knowledge based removal uses an NSM bit stream recorded by an independent GPS receiver (e.g., network of ground based receivers). The complete NSM sequence from the occulting satellite is then correlated in time with the received RS data and phase jumps matching the NSM bit transitions are removed. Knowledge based removal is more reliable than the automatic removal scheme, but requires continuous recording of the NSM sequences of all GPS satellites.

3 The Phase Transform Algorithm

The classical geometric optics algorithm is applicable provided no multi-path propagation occurs in the atmosphere. If multi-path propagation occurs, a more sophisticated algorithm is required to recover the neutral bending angle as a function of impact parameter, namely the phase transform algorithm. The phase transform algorithm was originally derived by A. S. Jensen (Jensen et al. 2003, 2004, 2006), in a slightly different form. The derivation given here is explicit.

To perform the phase transform algorithm the regenerated phase must be first corrected for (a) instrument characteristics, (b) general relativity, and (c) clock drifts. After these corrections have been performed a complex signal with unit amplitude is constructed from the resulting regenerated phase $\varphi_{\text{REG-B}}$ using the following equation:

$$R_{\text{REG-B}}\left(\tau_{\text{RX}}^{\text{IMT}}\right) = \exp\left(+i\,\varphi_{\text{REG-B}}\left(\tau_{\text{RX}}^{\text{IMT}}\right)\right) \tag{3}$$

Next the phase transform is performed:

$$u(p) = \int_0^{T_{\mathrm{IMT}}} \omega\left(\tau_{\mathrm{RX}}^{\mathrm{IMT}}\right) R_{\text{REG-B}}\left(\tau_{\mathrm{RX}}^{\mathrm{IMT}}\right) \exp\left(-i\,\beta\left(p, \tau_{\mathrm{RX}}^{\mathrm{IMT}}\right)\right) \mathrm{d}\tau_{\mathrm{RX}}^{\mathrm{IMT}}, \tag{4}$$

where ω is a weighting function introduced to prevent ringing and $\beta(p, \tau)$ is the reference phase function for impact parameter p. The bending angle is given by the following equation:

$$\alpha(p) = -\frac{\lambda}{2\pi}\frac{\mathrm{d}}{\mathrm{d}p}\left(\arg\left(u(p)\right)\right). \tag{5}$$

The bending angles from the L1 and L2 frequencies can be smoothed and then combined to give the neutral bending angle.

$$\alpha_{\mathrm{N}}(p) = \alpha_{\mathrm{L1}}(p) + \frac{f_{\mathrm{L2}}^2}{f_{\mathrm{L1}}^2 - f_{\mathrm{L2}}^2}\left(\alpha_{\mathrm{L1}}(p) - \alpha_{\mathrm{L2}}(p)\right). \tag{6}$$

The reference phase function is given by the following equations where the geometry is referred to the time in the phase transform integral (IMT time or reference time).

$$\begin{aligned}\beta(p, \tau) = +\frac{2\pi}{\lambda}\Bigg(&\sqrt{r_{\mathrm{LEO}}^2(\tau) - p^2} + \sqrt{r_{\mathrm{GPS}}^2(\tau) - p^2} + p\Gamma(\tau)\\ &-p \arctan\left(\frac{\sqrt{r_{\mathrm{LEO}}^2(\tau) - p^2}}{p}\right)\\ &-p \arctan\left(\frac{\sqrt{r_{\mathrm{GPS}}^2(\tau) - p^2}}{p}\right)\Bigg)\end{aligned} \tag{7}$$

$$\Gamma(\tau) = \arccos\left(\frac{\mathbf{r}_{\mathrm{LEO}}(\tau)\cdot\mathbf{r}_{\mathrm{GPS}}(\tau)}{|\mathbf{r}_{\mathrm{LEO}}(\tau)|\,|\mathbf{r}_{\mathrm{GPS}}(\tau)|}\right) \tag{8}$$

The phase transform algorithm is essentially a matched filter that selects from the signal received by the GRAS receiver that portion of the signal associated with a specific impact parameter. The phase transform algorithm thus allows the bending angle to be recovered in the presence of multi-path provided the atmosphere is (locally) spherically symmetric.

4 Derivation of the Phase Transform Algorithm

The phase transform algorithm is best understood by reviewing its derivation; this is given below. Consider the Fig. 1 (Born and Wolf 1983).

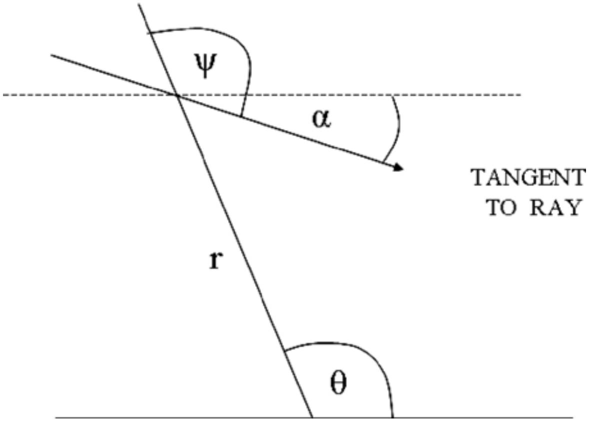

Fig. 1 Illustration of the formula of Bouguer (Born and Wolf 1983)

From Fig. 1 it is seen that:

$$ds = r\,\mathrm{cosec}(\psi)d\theta = \sqrt{(dr)^2 + r^2(d\theta)^2}. \tag{9}$$

For a spherically symmetric atmosphere the formula of Bouguer, Eq. (10), is valid

$$p = n(r)r\sin(\psi). \tag{10}$$

Therefore

$$\frac{d\theta}{dr} = \pm\frac{p}{r\sqrt{n^2(r)r^2 - p^2}}. \tag{11}$$

The phase along the ray path from a GPS satellite to the GRAS receiver on a METOP satellite is given by:

$$\varphi = \frac{2\pi}{\lambda}\int_s n(s)ds = \frac{2\pi}{\lambda}\int_s n(r)\sqrt{1 + r^2\left(\frac{d\theta}{dr}\right)^2}dr. \tag{12}$$

And thus

$$\varphi = \frac{2\pi}{\lambda}\int_{r_1}^{r_2}\frac{n^2(r)r\,dr}{\sqrt{n^2(r)r^2 - p^2}} \tag{13}$$

$$\varphi = \frac{2\pi}{\lambda}\int_{r_0}^{r_1}\frac{n^2(r)r\,dr}{\sqrt{n^2(r)r^2 - p^2}} + \frac{2\pi}{\lambda}\int_{r_0}^{r_2}\frac{n^2(r)r\,dr}{\sqrt{n^2(r)r^2 - p^2}}. \tag{14}$$

Above r_0 is the point of closest approach. Now consider one of these integrals:

$$\varphi_{0\mathrm{A}} = \frac{2\pi}{\lambda} \int_{r_0}^{r_\mathrm{A}} \frac{n^2(r) r \,\mathrm{d}r}{\sqrt{n^2(r) r^2 - p^2}}. \tag{15}$$

Using the identity:

$$n^2 r = \frac{1}{2} \frac{\mathrm{d}}{\mathrm{d}r} \left(n^2 r^2\right) - \left(n^2 r^2 - p^2\right) \frac{1}{n} \frac{\mathrm{d}n}{\mathrm{d}r} - p^2 \frac{1}{n} \frac{\mathrm{d}n}{\mathrm{d}r} \tag{16}$$

and the equation:

$$n^2(r_0) r_0^2 = p^2. \tag{17}$$

The integral becomes:

$$\begin{aligned} \varphi_{0\mathrm{A}} = & \frac{2\pi}{\lambda} \sqrt{n^2(r_\mathrm{A}) r_\mathrm{A}^2 - p^2} \\ & - \frac{2\pi}{\lambda} \int_{r_0}^{r_\mathrm{A}} \sqrt{n^2(r) r^2 - p^2} \frac{\mathrm{d}\,(\ln(n))}{\mathrm{d}r} \mathrm{d}r \\ & + \frac{2\pi p}{\lambda} \int_{r_0}^{r_\mathrm{A}} \frac{-p}{\sqrt{n^2(r) r^2 - p^2}} \frac{\mathrm{d}\,(\ln(n))}{\mathrm{d}r} \mathrm{d}r. \end{aligned} \tag{18}$$

Now from Fig. 1 and from the formula of Bouguer it is seen that:

$$\alpha = \psi - \theta \tag{19}$$

$$\frac{\mathrm{d}\psi}{\mathrm{d}\,r} = - \frac{p}{\sqrt{n^2(r) r^2 - p^2}} \frac{1}{n} \frac{\mathrm{d}\,(n)}{\mathrm{d}\,r} - \frac{p}{\sqrt{n^2(r) r^2 - p^2}} \frac{1}{r} \tag{20}$$

$$\frac{\mathrm{d}\theta}{\mathrm{d}r} = - \frac{p}{\sqrt{n^2(r) r^2 - p^2}} \frac{1}{r}. \tag{21}$$

Thus

$$\frac{\mathrm{d}\alpha}{\mathrm{d}r} = - \frac{p}{\sqrt{n^2(r) r^2 - p^2}} \frac{\mathrm{d}\,(\ln(n))}{\mathrm{d}r}. \tag{22}$$

Therefore

$$\begin{aligned} \varphi_{0\mathrm{A}} = & \frac{2\pi}{\lambda} \sqrt{n^2(r_\mathrm{A}) r_\mathrm{A}^2 - p^2} + \frac{2\pi p}{\lambda} \alpha_{\mathrm{A}0} \\ & - \frac{2\pi}{\lambda} \int_{r_0}^{r_\mathrm{A}} \sqrt{n^2(r) r^2 - p^2} \frac{\mathrm{d}\,(\ln(n))}{\mathrm{d}r} \mathrm{d}r. \end{aligned} \tag{23}$$

And therefore the phase is given by

$$\varphi = \frac{2\pi}{\lambda}\left(\sqrt{r_{\text{LEO}}^2 - p^2} + \sqrt{r_{\text{GPS}}^2 - p^2} + p\alpha \right. \\ \left. -2\int_{r_0}^{\infty} \sqrt{n^2(r)r^2 - p^2}\frac{\mathrm{d}\,(\ln(n))}{\mathrm{d}r}\mathrm{d}r\right). \tag{24}$$

Where, with reference to Fig. 2:

$$\alpha = \Gamma - \psi_{\text{GPS}} - \psi_{\text{LEO}} \\ = \Gamma - \arctan\left(\frac{\sqrt{r_{\text{GPS}}^2 - p^2}}{p}\right) - \arctan\left(\frac{\sqrt{r_{\text{LEO}}^2 - p^2}}{p}\right) \tag{25}$$

Now consider the integral:

$$u(p) = \int_0^{T_{\text{IMT}}} \omega\left(\tau_{\text{RX}}^{\text{IMT}}\right) R_{\text{REG-B}}\left(\tau_{\text{RX}}^{\text{IMT}}\right) \exp\left(-i\beta\left(p, \tau_{\text{RX}}^{\text{IMT}}\right)\right)\,\mathrm{d}\,\tau_{\text{RX}}^{\text{IMT}} \tag{26}$$

$$R_{\text{REG-B}}\left(\tau_{\text{RX}}^{\text{IMT}}\right) = A_{\text{REG-B}}\left(\tau_{\text{RX}}^{\text{IMT}}\right) \exp\left(+i\varphi\left(p, \tau_{\text{RX}}^{\text{IMT}}\right)\right). \tag{27}$$

Thus

$$u(p) = \int_0^{T_{\text{IMT}}} \omega\left(\tau_{\text{RX}}^{\text{IMT}}\right) A_{\text{REG-B}}\left(\tau_{\text{RX}}^{\text{IMT}}\right) \exp\left(i\,\varphi\left(p, \tau_{\text{RX}}^{\text{IMT}}\right) - i\,\beta\left(p, \tau_{\text{RX}}^{\text{IMT}}\right)\right)\mathrm{d}\,\tau_{\text{RX}}^{\text{IMT}} \tag{28}$$

The integral can be evaluated (approximately) by the method of stationary phase to be:

$$u(p) = \frac{\sqrt{2\pi i}\,\omega\left(\tau_{\text{RX-1}}^{\text{IMT}}\right) A_{\text{REG-B}}\left(\tau_{\text{RX-1}}^{\text{IMT}}\right) \exp\left(i\varphi\left(p, \tau_{\text{RX-1}}^{\text{IMT}}\right) - i\,\beta\left(p, \tau_{\text{RX-1}}^{\text{IMT}}\right)\right)}{\sqrt{\left.\left(\frac{\mathrm{d}^2\varphi}{\mathrm{d}\tau^2} - \frac{\mathrm{d}^2\beta}{\mathrm{d}\tau^2}\right)\right|_{\tau=\tau_1}}} \tag{29}$$

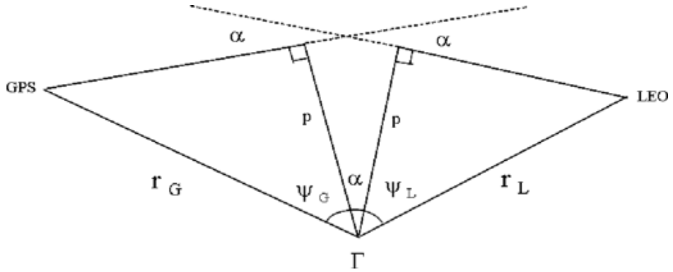

Fig. 2 Illustrating the occultation plane geometry

where

$$\varphi\left(p, \tau_{\text{RX-1}}^{\text{IMT}}\right) - \beta\left(p, \tau_{\text{RX-1}}^{\text{IMT}}\right) = \arg(u(p)). \tag{30}$$

Now $\beta(p, \tau)$ can be chosen arbitrarily; if $\beta(p, \tau)$ is chosen to be:

$$\beta(p, \tau) = \frac{2\pi}{\lambda}\left(\sqrt{r_{\text{LEO}}^2(\tau) - p^2} + \sqrt{r_{\text{GPS}}^2(\tau) - p^2} + p\,\alpha(p, \tau)\right), \tag{31}$$

where

$$\alpha(p, \tau) = \Gamma(\tau) - \arctan\left(\frac{\sqrt{r_{\text{GPS}}^2(\tau) - p^2}}{p}\right) - \arctan\left(\frac{\sqrt{r_{\text{LEO}}^2(\tau) - p^2}}{p}\right). \tag{32}$$

Then with reference to Eq. (24):

$$\varphi(p, \tau_1) - \beta(p, \tau_1) = -\frac{4\pi}{\lambda}\int_{r_0}^{\infty}\sqrt{n^2(r)r^2 - p^2}\,\frac{\mathrm{d}\,(\ln(n(r)))}{\mathrm{d}r}\mathrm{d}r. \tag{33}$$

Therefore we have:

$$\begin{aligned}\frac{\mathrm{d}}{\mathrm{d}p}\left(\varphi(p, \tau_1) - \beta(p, \tau_1)\right) &= -\frac{4\pi}{\lambda}\frac{\mathrm{d}}{\mathrm{d}p}\int_{r_0}^{\infty}\sqrt{n^2(r)r^2 - p^2}\,\frac{\mathrm{d}\,(\ln(n(r)))}{\mathrm{d}r}\mathrm{d}r \\ &= -\frac{4\pi}{\lambda}\int_{r_0}^{\infty} -\frac{p}{\sqrt{n^2(r)r^2 - p^2}}\,\frac{\mathrm{d}\,(\ln(n(r)))}{\mathrm{d}r}\mathrm{d}r \\ &= -\frac{4\pi}{\lambda}\left(\frac{\alpha}{2}\right) \\ &= -\frac{2\pi}{\lambda}\alpha.\end{aligned} \tag{34}$$

Equation (34) establishes the desired result. The main steps in the derivation are: (i) expressing the corrected phase between the transmitter and the receiver in the form given in Eq. (24), (ii) solving the Eq. (28) for $u(p)$ by the method of stationary phase, (iii) noticing that if $\beta(p, \tau)$ is chosen to be given by Eq. (31) then Eq. (33) will give $\arg(u(p))$ and (iv) observing that the derivative of $\arg(u(p))$ with respect to p is proportional to the bending angle as seen from Eq. (34). It is seen from the derivation that all the information about the bending angle is contained in the (corrected) regenerated phase measured by the GRAS receiver. The amplitude of the signal is not used.

The phase transform algorithm is valid for any spacecraft orbits provided an occultation plane exists (at least approximately). It is an exact algorithm and not an approximation. The Full Spectrum Inversion (FSI) algorithm (Jensen et al. 2003) is an approximation of the phase transform algorithm which is applicable assuming a spherical Earth and circular spacecraft orbits in the same plane. In this situation Eq. (4) can be approximated by a Fourier transform.

References

Born M, Wolf E (1983) Principles of Optics, 6th edn. Cambridge University Press, England

Jensen AS, Lohmann MS, Benzon HH, Nielsen AS (2003) Full spectrum inversion of radio occultation signals. Radio Science 38(3), doi:10.1029/2002RS002763

Jensen AS, Lohmann MS, Nielsen AS, Benzon HH (2004) Geometrical optics phase matching of radio occultation signals. Radio Science 39(RS3009), doi:10.1029/2003RS002899

Jensen AS, Benzon HH, Lohmann MS, Nielsen AS (2006) Processing radio occultation data by full spectrum inversion techniques: An overview and recent developments. In: Foelsche U, Kirchengast G, Steiner AK (eds) Atmosphere and Climate: Studies by Occultation Methods, Springer-Verlag, Berlin Heidelberg New York, pp 95–112

Loiselet M, Stricker N, Menard Y, Luntama LP (2000) GRAS – Metop's GPS-Based Atmospheric Sounder. ESA Bulletin 102, pp 38–44

Luntama JP (2006) The operational EPS GRAS measurement system. In: Foelsche U, Kirchengast G, Steiner AK (eds) Atmosphere and Climate: Studies by Occultation Methods, Springer, Berlin Heidelberg, pp 147–156, doi:10.1007/3-540-34121-8

Wilson JJW, Luntama JP (2007) Advanced processing algorithms for GRAS instrument data. In: Geoscience and Remote Sensing Symposium, IGARSS 2007, IEEE International, Barcelona, Spain, pp 1049–1054, doi:10.1109/IGARSS.2007.4422981

Using Airborne GNSS Receivers to Detect Atmospheric Turbulence

L.B. Cornman, A. Weekley, R.K. Goodrich, and R. Frehlich

Abstract A methodology for estimating turbulence intensity from GNSS-aircraft occultations is presented. The theoretical underpinnings are from standard weak-scattering theory for electromagnetic wave propagation in random media. These techniques are modified to deal with a transmitter and receiver moving relative to each other. A simulation method is then used to evaluate the sensitivity of the intensity estimates to two other unknown parameters, the turbulence length scale and the distance of the turbulence from the receiver. It is shown that the estimation is highly sensitive to the latter and relatively insensitive to the former. An iterative technique is presented that uses estimates of the distance parameters to improve the intensity estimation. It is shown that given the assumptions in the problem, the iterative technique provides relatively accurate estimates of the turbulence intensity parameter.

1 Introduction

There is a long and distinguished history in the study of electromagnetic (EM) wave propagation through random media (cf. Tatarskii 1971; Yeh and Liu 1982; Ishimaru 1997). These works have provided a firm theoretical foundation for estimating statistical properties of the neutral atmosphere and ionosphere via the statistical properties of the received EM signals. That is, the characteristics of the turbulent atmosphere can be deduced from, for example, correlation and/or spectral analysis of the phase and/or amplitude of the received signal. In the past, the bulk of the experimental analysis in this area has been performed with ground-based transmitters and receivers (e.g., radars and lidars), as well as with ground-based receivers and space-based transmitters. With the advent of Global Navigation Satellite System (GNSS) constellations, a new avenue has become available to investigate the turbulence properties of the Earth's atmosphere. The deployment of an ever-increasing number of Low Earth Orbiting (LEO) satellites—with high-quality, high-sampling rate receivers—provides a very valuable new source of turbulence measurements:

L.B. Cornman (✉)
National Center for Atmospheric Research, Boulder, USA
e-mail: cornman@ucar.edu

A. Steiner et al. (eds.), *New Horizons in Occultation Research*,
DOI 10.1007/978-3-642-00321-9_4, © Springer-Verlag Berlin Heidelberg 2009

GNSS-LEO occultations. There are numerous other practical applications which can benefit by having turbulence measurements (and resultant climatologies) from GNSS-aircraft occultations. For example: space weather (Hajj et al. 1994), trans-ionospheric communication links (Secan et al. 1997), aviation safety and navigation systems (Conker et al. 2003; Cornman et al. 2004), the accuracy of ground-based GNSS receivers (Ganguly et al. 2004), as well as the effect of turbulence on measuring atmospheric state variables from GNSS-LEO occultations (Kursinski et al. 1997; Gorbunov and Kirchengast 2005).

The methods and results presented below are extracted from a much more thorough report prepared for the Boeing Corporation.

2 Theory—Weak Scattering

The essential theory for the problem of wave propagation through a random media is described in a variety of references, e.g., Tatarskii (1971) or Ishimaru (1997). Specific application to ionospheric measurements which follows directly from the basic theory has also been developed (cf. Yeh and Liu 1982; Bhattacharyya et al. 1992). Further application of this theory to the GNSS-LEO problem is discussed in Vorob'ev and Kan (1999) and Cornman et al. (2004). In the following, this latter reference is used as a starting place.

Since the transmitter and receiver are moving relative to each other, the origin of the coordinate system for the problem is taken to be at the receiver. In this case, a displacement vector $\boldsymbol{\rho}$ in the plane perpendicular to the line-of-sight (LOS) between the transmitter and receiver is given to the first order by $\boldsymbol{\rho} = \mathbf{V}_{\text{eff}}\tau$, where τ is the change in time over which the displacement occurs. Assuming that the turbulence is isotropic in the perpendicular plane, it can only be a function of the length of the displacement vector, $\|\boldsymbol{\rho}\| = \|\mathbf{V}_{\text{eff}}\|\,\tau$, where $\|\mathbf{V}_{\text{eff}}\|$ for a non-moving atmosphere and spherical wave propagation is given by

$$\|\mathbf{V}_{\text{eff}}(\eta)\| = \left\|\mathbf{V}_{\text{R}}\frac{\eta}{R} + \mathbf{V}_{\text{T}}\left(1 - \frac{\eta}{R}\right)\right\|, \tag{1}$$

where η is the distance along the LOS from the transmitter ($\eta = 0$) to the receiver ($\eta = R$). $\mathbf{V}_{\text{T}}$ is the velocity of the transmitter and $\mathbf{V}_{\text{R}}$ is the velocity of the receiver, both computed as the projection of the full 3-D vectors into the plane transverse to the LOS. It can be shown that the frequency spectrum of a spherical wave measured in the plane perpendicular to the LOS, for the log-amplitude fluctuations of the index of refraction field, χ, is given by

$$\Phi_\chi(f) = \int\limits_{\eta_1-\Delta\eta/2}^{\eta_1+\Delta\eta/2} \frac{4\pi^{5/2}k^2AC_n^2(\eta)}{||\mathbf{V}_{\text{eff}}(\eta)||}y^{-4/3}\cdot \left\{\frac{2\Gamma(1/3)}{5\Gamma(5/6)} - \text{Re}\left[\mathrm{e}^{iax^2}U\left[1/2, -1/3, -iay\right]\right]\right\}\mathrm{d}\eta, \tag{2}$$

where it is assumed that the turbulence resides in a patch centered at η_1 and of length $\Delta\eta$ along the LOS; k is the wavenumber for the transmitted signal; Re refers to the real part; C_n^2 is the turbulence intensity (also referred to as the structure constant); U is the confluent hypergeometric function of the second kind, and Γ is the gamma function (Abramowitz and Stegum 1972); $x = 2\pi f/\|\mathbf{V}_{\text{eff}}\|$; $y = x^2 + L_0^{-2}$; L_0 is the integral length scale of the turbulence; $a = \eta(R-\eta)/kR$; and $A = 0.033$. A von Karman model for the isotropic index of refraction spectrum is used in Eq. (2) (Ishimaru 1997). Note that the Kolmogorov case is obtained by setting $L_0 \to \infty$. The Kolmogorov model is a power law at all wavenumbers. It is valid in the so-called inertial subrange of wavenumbers—far away from both the energy-producing scales (small wavenumbers) and the dissipation scales (large wavenumbers, Tatarskii (1971)). So, theoretically it cannot be a valid model at the smallest wavenumbers (it goes to infinity). In this subrange, the index of refraction spectrum is only a function of the single intensity parameter, C_n^2. The von Karman model has the same large wavenumber limit as the Kolmogorov model (power-law), but at small wavenumbers, it asymptotes to a constant (a function of both C_n^2 and L_0), which ensures finite energy. The plane wave propagation case is given by setting $a = (R-\eta)/k$. For turbulence in the ionosphere, a different set of coefficients are required as well as changing the k^2 factor to k^{-2}, but the rest of the formulation is the same. If it is further assumed that the length of the turbulence patch $\Delta\eta$ is small enough such that a mid-point approximation to the integral in Eq. (2) is an accurate one (given some criteria), then

$$\Phi_\chi(f) = \frac{4\pi^{5/2}k^2AC_n^2(\eta_1)\Delta\eta}{V_{\text{eff}}(\eta_1)}y^{-4/3}\cdot\left\{\frac{2\Gamma(1/3)}{5\Gamma(5/6)} - \mathrm{Re}\left[e^{iax^2}U\left[1/2,-1/3,-iay\right]\right]\right\} \tag{3}$$

It should be noted that typically $\Delta\eta$ will *not* be small enough such that a mid-point approximation is accurate; hence, the patch must be broken into a number of smaller segments such that the approximation is acceptable within each one. A detailed discussion on this topic is beyond the scope of this paper (a comment is made in Sect. 4). However, to simplify the problem, for the results presented below it is assumed that the mid-point approximation is accurate enough.

3 Results

3.1 Log-Amplitude Spectra: Analytic Forms

Next, consider the sensitivity of Eq. (3) to the unknown parameters, L_0 and η_1. The other unknown, the combined parameter $C_n^2(\eta_1)\Delta\eta$ will merely change the overall level of the curves. Figure 1a shows the log-amplitude spectra when L_0 is held fixed and $R-\eta_1$ (the distance along the LOS from the aircraft to the turbulence patch), is varied. The parameter values are: $L_0 = 3.0$ km and $R-\eta_1 = \{10, 50, 100, 200\}$ km. Note that in the following analyses, it has been assumed that the angle between

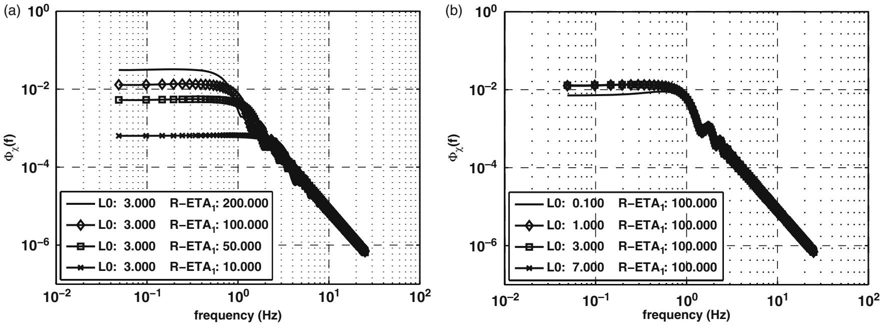

Fig. 1 (**a**) Log-amplitude spectra—showing the variation over different $R - \eta_1$ values, for fixed $L_0 = 3.0$ km. (**b**) Log-amplitude spectra—showing the variation over different L_0, for fixed $R - \eta_1 = 100$ km

the projections of the transmitter and receiver velocity vectors onto the plane perpendicular to the LOS is zero. That is, the projections are parallel. Clearly, this is not the general case, but for this heuristic analysis it will suffice. Next, consider holding η_1 fixed and varying L_0. This can be seen in Fig. 1b, where the parameter values are $R - \eta_1 = 100$ km and $L_0 = \{0.1, 1.0, 3.0, 7.0\}$ km. From Fig. 1a, it is clear that at low-frequencies the spectrum is highly sensitive to η_1, with lessening sensitivity for increasing frequencies. From Fig. 1b, it can be seen that excepting for $L_0 = 0.1$ km—a very small value for the upper atmosphere—the log-amplitude spectrum is fairly insensitive to the turbulence length scale. These considerations will be important when it comes to parameter estimation.

3.2 Simulation Studies and Parameter Estimation

An investigation into parameter estimation was performed, focusing on the log-amplitude spectra. Assuming that the received signal is a sample from a Gaussian process, its spectrum will have an exponential distribution. Using this fact, numerous realizations of the spectra can be generated, i.e., by replacing each spectral point with a sample from an exponentially-distributed random number sequence. An example of this is shown in Fig. 2. The simulation is intended to represent real-world situations; hence, it was assumed that the received signal would be available at 50 Hz, and approximately 10 s worth of data would go into a single spectrum (512 samples were used).

For this exercise, the parameter to be estimated is $C_n^2(\eta_1)\Delta\eta$. Two cases were examined, (i) holding η_1 fixed and varying L_0, and (ii) holding L_0 fixed and varying η_1. In each case, a single-parameter maximum-likelihood (ML) method was used to estimate $C_n^2(\eta_1)\Delta\eta$. Let $\Phi_g(f) = p\phi_g(f)$; where the subscript g refers to the function (here, the log-amplitude spectrum), and p is the parameter to be estimated. In this case, $\phi_g(f)$ is Eq. (3) with $C_n^2(\eta_1)\Delta\eta$ set to one. Then given a measured—or

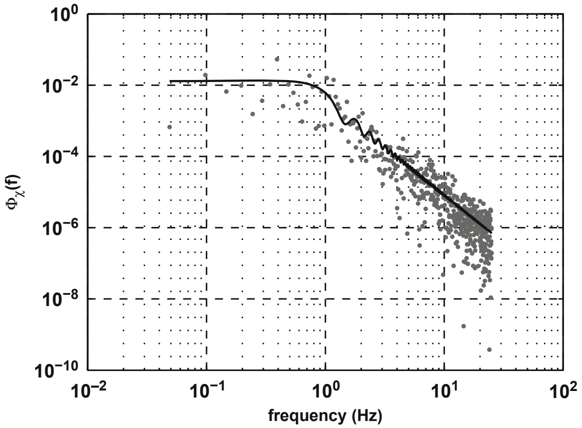

Fig. 2 Theoretical log-amplitude spectrum (*black curve*), and with values replaced by exponentially-distributed noise (*gray dots*)

in this case simulated—set of spectral points, $\hat{\Phi}_g(f_i)$, $i = 1, \ldots, N$ the maximum-likelihood estimate of p is given by

$$p = \frac{1}{N} \sum_{i=1}^{N} \frac{\hat{\Phi}_g(f_i)}{\phi_g(f_i)} \tag{4}$$

where the calculation is done over a set of N frequency values (Smalikho 1997).

Figure 3a illustrates results of the simulation exercise for the estimation of $C_n^2(\eta_1)\Delta\eta$ values, given fixed (and known) η_1, and varying L_0 around the true value. For the data in Fig. 3b, L_0 is fixed and η_1 is varied. The "true" values for L_0 and $R - \eta_1$ are 3 km and 100 km, respectively. This corresponds to the curve with diamond symbols in Fig. 1a. The concept is to determine the sensitivity in estimating $C_n^2(\eta_1)\Delta\eta$ given an uncertainty in the knowledge of one of the two other unknown parameters. That is, a realization of the log-amplitude spectrum is generated for a given set of input parameters $\{C_n^2(\eta_1)\Delta\eta, \eta_1, L_0\}$. This is $\hat{\Phi}_\chi(f)$ in Eq. (4). The model function, $\phi_\chi(f)$, is calculated from Eq. (3), (with $C_n^2(\eta_1)$ $\Delta\eta = 1$), using the same value of η_1 that was employed in generating $\hat{\Phi}_\chi(f)$; but with values of L_0 that range around the fixed value that was used in generating $\hat{\Phi}_\chi(f)$. These L_0 values constitute the ordinate in Fig. 3a. The black horizontal and vertical lines are the true values of L_0 and $C_n^2(\eta_1)\Delta\eta$, respectively. Figure 3a is a two-dimensional histogram for the $\{C_n^2(\eta_1)\Delta\eta, L_0\}$ parameter space, with the color representing the number of counts in that bin. One thousand realizations, such as the one shown in Fig. 2, were generated for each L_0 value. It can be seen that over a large range of length scales, the errors in estimating $C_n^2(\eta_1)\Delta\eta$ are mostly within $\pm 5\%$ of the true value—the spread being dominated by the statistics of the random realizations. These results confirm the qualitative discussion above regarding the relatively insensitivity of the log-amplitude spectrum with respect to the length scale. That is, given a two-parameter model where one of the parameters is known, and it is insensitive to the other one, it is not surprising to see these results.

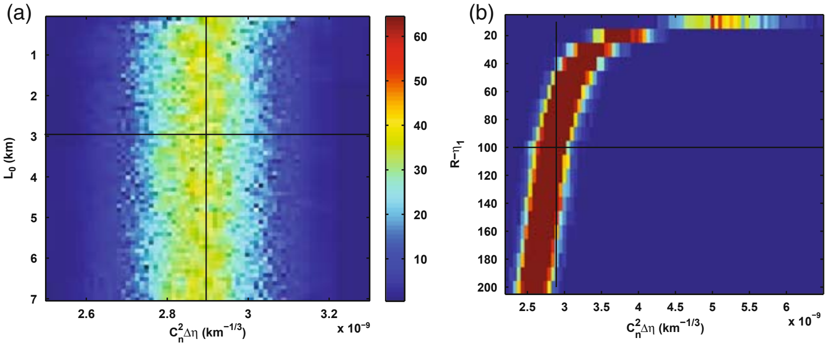

Fig. 3 (**a**) Distribution of $C_n^2(\eta_1)\Delta\eta$ estimates as a function of varying L_0, while holding $R - \eta_1 = 100$ km fixed. (**b**) Distribution of $C_n^2(\eta_1)\Delta\eta$ estimates as a function of varying $R - \eta_1$, while holding $L_0 = 3$ km fixed. The *black horizontal and vertical lines* are the true values of L_0 and $C_n^2(\eta_1)\Delta\eta$, respectively. Note that the scale for the abscissa on the two plots is different

A positive bias is visible at the smallest L_0 value ($L_0 = 0.1$ km). While this is a somewhat unrealistic value for the upper troposphere, the analysis of this case is instructive. From Fig. 1b, it can be seen that at low frequencies, the spectrum for this length scale value is about a factor of two smaller than that for the spectrum with $L_0 = 3$ km. Recall that the simulated spectrum is generated using the true value (3 km) and it is the model function that is given the erroneous value (0.1 km). Referring to Eq. (4), it can be seen why the high bias occurs. The model spectrum with the erroneous length scale is divided into the simulated spectrum, and since the former is smaller over a handful of low-frequency points, the ML estimator will produce a small positive bias.

Figure 3b illustrates the same procedure as above, but keeping L_0 fixed and varying η_1. For convenience, the ordinate of this figure is $R - \eta_1$, the distance to the turbulent patch from the receiver. The black horizontal and vertical lines are the true values of $R - \eta_1$ and $C_n^2(\eta_1)\Delta\eta$, respectively. Due to the larger sensitivities of the spectrum to η_1, the biases are even more apparent in this scenario. From Fig. 1a, it is obvious that the spectral points at low frequencies for the model spectra with the smaller $R - \eta_1$ value (10 km) are significantly lower than those from the simulated spectrum ($R - \eta_1 = 100$ km). In going from the low-frequency values on the 10 km curve to those on the 100 km curve, there is an increase by a factor of around 20. From the 50–100 km curve would result in an increase by a factor of around 2.5. Hence, the increasingly large positive biases for decreasing $R - \eta_1$ values. This is seen in the $R - \eta_1 < 100$ km region (above the black horizontal line) of Fig. 3b. Of course, the opposite is true: as the $R - \eta_1$ values used in the model spectrum increase over those in the true (e.g., simulated) spectrum, the bias will be increasingly negative. For example, in going from the low-frequency values on the 200 km curve to those on the 100 km curve, there is a decrease by a factor of around 2.5. This is seen in the $R - \eta_1 > 100$ km portion of the figure.

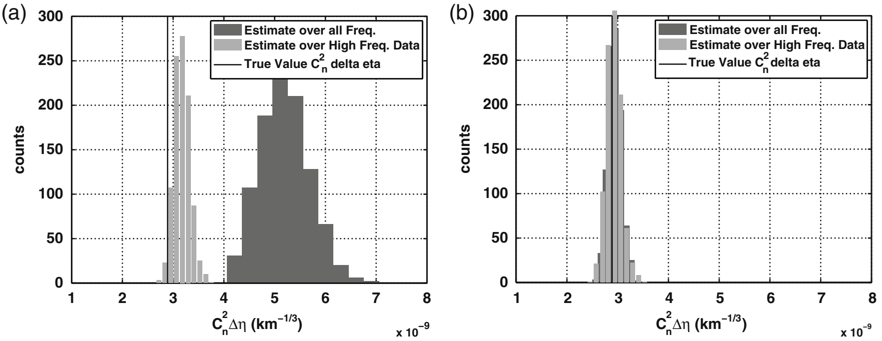

Fig. 4 Histograms of the distribution of $C_n^2(\eta_1)\Delta\eta$ values from the ML estimator, using log-amplitude spectrum. For the histograms in *dark gray*, all of the spectral points are used in the estimation; for the ones in *light gray* only the high frequency spectral points are used. In this case the true value of $R - \eta_1$ was 100 km and the model value was 10 km. (**a**) Prior to iteration using η_1 estimation, (**b**) After iteration using η_1 estimation

A partial solution to the bias problem is to restrict the spectral points used in the ML estimator to the high-frequency regime—where the effect of η_1 is lessened. The result of this exercise is shown in Fig. 4a. The histogram in dark gray is the distribution of $C_n^2(\eta_1)\Delta\eta$ estimates, over 1000 realizations, using all of the spectral points. In this case, a value of $R - \eta_1 = 10$ km is used for the model spectrum whereas the value for the simulated spectra is 100 km. This corresponds to the top line in Fig. 3b, where it can be seen that there is a significant positive bias, as well as a broader distribution. When the set of points used in the ML estimator is restricted to higher-frequency points, the bias and the spread are significantly reduced. This can be seen in the distribution in light gray. The input $C_n^2(\eta_1)\Delta\eta$ value is indicated by the vertical black line.

3.3 *Iterative Parameter Estimation*

As can be seen from Fig. 4a, there is still a non-trivial bias in the estimation of $C_n^2(\eta_1)\Delta\eta$ even when restricting the spectral points used in the ML estimator to those at higher frequency values. It can be shown that the bias in the ML estimator is directly proportional to the right-hand side of Eq. (4), minus one. At the higher frequencies, the ratios on the right-hand side of Eq. (4) are smaller than those at lower frequencies, but there are many more points at the higher frequencies so that the sum of these ratios can be significant. The reason that these ratios are not one in this case is that η_1 does not equal η. One approach to ameliorating this influence is to use a two-step method for calculating the estimates of $C_n^2(\eta_1)\Delta\eta$. The first step is to estimate $C_n^2(\eta_1)\Delta\eta$ from the method described in the previous section. That is, a value of η_1 is guessed, and used in the ML algorithm. Since the length scale value is not very pertinent, choose a reasonable physical value. Given these two parameters, the log-amplitude spectrum is now a function of the single unknown parameter η_1. A least-squares minimization method is then used to estimate η_1, which in turn is utilized in place of the "guessed" value in a second iteration of the ML estimation for $C_n^2(\eta_1)\Delta\eta$. In this case, the true value of $R - \eta_1$ is 100 km and the model value is 10 km. The η_1 estimates computed from the minimization method have a high bias. This is due to the positive bias in the first estimates of $C_n^2(\eta_1)\Delta\eta$. Referring to Eq. (4), if the $C_n^2(\eta_1)\Delta\eta$ estimates are too large, then the model function, $\phi_g(f, \hat{\eta}_1)$, must be smaller in order to minimize the difference between the data, $\hat{\Phi}_g(f_i)$, and the product of the $C_n^2(\eta_1)\Delta\eta$ estimates and the model. Making the model function smaller implies that larger η_1, or equivalently, smaller $R - \eta_1$ values, must be used (cf. Fig. 1a). Note that since the true value of $R - \eta_1$ is larger than the original model one, (100 km vs. 10 km); estimating larger η_1 values should reduce the bias in the iterated $C_n^2(\eta_1)\Delta\eta$ values. Figure 4b shows the results of the iterated $C_n^2(\eta_1)\Delta\eta$ estimation. Comparing these to Fig. 4a, it can be seen that the iterated estimates are superior to the original ones. There is still a small positive bias, but certainly less than in the original case. This is especially apparent in the $C_n^2(\eta_1)\Delta\eta$ estimates using all of the spectral points (in light gray). The discussion about biases in the η_1 and iterated $C_n^2(\eta_1)\Delta\eta$ values, was based on using a true $R - \eta_1$ value that is larger than the initial guess used in the model. The same logic holds for the case when the true $R - \eta_1$ value is smaller than the initial guess—all that changes is the directions of the biases—and the same movement of the estimates towards the true values occurs.

4 Conclusions and Outlook

This paper has focused on the use of airborne GNSS receivers to estimate turbulence intensity. The theoretical development follows methods described in the literature, with augmentations to account for specifics of the problem. The key results are Eq. (2) and Eq. (3). It should be noted that these results are valid—given the assumptions inherent in the method—for any pair of transmitters and receivers moving relative to each other. The rest of the paper described parameter estimation methodologies. A simple technique to simulate many independent realizations was used in order to provide a statistical evaluation of the methods. A maximum likelihood (ML) method was used to produce turbulence intensity estimates. The location of the turbulence along the LOS was seen to have a strong affect on the accuracy of the ML estimation method. In order to work around this problem, an iterative technique was developed. This technique uses the first estimates of the turbulence intensity to feed into a least-squares estimator for the location of the turbulence. These latter estimates were then feed back into the ML estimator to produce iterated estimates for the intensity parameter. It was shown that for the log-amplitude spectra—which are more sensitive to the unknown location parameter than the phase spectra—the iterative method produced significant improvements in the intensity parameter estimation.

There are a number of issues that still need to be investigated more thoroughly. Further analysis of the contamination due to electron density fluctuations in the ionosphere should be made. The results presented above were concerned with a single patch of turbulence along the LOS, using the mid-point approximation for the integral, Eq. (2). The effect of the mid-point approximation on the accuracy of the estimation methods for the turbulence intensity parameter needs further study. The log-amplitude spectra were analyzed, but the phase spectrum was not. An analysis should be performed to see if there are any advantages to using this spectrum for parameter estimation. Most of the analysis was performed with the angle between the projections of the transmitter and receiver velocities in the plane perpendicular to the LOS being zero. An analysis should be performed using non-zero angles to see the effect on parameter estimation. The effect of multiple patches of turbulence along the LOS on parameter estimation also needs to be addressed. The simulation methods used above can easily be modified to generate multiple patches of turbulence along the LOS—including ones in the ionosphere. Furthermore, the effects of layered turbulence regions—not uncommon in the upper-troposphere and lower stratosphere—could be evaluated by using an anisotropic index of refraction spectrum (Tereshchenko et al. 2004). A new approach to parameter estimation can also be studied. One candidate is to use one-dimensional tomography at each temporal frequency of the measured spectrum. In this approach the integral of the spectrum over the path length is subdivided into multiple intervals, such that over each interval, the mid-point approximation meets a required accuracy criterion. However, the width of these intervals, $\Delta\eta$, will be a function of the location of a given interval along the LOS and the frequency. The integral, i.e., the frequency spectrum, can then be discretized and viewed as the linear combination,

$$\hat{\Phi}_\chi(f_j) = \sum_{i=1}^{N} C_n^2(\eta_i)(\Delta\eta)_{ij} h_\chi(\eta_i, f_j) \tag{5}$$

where the log-amplitude spectrum has been used as an example. $\hat{\Phi}_\chi(f)$ is the measured frequency spectrum, and $h_\chi(\eta_i, f_j)$ is the theoretical frequency spectrum, Eq. (3), with $C_n^2(\eta_1)\Delta\eta$ set to one. Since $h_\chi(\eta_i, f_j)$ and $(\Delta\eta)_{ij}$ are known quantities, Eq. (5) represents a system of linear equations, which can then be solved for the $C_n^2(\eta_i)$ values using the Singular Value Decomposition (SVD) method (Press et al. 1989).

Acknowledgements The authors would like to acknowledge the great support provided by our sponsor, Brian Tillotson, from the Boeing Corporation.

References

Abramowitz M, Stegun IA (eds) (1972) Handbook of Mathematical Functions. National Bureau of Standards, Washington, D.C.

Bhattacharyya A, Yeh KC, Franke SJ (1992) Deducing turbulence parameters from transionospheric scintillation measurements. Space Sci Rev 61(3–4):335–386

Conker RS, El-Arini MB, Hegarty CJ, Hsiao T (2003) Modeling the effects of ionospheric scintillation of GPS/Satellite-Based Augmentation System availability. Radio Sci 38(1), doi:10.1029/2000RS002604

Cornman LB, Frehlich R, Praskovskaya E (2004) The Detection of Upper Level Turbulence via GPS Occultation Methods. In: Kirchengast G, Foelsche U, Steiner AK (eds) Occultations for Probing the Atmosphere and Climate, Springer-Verlag, Berlin Heidelberg New York, pp 365–373

Ganguly S, Jovancevic A, Brown A, Kirchner M, Zigic S, Beach T, Groves KM (2004) Ionospheric scintillation monitoring and mitigation using a software GPS receiver. Radio Sci 39(RS1S21), doi:10.1029/2002RS002812

Gorbunov ME, Kirchengast G (2005) Processing X/K band radio occultation data in the presence of turbulence. Radio Sci 40(RS6001), doi:10.1029/2005RS003263

Hajj GA, nez Meier RI, Kursinski ER, Romans LJ (1994) Imaging the ionosphere with the global positioning system. Int J Imaging Syst Technol 5:174–184

Ishimaru A (1997) Wave Propagation and Scattering in Random Media. IEEE Press, New York

Kursinski ER, Hajj GA, Schofield JT, Linfield RP, Hardy KR (1997) Observing Earth's atmosphere with radio occultation measurements using the Global Positioning System. J Geophys Res 102(D19):23429–23465

Press WH, Flannery BP, Teukolsky SA, Vetterling WT (1989) Numerical Recipes (FORTRAN version). Cambridge University Press, Cambridge

Secan JA, Bussey RM, Fremouw EJ, Basu S (1997) High-latitude upgrade to the Wideband ionospheric scintillation model. Radio Sci 32(4):1567–1574

Smalikho IN (1997) Accuracy of the turbulent energy dissipation rate stimation from the temporal spectra of wind velocity fluctuations. Atmos Ocean Opt 10(8):559–563

Tatarskii VI (1971) The Effects of the Turbulent Atmosphere on Wave Propagation. U.S. Department of Commerce and National Science Foundation, Washington, D.C.

Tereshchenko ED, Kozlova MO, Kunitsyn VE, Andreeva ES (2004) Statistical tomography of subkilometer irregularities in the high-latitude ionosphere. Radio Sci 39(RS1S35), doi:10.1029/2002RS002829

Vorob'ev VV, Kan V (1999) Background fluctuations in the GPS-Microlab-1 ionospheric radio sounding experiment. Radiophys Quantum Electron 42(6):451–462

Yeh KC, Liu CH (1982) Radio wave scintillations in the ionosphere. Proc IEEE 70(4):324–360

The GRAS SAF Radio Occultation Processing Intercomparison Project ROPIC

A. Löscher, K.B. Lauritsen, and M. Sørensen

Abstract Global Navigation Satellite System (GNSS) based radio occultation (RO) measurements promise to be valuable observations to supplement the data base used for numerical weather prediction, atmospheric process studies, and climate research. Especially in the latter case it is important to fully understand the influence of the particular processing (algorithms, implementations, and used parameters) on the quantities used for further studies. To assess the impact of different algorithms and implementations used to derive bending angles and refractivities and to identify possible systematic deviations three centers routinely processing RO data had been given an identical excess phase and orbit (Level 1a) CHAllenging Minisatellite Payload (CHAMP) data set comprising observations from two months. To probe the robustness and possible dependences of the processing results on atmospheric conditions the middle month of the winter and summer season 2005 had been chosen. The results after an external quality control indicate a good agreement of the data sets between 5 km and 40 km for bending angles and refractivity depending on latitude, although the Wegener Center for Climate and Global Change (WEGC) data set exhibits systematic deviations compared to Danish Meteorological Institute (DMI) and Deutscher Wetterdienst (DWD). At high altitudes, the different initialization strategies are visible in the processed data. The Radio Occultation Processing Center Intercomparison Campaign (ROPIC) was conducted by the Global Navigation Satellite System Receiver for Atmospheric Sounding (GRAS) Satellite Application Facility (SAF).

1 Introduction

Radio occultation (RO) proved to be a reliable technical concept meeting requirements like global coverage, all weather capability (the signals are not hampered by clouds and precipitation), *a priori* long term stability and self-calibration

---

A. Löscher (✉)
European Space Agency (ESA), 2200 AG Noordwijk, The Netherlands
e-mail: armin.loescher@esa.int

A. Steiner et al. (eds.), *New Horizons in Occultation Research*,
DOI 10.1007/978-3-642-00321-9_5,

(Kursinski et al. 1997; Hajj et al. 2004) which favors RO data utilization within frameworks conducting climate studies (Foelsche et al. 2009; Löscher and Kirchengast 2008). The latter property, which distinguishes RO from most other space-borne observational techniques, should allow for rather easy inter-comparison and combination of data, offering the opportunity to get a comprehensive time series. Over the next decades, observations from different receivers and platforms (e.g., Constellation Observing System for Meteorology, Ionosphere, and Climate COSMIC (Rocken et al. 2000), or the Global Navigation Satellite System (GNSS) Receiver for Atmospheric Sounding (GRAS), a new state of the art GNSS based RO instrument (Loiselet et al. 2000; Luntama et al. 2008) onboard the Metop series of satellites operated by EUropean Organisation for the Exploitation of METeorological SATellites (EUMETSAT)) will be available.

Since RO data should serve as a climate benchmark the processing must be robust and deliver reproducible results, the GRAS Satellite Application Facility (SAF). located at the Danish Meteorological Institute (DMI) in Copenhagen, Denmark, initiated the Radio Occultation Processing Intercomparison Campaign (ROPIC). A similar project the Radio Occultation Sensor Evaluation (ROSE) had been conducted a while ago (Ao et al. 2003). The main finding had been a surprisingly small overlap of profiles processed by three different centers (University Cooperation for Atmospheric Research (UCAR), GeoForschungsZentrum Potsdam (GFZ), and Jet Propulsion Laboratory (JPL)) drawing from the same pool of raw data which lead to further investigations. The monthly mean of refractivity difference turned out to be less than 0.3% with a standard deviation of 0.5% in an altitude range of 10–25 km. In the lower troposphere, the agreement was worse in the tropics than elsewhere, with the mean refractivity difference exceeding 1% in the lower altitudes. Bending angles were not analyzed.

RO processing chains are composed of a number of algorithms which differ between the centers; even if the same underlying algorithm is used the specific implementations will be different thus slightly different results can be expected. As shown by von Engeln (2006a,b) this uncertainty cannot be neglected. This study serves to assess those variations by comparing the data products of different processing chains.

The intention is not the assessment of the absolute accuracy but to reveal possible inconsistencies and systematic deviations between different centers. This study should serve as a baseline to identify benefits from using certain algorithms and methods, which in turn could be used to optimize the processing chains. Most likely, the optimal processing method is complex (e.g., it may vary with altitude range and spatial location of the observation).

In our study, we focus on the assessment of the processing chains from excess phase level to bending angles and refractivities. Those are the quantities used in Numerical Weather Prediction (NWP) systems (Healy and Thépaut 2006) and are possibly the best candidates for long-term climate monitoring applications (Ringer and Healy 2008). Data even closer to the raw observation state might be even better but are not used yet. As a matter of fact it is difficult to quantify the uncertainties introduced by the different processing steps, thus it is an advantage to keep them at a minimum. Although for climate applications where mostly relative changes are of interest (Löscher et al. 2008) a possible bias for example is not posing a problem as long as it is stable in time (which is difficult to guarantee if it is not entirely clear where it stems from). Other quantities like suggested in Leroy et al. (2006) might prove to be appropriate for climate applications too which still has to be studied in detail concerning its sensitivity to the processing.

As a common baseline a CHAllenging Minisatellite Payload (CHAMP) (Wickert et al. 2004) based data set had been compiled containing the occultation events from January and July 2005 covering the middle month of the Northern Hemisphere winter and summer season to represent different atmospheric conditions. The occultations had been processed from raw to excess phase and orbit data by GFZ Potsdam (Germany). The participating centers Deutscher Wetterdienst (DWD) in Offenbach (Germany), GRAS-SAF at DMI, and Wegener Center for Climate and Global Change (WEGC) in Graz (Austria) processed the common data set to bending angles, refractivities, and higher-level products like dry temperature. The activity was coordinated by the GRAS-SAF. We present here the results of the bending angle and refractivity intercomparison.

2 Data Set

To conduct the ROPIC campaign, a comprehensive set of phase delay and orbit data from CHAMP had been compiled for the participating processing facilities. This serves several purposes, it enables the participation of centers not capable of processing the data up to Level 1a (excess phase and orbit), it avoids that the overlap of processed profiles at that point is small as it happened in the ROSE campaign[1], and finally we are interested in investigating the processing from Level 1a to bending angles and refractivities thus respective effects are effectively isolated.

GFZ Potsdam provided the data of the CHAMP GPS radio occultation experiment, generated the phase delay data, and made the orbit data available for ROPIC. The GRAS-SAF edited the data and compiled the final ROPIC input data set including instructions. The package was distributed either in GFZ ASCII or ROPP (Radio Occultation Processing Package) NetCDF format via a dedicated web page.

To clarify the notation and avoid confusion Table 1 shows some data level definitions used for the excess phase (PD) and corresponding orbit data by different centers, in this paper the GRAS-SAF convention is used.

Table 1 Definitions used for the same data level

GFZ	GRAS-SAF	UCAR	EUMETSAT
Level 2	Level 1a	Level 2	Level 1a

---

[1] The overlap issue had been a bit relaxed meanwhile pers. communication J. Wickert

Table 2 ROPIC excess phase data set from GFZ

	January	July	Total
GFZ Data	5246	5928	11174

The data set consists of two months (January and July 2005) to cover the atmospheric variability throughout the Northern Hemisphere summer and winter seasons providing a representative baseline. It comprises 5246 profiles from January 1, 2005 to January 31, 2005 and 5928 profiles from July 1, 2005 to July 31, 2005; in total 11,174 profiles (Table 2), a number, which allows to generate meaningful statistics. Due to problems in the attitude stabilization of CHAMP no precise orbits are provided from January 30, 22 UTC to January 31, 22 UTC, thus only a limited number of occultations could be processed.

The space based single differencing technique had been used to eliminate the CHAMP satellite clock error and to derive the atmospheric excess phase data for ROPIC (which is not equal to the GFZ standard data stream where the double differencing technique is employed). The GPS clock errors are corrected by using 5 min clock solutions, provided by the GFZ orbit processing facility (König et al. 2005). The use of the single differencing technique seems to introduce no significant deviations compared to the operational double differencing. Details concerning the GFZ RO data processing using the single differencing technique are given by Wickert et al. (2002). Further references related to the derivation of the atmospheric excess phase from GPS RO data are, e.g., Schreiner et al. (1998) and Hajj et al. (2002).

The DWD reference data (especially the ray-traced bending angles which are usually not available) proved to be essential for quality control. For all data sets, the mean tangent point had been recalculated as in Sect. 3 described (except for the WEGC data, since the tangent point track was not provided the given coordinates had been used). Since the aim of this project is to assess the relative deviations between different retrieval procedures, the processing chains of the centers are treated as "black boxes" in a first step. The delivered profiles are assumed to be the quality controlled standard output. A next step will be to analyze where differences originate which will call for a close look at the specific implementations.

The DMI and DWD processing chains are based on the same underlying algorithm (a combination of geometric optics (GO) and wave optics, where the Canonical Transform 2nd Type (CT2) is used). The WEGC data was retrieved with the Occultation Processing System version OPSv5.3, an enhanced version of OPSv5.2 (Foelsche et al. 2008) based on the heritage of the CHAMPCLIM retrieval (Foelsche et al. 2005). This retrieval is a dry air retrieval based on geometric optics.

More subtle differences exist concerning quality control, initialization methods, smoothing, and implementation particularities, which cause differences in the output. Details on the processing applied by DMI cf. Gorbunov (2005); Gorbunov and Lauritsen (2006); Gorbunov et al. (2006), by DWD cf. Gorbunov (2002); Gorbunov and Lauritsen (2002); Gorbunov (2005) and by WEGC cf. Gobiet et al. (2007); Foelsche et al. (2008).

The ROPIC data consists of Level 1a, bending angle, refractivity profiles, and data processed to a higher level like dry temperature including the respective (ECMWF) reference data (collocated reference profiles of temperature, specific humidity, pressure including the derived refractivity, surface pressure, and for the DWD data set the derived bending angles).

To ease processing and general handling all data sets had been converted to the ROPP[2] (Radio Occultation Processing Package) NetCDF format in a pre-processing step. To filter outliers, which would spoil the statistics, quality control procedures are executed as part of the analysis. The quality controls are based on external data (bending angles and refractivities) which rules are as follows: Any profile, which deviates from the respective reference between 10 km and 20 km more than 10% is considered an outlier and flagged as failed. From 10 km down every level of a profile is checked against the respective reference and if the deviation exceeds 20% the first time the value at that level and all consecutive levels is set to missing values. The same procedure is applied to all levels from 20 km up.

As reference data the DWD provided collocated ray-traced bending angles and reference refractivities, both derived from ECMWF data, are used. If a profile is flagged as outlier in bending angle space, it is not carried on to the refractivity analysis.

Those procedures are empirical and proved to be reliable measures to account for outliers and un-physical values, which seem to appear in a few profiles on a random base. Since the observations are compared to the DWD derived reference profiles in the analysis only profiles with a difference of $\leq$ 50 km in the mean tangent point location with respect to DWD enter the calculations.

Careful quality control at all stages of the analysis proved to be essential to reliably remove outliers in bending angle and refractivity space, which would spoil the statistics, where one has to be careful not to exclude too many observations from the analysis. Sensitivity tests using different percentage thresholds for data filtering suggest that the method used here provides a simple but reliable quality monitoring framework. The complication for standard RO data products is the in general missing bending angle reference.

3 Baseline of the Comparison

The baseline of the comparison are bending angles as function of 247 fixed impact heights (impact parameter minus radius of curvature) up to $\sim$60 km and refractivities at an equidistant 200 m grid above ellipsoid (WGS-84) covering an altitude range from 0–45 km (226 vertical levels). This data is complemented by collocated ECMWF profiles (at the profile's mean tangent point location) and the respective

---

[2] For instructions to download the ROPP-Package go to http://www.grassaf.org/ROPP_package.php

derived refractivities (plus the ray-traced bending angles for DWD). The mean tangent point is calculated as the average of the tangent point track of the observations from the lowermost 20 km of a profile. By doing so, the mean tangent point is effectively weighted towards lower altitudes (von Engeln 2006a). The ECMWF collocated profiles are derived from operational analysis fields retrieved at a 1° by 1° spatial resolution comprising 60 vertical levels, which are interpolated to the comparison grid. The time layer (of four available per day) closest (in time) to the profile had been used.

DWD provided beside the ECMWF derived reference refractivity two sets of reference bending angle data sets, based on an Inverse Abel procedure and raytracing. Since the DWD data set contains most profiles, which enter the comparison (cf. Table 3) the ray-traced bending angles and consequently the respective reference refractivities have been used as data to compare against. Still one has to keep in mind that in our comparison the differences between the retrieved results are most important, although the comparison to ECMWF (in bending angle and refractivity space) provides some added value to the analysis.

To analyze the data, basic statistical quantities like bias, median, standard deviation, and variance had been used. First assessments indicated the presence of outliers or unphysical values in the data set. This assumption had been verified by comparing the median (median of the differences to the reference) of the deviations against the bias. After introducing the quality control procedures (cf. Sect. 2), both values agree well indicating the successful removal of corrupted profiles and data points, although the agreement between the different centers is still slightly better using the median in refractivity space. That indicates that a few profiles influence the statistics disproportionately. The calculations had been performed for each set of profiles separately where first the matches with the DWD data set had been determined. The analysis was then performed based on differences to the DWD reference data as common baseline. One has to notice that DWD is compared against its own provided reference in contrast to WEGC and DMI. Since the relative differences between the centers are the focus of this study, no side effects are expected to be introduced due to that fact.

Table 3 Processed ROPIC data set where the difference between passed profiles in Table 3 and raw data profiles in Table 2 is composed of profiles, which could not be processed to bending angles and profiles flagged as bad by the centers. Matches indicates profiles entering the analysis (matching DWD profiles and a mean tangent point location agreeing $\leq 50\,\mathrm{km}$), QC refers to the quality control conducted by the centers

	January		July		Total	
	Processed and passed QC	Matches	Processed and passed QC	Matches	Processed and passed QC	Matches
DMI	4262	4142	5043	4944	9305	9086
DWD	4454	–	5066	–	9520	–
WEGC	3520	2939	4138	3398	7658	6337

A different number of profiles per center enters the analysis thus the sample sizes are different. To assess if this approach has any implications the analysis was performed a second time only taking profiles into consideration, which are present in each data set, thus the sample size was equal for each center. The differences are negligible proving that our approach to maximize the number of analyzed profiles does not introduce any sampling error.

4 Results

To illustrate the results a subset of plots based on the differences between profiles and respective references is shown. We focus here on the low, mid, and high latitude Southern Hemisphere for July as exemplary cases. The high latitude Southern Hemisphere case demonstrates the level of consistency between the different data sets concerning the pronounced increments (Gobiet et al. 2005) present during the Antarctic winter in the ECMWF analyses 2005.

The overall agreement between the bending angles derived by the different centers is good up to an altitude of 30 km at southern high, 35 km at mid respectively up to 40 km at low latitudes. The agreement gets worse within the last few kilome-ters above the ground but as can be seen in the plots the number of profiles equally declines (WEGC profiles terminate at 4 km for high, at 5 km for mid and at 8 km for low latitudes in refractivity space) although WEGC exhibits a systematic deviation compared to DWD and DMI. The atmospheric increments compared to ECMWF at southern high latitudes are captured by all data sets consistently. At high altitudes WEGC derived values start to deviate from the other two centers at 30 km in the high, 35 km in the mid, and 40 km at low latitudes whereas DWD and DMI still agree with each other. This effect most likely stems from the different high altitude initialization where DMI and DWD are using the MSISE-90 (Mass Spectrometer Incoherent Scatter) model (Hedin 1991). The fit to (and selection of) MSISE is done in the range from 40–60 km in a dynamical way for each occultation. The actual transition from measurement to MSISE is on average done between 30 km and 50 km such that MSISE represents 0% at 30 km and 100% at 50 km in the results (this description applies for DMI, DWD uses similar procedures). The WEGC bending angle profile is statistically optimized between 30 km and 120 km, at the lower part with co-located ECMWF profiles and above ∼60 km with profiles from the MSISE-90 climatology.

This explains the rapid decrease in the number of the accepted profiles in the DWD and DMI cases at altitudes of ∼45 km and above (QC threshold 20% relative deviation from reference) since the difference between MSISE-90 and the observed atmosphere can be significant.

These results give a hint that we have here one example of parametric uncertainty caused by auxiliary information introduced during the processing. This information leaves a signature in the data, which in theory exponentially decreases with altitude (in the case of high altitude initialization) but still might influence observations in the atmospheric domain of interest. That is important if the data is used within a climate context and non static (in time) auxiliary data is present in the processing. What can be observed in bending angle space is to a certain extend translated to refractivity space where WEGC seems to be drawn to the reference at altitudes above 30 km. WEGC's systematic deviations to DMI and DWD apparent in all plots are somewhat reduced in the median compared to the bias. The altitude dependent pattern of the deviation is significantly different in the high, mid, and low latitudes thus it is very unlikely that they are caused by a single effect; the pattern appears in a reduced height interval in the mid latitudes.

One can notice the decrease of penetration depth of profiles towards the tropics in Figs. 1, 2, and 3 (refractivity space) which can be clearly related to the moist atmosphere, which is still a challenge for the processing algorithms. In any latitude band DWD profiles exhibit the best penetration performance, in the WEGC data set

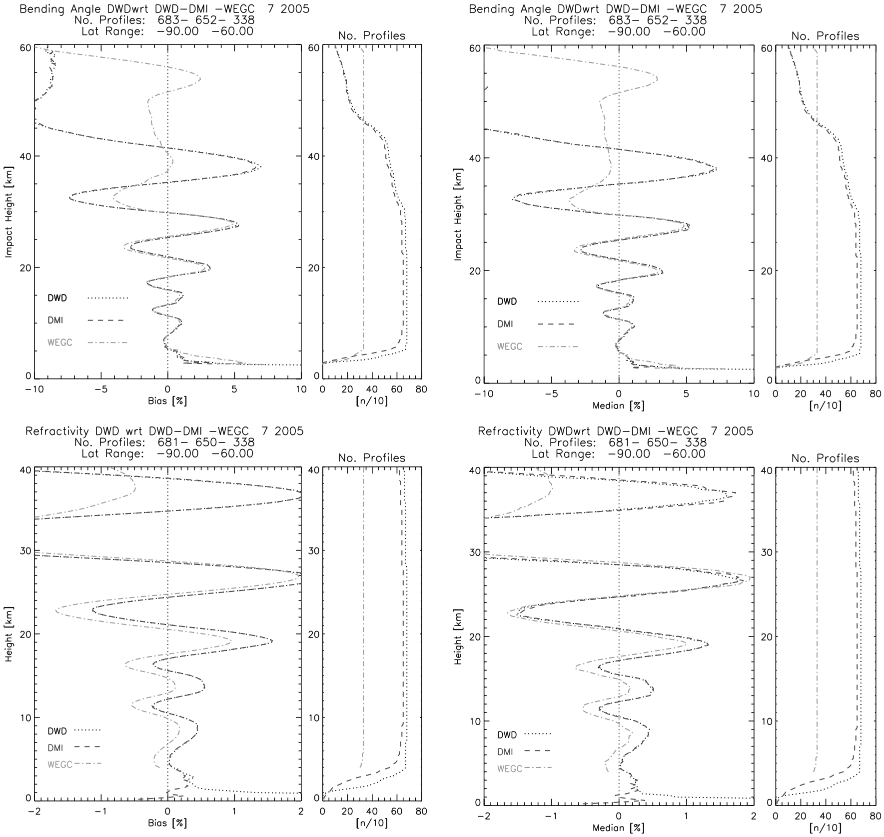

Fig. 1 This panel shows bending angle and refractivity bias to the *left* and the respective median of difference profiles between 60° and 90° south from July 2005 on the *right* (different vertical and horizontal axes for bending angle and refractivity)

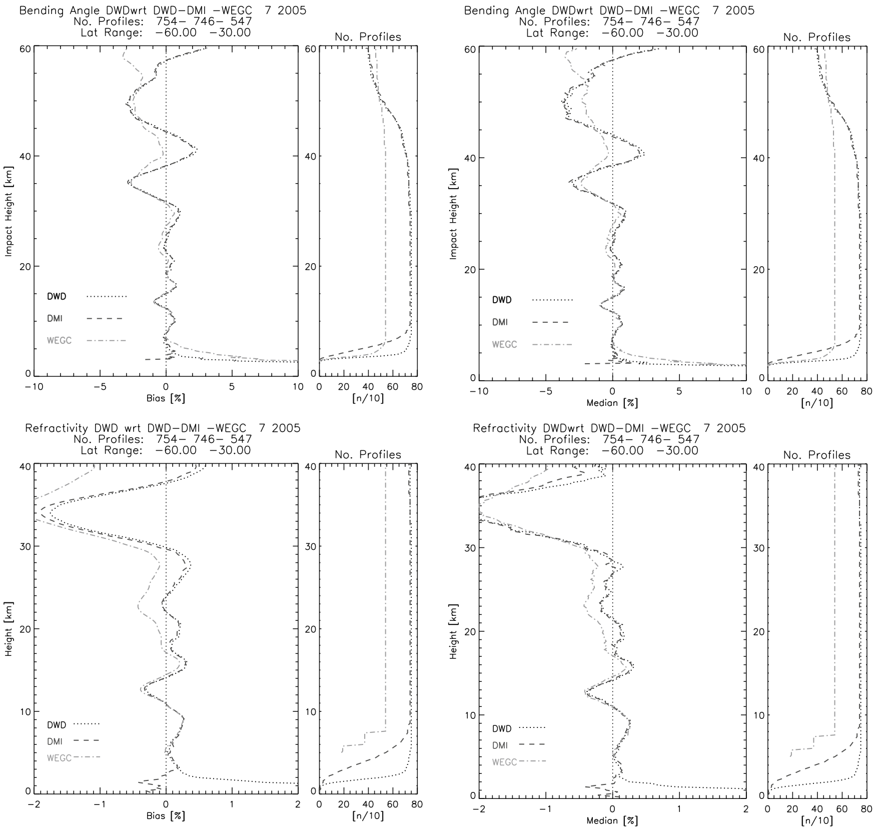

Fig. 2 This panel shows bending angle and refractivity bias to the *left* and the respective median of difference profiles between 30° south and 60° south from July 2005 on the *right* (different vertical and horizontal axes for bending angle and refractivity)

observations are completely absent from a certain altitude which increases from the poles towards the equator in refractivity space. This can be attributed to the used GO processing which cannot cope with the strong refractivity gradients present in moist dense atmospheric regimes, wave optics methods are performing better in such an environment. That is reflected in bending angles, which apparently cannot be processed to refractivities.

Another interesting feature to note is that the median seems to move the DMI and DWD results a bit away from the reference compared to the deviations visible in the bias plots, an effect which appears at high altitudes.

The results suggest that all retrieval chains capture the same atmospheric features below 30–40 km depending on latitude, but the systematic differences relative to each other show that those features are captured at different magnitude. This behavior had been confirmed for the rest of the data set not presented here. The indication

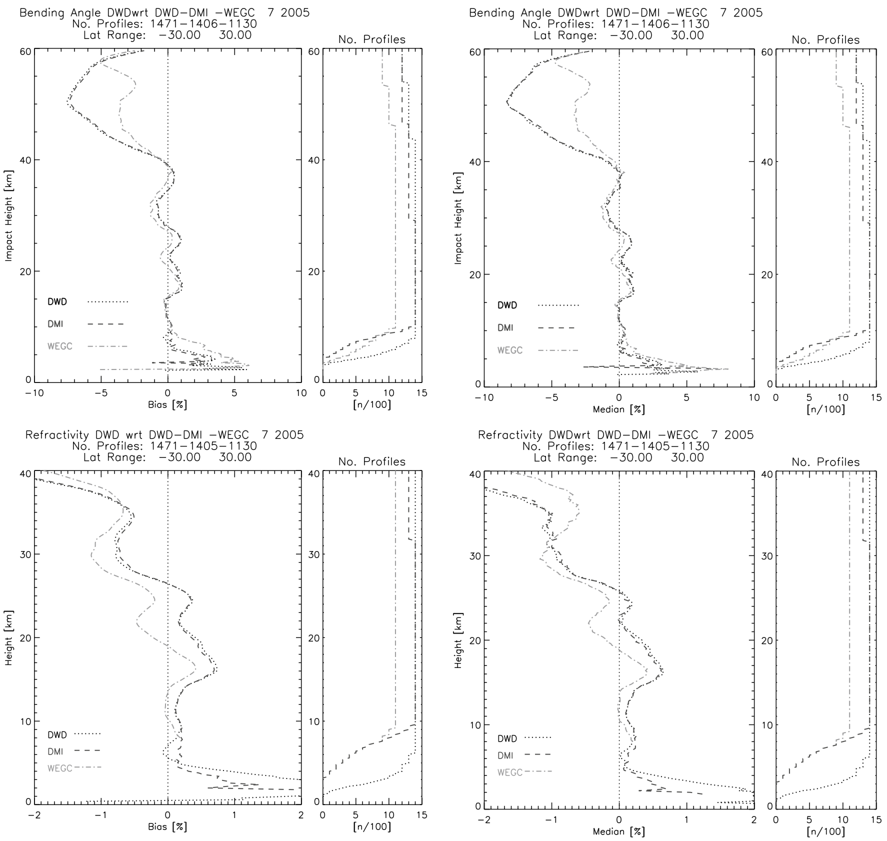

Fig. 3 This panel shows bending angle and refractivity bias to the *left* and the respective median of difference profiles between 30° south and 30° north from July 2005 on the *right* (different vertical and horizontal axes for bending angle and refractivity)

is that outliers can be ruled out as possible cause of the remaining deviations (as the median suggests).

5 Conclusion

The ROPIC campaign serves to assess the level of independence RO data exhibits concerning the used processing chain. Not surprising DMI and DWD derived results agree very well with each other since the underlying processing chains are based not only on the same theory (combination of geometrical optics at high altitudes and CT2 at lower altitudes) but also exhibit similar initialization strategies and partly share the same code base. WEGC is using a different approach (only geometrical optics processing) but still the results agree reasonably well in the altitude domain of interest concerning the representation of atmospheric features. Nevertheless, the data still exhibits systematic deviations, which are latitude dependent. This behavior should be assessed further; the deviations apparent at high altitudes most likely stem from the different initialization strategies. If this assumption is correct, it would illustrate an example for parametric uncertainty of RO processing.

These results highlight the potential of RO data for climate applications on one hand but also indicate the need of close cooperation between the different centers to consolidate their processing, to identify systematic deviations, and improve overall robustness. The output of more independent processing chains is needed to better quantify the bandwidth of variations (DMI and DWD processing chains are not strictly independent) and to realistically estimate the magnitude of structural uncertainty.

Agreement should be reached on open issues like a common definition of the mean tangent point or discretization schemes making it easier to relate differently processed data to each other. Since agreement on internal processing procedures is not expected to be reached, I would suggest to provide at least the tangent point track as a standard data product.

Another important step would be the development of reliable quality standards for data products in an ideal case relying on methods for filtering based purely on observed quantities not dependent on auxiliary reference data.

This first assessment should provide a starting point for further investigations, which should have a thorough look at the different processing strategies and auxiliary data used. In an ideal scenario, the current data set would be supplemented by more independently derived data sets to have a better chance of estimating the performance envelope of RO defined by structural and parametric uncertainty.

Especially for climate applications which can rely on the monitoring of relative changes instead of the absolute values the auxiliary data used should be static (static in the sense of not changing as a function of time). In that case, any systematic deviation introduced by the auxiliary data is static too and relative changes are not masked by their variation.

Acknowledgements The authors want to thank J. Wickert and T. Schmidt (GFZ, Potsdam, Germany) for making available the excess phase and orbit CHAMP data, M. Borsche (WEGC, Austria), and D. Pingel, A. Rhodin (DWD, Germany) for providing the processed CHAMP profiles. The GRAS- SAF (supported by DMI and EUMETSAT), Georg Bergeton Larsen (DMI, Denmark) is thanked for enabling this study within a visiting scientist project. The authors are further thankful for fruitful discussions with A. v. Engeln (EUMETSAT), and M. E. Gorbunov (Institute for Atmospheric Physics, Russia).

References

Ao CO, Schreiner WB, Wickert J (2003) First report on the CHAMP Radio Occultation Intercomparison Study. JPL Publication 03–016, Pasadena

von Engeln A (2006a) An Analysis of CHAMP Radio Occultation Data. Forecasting Technical Report No 471, MetOffice, UK von Engeln A (2006b) A first test of climate monitoring with radio occultation instruments: Comparing two processing centers. Geophys Res Lett 33(L22705), doi: 10.1029/2006GL027767

Foelsche U, Gobiet A, Löscher A, Kirchengast G, Steiner AK, Wickert J, Schmidt T (2005) The CHAMPCLIM project: An overview. In: Reigber C, Luehr H, Schwintzer P, Wickert J (eds) Earth Observation with CHAMP: Results from Three Years in Orbit, Springer Verlag, Berlin, pp 615–619

Foelsche U, Borsche M, Steiner AK, Gobiet G, Pirscher B, Kirchengast G, Wickert J, Schmidt T (2008) Observing upper troposphere-lower stratosphere climate with radio occultation data from the CHAMP satellite. Clim Dyn 31:49–65, doi:10.1007/s00382-007-0337-7

Foelsche U, Pirscher B, Borsche M, Kirchengast G, Wickert J (2009) Assessing the climate monitoring utility of radio occultation data: From CHAMP to FORMOSAT-3/COSMIC. Terr Atmos Oceanic Sci 20(1):155–170, doi:10.3319/TAO.2008.01.14.01(F3C)

Gobiet A, Foelsche U, Steiner AK, Borsche M, Kirchengast G, Wickert J (2005) Climatological validation of stratospheric temperatures in ECMWF operational analyses with CHAMP radio occultation data. Geophys Res Lett 32(L12806), doi:10.1029/2005GL022617

Gobiet A, Kirchengast G, Manney GL, Borsche M, Retscher C, Stiller G (2007) Retrieval of temperature profiles from CHAMP for climate monitoring: intercomparison with Envisat MIPAS and GOMOS and different atmospheric analyses. Atmos Chem Phys 7:3519–3536

Gorbunov ME (2002) Canonical transform method for processing radio occultation data in lower troposphere. Radio Sci 37(5), doi:10.1029/2000RS002592

Gorbunov ME (2005) Operational Processing of CHAMP Data: Mathematical Methods, Data Filtering and Quality Control. Scientific Report 05-07, Danish Meteorological Institute, Copenhagen, Denmark, http://www.dmi.dk/dmi/SR05-07.pdf

Gorbunov ME Lauritsen KB (2002) Canonical Transform Methods for Radio Occultation Data. Scientific Report 02–10, Danish Meteorological Institute, Copenhagen, Denmark, http://www.dmi.dk/dmi/Sr02-10.pdf

Gorbunov ME, Lauritsen KB (2006) Radio holographic filtering of noisy radio occultations. In: Foelsche U, Kirchengast G, Steiner AK (eds) Atmosphere and Climate: Studies by Occultation Methods, Springer-Verlag, Berlin Heidelberg New York, pp127–134

Gorbunov ME, Lauritsen KB, Rhodin A, Tomassini M, Kornblueh L (2006) Radio holographic filtering, error estimation, and quality control of radio occultation data. J Geophys Res 111(D10105), doi:10.1029/2005JD006427

Hajj GA, Kursinski ER, Romans LJ, Bertiger WI, Leroy SS (2002) A technical description of atmospheric sounding by GPS occultation. J Atmos Solar-Terr Phys 64:451–469

Hajj GA, Ao CO, Iijima BA, Kuang D, Kursinski ER, Mannucci AJ, Meehan TK, Romans LJ, de la Torre Juarez M, Yunck TP (2004) CHAMP and SAC-C atmospheric occultation results and intercomparisons. J Geophys Res 109(D06109), doi:10.1029/2003JD003909

Healy SB, Thépaut JN (2006) Assimilation experiments with CHAMP GPS radio occultation measurements. Quart J Roy Meteorol Soc 132:605–623, doi:10.1256/qj.04.182

Hedin AE (1991) Extension of the MSIS thermosphere model into the middle and lower atmosphere. J Geophys Res 96(A2):1159–1172

König R, Michalak G, Neumayer K, Schmidt R, Zhu S, Meixner H, Reigber C (2005) Recent developments in CHAMP orbit determination at GFZ. In: Reigber C, Schwintzer P, Lühr H, Wickert J (eds) Earth Observation with CHAMP: Results from Three Years in Orbit, Springer Verlag, Berlin, pp 65–70

Kursinski ER, Hajj GA, Schofield JT, Linfield RP, Hardy KR (1997) Observing Earth's atmosphere with radio occultation measurements using the global positioning system. J Geophys Res 102:23429–23465

Leroy SS, Anderson JG, Dykema JA (2006) Testing climate models using GPS radio occultation: A sensitivity analysis. J Geophys Res 111(D17105), doi:10.1029/2005JD006145

Löscher A, Kirchengast G (2008) Variational data assimilation for deriving global climate analyses from GNSS radio occultation data. GPS Solut 12(4):227–235, doi:10.1007/s10291-008-0087-y.

Löscher A, Retscher C, Fusco L, Goncalves P, Brito F, Kirchengast G (2008) Variational optimization for global climate analysis on ESA's high performance computing grid. Remote Sensing of Environment, Special Issue: Remote Sensing Data Assimilation 112:1450–1463, doi:10.1016/j.rse.2007.05.022

Loiselet M, Stricker N, Menard Y, Luntama JP (2000) GRAS – MetOp's GPS-based atmospheric sounder. ESA Bull 102:38–44

Luntama JP, Kirchengast G, Borsche M, Foelsche U, Steiner AK, Healy SB, von Engeln A, O'Clerigh E, Marquardt C (2008) Prospects of the EPS GRAS mission for operational atmospheric applications. Bull Amer Meteorol Soc 89:1863–1875, doi:10.1175/2008BAMS2399.1

Ringer MA, Healy SB (2008) Monitoring twenty-first century climate using GPS radio occultation bending angles. Geophys Res Lett 35(L05708), doi:10.1029/2007GL032462

Rocken C, Kuo YH, Schreiner WS, Hunt D, Sokolovskiy SV, McCormick C (2000) COSMIC system description. Terr Atmos Ocean Sci 11:21–52

Schreiner WS, Hunt DC, Rocken C and Sokolovskiy S (1998) Precise GPS data processing for the GPS/MET radio occultation mission at UCAR. Proceedings of the Institute of Navigation 2000, Alexandria, VA, pp 103–112

Wickert J, Beyerle G, Hajj GA, Schwieger V, Reigber C (2002) GPS radio occultation with CHAMP: Atmospheric profiling utilizing the space-based single difference technique. Geophys Res Lett 29(8), doi:10.1029/2001GL013982

Wickert J, Schmidt T, Beyerle G, König R, Reigber C, Jakowski N (2004) The radio occultation experiment aboard CHAMP: Operational data analysis and validation of vertical atmospheric profiles. J Meteorol Soc Japan 82:381–395

Radio Occultation Soundings in Ionosphere and Space Weather Applications: Achievements and Prospects

J.-P. Luntama

Abstract It is well known that the GNSS (Global Navigation Satellite System) signals are affected by the dispersive ionosphere, when the signals pass through it on their way from the transmitter to the receiver. The impact of the ionosphere is an error source that is usually eliminated in the ground based GNSS navigation applications and in the retrieval of the characteristics of the neutral atmosphere from the RO (Radio Occultation) soundings. However, both RO soundings and ground based GNSS observations can also be used to monitor the characteristics of the ionosphere and the plasmasphere. RO soundings for ionospheric tomography were proposed for the first time already in 1988 (Austen et al. 1988). The first demonstration of the soundings were performed by the GPS/MET mission. Many other RO missions (Oersted, CHAMP, SAC-C, and GRACE) have also included ionospheric soundings into their mission objectives. IOX (Ionospheric Occultation Experiment) was a dedicated ionospheric RO instrument onboard the PICOSat satellite. The ongoing FORMOSAT-3/COSMIC mission has already provided over 800 000 ionospheric soundings during the first 14 months of the mission. The new data produced by the GNSS soundings has generated significant advances in the radio science of the Earth's atmosphere and the ionosphere. Global coverage and continuous data production have enabled new types of services providing information about the status of the ionosphere in NRT (Near Real Time). Some emerging applications of GNSS observations include e.g., regional high resolution ionospheric tomography and monitoring and prediction of ionospheric scintillation. This paper gives an overview of the scientific achievements with the ionospheric RO soundings from the past and from the current RO missions, and discusses the prospects of the GNSS "space weather" applications in the near future.

J.-P. Luntama (✉)
Finnish Meteorological Institute, Helsinki, Finland
e-mail: juha-pekka.luntama@fmi.fi

A. Steiner et al. (eds.), *New Horizons in Occultation Research*,
DOI 10.1007/978-3-642-00321-9_6,

1 Introduction

"Space Weather" is a generic name for the variations caused by the solar wind in the electromagnetic and the particle environment in the Earth's ionosphere and magnetosphere above the height of 100 km. Space weather effects may impact also the lower ionosphere below 100 km, e.g., during proton events, causing polar cap absorption and changes in the upper atmosphere chemistry. Space weather is driven by the Sun. Thus, also the disturbances caused by the space weather follow the 11 year solar activity cycle. Currently the solar activity (the number of Sun spots) is very low, i.e., we are at a solar minimum. The next solar maximum is expected to take place in 2011/2012. At the moment we cannot reliably predict whether the next solar maximum will be stronger or weaker than the previous maximum in 2001. The official prediction issued by the Solar Cycle 24 Prediction Panel is available from the NOAA (National Oceanic and Atmospheric Administration) SWPC (Space Weather Prediction Center) web page (http://www.swpc.noaa.gov/SolarCycle/SC24/index.html).

Space weather impacts the human activities in many ways. The most obvious dangers are of course the solar radiation and the charged particles damaging the Earth orbiting satellites or an interplanetary spacecraft. The radiation and the particles can also endanger the health of the humans during a spaceflight. The danger from the solar radiation and the particles is significantly bigger outside the Earth's magnetosphere, i.e., in a spacecraft on the way to the Moon or to other planets. Space weather can also damage ground based systems on the Earth through electromagnetic induction. Space weather events can also cause problems in commercial aviation by disturbing HF and VHF radio communications at polar regions and by increasing the radiation doses of the crew members of the high flying aircraft.

The final report of the COST 724 action defines the "space weather" as *Space weather is the physical and phenomenological state of natural space environments. The associated discipline aims, through observation, monitoring, analysis and modelling, at understanding and predicting the state of the sun, the interplanetary and planetary environments, and the solar and non-solar driven perturbations that affect them; and also at forecasting and nowcasting the possible impacts on biological and technological systems* (http://cost724.obs.ujf-grenoble.fr/). RO soundings of the planetary ionospheres and the interplanetary plasma fit very nicely to observation and monitoring aspects of this definition. In this paper, the focus is especially in the observation of the ionosphere of the Earth.

2 History of Ionospheric RO Soundings

The first RO ionospheric soundings related proposal was made by a group at the Stanford University in 1962. The objective of this proposal was to study interplanetary charged particles and plasma with the radio signals transmitted by the Mariner probes. Another measurement scheme was proposed independently by a group at the

Jet Propulsion Laboratory (JPL) in 1963 (Kliore et al. 1964). The result of these two proposals was the establishment of a collaborating experiment team for the NASA Mariner 3 and 4 missions. This collaboration between JPL and Stanford University continued over 20 years developing "radio science" as a technique for planetary exploration. A more detailed history of the early years of the RO soundings is presented in Melbourne et al. (1994).

The sounding of the Earth's ionosphere with the GNSS observations was first introduced in 1988. The ionospheric soundings were included into a memo written by Dr. Gunnar Lindal in the framework of the preparation of an instrument proposal for the NASA Earth Observing System (EOS) (Lindal 1988). Almost simultaneously a paper envisioning ionospheric tomography with multiple observations of the Earth satellite links was published (Austen et al. 1988). Despite some setbacks due to e.g., changes in the NASA program plans, these two publications led into series of publications and proposals to promote RO soundings (e.g., Yunck et al. 1988; Yunck and Melbourne 1989; Melbourne et al. 1994).

The starting point of the first RO demonstration mission was a proposal submitted to the National Science Foundation (NSF) in the US by a group at the University Corporation for Atmospheric Research (UCAR). With the support from NSF and with co-sponsorship by the US National Oceanic and Atmospheric Administration (NOAA), the Federal Aviation Administration, and the Orbital Sciences Corporation, the GPS/MET mission was initialized. The launch of the GPS/MET instrument onboard NASA's MicroLab I spacecraft took place in April 1995.

The history of the neutral atmosphere soundings by RO and many details of e.g., the GPS/MET mission are described by Yunck et al. (2000). It is important to note that the ionospheric soundings have been included into the mission planning from the beginning of RO. The GPS/MET mission already included dedicated ionospheric measurement campaigns e.g., in October 1996 and in January 1997. Ionospheric soundings have been performed more continuously in later RO missions like CHAMP, SAC-C, and GRACE. The most comprehensive amount of ionospheric soundings has been naturally provided by the ongoing, multi-satellite FORMOSAT-3/COSMIC mission.

Table 1 lists the past RO satellite missions and their status. It should be noted that both Oersted and SUNSAT had severe technical problems with their RO receivers and very little useful data was generated (but both missions were highly successful in their other objectives). Both UCAR (University Corporation for Atmospheric Research) and JPL have archives containing data from the RO missions in which they have been involved. These data are available for free for registered scientific users. The name of the UCAR data archive is CDAAC (COSMIC Data Analysis and Archive Center) and it can be accessed over the Internet (http://cosmic-io.cosmic.ucar.edu/cdaac/index.html). The JPL RO data archive is called GENESIS (Global Environmental & Earth Science Information System) and it is also accessible over the Internet (http://genesis.jpl.nasa.gov/zope/GENESIS). The data from the GRAS instrument is disseminated in NRT to the EUMETSAT user community. Scientific users can also access the archived data via the EUMETSAT UMARF (Unified Meteorological ARchive Facility) service (http://www.eumetsat.int/).

Table 1 RO satellite missions

Launch year	Mission	Status
1995	GPS/MET	Decommissioned
1999	Oersted	Decommissioned
1999	SUNSAT	Decommissioned
2000	CHAMP	Active
2000	SAC-C	Active
2001	PICOSat IOX	Decommissioned
2002	GRACE	Active
2006	FORMOSAT-3/COSMIC	Active
2006	EPS GRAS	Active
2007	TerraSAR-X	Commissioning Phase

3 Achievements

The achievements of the ionospheric RO soundings naturally include all observations of the interplanetary plasma and the ionospheres of the planetary bodies. Some of the early achievements of the radio science have already been noted in Sect. 2. The use of RO soundings to monitor the ionospheres of the planets is far from over. For example Hinson et al. (2007) have recently presented new results from observing the neutral atmosphere of Mars and Häusler et al. (2006) have published results from the Venus Express Radio Science Experiment (VeRa) onboard the Venus Express spacecraft. RO soundings have also been used to observe the characteristics of the plasma turbulence in the solar wind (e.g., Chashei et al. 2005).

This section provides a look at the achievements of the ionospheric RO soundings in the monitoring of the Earth's ionosphere and the plasmasphere. This discussion includes also the monitoring of the ionosphere with ground based GNSS observations, because it is very often necessary or at least useful to combine these two types of observations. The combined data provides a better coverage and potentially provides a better resolution e.g., in ionospheric tomography.

One aspect that has significantly contributed to the success of the RO science for the Earth is the open source data policy that has been adopted by most RO missions. This policy was started by the GPS/MET experiment. The opportunity for the whole scientific community to access and "play" with the GPS/MET data was an important factor for the success of the mission. Without doubt the possibility to use GPS/MET data in research projects also triggered quite a few new scientific careers.

3.1 Ionospheric RO Science

The basic application of the ionospheric RO soundings is clearly the possibility to measure the vertical electron density profile. This measurement shares the same benefits and drawbacks as the RO soundings of the neutral atmosphere. The vertical resolution provided by the ionospheric RO soundings is in principle very high. However, the retrieved TEC (Total Electron Content) values represent an integral of the electron content over a very long horizontal propagation path. In neutral atmosphere the pressure dependence of the atmospheric refraction index makes the inversion of the measurement time series into a vertical profile relatively easy. In the case of the ionosphere, the inversion of the measured TEC to a vertical electron density profile can be performed by using an assumption of a spherical symmetry (Lei et al. 2007). However, in the presence of horizontal electron density gradients, this technique will produce only an approximation of the true profile. Taking additional information about the horizontal structure of the ionosphere into account makes the inversion significantly more complicated. In this case the inversion requires the use of a background electron density model (e.g., Heise et al. 2002; Jakowski et al. 2002; Stolle et al. 2004). An example of electron density and plasma frequency profiles retrieved from a CHAMP sounding is presented in Fig. 1. An example of an intercomparison of electron density retrievals from CHAMP RO soundings and collocated ionosonde observations is provided in Fig. 2.

Many RO missions use GNSS observations for the Precise Orbit Determination (POD). Because the data for POD should be as free from the atmospheric disturbance as possible, these measurements are normally made to the direction of the spacecraft zenith. This gives another possibility to monitor the ionosphere and the

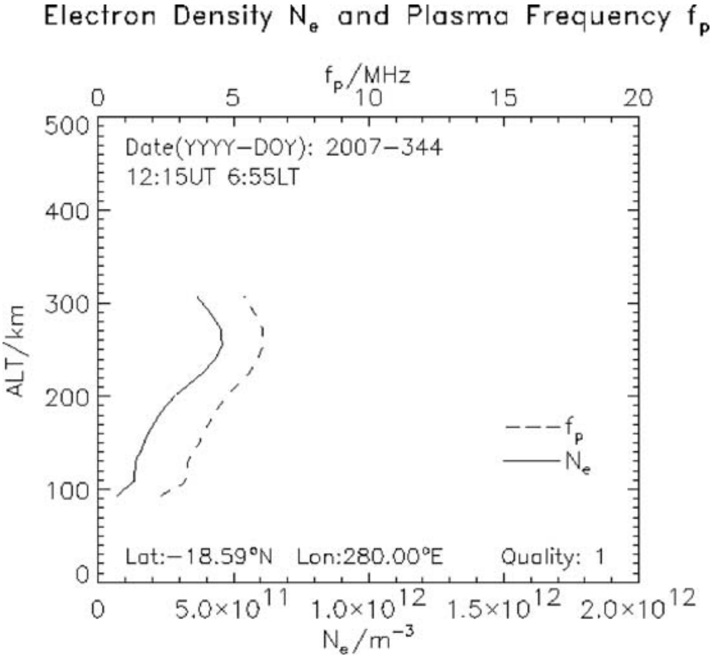

Fig. 1 Electron density and plasma frequency profiles from CHAMP sounding on December 10, 2007. Picture courtesy of DLR project Space Weather Application Center – Ionosphere

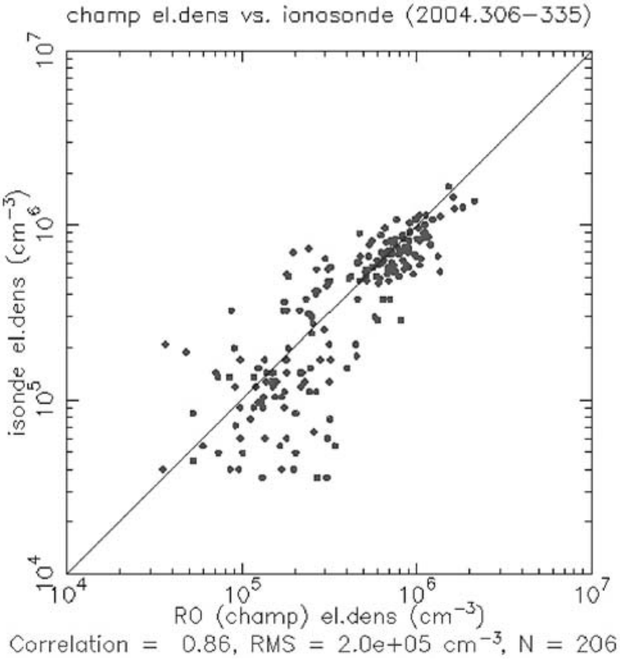

Fig. 2 Intercomparison of electron density profiles from CHAMP soundings and collocated ionosonde measurements. Picture courtesy of UCAR/CDAAC

plasmasphere. The zenith GNSS observations can be used to calculate the TEC above the spacecraft and they can also be assimilated into an electron density model for ionospheric tomography.

Ionospheric tomography is a research field that has gained significantly from the development of the GNSS. The most significant advantages of the GNSS observations are the global coverage and the continuity of the observations. For example, the network of the observing stations in the IGS (International GNSS Service) provides globally GPS tracking data sampled as minimum at 30 s intervals (Dow et al. 2005). Many IGS stations provide currently also observations at 1 Hz sampling. IGS observations are used by many groups and institutes to retrieve global TEC estimates. Also IGS products available through the IGS website (http://igscb.jpl.nasa.gov/) include global TEC maps. However, high resolution ionospheric tomography is difficult by using only ground based observations. A possible approach is to combine spaceborne RO soundings with the ground based observations (e.g., Jakowski et al. 2002; Mandrake et al. 2004). The horizontal resolution of the ionospheric tomography can be improved significantly by using dense regional GNSS networks (e.g., Luntama et al. 2007). The research on combining ground based observations from dense regional networks with the spaceborne RO soundings is ongoing.

In addition to the ionospheric electron distribution profiling, new innovations to take advantage of the ionospheric RO soundings are continuously coming up. An example of a new idea is e.g., the detection of the sporadic E-layer by monitoring the amplitude data from the RO soundings (Viehweg et al 2007). Another interesting new area is the "GNSS reflectometry". Using the reflected GNSS signals to determine the wind speed over the oceans and for ocean surface altimetry has been demonstrated with real RO data (Beyerle et al. 2002; Gleason et al. 2005; Yunck and Hajj 2005). To use the reflected GNSS signals also to measure the electron density distribution in the ionosphere has been proposed by Pallares et al. (2005).

Another area where the ionospheric RO soundings have made a big impact is the development of the ionospheric models. One reason for this is that the GNSS applications also need the support of the ionospheric models to mitigate the error caused by the ionosphere in the navigation applications based on single frequency GNSS receivers. The continuous development of the ionospheric "climatology" models like IRI (International Reference Ionosphere), NeQuick, and GIM (Global Ionospheric Mapping) is potentially very useful for the single frequency GNSS applications. All these models can also be driven with observation based input parameters. This means that the models can be used to pass the observed ionospheric characteristics to the users globally or regionally.

GNSS observations have driven also the development of ionospheric models for data assimilation. The basic need has been the feasibility to combine the ground based and the spaceborne GNSS observations with the other types of observations. The development of the physical based models is still very much ongoing, but some models are already rather advanced. Two models under development in the US are both called GAIM (Global Assimilation of Ionospheric Measurements). One GAIM model is being developed by the JPL/USC (Wang et al. 2004) and the other one by the Utah State University (Schunk et al. 2004). Another model that has been used in data assimilation is the PIM (Parametric Ionospheric Model) (e.g., Daniell et al. 1995; Stankov et al. 2007).

Observation of the ionospheric scintillations is an area that has not yet been much addressed with RO soundings. One reason for this is that the measurement of the scintillation characteristics is not easy and the spaceborne RO receivers have not yet been specially designed for this purpose. Amplitude variations in the CHAMP RO soundings have been analyzed and compared to the scintillation observations in the satellite telecommunication links (e.g., Wickert et al. 2004). New results from the scintillation monitoring from the COSMIC mission have recently been presented by Starks et al. (2007) in the AGU 2007 Joint Assembly.

3.2 Operational Services

Operational space weather services are an area, where the ionospheric RO soundings are gradually making an impact (see Table 2). It is very clear, that the spaceborne observations of the Sun are the main source of information for the services like the NOAA SWPC (Space Weather Prediction Center). However, the GNSS observations have enabled the monitoring of the impacts of the solar activity on

Table 2 Examples of the space weather services

Name	Web address
SWPC (Space Weather Prediction Center)	http://www.swpc.noaa.gov/
ESA Space Weather Web Server	http://esa-spaceweather.net/
SWACI (Space Weather Application Center – Ionosphere)	http://w3swaci.dlr.de/
CODE (Center for Orbit Determination in Europe)	http://cmslive2.unibe.ch/unibe/philnat/aiub/content/research/gnss/code___research/index_eng.html
JPL	http://iono.jpl.nasa.gov/
Radio Propagation Project	http://wdc.nict.go.jp/IONO/index_E.html

the ionosphere in the real time. This is very important because the ionospheric conditions affect the satellite applications like telecommunications and satellite navigation. The research to use the GNSS observations to predict the ionospheric storms and scintillation is ongoing.

Most operational or semi-operational ionospheric monitoring services are concentrating on the monitoring of the TEC. Many services like CODE at the University of Bern and SWACI at DLR (Deutsches Zentrum für Luft- und Raumfahrt) provide NRT TEC maps through their web portals. Examples of a global TEC map provided by the CODE service and an European TEC from the SWACI service are presented in Fig. 3 (a) and (b), respectively. The SWACI service provides also maps of the TEC error estimates, the TEC latitude and longitude gradients, and the TEC rate of change. SWACI is also producing three dimensional maps of the ionospheric

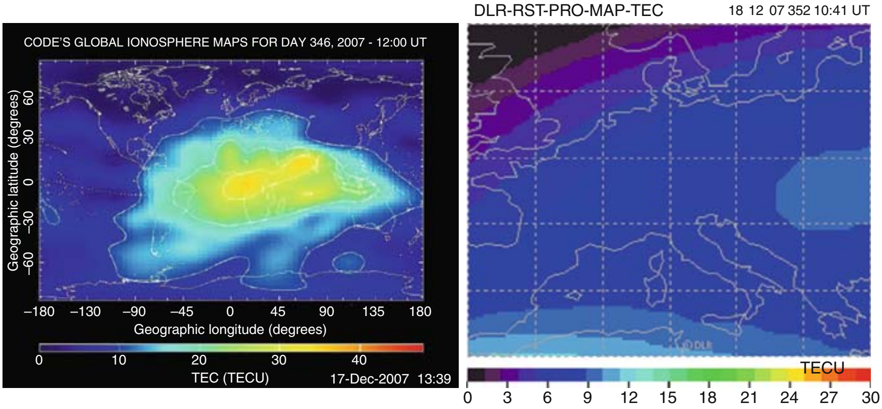

(a) (b)

Fig. 3 (**a**) Global NRT TEC map produced by the CODE service at the University of Bern. (**b**) TEC map over Europe from the SWACI service at DLR. Pictures courtesy of University of Bern and DLR project Space Weather Application Center–Ionosphere and plasmaspheric electron density. This activity is based on combining spaceborne ionospheric GNSS observations with the PIM model (Heise et al. 2002).

4 Prospects for the Future

The future of the RO science looks very promising—at least from the point of view of the signal sources. The GNSS (Global Navigation Satellite System) is expanding with three new satellite constellations. Russia is gradually upgrading the GLONASS system into a fully operational status with 21 active and 3 in-orbit spare satellites. China is rapidly developing the Compass navigation satellite system that will include 30 MEO (Middle Earth Orbit) satellites and 5 GEO (Geostationary Earth Orbit) satellites. Finally, EU has recently agreed on the final funding to fully deploy the Galileo satellite constellation with 27 operational satellites and 3 in-orbit spares. With all four satellite systems fully operational, the RO community will be able to enjoy an environment with more than 100 satellites transmitting signals suitable for RO soundings. This is of course feasible only in the case that all GNSS systems are open for civilian use.

The multitude of the GNSS constellations creates naturally also challenges. The spaceborne RO receivers should be designed to take advantage of all GNSS constellations. At least that would maximize the number of observations per receiver. However, it is not yet clear if the compatibility is sufficient to allow designing of spaceborne receivers that can use all future GNSS satellites.

Another promising indication for the RO community is the very positive signal from the NWP users. The results from assimilating the CHAMP and the COSMIC observations into the NWP models have been very promising (Healy et al. 2005; Healy and Thépaut 2006; Luntama et al. 2008). One result from this success has been that the EUMETSAT user community has given RO soundings a high ranking in the Post-EPS candidate mission assessment. This is a very strong message supporting the continuity of the RO soundings in the EUMETSAT mission framework. However, the ionospheric user community should ensure that their requirements are properly taken into account in the RO mission planning. The EPS GRAS mission shows that it is possible to design a mission that provides an excellent service to the NWP users, but very little for ionospheric user community (Luntama 2005).

Recent results from the regional ionospheric tomography show that the RO soundings are needed to support the ground based observations (e.g., Luntama et al. 2007). Even dense ground based GNSS networks cannot provide enough observations to allow the retrieval of the electron density maps with a high vertical resolution. Currently the number of RO soundings through a regional tomography grid is unfortunately limited to a few observations per day. A large number of GNSS satellites and a constellation of RO satellites would increase this number significantly.

It is fairly safe to assume that the need for ionospheric monitoring information will increase in the near future. The first reason for this is that at the moment the solar activity is at its minimum (http://www.swpc.noaa.gov/SWN/index.html). With the increasing solar activity over the next 4–5 years it can be expected that the disturbances caused by the solar events in e.g., the satellite communication links will increase. The second reason for the growing interest for ionospheric information is the increasing number of GNSS applications and users. Especially the users of the single frequency GNSS receivers will notice the increasing solar activity as degraded positioning accuracy and as an increasing number of navigation problems. This user community will benefit from the services providing real time user warnings and ionospheric forecasts of degraded navigation conditions. The professional users for high precision or safety critical GNSS applications will almost certainly need precise and reliable information about the moments when navigation performance can be degraded due to the ionospheric disturbances. Even with the multi-frequency GNSS receivers and the navigation augmentation systems like EGNOS (European Geostationary Navigation Overlay Service) and WAAS (Wide Area Augmentation System) a transient problem like the ionospheric scintillation may cause a complete loss of the GNSS signal temporarily.

The services described above already give an indication of what the potential prospects for the ionospheric RO soundings are in the near future. The operational applications will require high accuracy and near real time data processing and dissemination. These requirements are actually the same that are applied to the NWP systems today. So, one of the conclusions is that the collection, archiving, and dissemination of the space weather observations should be organized in the same way as the meteorological observations are organized. This means that an operational organization should carry out the baseline satellite missions and take care of the data dissemination. For some observations this is already true (e.g., the space weather instrument onboard the GOES satellites and the most recently the SEM (Space Environment Monitor) instrument package onboard the Metop satellite series). For the ionospheric RO soundings the continuity of the measurements is not as certain. A number of RO missions are currently planned (ROSA, GOCE, KOMPSAT-5, Post-EPS), but it is not certain if ionospheric soundings are included into the mission planning. Coordination of the potential next generation RO sounding missions (e.g., ATOMMS, ACCURATE, CICERO, COSMIC-2, CHAMP-2, . . .) would be very important also to improve the temporal and the spatial coverage for the high resolution regional ionospheric tomography applications.

Another great challenge for the future of the RO soundings will be the data policy. The open source data policy adopted by the most RO missions this far has been very successful. It is not clear if the same approach can be continued in the future, when the operational users will form a large part of the RO user community. The problem is that there will always be a part of the user community (scientific users) that will not be able to pay for the observations. It also seems that the trend at the moment e.g., in the meteorological observations is that the raw data should be available for the users for free. So, the data policy for the future RO missions should be considered very carefully.

A number of scientific challenges is still left in the ionospheric RO soundings. The first challenge is the monitoring of the local plasma bubbles causing ionospheric scintillation. Detection of the small scale structures will most likely require combining the RO soundings, the ground based GNSS observations, and potentially other types of observations. It may also be necessary to adjust the characteristics of the RO receivers to improve their scintillation measurement capability. Combining the GNSS observations with the other types of observations will require development of the data assimilation techniques. Combining different types of observations will most likely also require development of the physically based models for the ionosphere and the magnetosphere. This would presumably be the best way to develop more accurate nowcasting and forecasting techniques for the space weather applications. For the ionospheric RO sounding community this means close collaboration with the traditional space weather community to trace the origins of the ionospheric events back to the source, i.e., the Sun.

A particular challenge in nowcasting is that observations will have to be disseminated to the users with a very small latency (typically 5–15 min). This will make the design and the implementation of the mission ground segments more demanding.

5 Conclusions

The short history of the RO science in the monitoring of the Earth's atmosphere and the ionosphere is very impressive. It is likely that the experience from the planetary RO science has contributed to this. In any case, huge advances both in the RO science and in the infrastructure have been reached in a rather short time. It is very impressive that ten RO missions have been accomplished over the last 12 years.

The future of RO looks bright. The GNSS is getting bigger and better. Thus, the lack of signal sources should not at least become a problem for the future RO missions. The third frequency in the next generation GNSS satellites can potentially further improve the accuracy of the ionospheric soundings. However, many challenges are related to the evolution of the GNSS. The compatibility of the different GNSS elements may become an issue, especially with spaceborne instruments. The political and legal constrains may also become more important in the future.

In meteorological applications RO has matured into one of the baseline observations required by the NWP users. A good indication of this is the high status given by the meteorological users to the RO soundings in the ranking of the EUMETSAT Post-EPS candidate missions. This is good news also for the users of the ionospheric soundings, because both soundings can be performed with the same instrument. It is just the task of the ionospheric user community to ensure that their requirements are taken into account in the RO mission planning.

The applications for the ionospheric RO soundings will most likely become more operational and require NRT dissemination of the data and the products. This will create more challenges for the ionospheric sounding missions. Coordination in the mission planning, in the data processing and in the data archiving will be very important. Also the access of the scientific users to the archived data will have to be organized. These challenges are linked to the data policy issues. The past success of the RO science has been very much based on the open source data policy adopted by the most RO missions. This policy should be continued at least for the scientific use of the data. For commercial applications the data policy has to be considered very carefully.

Finally, an important area of activity for space agencies in the near future is the "space situation awareness". This means the capability of monitoring what is happening in the near Earth space. For example in the case of satellite failure, the space agencies will want to know if the failure was caused by natural events, space debris, or if it was caused intentionally by somebody. Nowcasting and forecasting space weather will be one aspect of this activity. The ionospheric RO soundings will certainly be a part of the observation system required for space weather prediction. Combining the RO soundings with other types of space weather observations will require development of the data assimilation systems and most likely physically based ionosphere and magnetosphere models. These activities will require a close cooperation between the RO and the other space weather science communities. Links to the NWP community will also certainly be useful to benefit from their long term experience in the development of the data assimilation systems.

References

Austen J, Franke S, Liu CH (1988) Ionospheric imaging using computerized tomography. Radio Sci 23:23–307

Beyerle G, Hocke K, Wickert J, Schmidt T, Marquardt C, Reigber C (2002) GPS radio occultations with CHAMP: A radio holographic analysis of GPS signal propagation in the troposphere and surface reflections. J Geophys Res Atmos 107(D24):4802, doi:10.1029/2001JD001402

Chashei IV, Efimov AI, Samoznaev LN, Plettemeier D, Bird MK (2005) Properties of solar wind turbulence near the Sun as deduced from coronal radio sounding experiments. Adv Space Res 36:1454–1460, doi:10.1016/j.asr.2005.05.128

Daniell RE, Brown LD, Anderson DN, Fox MW, Doherty PH, Decker DT, Sojka JJ, Schunk RW (1995) Parameterized ionospheric model: A global ionospheric parameterization based on first principles models. Radio Sci 30(5):1499–1510, doi:10.1029/95RS01826

Dow JM, Neilan RE, Gendt G (2005) The International GPS Service: Celebrating the 10th anniversary and looking to the next decade. Adv Space Res 36(3):320–326, doi:10.1016/j.asr.2005.05.125

Gleason S, Hodgart S, Yiping Sun, Gommenginger C, Mackin S, Adjrad M, Unwin M (2005) Detection and Processing of bistatically reflected GPS signals from low Earth orbit for the purpose of ocean remote sensing. IEEE Trans Geosci Remote Sens 43(6):1229–1241, doi:10.1109/TGRS.2005.845643

Häusler B, Pätzold M, Tyler GL, Simpson RA, Bird MK, Dehant V, Barriot JP, Eidel W, Mattei R, Remus S, Selle J, Tellmann S, Imamura T (2006) Radio science investigations by VeRa onboard the Venus Express spacecraft. Planet Space Sci 54:1315–1335, doi:10.1016/j.pss.2006. 04.032

Healy SB, Thépaut JN (2006) Assimilation experiments with CHAMP GPS radio occultation measurements. Quart J Roy Meteor Soc 132:605–623, doi: 10.1256/qj.04.182

Healy SB, Jupp AM, Marquardt C (2005) Forecast impact experiment with GPS radio occultation measurements. Geophys Res Lett 32(L03804), doi:10.1029/2004GL020806

Heise S, Jakowski N, Wehrenpfennig A, Reigber C, Lühr H (2002) Sounding of the topside ionosphere/plasmasphere based on GPS measurements from CHAMP: Initial results. Geophys Res Lett 29(14), doi:10.1029/2002GL014738

Hinson D, Pätzold M, Simpson R, Tellmann S, Tyler L (2007) The Neutral Atmosphere of Mars as Observed Through Radio Occultation Measurements With MEX and MGS. AGU Fall Meeting Abstracts p A247

Jakowski N, Wehrenpfennig A, Heise S, Reigber C, Lühr H, Grunwaldt L, Meehan TK (2002) GPS radio occultation measurements of the ionosphere from CHAMP: Early results. Geophys Res Lett 29(10), doi:10.1029/2001GL014364

Kliore AJ, Hamilton TW, Cain DL (1964) Determination of some physical properties of the atmosphere of Mars from changes in the Doppler signal of a spacecraft on an Earth occultation trajectory. Technical Report 32–674, JPL, Pasadena, CA, USA

Lei J, Syndergaard S, Burns AG, Solomon SC, Wang W, Zeng Z, Roble RG, Wu Q, Kuo YH, Holt JM, Zhang SR, Hysell DL, Rodrigues FS, Lin CH (2007) Comparison of COSMIC ionospheric measurements with ground-based observations and model predictions: Preliminary results. J Geophys Res 112(A07308), doi:10.1029/2006JA012240

Lindal GF (1988) Radio occultation measurements with L band links between GPS and EOS satellites, JPL Internal Memo to T. P. Yunck

Luntama JP (2005) Ionosphere monitoring with Metop GRAS mission. In: Proceedings of the Second European Space Weather Week (Available Online), European Space Agency, Noordwijk, the Netherlands

Luntama JP, Mitchell C, Spencer P (2007) Mesoscale Ionospheric Tomography Over Finland. In: Fourth European Space Weather Week, 5–9 November, 2007, Brussels, Belgium

Luntama JP, Kirchengast G, Borsche M, Foelsche U, Steiner AK, Healy SB, von Engeln A, O'Clerigh E, Marquardt C (2008) Prospects of the EPS GRAS mission for operational atmospheric applications. Bull Amer Meteorol Soc 89:1863–1875, doi:10.1175/2008BAMS2399.1

Mandrake L, Wilson BD, Hajj G, Wang C, Pi X, Iijima B (2004) USC/JPL GAIM: A Real-Time Global Ionospheric Data Assimilation Model. AGU Fall Meeting Abstracts, Abstract SA44A-01

Melbourne WG, Davis ES, Duncan CB, Hajj GA, Hardy KR, Kursinski ER, Meehan TK, Young LE, Yunck TP (1994) The application of spaceborne GPS to atmospheric limb sounding and global change monitoring. Tech. Rep. JPL Publication 94–18, Jet Propulsion Laboratory, Pasadena, USA

Pallares JM, Ruffini G, Ruffini L (2005) Ionospheric tomography using GNSS reflections. IEEE Trans Geosci Remote Sens 43(2):321–326, doi:10.1109/TGRS.2004.841253

Schunk RW, Scherliess L, Sojka JJ, Thompson DC, Anderson DN, Codrescu M, Minter C, Fuller-Rowell TJ, Heelis RA, Hairston M, Howe BM (2004) Global Assimilation of Ionospheric Measurements (GAIM). Radio Sci 39(RS1S02), doi:10.1029/2002RS002794

Stankov SM, Marinov P, Kutiev I (2007) Comparison of NeQuick, PIM, and TSM model results for the topside ionospheric plasma scale and transition heights. Adv Space Res 39:767–773, doi:10.1016/j.asr.2006.10.023

Starks MJ, Lin CS, Groves KM, Pedersen TR, Basu S, Syndergaard S, Rocken C (2007) Characterization of ionospheric scintillation using simultaneous Formosat-3/COSMIC radio occultation observations and AFRL SCINDA ground scintillation measurements. In: Eos Trans. AGU, Jt. Assem. Suppl., abstract SA31A-03

Stolle C, Jakowski N, Schlegel K, Rietveld M (2004) Comparison of high latitude electron density profiles obtained with the GPS radio occultation technique and EISCAT measurements. Ann Geophys 22:2015–2022

Viehweg C, Wickert J, Heise S, Jacobi C, Beyerle G, Schmidt T, Rothacher M (2007) Global distribution of plasma irregularities in the lower ionosphere derived from GPS radio occultation data. In: European Geosciences Union General Assembly 2007, Vienna, Austria, April 15–20, 2007. Poster presentation

Wang C, Hajj G, Pi X, Rosen IG, Wilson B (2004) Development of the global assimilative ionospheric model. Radio Sci 39(RS1S06), doi:10.1029/2002RS002854

Wickert J, Pavelyev AG, Liou YA, Schmidt T, Reigber C, Igarashi K, Pavelyev AA, Matyugov S (2004) Amplitude variations in GPS signals as a possible indicator of ionospheric structures. Geophys Res Lett 31(L24801), doi:10.1029/2004GL020607

Yunck TP, Hajj GA (2005) Atmospheric and ocean sensing with GNSS. In: Reigber C, Lühr H, Schwintzer P, Wickert J (eds) Earth Observation with CHAMP, Results from Three Years in Orbit, Springer, Berlin Heidelberg, pp 421–430, doi:10.1007/3-540-26800-6_67

Yunck TP, Melbourne WG (1989) Geoscience from GPS tracking by Earth satellites. In: Proc. IUGG/IAG Symposium No. 102, Edinburgh, Scotland

Yunck TP, Lindal GF, Liu CH (1988) The role of GPS in precise Earth observation. In: Proc. IEEE Position Location and Navigation Symposium (PLANS 88), doi:10.1109/PLANS.1988.195491

Yunck TP, Liu CH, Ware R (2000) A history of GPS sounding. Special issue of Terr Atmos Ocean Sci 11(1):1–20

Part II
Solar, Lunar, and Stellar Occultation for Atmospheric Studies

SCIAMACHY Solar Occultation: Ozone and NO_2 Profiles 2002–2007

K. Bramstedt, L.K. Amekudzi, A. Rozanov, H. Bovensmann, and J.P. Burrows

Abstract SCIAMACHY on-board ENVISAT is measuring solar irradiances and Earthshine radiances from the UV to the NIR spectral region in nadir, limb, and lunar as well as solar occultation geometry. Solar occultation measurements are performed in Sun-scanning mode during sunset at northern latitudes between 49°N and 69°N, depending on season. The radiative transfer and retrieval code SCIATRAN 2.1 is used to derive vertical profiles of ozone and NO_2 from the SCIAMACHY solar occultation measurements. The retrieval scheme is an optimal estimation approach with Twomey-Tikhonov regularization. Ozone and NO_2 are simultaneously retrieved in the fit windows 524–590 nm and 425–453 nm, respectively. Here we present an almost complete dataset from August 2002 to August 2007, including validation results with independent measurements from the satellite instruments HALOE and SAGE II.

1 Introduction

SCIAMACHY (SCanning Imaging Absorption spectroMeter for Atmospheric CHartographY) is a passive remote sensing moderate-resolution imaging UV-Vis-NIR spectrometer on board the European Space Agency's (ESA) Environmental Satellite (ENVISAT). ENVISAT was launched in March 2002 from Kourou, French Guiana to a Sun-synchronous orbit with an equator crossing time in the descending node of 10.00 am. The instrument observes the Earth atmosphere in nadir, limb, and solar/lunar occultation geometries and provides column and profile information of atmospheric trace gases of relevance to ozone chemistry, air pollution, and climate monitoring issues (Bovensmann et al. 1999).

SCIAMACHY performs solar occultation measurements every orbit between 49°N and 69°N depending on season (Fig. 1). From the instrument point of view, the Sun rises above the horizon, but the local time at the tangent point corresponds

---

K. Bramstedt (✉)
Institute of Environmental Physics and Remote sensing (IUP/Ife), University of Bremen,
Otto-Hahn-Allee 1, 28334 Bremen, Germany
e-mail: klaus.bramstedt@iup.physik.uni-bremen.de

A. Steiner et al. (eds.), *New Horizons in Occultation Research*,
DOI 10.1007/978-3-642-00321-9_7,

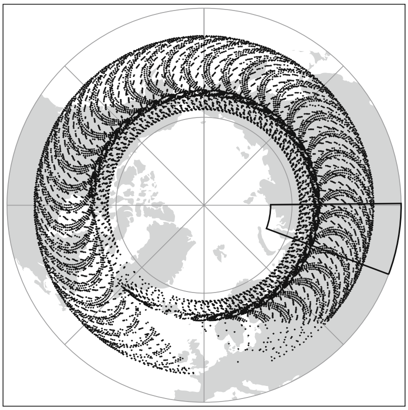

Fig. 1 Geographical distribution of SCIAMACHY solar occultation events used for profile retrieval. Each dot represents the tangent point of one measurement. All events for the years 2002–2007 are plotted, but the pattern repeats after 35 days (the repeat cycle of the ENVISAT orbit). Once per day the nominal occultation measurement stops at 100 km and instrument monitoring measurements are performed above the atmosphere. Because the measurements above the atmosphere are used for a precise tangent height determination, the truncated sequence is not yet used for profile retrieval. Therefore, tangent points in the Atlantic region are missing. The occultation measurements inside the marked area over Siberia are used for the time series in Fig. 6 and Fig. 7

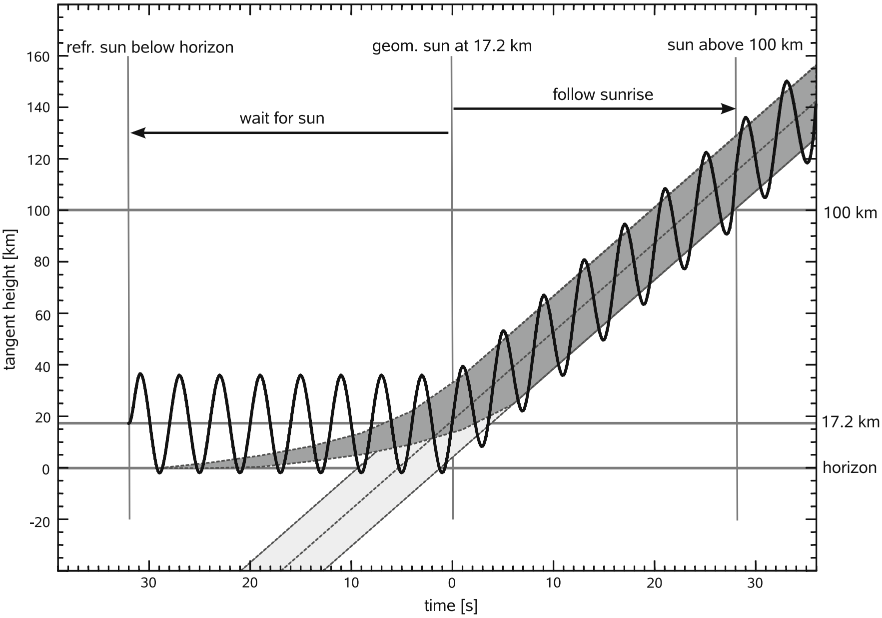

Fig. 2 Outline of the SCIAMACHY solar occultation measurement sequence. The *light gray* area indicates the geometrical position of the solar disk. The *dark gray* area shows the visibility of the Sun, changed from the geometrical position by refraction in Earth's atmosphere. The sinusoidal line gives the viewing direction of the instrument during the sequence, which is continued up to an altitude of 300 km

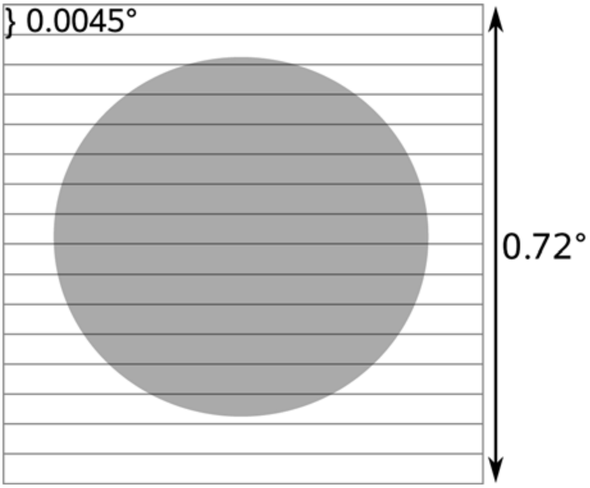

Fig. 3 Coverage of the solar disk by one scan across the solar disk above the atmosphere. The *rectangles* indicate SCIAMACHY's FOV for one individual measurement. In lower altitudes, the image of the solar disk would be flattened due to the refraction in Earth's atmosphere

to a sunset event. The scan sequence is as illustrated in Fig. 2: In an initial phase, SCIAMACHY scans around 17.2 km above the horizon, waiting for the Sun to appear. When the Suns geometrical altitude exceeds 17.2 km, the instrument follows (continuously scanning) the rising Sun up to an altitude of about 300 km. The field of view (FOV) of SCIAMACHY in horizontal direction is 1.8°. In case of solar occultation a small aperture to reduce the amount of incoming light is put into the light path and reduces the FOV to 0.72°. In vertical direction, the FOV is 0.0045° corresponding to an altitude range of about 2.5 km at the tangent point. With measurements performed every 62.5 ms, 16 spectra are taken during one sweep of 0.72° over the solar disk. The solar disk with a diameter of 0.53° is completely covered, as illustrated in Fig. 3.

Only directly transmitted light contributes significantly in occultation geometry. Transmissions are calculated dividing atmospheric measurements by an appropriate measurement from above the atmosphere. In southern latitudes (40°S–90°S) SCIAMACHY performs lunar occultation measurements, depending on visibility and phase of the Moon (Amekudzi et al. 2005).

2 Retrieval Scheme

The SCIATRAN version 2.1 radiative transfer code (Rozanov et al. 2005) is used for forward modeling and retrieval. An optimal estimation approach with Twomey-Tikhonov regularization is used to fit simultaneously NO_2 and ozone in the spectral windows of 425–453 nm and 524–590 nm respectively at the spectral resolution of the SCIAMACHY instrument, which is 0.44 nm for these windows. The SCIAMACHY ozone and NO_2 cross sections are used (Bogumil et al. 2000).

Ozone profile a priori information is taken from the Fortuin and Kelder ozone climatology (Fortuin and Kelder 1998). An NO_2 climatology has been compiled from HALOE sunset measurements from 1992 to 2005.

Broadband absorption features of the atmosphere and broadband instrument effects were removed from the measured spectra by subtracting a third order polynomial. Precise tangent height information is derived geometrically using the Sun as well-known target in space (Bramstedt et al. 2007).

From the 1040 spectra taken in one occultation measurement sequence, a set of 11 spectra taken around the center of the solar disk between 12 km and 45 km is selected. One measurement well above the atmosphere is used as reference to calculate the Sun-normalized transmission spectra.

The theoretically calculated errors for the retrieved profiles are for ozone between 17 km and 48 km below 2% and for NO_2 between 23 km and 38 km below 4%. However, these values do not recognize systematic errors (such as calibration errors in the spectra) and are influenced by the amount of regularization applied in the retrieval.

3 Validation with the Satellite Instruments HALOE and SAGE II

The Halogen Occultation Experiment (HALOE) was launched on the Upper Atmosphere Research Satellite (UARS) spacecraft in September 1991, operations were stopped in November 2005. For this work, ozone and NO_2 profiles from version 19 of the HALOE data are used. The Stratospheric Aerosol and Gas Experiment II (SAGE II) was launched on the Earth Radiation Budget Satellite (ERBS) in October 1984 and stopped operation in August 2005. The current version 6.2 is used for the comparisons. Both instruments also measured in solar occultation mode.

For the study presented here, all coincidences within 500 km distance between the tangent points and with no more than 6 h between the measurements are used. Because of the diurnal cycle of NO_2, the coincidences NO_2 are restricted to sunset events of HALOE and SAGE II. Due to the strict coincidence criteria, most of the matches are sunset events anyway.

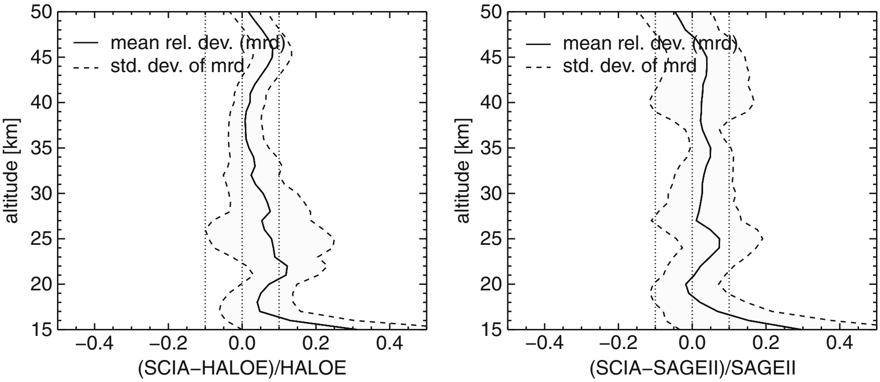

Fig. 4 Mean relative deviation (mrd) and standard deviation of mrd for ozone profiles compared to co-located profiles from HALOE (*left*, 125 co-locations) and SAGE II (*right*, 219 co-locations)

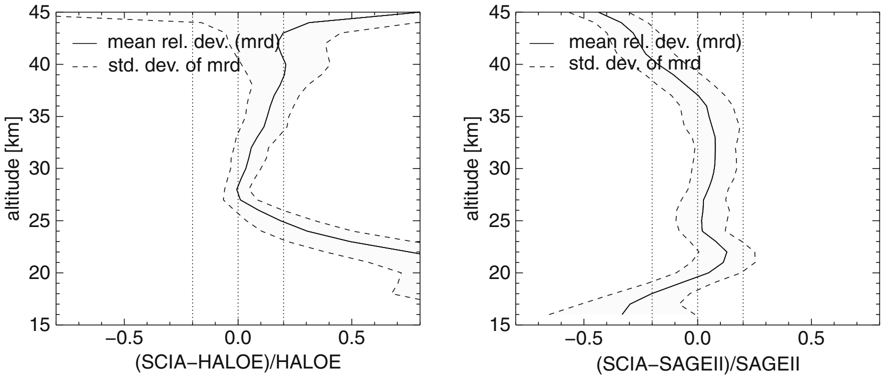

Fig. 5 Mean relative deviation (mrd) and standard deviation of mrd for NO_2 profiles compared to co-located profiles from HALOE (*left*, 113 co-locations) and SAGE II (*right*, 214 co-locations)

Figure 4 shows the mean relative deviation (mrd) and the standard deviation of mrd of the SCIAMACHY ozone profiles compared to HALOE and SAGE II. There is a remarkable good agreement with less than 10% mrd from 17–50 km. In general, SCIAMACHY gives slightly higher ozone values in the order of 5% for most altitudes.

Figure 5 shows the same plots for NO_2. The comparison with SAGE II shows good agreement from 18–40 km with mrd below 20% and a bias of about 5%. The comparison with HALOE gives mrd below 20% only above an altitude of 24 km, below the HALOE profiles give much smaller values. NO_2 has a strong gradient along the line-of-sight in case of occultation geometry, because its concentration changes rapidly during sunset (and sunrise). Therefore, the measured NO_2 value is not completely representative for the solar zenith angle of 90° at the tangent point, especially at lower altitudes. The HALOE retrieval recognizes this and performs a correction to get profiles representative for 90° solar zenith angle (Bracher et al. 2005), whereas for SCIAMACHY and SAGE II no such correction is done. This might explain the larger deviation to HALOE at lower altitude and has to be further investigated.

4 Ozone and NO_2 Profiles 2002–2006

About 19000 solar occultation measurements from the begin of measurements in August 2002 until August 2007 have been evaluated so far. Figure 6 shows a time series of the vertical ozone distribution from SCIAMACHY's measurements (one profile per day over Siberia, see Fig. 1). Figure 7 is the equivalent time series for NO_2.

From October to February, solar occultation events take place north of 63°N, whereas from May to August the events are south of 54°N, as indicated in the lower part of the panels. Both time series show a pattern corresponding to the variation

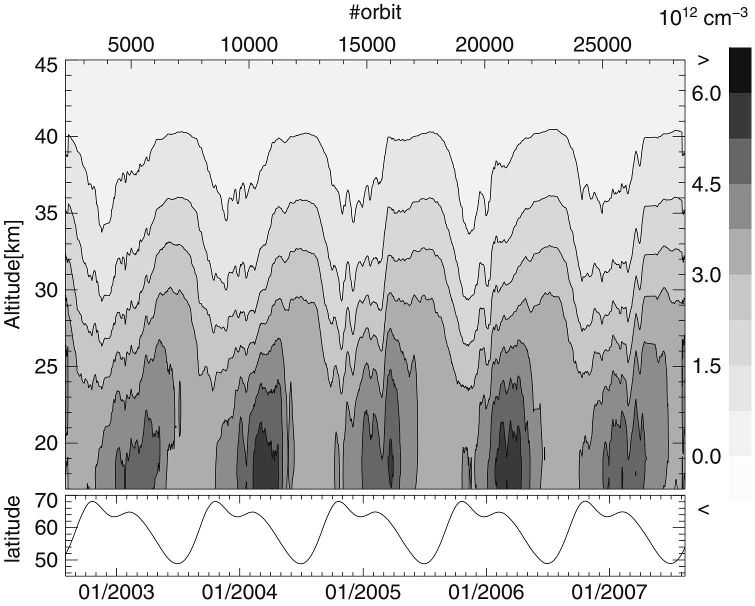

Fig. 6 Time series of ozone profiles derived from the solar occultation measurements over Siberia between 69°E and 90°E with one measurement per day (see Fig. 1). The *small charts* below indicate the latitudes of the tangent points of the measurements

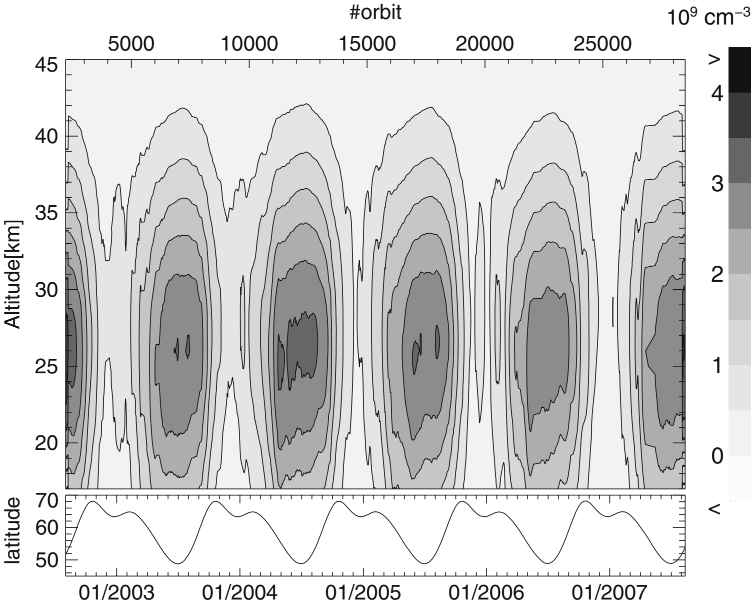

Fig. 7 As Fig. 6, but for NO_2

in latitude. From May to November, ozone concentrations as expected for mid-latitudes in summer and autumn are observed. From December to April, the measurements at higher latitudes are influenced by the development of the Arctic ozone hole. In 2003, 2005, and 2007, higher ozone loss in the Arctic ozone hole season than in the years 2004 and 2006 were observed.

Also the NO_2 time series is dominated by the variation in latitude over the year. At higher latitudes from October to February, low concentrations are observed, whereas at mid-latitudes increased NO_2 values are observed.

5 Conclusions

SCIAMACHY solar occultation gives ozone profiles of excellent quality, and NO_2 profiles of good quality in the Northern Hemisphere as shown by comparison with co-located measurements of HALOE and SAGE II. An almost complete dataset of ozone and NO_2 profiles from 5 years in orbit is presented. With the extension of the mission until 2013, which is under investigation by ESA at the time of writing, SCIAMACHY solar occultation will continue the long term datasets of previous solar occultation instruments such as HALOE and SAGE II and contribute to a better understanding of atmospheric chemistry and dynamics in the Northern Hemisphere. The presented data are available upon request from the first author.

Acknowledgements We thank the European Space Agency (ESA) for providing SCIAMACHY level-1 data, the HALOE team (at Hampton University, especially J. M. Russell III, and at NASA LaRC, especially E. Thompson), and the SAGE II group (at NASA LaRC, especially Larry Thomason and the NASA Langley Radiation and Aerosols Branch) for providing data and information from their instruments. This work was funded in parts by the German Ministry of Education and Research (BMBF) via grant 07UFE12/8, the DLR-Born via grant 50EE0502, the University of Bremen and the state of Bremen.

References

Amekudzi LK, Bracher A, Meyer J, Rozanov A, Bovensmann H, Burrows JP (2005) Lunar occultation with SCIAMACHY: First retrieval results. Adv Space Res 36(5):906–914, doi:10.1016/j.asr.2005.03.017

Bogumil K, Orphal J, Burrows JP (2000) Temperature dependent absorption cross sections of O3, NO2, and other atmospheric trace gases measured with the SCIAMACHY spectrometer. In: Proc ERS Envisat Symposium, Goteborg, Sweden

Bovensmann H, Burrows JP, Buchwitz M, Frerick J, Noël S, Rozanov VV, Chance KV, Goede APH (1999) SCIAMACHY: Mission objectives and measurement modes. J Atmos Sci 56(2): 127–150

Bracher A, Sinnhuber M, Rozanov A, Burrows JP (2005) Using a photochemical model for the validation of NO_2 satellite measurements at different solar zenith angles. Atmos Chem Phys 5:393–408

Bramstedt K, Amekudzi LK, Bracher A, Rozanov A, Bovensmann H, Burrows JP (2007) SCIAMACHY solar occultation: Ozone and NO_2 profiles 2002–2006. Proc Envisat Symposium 2007, Montreux Switzerland 23–27 April, SP-636

Fortuin JPF, Kelder H (1998) An ozone climatology based on ozonesonde and satellite measurements. J Geophys Res 103(D24):31709–31734

Rozanov A, Rozanov V, Buchwitz M, Kokhanovsky A, Burrows JP (2005) SCIATRAN 2.0 A new radiative transfer model for geophysical applications in the 175–2400 nm spectral region. Adv Space Res 36:1015–1019, doi: 10.1016/j.asr.2005.03.012

Retrieval of Trace Gas Concentrations from Lunar Occultation Measurements with SCIAMACHY on ENVISAT

L.K. Amekudzi, K. Bramstedt, A. Rozanov, H. Bovensmann, and J.P. Burrows

Abstract SCIAMACHY (Scanning Imaging Absorption Spectrometer for Atmospheric Chartography) is a UV-Vis-NIR spectrometer on-board ENVISAT, dedicated to measure atmospheric trace gas distributions in nadir, limb, and occultation geometries. In occultation mode, SCIAMACHY tracks the rising Sun or Moon directly through the atmosphere. Dividing the atmospheric measurements by extraterrestrial references gives transmission spectra, which are suitable for a DOAS-like retrieval approach. Here, we report on the major retrieved data products (ozone, NO_2, and NO_3) obtained from SCIAMACHY lunar occultation observations. We validated our ozone and NO_2 data products. Ozone validation was carried out with other satellite instruments (HALOE, SAGE II, and POAM III). The NO_2 results were validated with photochemically scaled HALOE and SAGE II profiles. The validation results reveal that the biases in the SCIAMACHY lunar occultation ozone and NO_2 are within ±15%, with standard deviations and the uncertainties of the biases are less than 20% and 6%, respectively. Comparisons of NO_3 results carried out with a 1-D photochemical model show that the accuracy of our NO_3 data product is better than 30%.

1 Introduction

The **SC**anning **I**maging **A**bsorption Spectro**M**eter for **A**tmospheric **CH**artograph**Y** (SCIAMACHY) is a passive remote sensing moderate-resolution UV-Vis-NIR spectrometer on-board the European Space Agency's **ENVI**ronmental **SAT**ellite (ENVISAT) launched into a near-circular Sun-synchronous polar orbit in March 2002 from Kourou, French Guiana. The instrument observes the Earth's atmosphere in nadir, limb, and solar/lunar occultation geometries, recording spectroscopic data in eight channels; covering the spectral range of 240–2380 nm with spectral

---

L.K. Amekudzi (✉)
Institute of Environmental Physics and Remote Sensing (IUP/IFE), University of Bremen, Germany and Department of Physics, Kwame Nkrumah University of Science and Technology (KNUST), Kumasi, Ghana
e-mail: leoamekudzi@yahoo.com

A. Steiner et al. (eds.), *New Horizons in Occultation Research*,
DOI 10.1007/978-3-642-00321-9_8,

resolution of 0.24–1.5 nm. Various atmospheric components (column and profile information of trace gases) are derived from SCIAMACHY measurements relevant to ozone chemistry, air pollution, and climate monitoring issues (Bovensmann et al. 1999; Gottwald et al. 2006).

Due to the Sun-synchronous orbit and the position of the SCIAMACHY instrument on ENVISAT, lunar occultation events are observed by SCIAMACHY in the Southern Hemisphere between 40°S and 90°S, when the phase of the Moon is 0.6–0.7 and ends shortly after full Moon, yielding measurements about 6–8 days per month. In the Northern Hemisphere between 49°N and 70°N, SCIAMACHY performs solar occultation measurements (Meyer et al. 2005; Bramstedt et al. 2007).

The SCIAMACHY lunar occultation measurements are successfully executed when the Moon's visibility is on the nightside of ENVISAT orbit, because on the day-side, stronger signals (stray light) from the brighter Earth's atmosphere contaminate the measurements. The duration of the useful SCIAMACHY lunar occultation measurements is highly variable (about 4–8 months per year), as seen in Fig. 1. The SCIAMACHY lunar occultation measurements are performed in Moon pointing mode, usually starting around 17 km the Moon is followed up to 100 km tangent height. The integration time for the lunar occultation measurements is 1.0 s resulting in a vertical sampling of approximately 2.5 km. The horizontal resolution is 30 km across track and extending approximately 400 km along track. Detailed information about SCIAMACHY lunar occultation is given in Amekudzi (2005) and Amekudzi et al. (2005).

The scientific objective of SCIAMACHY lunar occultation measurements is to provide nighttime vertical profiles of trace gases such as O_3, NO_2, and NO_3, which are important in stratospheric chemistry. Simultaneous measurements of O_3, NO_2, and NO_3 are crucial for understanding of NO_x budget and long-term trends in stratospheric ozone loss.

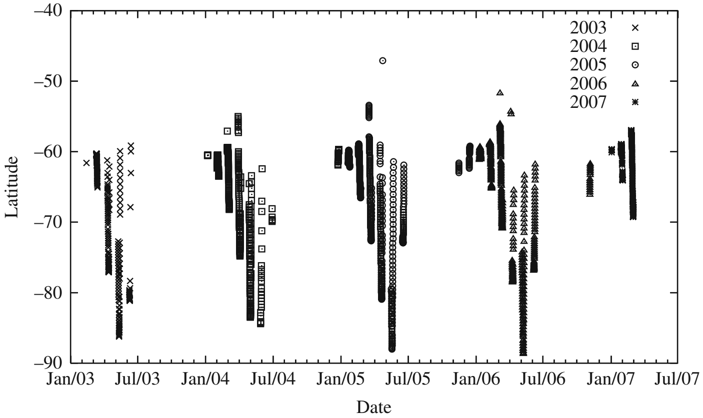

Fig. 1 Latitudinal distribution of SCIAMACHY lunar occultation measurements from 2003 to March 2007. Most measurements were taken in March, April, and May

In this paper, we describe briefly the retrieval method used to process the measured SCIAMACHY lunar occultation data. This is followed by O_3, NO_2, and NO_3 retrieval results. Thereafter the validation carried out for the retrieved O_3 and NO_2 is presented, and finally, summary and conclusions of our findings.

2 Retrieval Methodology

In this section we described briefly the SCIAMACHY lunar occultation retrieval scheme. Detailed description of the retrieval method is given in Amekudzi (2005).

SCIATRAN version 2.1 radiative transfer and retrieval code (Rozanov et al. 2005) is used to process the calibrated (level-1, version 6.01) SCIAMACHY lunar occultation data to derive vertical profiles of O_3, NO_2, and NO_3. The radiative transfer for simulating SCIAMACHY lunar transmission spectra and computing the Jacobian (the weighting function matrices) is based on Lambert-Beer's law. The simulated transmission $\Upsilon^s(h_i, \lambda)$ for a given tangent height, h_i, and wavelength, λ, is given by

$$\Upsilon^s(h_i, \lambda) = \int_{\Omega} \int_{\triangle\lambda} S(\lambda, \lambda') F(\omega) e^{-\tau(h_i, \lambda)} \mathrm{d}\lambda' \mathrm{d}\omega, \quad (1)$$

where $\triangle\lambda$ is the total width of SCIAMACHY slit function $S(\lambda, \lambda')$, Ω is the field of view of the instrument, and $F(\omega)$ is the apparatus function. $\tau(h_i, \lambda)$ is the full optical depth along the line of sight through the atmosphere and i represents the tangent height index.

The global fitting method coupled with the differential optical depth approach is applied to fit simultaneously NO_2 and O_3 within the spectral window of 420–454 nm and 520–580 nm, respectively. NO_3 is fitted using the spectral window of 610–680 nm containing the most intense NO_3 absorption band at 623 nm ν_1(1,0) and 662 nm ν_1(0,0). The NO_3 retrieval window has significant contributions from other absorbers such as O_3, O_2, O_4, and H_2O. Therefore, to accurately fit and retrieve NO_3 profiles, these interfering gases are fitted. O_2 and H_2O are line absorber, hence their absolute cross sections are calculated by using the exponential sum fitting of transmittance (ESFT) method (Buchwitz et al. 2000). Broadband absorption features of the atmosphere and instrument are removed from the measured spectra by subtracting a third order polynomial.

Typical spectral fits for NO_2 and O_3 are shown in Fig. 2 (top). Also in Fig. 2 (bottom) are shown the spectra residuals, which are the differences between the model differential spectra and the measurement contribution. The spectral residuals shown here are less than 0.5%.

The total model errors for the retrieval are within 2% and 10% for ozone and NO_2 (Amekudzi 2005) and less than 20% for NO_3 retrieval (Amekudzi et al. 2005). The total model errors include the uncertainties in the absorption cross sections for all interfering gases, which are fitted or retrieved with the targeted gases and errors due to tangent height shift, instrumental line shape, and temperature profiles.

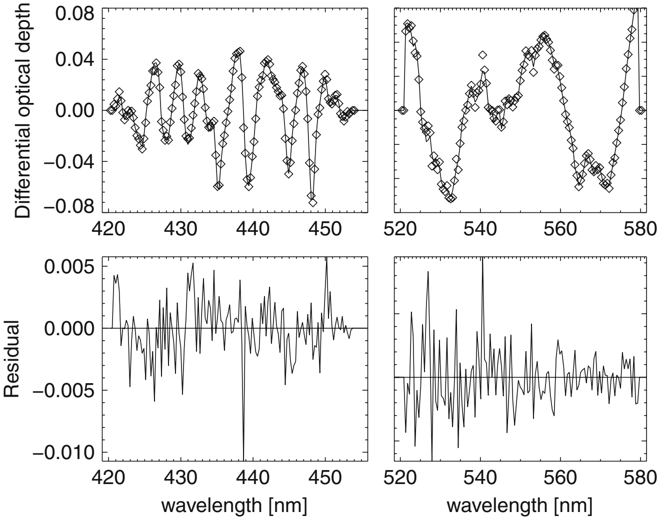

Fig. 2 Example of spectral fits (*top*) and residuals (*bottom*) at about 25 km tangent height showing absorption features of NO_2 (*top left*) and O_3 (*top right*) for measurement in orbit 15 598, day February 22, 2005. The diamond points represent the modeled differential optical depth and the *solid line* the measurement contribution

The European Centre for Medium-Range Weather Forecasts (ECMWF) temperature and pressure profiles information as well as O_3 and NO_2 absorption cross sections at five different temperatures measured at University of Bremen (Burrows et al. 1998) are used in the retrieval schemes. NO_3 absorption cross section at 298 K (Sander et al. 2003) is used. The a priori trace gases are taken from model calculations from the Max-Planck Institute, Mainz. The inversion technique used in the retrieval algorithm is similar to the optimal estimation method (OEM) with additional smoothing constrain. Although the measurement vertical resolution is ∼3–4 km, the retrievals were carried out with 1 km vertical sampling. The total retrieval errors, (i.e., the random, smoothing, and systematic errors) are within 5% and 15% between 18 km and 40 km for ozone (Amekudzi 2005). The retrieval errors for NO_2 are within 5% and 20% in the altitude range of 18–36 km and for NO_3 profiles the total retrieval errors are within 20% and 35% between 20 km and 45 km.

3 Retrieval Results

In this section we present zonal mean concentrations inferred from the retrieved number density profiles reported in Amekudzi et al. (2007b). In addition, monthly means of NO_2 and NO_3 are presented.

The zonal mean number densities derived from the retrieved lunar occultation O_3, NO_2, and NO_3 vertical profiles are shown in Figs. 3, 4, and 5 respectively for 2003 (left) and 2004 (right). These results represent number density averages

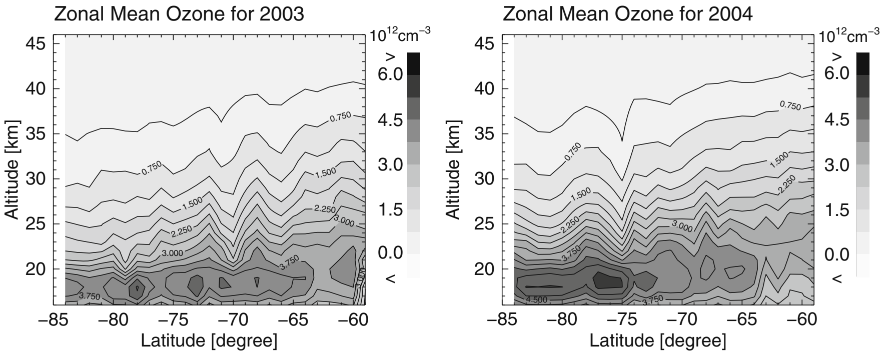

Fig. 3 Zonal mean of ozone for 2003 and 2004 derived from SCIAMACHY lunar occultation measurements averaged over 1° latitude. *Left* are the 2003 results and *right* are 2004 results

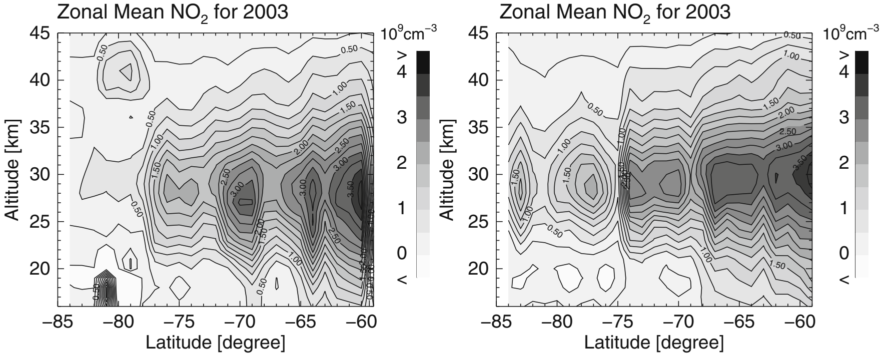

Fig. 4 As in Fig. 3, but for NO$_2$

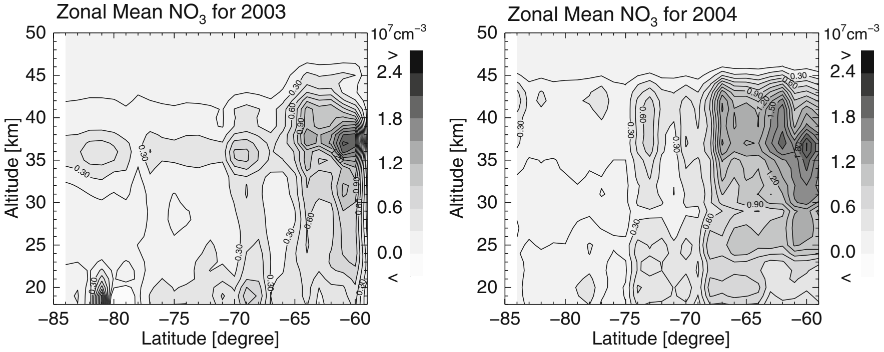

Fig. 5 As in Fig. 3, but for NO$_3$

corresponding to the latitudinal distributions shown in Fig. 1. There are 2–10 profiles per latitude bin between 85–76°S and between 75–60°S, there are 9–58 profiles per latitude bin. The 2003 results are derived from measurements for March to June and 2004 results for January to June.

In general higher values of ozone in the range of 3.0×10^{12} molec cm^{-3} to 4.5×10^{12} molec cm^{-3} are observed for the altitude range 15–22 km. In 2004, much higher concentrations of ozone (4.5×10^{12} to 5.2×10^{12} molec cm^{-3}) are retrieved for 70–84°S. Above 35 km very low values ($< 0.5 \times 10^{12}$ molec cm^{-3}) of ozone are retrieved and between 22 km and 28 km the retrieved ozone concentrations are within 1.0×10^{12} molec cm^{-3} and 2.5×10^{12} molec cm^{-3}.

The NO_2 and NO_3 results displayed in Figs. 4 and 5 show higher concentration values between latitudes 60°S and 65°S. The higher values of NO_3 seen at these latitudes are mainly from measurements taken in March for 2003 and January to March for 2004 (see Fig. 7). March and April measurements contribute significantly to higher values of NO_2 as seen at latitudes 60–65°S for 2003 and for NO_2 results in 2004, higher values are from measurements in February to April (see Fig. 6). The maximum concentration of retrieved NO_2 are in the range of 2.0×10^9 molec cm^{-3} to 4.0×10^9 molec cm^{-3} at altitudes of 25–35 km and those of NO_3 are in the range of 1.2×10^7 molec cm^{-3} to 2.4×10^7 molec cm^{-3} at 34–42 km altitude.

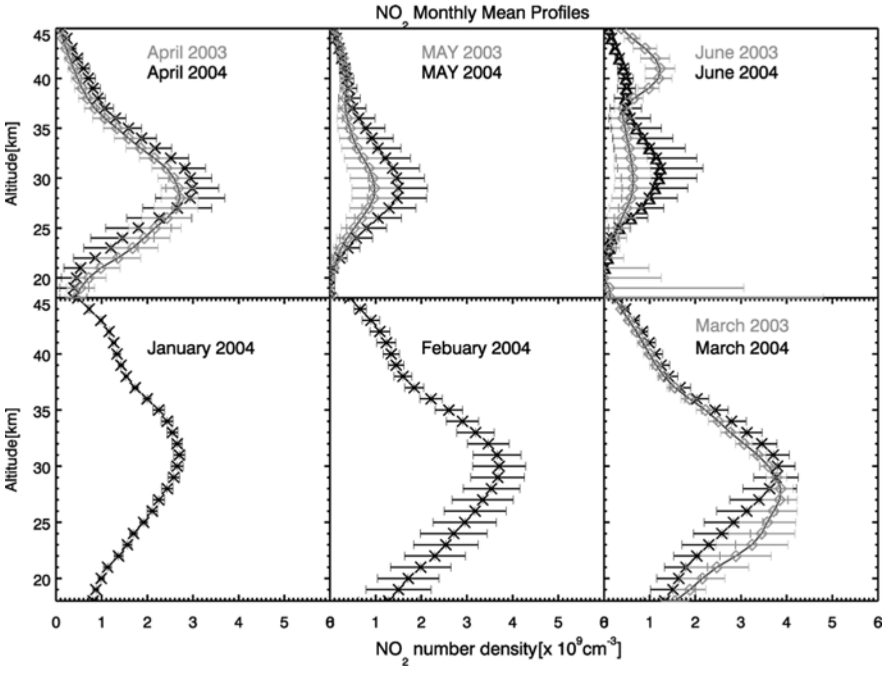

Fig. 6 Monthly mean of NO_2 for 2003 and 2004 derived from SCIAMACHY lunar occultation measurements. 2003 results in *gray* and 2004 in *black*. The error bars are the standard deviations of mean profiles

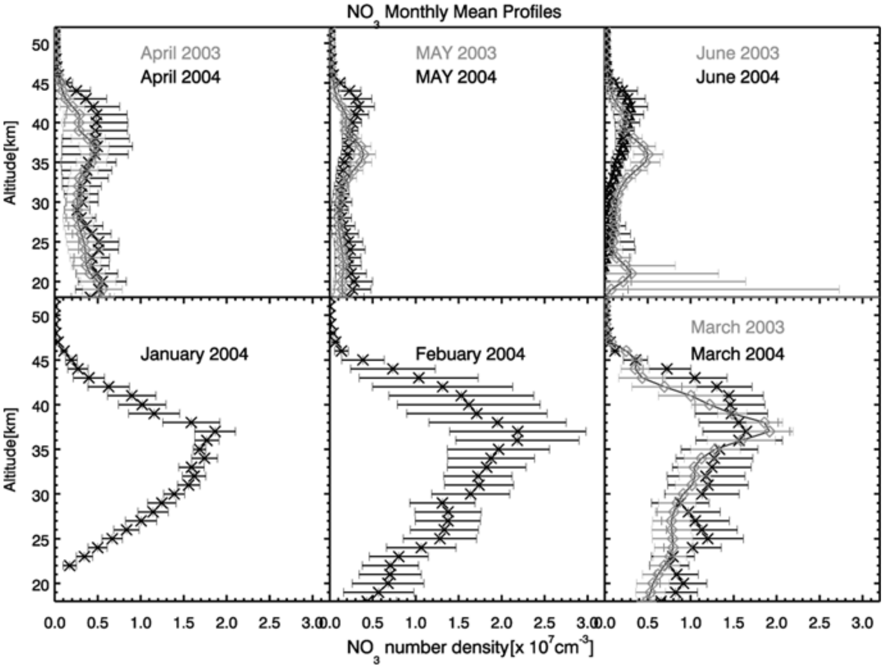

Fig. 7 As in Fig. 6, but for NO_3

Immediately after sunset, the stratospheric NO is rapidly oxidized to NO_2 by O_3. The NO_2 formed, reacts more slowly with O_3 to form NO_3. The concentrations of both NO_2 and NO_3 thus build up within few hours after sunset. The NO_2 and NO_3 formed could react in the presence of a collision partner to form N_2O_5. In relatively warm stratosphere, N_2O_5 can be converted in the presence of collision partner to NO_2 and NO_3. At relatively cold temperatures N_2O_5 serves as the reservoir of the nighttime NO_x or in the presence of polar stratospheric clouds N_2O_5 is converted to nitric acid (HNO_3) and eventually to the stable complex nitric acid trihydrate ($HNO_3 \cdot 3H_2O$). Kumer et al. (1997) have shown that at relative warm temperatures ($T > 255$ K), NO_3 has lifetime of the order of a day and thermal lifetime of N_2O_5 is few minutes. This implies that more NO_3 is produced in warmer nights. Hence our observations in January–March shown in Fig. 7 are consistent with nighttime NO_y chemistry.

4 Validation Results

Retrieved profiles from remote sensing measurements require validation in order to access the overall confidence in the data products. Validation will help to detect and remove potential biases in the new retrieval products and also will provide information about estimated retrieval accuracy (Rodgers and Connor 2003). The major NO_2 and O_3 validation results are reported in Amekudzi et al. (2007a,c). Here we present a summary of the validation results. The reference validation data sources are retrieval results from the Halogen Occultation Experiment (HALOE), Stratospheric Aerosol and GAS Experiment II (SAGE II), and The Polar Ozone and Aerosol Measurement III (POAM III). The O_3 data quality of these instruments is described in Cunnold et al. (1989); Brühl et al. (1996); Randall et al. (2003) and NO_2 data quality is assessed in Cunnold et al. (1991); Gordley et al. (1996). The coincidences with HALOE are found in 2003–2005, SAGE II in 2004, and POAM in 2003–2004.

The statistics of O_3 validation results (i.e., the mean relative deviations (mrd), the standard deviations of the mrd, and uncertainty) are shown in Table 1. The statistics of NO_2 validation results are presented in Table 2. Due to the strong diurnal cycle of NO_2, a photochemical correction scheme described in Bracher et al. (2005) has been applied to scale HALOE or SAGE II measurements to SCIAMACHY solar zenith angle. In general, very good agreements are obtained.

We compared our retrieved NO_3 profiles with photochemical model calculations to check the validity and internal consistency of our results. Two photochemical model schemes were used. The first model scheme, called a full photochemical model is a 1-d chemistry model containing a comprehensive chemistry and dynamics of the stratosphere. Details of this model are described in Amekudzi et al. (2005) and references therein. The second model is a relatively simple chemical model, which assumed that at steady state, the nighttime concentration of NO_3 depends on the concentration of ozone, NO_2, temperature, and pressure. We found that NO_3 profiles calculated from the full 1-D photochemical model are in good agreement with the retrieved NO_3 profiles within 20% and 35% between 24 km and 45 km (Amekudzi 2005; Amekudzi et al. 2005). A comparison with a simple chemical

Table 1 Summary of lunar occultation ozone validation results, the coincidence criteria applied are measurement time difference of 12 h and correlative radius of 1000 km

Instruments	mrd (%)	rms (%)	Uncert.[a] (%)	Height (km)
HALOE $N = 154$	−5 to +15	5–25	2–5	20–45
SAGE II $N = 92$	−15 to +15	6–20	< 2	20–45
POAM III $N = 149$	−8 to +2	12–20	1–4	24–43

[a] The uncertainty is the $\mathrm{rms}/\sqrt{N}$, where N is the number of coincidences.

Table 2 Summary of lunar occultation NO_2 validation results. The coincidence criteria applied are similar to the ozone validation

Instruments	mrd (%)	rms (%)	Uncert. (%)	Height (km)
HALOE $N = 65$	−16 to +3	4–16	1–6	25–38
SAGE II $N = 72$	−9 to +7	10–17	< 2	22–39

model calculation showed good agreement between 22 km and 38 km with accuracy better than 30% (Amekudzi et al. 2005, 2007a).

5 Summary and Conclusions

The retrieval results of SCIAMACHY lunar occultation measurements of O_3, NO_2, and NO_3 are presented. Relatively high concentration values were retrieved for NO_3 in the months of January–March due to warmer temperatures. These results are consistent with nighttime NO_y chemistry.

Validation performed with correlative satellite instruments showed that the SCIAMACHY lunar occultation O_3 and NO_2 results are very promising. The biases in the O_3 and NO_2 validation were within ±15%, with standard deviations and the uncertainties of the biases better than 20% and 6%, respectively. Comparisons of NO_3 results carried out with a 1-D photochemical model showed that the accuracy of our NO_3 data products were better than 30%. Re-processing of the complete dataset and validation activities are currently in progress. Comparisons of our NO_3 profiles with stellar occultation NO_3 measurements from GOMOS (Global Ozone Monitoring by Occultation of Stars) instrument will be considered in the future.

Acknowledgements We are thankful to the following institutions: European Space Agency (ESA) for providing SCIAMACHY level-1 data. The HALOE and SAGE II teams at Hampton University and NASA Langley Research Center (LaRC), USA, for providing us with HALOE and SAGE II data. The ECMWF special project SPDECDIO provided the temperature and pressure profiles for this work. This work was funded in parts by the German Ministry of Education and Research (BMBF) via grant 07UFE12/8, the DLR-Bonn via grant 50EE0502, the University of Bremen and the state of Bremen. We are grateful to our anonymous reviewers for their helpful comments and suggestions.

References

Amekudzi LK (2005) Stratospheric O_3, NO_2, and NO_3 number density profiles from SCIAMACHY lunar occultation spectroscopic measurements: Retrieval, validation and interpretation. PhD thesis, Universität Bremen, ISBN 3-8325-1131-8, Logos Verlag Berlin

Amekudzi LK, Sinnhuber BM, Sheode NV, Meyer J, Rozanov A, Lamsal LN, Bovensmann H, Burrows JP (2005) Retrieval of stratospheric NO_3 vertical profiles from SCIAMACHY lunar occultation measurement over the Antarctic. J Geophys Res 110(D20304), doi:10.1029/2004JD005748

Amekudzi LK, Bracher A, Bramstedt K, Rozanov A, Bovensmann H, Burrows JP (2007a) Towards validation of SCIAMACHY lunar occultation NO_2 vertical profiles. Adv Space Res 41(11):1921–1932, doi:10.1016/j.asr.2007.06.055

Amekudzi LK, Bramstedt K, Bracher A, Rozanov A, Bovensmann H, Burrows JP (2007b) Current retrieval and intercomparisons results of SCIAMACHY nighttime NO_X. In: Proc. of Envisat Symposium 2007, ESA Publication Division, ESTEC, Noordwijk, The Netherlands, SP-636

Amekudzi LK, Bramstedt K, Bracher A, Rozanov A, Bovensmann H, Burrows JP (2007c) SCIAMACHY solar and lunar occultation: validation of ozone, NO_2 and NO_3 profiles. In: Proc of Atmospheric Chemistry Validation (ACVE-3) December 2006, ESA Publication Division, ESTEC, Noordwijk, The Netherlands, SP-642

Bovensmann H, Burrows JP, Buchwitz M, Frerick J, Noël S, Rozanov VV, Chance KV, Goede APH (1999) SCIAMACHY: Mission objectives and measurement modes. J Atmos Sci 56(2): 127–150, doi:10.1175/1520-0469(1999)056¡0127:SMOAMM¿2.0.CO;2

Bracher A, Sinnhuber M, Rozanov A, Burrows JP (2005) Using a photochemical model for the validation of NO_2 satellite measurements at different solar zenith angles. J Atmos Chem Phys 5:393–408

Bramstedt K, Amekudzi LK, Bracher A, Rozanov A, Bovensmann H, Burrows JP (2007) SCIAMACHY solar occultation: Ozone and NO_2 profiles 2002–2006. In: Proc. of Envisat Symposium 2007, ESA Publication Division, ESTEC, Noordwijk, The Netherlands, SP-636

Brühl C, Drayson SR, Russell JM, Crutzen PJ, Mclnerney JM, Purcell PN, Claude H, Gernandt H, McGee TJ, McDermid IS, Gunson MR (1996) Halogen occultation experiment ozone channel validation. J Geophys Res 101(D6):10 217–10 240, doi:10.1029/95JD02031

Buchwitz M, Rozanov VV, Burrows JP (2000) A correlated-*k* distribution scheme for overlapping gases suitable for retrieval of atmospheric constituents from moderate resolution radiance measurements in the visible/near-infrared spectral region. J Geophys Res 105(D12): 15 247–15 262, doi:10.1029/2000JD900171

Burrows JP, Dehn A, Deters B, Himmelmann S, Richter A, Voigt S, Orphal J (1998) Atmospheric remote-sensing reference data from GOME: Part 1. Temperature-dependent absorption cross sections of NO_2 in the 231–794 nm range. J Quant Spectrosc Radiat Transf 60(6):1025–1031

Cunnold DM, Chu WP, Barnes RA, McCormick MP, Veiga RE (1989) Validation of SAGE II ozone measurements. J Geophys Res 94:8447–8460

Cunnold DM, Zawodny JM, Chu WP, Pommereau JP, Goutail F, Lenoble J, McCormick MP, Veiga RE, Murcray D, Iwagami N, Shibasaki K, Simon PC, Peetermans W (1991) Validation of SAGE II NO_2 measurements. J Geophys Res 96(D7):12913–12925

Gordley LL, Russell JMI, Mickley LJ, Frederick JE, Park JH, Stone KA, Beaver GM, McInerney JM, Deaver LE, Toon GC, Murcray FJ, Blatherwick RD, Gunson MR, Abbatt JPD, Mauldin RLI, Mount GH, Sen B, Blavier JF (1996) Validation of nitric oxide and nitrogen dioxide measurements made by the halogen occultation experiment for the UARS platform. J Geophys Res 101(D6):10241–10266

Gottwald M, Bovensmann H, et al. (2006) SCIAMACHY monitoring the changing Earth‘s atmosphere. DLR, Germany, Institut für Methodik der Fernerkundung (IMF)

Kumer JB, Kawa SR, Roche AE, Mergenthaler JL, Smith SE, Taylor FW, Connell PS, Douglass AR (1997) UARS first global N_2O_5 data set: Application to a stratospheric warming event in January 1992. J Geophys Res 102(D3):3575–3582

Meyer J, Bracher A, Rozanov A, Schlesier AC, Bovensmann H, Burrows JP (2005) Solar occultation with SCIAMACHY: algorithm description and first validation. J Atmos Chem Phys 5:1589–1604

Randall CE, Rusch DW, Bevilacqua RM, Hoppel KW, Lumpe JD, Shettle E, Thompson E, Deaver L, Zawodny J, Kyrö E, Johnson B, Kelder H, Dorokhov VM, König-Langlo G, Gil M (2003) Validation of POAM III ozone: Comparisons with ozonesonde and satellite data. J Geophys Res 108(D12):4367, doi:10.1029/2002JD002944

Rodgers CD, Connor BJ (2003) Intercomparison of remote sounding instruments. J Geophys Res 108:4116, doi:10.1029/2002JD002944

Rozanov A, Rozanov V, Buchwitz M, Kokhanovsky A, Burrows JP (2005) SCIATRAN 2.0 – A new radiative transfer model for geophysical applications in the 175–2400 nm spectral region. Adv Space Res 36(5):1015–1019

Sander SP, et al. (2003) Chemical kinetics and photochemical data for use in stratospheric modeling. NASA Panel Data Eval 14:1–119–4–111, JPL Publication 02–25

Validation of GOMOS/Envisat High-Resolution Temperature Profiles (HRTP) Using Spectral Analysis

V.F. Sofieva, J. Vira, F. Dalaudier, A. Hauchecorne, and the GOMOS Team

Abstract The GOMOS (Global Ozone Monitoring by Occultation of Stars) instrument on board the Envisat satellite is equipped with two fast photometers operating at 1 kHz sampling frequency in blue and red wavelengths. The bi-chromatic scintillations recorded by the photometers allow the determination of refractive angle, which is proportional to the time delay between the photometer signals. The high resolution density and temperature profiles can be reconstructed (with a vertical resolution of about 200 m) from these data in the altitude range $\sim$15–35 km. The validation of small-scale fluctuations in HRTP requires a very close collocation in time and space with high-quality data having comparable or better vertical resolution. Comparing spatial spectra of temperature profile fluctuations requires less strict collocation criteria. In this paper, we compared vertical wavenumber spectra of temperature fluctuations in HRTP and in collocated radiosonde data. We found that the vertical wavenumber spectra of HRTP and radiosonde temperature fluctuations are very similar in case of vertical occultations of bright stars. In case of oblique occultations or of dim stars, the HRTP fluctuations often have a larger spectral magnitude, despite of several good agreements. The spectral analysis has confirmed that the actual resolution of HRTP is 150–200 m.

1 HRTP: Measurement Principle and Retrievals

GOMOS on board Envisat is the first instrument performing synchronous scintillation measurements at two wavelengths. It is equipped with two fast photometers operating at blue (470–520 nm) and red (650–700 nm) wavelengths with a sampling frequency of 1 kHz (http://envisat.esa.int/instruments/gomos, Bertaux et al. 2004; Kyrölä et al. 2004).

The retrieval of high-resolution temperature and density exploits chromatic refraction in the atmosphere. Due to dependence of air density (and, consequently,

---

V.F. Sofieva (✉)
Finnish Meteorological Institute, Earth Observation, Helsinki, Finland
e-mail: viktoria.sofieva@fmi.fi

A. Steiner et al. (eds.), *New Horizons in Occultation Research*,
DOI 10.1007/978-3-642-00321-9_9, © Springer-Verlag Berlin Heidelberg 2009

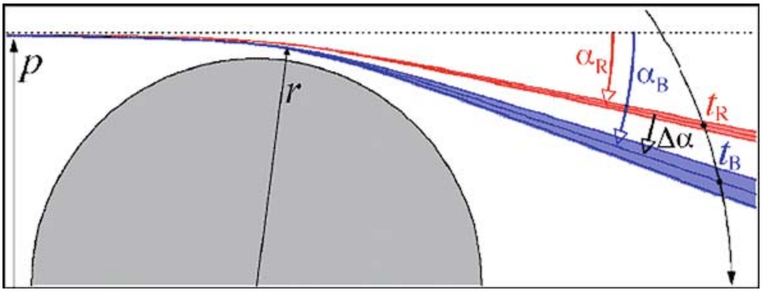

Fig. 1 The schematic representation of chromatic refraction and the principle of refraction angle measurements by GOMOS

refractivity) on wavelength, the blue ray bends more than red one (Fig. 1), thus it is observed later by GOMOS.

The intensity structures (scintillation spikes), which are caused by atmospheric density fluctuations, are observed by both photometers with a time delay t_B–t_R (Fig. 2) proportional to the difference in refraction angle $\Delta\alpha = \alpha_B - \alpha_R$. In the HRTP processing, the time delay is estimated as the position of the maximum of the cross-correlation function of photometer signals.

The difference in refractive angles $\Delta\alpha$ is transformed into the refractive angle α_B at the reference wavelength. After that, the retrieval method is similar to the one used in radio occultation. Assuming local spherical symmetry of the atmosphere, the refractivity profile is retrieved from the refractive angle profile using the Abel transform. The refractivity is proportional to air density. The corresponding pressure

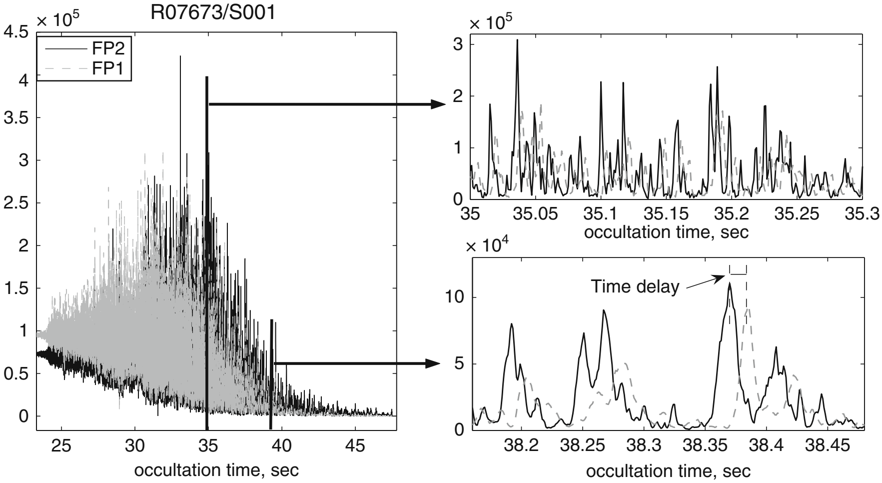

Fig. 2 Signals of GOMOS fast photometers (FP1, blue, and FP2, red). Time delay is clearly seen in the photometer data

profile is deduced by integrating the hydrostatic equation and, finally, the temperature profile is obtained from the state equation of a perfect gas. The details of the HRTP processing are described in Dalaudier et al. (2006).

At altitudes ∼18–35 km, the estimated accuracy of HRTP is 1–2 K. The best accuracy is achieved for vertical (in orbital plane) occultations of bright stars. Below ∼15 km, the quality of HRTP decreases due to low signal-to-noise ratio, broadening of scintillation peaks as a result of chromatic smoothing and the violation of the assumptions used in the retrievals (in particular, the weak scintillation assumption). The vertical resolution of HRTP profiles is ∼200 m.

The HRTP profiles used in this validation were processed with the research software, which was developed within the scope of the ESA funded project "Algorithms for the estimation of high resolution temperature and density profiles from GOMOS measurements" aimed at optimization of HRTP retrievals. GOMOS data from September 2002 to January 2005 were used. Collocated sounding data available in the Envisat calibration/validation database at NILU (Norwegian Institute for Air Research) and in the SHADOZ (Southern Hemisphere Additional Ozonesondes) database (Thompson et al. 2001) were used for the validation.

2 Using Spectral Analysis for HRTP Validation: Motivation

The beneficial feature of HRTP is a good vertical resolution. In order to validate small-scale fluctuations in HRTP that are assumed to be generated by internal gravity waves (IGW), correlative measurements should provide high-quality temperature in the same altitude range with a similar or better resolution.

Let us discuss the data collocation criteria, i.e., a space-time window, where the temperature field does not change much and where we can expect similarity of temperature profiles, including their small-scale fluctuations. In the stratosphere, the characteristic ratio of horizontal and vertical scales is typically equal to the ratio of maximal and minimal intrinsic frequencies of the gravity waves field (N/f is typically larger than 100, N is the Brunt-Väisälä frequency and f is the Coriolis parameter). Since the vertical resolution of HRTP is ∼200 m, the horizontal separation of collocated measurements should ideally be less than 20 km. HRTP is most sensitive to gravity waves with small vertical and large horizontal wavelengths, i.e., waves of low intrinsic frequencies (Fritts and Alexander 2003). Since the characteristic time for evolution of such gravity waves is few hours, the time difference between collocated profiles should not exceed 2–3 h.

The criteria for data selection derived above are very strict. In the altitude range of HRTP, only radiosonde data satisfy the vertical resolution requirements. It is important to note that the time separation results in additional spatial separation in the atmosphere caused by advection of air masses. For example, provided a very moderate wind speed of 20 m/s for altitudes 15–30 km, air parcels probed at the same geographical location with a time interval of 30 min will be separated by 36 km in the atmosphere. Relatively long measurement time of temperature profiles by radiosondes during balloon flights (it takes ~1 hour for balloon to raise from 10–30 km) has a similar effect. If a satellite (nearly instantaneous) measurement is perfectly collocated in time and space with a radiosonde measurement at 10 km, then they will be separated in the atmosphere up to several tens of kilometers at 30 km due to displacement by wind.

It is nearly impossible to find data satisfying these very strict collocation criteria (all our searches were not successful so far). According to the analysis of collocated radiosonde data (Sofieva et al. 2008), difference in temperature rapidly grows with increasing separation distance. Rms of temperature differences for profiles having ~200 m vertical resolution is ~0.4 K for 40 km separation, ~0.7 K for 80 km separation, and it is ~1–1.5 K for separations 200–1000 km.

If the separation of measurements in the atmosphere exceeds 20–30 km, the small scale structures of temperature profiles should not coincide. However, we can expect similar spectral properties of the temperature field at locations not far from each other (e.g., less than 500 km) during some time period (few hours). The spectral analysis of collocated radiosonde profiles (Sofieva et al. 2008) has confirmed this hypothesis: the spectra of temperature fluctuations look similar, even for profiles significantly separated in time and space (a few hundreds of kilometers, several hours). The values of rms of profile fluctuations are found to be very close to each other (the smaller distance, the smaller difference in rms of fluctuations). For radiosonde profiles separated in the stratosphere by 300–600 km, rms of temperature fluctuations are within ± 40% interval in majority of cases (Sofieva et al. 2008).

The spectral analysis approach allows using data collocated in a wider space-time window, thus more data are suitable for validation. Furthermore, the validation of the HRTP spectra is of high importance, as one of the possible HRTP applications is the study of internal gravity wave activity in the stratosphere.

The vertical resolution of HRTP is expected to be ~200 m (worse than of radiosonde profiles but better than that from radio-occultation measurements). This resolution is sufficient for probing vertical spectra of gravity waves. Comparison of vertical spectra of temperature fluctuations in HRTP and collocated radiosonde profiles allows experimental estimation of actual HRTP vertical resolution: it corresponds to a cut-off of vertical spectra at large wavenumbers.

However, comparing spectra of temperature fluctuations in HRTP and collocated radiosonde profiles should be performed with care, because the vertical wavenumber spectra of temperature fluctuations in the ground-based (HRTP) and in GW intrinsic reference frame (balloon measurements) can differ as a result of the wind-shifting effect (e.g., Eckermann 1995). Gardner and Gardner (1993) estimated influence of horizontal winds on vertical wavenumber spectra. They found that modifications in vertical wavenumber spectra caused by background winds are negligible if:

(i) ratio of horizontal wind speed to balloon ascend speed is much smaller than the anisotropy coefficient η (in Gardner and Gardner (1993), $\eta \approx 22$ is taken). This means that the time required to ascend through a temperature irregularity of characteristic vertical dimension is short compared to the time required to advect the balloon horizontally through the irregularity with the characteristic horizontal size.

(ii) the time required to ascend through a temperature irregularity of characteristic vertical dimension is short compared to the lifetime of the irregularity.

The second condition can be considered as always satisfied, as balloons ascend with the mean velocity of 4–5 m/s. The first condition can be violated only in case of very strong horizontal winds.

For HRTP, the influence of obliquity of occultation on the distortion of vertical wavenumber can be estimated in a similar way. The difference between spectra obtained using instantaneous vertical and oblique profiles is expected to be small, if obliquity α of occultation satisfies $\tan \alpha << \eta$ (α is the angle between the local vertical and the direction of star motion). This condition is satisfied for all occultations considered in the present work.

3 Validation Results

3.1 Data Selection

We selected temperature profiles from PTU (pressure, temperature, humidity) and ozone soundings at high and mid latitudes available in NILU database, located at < 300 km distance and having < 4 h time difference with the corresponding GOMOS measurements. The location of stations and sonde characteristics are collected in Table 1. 63 profiles were found satisfying the collocation criterion. However, only 27 sounding profiles were covering a significant part the HRTP altitude range, i.e., altitudes ∼18–30 km. Most of the selected GOMOS occultations are in "stray light" illumination conditions (i.e., not in full dark) and oblique (off orbital plane). Vertical occultations of bright stars ($|\alpha| \leq 5°$), where the best accuracy of HRTP is expected, were not presented within this selected set. In order to have possibility to estimate HRTP quality in "the best" occultations, we found 12 vertical occultations of bright stars collocated with SHADOZ soundings. However, the spatial separation of these occultations and SHADOZ soundings is large, 300–600 km, as well as time difference, ∼12 h. The information about the

Table 1 Location of sounding stations at mid and high latitudes and some characteristics of soundings

Station	Location	Sonde type and typical vertical resolution
Legionowo	52.40°N, 20.97°E	50 m (PTU)
Uccle	50.8°N, 4.35°E	75 m (PTU and ozone sondes)
Jokioinen	52.40°N, 20.97°E	10 m (PTU), 50 m (ozone sondes)
Sodankylä	67.37°N, 26.63°E	10 m (PTU and ozone sondes)
Ny-Ålesund	78.92°N, 11.93°E	50 m (ozone sonde)
Scorebysund	70.50°N, 22.00°W	50 m (ozone sonde)
Marambio	64.2°S, 56.7°W	50 m (ozone sonde)
Dumont D'Urville	66.67°S, 140.01°E	90 m (ozone sonde)

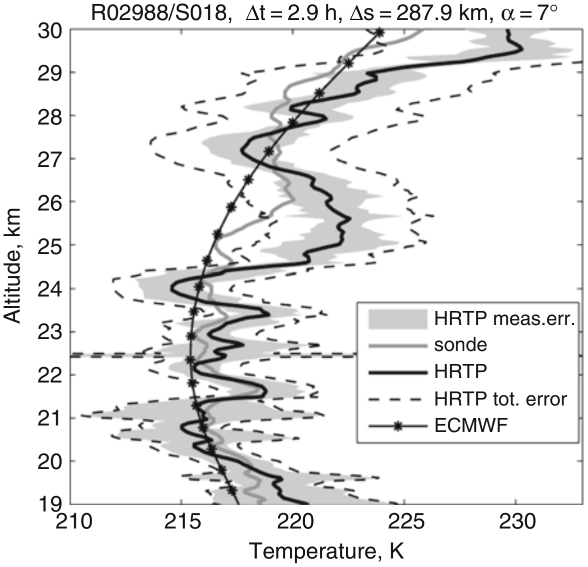

Fig. 3 GOMOS HRTP from occultation of star S018 and collocated radiosonde temperature profile at Jokioinen on September 25, 2002. Distance between profiles, time difference and obliquity of occultation α (the angle between the local vertical and the direction of star motion in the phase screen) are specified in the figure header

location of SHADOZ sounding stations and sonde characteristics can be found at http://croc.gsfc.nasa.gov/shadoz/and in Thompson et al. (2001).

An example of collocated HRTP and sounding profiles is shown in Fig. 3. Two error estimates are shown for HRTP: measurement error (shaded area) and the total error estimate, which includes the measurement error and the upper limit initialization error (dashed lines). ECMWF temperature profile at the occultation location is also shown.

3.2 Results of Spectra Comparison

For computing power spectral density, the profiles were interpolated to a common equidistant 30 m altitude grid. For detection of temperature fluctuations, the smooth component is obtained using Hanning filtering with the cut-off scale 3 km.

The power spectral density of relative fluctuations of temperature $\delta T/T$ is estimated using the method of averaged periodogram. In our analysis, we focus on wave numbers lower than 0.01 cy/m, as the high-frequency part of spectra is influenced by aliasing. For the spectral analysis, we used profiles in the altitude range 20–30 km.

Figure 4 shows several spectra of relative temperature fluctuations in the collocated HRTP and sounding profiles at mid and high latitudes (occultations of different types, mostly oblique). The "model" lines correspond to the model of the saturated gravity waves, which predicts κ_z^{-3} shape of the vertical wavenumber spectrum $V_{\delta T/T}$ of the relative temperature fluctuations:

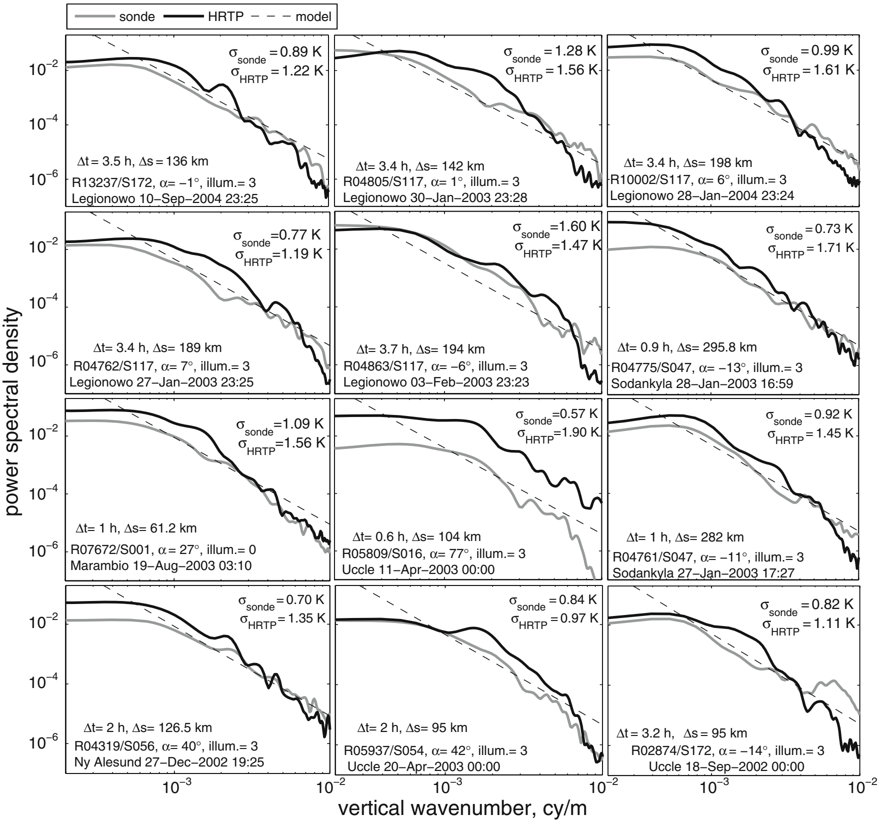

Fig. 4 Spectra of relative temperature fluctuations in sounding profiles and in HRTP, collocations at high and mid latitudes

$$V_{\delta T/T}(\kappa_z) = A\frac{N^4}{g^2}\kappa_z^{-3}, \tag{1}$$

where κ_z is the vertical wave number, g is the acceleration of gravity, and $A{\approx}0.1$ is an experimental constant (Smith et al. 1987). They are presented only for reference, as the current analysis is not aimed at checking the hypothesis on universality of GW vertical spectra. It is known that departures from the spectrum (1) are rather common in the stratosphere (Eckermann 1995; Fritts and Alexander 2003).

The rms of temperature fluctuations (computed as a sample standard deviation) and information about GOMOS occultations and sonde measurements are also specified in Fig. 4.

The spectral density of HRTP fluctuations shown in Fig. 4 is usually larger than that of soundings fluctuations. The horizontal wind velocity is not more than about 10 times the balloon ascent velocity in all the considered collocations. Thus the difference of HRTP and radiosonde wavenumber spectra is unlikely explained by the influence of background wind estimated in Gardner and Gardner (1993) and discussed in Sect. 2 of this chapter. We have not found any clear dependence of spectra discrepancy on magnitude of horizontal winds. All occultations selected at high and mid latitudes are either of dim stars (thus the measurement noise is significant) or/and oblique. In oblique occultations, isotropic scintillations caused by turbulence disturb the correlation between photometer signals. Thus accuracy of HRTP retrievals, which are based on finding the correlation between photometer signals, decreases in oblique occultations. Therefore, disagreement in spectral characteristic for these occultations is not very surprising. The situation drastically changes for vertical occultations of bright stars (Fig. 5, these occultations are collocated with SHADOZ soundings in tropics). The vertical wavenumber spectra are very similar for HRTP and sondes, as well as the rms of fluctuations.

Figure 6 shows the scatter plot of rms of temperature fluctuations in HRTP and radiosonde profiles, for these two datasets. Figure 6 summarizes observations described above. For vertical occultations of bright stars, rms of HRTP fluctuations

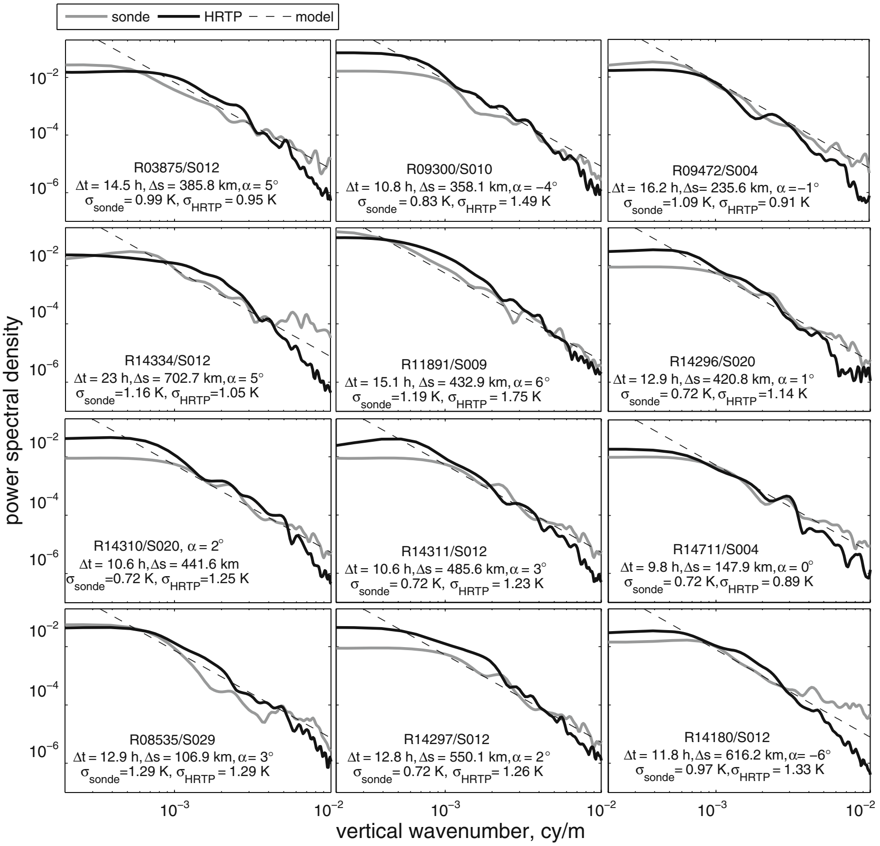

Fig. 5 Spectra of relative temperature fluctuations in SHADOZ sounding profiles and in HRTP

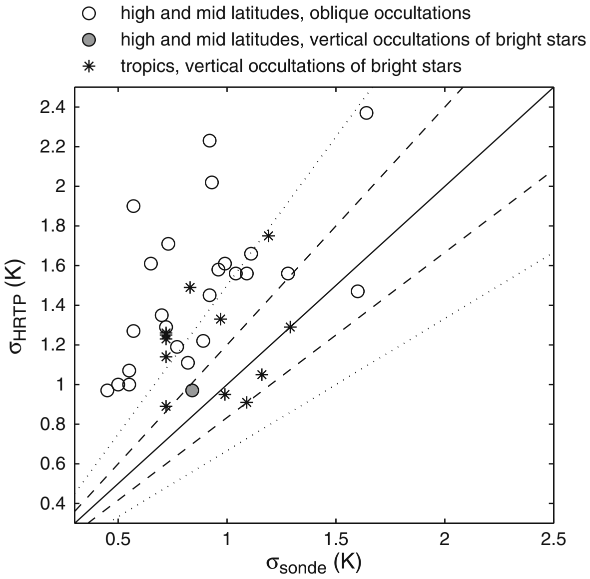

Fig. 6 Rms of temperature fluctuations of HRTP profiles versus that of sounding profiles. *Solid line*: $y=x$, *dashed lines*: $y=1.2x$ and $y=(1/1.2)\,x$; *dotted lines*: $y=1.5x$ and $y=(1/1.5)x$

is close to that in the collocated radiosonde temperature profiles. The scattering of the data is very similar to that observed in collocated radiosonde data (Sofieva et al. 2008). In case of oblique occultations or dim stars, fluctuations in HRTP are larger than in radiosonde temperature profiles, but several good agreements were also observed.

A clear cut-off corresponding to scales ~150–200 m is observed in HRTP spectra (Fig. 5). This confirms that the actual HRTP vertical resolution is 150–200 m.

4 Conclusions and Outlook

The validation of small-scale structures in high-resolution profiles is the problem of high complexity, because the collocated data with the same vertical resolution should be available nearly at the same time and location. In this work, we based and described the spectral analysis approach to validation of high-resolution profiles, which requires less strict collocation criteria.

The application of this method for validation of high-resolution temperature profiles retrieved from bi-chromatic stellar scintillation measurements by GOMOS fast photometers has shown that HRTP fluctuations are realistic (in terms of their 1D vertical spectra) in vertical occultations of bright stars. In case of oblique occultations or of dim stars, the HRTP fluctuations often have a larger spectral magnitude, despite of several good agreements. The spectral analysis has confirmed that the actual resolution of HRTP is 150–200 m.

The large class of occultations – close to vertical occultations of medium-brightness stars (with visual magnitude $1 < m < 2.5$) is not presented in the considered data sets. We expect that the accuracy of HRTP profile retrievals from such occultations is close to that with bright stars, as moderate noise does not affect the computation of cross-correlation function and thus the accuracy of time delay reconstruction. The validation of these occultations is the subject of future work.

In addition, it is possible also to use all available radiosonde data world-wide and find suitable collocations with the GOMOS occultations for spectral validation of HRTP. This will possibly give a larger statistics and a better coverage of different types of occultations.

Excessive amplitude of HRTP fluctuations, which was detected in this study in case of dim stars or oblique occultations, can potentially be reduced by applying regularization in retrievals. The HRTP profiles presented in this study were processed with the minimum of a priori information used in the inversion. The inversion method based on statistical optimization (Bayesian approach) has also been developed within the scope of the project "Algorithms for the estimation of high resolution temperature and density profiles from GOMOS measurements". Validation of retrievals with the regularization applied will also be the subject of future work.

Acknowledgements This work has been performed within the scope of the ESA funded project "Algorithms for the estimation of high resolution temperature and density profiles from GOMOS measurements" (Contract number 17895/04/I-LG). The authors thank ESA and the GOMOS team for the GOMOS data. The authors greatly appreciate the use of correlative data from the ENVISAT Cal/Val database at NILU, and thank the principal investigators of the radiosondes and SHADOZ sondes. The work of V.F. Sofieva was supported by the Academy of Finland (postdoctoral researcher project).

References

Bertaux JL, Hauchecorne A, Dalaudier F, Cot C, Kyrola E, Fussen D, Tamminen J, Leppelmeier GW, Sofieva V, Hassinen S, Fanton d′Andon O, Barrot G, Mangin A, Theodore B, Guirlet M, Korablev O, Snoeij P, Koopman R, Fraisse R (2004) First results on GOMOS/Envisat. Adv Space Res 33:1029–1035, doi:10.1016/j.asr.2003.09.037

Dalaudier F, Sofieva V, Hauchecorne A, Kyrölä E, Blanot L, Guirlet M, Retscher C, Zehner C (2006) High-resolution density and temperature profiling in the stratosphere using bi-chromatic scintillation measurements by GOMOS. Proceedings of the First Atmospheric Science Conference, European Space Agency, ISBN 92-9092-939-1-ISSN 1609-042X

Eckermann SD (1995) Effect of background winds on vertical wavenumber spectra of atmospheric gravity waves. J Geophys Res 100(D7):14097–14112

Fritts DC, Alexander MJ (2003) Gravity wave dynamics and effects in the middle atmosphere. Rev Geophys 41(1):1003, doi:10.1029/2001RG00106

Gardner C, Gardner N (1993) Measurement distortion in aircraft, space shuttle, and balloon observations of atmospheric density and temperature perturbation spectra. J Geophys Res 98(D1):1023–1033

Kyrölä E, Tamminen J, Leppelmeier GW, Sofieva V, Hassinen S, Bertaux JL, Hauchecorne A, Dalaudier F, Cot C, Korablev O, Fanton d'Andon O, Barrot G, Mangin A, Theodore B, Guirlet M, Etanchaud F, Snoeij P, Koopman R, Saavedra L, Fraisse R, Fussen D, Vanhellemont F (2004) GOMOS on Envisat: An overview. Adv Space Res 33:1020–1028, doi:10.1016/S0273-1177(03)00590-8

Smith SA, Fritts DC, VanZandt TE (1987) Evidence of a saturation spectrum of atmospheric gravity waves. J Atmos Sci 44(10):1404–1410

Sofieva VF, Dalaudier F, Kivi R, Kyrö E (2008) On the variability of temperature profiles in the stratosphere: Implications for validation. Geophys Res Lett 35(L23808), doi:10.1029/2008GL035539

Thompson AM, Witte JC, McPeters RD, Oltmans SJ, Schmidlin FJ, Logan JA, Fujiwara M, Kirchhoff VWJH, Posny F, Coetzee GJR, Hoegger B, Kawakami S, Ogawa T, Johnson BJ, Vömel H, Labow G (2001) Southern Hemisphere Additional Ozonesondes (SHADOZ) 1998–2000 tropical ozone climatology 1. Comparison with Total Ozone Mapping Spectrometer (TOMS) and ground-based measurements. J Geophys Res 108(D2):8238, doi:10.1029/2001JD000967

Part III

GNSS Occultation for Atmospheric Studies

Assimilation of Radio Occultation Data in the Global Meteorological Model GME of the German Weather Service

D. Pingel and A. Rhodin

Abstract The assimilation of GPS radio occultations within the three-dimensional variational data assimilation system of the German Weather Service requires GPS radio occultation bending angle forward operators. To optimize the forward operator setup, different one- and three-dimensional bending angle forward operators are evaluated. The innovation statistics for radio occultation data from the CHAMP, GRACE-A, and FORMOSAT-3/COSMIC satellites are compared with estimates based on the background- and observation errors specified in the assimilation scheme. A numerical experiment is performed to assess the impact of assimilated radio occultation data on the weather forecast scores, to be compared to an experiment assimilating conventional observation data only.

1 Data Assimilation at the DWD

In the assimilation step of the numerical weather forecasting procedure, preceding the forecast run itself, the state of the meteorological model is updated using observational information. Conventional sources of meteorological observations are in-situ data such as radiosondes, ground station measurements, data from aircrafts, and buoys. They are complemented by satellite remote-sensing measurements, e.g., radiances of a given wavelength at nadir.

Global positioning system radio occultation (GPS RO) data is a relatively new and valuable source of observational information introducing additional information on temperature and humidity into the model (Healy et al., 2007b; Wickert et al., 2009). Benefits of RO data are good vertical resolution, independence of cloudy conditions (that generally afflict radiance measurements, cf. McNally (2002)), the lack of fundamental biases, and a nearly uniform global coverage.

At the German weather service (Deutscher Wetterdienst, DWD), the assimilation of observational data (including GPS radio occultation data) will be performed by

---

D. Pingel (✉)
Deutscher Wetterdienst (DWD), Offenbach, Germany
e-mail: detlef.pingel@dwd.de

A. Steiner et al. (eds.), *New Horizons in Occultation Research*,
DOI 10.1007/978-3-642-00321-9_10, © Springer-Verlag Berlin Heidelberg 2009

the three-dimensional variational (3D-Var) assimilation method. The assimilation is done in a statistically optimal way, taking into account the observations **y**, the forecast $\mathbf{x}_b$ (model background) from the previous analysis and error characteristics of both model and observations, given by their respective error covariance matrices **B** and **R**. Therefore, a thorough specification of observational and forecast errors is of high relevance in data assimilation. Within the assimilation process, a cost function J containing penalty terms for deviances of the control variables **x** (gridded model field) from the background $\mathbf{x}_b$ on the one side, and of the observations **y** from their model equivalents $\mathbf{H}(\mathbf{x})$ on the other side is minimized:

$$J(\mathbf{x}) = J_b + J_o = \frac{1}{2}[\mathbf{x} - \mathbf{x}_b]^T\mathbf{B}^{-1}[\mathbf{x} - \mathbf{x}_b] + \frac{1}{2}[\mathbf{y} - H(\mathbf{x})]^T\mathbf{R}^{-1}[\mathbf{y} - H(\mathbf{x})]. \quad (1)$$

A forward operator H maps the model background data into observation space. For in situ measurements, H simply performs an interpolation to the location of the observation. In the case of remote sensing measurements, H is more complex and generally nonlinear. The analysis **x** is given by the zero of the gradient of the cost function J with respect to the control variables **x**,

$$\frac{\partial J}{\partial \mathbf{x}} = \mathbf{B}^{-1}[\mathbf{x} - \mathbf{x}_b] + \mathbf{H}^T\mathbf{R}^{-1}[\mathbf{y} - H(\mathbf{x})] \quad (2)$$

with **H** being the Jacobi matrix of H. Tangent-linear and adjoint operators calculate the product of **H** with a vector to the right and to the left, respectively. The analysis increment is

$$\begin{aligned}\mathbf{x} - \mathbf{x}_b &= [\mathbf{H}^T\mathbf{R}^{-1}\mathbf{H} + \mathbf{B}^{-1}]^{-1}\mathbf{H}^T\mathbf{R}^{-1}[\mathbf{y} - H(\mathbf{x}_b)] \\ &= \mathbf{B}\mathbf{H}^T[\mathbf{H}\mathbf{B}\mathbf{H}^T + \mathbf{R}]^{-1}[\mathbf{y} - H(\mathbf{x}_b)].\end{aligned} \quad (3)$$

The solution of Eq. (3) is performed in observation space (Physical-space Statistical Assimilation System, PSAS). This implies a reduction of the size of the numerical equations to solve significantly compared to a minimization in model space. It is done by substituting

$$\mathbf{x} - \mathbf{x}_b = \mathbf{B}\mathbf{H}^T\mathbf{z} \quad (4)$$

and solving

$$[\mathbf{H}\mathbf{B}\mathbf{H}^T + \mathbf{R}]\mathbf{z} = [\mathbf{y} - H(\mathbf{x}_b)] \quad (5)$$

for **z** in observation space. The nonlinear problem is solved in an iterative procedure with a combination of an outer Newton algorithm and an inner preconditioned Conjugate Gradient (CG) algorithm. Nonlinearities are accounted for by iterating Eq. (5) with H linearized at the current estimate $\mathbf{x}_i$, denoted by $\mathbf{H}_i$ (Daley and Barker, 2000):

$$[\mathbf{H}_i\mathbf{B}\mathbf{H}_i^T + \mathbf{R}]\mathbf{z} = [\mathbf{y} - H(\mathbf{x}_i) + \mathbf{H}_i\mathbf{x}_i - \mathbf{H}_i\mathbf{x}_b] \quad (6)$$

Subsequently, the analysis increments of the model state variables are determined by post-multiplication of the solution **z** with the forecast error covariance according to Eq. (4).

Basically, phase delay, bending angle, or refractivity fields can play the role of the observations to be assimilated. At the DWD, bending angles have been chosen as observations, as they allow for a reliable specification of significant background and observational errors and can be derived without any assumptions regarding horizontal homogeneity or isotropy. Hence an appropriate forward operator H is to be implemented to map the model background at the location of the observation to the corresponding first guess bending angle.

2 Evaluation of Bending Angle Forward Operators

An essential step in the preparation of the assimilation of radio occultations is to find a reasonable setup for the forward operator that is suitable for data assimilation under the specific terms of operational application. One- and three-dimensional bending angle forward operators are evaluated, with the standard deviation of the innovations (differences of observation and first guess value) being considered as a benchmark criterion. While the three-dimensional ray-tracing operator shows the smallest standard deviation, the result of optimized one-dimensional forward operators come close to the performance of the three-dimensional operator.

The evaluation of a possible bending angle forward operator setup, providing a background profile of bending angles $\alpha(p)$ as function of impact height p, is a prerequisite for the assimilation of RO observations. A three-dimensional ray tracing model and a one-dimensional model have been considered to serve as forward operators:

The ray-tracing operator $H_{3\mathrm{d}}$ (Gorbunov and Kornblueh, 2003) is supposed to be the best fit to the physical reality, as it takes into account the along-ray and transverse-ray horizontal gradients of the temperature and humidity atmospheric fields as well as the drift of the ray's tangential points in the course of an occultation. A certain disadvantage of the ray-tracing operator is the high demand of computing resources (time and memory).

The one-dimensional forward operator is based on the assumption of spherically symmetric atmospheric fields. It applies an inverse Abel transform

$$\alpha(p) = -2p \int_p^\infty \frac{\mathrm{d}\ln n}{\mathrm{d}r} \cdot \frac{\mathrm{d}r}{\sqrt{(nr)^2 - p^2}} \tag{7}$$

to the refractivity profile

$$n = 1 + 10^{-6}\left(c_1 \frac{p}{T} + c_2 \frac{p_v}{T^2}\right) \tag{8}$$

(with $c_1 = 77.6$ K hPa^{-1} and $c_2 = 3.73 \cdot 10^5$ K^2 hPa^{-1}) derived from the temperature T, pressure p, and water vapor partial pressure p_v above a single point in the horizontal, the occultation point x_{oc}. By reducing the horizontally extended occultation event to a single point x_{oc}, the tangential point drift is neglected. Furthermore, the choice of x_{oc} introduces a certain indefiniteness to the forward model. To model the drift of the tangential points at least to some extent, three versions of the one-dimensional forward operator have been implemented for test purposes, each of them considering a differently determined x_{oc}: The first version H_{1d} performs the inverse Abel transform at x_{oc} as given in the corresponding observation data set of bending angles. For the second version H_{1dmn}, x_{oc} is determined as the mean of the individual ray's tangential points in the lowest 20 km of the occultation profile (indicated by the additional abbreviation "mn" in the acronym "1dmn"). The third version H_{2d} applies the inverse Abel transform to each ray of the occultation profile separately, with x_{oc} being the tangential point of the ray. This approach is expected to model the tangential point drift best compared to the two preceding versions.

The data set to test the performance of the different forward operators is a CHAMP (CHAllenging Minisatellite Payload) and GRACE-A (Gravity and Climate Recovery Experiment) phase delay data set provided by the GeoForschungsZentrum (GFZ) Potsdam for January and July 2005, processed to bending angles at the DWD with the method of canonical transform CT2 (Gorbunov and Lauritsen, 2002, 2004a,b; Gorbunov et al., 2006). DWD global meteorological model GME (Majewski et al., 2002) three-hourly forecast fields served as model background. The statistical properties of the innovations, i.e., of the differences of observation and first guess, are then taken into account as a criterion to evaluate the different forward operators.

Figure 1a–c shows zonal averages of the ratio of the $(O-B)$ standard deviation of the three versions H_{1d}, H_{1dmn}, and H_{2d} of the one-dimensional forward operator to the respective value of the three-dimensional ray-tracing operator H_{3d} for January 2005 (bin size 1 km$\times$10°). For all three one-dimensional forward operators, the values of the ratios are larger than unity for most areas and heights (they are strictly larger than unity when considering global means). This indicates that the ray-tracing forward operator performs best in terms of standard deviation.

When comparing the different one-dimensional forward operators, the operator H_{1d}, accepting the occultation point as given by the CT2, performed poorest (Fig. 1a). The corresponding standard deviation exceeds the respective value for H_{3d} by up to 8%. However, the ratio is significantly smaller for the tropics compared to the extra tropics. This is related to the fact that due to differences of the atmospheric dynamics horizontal gradients of temperature and humidity are less pronounced in the tropics than in the extra tropics. As the provision for these gradients is one of the characteristics of the operator H_{3d} compared to H_{1d}, the bending angle values of the one- and three-dimensional operators tend to be comparable in the tropics.

Compared to the operator H_{1d}, the operator H_{1dmn} shows a reduced standard deviation for impact heights above ~8 km (Fig. 1b). This indicates that the averaging process brings x_{oc} closer to the tangential points of the rays in the upper troposphere and lower stratosphere.

The first guess values of the version H_{2d}, applying the inverse Abel transform to each individual ray, are closest to the ray-tracing results (Fig. 1c) as expected.

Fig. 1 Evaluation of bending angle forward operators: Ratio of the standard deviation of the one-dimensional forward operators (**a**) H_{1d} (*top*), (**b**) H_{1dmn} (*middle*) and (**c**) H_{2d} (*bottom*) with respect to the ray tracing forward operator H_{3d}, January 2005

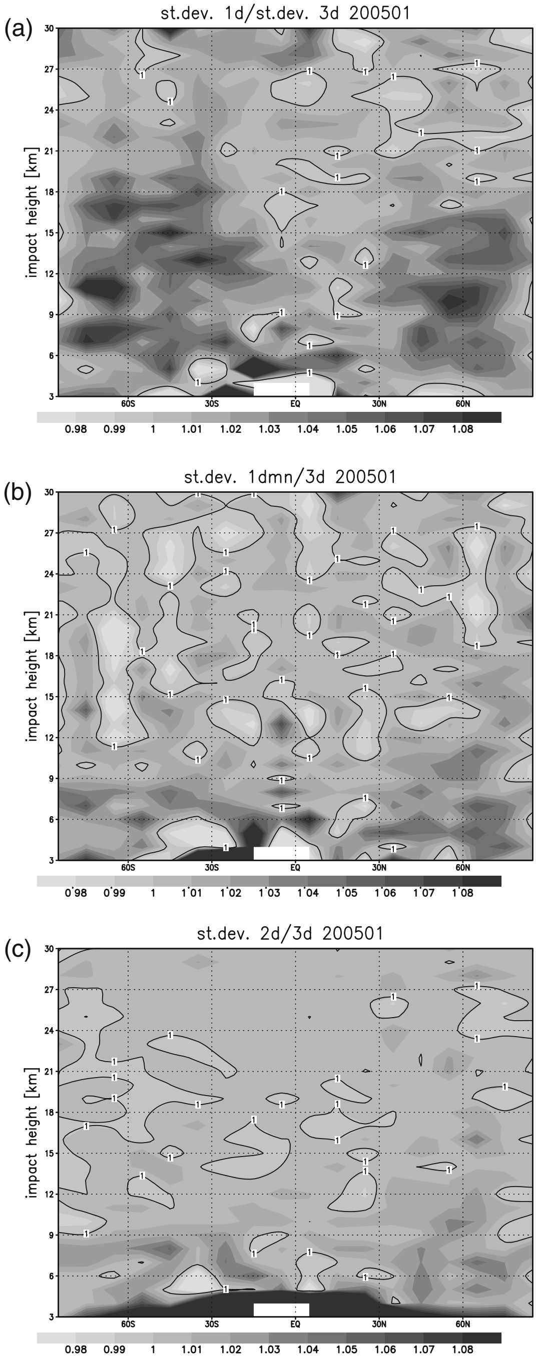

Above an impact height of ~10 km, the difference to the operator $H_{3\mathrm{d}}$ is less than 1% for most areas. Additionally, the ratio of the standard deviations is more uniform for $H_{2\mathrm{d}}$ than for $H_{1\mathrm{d}}$ and $H_{1\mathrm{dmn}}$.

However, for the lowermost rays especially at tropical latitudes, the more refined version $H_{2\mathrm{d}}$ performs worse than the more simple versions $H_{1\mathrm{d}}$ and $H_{1\mathrm{dmn}}$. This effect might be related to the fact that for most occultation events the positions of the tangent points of the lowest lying rays lie off the more or less straight line described by tangent points of higher rays. These "kinks" might be an inappropriate choice as a location for georeferencing points. A thorough investigation of this effect is necessary, though.

Below an impact height of ~8 km, the ray tracing forward operator $H_{3\mathrm{d}}$ is significantly better in terms of standard deviation. This may be attributed to the fact that below this height the bending angle signal contains predominantly humidity information (especially in the tropics). Water vapor is, contrary to temperature, a quantity that fluctuates significantly on a horizontal scale comparable with the extent of the occultation. These fluctuations are considered for by the operator $H_{3\mathrm{d}}$, but not by the one-dimensional forward operators.

Figure 2 shows the same quantity as Fig. 1c, but for July 2005. The shift of the maxima of the ratio of the standard deviations in the lower troposphere towards the north is clearly visible, corresponding to the increase of humidity in these regions in the summer of the northern hemisphere.

The results of the evaluation of the bending angle forward operators are confirmed in another way: To expose the differences of the performance of the operators (in terms of standard deviations) more clearly, we consider the innovation statistics for those observations $(\mathbf{y})_i$ whose respective first guess bending angle

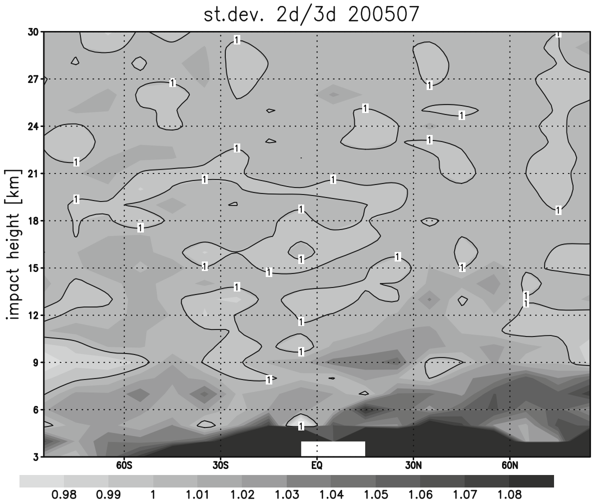

Fig. 2 As Fig. 1c, but for the summer month

values $(H(\mathbf{x}_b))_i$ differ by at least a given fraction of the ray-tracing first guess value $(H_{3d}(\mathbf{x}_b))_i$

$$|(H_F(\mathbf{x}_b))_i - (H_{3d}(\mathbf{x}_b))_i| > \varepsilon \cdot (H_{3d}(\mathbf{x}_b))_i \tag{9}$$

with $F \in \{1\mathrm{d}, 1\mathrm{dmn}, 2\mathrm{d}\}$ denoting the version of one-dimensional forward operator and components of H denoted by $(H)_i$. Each observation value $(\mathbf{y})_i$ selected by Eq. (9) corresponds to background values evaluated with the different versions of the one-dimensional forward operator and with the 3d operator. To measure the closeness of the observations to the background value, we determined the innovation $(\mathbf{y} - H(\mathbf{x}_b))$ statistics for each of the different combinations of observations $\mathbf{y}$ and background values $H_{1d}(\mathbf{x}_b)$, $H_{1dmn}(\mathbf{x}_b)$, $H_{2d}(\mathbf{x}_b)$, $H_{3d}(\mathbf{x}_b)$. Figure 3 shows the standard deviations (percentage of first guess value, global average, July 2005) for data sets selected this way with operators H_{1dmn} and H_{3d}, and $\varepsilon = 5\%$. The standard deviation of H_{3d} is significantly smaller than the corresponding value of H_{1dmn}, i.e., the first guess values derived with H_{3d} tend to be closer to the observations than those calculated with H_{1dmn}. Corresponding calculations with other combinations of forward operators and different values of ε clearly indicate that the performance

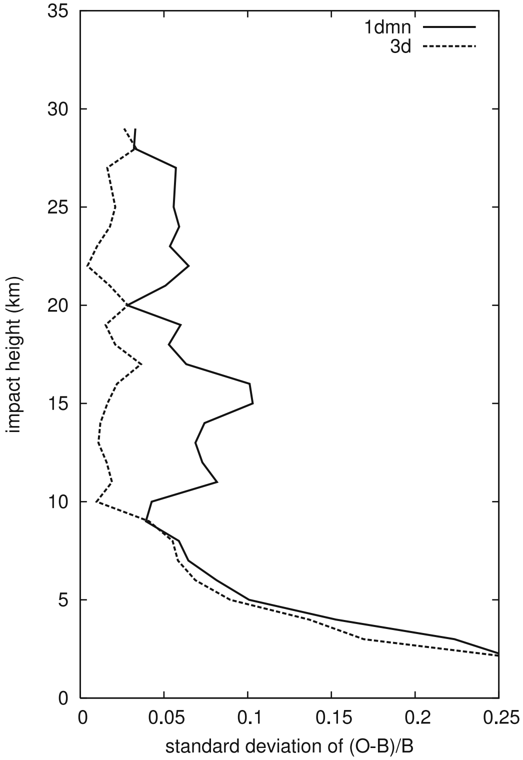

Fig. 3 Evaluation of bending angle forward operators: Standard deviation of H_{1dmn} and H_{3d} ($\varepsilon = 5\%$) for observations selected according Eq. (9)

of the bending angle forward operator in terms of standard deviation increases in the order $H_{1\mathrm{d}} \rightarrow H_{1\mathrm{dmn}} \rightarrow H_{2\mathrm{d}} \rightarrow H_{3\mathrm{d}}$.

Although there are significant differences on the level of innovation statistics, the overall deviances of the optimized one-dimensional forward operators from the ray tracing result are only minor (1–2%) for impact heights above 8 km. As the statistical weight of GPS RO observations is small below this height (large observation errors due to humidity gradients), this suggests the usage of an appropriately optimized one-dimensional bending angle forward operator for the operational assimilation, in agreement with results of other studies (Poli 2006; Healy et al., 2007a).

For the following monitoring and assimilation experiments, the optimized one-dimensional forward operator $H_{1\mathrm{dmn}}$ is applied rather than the ray-tracing operator.

3 Monitoring

A long-term monitoring of the radio occultation observations is arranged. To this end, the statistical parameters of the differences of observations and background values $(O - B)$ are determined on a monthly basis. Generally, the observed bending angles agree with the background equivalents with a deviation that corresponds to the assumptions made for the background and observation errors in the assimilation system.

The bending angle observations are compared with the corresponding background equivalents, derived from the forecast fields of the GME by application of the one-dimensional inverse Abel transform forward operator (version $H_{1\mathrm{dmn}}$, see Sect. 2). Near real time (NRT) bending angle data sets of CHAMP and GRACE-A from GFZ and FORMOSAT-3/COSMIC (Constellation Observing System for Meteorology, Ionosphere, and Climate) by CDAAC/UCAR (COSMIC Data Analysis and Archive Center/University Corporation for Atmospheric Research) are considered. In addition, a third data set is generated by applying the CT2 method (at the DWD) to near real time phase delay data sets of CHAMP and GRACE-A by GFZ. The CT2 method allows to estimate values of the bending angle observational error, which are not included in the near real time bending angle data set from GFZ. Thus, additional statistical information on the occultation data is gained.

A quality control is applied to the GPS RO data to be monitored: A 3σ $(O - B)$ check is applied to remove outliers. Observations with a relative observation error larger than 5% (with respect to observed bending angle value) are discarded, which removes observations mostly in the tropical lower troposphere (influence of humidity fluctuations) and in the stratosphere (residual stratospheric fluctuations induce additional noise). In addition, the value of the bending angle is confined to the interval [0, 0.02] to exclude errors due to ducting processes. These parameters of the quality control are also applied in the assimilation experiment (see Sect. 4).

The statistical properties of the corresponding differences, the innovations, are taken into account to assess the consistency of model and observational bending angle values and corresponding error estimates and are discussed in the following paragraph.

Figure 4a–c shows the global distribution of the number of RO profiles (bin size 1 km × 10°) available after quality control. The different orbit geometry of CHAMP/GRACE-A on the one hand and COSMIC on the other hand leads to the different patterns in the respective diagrams.

Figures 5, 6, 7, 8, and 9 show zonal averages (bin size 1 km × 10°) of statistical parameters of the $(O - B)$ innovations of the three data sets for the time of March 2007, to be discussed in the following.

As the CHAMP and GRACE-A near real time data not yet include estimates for the observational error, a simple, partially linear functional dependence of the observation error on the impact height (Healy and Thépaut, 2006) is assumed for this data set (see Fig. 5a): The relative observation error decreases linearly from 10–1% for 0 km to 10 km impact height. Above 10 km, the observation error is assumed to be 1% of the bending angle value, until it reaches a lower absolute limit of 6×10^{-6} radians. This observation error model is in contrast to the zonally varying observation error for CHAMP and GRACE-A by the CT2 method (Fig. 5b) and COSMIC (Fig. 5c).

Stratospheric observation errors are to the largest part due to ionospheric fluctuations. For both the COSMIC and the CT2 derived CHAMP/GRACE-A bending angle data sets observation errors are estimated from differences between bending angles derived by geometrical optics and a climatology. For the tropospheric sections of the occultation profile, signal tracking in multipath areas (to be resolved by radio-holographic approaches) dominate the observation error. For COSMIC data, observation errors are derived by direct propagation of fluctuation in the excess phase signal to bending angles. For the CT2 method, the spectral width of the running spectra of the transformed signal wave field is used for the estimation. For details of the methods involved in the estimation of observation errors, see Gorbunov (2002); Gorbunov et al. (2006) (CHAMP/GRACE-A with CT2) and CDAAC/TACC (2007a,b) (FORMOSAT-3/COSMIC) and references therein.

The influence of tropical humidity on the observation error is consistent with higher values of the relative observation error in the lower latitudes. Above 20 km impact height, a difference in the observation errors of CHAMP and GRACE-A by CT2 on the one hand and COSMIC on the other hand is noticeable. It is due to the usage of a different climatology for estimation of the stratospheric component of the error. Comparing the near real time bending angles by GFZ with the bending angles obtained by applying CT2 at the DWD, it is apparent that the CT2 generally tends to keep more occultation data than the method of GFZ (cf. Fig. 4a,b in 10–20 km impact height), but assigns a relatively high observation error, especially in the lower and upper troposphere (see Fig. 5b). High values for the observation error cause more observations to be discarded at these height levels, see Fig. 4b. For all data sets, the estimated observational errors (Fig. 5a–c) are generally smaller than the model background errors (Fig. 6, model background errors are the same for the different RO data sets), especially in the upper troposphere of the extra tropics. The background error of the bending angle $\mathbf{B}_\mathrm{b}$ is calculated from the background error covariances of temperature and relative humidity $\mathbf{B}_{t,rh}$ specified in the 3D-Var by application of the linearized observation operator:

Fig. 4 Number of GPS RO profiles (bin size 1 km ×10°) for (**a**) CHAMP/GRACE-A (bending angles by GFZ), (**b**) CHAMP/GRACE-A (phase delays by GFZ, bending angles by CT2 at DWD), (**c**) COSMIC (bending angles by CDAAC/UCAR)

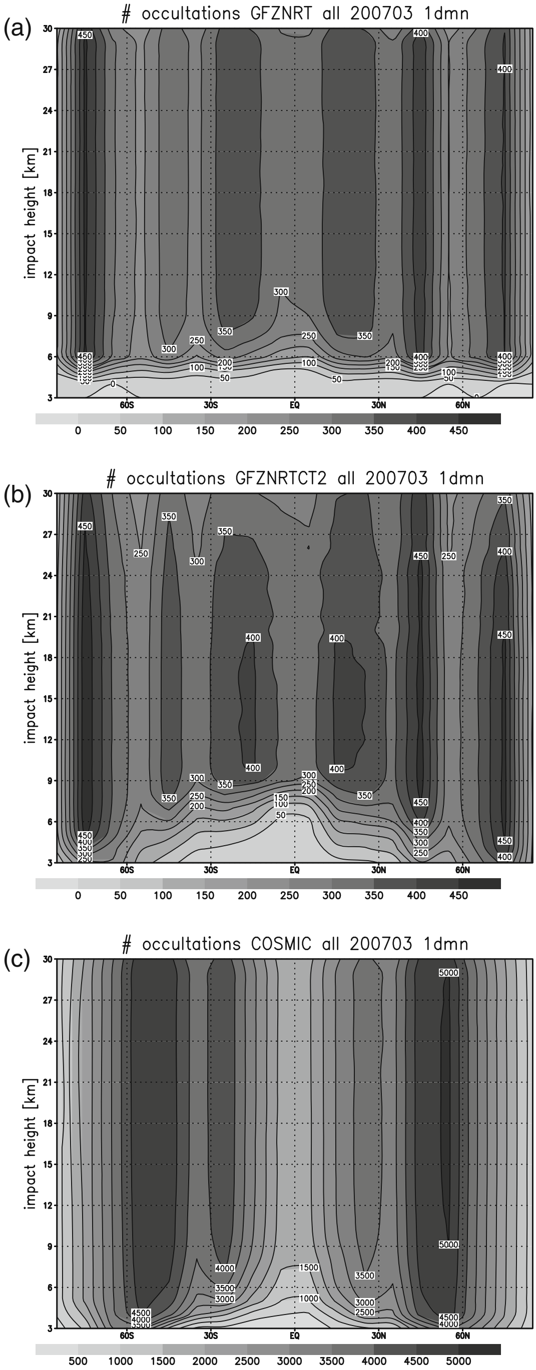

Fig. 5 Estimated bending angle observation error for (**a**) CHAMP/GRACE-A (functional approach, bending angles by GFZ), (**b**) CHAMP/GRACE-A (phase delays by GFZ, bending angles by CT2 at DWD), (**c**) COSMIC (bending angles by CDAAC/UCAR)

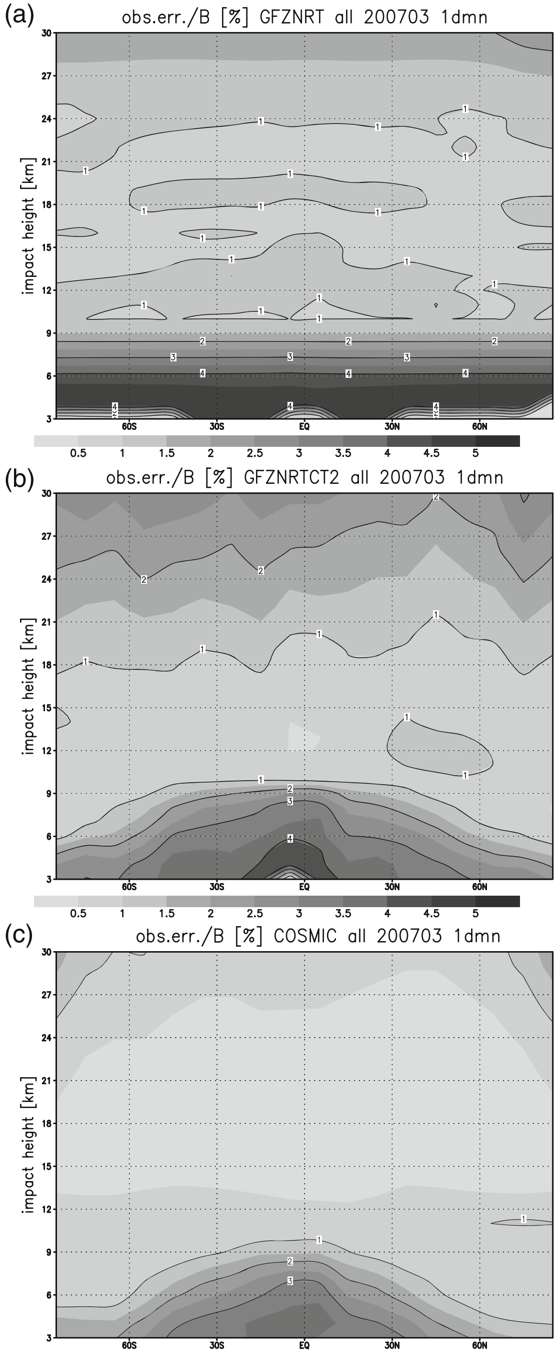

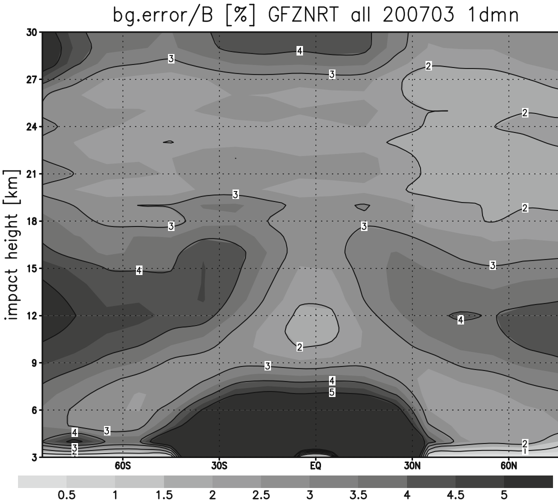

Fig. 6 Estimated bending angle background error in the GME model (percentage of first guess value, derived from the background error covariances at *t* and *rh* by means of the tangent linear operator $H_{1\mathrm{dmn}}$)

$$\mathbf{B}_{\mathrm{b}} = \mathbf{H}\,\mathbf{B}_{t,rh}\,\mathbf{H}^{\mathrm{T}} \tag{10}$$

The background error distribution of the bending angles are large in the extra-tropical jet stream regions where atmospheric variations are large. Another maximum is found in the lower tropical troposphere. Here humidity variations give the largest contribution to the bending angle background errors, reaching values of up to 15%. The observation errors estimated by the COSMIC and CT2 algorithm (Fig. 5) show maxima in the tropics as well. If no quality control was applied, these observational errors would be much larger and would reach values similar to the background errors. In the lower tropics only relatively few observations pass the criteria (cf. Fig. 4) so that the observational error is of the same order or less than the background error, which is a prerequisite for using the observations in the assimilation.

Figure 7a–c displays the standard deviation σ of the innovation for the three data sets. The standard deviation has generally higher values in the tropics, due to the more pronounced influence of humidity. A maximum of the standard deviation at the impact height of $\sim$18 km is caused probably by the presence of gravity waves. The deviations above 25 km result from ionospheric fluctuations which can only be partly corrected by taking into account the differences of the L1 and L2 phase. Remaining large differences of the retrieved bending angles from climatology are usually suppressed by fitting to the climatology. Reasonable bending angle values at higher altitudes are important if temperature profiles are derived from the bending angles by the Abel inversion. They are not essential if a forward operator is applied to the atmospheric profiles to derive model counterparts to the retrieved bending angles so long as the errors of the retrieval are specified correctly. This is done by the CT2 retrieval algorithm. In this case the model background will be used for

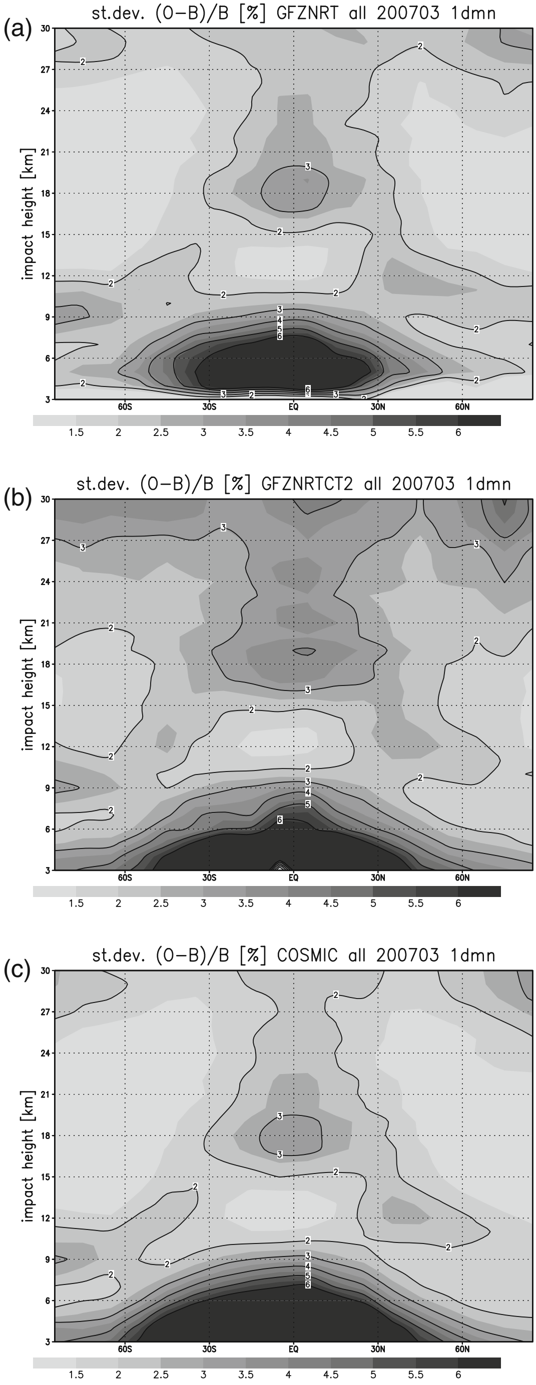

Fig. 7 Standard deviation of innovations $(O - B)/B$ (percentage of first guess value, H_{1dmn} bending angle forward operator) for (**a**) CHAMP/GRACE-A (bending angles by GFZ), (**b**) CHAMP/GRACE-A (phase delays by GFZ, bending angles by CT2 at DWD), (**c**) COSMIC (bending angles by UCAR/CDAAC)

Fig. 8 Ratio of standard deviation of innovations $(O - B)$ with respect to estimated standard deviation for (**a**) CHAMP/GRACE-A (bending angles by GFZ), (**b**) CHAMP/GRACE-A (phase delays by GFZ, bending angles by CT2 at DWD), (**c**) COSMIC (bending angles by UCAR/CDAAC)

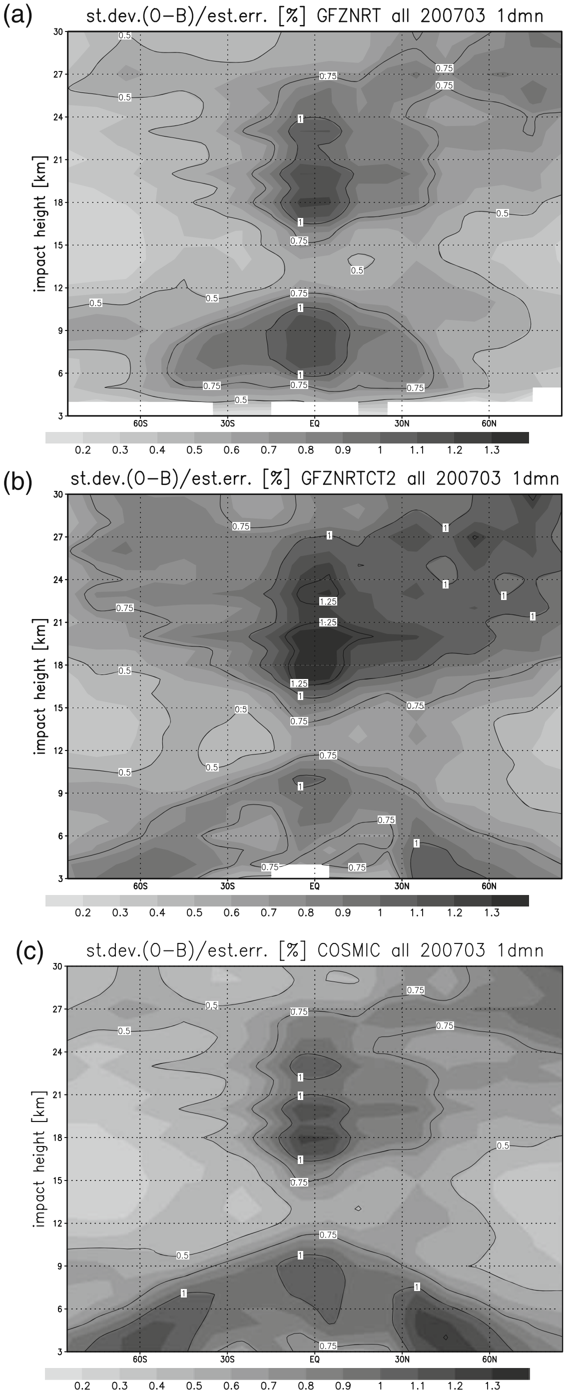

Fig. 9 Bias of innovations $(O - B)/B$ (percentage of first guess value, $H_{1\mathrm{dmn}}$ bending angle forward operator) for (**a**) CHAMP/GRACE-A (bending angles by GFZ), (**b**) CHAMP/GRACE-A (phase delays by GFZ, bending angles by CT2 at DWD), (**c**) COSMIC (bending angles by UCAR/CDAAC)

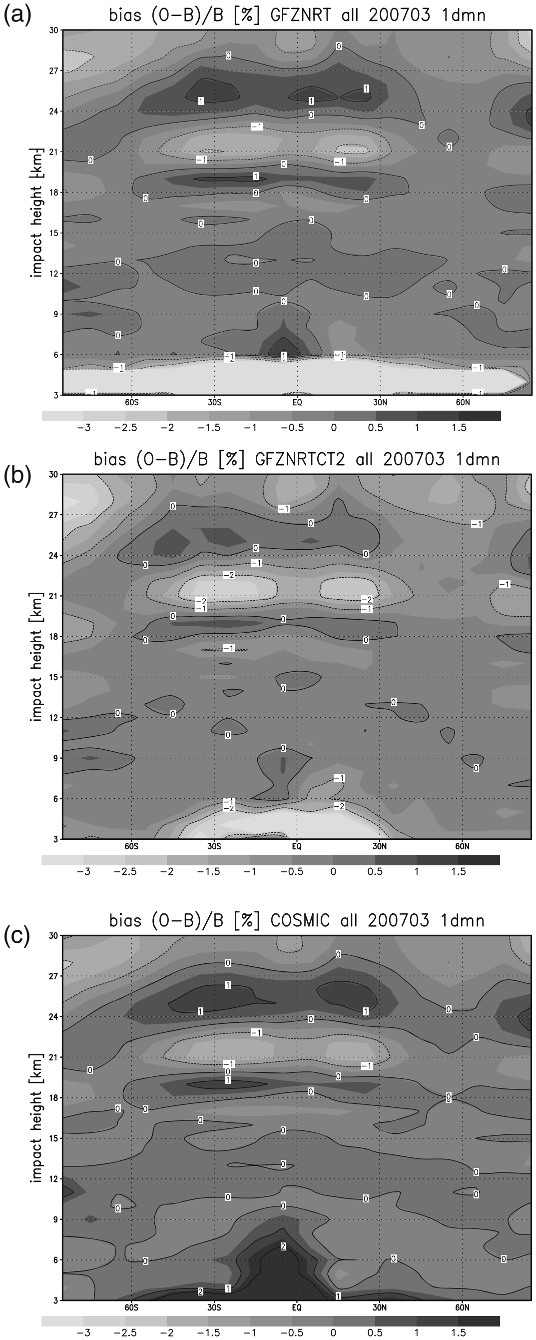

the regularization in the variational assimilation scheme. The innovation's standard deviation is compared to its estimate, the quadratic sum of the observation error and background error $e_{\mathrm{est}} = (e_{\mathrm{obs}}^2 + e_{\mathrm{bg}}^2)^{1/2}$. Figure 8a–c shows the ratio of the standard deviation to the estimated deviation σ/e_{est}. In general, the CHAMP and GRACE-A observed bending angles agree with the corresponding background equivalents reasonably well and within the assumptions made for the background and observation errors in the assimilation system. The ratio is less than unity for most areas and height levels, indicating a better agreement of observations and background values than estimated from the error specification. In the upper tropical troposphere, the relatively high value of the ratio σ/e_{est} again indicates the presence of gravity waves not accounted for in the background error model.

The bias of the innovations as depicted in Fig. 9a–c is reasonably small, but shows a remarkable vertically oscillating pattern in the upper troposphere and stratosphere in the tropics and mid-latitudes, which might be related to properties of the GME background model. In addition, the overall bias of the CT2 processed CHAMP and GRACE-A data (Fig. 9b) seems to be slightly more negative than the corresponding NRT result by GFZ and COSMIC (Fig. 9a,c).

4 Assimilation Experiments

The assimilation setup, including the optimized bending angle forward operator, is tested in assimilation experiments. The impact of the radio occultation observations on the weather forecast quality is assessed by an experiment assimilating RO data from the six FORMOSAT-3/COSMIC satellites in addition to conventional data only. A positive impact on the forecast scores in the southern hemisphere is observed.

A first assimilation experiment with RO observations has been performed, in order to estimate the maximal impact of the RO data and to apply the necessary optimization to the assimilation system. The assimilation experiment is carried out for the time of May 2007 by the DWD 3D-Var with a three-hourly assimilation time window. The assimilated observations are RO bending angle data from the six FORMOSAT-3/COSMIC satellites and conventional in-situ-data. In the corresponding control experiment, conventional data is the only observational source.

Figure 10a shows a significant reduction of the standard deviation of the differences of the experiment's analysis to the IFS analysis (ECMWF) for the geopotential at 500 hPa in the southern hemisphere. For the northern hemisphere, the average change in the analyzed fields is neutral (not shown).

Subsequent forecast runs are performed to assess the impact on the forecast results. The forecast quality can be quantified by the anomaly correlation coefficient (ANOC) of an atmospheric field, measuring the correlation of deviances of forecasts with those of coinciding analysis with respect to the model climatology. Figure 10b shows the anomaly correlation coefficient of the geopotential field at 500 hPa in the southern hemisphere for the control experiment, the experiment

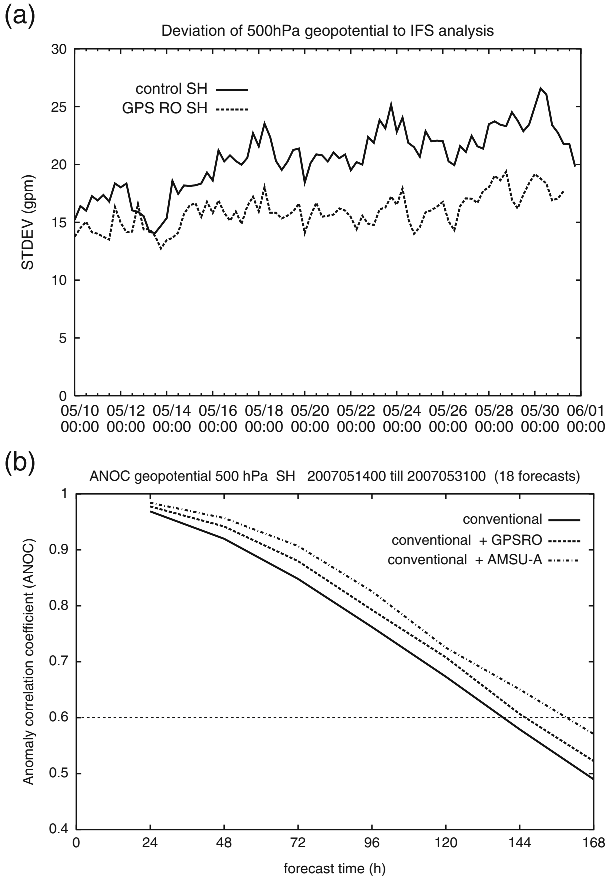

Fig. 10 Assimilation of GPS RO observation data in experiment, southern hemisphere: (**a**) standard deviation of analysis differences of geopotential at 500 hPa to IFS, (**b**) Anomaly correlation (ANOC) coefficient

additionally including RO observations, and an experiment that assimilates conventional observations and AMSU-A data (using 18 forecasts). The assimilation of RO results in a significant increase of the ANOC in the southern hemisphere, with a similar result for the temperature field. It is remarkable that the improvement of the forecast scores due to RO is already half of the improvement to be expected when assimilating AMSU-A radiance observations in addition to conventional data. In the northern hemisphere, still a slight degradation of the ANOC is visible for geopotential and temperature, the reason for this is still to be identified.

The verification of temperature and humidity against corresponding measurements of radio soundings and aircraft data indicates a significant reduction of the standard deviation for the experiment with assimilation of RO observations in the southern hemisphere (not shown).

5 Conclusions

The performance of three different versions of a one-dimensional and a three-dimensional ray-tracing bending angle forward operator is evaluated for use in a three-dimensional variational data assimilation system. The ray-tracing operator takes horizontal gradients and the ray's tangential point drift into account. The different versions of the one-dimensional operator all apply the inverse Abel transform, assuming spherically symmetric atmospheric fields, but reflect the tangential point drift each to a different degree. Considering the standard deviation of the differences of first guess to observed occultation data above the impact height of 8 km, the three-dimensional and the optimized one-dimensional forward operator differ by less than 2%. Therefore, a choice of a properly optimized, numerically less expensive one-dimensional forward operator for the use in an operational data assimilation system seems legitimate. Monitoring of near real time radio occultation bending angle data sets from CHAMP, GRACE-A, and FORMOSAT-3/COSMIC has been carried out for the time of several months. The standard deviation of the observations-first guess differences are well within the error bound estimation of the assimilation system. An experiment assimilating bending angle observations shows a significant improvement of the forecast quality in the southern hemisphere when compared to a control experiment assimilating conventional data only, proving radio occultation data to be a valuable source of meteorological information.

Acknowledgements We thank the GeoForschungsZentrum (GFZ) Potsdam for reliably providing CHAMP and GRACE-A data sets of radio occultation data, both offline and near real time processed. The FORMOSAT-3/COSMIC project is gratefully mentioned for free provision of radio occultation data. We thank Michael Gorbunov for making the CT2 processing method and both bending angle forward operators available to us. The German Ministry for Education and Research supported the research project NRT-RO related to the near real time provision and usage of radio occultation data within the GEOTECHNOLOGIEN research program.

References

CDAAC/TACC (2007a) Atmospheric data inversion (ROAM): Algorithms for inverting radio occultation signals in the neutral atmosphere. http://cosmic-io.cosmic.ucar.edu/cdaac/doc/documents/roam05.doc, http://tacc.cwb.gov.tw/cdaac/doc/documents/roam05.doc

CDAAC/TACC (2007b) Ionospheric data inversion (GMRION): Algorithms for inverting radio occultation signals in the ionosphere. http://cosmic-io.cosmic.ucar.edu/cdaac/doc/documents/gmrion.pdf, http://tacc.cwb.gov.tw/cdaac/doc/documents/gmrion.pdf

Daley R, Barker E (2000) NAVDAS Source Book 2000: NRL Atmospheric Variational Data Assimilation System. Tech. rep., Naval Research Laboratory, Monterey, Canada

Gorbunov ME (2002) Ionospheric correction and statistical optimization of radio occultation data. Radio Sci 37(5):1084, doi:10.1029/2000RS002370

Gorbunov ME, Kornblueh L (2003) Principles of variational assimilation of GNSS radio occultation data. Report 350, Max-Planck-Institut für Meteorologie, Bundesstrasse 55, D-20146 Hamburg

Gorbunov ME, Lauritsen KB (2002) Canonical Transform Methods for Radio Occultation Data. Sci Rep 02-10, Danish Meteorological Institute Copenhagen, available at http://www.dmi.dk/dmi/Sr02-10.pdf

Gorbunov ME, Lauritsen KB (2004a) Analysis of wave fields by Fourier integral operators and their application for radio occultations. Radio Sci 39(RS4010), doi:10.1029/2003RS002971

Gorbunov ME, Lauritsen KB (2004b) Canonical transform method for radio occultation data. In: Kirchengast G, Foelsche U, Steiner AK (eds) Occultations for Probing Atmosphere and Climate, Springer, Berlin Heidelberg, pp 61–68

Gorbunov ME, Lauritsen KB, Rhodin A, Tomassini M, Kornblueh L (2006) Radio holographic filtering, error estimation, and quality control of radio occultation data. J Geophys Res 111(D10105), doi:10.1029/2005JD006427

Healy SB, Thépaut JN (2006) Assimilation experiments with CHAMP GPS radio occultation measurements. Q J R Meteorol Soc 132:605–623, doi:10.1256/qj.04.182

Healy SB, Eyre JR, Hamrud M, Thépaut JN (2007a) Assimilating GPS radio occultation measurements with two-dimensional bending angle observation operators. Q J R Meteorol Soc 133 (626):1213–1227

Healy SB, Wickert J, Michalak G, Schmidt T, Beyerle G (2007b) Combined forecast impact of GRACE-A and CHAMP GPS radio occultation bending angle profiles. Atmos Sci Let 8(2): 43–50

Majewski D, Liermann D, Prohl P, Ritter B, Buchhold M, Hanisch T, Paul G, Wergen W (2002) The operational global icosahedral-hexagonal gridpoint model GME: Description and high-resolution tests. Mon Wea Rev 130:319–338

McNally AP (2002) A note on the occurence of cloud in meteorologically sensitive areas and the implications for advanced infrared sounders. Q J R Meteorol Soc 128:2551–2556, doi:10.1256/qj.01.206

Poli P (2006) Effects of horizontal gradients on GPS radio occultation observation operators. II: A Fast Atmospheric Refractivity Gradient Operator (FARGO). Q J R Meteorol Soc 130(603):2807–2825, doi:10.1256/qj.03.229

Wickert J, Michalak G, Schmidt T, Beyerle G, Cheng C, Healy SB, Heise S, Huang CY, Jakowski N, Köhler W, Mayer C, Offilier D, Ozawa E, Pavelyev A, Rothacher M, Tapley B, Viehweg C (2009) GPS radio occultation: Results from CHAMP, GRACE and FORMOSAT-3/COSMIC. Terr Atmos Oceanic Sci 20(1):35–50, doi:10.3319/TAO.2007.12.26.01(F3C)

Sampling of the Diurnal Tide of Temperature Using Formosat-3/COSMIC Data

B. Pirscher, U. Foelsche, M. Borsche, and G. Kirchengast

Abstact The Formosat-3/COSMIC satellite constellation, performing radio occultation measurements, allows for an adequate measurement density in space and time to determine the temperature diurnal tide typical for one month, i.e., on a monthly basis. In this initial study on the topic we investigated the diurnal amplitude and phase between 4 km and 35 km altitude in different geographical regions in July 2007. The tropical diurnal tide shows a distinctive downward phase progression. The corresponding amplitude is increasing towards higher altitudes but it always remains smaller than 0.5 K up to an altitude of 35 km. Natural temperature variability within large latitudinal domains seems to interfere with the diurnal tide, which complicates the interpretation of our extratropical results. We found maximum temperature amplitude within a day in the afternoon at high latitudes with an increase in amplitude with altitude. The tide is more pronounced in the winter hemisphere.

1 Introduction

Nearly continuous measurements at synoptic land stations, ships, and buoys allow an adequate determination of the diurnal tide of atmospheric parameters, e.g., temperature or humidity, at the surface. Some of these data are available since the end of the 19th century. From 1950 until 2004 a decrease in the diurnal surface temperature range occurred due to a steeper increase in daily minimum surface temperatures than in daily maximum surface temperatures (Vose et al. 2005; Easterling et al. 2006). Since 1979, however, no change in temperature range is observed (Trenberth et al. 2007).

The number of measurements and the spatial density in the upper troposphere and lower stratosphere (UTLS) region was very sparse in the pre-satellite era (before

---

B. Pirscher (✉)
Wegener Center for Climate and Global Change (WegCenter) and Institute for Geophysics, Astrophysics, and Meteorology (IGAM), University of Graz, Austria
e-mail: barbara.pirscher@uni-graz.at

A. Steiner et al. (eds.), *New Horizons in Occultation Research*,
DOI 10.1007/978-3-642-00321-9_11, © Springer-Verlag Berlin Heidelberg 2009

1979), since radiosonde, lidar, and radar data were the only measurements available in the free atmosphere. To estimate the diurnal tide in the free atmosphere it is necessary to analyze data from radiosonde measurement campaigns with at least four radiosonde ascends per day (e.g., Seidel et al. 2005; Alexander and Tsuda 2008), to examine lidar/radar data (e.g., Revathy et al. 2001; Riggin et al. 2002) or to investigate satellite data (e.g., Zeng et al. 2008). The lack of long term measurements in the UTLS region prevents the examination of a possible climate change impact on the diurnal tide in the free atmosphere.

In the recent past, discussion about temperature trends in the free atmosphere derived from (Advanced) Microwave Sounding Unit (MSU/AMSU) satellite data received much attention. Discrepancies in sign and magnitude of the trends arose from incorrect inter-calibration and correction procedures between the different satellites (e.g., Karl et al. 2006). Radio occultation (RO) data (Kursinski et al. 1997; Steiner et al. 2001), however, are self-calibrated, and inter-calibration between measurements of different satellites is, in principle, not needed (Foelsche et al. 2009). Continuous RO data, available since 2001, are thus suitable to perform climate monitoring and related change analyses such as of the diurnal tide, because the data are expected to be stable on a long term basis (Foelsche et al. 2008).

A satellite's inclination and its orbit altitude determine the drifting rate and hence its local time sampling. The RO mission CHAMP (CHAllenging Minisatellite Payload) yields the longest available RO data set, but since the CHAMP satellite only drifts by three hours within one month, it is not able to observe the diurnal tide within one month, nor within one season (e.g., Pirscher et al. 2007). To determine the diurnal tide with CHAMP data, it is necessary to merge data from different years. In doing so, Zeng et al. (2008) removed atmospheric seasonal and interannual variability.

Until 2006 no RO mission was able to sample at all local times within one month. However, the six Formosat-3/COSMIC (Rocken et al. 2000; Anthes et al. 2008) satellites, launched in April 2006, are able to observe the diurnal tide of a measurand within 10 days at low latitudes. We used these data to estimate the temperature diurnal tide at different latitudes and vertically from 4 km to 35 km for an example month (July 2007). Section 2 gives an introduction to local time sampling with the Formosat-3/COSMIC constellation. Section 3 briefly describes the data set and the method used to estimate the diurnal tide. Results are discussed in Sect. 4. Section 5 closes with a summary and conclusions.

2 Local Time Sampling Using Formosat-3/COSMIC

The secular drift in satellite orbit planes is mainly caused by the Earth's polar oblateness. Assuming a circular orbit, the orbit's precession rate $\dot{\Omega}$ [rad s^{-1}] can be calculated from

$$\dot{\Omega} = -\frac{3}{2} J_2 \left(\frac{a_\mathrm{e}}{a}\right)^2 n \cos i, \tag{1}$$

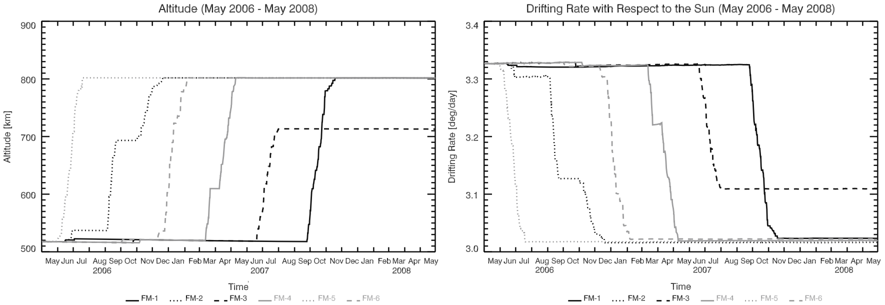

Fig. 1 Time series from May 2006 until May 2008: Altitudes of the six Formosat-3/COSMIC satellites (*left*) and resulting orbital drifting rates (*right*)

where $J_2 = 1082.63 \times 10^{-6}$ is a constant factor describing the Earth's polar oblateness, $a_e = 6378.137$ km is the Earth's mean equator radius, a is the semi-major axis of the satellite's orbit, i its inclination, and $n = n(a)$ is the mean motion of the satellite [rad s^{-1}] (Hoffmann-Wellenhof et al. 1997; Larson and Wertz 1997; Boain 2005). As can be inferred from Eq. (1), the orbit parameters i and a yield the precession rate of the satellite. It is often referred to as the Earth's mean motion of $360°/365.242199\mathrm{d} = 0.9856°/\mathrm{d}$, resulting in $\dot{\Omega}_{\odot}$ ($\dot{\Omega}_{\odot} = 0.9856°/\mathrm{d} - \dot{\Omega}$).

Figure 1 depicts the consecutive orbital raising of the six Formosat-3/COSMIC satellites and the effects on their drifting rates with respect to the Earth's mean motion from May 2006 until May 2008. Complementarily, Fig. 2 shows the equator crossing times.

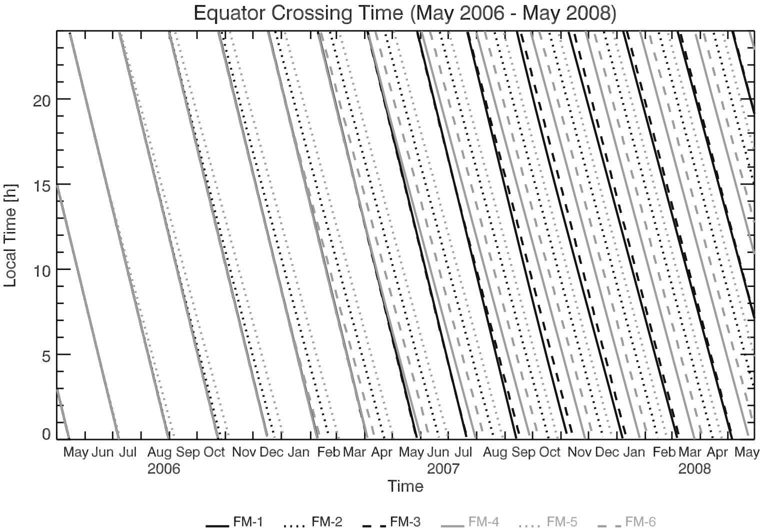

Fig. 2 Equator crossing time of the Formosat-3/COSMIC satellites from May 2006 until May 2008

The satellites were raised from about 520–800 km while the inclination $i = 72^\circ$ was kept constant. The respective orbital drifting rates decreased from $\dot{\Omega}_\odot \approx 3.33^\circ/\mathrm{d}$ at 520 km to $\dot{\Omega}_\odot \approx 3.02^\circ/\mathrm{d}$ at 800 km. The gradual change in drifting rate results in a (desired) orbital separation. Shortly after launch (April 2006), all satellites were close to each other. In June 2006, FlightModel-5 (FM-5) was the first satellite which separated from the others because of its orbital raising and the resulting slower drifting rate. By the end of May 2008 all satellites were separated from each other but the final constellation was not fully developed because the solar panels of FM-3 are stuck resulting in non-optimal power and limited payload operation for this spacecraft (D. Hunt, UCAR, pers. comm. May 2008). For this reason, the orbit raising for FM-3 has been halted in July 2007. It is currently not clear, if it is possible to raise FM-3 to its final altitude to 800 km.

The precession rate of a satellite determines the sampling behavior with respect to local time. Thereby, it is convenient to refer the precession rate to the mean motion of the Earth of $0.9856^\circ/\mathrm{d}$. Satellites with orbital precession rates equal to $0.9856^\circ/\mathrm{d}$ are in a Sun-synchronous orbit ($\dot{\Omega}_\odot = 0$). These satellites are never able to observe the diurnal tide of an atmospheric parameter. The larger the difference between the orbital precession rate and the mean motion of the Earth, the shorter the time span to sample through all local times.

Figure 3 shows the local time coverage of all six Formosat-3/COSMIC satellites in December 2006 and in July 2007. Each gray dot corresponds to an RO event (as a function of local time and latitude). In December 2006, FM-5 and FM-2 were the only two satellites in their final orbits. Thus, the plane separation was incomplete, which becomes apparent in less optimal local time sampling (left panel). On the other hand, in July 2007 FM-1 was the only satellite still in its parking orbit and plane separation was well advanced. Local time sampling (right panel) was therefore more uniform compared to December 2006 even though not as good as it will be when all satellites are in their final orbits.

The 30° separation in the ascending node and the orbital drifting rate with respect to the Sun of $\approx 3.02^\circ/\mathrm{d}$ in the final constellation enables the diurnal tide to be sampled fully every 10 days at low latitudes. At higher latitudes the ascending and descending branch of the orbit move closer together in terms of local time sampling. Thus, local time sampling at high latitudes is insufficient and irregular within

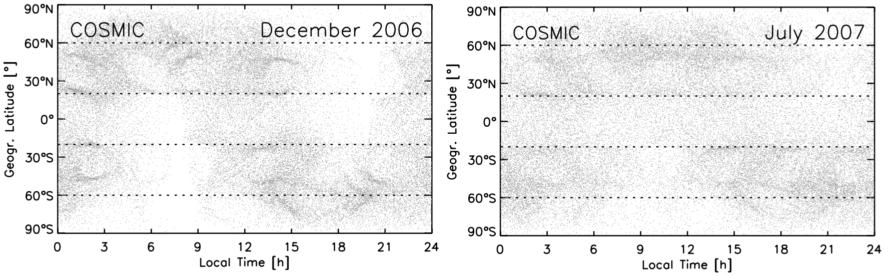

Fig. 3 Local time sampling in December 2006 (*left panel*) and July 2007 (*right panel*)

one month, limiting the monthly reconstruction of the diurnal tide of atmospheric parameters.

3 Determination of the Diurnal Tide

Formosat-3/COSMIC RO data are provided by the COSMIC Data Analysis and Archive Center (CDAAC) (http://cosmic-io.cosmic.ucar.edu/cdaac/). In this initial study we use CDAAC dry temperature profiles (post-processed profiles, version 2007.3200). Dry temperature is equivalent to physical temperature when atmospheric humidity is small, which is true everywhere above 8–14 km altitude (Foelsche et al. 2008). Since local time is not well sampled in December 2006, we only use data from July 2007 to estimate the diurnal tide.

In addition to this data set we use co-located ECMWF (European Centre for Medium-Range Weather Forecasts) analysis data, which are available at four UTC (coordinated universal time) time layers (00 UTC, 06 UTC, 12 UTC, and 18 UTC). Co-location means that the ECMWF profile is drawn from the ECMWF time layer nearest to the RO event time (no interpolation in time) and that the ECMWF field is spatially interpolated to the geographic RO event location, where the co-located RO profile is extracted. This temporal adjustment in UTC (by up to three hours) also yields corresponding shifts in local time. But since we use profiles at all longitudes, all local times are also covered by co-located ECMWF profiles.

To determine the diurnal tide, we divide all RO events within one month into five zonal bands with latitude-dependent width (30° or 40°). The specifications of the regions are shown in Table 1. The use of zonal bands prevents the examination of non-migrating tidal modes which are forced by the land-sea distribution (Tsuda and Kato 1989).

Table 1 shows the number of profiles considered in the calculation processes. The smaller total number of profiles at high latitudes results from the comparatively small inclination of the Formosat-3/COSMIC satellites of $i = 72^\circ$. A larger amount of RO measurements is obtained at mid- and sub-tropical latitudes. When comparing the number of profiles at high southern and high northern latitudes within three hours local time, the asymmetric local time sampling can be seen best. A lot of RO events at high southern latitudes in the early morning correspond to only a few measurements at high northern latitudes at the same time. Twelve hours later, local time sampling is opposite – more measurements occur in the Northern Hemisphere than in the Southern Hemisphere. The most uniform local time sampling is obtained in the tropical region. July 2007 allows for all local times to be sampled sufficiently within three hour intervals: there are always more than 180 RO events in polar regions, more than 500 events in the subtropics and midlatitudes, and more than 800 measurements in the tropical region within each three hour time interval.

Collecting all profiles within three hours in local time in one geographical region and weighting each of these profiles with the cosine of its geographical latitude φ gives the mean profile typical for one region and for a three hour time interval. The cosine-weighting accounts for area changes between meridians at varying latitudes

Table 1 Geographical regions and their local time coverage in July 2007

Latitudinal domain	SHP[a] 60°S to 90°S	SHSM[b] 20°S to 60°S	TRO[c] 20°S to 20°N	NHSM[d] 20°N to 60°N	NHP[e] 60°N to 90°N
00 LT to 03 LT	1 219	2 770	1 346	1 572	264
03 LT to 06 LT	627	2 177	1 573	2 422	747
06 LT to 09 LT	312	1 424	1 157	2 347	1 116
09 LT to 12 LT	221	649	982	2 255	1 047
12 LT to 15 LT	292	1 655	1 262	2 356	1 127
15 LT to 18 LT	749	2 492	1 408	1 812	628
18 LT to 21 LT	1 066	2 744	1 076	1 178	287
21 LT to 24 LT	983	2 625	964	598	185
Total	5 469	16 536	9 768	14 540	5 401

[a] Southern Hemisphere Polar Region
[b] Southern Hemisphere Subtropics and Midlatitudes
[c] Tropics
[d] Northern Hemisphere Subtropics and Midlatitudes
[e] Northern Hemisphere Polar Region

(Foelsche et al. 2008), i.e., due to convergence of meridians towards the poles the geographic area per latitude increment shrinks by $\cos\varphi$. Anomalies for each region are derived by subtracting the mean profile (i.e., average over all time intervals). The amplitude is derived by calculating the half of the difference between maximum and minimum temperature at each altitude. The phase corresponds to the local time of the temperature maximum.

The determination of the diurnal tide is based on all high quality profiles available in the geographical regions. Since the number of events differs significantly from one to the other time interval, the robustness of the calculation method was investigated. This was done by reducing the number of RO events so that they were evenly distributed over all time intervals. The reduced number was thus chosen to be about the minimum number of events available within each time interval. 180, 500, and 800 profiles were randomly selected from the respective set and used for the polar, midlatitude, and tropical region, respectively.

The attempt to estimate the diurnal tide with a temporal resolution of one hour was discontinued because the number of events within one hour time intervals was too small.

4 Results and Discussion

Figure 4 shows the mean dry temperature profile for each geographical region (left), the diurnal tide (anomalies with respect to the mean profile) as function of local time (middle), and the diurnal amplitude (right) obtained from Formosat-3/COSMIC RO data in July 2007. All results are shown as a function of mean sea level (MSL) altitude, from high northern latitudes (top) to high southern latitudes (bottom). The

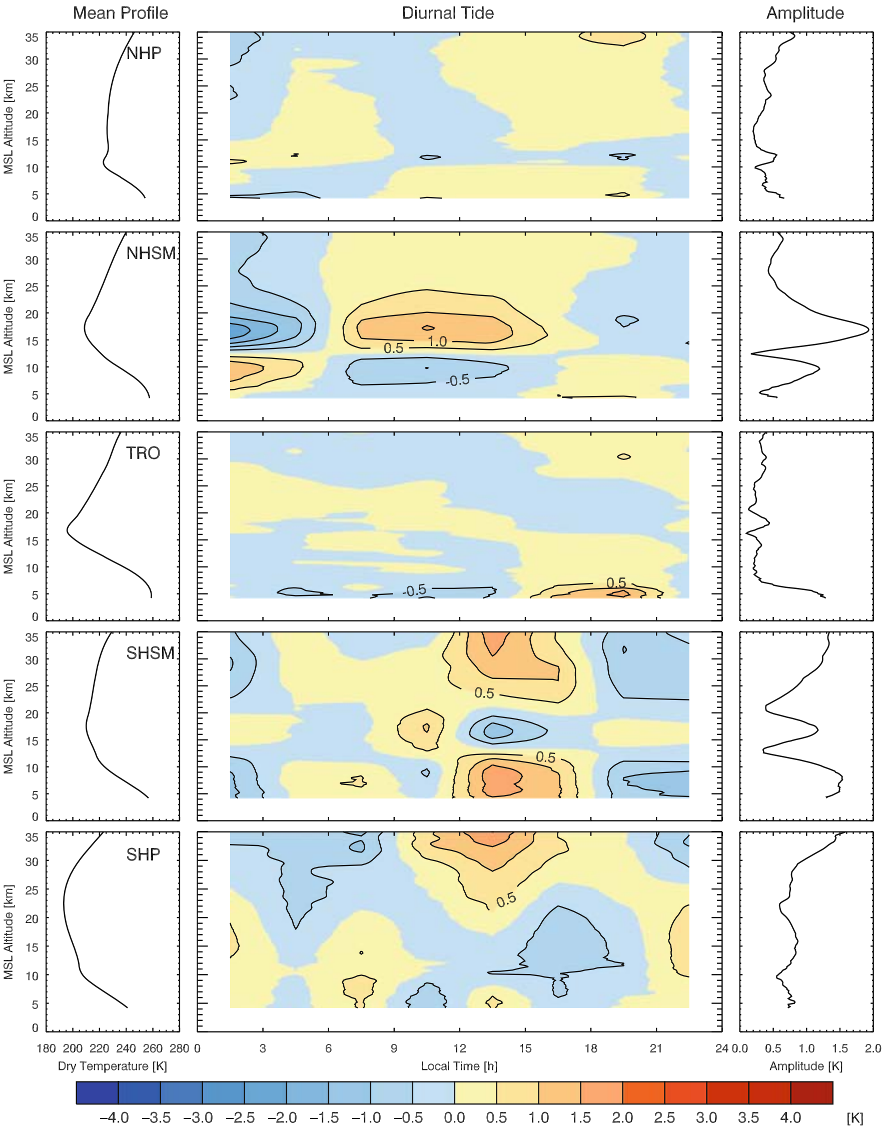

Fig. 4 Mean profiles (*left*), diurnal tide (*middle*), and amplitude (*right panels*) in July 2007 calculated with a local time resolution of three hours

mean atmospheric temperature structure is typical for a Northern Hemisphere summer month with a well pronounced tropopause in the summer hemisphere.

The diurnal tide shows comprehensible results in the tropics that are in very good agreement with other studies, (e.g., Alexander and Tsuda 2008; Zeng et al. 2008). Natural temperature variability within large latitudinal regions with 30° or 40° width and diverse atmospheric characteristics seem to interfere with the estimated diurnal tide complicating the interpretation of extratropical results. Particularly, the mid latitude (plus subtropical) regions (between 20°N/S and 60°N/S) seem to be too large to estimate a "typical" diurnal tide because atmospheric properties are too diverse in that extended latitudinal domain. Therefore, the discussion of the results of this initial study will be focused on the tropical latitudes. The interpretation of the results obtained at high latitudes should be regarded with reasonable care.

At high northern latitudes the diurnal amplitude slowly decreases from ∼0.65 K to ∼0.25 K from 4 km up to the tropopause level near 10 km. Above about 15 km up to 35 km the amplitude increases from ∼0.2 K to ∼0.8 K. The temperature phase (local time of the maximum) shifts from afternoon (in the troposphere) to early morning (at tropopause level) to afternoon and evening (in the lower stratosphere).

At high southern latitudes the diurnal amplitude decreases from ∼0.8 K (at an altitude of 5 km) to ∼0.5 K (near 10 km). Above that height it increases again to reach ∼1.6 K at an altitude of 35 km. Maximum temperature in the Southern Hemisphere winter is observed in the early afternoon.

In the tropical region, the diurnal temperature tide above about 8 km is less pronounced (amplitude ∼0.3 K only) than in the lower troposphere (amplitude reaches ∼ 1.2 K near 5 km). The distinctive increase in amplitude below 8 km may be associated with the use of dry temperature which depends on physical temperature as well as on humidity. Dry temperature is colder than physical temperature if humidity becomes important (see also the distinct decrease of lapse rate towards 4 km in the tropical mean profile in Fig. 4). The diurnal variability of humidity in tropical regions may thus cause the observed pronounced dry temperature diurnal tide at altitudes below 8 km.

Minimum diurnal amplitude values (∼0.1 K) can be observed near 11 km as well as near the tropopause (∼16 km). Above 21 km, the amplitude generally increases with height reaching to near 0.4 K above 27 km; below the tropical tropopause the phase remains constant with maximum temperature in the (late) afternoon. It shifts from afternoon to early morning from the tropopause to approximately 27 km. Maximum temperature perturbation above that height is observed at night. This downward propagating phase may be attributed to an upward propagating diurnal tide which is caused by tropospheric water vapor heating rather than stratospheric ozone heating (Chapman and Lindzen 1970).

The tropical vertical structure of the diurnal temperature tide, particularly the phase, is in good agreement with investigations of Alexander and Tsuda (2008) and Zeng et al. (2008). Even though an increase in diurnal amplitude with height is noticeable in Formosat-3/COSMIC RO data, it is smaller compared to the other studies (e.g., 1.2–2.2 K around 30 km in Zeng et al. (2008)) and only amounts to < 0.5 K at an altitude near 30 km.

Results obtained with a reduced number of Formosat-3/COSMIC profiles (flat number for all zonal bands and time intervals) are similar to the results discussed above (not shown). From this we infer that the results are basically robust, i.e., they do not depend on the number of profiles or sample details.

The diurnal tide obtained from ECMWF profiles co-located to Formosat-3/COSMIC RO events (not shown) is also in good agreement with results obtained from RO data. This result is not unexpected, since Formosat-3/COSMIC data are assimilated in ECMWF analyses. Best agreement is observed in the tropical region, with some minor differences noticed in high latitude regions: at high northern latitudes maximum temperatures are predominantly observed in the afternoon (no maximum in the morning) and the amplitude at high southern latitudes is less pronounced.

5 Summary and Conclusions

The diurnal tide of temperature was determined and analyzed in the atmosphere between 4 km and 35 km in selected geographical regions (five zonal bands with 30° or 40° width), based on Formosat-3/COSMIC RO data of July 2007 (Northern Hemisphere summer month). The satellite constellation consisting of six single platforms enables the estimation of the diurnal phase and amplitude on a monthly basis.

An increase in diurnal amplitude is noticeable in the tropical lower stratosphere but it always remains smaller than 0.5 K (considerably smaller than in other studies with sparser data sets). Maximum temperatures in the tropics show downward phase progression from late afternoon to evening.

At extratropical latitudes atmospheric variability is determined by a combination of physical processes so that it is not possible to estimate a “typical” diurnal tide for these regions in the large-scale domains of this initial study. Geographical domains have to be selected carefully. On the one hand, the latitudinal width of regions must not be too large because the mean profile has to be representative for a region. On the other hand, a sufficient number of RO profiles is of high priority. Work on choosing the optimal size of the geographical regions for the given RO data set is currently on-going.

In order to estimate the diurnal tide with Formosat-3/COSMIC RO data in months other than July 2007 a longer period of data from the satellite constellation will be analyzed. Since mid-2007 local time coverage is sufficient to allow the observation of the diurnal tide typical for one month. Annual/longer term variations of the diurnal tide cannot be properly determined until the second half of 2008; then local time coverage is sufficient for more than one year of data.

Acknowledgements We thank CelesTrak (Colorado Springs, CO, USA) for the provision of Formosat-3/COSMIC Two-Line Element-files, UCAR/CDAAC (Boulder, CO, USA) for providing Formosat-3/COSMIC data and ECMWF (Reading, UK) for analysis data. The work was carried out with financial support from the Austrian Science Fund (FWF) under research grant P18837 (CLIMROCC). UF received financial support from the Max Kade Foundation (New York, NY, USA) and from UCAR.

References

Alexander SP, Tsuda T (2008) Observations of the diurnal tide during seven intensive radiosonde campaigns in Australia and Indonesia. J Geophys Res 113(D04109), doi:10.1029/2007JD008717

Anthes RA, Bernhardt PA, Chen Y, Cucurull L, Dymond KF, Ector D, Healy SB, Ho SP, Hunt DC, Kuo YH, Liu H, Manning K, McCormick C, Meehan TK, Randel WJ, Rocken C, Schreiner

WS, Sokolovskiy SV, Syndergaard S, Thompson DC, Trenberth KE, Wee TK, Yen NL, Zeng Z (2008) The COSMIC/FORMOSAT-3 mission: Early results. Bull Am Met Soc 89(3):313–333, doi:10.1175/BAMS-89-3-313

Boain RJ (2005) A-B-Cs of Sun-synchronous orbit mission design (AAS 04-108). In: Coffey SL, Mazzoleni AP, Luu KK, Glover RA (eds) Spaceflight Mechanics 2004 – Part I, Univelt, Inc, San Diego, CA

Chapman S, Lindzen RS (1970) Atmospheric Tides. D. Reidel, Norwell, Mass

Easterling DR, Gleason B, Vose RS, Stouffer RJ (2006) A comparison of model produced maximum and minimum temperature trends with observed trends for the 20th and 21st centuries. Paper presented at 18th Conference on Climate Variability and Change, Session 5: Climate Modeling: Studies of Climate Change on 01.02.2006, Am. Meteorol. Soc., Atlanta, GA, extended abstract

Foelsche U, Borsche M, Steiner AK, Gobiet A, Pirscher B, Kirchengast G, Wickert J, Schmidt T (2008) Observing upper troposphere-lower stratosphere climate with radio occultation data from the CHAMP satellite. Clim Dyn 31:49–65, doi:10.1007/s00382-007-0337-7

Foelsche U, Pirscher B, Borsche M, Kirchengast G, Wickert J (2009) Assessing the climate monitoring utility of radio occultation data: From CHAMP to FORMOSAT-3/COSMIC. Terr Atmos Oceanic Sci 20(1):155–170, doi:10.3319/TAO.2008.01.14.01(F3C)

Hoffmann-Wellenhof B, Lichtenegger H, Collins J (1997) GPS Theory and Practice. Springer, Wien New York

Karl TR, Hassol J, Miller CD, Murray WL (2006) Temperature Trends in the Lower Atmosphere: Steps for Understanding and Reconciling Differences. A Report by the Climate Change Science Program and the Subcommittee on Global Change Research, Washington, DC

Kursinski ER, Hajj GA, Schofield JT, Linfield RP, Hardy KR (1997) Observing Earth's atmosphere with radio occultation measurements using the Global Positioning System. J Geophys Res 102:23429–23465

Larson WJ, Wertz JR (eds) (1997) Space Mission Analysis and Design. Space Technology Library, Microcosm, Inc. and Kluwer Academic Publishers, USA, The Netherlands

Pirscher B, Foelsche U, Lackner BC, Kirchengast G (2007) Local time influence in single-satellite radio occultation climatologies from sun-synchronous and nun-sun-synchronous satellites. J Geophys Res 112(D11119), doi:10.1029/2004JD005526

Revathy K, Prabhakaran Nayar SR, Krishna Murthy BV (2001) Diurnal variation of tropospheric temperature at a tropical station. Ann Geophys 19:1001–1005

Riggin DM, Kudeki E, Feng Z, Sarango MF, Lieberman RS (2002) Jicamarca radar observations of the diurnal and semidiurnal tide in the troposphere and lower stratosphere. J Geophys Res 107(D8):4062, doi:10.1029/2001JD001216

Rocken C, Kuo YH, Schreiner W, Hunt D, Sokolovskiy S, McCormick C (2000) COSMIC system description. Terr Atmos Ocean Sci 11:21–52

Seidel DJ, Free M, Wang J (2005) Diurnal cycle of upper-air temperature estimated from radiosondes. J Geophys Res 110(D09102), doi:10.1029/2004JD005526

Steiner AK, Kirchengast G, Foelsche U, Kornblueh L, Manzini E, Bengtsson L (2001) GNSS occultation sounding for climate monitoring. Phys Chem Earth 26(3):113–124, D09102

Trenberth KE, Jones PD, Ambenje P, Bojariu R, Easterling D, Tank AK, Parker D, Rahimzadeh F, Renwick JA, Rusticucci M, Soden B, Zhai P (2007) Observations: Surface and atmospheric climate change. In: Solomon S, et al. (eds) Climate Change 2007: The Physical Science Basis., Cambridge Univ Press, Cambridge, UK and New York, NY, USA, pp 235–336

Tsuda T, Kato S (1989) Diurnal non-migrating tides excited by a differential heating due to land-sea distribution. Soc Jpn 67:43–54

Vose RS, Easterling DR, Gleason B (2005) Maximum and minimum temperature trends for the globe: An update through 2004. J Geophys Res 32(L23822), doi:10.1029/2005GL024379

Zeng Z, Randel W, Sokolovskiy S, Deser C, Kuo YH, Hagan M, Du J, Ward W (2008) Detection of migrating diurnal tide in the tropical upper troposphere and lower stratosphere using the Challenging Minisatellite Payload radio occultation data. J Geophys Res 113(D03102), doi:10.1029/2007JD008725

Recent Advances in the Study of Stratospheric Wave Activity Using COSMIC and CHAMP GPS-RO

S.P. Alexander and T. Tsuda

Abstract Gravity (buoyancy) waves are mainly generated in the lower atmosphere and propagate upwards, transporting energy and momentum. They must be characterized and parameterized in models because their cumulative effect on the atmosphere is important. GPS Radio Occultation (RO) satellites are able to measure the temporal and spatial evolution of gravity waves with global coverage. COSMIC enables their study at a much higher temporal and spatial resolution than was previously possible, while CHAMP provides a multi-year dataset. New CHAMP and COSMIC gravity wave results are presented here and discussed in both a global and regional scale context.

1 Introduction

The study of atmospheric waves using Global Positioning System (GPS) Radio Occultation (RO) has expanded markedly since the seminal paper of Tsuda et al., (2000), where data from the GPS/MET satellite were used to construct seasonal maps of stratospheric gravity wave potential energy (E_{p}). These showed that large E_{p} occurred above deep convection, especially over the Indonesian Maritime Continent region.

The launch in 2000 of the CHAllenging Minisatellite Payload (CHAMP) mission and its continuing operation has allowed the construction of multi-year gravity wave global and regional climatologies (Ratnam et al. 2004; Randel and Wu 2005; de la Torre et al. 2006; Baumgaertner and McDonald 2007; Hei et al. 2008). Results from the tropical regions have been favorably compared with ground-based instrumentation (Tsuda et al. 2004, 2006) allowing an extension of local scale results to a regional scale understanding of wave energy. CHAMP and SAC-C (Satélite de Aplicaciones Científicas-C) data have also been used to study the generation of mountain waves by the Andes, and subsequent propagation upwards (de la Torre et al. 2004,

---

S.P. Alexander (✉)
Research Institute for Sustainable Humanosphere (RISH), Kyoto University, Kyoto, Japan
e-mail: simon.alexander@aad.gov.au

A. Steiner et al. (eds.), *New Horizons in Occultation Research*,
DOI 10.1007/978-3-642-00321-9_12, © Springer-Verlag Berlin Heidelberg 2009

de la Torre and Alexander 2005). Stratospheric gravity wave activity measured by GPS-RO above the Andes has shown clear correlations with ionospheric fluctuations (Hocke et al. 2002), indicating the important role that these waves play in coupling the entire atmospheric system. Results obtained from GPS-RO have been compared with model data. For example, large stratospheric E_p noticed by Tsuda et al. (2000) above the Bay of Guinea (10°S) away from any convective or topographic wave source were investigated using high-resolution GCM data (Kawatani et al. 2003), where it was found to be due to waves generated by a region of moist heating near 10°N crossing the equator and converging near 10°S.

Gravity wave energy is the sum of kinetic energy E_k and potential energy E_p terms, with the former only calculable with knowledge of the wind velocities. However, the temperature and wind velocities are coupled to each other via the wave polarization equations. When the intrinsic frequency is significantly greater than the inertial frequency and much less than the squared Brunt-Väisälä frequency N^2, linear gravity wave theory predicts that the ratio of E_k to E_p is constant and therefore we can consider the total energy of the atmospheric system by studying temperature perturbations alone (Tsuda et al. 2000). It should be noted that the distribution of E_k and E_p are sometimes different in the atmosphere (Sato et al. 1999; Liou et al. 2003; Liou et al. 2006) and so E_p does not always constitute half of the total atmospheric energy.

2 COSMIC

The April 2006 launch of the Constellation Observing System for Meteorology, Ionosphere, and Climate (COSMIC) satellites promises to further increase our understanding of these waves and their influence on the atmosphere. COSMIC provides a much increased temporal and spatial resolution, which allows the study of waves and their variability on smaller scales than was possible with CHAMP. The COSMIC data analysis method and initial results are discussed below.

2.1 Data Analysis Method

The analysis of the COSMIC data presented below is broadly similar to that used with the previous generation CHAMP satellite (Hei et al. 2008), except that a smaller grid cell size and higher temporal resolution are employed. The raw profiles are interpolated to 1 km vertical resolution both for computational reasons and because the original ~50 m resolution data are not height independent (Baumgaertner and McDonald 2007). The data are binned into grid cells of size 20° × 5° × 7 days, from which the mean background temperature $\overline{T}$ is calculated. The temperature perturbation of an individual profile T' is calculated in the following way. A profile's T is subtracted from $\overline{T}$ and the linear mean is removed using a least squares fitting method. Any missing data points are linearly interpolated across (in reality this is not often necessary to do). The data are then Welch windowed to reduce spectral leakage before being 7 km vertically high-pass filtered. The resultant perturbation profile is referred to as T'. These perturbations from the mean are interpreted as being due mainly to gravity waves. The potential energy per unit mass E_{p} is then calculated using:

$$E_{\mathrm{p}} = \frac{1}{2}\left(\frac{g}{N}\right)^2 \left(\frac{T'}{\overline{T}}\right)^2, \tag{1}$$

where N is the Brunt-Väisälä frequency and g is the gravitational acceleration. E_{p} is calculated over 7 km vertically and then stepped up by 1 km, thus consecutive heights are not independent. So E_{p} can be referred to as the mean specific (per unit mass) potential energy. This analysis procedure is stepped forward in time by one day, therefore consecutive days are also not independent. This time resolution compares favorably with that used with GPS/MET (seasonal) and CHAMP (monthly).

T' may be obtained by removing an individual low pass filtered T profile and then forming the relevant grid cell perturbation average (Tsuda et al. 2000; de la Torre et al. 2006). Polynomial fitting individual T profiles to obtain T', which are then averaged over the appropriate grid domain result in E_{p} differences of < 0.4 J kg^{-1} except around the tropopause, when compared with forming the grid cell mean T firstly. Seven day averaging is optimum given the data constraints (these results are not shown).

Two examples of COSMIC profiles and their resultant E_{p} are shown in Fig. 1 during August 2007. The top row shows data obtained at 50°S while the bottom row

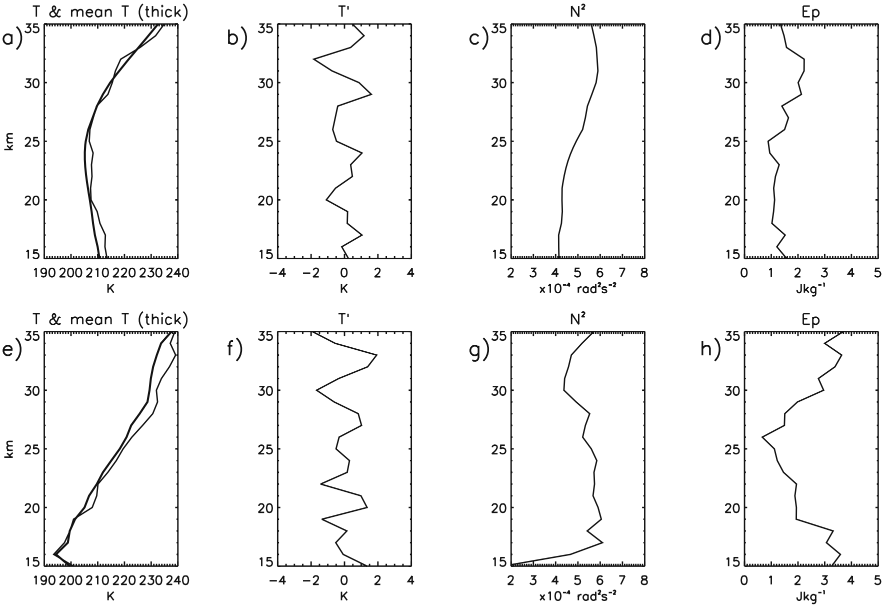

Fig. 1 (*Top row*) Profile obtained in the grid cell [260°E, 50°S] at 0633 UT, August 25, 2007. (*Bottom row*) Profile obtained in the grid cell [160°E, 5°S] at 0103 UT, August 28, 2007. From left to right, the panels show raw T and background $\overline{T}$, filtered T', N^2, and E_{p}

shows data at 5°S. Differences between the individual profile's T and the $20^\circ \times 5^\circ \times 7$ day background $\overline{T}$ are readily apparent in Fig. 1a,e. Note also the sharp cold-point tropopause at 16 km in the tropical profile of Fig. 1e. The resultant T' perturbation profiles are shown in Fig. 1b,f respectively, which together with the N^2 of Fig. 1c,g are used to calculate E_p. The E_p at 50°S in Fig. 1d shows a maximum of 2.2 J kg^{-1} at 32 km. This large E_p probably is a result of gravity wave emission, Doppler shifting, and reduced critical level filtering activity associated with the stratospheric polar night jet (Baumgaertner and McDonald 2007; Hei et al. 2008). In the tropics (Fig. 1h), the E_p shows a maximum around 16 km as a result of the cold-point tropopause and the low N^2. Another maximum of 3.5 J kg^{-1} is observed at 33 km. This is due to critical level wave interactions which depends upon the phase of the Quasi-Biennial Oscillation (QBO), to be discussed below.

NCEP re-analysis zonal wind velocity u data from 1000 hPa to 10 hPa (about 31 km) (Kalnay et al. 1996) are used for comparison with the COSMIC E_p. Use is also made of Outgoing Longwave Radiation (OLR) data in the tropics, which is widely used as a proxy for deep convective activity (Wheeler and Kiladis 1999).

2.2 Tropics

Randel and Wu (2005) pointed out that large scale temperature variances associated with Kelvin wave activity were two to three times smaller than those associated with regional or mesoscale phenomena. COSMIC provides dense enough data to be able to study these regional differences in E_p due to both the differences in source (convection) and subsequent wave-mean flow interaction. A discussion of the Madden-Julian Oscillation (MJO) is presented here. Full results, including latitude-longitude E_p maps and an analysis of equatorially trapped waves during 2007 are discussed by Alexander et al. (2008b).

The $20^\circ \times 5^\circ \times 7$ day resolution of COSMIC E_p allows direct mesoscale study of the effects of deep convection on the Upper Troposphere and Lower Stratosphere (UTLS) and mid-stratosphere. Deep convection is responsible for the emission of a broad spectrum of equatorially trapped and 3-D gravity waves, some of which are resolvable using COSMIC. Tropical mesoscale convection is associated with the intraseasonal MJO (Madden and Julian 1994; Wheeler and Kiladis 1999) which has a periodicity of ∼30–90 days and is especially dominant between the Indian Ocean and Western Pacific regions.

A time-height contour plot of equatorial E_p (2.5°S to 2.5°N) centered on 80°E is shown in Fig. 2. This region is above the Eastern Indian Ocean, close to Sumatra, Indonesia. Data are plotted where at least three profiles are available during each seven day interval in this cell. The background cold-point tropopause height is fairly constant at 17 km. Because the E_p are calculated over 7 km vertically, the value at e.g., 25 km is the average of the region 22–28 km inclusive. OLR data are also averaged over the region 2.5°S to 2.5°N and are plotted directly below the main E_p panel in Fig. 2. The 30–90 day bandpass filtered OLR are also shown (MJO intra-seasonally filtered).

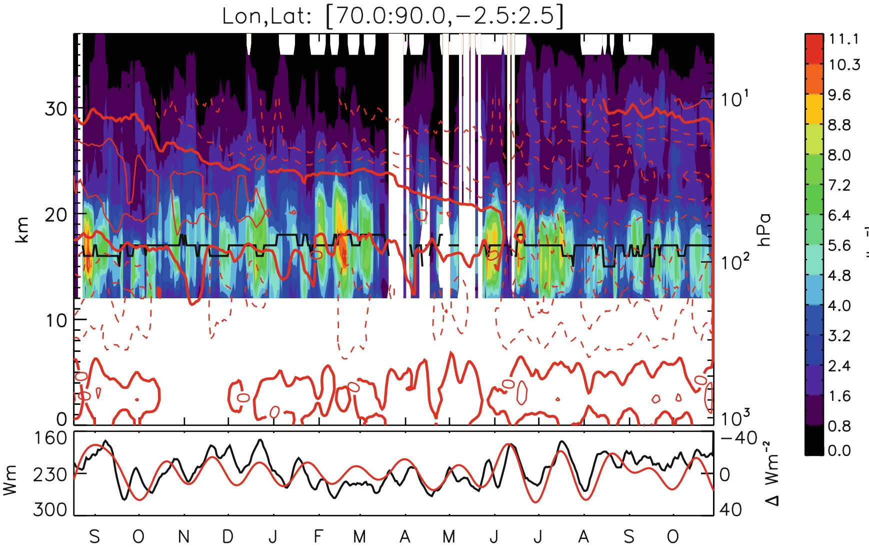

Fig. 2 August 2006–October 2007 E_p at [0°S, 80°E] marked as the color contours in the *upper panel*, with u overplotted (units of m s^{-1}, *solid* eastward and *dashed* westward). The cold-point tropopause is marked by the *black line*. The OLR is shown in the *bottom panel* (*black*, scale to left) with the MJO bandpass filtered overplotted (*red*, scale to right). Missing E_p data are marked *white*

In most cases, high cloud tops (low OLR) correspond directly to large tropopause E_p, with the bandpass filtered perturbations showing this even more clearly. Deep convection produces gravity waves which increase the temperature variance from the mean as they propagate upwards, thus increased E_p is observed at these times. It should be noted that the E_p calculated in the tropical UTLS region over-estimates the true value because the very sharp cold-point tropopause in the tropics increases the temperature variance.

Increases in UTLS E_p are usually accompanied by enhanced stratospheric E_p, extending up to about 30 km, emphasizing that some of these convectively generated waves propagate to high altitudes.

Stratospheric QBO background mean flow filtering occurs, with changes in E_p dependent upon the QBO phase. During 2006 and 2007, the winds move from eastward to westward. As the QBO phase descends, increasing amounts of waves are filtered. This results in less wave energy reaching higher altitudes and can be noted in Fig. 2 by considering the higher 30 km E_p in October 2006 than in April 2007. The 30 km E_p is again large in October 2007 because of the QBO phase structure, consistent with the CHAMP results of de la Torre et al. (2006). Upward propagating gravity waves after June 2007 are encountering increasingly weak westward winds as they approach the 0 m s^{-1} phase line. Given a typical gravity wave source spectrum centered around 0 m s^{-1}, temperature variance increases as the critical level is approached (Randel and Wu 2005). Furthermore, the decreasing vertical wave velocities towards the waves' critical levels increases the likelihood of their observability (Alexander and Barnet 2007). The latitude-longitude variability of gravity wave propagation, filtering, and mean-flow interaction observed by COSMIC is discussed fully by Alexander et al. (2008b).

2.3 Northern Hemisphere Winter

A detailed study of Northern Hemisphere lower stratospheric E_p during the boreal winter of 2006/07 reveals large values above mountainous regions such as the Himalayas, Canadian Rockies, and Japan (Alexander et al. 2008a). It is not possible from the COSMIC data to separate the jet-stream geostrophic adjustment contribution to total E_p from the mountain wave E_p contribution, but it is likely that some of the enhanced E_p above these mountains is due to mountain waves. Results from an Atmospheric General Circulation Model (AGCM) show that most of the large E_p observed by COSMIC is due to sub-tropical jet processes, with energy propagating upward.

Ground-based radar and radiosonde observations in Japan showed large wintertime stratospheric E_p (Murayama et al. 1994; Ogino et al. 1999). COSMIC results from the winter of 2006/07 independently confirmed this to be the case. The large E_p are a combination of the strong winter sub-tropical jet-stream above Japan and the islands' moderate topography (Alexander et al. 2008a). Previous generation GPS-RO satellite mean E_p results from the Northern Hemisphere winter did not reveal the large Japanese peak (Tsuda et al. 2000; Ratnam et al. 2004) because their data were not of sufficiently high temporal resolution. The enhancements in E_p above Japan occur on time scales on the order of a week or two, thus could not be captured previously. These short-term processes do, however, have a significant impact on the mean winter E_p and demonstrate the relevance of using the higher resolution COSMIC data for constructing seasonal means.

3 Champ

3.1 Tropics

CHAMP data have been compared with intensive radiosonde campaigns in equatorial Indonesia to study the effects on the tropopause of Kelvin wave activity (Tsuda et al. 2006). Zonal mean time-height profiles of equatorial CHAMP results showed the interaction between gravity waves and the stratospheric QBO but were unable to resolve longitudinal variability. Temperature variance increases as the 0 m s^{-1} phase speed line is encountered (Randel and Wu 2005). de la Torre et al. (2006) showed that large E_p of waves with vertical wavelength between 4 km and 10 km occurred only during the eastward wind shear phase of the QBO. Potential energy calculated from CHAMP and from intensive ground based radiosonde campaigns in Northern Australia show favorable agreement (Tsuda et al. 2004).

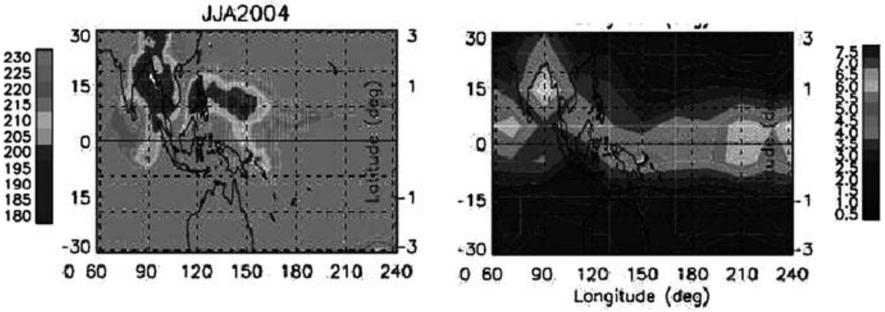

Fig. 3 (*Left panel*) Cloud top height in Kelvin from OLR data during JJA 2004 in units of W m^{-2}. (*Right panel*) CHAMP E_p at 19–26 km during JJA 2004 with units of J kg^{-1}

The zonal propagation of Kelvin waves was studied previously (Tsai et al. 2004; Ratnam et al. 2006). Here we show the relationship between large scale convection and CHAMP derived 19–26 km E_p (Fig. 3) for the Northern Hemisphere summer months of JJA 2004, when the QBO is in its eastward phase. The CHAMP E_p are calculated using a similar procedure to that for COSMIC detailed above, except that the background $\overline{T}$ is calculated over a three month interval and smoothed by applying a low-pass filter with cut-off at 7 km. The T' are extracted for waves shorter than 7 km vertical wavelength. The E_p are then determined using Eq. (1) over three height intervals, including 19–26 km.

The seasonal OLR are shown as cloud top temperature in the left hand panel of Fig. 3, with colder temperatures indicating deeper convection. Cloud convection is centered over the Bay of Bengal and is part of the Asian monsoon. Another region of deep convection is above and to the east of the Philippines. The large convection above the Bay of Bengal corresponds to a seasonal mean 19–26 km E_p of 6.5 J kg^{-1}. Large E_p are also observed over the Indian Ocean at 70°E and east of Papua New Guinea.

Large equatorial E_p are observed east of 120°E, increasing from 4.0 J kg^{-1} to 6.0 J kg^{-1} in the Central Pacific Ocean. This region does not correspond to deep convective activity but what may be being observed here are (equatorially trapped) Kelvin wave-like disturbances.

3.2 Polar Regions

A polar climatology of stratospheric gravity wave activity was assembled by Hei et al. (2008) using CHAMP data between 2001 and 2005. In the Arctic region, E_p showed an annual variation with a maximum in winter, which is consistent with stronger zonal mean horizontal wind speeds and larger Eliassen-Palm flux F_z. Larger values of F_z indicate higher planetary wave activity which can distort the polar night jet. Gravity waves can then be emitted as the jet re-aligns through geostrophic adjustment.

In contrast, the Antarctic E_p and horizontal wind speed are maximum in spring, concurrent with the break-up time of the polar night jet (Hei et al. 2008). These Antarctic lower stratospheric results are summarized in Fig. 4 for the period 2001–2005. Planetary wave activity generates gravity waves via geostrophic adjustment related to planetary wave transience and/or breaking thus increasing the E_p during winter and spring. The spring peak E_p corresponds to the time of the largest rate of change of the mean wind speed. Hei et al. (2008) also showed a correlation between gravity wave energy and the Eliassen-Palm flux divergence. Baumgaertner and McDonald (2007) explained the smaller summertime Antarctic E_p to be a result of critical level wave filtering. During other seasons, strong eastward winds are observed throughout the troposphere and stratosphere which increase in

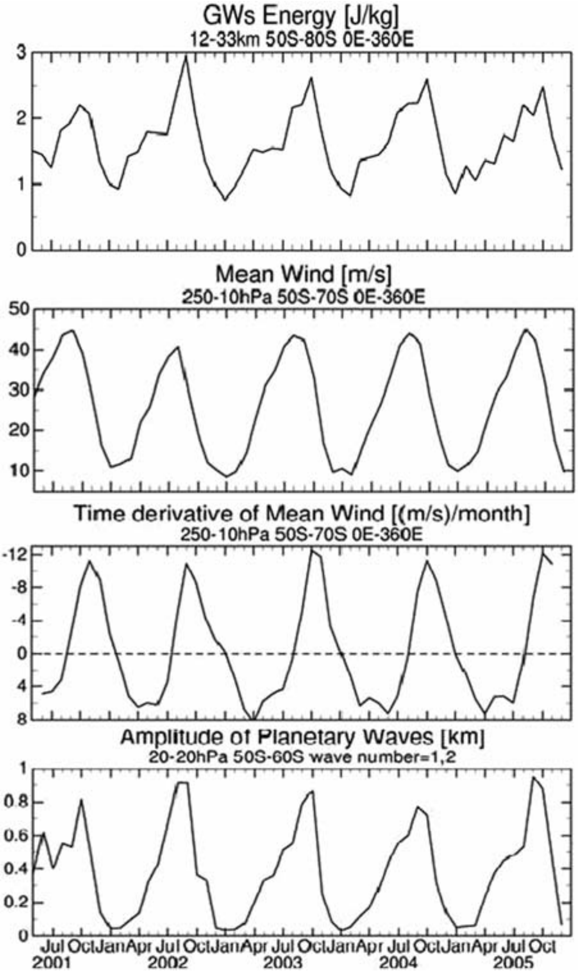

Fig. 4 (*Top panel*) Zonal mean gravity wave potential energy from 12–33 km and 50°S to 80°S. (*Second panel*) Mean horizontal wind speed, 250–10 hPa. (*Third panel*) Time derivative of mean horizontal wind speed. (*Bottom panel*) Planetary wave $s = 1, 2$ amplitude

strength with height. This results in less wave filtering and can also Doppler shift gravity waves to larger vertical wavelengths with larger amplitudes. The decrease in filtering at the vortex edge leads to wave enhancement.

The topography of the Antarctic Peninsula and the Trans-Antarctic Mountains are a strong local source of gravity wave activity (Baumgaertner and McDonald 2007; Hei et al. 2008) but topography is less important than the stratospheric polar night jet in determining the overall gravity wave climatology (Hei et al. 2008).

4 Future Directions

The benefits of an increasingly dense array of GPS-RO profiles obtained from different instruments over the last ten years has enabled the study of many more atmospheric waves and coupling processes, especially in regions where ground-based profiles of temperature are not obtainable. The GPS-RO results will eventually allow more accurate wave parameterizations in models.

Initial investigations of the spatial and temporal variability of stratospheric gravity waves using COSMIC reveal the potential to increase substantially our knowledge of the atmospheric system and stratosphere-troposphere coupling. The results presented above also show the ability of COSMIC to monitor changes in potential energy on the order of a week over relatively small grids of $20^\circ \times 5^\circ$.

Future possibilities for using COSMIC include a detailed analysis of regional scale convective wave generation, propagation, and mean-flow interaction; model comparisons to determine the waves responsible for the observed potential energy; and incorporation with ground based instruments to expand understanding of the coupled stratosphere-troposphere system. The Antarctic region is an active area of research using COSMIC.

Acknowledgements The COSMIC research was undertaken while one of the authors (SPA) was in receipt of a Japan Society for the Promotion of Sciences (JSPS) post-doctoral fellowship. This study was supported in part by the Japanese Ministry of Education, Culture, Sports, Science and Technology (MEXT) through a Grant-in-Aid for Scientific Research (19403009) and the Kyoto University Active Geosphere Investigation (KAGI) for the 21st century COE program. COSMIC data were obtained from the COSMIC Data Analysis and Archive Center (CDAAC). NCEP zonal wind and uninterpolated OLR data used in the study were provided by the NOAA/OAR/ESRL PSD, Boulder, Colorado, USA, from their Web site at http://www.cdc.noaa.gov/. The helpful comments of two anonymous reviewers are gratefully acknowledged.

References

Alexander MJ, Barnet C (2007) Using satellite observations to constrain parameterizations of gravity wave effects for global models. J Atmos Sci 64(5):1652–1665, doi:10.1175/JAS3897.1

Alexander SP, Tsuda T, Kawatani Y (2008a) COSMIC GPS observations of Northern Hemisphere winter stratospheric gravity waves and comparisons with an atmospheric general circulation model. Geophys Res Lett 35(L10808), doi:10.1029/2008GL033174

Alexander SP, Tsuda T, Kawatani Y, Takahashi M (2008b) Global distribution of atmospheric waves in the equatorial upper troposphere and lower stratosphere: COSMIC observations of wave mean flow interactions. J Geophys Res 113(D24115), doi:10.1029/2008JD010039

Baumgaertner AJG, McDonald AJ (2007) A gravity wave climatology for Antarctica compiled from Challenging Minisatellite Payload/Global Positioning System (CHAMP/GPS) radio occultations. J Geophys Res 112(D05103), doi:10.1029/2006JD007504

Hei H, Tsuda T, Hirooka T (2008) Characteristics of atmospheric gravity wave activity in the polar regions revealed by GPS radio occultation data with CHAMP. J Geophys Res 113(D04107), doi:10.1029/2007JD008938

Hocke K, Tsuda T, de la Torre A (2002) A study of stratospheric GW fluctuations and sporadic E at midlatitudes with focus on possible orographic effect of Andes. J Geophys Res 107(D20):4438, doi:10.1029/2001JD001330

Kalnay E, Kanamitsu M, Kistler R, Collins W, Deaven D, Gandin L, Iredell M, Saha S, White G, Woollen J, Zhu Y, Chelliah M, Ebisuzaki W, Higgins W, Janowiak J, Mo KC, Ropelewski C, Wang J, Leetmaa A, Reynolds R, Jenne R, Joseph D (1996) The NCEP/NCAR 40-year reanalysis project. Bull Am Meteor Soc 77(3):437–471

Kawatani Y, Dhaka SK, Takahashi M, Tsuda T (2003) Large potential energy of gravity waves over a smooth surface with little convection: Simulation and observation. Geophys Res Lett 30(8):1438, doi:10.1029/2003GL016960

Liou YA, Pavelyev AG, Huang CY, Igarashi K, Hocke K, Yan SK (2003) Analytic method for observation of the gravity waves using radio occultation data. Geophys Res Lett 30(20):2021, doi:10.1029/2003GL017818

Liou YA, Pavelyev AG, Wickert J, Liu SF, Pavelyev AA, Schmidt T, Igarashi K (2006) Application of GPS radio occultation method for observation of the internal waves in the atmosphere. J Geophys Res 111(D06104), doi:10.1029/2005JD005823

Madden RA, Julian PR (1994) Observations of the 40–50 day tropical oscillation – A review. Mon Wea Rev 122(5):814–837

Murayama Y, Tsuda T, Fukao S (1994) Seasonal variation of gravity wave activity in the lower atmosphere observed with the MU radar. J Geophys Res 99(D11):23, 057–23, 069

Ogino S, Yamanaka MD, Fukao S (1999) Interannual and day-to-day variations of gravity wave activity in the lower stratosphere over the eastern part of Japan observed in winter 1989–1995. J Met Soc Jpn 77(2):413–429

Randel WJ, Wu F (2005) Kelvin wave variability near the equatorial tropopause observed in GPS radio occultation measurements. J Geophys Res 110(D03102), doi:10.1029/2004JD005006

Ratnam MV, Tetzlaff G, Jacobi C (2004) Global and seasonal variations of stratospheric gravity wave activity deduced from the CHAMP/GPS satellite. J Atmos Sci 61(13):1610–1620

Ratnam MV, Tsuda T, Mori S, Kozu T (2006) Modulation of tropopause temperature structure revealed by simultaneous radiosonde and CHAMP GPS measurements. J Met Soc Japan 84(6):989–1003

Sato K, Kumakura T, Takahashi M (1999) Gravity waves appearing in a high-resolution GCM simulation. J Atmos Sci 56(8):1005–1018

de la Torre A, Alexander P (2005) Gravity waves above Andes detected from GPS radio occultation temperature profiles: Mountain forcing? Geophys Res Lett 32(L17815), doi:10.1029/2005GL022959

de la Torre A, Tsuda T, Hajj GA, Wickert J (2004) A global distribution of the stratospheric gravity wave activity from GPS occultation profiles with SAC-C and CHAMP. J Met Soc Jpn 82(1B):407–417

de la Torre A, Schmidt T, Wickert J (2006) A global analysis of wave potential energy in the lower stratosphere derived from 5 years of GPS radio occultation data with CHAMP. Geophys Res Lett 33(L24809), doi:10.1029/2006GL027696

Tsai HF, Tsuda T, Hajj GA, Wickert J, Aoyama Y (2004) Equatorial Kelvin waves observed with GPS occultation measurements (CHAMP and SAC-C). J Met Soc Jpn 82(1B): 397–406

Tsuda T, Nishida M, Rocken C, Ware RH (2000) A global morphology of gravity wave activity in the stratosphere revealed by the GPS occultation data GPS/MET. J Geophys Res 105(D6):7257–7273

Tsuda T, Ratnam MV, May PT, Alexander MJ, Vincent RA, MacKinnon A (2004) Characteristics of gravity waves with short vertical wavelengths observed with radiosonde and GPS occultation during DAWEX (Darwin Area Wave Experiment). J Geophys Res 109(D20S03), doi:10.1029/2004JD004946

Tsuda T, Ratnam MV, Kozu T, Mori S (2006) Characteristics of 10-day Kelvin wave observed with radiosondes and CHAMP/GPS occultation during the CPEA campaign (April-May, 2004). J Met Soc Jpn 84A:277–293

Wheeler M, Kiladis GN (1999) Convectively coupled equatorial waves: Analysis of clouds and temperature in the wavenumber-frequency domain. J Atmos Sci 56(3):374–399

Recent Advances in Gravity Wave Analysis from Long Term Global GPS Radio Occultation Observations

A. de la Torre, P. Alexander, P. Llamedo, T. Schmidt, and J. Wickert

Abstract A previous global analysis of wave potential energy using Global Positioning System (GPS) radio occultation (RO) temperature profiles revealed a considerable intense gravity wave activity (WA) at middle latitudes near to the Andes Range. WRF (Weather Research and Forecasting) and MM5 (Mesoscale Model 5) mesoscale model results for two selected cases in the vicinity of RO lines of tangent points, confirm an intense activity near to the mountains. A wavelet analysis led us to identify principal modes with two main horizontal wavelengths, clearly corresponding to mountain waves. Different hodograph analyses evidence that inertio gravity waves (IGWs) are due to mountain forcing and not to geostrophic adjustment at jet levels, as could be expected too. One of the simulations does not show intense WA in the vicinity of the tangent points, even though that the GPS-RO temperature profile detects it. We conclude that the GPS-RO technique is not by itself reliable enough to quantify and locate accurately WA of single events, but it should be considered as a useful tool to detect the global distribution of WA.

1 Introduction

As it is well known, gravity waves (GWs) play an important role in the momentum and energy budget of the lower and middle atmosphere. One form of momentum deposition is wave breaking, yielding body forces exerted on the synoptic circulation (Lindzen 1990). This drag effect has to be included, via parameterizations, for an accurate general circulation model (GCM). The other two main sources of GWs are (i) adjustment of the mean flow after departures from geostrophic equilibrium and (ii) upwards forcing during deep convection events. Any realistic parameterization of GW drag needs a sufficient coverage of observational evidence on the global scale (Fritts and Alexander 2003).

A. de la Torre (✉)
Departamento de Fisica, FCEN, Universidad de Buenos Aires, Argentina
e-mail: alejandrodelatorre@yahoo.com

A. Steiner et al. (eds.), *New Horizons in Occultation Research*,
DOI 10.1007/978-3-642-00321-9_13, © Springer-Verlag Berlin Heidelberg 2009

The GPS-RO (Global Positioning System Radio Occultation) technique allows to localize and identify single large amplitude GW events, detected from tomographic global maps of GW activity (WA) (de la Torre et al. 2004). The GPS-RO technique provides important advantages in comparison with regular radiosoundings: Global coverage under all weather conditions, sub-Kelvin temperature (*T*) accuracy, high vertical resolution, and long-term stability (see e.g., Kirchengast 2004, and references therein). Nevertheless, several limitations to the specific observation of GWs could be pointed out: (i) the capability of GPS-RO (as any other limb sounding devices) observations to detect only GWs with horizontal wavelengths longer than 150 km (horizontal resolution), (ii) the distinction between detected (apparent) and real wavelengths depending on the angle defined by the line of sight (LOS) between satellites and the wave phase surfaces (de la Torre and Alexander 1995), (iii) the wavelength refraction due to the background wind (de la Torre and Alexander 1995; de la Torre et al. 2006a,b), and (iv) the spherical symmetry assumption used to retrieve the *T* profiles even though the GW field is essentially three-dimensional. Moreover, the horizontal averaging during a GPS-RO event results in an amplitude attenuation and phase shift in any retrieved wave, which may lead to significant discrepancies with respect to the original values.

The main purposes of this work are to interpret, via mesoscale simulations, the capabilities of RO techniques to detect, localize, and properly quantify WA. Section 2 discusses the capability of the GPS-RO technique to detect GWs. In Sect. 3 we analyze GWs signatures in mesoscale numerical results. In Sect. 4 we present our conclusions.

2 GPS-RO Capabilities

The SAC-C, CHAMP (since 2001), GRACE, and COSMIC satellites (since 2002 and 2006, respectively) provide atmospheric parameters retrieved during RO events such as temperature, pressure, water vapor, and geopotential height. The obtained profiles have vertical resolutions ranging from 0.5 km in the troposphere up to 1.4 km in the stratosphere (Kursinski et al. 1997) (nevertheless, the data are usually interpolated every 200 m) and horizontal resolution of 150 km along each LOS.

The perigee of the LOS between the satellites projected on the Earth's surface determines the geographical coordinates where the atmospheric parameters are given. Each one of these points is usually denoted as tangent point (TP). Successive perigees during the occultation form the line of tangent points (LTP). There is an uncertainty in the determination of the exact position of each TP position in geographical coordinates. TPs may be displaced away from the perigee along each ray path. This displacement is bounded between 25 km and 50 km in the 10–16 km and 16–35 km altitude intervals, respectively (Liou et al. 2007). This introduces uncertainties in localizing WA. The capability of this technique to detect GWs depends principally on the angle defined by LOS and wave surfaces. For example, surprisingly GW with horizontal wavelengths shorter than the horizontal resolution of GPS-ROs are frequently detected in the region considered. This happens because LOS directions and constant wave surfaces due to mountain waves (MWs) have a predominant and nearly coincident North-South direction (de la Torre et al. 2006a).

The GWs activity has been usually quantified from GPS-RO T profiles, by calculating the mean specific potential energy (E_p) or the relative T variance content (σ) in a vertical column of air C between altitudes z_1 and z_2:

$$E_\mathrm{p} = \frac{g^2}{N^2}\sigma \qquad \sigma = \frac{1}{z_2 - z_1}\int_{z_1}^{z_2}\left(\frac{\delta T}{T_\mathrm{B}}\right)^2 \mathrm{d}z \tag{1}$$

where δT is the band-pass filtered T perturbations between cutoffs at 3 km and 9 km, T_B is the background T, g is the gravitational acceleration, and N the buoyancy frequency. Due to the T behavior in the tropopause, the filtering process may lead to an overestimation of δT at some wavelengths (Schmidt et al. 2004). The lowest altitude limit is chosen above the tropopause, to avoid artificial contributions to the integral due to this effect. The potential energy could be inferred also from another occultation parameter like refractivity, which decreases monotonically with height. However, this decrease is nearly exponential, around two orders of magnitude from the lowest to the highest TP altitude, making it difficult to distinguish between the mean and perturbation values at different altitudes. Despite of the tropopause problem, it

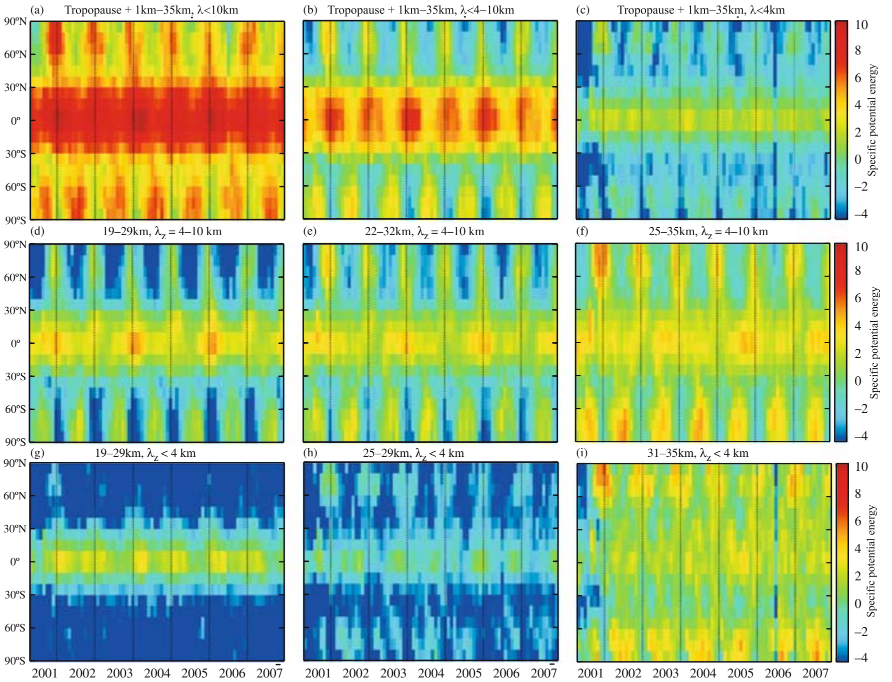

Fig. 1 **a–c**: Specific mean potential energy distribution, averaged between 1 km above the tropopause and 35 km, for different bandpass cut-offs. **d–i**: The same, for representative vertical columns consistent with the band-pass upper cutoffs selected: 10 km and 4 km, respectively (reproduced from de la Torre et al. (2006b))

is more adequate to use the *T* rather than refractivity, as its variations in the lower and middle atmosphere remain within the same order of magnitude.

Monthly global observations of WA between 2001 and 2006 reported in de la Torre et al. (2006b) revealed, in addition to general and specific features of energy distribution in the middle atmosphere (Fig. 1), the existence of singular extratropical locations with anomalously strong signatures. From each monthly tomographic latitude-longitude plot (not shown here), we selected two months that show intense WA in the region considered, during August and November 2001. A detailed insight among all the occultations registered in those periods, evidenced the influence in the mean of two intense events: August 30, 2001, 04:10 UTC and November 20, 2001, 03:58 UTC; hereinafter S1 and S2, respectively. In the following, we concentrate on the description of these events.

3 Case Studies: Two WA Events over Andes

3.1 Specific Features of GW Generation and Propagation

De la Torre et al. (2006b) performed an analysis of global distribution of WA in the upper troposphere and lower stratosphere between June 2001 and March 2006, using GPS-RO *T* profiles retrieved from the CHAMP satellite. A significant WA with respect to the remaining extra-equatorial regions in the Southern Hemisphere was detected in Mendoza, at the eastern side of the highest Andes Mountains (70°W to 65°W and 30°S to 40°S).

As it was pointed out by the authors, this region constitutes a natural laboratory where the known sources of GWs coexist: (i) Between October and March, frequent severe deep convection processes and intense hail storms take place. Waves throughout the full range of phase speeds, intrinsic frequencies, vertical and horizontal scales are generated. (ii) The Andes mountains represent a very important obstacle to the intense westerlies blowing from the Pacific Ocean, generating large amplitude GWs. This North-South barrier (tops around 7 km) generates mountain waves (MWs), whose phase surfaces are aligned nearly parallel to the mountains. The presence of an intense tropospheric jet allows for GWs propagation in the upper troposphere and stratosphere, because possible critical level filtering is avoided. (iii) This jet is observed above the highest orographic tops and its space and time variability may affect the geostrophic balance (de la Torre and Alexander 2005). As a consequence, possible generation of inertia gravity waves (IGWs) by geostrophic adjustment near the permanent jet is expected. This process may take place when the timescale of the wind evolution becomes comparable or shorter than the inertial period (around 1 day at 30°S). This perturbed flow, relaxes then to a new balanced state with redistribution of momentum, energy, and potential vorticity, with an additional radiation of excess energy as IGWs. In fact, downward/upward phase propagations above/below jets have been reported (Hirota and Niki 1985), in spite of the ignorance of the dynamical mechanism of wave emission (Plougonven et al. 2003).

3.2 Mesoscale Numerical Simulation and GWs Analysis

Mesoscale models can simulate realistic GW distributions in the troposphere and stratosphere and have been recently a major tool to study wave generation and propagation mechanisms (Zhang 2004). Mesoscale models can reveal detailed wave structures, energy sources, and maintenance mechanisms that are difficult to measure by satellite sensors. However, modeled GW properties and effects require observational verifications that are rarely available (Wu and Zhang 2004).

We performed simulations with the WRF (Weather Research and Forecasting) model during S1 and S2. In both cases, we employed three nested domains with effective horizontal grid spacing of 36 km, 12 km, and 4 km, respectively, and a time step equal to 30 s. The experiments were driven by assimilating lateral boundary conditions and sea surface temperatures from NCEP reanalysis. The simulations were initialized at least one day before the RO event in order to stabilize it. The physical parameterizations employed are described in Menéndez et al. (2004). The results showed a reasonably good performance in reproducing various features of southern South America regional climatology. We recall that these simulations were performed with the MM5 model too, reproducing the same numerical results obtained with WRF. Figure 2 shows the topography in the highest resolution domain, for S1 and S2. The horizontal projections of LTPs and LOSs corresponding to each RO event are shown. It can be seen that the LTP corresponding to S1 is

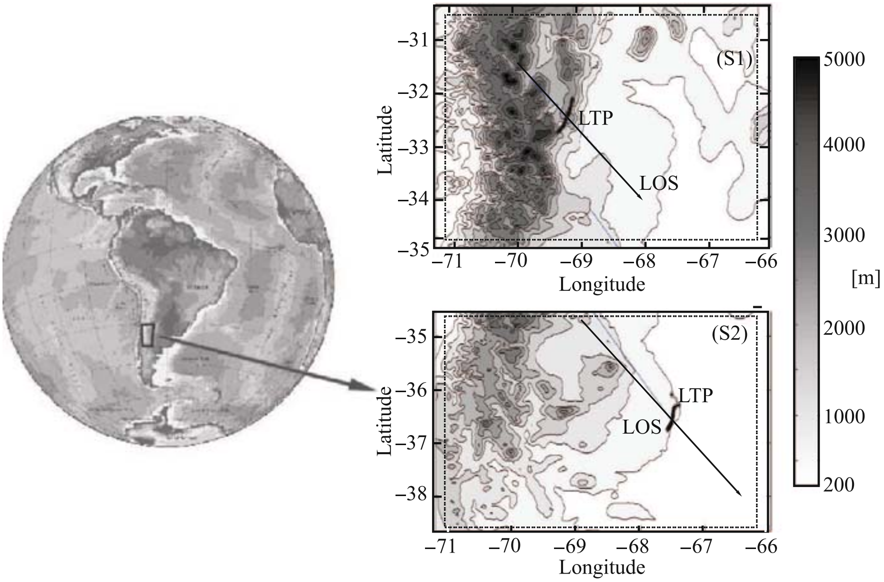

Fig. 2 Topography at the highest resolution domain for both simulations S1 and S2 and their corresponding horizontal projections of LTP and LOS. Observe that LTP corresponding to S1 is situated almost over the highest Andes Mountain, whereas for S2 it is situated approximately 200 km East of a lower part of the mountain range

situated over the mountains, whereas S2 is situated, on average, at 200 km East of the mountains, over a plateau region. Note that in both cases, the respective LOSs (and LTPs) are close to parallel.

Typical westerlies are seen at and above 700 hPa during both events. An intense jet core with zonal speed greater than 50 m/s is seen in both simulations at 250 hPa. Figure 3 shows the jet core intensity variation for both events. It can be seen that the zonal wind speed, *U*, varies approximately 30% in a period shorter than the inertial (24 h) in both events. Probable IGWs radiated by geostrophic adjustment must then be considered here. It may be noted that the largest wind variation occurs just over the mountains. MWs generated at the Andes Range transfer energy upwards, decelerating the mean flow and possibly altering the geostrophic equilibrium.

We removed the background *T* and wind components, to study δT and the zonal, meridional, and vertical velocity perturbations δU, δV, and δW. Figure 4 shows a typical MW with λ_x and λ_z around 50 km and 5 km, propagating from the troposphere to the lower stratosphere without finding any obstacle at the tropopause. As from cloud imagery we know that possible deep convection sources were absent during S1 and S2, the enhanced signatures registered by GPS RO could be explained by (i) the presence of MWs like this one, or instead, by (ii) longer waves originated

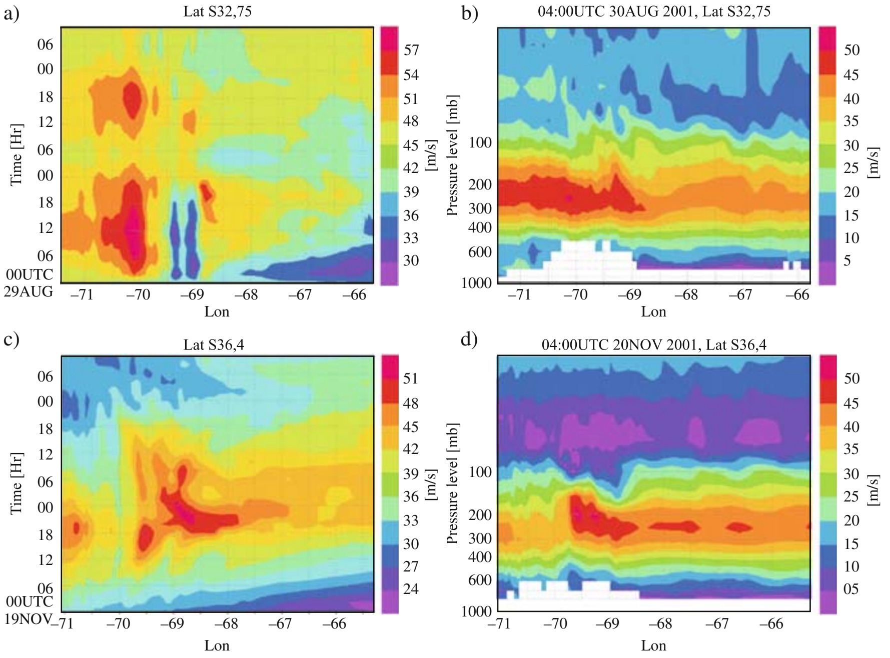

Fig. 3 (**a**) and (**c**): *U* time and zonal variability, at constant latitude, for S1 and S2, respectively. The largest variability occurs over the mountain range in both simulations. (**b**) and (**d**): *U* vertical and zonal variability, at constant latitude, for S1 and S2, respectively. A jet with zonal speed greater than 45 m/s is seen at approximately 250 hPa in both simulations

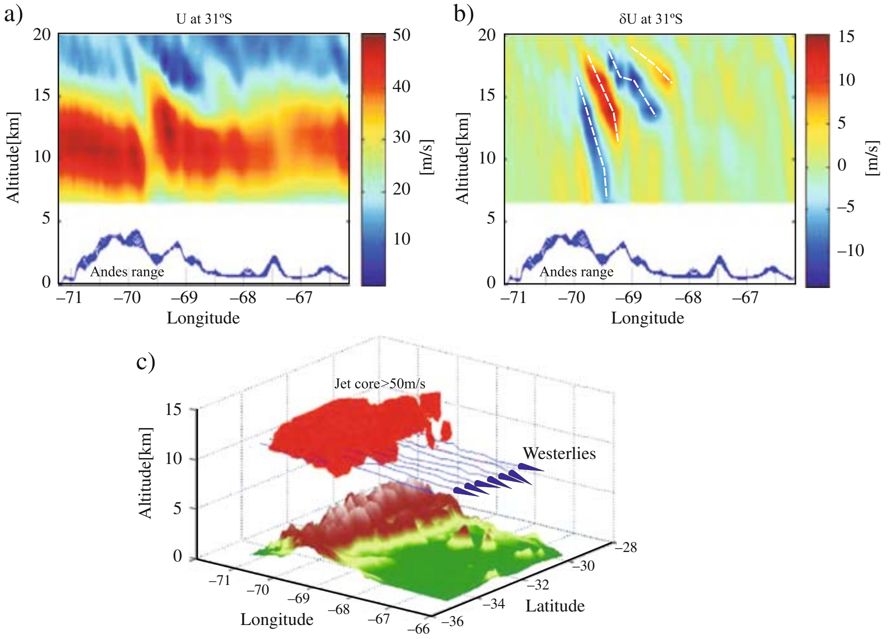

Fig. 4 a–b: U and δU vertical and zonal variability, at constant latitude, for S1. Note the wave constant phase surfaces due to the orographic forcing. (**c**) 3D view of the jet core (speed > 50 m/s). The Andes Range generates MWs and decelerates the mean flow, possibly altering the geostrophic balance

in the radiation of the atmosphere during the restitution of geostrophic equilibrium after the departure induced by the MW.

Figure 5 shows δW and δU at 300 hPa at the closest simulation time step output to each event. A stationary wave pattern with horizontal $\lambda_h > 50$ km along LOS, both during S1 and S2 are found in δW and δU. The mesoscale waves coincide with the highest orographic tops, as well as constant phase surfaces quite parallel to topography, suggesting their topographic origin. Note that in these cases, due to the relative oblique orientation of LOS and constant wave phases, in spite of the short horizontal wavelengths revealed during the simulations, it may be possible for the RO technique to resolve MWs with horizontal wavelengths shorter than its horizontal resolution.

In Fig. 6 we show the continue Morlet wavelet transform (CWT) for δU and δV during both events for two representative latitudes, at 300 hPa and the closest time step output to each one. Two principal modes were found both in δU and δV, longer and shorter than 100 km, respectively, and mostly located above the main mountains. One question arising here is whether the longer modes are due to the direct forcing of the mountains. To answer this, we recall that two important fundamental properties of GWs are (i) their phase front progression at right angles with group velocity (energy propagation) and (ii) their tendency to grow in amplitude

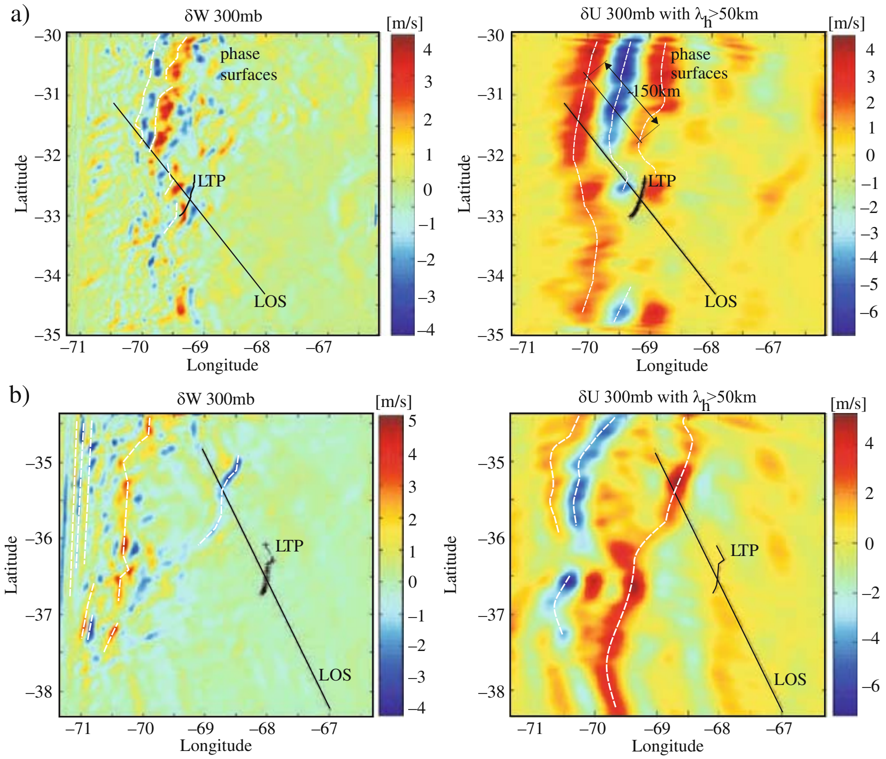

Fig. 5 δW and δU at 300 hPa at the closest simulation time step output to (**a**) S1 and (**b**) S2. A stationary wave pattern with $\lambda_h > 50$ km along LOS, during the events are found in both variables

with height, proportionally to the inverse square root of the exponentially decreasing air density. To identify internal waves in the atmosphere, it is necessary to know how the velocity components vary in space and time. Taking into account the Earth rotation effects, linear wave theory predicts an elliptic polarization relation between zonal and meridional velocity perturbation components. This means that the velocity vector rotates anticyclonically (counter-clockwise in the Southern Hemisphere) with time and hence also in space, as one moves in a direction opposite to the phase velocity (e.g., Gill 1982). Rotation effects are important in waves with horizontal scales greater than 100 km and they have no effect on shorter waves, which linear wave theory predicts a lineal polarization relation between δU and δV.

In the GWs literature, examples may be found where the polarization is analyzed from vertical regular radiosoundings, soundings from stratospheric balloons, etc.(e.g., de la Torre et al. 1996; Zhang et al. 2004). Nevertheless, GWs represent 3D structures without preferred symmetries, thus they can be observed in any direction or orientation. If the main wave source is at the ground and additional wave contributions from other sources are absent, the sense of rotation never changes. When a source is situated at a given altitude, energy is radiated at this level. In this case, the

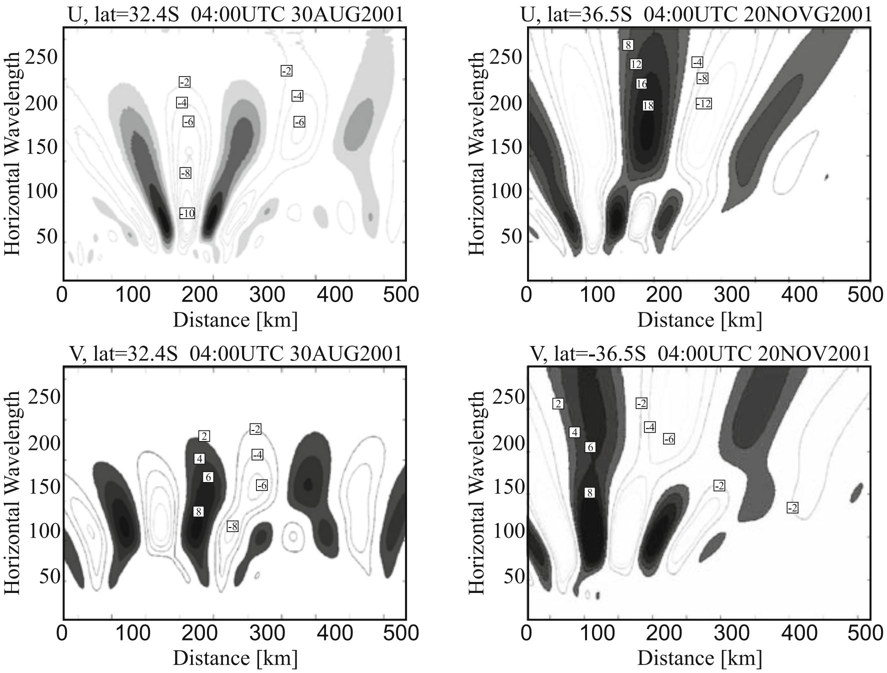

Fig. 6 Morlet CWT for δU (*above*) and δV (*below*) for S1 (*left*) and S2 (*right*), at 300 hPa and the closest time step output to each event. Two principal modes were found both δU and δV. The origin of the horizontal axis coincides with the western limit of the domain (71°W)

sense of rotation must be different above and below it. In order to identify the main source of GWs we studied the sense of rotation of the perturbation velocity vectors (δU, δV) at different pressure levels, above and below the jet, along different paths: (i) at constant latitudes and (ii) parallel to the LOS. We applied two different methods to identify the principal modes of oscillation in both velocity components: (1) a non recursive bandpass filter and (2) a CWT wavelet transform. The CWT coefficient corresponding to a certain wavelength can be interpreted as a bandpass filter for this wavelength. From both filtering methods we observe the velocity vector for modes with wavelengths greater than 100 km rotating in the same sense above and below the jet along all paths. From these results, we conclude that IGWs do not stem from geostrophic adjustment and the major source must be topographic forcing.

3.3 Comparison of Observed and Simulated GW Activity

The RO bending angle is an integrated measure of the refractive index (and therefore *T*) in the atmosphere traversed by the optical ray. The contribution peaks at the perigee and decays exponentially away from it. Due to uncertainties in the determination the exact position of the perigee, the peak of the exponential decay does not always coincide with each TP. In some cases, a LOS traversing through wave packets away from a TP, may reveal a vertical *T* profile evidencing an apparent larger (or nonexistent) WA at the LTP locations, as it is the case during S2 (Fig. 7b). We must be careful to interpret the atmospheric region where a given RO event predicts intense WA. If we are interested only in the mean *T* profile, the consideration of a rectangular parallelepiped defined by the first and last TP would be enough. If we are interested in the WA associated with it, the proper interpretation must consider the region defined by the set of optical rays. The 3D contours corresponding to $\pm\delta T = 3.0$ K for S1 and $\pm\delta T = 2.0$ K S2 are shown in left panel of Fig. 7. LTPs and LOSs are included. The right panels show δT along the vertical planes defined by the LOSs' sets. Note the wave phase surfaces tilting westward, evidencing a downward-westward phase progression clearly corresponding to MWs. A first insight shows an intense WA in S1 close to the TP (as predicted by the corresponding RO); whereas for S2, there are only weak wave packets in the troposphere at approximately 100 km away from the tangent points. Note in Fig. 7b for S2, the

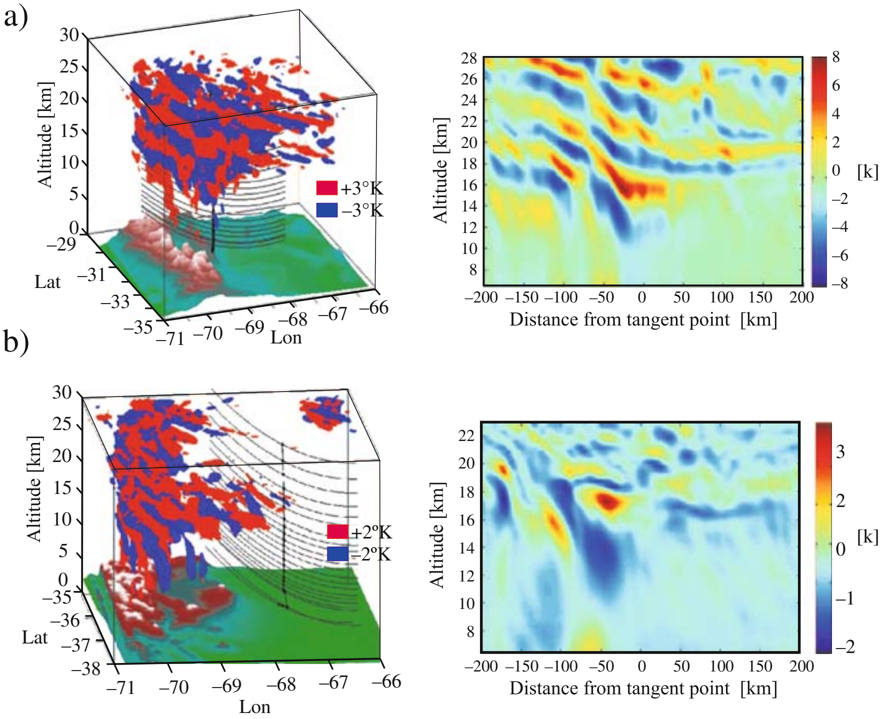

Fig. 7 Sets of LOS corresponding to each tangent point (TP) for (**a**) S1 and (**b**) S2. The relative weighting of the contribution rises with decreasing distance to the LOS center (TP). The *T* perturbations in 3D contours corresponding to $\pm\delta T = 3.0$ K for S1 and $\pm\delta T = 2.0$ K for S2 are shown. The *right* panels show δT along the vertical planes defined by the LOSs' sets

partial penetration of LOSs into the high wave amplitude atmospheric region. Taking into account these two examples, in addition to the systematic GPS-RO uncertainties mentioned above, it appears that GPS-RO *T* data alone are not enough to quantify and locate accurately WA during single events. At most, they would provide a useful qualitative indication. This should be complemented with independent observations or with mesoscale simulations. On the other hand, it seems reasonable to draw statistical conclusions from the global WA distribution derived from GPS-RO measurements alone.

4 Conclusions

A previous global analysis of wave potential energy using GPS-RO *T* profiles in the period 2001–2006 revealed a considerable intense WA in the Mendoza (Argentina) region, in comparison with other non-equatorial areas. After examining WRF and MM5 results for two selected cases in the vicinity of the RO LTPs, we found intense activity only near to the mountains. A wavelet analysis led us to identify principal modes with two main horizontal wavelengths, clearly corresponding to mountain waves. A hodograph analysis performed from the bandpassed results and from the wavelet coefficients evidences that IGWs do not stem from geostrophic adjustment at jet levels, but the source seems to be the topographic forcing. One of the simulations does not show intense WA in the vicinity of the tangent points, even though that the GPS-RO *T* profile detects it. The GPS-RO technique is not by itself reliable enough to quantify and locate accurately WA of single events, but it may be considered as a useful tool to measure the global distribution of WA.

Acknowledgements Manuscript prepared under grants UBA X021 and CONICET PIP 5932. A. de la Torre and P. Alexander are members and P. Llamedo holds a fellowship of CONICET. The GFZ contribution was partially funded through DFG project GW-CODE (WI 2634/2-1), DFG priority program CAWSES SPP 1176. We acknowledge data provided by the NOAA-CIRES/Climate Diagnostics Center, Boulder (CO), from their website http://www.cdc.noaa.gov and GFZ Potsdam and JPL for making available CHAMP and SAC-C GPS RO data for our study.

References

Fritts DC, Alexander MJ (2003) Gravity wave dynamics and effects in the middle atmosphere. Rev Geophys 41(1):1003, doi:10.1029/2001RG000106

Gill AE (1982) Atmosphere-Ocean Dynamics. Academic Press, San Diego London

Hirota I, Niki T (1985) A statistical study of inertia-gravity waves in the middle atmosphere. J Met Soc Jpn 63:1055–1066

Kirchengast G (2004) Occultations for probing atmosphere and climate: Setting the scene. In: Kirchengast G, Foelsche U, Steiner AK (eds) Occultations for Probing Atmosphere and Climate, Springer-Verlag, Berlin Heidelberg New York, pp 1–8

Kursinski ER, Hajj GA, Schofield JT, Linfield RP, Hardy KR (1997) Observing the Earth's atmosphere with radio occultation measurements using the Global Positioning System. J Geophys Res 102(D19):23429–23465

Lindzen RS (1990) Dynamics in Atmospheric Physics. Cambridge University Press, Cambridge

Liou YA, Pavelyev AG, Liu SL, Pavelyev AA, Yen N, Huang CY, Fong CJ (2007) FORMOSAT-3/COSMIC GPS radio occultation mission: Preliminary results. IEEE Trans Geosci Remote Sens 45(11):3813–3826, doi:10.1109/TGRS.2007.903365

Menéndez CG, Cabré MF, Núñez M (2004) Interannual and diurnal variability of January precipitation over subtropical South America simulated by a regional climate model. CLIVAR Exch 29:1–3

Plougonven R, Teitelbaum H, Zeitlin V (2003) Inertia gravity wave generation by the tropospheric midlatitude jet as given by the Fronts and Atlantic Storm-Track Experiment radio soundings. J Geophys Res 108(D21):4686, doi:10.1029/2003JD003535

Schmidt T, Wickert J, Beyerle G, Reigber C (2004) Tropical tropopause parameters derived from GPS radio occultation measurements with CHAMP. J Geophys Res 109(D13105), doi:10.1029/2004JD004566

de la Torre A, Alexander P (1995) The interpretation of wavelengths and periods as measured from atmospheric balloons. J Appl Meteor 34(12):2747–2754

de la Torre A, Alexander P (2005) Gravity waves above Andes detected from GPS radio occultation temperature profiles: Mountain forcing? Geophys Res Lett 32(L17815), doi:10.1029/2005GL022959

de la Torre A, Teitelbaum H, Vial F (1996) Stratospheric and tropospheric wave measurements near the Andes mountains. J Atmos Terr Phys 58(5):521–530

de la Torre A, Tsuda T, Hajj G, Wickert J (2004) A global distribution of the stratospheric gravity wave activity from GPS occultation profiles with SAC-C and CHAMP. J Meteor Soc Jpn 82(1B):407–417

de la Torre A, Alexander P, Llamedo P, Menéndez C, Schmidt T, Wickert J (2006a) Gravity waves above Andes detected from GPS radio occultation temperature profiles: Jet mechanism? Geophys Res Lett 33(L24810), doi:10.1029/2006GL027343

de la Torre A, Schmidt T, Wickert J (2006b) A global analysis of wave potential energy in the lower stratosphere derived from 5 years of GPS radio occultation data with CHAMP. Geophys Res Lett 33(L24809), doi:10.1029/2006GL027696

Wu DL, Zhang F (2004) A study of mesoscale gravity waves over North Atlantic with satellite observations and a mesoscale model. J Geophys Res 109(D22104), doi:10.1029/2004JD005090

Zhang F (2004) Generation of mesoscale gravity waves in upper-tropospheric jet-front systems. J Atmos Sci 61(4):440–457

Zhang F, Wang S, Plougonven R (2004) Uncertainties in using the hodograph method to retrieve gravity wave characteristics from individual soundings. Geophys Res Lett 31(L11110), doi:10.1029/2004GL019841

New Applications and Advances of the GPS Radio Occultation Technology as Recovered by Analysis of the FORMOSAT-3/COSMIC and CHAMP Data-Base

A.G. Pavelyev, Y.A. Liou, J. Wickert, V.N. Gubenko, A.A. Pavelyev, and S.S. Matyugov

Abstact Comparative analysis of phase and amplitude variations of GPS radioholograms allows one to separate the influence of the layered and irregular structures. A possibility exists to measure important parameters of internal waves: the intrinsic phase speed, the horizontal wind perturbations, and, under some assumptions, the intrinsic frequency as function of height in the atmosphere. A new technique was applied to measurements provided during CHAllenging Minisatellite Payload (CHAMP) and the Formosa Satellite-3/Constellation Observing System for Meteorology, Ionosphere, and Climate (FORMOSAT-3/COSMIC) radio occultation (RO) missions. As an example of this approach, we establish the atmospheric origin of amplitude and phase variations in the RO signal at altitudes 10–26 km. We observed for the first time in the RO practice examples of internal wave breaking at altitudes between 38 km and 45 km. We obtained geographical distributions and seasonal dependence of atmospheric wave activity with global coverage within the years 2001–2003.

1 Introduction

Atmospheric gravity waves (GW) have been a subject of intense research activities in recent years because of their various effects and their major contributions to atmospheric circulation, structure, and variability (Fritts and Alexander 2003). Radiosonde and rocketsonde GW measurements, balloon soundings, radar observations, and lidar studies have been limited to ground-based sites (Fritts et al. 1988; Wilson et al. 1991; Eckermann et al. 1995; Steiner and Kirchengast 2000; Tsuda et al. 2004; Wang et al. 2005) mainly over specific land parts of the Northern and Southern Hemispheres.

A.G. Pavelyev (✉)
Institute of Radio Engineering and Electronics of the Russian Academy of Sciences (IRE RAS), Moscow, Russia
e-mail: pvlv@ms.ire.rssi.ru

A. Steiner et al. (eds.), *New Horizons in Occultation Research*,
DOI 10.1007/978-3-642-00321-9_14, © Springer-Verlag Berlin Heidelberg 2009

The radio occultation technology incorporates high-precision GPS radio signals at two frequencies ($f_1 = 1575.42$ MHz and $f_2 = 1227.6$ MHz) for the investigation of internal waves. It allows the analysis of phase and amplitude of radio waves after propagating through the atmosphere. Analysis of temperature variations found from RO phase data furnishes an opportunity to measure the GW's statistical characteristics in the atmosphere (Steiner and Kirchengast 2000; Tsuda et al. 2000; Tsuda and Hocke 2002; Tsuda et al. 2004). Of particular importance are new ways to investigate locations of the layered plasma structures in the ionosphere. Radio-holographic methods for the analysis of RO signals have the potential and capability for the research and simultaneous observation of atmospheric and ionospheric waves (Igarashi et al. 2000, 2001; Pavelyev et al. 2002, 2003, 2004; Liou et al. 2002, 2003, 2006). However, up to now the assumption of global spherical symmetry of the atmosphere and ionosphere is a cornerstone in the analysis of GPS RO measurements (Hajj et al. 2002; Wickert et al. 2004).

The aim of this paper is to introduce a new technique for estimating parameters of internal waves, to demonstrate the examples of direct observation and location of quasi-regular internal waves, and to analyze seasonal and geographical distributions of internal wave activity at different levels in the atmosphere using amplitude and phase variations in GPS occultation signals.

2 Radio Occultation Method

The scheme of the RO geometry is shown in Fig. 1. The point O is the center of the global spherical symmetry of the Earth's atmosphere and ionosphere. Radio waves emitted by the GPS satellite (point G) arrive at the receiver on board of the LEO satellite (point L) along the ray GTL, where T is the tangent point in the atmosphere. The results of registration which are 1-D radio-holographic images of the propagation medium consist of the phase path excesses $\Phi_1(t)$ and $\Phi_2(t)$ along the amplitudes $A_1(t)$ and $A_2(t)$ of the radio field as functions of time at two GPS frequencies. These variations are caused mainly owing to the medium influence at the tangent point T, where the refractivity gradient is perpendicular to the ray GTL. In the case of spherical symmetry the point T coincides with the perigee of ray GTL, where the distance from the center of spherical symmetry—point O is minimal and

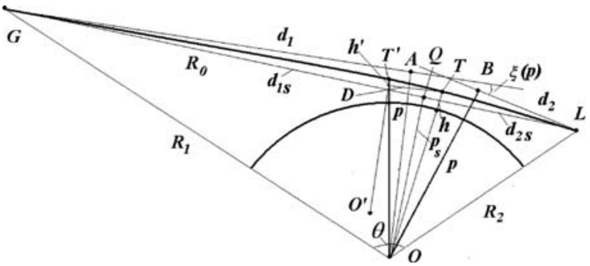

Fig. 1 Key geometrical parameters for RO measurements

equal to r_0. The geographical coordinates of the ray perigee can be evaluated by use of orbital data of the GPS and LEO satellites. Analysis of RO data delivers the vertical profile of refractivity $N(h)$ in the atmosphere and then vertical profiles of pressure $p(h)$ and temperature $T(h)$.

The projection of the point T on the Earth's surface determines the geographical coordinates of the RO region. The vertical velocity of the occultation beam path $v_\perp$ is about of 2 km/s. This value of $v_\perp$ is many times greater than those corresponding to the motion of layers in the atmosphere and ionosphere. Thus the RO radio-holograms record practically simultaneously the impact of the internal waves on the RO signal because the vertical displacement of a wave structure is negligible during the movement of the beam across it. However, the horizontal gradients in the atmosphere and ionosphere can disturb the spherical symmetry of the atmosphere and ionosphere (Wickert et al. 2004). Actually a local spherical symmetry can exist for inclined layered structures in the propagation medium. In the case of local spherical symmetry one can use the same relationships, which have been previously obtained for the case of global spherical symmetry (Pavelyev et al. 2002, 2004) with a change of the designation of the impact parameter from p to p' (Fig. 1). For simplicity we will not use the primes on p and O below.

In the case of local spherical symmetry with center at point O (Fig. 1) there are fundamental relations between the phase path excess $\Phi(p)$ (in m) and the refraction attenuation of radio waves $X(p)$ (dimensionless), which characterizes the decreasing/increasing of the intensity of radio waves because of the influence of the refraction effect in the atmosphere (Pavelyev et al. 2002, 2004; Liou et al. 2006)

$$\Phi(p) = L(p) + \kappa(p) - R_0, \quad L(p) = d_1 + d_2 + p\xi(p), \tag{1}$$

$$X(p) = pR_0^2 \left[R_1 R_2 d_1 d_2 \sin\theta \left| \frac{\partial \theta}{\partial p} \right| \right]^{-1}, \tag{2}$$

$$\frac{\partial \theta}{\partial p} = \frac{\mathrm{d}\xi}{\mathrm{d}p} - \left(\frac{1}{d_1} + \frac{1}{d_2} \right), \tag{3}$$

$$L(p) = \left(R_1^2 - p^2\right)^{1/2} + \left(R_2^2 - p^2\right)^{1/2} + p\xi(p), \tag{4}$$

$$R_0 = d_1 + d_2, \quad d_{1,2} = \left(R_{1,2}^2 - p^2\right)^{1/2}, \tag{5}$$

where $\kappa(p)$ is the main refractivity part of the phase path excess, $\xi(p) = -\mathrm{d}\kappa(p)/\mathrm{d}p$ is the refraction angle, $\theta(p)$ is the central angle, p, p_s are the impact parameters of the ray trajectory GTL, and the line of sight GQL, respectively, R_0, R_1, R_2 are the distances GL, OG, and OL, correspondingly, $L(p)$ is the distance GABL. $L(p)$ is a sum of two short lengths GA (d_1), BL (d_2), and arc AB, which is equal to the product $p\xi(p)$. Because smallness of the refraction effects the distances d_1, d_2 are approximately equal to GQ and QL. According to Eq. (1) the phase path excess $\Phi(p)$ contains only one term $\kappa(p)$, which depends directly on the refractivity. This justifies the designation "main refractivity part" for $\kappa(p)$. The refraction angle $\xi(p)$ is connected with the central angle θ (Fig. 1):

$$\theta = \pi + \xi(p) - \sin^{-1}\left(\frac{p}{R_1}\right) - \sin^{-1}\left(\frac{p}{R_2}\right), \tag{6}$$

$$\theta = \pi - \sin^{-1}\left(\frac{p_s}{R_1}\right) - \sin^{-1}\left(\frac{p_s}{R_2}\right), \tag{7}$$

$$\xi(p) = \sin^{-1}\left(\frac{p}{R_1}\right) + \sin^{-1}\left(\frac{p}{R_2}\right) - \sin^{-1}\left(\frac{p_s}{R_1}\right) - \sin^{-1}\left(\frac{p_s}{R_2}\right). \tag{8}$$

Two different expressions (Eqs. 6 and 7) can be used to obtain the connections between the impact parameters p_s and p and the refraction angle $\xi(p)$. From Eqs. (1) and (6) or (7) one can obtain by time differentiation of the phase excess $\Phi(p)$ and the central angle θ the relationship connecting the Doppler frequency F_d of the RO signal with the impact parameters p and p_s:

$$\frac{\mathrm{d}\Phi(p)}{\mathrm{d}t} = F_\mathrm{d} = (p - p_s)\frac{\mathrm{d}\theta}{\mathrm{d}t} + (d_1 - d_{1s})R_1^{-1}\frac{\mathrm{d}R_1}{\mathrm{d}t} + (d_2 - d_{2s})R_2^{-1}\frac{\mathrm{d}R_2}{\mathrm{d}t}, \tag{9}$$

$$\frac{\mathrm{d}\theta}{\mathrm{d}t} = \frac{\partial\theta}{\partial p_s}\frac{\mathrm{d}p_s}{\mathrm{d}t} - p_s\left[(d_{1s}R_1)^{-1}\frac{\mathrm{d}R_1}{\mathrm{d}t} + (\mathrm{d}_{2s}R_2)^{-1}\frac{\mathrm{d}R_2}{\mathrm{d}t}\right], \tag{10}$$

$$d_{1s} = (R_1^2 - p_s^2)^{1/2}, \quad d_{2s} = \left(R_2^2 - p_s^2\right)^{1/2}, \tag{11}$$

where d_{1s}, d_{2s} are the distances GQ and QL, correspondingly. After substitution of Eq. (10) into Eq. (9) one can obtain:

$$\begin{gathered} F_\mathrm{d} = -(p - p_s)\left\{\left(\frac{1}{d_{1s}} + \frac{1}{d_{2s}}\right)\frac{\mathrm{d}p_s}{\mathrm{d}t} - (p^2 - p_s^2)(Q_1 + Q_2)\right\} \\ Q_{1,2} = R_{1,2}\frac{\mathrm{d}R_{1,2}}{\mathrm{d}t}\left[d_{1,2s}(d_{1,2s} + d_{1,2s})(pd_{1,2s} + p_s d_{1,2s})\right]^{-1} \end{gathered} \tag{12}$$

Equations (9), (10), (11), and (12) are valid for general case of non-circular orbits of the GPS and LEO satellites. Usually in RO experiments the absolute values of difference $p - p_s$ and vertical velocities $\mathrm{d}R_{1,2}/\mathrm{d}t$ are far below (by factor 10^{-2}–10^{-4}) the absolute magnitudes of the impact parameter p (or p_s) and vertical velocity of ray perigee $\mathrm{d}p_s/\mathrm{d}t$. Under condition $|(p - p_s)\mathrm{d}R_{1,2}/\mathrm{d}t| \ll p_s|\mathrm{d}p_s/\mathrm{d}t|$ one can obtain from Eq. (12) a simple formula for estimation of the difference $p - p_s$ on the Doppler frequency

$$F_\mathrm{d} = -(p - p_s)\left(\frac{1}{d_{ts}} + \frac{1}{d_{2s}}\right)\frac{\mathrm{d}p_s}{\mathrm{d}t}. \tag{13}$$

The values p_s, $\mathrm{d}p_s/\mathrm{d}t$, d_{1s}, d_{2s} can be delivered from orbital data and the phase delays $\Phi_{1,2}(p)$ are the objects of measurements and given in the phase parts of radio-holograms at frequencies f_1 and f_2. Below we will consider new relationships, which connect the phase acceleration $a = \mathrm{d}^2\Phi(t)/\mathrm{d}t^2$, Doppler frequency $F_\mathrm{d}(t)$, and refraction attenuation of radio waves $X(t)$. Under conditions

$$|p - p_s| \ll p_s, \qquad \left|\frac{(p - p_s)\mathrm{d}(\partial\theta/\partial p_s)}{\mathrm{d}t}\right| \ll \left|\left(\frac{\mathrm{d}p}{\mathrm{d}t} - \frac{\mathrm{d}p_s}{\mathrm{d}t}\right)\frac{\partial\theta}{\partial p}\right|, \tag{14}$$

and by use of equation $\mathrm{d}p/\mathrm{d}t - \mathrm{d}p_s/\mathrm{d}t \approx [X(t) - 1]\mathrm{d}p_s/\mathrm{d}t$ (Liou et al. 2006), one can obtain from Eq. (13):

$$1 - X(t) = \frac{m\,\mathrm{d}F_\mathrm{d}(t)}{\mathrm{d}t} = \frac{m\,d^2\Phi(t)}{\mathrm{d}t^2} = ma, \tag{15}$$

$$m = \left(\frac{\mathrm{d}p_s}{\mathrm{d}t}\right)^{-2}\frac{d_1 d_2}{d_1 + d_2}. \tag{16}$$

Equations (15) and (16) relate the refraction attenuation and the excess phase path acceleration via a classical dynamics equation-type, first published in 2006 (Liou and Pavelyev 2006). The coefficient m, having the dimension s^2/m, is a slowly changing function of vertical velocity $\mathrm{d}p_s/\mathrm{d}t$ of the ray perigee T and distances d_1, d_2. Equation (15) indicates equivalence between variations of the excess phase path acceleration a, derivative of the Doppler frequency $F_\mathrm{d}(t)$, and refraction attenuation $X(t)$. Usually during RO experiments parameters m and $\mathrm{d}p_s/\mathrm{d}t$ are known from orbital data because the location of the spherical symmetry center O and its projection on the line of sight—point Q are supposed to be known, and the distances GT d_1 and TL d_2 can be estimated as $d_{1,2} = (R_{1,2}^2 - p^2)^{1/2}$. Therefore, Eq. (15) gives the possibility to recalculate the phase acceleration a and/or Doppler frequency F_d to the refraction attenuation X_p. This is useful for excluding systematic errors from phase and/or amplitude data. This is also useful for the estimation of absorption in the atmosphere. The refraction attenuation X_a is determined from amplitude data as a ratio of intensity of radio waves propagating through the atmosphere $I_a(t)$ to its intensity in free space I_s:

$$X_a(t) = \frac{I_a(t)}{I_s}. \tag{17}$$

The experimental value X_a (dimensionless) is the product of the refractive and absorption contributions. However, the phase acceleration depends on the refraction effect only. This gives a possibility to determine the absorption in the atmosphere $Y(t)$ as a ratio:

$$\begin{aligned} Y(t) &= \frac{X_a(t)}{(1 - ma)}, \text{ or} \\ Y(t) &= X_a(t)\left(1 - \frac{m\,\mathrm{d}F_\mathrm{d}(t)}{\mathrm{d}t}\right)^{-1}. \end{aligned} \tag{18}$$

This possibility must be investigated in detail because in future satellite RO missions measurements of absorption effects due to water vapor and minor atmospheric gas constituents are planning and difficulties will consist of removing the refraction attenuation effect from amplitude data. Equations (18) indicate the feasible way to solve this problem. Also Eqs. (18) may be useful for estimation the conditions for communication in the Ku/K bands between two LEO satellites in a radio occultation geometry (Martini et al. 2006).

Phase variations of the RO signal as function of time $\Phi(t)$ at each GPS frequency f_1 and f_2 contain slowly and quickly changing parts $\Phi_s(t)$ and $\Phi_f(t)$:

$$\Phi(t) = \Phi_s(t) + \Phi_f(t) \tag{19}$$

After substitution of Eq. (19) in Eq. (15) one can obtain:

$$1 - X(t) = m\left[\frac{\mathrm{d}^2\Phi_s(t)}{\mathrm{d}t^2} + \frac{\mathrm{d}^2\Phi_f(t)}{\mathrm{d}t^2}\right] \approx m\frac{\mathrm{d}^2\Phi_f(t)}{\mathrm{d}t^2}. \tag{20}$$

Equation (20) is valid under condition: $|\mathrm{d}^2\Phi_s(t)/\mathrm{d}t^2| \ll |\mathrm{d}^2\Phi_f(t)/\mathrm{d}t^2|$, which is fulfilled if the influence of irregularities in the atmosphere and ionosphere is far below the effect of the standard atmosphere (or ionosphere) near the ray perigee. The contribution of layered structures to phase excess variations in some cases may be considered as a quasi-periodical process, and the second derivative $\mathrm{d}^2\Phi(t)/\mathrm{d}t^2$ may be presented in the form:

$$\frac{\mathrm{d}^2\Phi_f(t)}{\mathrm{d}t^2} \approx -\omega_0^2\Phi_f(t), \quad \omega_0^2 = 4\pi^2 v_p^2 \lambda_v^{-2}, \tag{21}$$

where v_p is the vertical velocity of the RO ray near the perigee T. Parameter ω_0^2 depends on the vertical period λ_v of the layered structure. After substitution of Eq. (21) in Eq. (15) one can obtain:

$$\begin{aligned} X(t) - 1 &= c_0\Phi_f(t), \\ c_0 &= m\omega_0^2 = k_v^2 d_1 d_2/R_0, \\ k_v^2 &= 4\pi^2/\lambda_v^2, \end{aligned} \tag{22}$$

where k_v is the vertical wave number of the vertical quasi-periodical structure in the atmosphere (ionosphere), d_1, d_2 are the distances along the ray GTL from the points L and G up to the ray perigee T, respectively, R_0 is the distance GL. Equation (22) connects the high-frequency part of phase path excess variations $\Phi_f(t)$ with refraction attenuation changes $X(t) - 1$ of the RO signal. Note that the coefficient c_0 in Eq. (22) does not depend on the vertical velocity of the ray perigee. Equations (22) allow one to recalculate refraction attenuation variations of GPS radio-holograms to phase path excess variations and vice versa. The form of phase path excess variations $\Phi_f(t)$ is similar to the form of intensity variations $X(t) - 1$. It follows from Eqs. (22) that variations of the intensity of the RO signal are proportional to phase path excess oscillations and inversely proportional to the second power of the vertical spatial period of the layered structure. One can estimate from Eqs. (22) the value of parameter c_0 by comparison of amplitude and phase variations of the RO signal.

As follows from our analysis the practical algorithm for revealing the contribution of the lower ionosphere in the phase data can be described by:

$$\Phi_l(t) = \Phi(t) - \langle \Phi(t) \rangle, \tag{23}$$

where $\langle \Phi(t) \rangle$ denotes the trend in the phase data. An alternative approach to find $\langle \Phi(t) \rangle$ consists in averaging of the phase path excess over a sliding interval; the size of the sliding averaging interval must be long enough to account for the long-scale influence of the atmosphere or upper ionosphere.

Usually during RO experiments the parameter m (Eqs. 15 and 16) is a slowly changing function of time. Parameter $\mathrm{d}p_s/\mathrm{d}t$ depends on the velocity components v, w of the GPS and LEO satellites, respectively. Components v, w are perpendicular to the straight line GL in the plane GOL. The components v, w are positive when oriented in direction to the point O and are negative in the opposite case. Components v, w are connected with the parameter $\mathrm{d}p_s/\mathrm{d}t$ by:

$$\frac{\mathrm{d}p_s}{\mathrm{d}t} = v + (w - v)\frac{d_{1s}}{R_0}. \tag{24}$$

Equations (15), (16), and (24) can be used to find the distance LT d_{2s} from simultaneous observations of phase and intensity variations of radio waves. To achieve this, one can find m from Eq. (15) from the ratio of refraction attenuation changes to phase acceleration variations and then the distance d_{2S} can be evaluated from the relationship

$$d_{2s} = 2mw^2\left[1 + 2b\left(\frac{v}{w} - 1\right) + \left(1 - 4b\frac{v}{w}\right)^{1/2}\right]^{-1}, \quad b = \frac{mw^2}{R_0}. \tag{25}$$

Equations (15) and (25) may be applied for the location of the tangent point T (or locally spherical symmetric layers) in the propagation medium.

3 Connection Between the Phase Acceleration and Intensity Variations: Experimental Validation

The phase acceleration a calculated as the second temporal derivative of the phase path excess and intensity variations $X(t) - 1$ at the frequency f_1 are shown in Fig. 2, (curves 1 and 2, respectively) for CHAMP RO events 0136 (January 14, 2003) and 0023 (September 21, 2003). As seen in Fig. 2, there is a good correspondence between variations of the phase acceleration and the refraction attenuation of the RO signal. The coefficient m is different in RO events 0136 and 0023. The average ratio of the refraction attenuation and the phase acceleration m is about 1.0 s^2/m in the 5–40 km height interval for RO event 0136 (Fig. 2, left panel) but for event 0023 (Fig. 2, right panel) is about 1.5 times greater. As follows from orbital data, the change in parameter m during these RO events is about 10%. As follows from

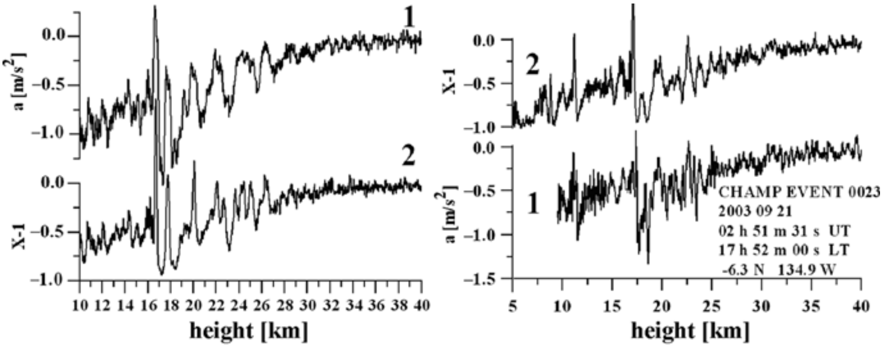

Fig. 2 Phase acceleration a and refraction attenuation variations $X - 1$ at the first GPS frequency f_1 (curves 1 and 2, respectively) for two CHAMP RO events: No. 0136 on January 14, 2003 (*left panel*) and No. 0023 on September 21, 2003 (*right panel*)

analysis of data shown in Fig. 2, Eqs. (15) and (16) are valid and they may allow one to locate the layered structures in the atmosphere and ionosphere, which are responsible for the variations of the intensity and phase acceleration of radio waves in the satellite-to-satellite links.

An example of the determination of the displacement $D = d_{2s} - d_2$ is shown in Fig. 3 for the FORMOSAT-3/COSMIC RO event 0006, April 23, 2006, 15 h 54 m 28 s LT, with geographical coordinates 9.5°S, 288.9°W. Curves 1 and 2 in Fig. 3, left panel, demonstrate good correspondence between the refraction attenuation X_p estimated from the phase acceleration a and parameter m by use of formula $1 - X_p = ma$, and X_a evaluated from amplitude data, respectively, at the first GPS frequency f_1.

The results of evaluation of the displacement D by use of Eqs. (15) and (25) are shown in Fig. 3, right panel. According to Fig. 3 (right panel) the displacement D is bound between ±50 km in the 10–25 km altitude interval and between ±100 km

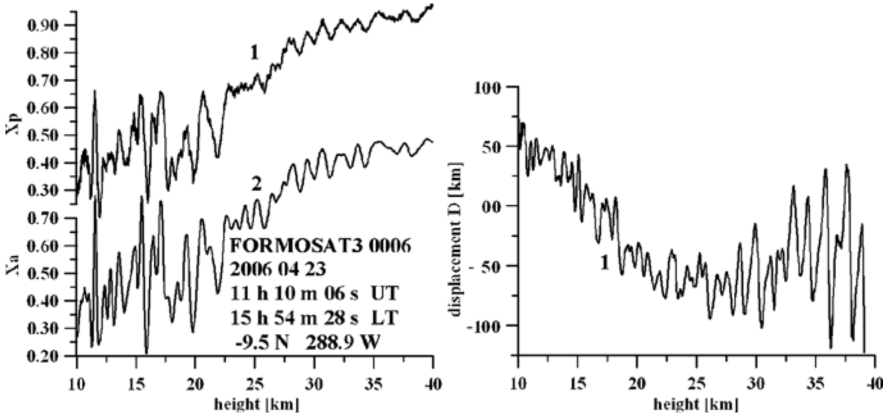

Fig. 3 *Left panel*: comparison of the refraction attenuations X_a and X_p calculated from the phase (curve 1) and amplitude (curve 2) data. *Right panel*: displacement D of the tangent point T calculated by use of Eqs. (15) and (25)

in the 25–40 km height interval. It follows that the phase acceleration has the same importance for RO experiments as the well-known Doppler frequency.

4 Wave-Breaking Effect and Determination of Internal Wave Parameters

The amplitude channel of the radio-hologram can be used to obtain information on the vertical distribution of refractivity, temperature, and their vertical gradient (Pavelyev et al. 2002, 2003; Liou et al. 2002, 2003, 2006). Amplitude variations of the RO signal depend mainly on the high-frequency part of the derivative of the refraction angle on the impact parameter $\mathrm{d}\xi(p)/\mathrm{d}p$. For obtaining the corresponding variations in the vertical gradient of refractivity $\mathrm{d}N(h)/\mathrm{d}h$ the low frequency part in the function $\mathrm{d}\xi(p)/\mathrm{d}p$ corresponding to the low frequency noise in the amplitude data has been excluded by numerical filtration. The remaining high-frequency part of $\mathrm{d}\xi_h(p)/\mathrm{d}p$ was transformed by use of the Abel transformation technique (Liou et al. 2002), to find perturbations in the vertical gradient of refractivity $\mathrm{d}N_h(h)/\mathrm{d}h$. This procedure does not need an optimization technique because (1) absence of the low frequency noise in the function $\mathrm{d}\xi_h(p)/\mathrm{d}p$ and (2) high sensitivity of the amplitude to high-frequency variations in the vertical gradient of refractivity (variations of the intensity of the RO signal are inversely proportional to the second power of the vertical spatial period of the layered structure).

Variations in the vertical gradient of refractivity retrieved from the RO amplitude data are shown in Fig. 4 for CHAMP RO events No. 0140 and No. 0001,

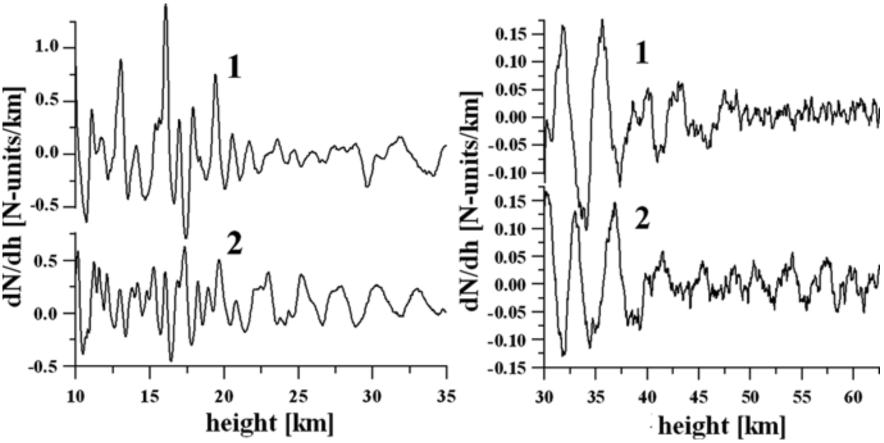

Fig. 4 Vertical gradient of refractivity perturbations at the first GPS frequency f_1 in the 10–30 km (*left*) and 30–65 km height interval (*right*). Abrupt changes in the amplitude and phase of refractivity perturbations are seen between the altitudes 38 km and 40 km (curves 1 and 2, *right panel*) and 45–50 km (curve 1, *right panel*). Curves 1 and 2 correspond to CHAMP RO events No. 0140 (02 h 35 m 34 s LT, 21.9°N, 172.5°W) and No. 0001 (02 h 09 m 51 s LT, 15.9°N, 330.0°W), January 23, 2003, respectively

January 23, 2003 (curves 1 and 2, respectively). The wave structure is clearly seen in the perturbations of the vertical refractivity gradient in the 10–45 km interval (curves 1 and 2, left and right panels in Fig. 4). The vertical period of the wave structure grew from 0.8–1.0 km in the 10–25 km interval and from 2–4 km in the 30–40 km interval. Abrupt changes in the amplitude and phase of the refractivity perturbations are seen between the altitudes 38 km and 40 km (curves 1 and 2, right panel) and 45–50 km (curve 1, right panel). These changes may be connected with wave-breaking altitudes where the wave energy dissipates to eddies and turbulence. Previously the wave breaking effect has been observed from space during CRISTA experiments (Eckermann and Preusse 1999) at altitudes between 30 km and 40 km. There are indications for GW breaking at altitudes of about 50–60 km (Ern et al. 2006). Note that phenomena of wave breaking shown in Fig. 4 are the first direct observations by use of the GPS RO method.

5 Integral Behavior of Wave Activity in the Years 2001–2003

The wave activity in the atmosphere over a global scale can be characterized by the RO index β: probability of strong wave amplitudes exceeding the fixed level of the vertical gradient of refractivity q. This index has a global importance for the description of wave activity in the atmosphere as seen in Figs. 5 and 6 based on the analysis of CHAMP RO data for the time period 2001–2003. The magnitude β has been defined in this analysis as a ratio of numbers of intense wave amplitude greater than $q > 0.6$ N-units/km for the 12–16 km and with $q > 0.24$ N-units/km for the 18–26 km to total number of measurements over the Earth globe. The value β is marked in percents at vertical axis in Figs. 5 and 6. The smooth curves are obtained as approximation of the experimental data (broken lines) by least squares method. The data, shown in Figs. 5 and 6, are relevant to three year time interval September 2001–September 2003, with three data gaps: (1) from October 15, 2001, up to February 28, 2002; (2) from May 16, 2002, up to October 31, 2002; (3) from January 1 up to January 12, 2003. The seasonal and annual changes of wave activity are seen at all altitudes 12–26 km. For example, changes with period of about 12 months are seen at altitudes 12 km, 16 km, and 20–26 km (Figs. 5 and 6) for period January–September 2003. The phases of one-year oscillations at altitudes 12 km and 16 km are opposite to the phases of wave activity variations at the heights 20–26 km. The wave activity behavior at the altitudes 14 km and 18 km is different from that at the heights 12 km, 16 km, and 20–26 km. The wave activity at the heights 14 km and 18 km is increasing when the time goes to the end of the considered period—September 2003. This may be connected with tropopause effects. Changes in tropopause height, significant variations in refractivity gradients near the tropopause, and other phenomena can produce strong scintillations in amplitude variations of the RO signal. Analysis of these effects is a task of future investigation. At altitudes 12 km, 16 km, and 20–26 km the wave activity is gradually diminishing by 10–40% when time changes from September 2001 to September 2003. This diminishing may be connected with

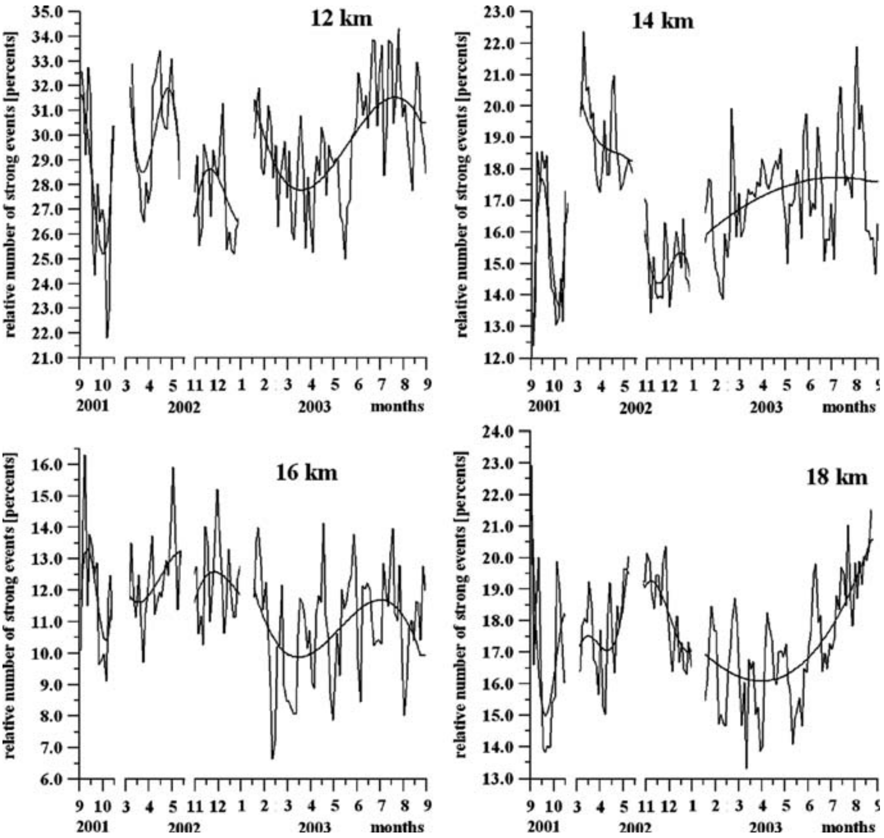

Fig. 5 Changes in internal wave activity (averaged over the Earth globe) during 2001 and 2003 at different altitudes in the atmosphere: 12 km and 14 km (*top left and right panels*, respectively), 16 km and 18 km (*bottom left and right panels*, respectively)

changes in the intensity of meteorological processes, types of atmospheric circulations, and, very likely, with reduction in solar activity in the considered period of time. In that respect internal wave activity may be considered among the other important parameters described in various publications (e.g., Suh and Lim 2006, and references therein), which characterize effects of solar activity on the Earth's atmosphere.

6 Conclusion

Comparative theoretical and experimental analysis of phase and amplitude variations of GPS radio-holograms discovered new relationships, which relate the refraction attenuation and the excess phase path acceleration via a classical dynamics equation-type. The advantages of the introduced relationship consist in (1) a

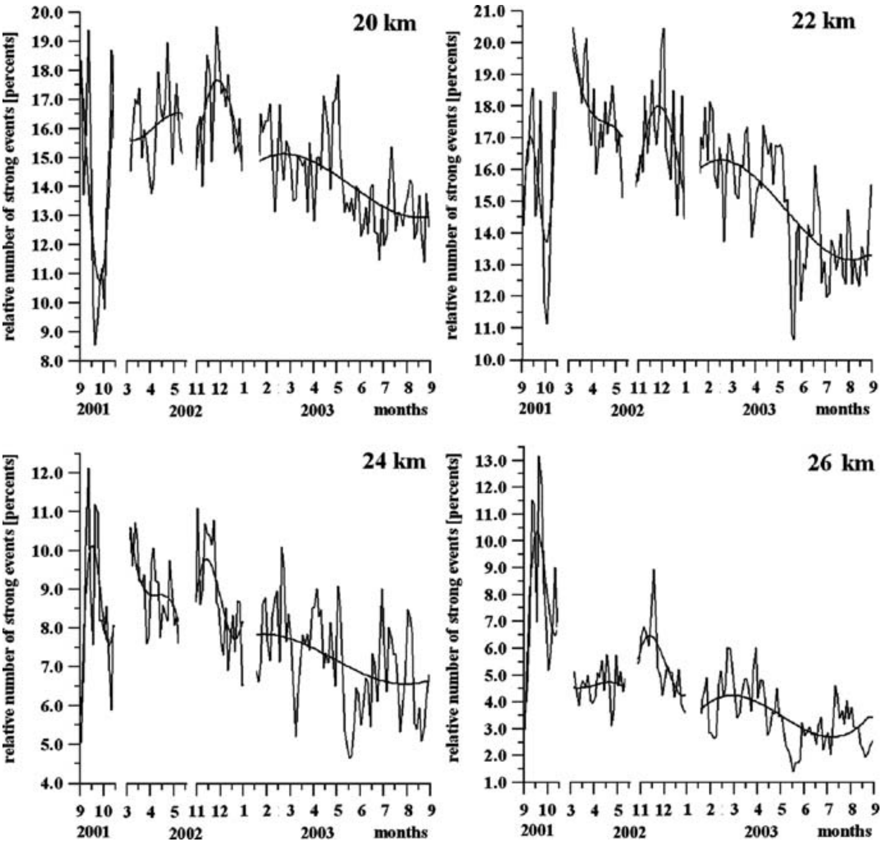

Fig. 6 Changes in internal wave activity (averaged over the Earth globe) during 2001 and 2003 at different altitudes in the atmosphere: 20 km and 22 km (*top left and right panels*, respectively), 24 km and 26 km (*bottom left and right panels*, respectively)

possibility to separate the layered structure and turbulence contributions to the RO signal; (2) a possibility to estimate the absorption in the atmosphere by dividing refraction attenuations found from amplitude and phase data; (3) a possibility to locate the tangent point in the atmosphere with accuracy in the distance from the standard position of about ±100 km. The suggested method has a general importance (for example, it may be applied for analysis of amplitude and phase variations in the trans-ionospheric satellite-to-Earth links). We showed also that amplitude variations of GPS occultation signals are very sensitive sensors to internal waves in the atmosphere. The sensitivity of the amplitude method is inversely proportional to the square of the vertical period of the internal wave, indicating high sensitivity of amplitude data to wave structures with small vertical periods in the 0.8–4 km interval. By use of the amplitude data analysis the internal wave breaking phenomenon has been observed at the first time in RO practice at altitudes between 38 km and 45 km.

The amplitude GPS occultation method presents a possibility to obtain the geographical distribution and seasonal dependence of atmospheric wave activity with global coverage. At the altitudes 12 km, 16 km, and 20–26 km the wave activity is gradually diminishing by 10–40% from September 2001 to September 2003. This diminishing may be connected with changes in the intensity of meteorological processes, types of atmospheric circulations, and, very likely, with reduction in solar activity.

Acknowledgements We are grateful to the GeoForschungZentrum Potsdam for delivering the CHAMP RO data and to UCAR/CDAAC (Boulder, CO, USA) for the provision of FORMOSAT-3/ COSMIC data. We are grateful to the National Science Council of Taiwan, R.O.C., for financial support under the grants NSC 92-2811-M008-001, NSC 91-2111-M008-029, and the Office of Naval Research (ONR) of USA under grant N00014-00-0528. Work has been partly supported by the Russian Fund of Basic Research, grant No. 06-02-17071. In addition, assistance was provided by the Russian Academy of Sciences, program OFN-16 and OFN-17.

References

Eckermann SD, Preusse P (1999) Global measurements of stratospheric mountain waves from space. Science 286(5444):1534–1537, doi:10.1126/science.286.5444.1534

Eckermann SD, Hirota I, Hocking WA (1995) Gravity wave and equatorial wave morphology of the stratosphere derived from long-term rocket soundings. QJR Meteorol Soc 121: 149–186

Ern M, Preusse P, Warner CD (2006) Some experimental constraints for spectral parameters used in the Warner and McIntyre gravity wave parameterization scheme. Atmos Chem Phys 6: 4361–4381

Fritts DC, Alexander MJ (2003) Gravity wave dynamics and effects in the middle atmosphere. Rev Geophys 41(1):1–64, doi:10.1029/2001RG000106

Fritts DC, Tsuda T, Sato T, Fukao S, Kato S (1988) Observational evidence of a saturated gravity wave spectrum in the troposphere and lower stratosphere. J Atmos Sci 45:1741–1759

Hajj GA, Kursinski ER, Romans LJ, Bertiger WI, Leroy SS (2002) A technical description of atmospheric sounding by GPS occultation. J Atmos Solar Terr Phys 64(4):451–469

Igarashi K, Pavelyev A, Hocke K, Pavelyev D, Kucherjavenkov IA, Matugov S, Zakharov A, Yakovlev O (2000) Radio holographic principle for observing natural processes in the atmosphere and retrieving meteorological parameters from radio occultation data. Earth Planets Space 52(11):893–899

Igarashi K, Pavelyev A, Hocke K, Pavelyev D, Wickert J (2001) Observation of wave structures in the upper atmosphere by means of radio holographic analysis of the radio occultation data. Adv Space Res 27(6/7):1321–1327

Liou YA, Pavelyev AG (2006) Simultaneous observations of radio wave phase and intensity variations for locating the plasma layers in the ionosphere. Geophys Res Lett 33(L23102), doi:10.1029/2006GL027112

Liou YA, Pavelyev AG, Huang CY, Igarashi K, Hocke K (2002) Simultaneous observation of the vertical gradients of refractivity in the atmosphere and electron density in the lower ionosphere by radio occultation amplitude method. Geophys Res Lett 29(19):1937, doi:10.1029/2002GL015155

Liou YA, Pavelyev AG, Huang CY, Igarashi K, Hocke K, Yan SK (2003) Analytic method for observation of the gravity waves using radio occultation data. Geophys Res Lett 30(20):2021, doi:10.1029/2003GL017818

Liou YA, Pavelyev AG, Wickert J, Liu SF, Pavelyev AA, Schmidt T, Igarashi K (2006) Application of GPS radio occultation method for observation of the internal waves in the atmosphere. J Geophys Res Atmos 111(D06104), doi:10.1029/2005JD005823

Martini E, Freni A, Facheris L, Cuccoli F (2006) Impact of tropospheric scintillation in the Ku/K bands on the communications between two LEO satellites in a radio occultation geometry. IEEE Trans Geosci Remote Sens 44(8):2063–2071

Pavelyev A, Igarashi K, Reigber C, Hocke K, Wickert J, Beyerle G, Matyugov S, Kucherjavenkov A, Pavelyev D, Yakovlev O (2002) First application of radioholographic method to wave observations in the upper atmosphere. Radio Sci 37(3):1034, doi:10.1029/2000RS002501

Pavelyev AG, Tsuda T, Igarashi K, Liou YA, Hocke K (2003) Wave structures in the electron density profile in the ionospheric D- and E-layers observed by radio holography analysis of the GPS/MET radio occultation data. J Atmos Solar Terr Phys 65(1):59–70

Pavelyev AG, Liou YA, Wickert J (2004) Diffractive vector and scalar integrals for bistatic radio holographic remote sensing. Radio Sci 39(RS4011), doi:10.1029/2003RS002935

Steiner AK, Kirchengast G (2000) Gravity wave spectra from GPS/MET occultation observations. J Atmos Ocean Tech 17(4):495–503

Suh YC, Lim GH (2006) Effects of the 11-year solar cycle on the Earth atmosphere revealed in ECMWF reanalyses. Geophys Res Lett 33(L24705), doi:10.1029/2006GL028128

Tsuda T, Hocke K (2002) Vertical wave number spectrum of temperature fluctuations in the stratosphere using GPS occultation data. J Meteorol Soc Jpn 80(4B):925–938

Tsuda T, Nishida M, Rocken C, Ware RH (2000) A global morphology of gravity wave activity in the stratosphere revealed by the GPS occultation data (GPS/MET). J Geophys Res 105: 7257–7273

Tsuda T, Ratnam MV, May PT, Alexander MJ, Vincent RA, MacKinnon A (2004) Characteristics of gravity waves with short vertical wavelengths observed with radiosonde and GPS occultation during DAWEX (Darwin Area Wave Experiment). J Geophys Res 109(D20S03), doi:10.1029/2004JD004946

Wang L, Geller MA, Alexander MJ (2005) Spatial and temporal variations of gravity wave parameters. Part I: Intrinsic frequency, wavelength, and vertical propagation direction. J Atmos Sci 62:125–142

Wickert J, Pavelyev AG, Liou YA, Schmidt T, Reigber C, Igarashi K, Pavelyev AA, Matyugov S (2004) Amplitude variations in GPS signals as a possible indicator of ionospheric structures. Geophys Res Lett 31(L24801), doi:10.1029/2004GL020607

Wilson R, Chanin ML, Hauchecorne A (1991) Gravity waves in the middle atmosphere observed by Rayleigh lidar, 2. Climatology. J Geophys Res 96(D3):5169–5183

Part IV
GNSS Occultation for Climate Studies

Climatologies Based on Radio Occultation Data from CHAMP and Formosat-3/COSMIC

U. Foelsche, B. Pirscher, M. Borsche, A.K. Steiner, G. Kirchengast, and C. Rocken

Abstract Radio Occultation (RO) data using Global Navigation Satellite System (GNSS) signals have the potential to deliver climate benchmark measurements, since they can be traced, at least in principle, to the international standard for the second. The special climate utility of RO data arises from their accuracy and long-term stability due to self-calibration. The German research satellite CHAMP (CHAllenging Minisatellite Payload for geoscientific research) provided the first opportunity to create RO based climatologies over more than 6 years. Overlap with data from the Taiwan/US Formosat-3/COSMIC (Formosa Satellite Mission 3/Constellation Observing System for Meteorology, Ionosphere, and Climate, F3C) mission allows testing the consistency of climatologies derived from different satellites. We show results for altitude- and latitude-resolved seasonal zonal mean dry temperature climatologies. Our results indicate excellent agreement between RO climatologies from different F3C satellites: After subtraction of the estimated respective sampling errors, differences are smaller than 0.1 K almost everywhere in the considered domain between 8 km and 35 km altitude. Mean differences (over the same domain) are smaller than 0.03 K in any case and can be as small as 0.003 K. Differences between F3C and CHAMP are only slightly larger. The assimilation of RO data at ECMWF (European Centre for Medium-Range Weather Forecasts) considerably improved operational analyses in regions where the data coverage and/or the vertical resolution and accuracy of RO data is superior to traditional data sources.

1 Introduction

Any attempts to detect, understand, and attribute climate variability and change require accurate, consistent, long-term data. Our knowledge about changes in the free atmosphere is still limited (GCOS 2004), despite notable efforts to build

---

U. Foelsche (✉)
COSMIC Project Office, University Corporation for Atmospheric Research (UCAR), Boulder, CO, USA; Wegener Center for Climate and Global Change (WegCenter) and Institute for Geophysics, Astrophysics, and Meteorology (IGAM), University of Graz, Austria
e-mail: ulrich.foelsche@uni-graz.at

A. Steiner et al. (eds.), *New Horizons in Occultation Research*,
DOI 10.1007/978-3-642-00321-9_15, © Springer-Verlag Berlin Heidelberg 2009

long-term upper air temperature records. This has been done using data from radiosondes (e.g., Sherwood et al. 2005; Thorne et al. 2005) and from MSU (Microwave Sounding Unit) as well as AMSU (Advanced MSU) instruments on board of polar orbiting satellites (e.g., Christy and Spencer 2005; Mears and Wentz 2005; Vinnikov et al. 2006). After intense discussions over many years, temperature trend estimates based on these data sets now seem to be consistent with surface warming estimates and results from climate models but discrepancies still remain (Karl et al. 2006). Independent high-quality upper air records are therefore desirable.

A promising data source for climate monitoring, which can overcome some of the problems of established ones, is the Global Navigation Satellite System (GNSS) Radio Occultation (RO) technique. It has the potential to deliver climate benchmark measurements, since they can be traced, at least in principle, to the international standard for the second (Leroy et al. 2006a, b). The RO technique has been developed in the 1960s for the study of planetary atmospheres and ionospheres (see Yunck et al. 2000 for a review). Accurate sensing of the Earth's atmosphere became feasible with the precise signals of the GPS (Global Positioning System) satellites, successfully demonstrated with the GPS Meteorology (GPS/MET) experiment. Data from several measurement campaigns (April 1995–March 1997) proved most of the expected strengths of the technique, like high vertical resolution, high accuracy of retrieved parameters, and insensitivity to clouds (Kursinski et al. 1997; Rocken et al. 1997; Steiner et al. 1999). For detailed descriptions of the GNSS RO method see, e.g., Ware et al. (1996), Kursinski et al. (1997), Steiner et al. (2001), and Hajj et al. (2002). For the general utility of occultation methods for probing atmosphere and climate see Kirchengast (2004) and Foelsche et al. (2006a).

The German research satellite CHAMP (CHAllenging Minisatellite Payload for geoscientific research) was launched in July 2000 into low Earth orbit (LEO) and since September 2001 it continuously records RO profiles (Wickert et al. 2001, 2004); the mission is expected to last until 2009. CHAMP RO data, now covering more than 6 years, provide the first opportunity to create RO based multi-year climatologies. The number of RO profiles is sufficient to build seasonal (and monthly mean) zonal mean climatologies (Foelsche et al. 2008a).

In April 2006, Formosat-3/COSMIC (Formosa Satellite Mission 3/Constellation Observing System for Meteorology, Ionosphere, and Climate, F3C), a Taiwan/US RO mission consisting of six receiving satellites (Anthes et al. 2000; Rocken et al. 2000; Wu et al. 2005; Schreiner et al. 2007; Anthes et al. 2008) was successfully launched. All six F3C satellites have been launched into the same parking orbit with $\sim$515 km orbit altitude. The satellites have then been sequentially raised to their final orbit altitudes of $\sim$800 km. At this altitude the precession due to the oblateness of the Earth is smaller than in the parking orbit, leading to a (desired) deployment of the orbit planes to a final separation of 30°. The final orbit constellation (with optimal distribution of RO events in space and local time) has nearly been reached by early 2008. Early results on F3C climatologies have been presented by Foelsche et al. (2009). Here we continue the work of Foelsche et al. (2008a and 2009) and address the accuracy of RO climatologies by comparing also to more recent ECMWF-based climatologies and via cross-validation of RO climatologies.

Section 2 shall give the context to previous work. Data and methods are explained in Sect. 3. The comparison results are presented and discussed in Sect. 4, followed by concluding remarks.

2 Context

The special climate monitoring utility of RO data arises from the fact that atmospheric profiles are not derived from absolute values (phase delays) but from Doppler shift (phase change) profiles. Therefore, RO measurements require no external calibration and only short-term measurement stability over the occultation event duration (1–2 min), which is provided by very stable oscillators onboard the GNSS satellites. Potential residual GNSS clock errors and clock errors on the receiving satellites can be corrected by relating the measurements to even more stable oscillators on the ground (Hajj et al. 2002). Given this "self-calibration", data from different sensors and different occultation missions can be combined without need for inter-calibration and overlap, provided that the same data processing scheme is used (von Engeln 2006) and spatio-temporal sampling (Foelsche et al. 2008a; Pirscher et al. 2007) is well understood.

The active use of L-band signals with wavelengths of 19.0 cm and 24.4 cm (in case of GPS), allows for measurements during day and night and for the penetration of clouds. RO data have their highest quality at altitudes between $\sim$8 km and $\sim$35 km and are thus well suited to build climatologies of the upper troposphere and lower stratosphere (UTLS, which we understand as the altitude range between 5 km and 35 km). In the lower troposphere the error budget is dominated by horizontal variations of the refractivity and consequent deviations from the spherical symmetry assumption (e.g., Healy 2001a), the data can be affected by processes like signal multi-path and super-refraction (e.g., Sokolovskiy 2003; Beyerle et al. 2006), and the temperature (and water vapor) retrieval requires background information. Above $\sim$35 km error sources like residual ionospheric effects become important, given the exponential decrease of refractivity with height and therefore a comparatively weak atmospheric signal (e.g., Kursinski et al. 1997). The horizontal resolution is low (200–300 km, Kursinski et al. 1997) compared to (A)MSU or radiosonde data, but especially for climate applications, where data are averaged anyway, the inherent horizontal averaging of RO data is also an advantage.

The climate monitoring potential of RO data has been demonstrated with the aid of simulation studies (e.g., Yuan et al. 1993; Steiner et al. 2001; Foelsche et al. 2003, 2008b; Leroy et al. 2006a, 2006b; Ringer and Healy 2008). RO records have been successfully validated against (A)MSU data (Schrøder et al. 2003; Steiner et al. 2007, 2009; Ho et al. 2007, 2009) as well as data from MIPAS (Michelson Interferometer for Passive Atmospheric Sounding) and GOMOS (Global Ozone Monitoring for Occultation of Stars) on Envisat (Gobiet et al. 2007). They have been validated against climatological analyses (Gobiet et al. 2005, 2007; Foelsche et al. 2006b, 2008a) and RO data from different satellites (Hajj et al. 2004; Schreiner et al. 2007; Ho et al. 2009; Foelsche et al. 2009). The utility of RO data for monitoring tropopause parameters has been shown by Schmidt et al. (2005, 2006), Borsche et al. (2007), and Foelsche et al. (2009) while von Engeln et al. (2005) and Sokolovskiy et al. (2006) have investigated monitoring of the atmospheric boundary layer with RO data.

3 Data and Method

We developed a retrieval scheme at the Wegener Center (Occultation Processing System version 5.2), which is focused on minimizing potential biases and on using background information (which is needed for high altitude initialization) in a transparent way (Gobiet and Kirchengast 2004; Borsche et al. 2006; Gobiet et al. 2007; Foelsche et al. 2008a, 2009). The profile retrieval starts with phase and orbit data from GFZ (GeoForschungsZentrum) Potsdam (CHAMP, level 2 data set) and UCAR (Formosat-3/COSMIC, version 2007.1200). For the setup of RO climatologies we used the approach explained by Foelsche et al. (2008a) and (2009); the RO climatologies are obtained by "binning and averaging". All RO profiles in a prescribed geographic domain ("bin") are sampled and averaged (weighted by the cosine of the latitude), using a common (mean-sea-level, MSL) altitude grid with regular 200 m spacing of altitude levels. The cosine-weighting accounts for area changes between meridians at varying latitudes. We use "fundamental" bins with $5^\circ \times 60^\circ$ width in latitude and longitude to build monthly mean climatologies. From the 6 fundamental bins in each 5° latitude band we derive 5° zonal means by weighting with the respective number of occultation events. The basic latitudinal resolution (used for the results shown here) finally is 10°, i.e., each of the 18 latitude bands (pole–pole) contains two 5° bands, and the mean profiles for these two bands are averaged, weighted with the surface area of the respective bins. Compared to direct averaging, this particular spatial averaging approach slightly reduces the effect of uneven sampling within the latitude bands. Seasonal climatologies are obtained by averaging over three monthly climatologies.

For comparison we use analysis data from the European Centre for Medium-Range Weather Forecasts (ECMWF), since they have widely recognized quality, adequate spatial and temporal resolution and contain a vast amount of observations, assimilated in a statistically optimal way. ECMWF operationally produces daily analyses for four time layers, 00, 06, 12, and 18 UTC (coordinated universal time), by dynamically combining a short-range forecast with observational data via four-dimensional variational data assimilation (ECMWF 2004). On February 1, 2006, a major resolution upgrade has been implemented at ECMWF with a vertical resolution increase from 60 to 91 levels and a raise of the model top from 0.1–0.01 hPa. The horizontal resolution has been increased from T511 (spectral representation with triangular truncation at wave number 511) to T799 (Untch 2006), allowing more atmospheric variability to be represented. On December 12, 2006 ECMWF started operationally assimilating RO profiles (Healy 2007).

Here we focus on the northern summer season (June-July-August) that shows the most interesting differences to reference fields. The summer season (JJA) 2006 provides furthermore an unplanned test of the robustness of single-satellite seasonal climatologies. Due to technical problems, there is a period of about five weeks (from July 3 to August 8) where no data from CHAMP are available. Fortunately, RO data from the satellite GRACE (Gravity Recovery and Climate Experiment), which has essentially the same receiver and associated error characteristics as CHAMP (Wickert et al. 2005), are available for this time period. We thus decided to fill the "gap" in the CHAMP record with GRACE data (based on GFZ input data). Figure 1 shows the distribution of ~11 700 CHAMP RO events during summer 2005 (a), the related RO dry temperature climatology (b), the estimated sampling error (c), and the ECMWF-based reference climatology (d). A selective sampling effect from different penetration depths of RO events leads to the chosen tropospheric cut-off heights for CHAMP climatologies (Foelsche et al. 2008a).

When generating RO climatologies, in addition to the observational error we have to consider the sampling error due to incomplete sampling of the full spatial and temporal variability. The sampling error can be quantitatively estimated when an adequate representation of the "true" spatio-temporal evolution of the atmosphere is available and the times and locations of RO events are known. As a proxy for this

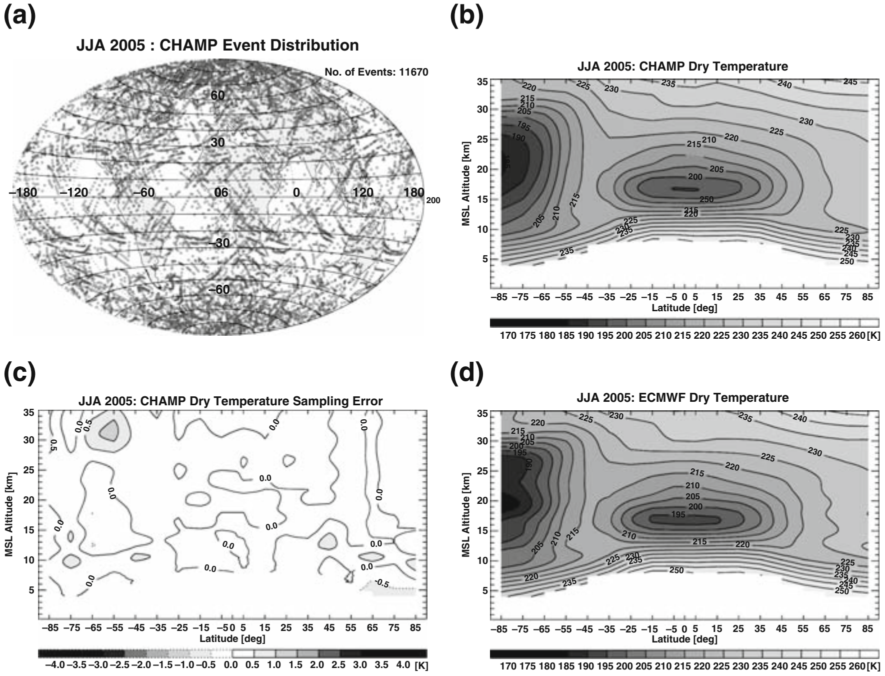

Fig. 1 Distribution of ~11 700 CHAMP RO events during the summer season (Jun-Jul-Aug) 2005 in zonal 10° bands (**a**), zonal mean dry temperature climatology resulting from these RO profiles (**b**), estimated sampling error of the CHAMP climatology (based on ECMWF fields) (**c**), and reference climatology based on ECMWF analysis fields (**d**)

atmospheric evolution we use ECMWF analyses, whose four time layers per day are sufficient to sample the diurnal cycle up to the second harmonic (the semidiurnal cycle). We estimate the sampling error by comparing climatologies derived from vertical ECMWF profiles at the RO times and locations with climatologies derived from the complete 4D ECMWF field (see Foelsche et al. 2008a, for further details).

4 Results and Discussion

The absolute accuracy of latitude-resolved RO climatologies is hard to determine to a level < 0.5 K, since all available validation data have their limitations as well (e.g., Gobiet et al. 2007). In this section we want to further test RO data, and raise confidence in their climate utility, by comparing with ECMWF-based climatologies and via cross-validation of RO climatologies from different satellites.

4.1 Comparison with ECMWF Analyses

The comparison between CHAMP and ECMWF is based on difference profiles. For each CHAMP RO profile we extracted a co-located vertical ECMWF profile from the nearest time layer of the analysis at the mean location of the (not exactly vertical) RO profile, using spatial interpolation. We define the mean location as the latitude and longitude of the point, where the straight-line connection between transmitting and receiving satellite during the occultation event touches the Earth's ellipsoidal surface (corresponding to the tangent point location of real RO profiles at about 12–15 km altitude). We note that ECMWF profiles have been used for the high-altitude initialization of the RO profiles via statistical optimization (Healy 2001b; Gobiet et al. 2007); results above $\sim$30 km are therefore not completely independent from ECMWF data.

Figure 2 shows systematic differences between ECMWF and RO climatologies (taking RO as reference). JJA 2005 (a) is also representative for all previous summer seasons (see Fig. 3 in Foelsche et al. 2008a). The wave-like bias structure in the southern winter polar vortex (Gobiet et al. 2005) is caused by deficiencies in the representation of the Austral polar vortex in the ECMWF analyses (see Fig. 1d). This feature appears also during JJA 2002–2004.

Above 30 km ECMWF is almost consistently colder than CHAMP by up to 2 K (more pronounced in fall, winter, and spring seasons). The persistent difference at the tropical tropopause (ECMWF being consistently colder than CHAMP), which is typical for all seasons until February 2006, is caused by a weak representation of tropopause height variability in ECMWF fields (Borsche et al. 2007). With the major resolution increase at ECMWF in February 2006 (see Sect. 3) this feature almost entirely disappeared, as can be seen in JJA 2006 (b). Interestingly, the wave-like bias structure appeared now in the Arctic. The assimilation of RO data at ECMWF (from Dec 12, 2006 onwards) had an amazingly large impact on mean ECMWF

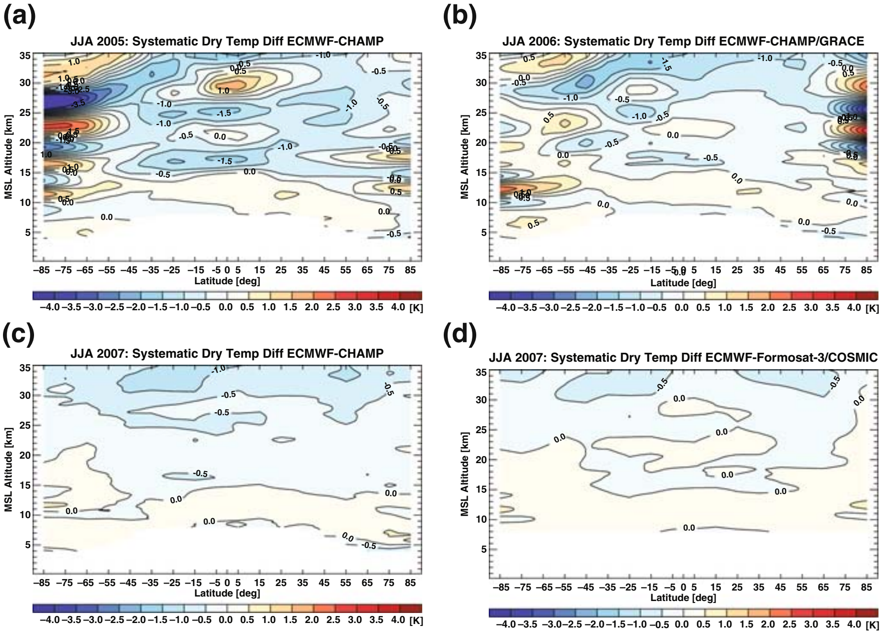

Fig. 2 Systematic differences between RO dry temperature climatologies and ECMWF analyses for northern summer seasons June-July-August (JJA): 2005 (**a**) and 2006 (**b**) based on CHAMP and CHAMP + GRACE data, respectively; JJA 2007 based on CHAMP data (**c**) and JJA 2007 based on F3C data (**d**)

analysis fields and obviously corrected these bias problems (see also Healy 2007): In JJA 2007 (c), systematic differences exceeding 1 K are entirely confined to altitudes above 30 km; the wave-like bias structures known from all previous summer seasons have disappeared. F3C results for JJA 2007 (d) are very similar to CHAMP results, with even smaller differences above 30 km (so far, we used only closed-loop F3C data above 8 km). After the assimilation of RO data, ECMWF analyses are certainly not an independent validation data source anymore. Nevertheless, the continuous convergence between RO and ECMWF with improvements at ECMWF and the assimilation of RO data suggests that the differences known from previous seasons had largely been attributable to the ECMWF rather than the RO data.

In the near future we will investigate the agreement between RO climatologies and global analyses from NCEP (National Centers for Environmental Prediction).

As noted above (Sect. 3), there is a period of ∼5 weeks of missing CHAMP data from July 3 to August 8, 2006. The JJA 2006 CHAMP climatology was thus supplemented with data from GRACE. Figure 3 (top) shows the dry temperature sampling error during JJA 2006 for CHAMP + GRACE (left) and for CHAMP alone (right). The latter is considerably larger, especially the southern polar vortex is clearly too warm, since essentially all data from the cold July (in southern winter) are missing. Nevertheless, the results show that seasonal mean, zonal mean single-satellite

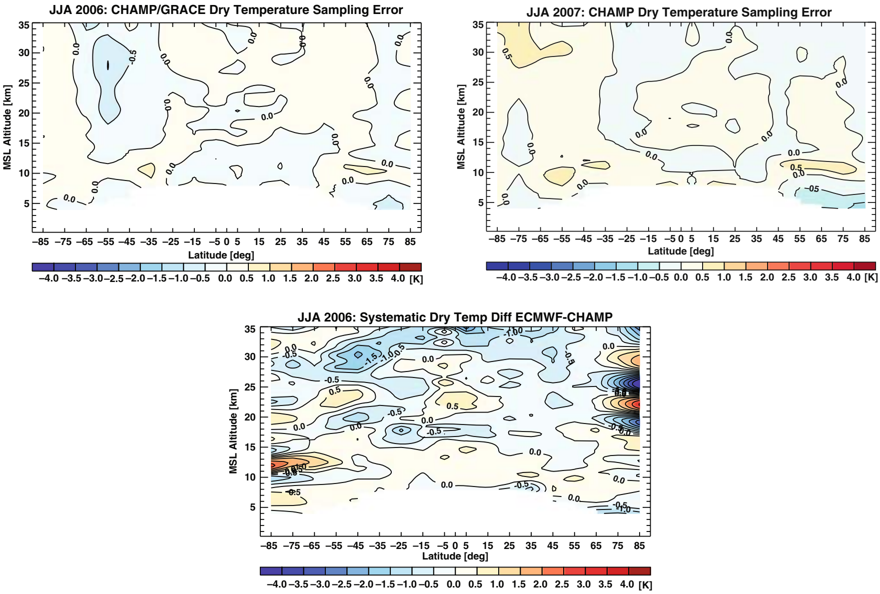

JJA 2006: CHAMP/GRACE Dry Temperature Sampling Error

JJA 2007: CHAMP Dry Temperature Sampling Error

JJA 2006: Systematic Dry Temp Diff ECMWF-CHAMP

Fig. 3 *Top*: Dry temperature sampling error for JJA 2006 using CHAMP + GRACE data (*left*) and CHAMP data alone (*right*, with a data gap of ~5 weeks). *Bottom*: Systematic dry temperature difference between ECMWF and CHAMP for JJA 2006

climatologies are surprisingly robust, even when several weeks of data are missing. The systematic difference for June and August between ECMWF and CHAMP alone (bottom) displays essentially the same large scale features as Fig. 2b; only at small scales there is more variability. It seems therefore justified to combine data from CHAMP and GRACE to a single record.

4.2 Consistency of Data from Different Satellites

Previous studies addressed the consistency of data from different RO satellites by selecting RO profiles in close spatial and temporal vicinity (Hajj et al. 2004; Schreiner et al. 2007; Ho et al. 2009). Data from CHAMP and SAC-C (Satélite de Aplicaciones Científicas-C), e.g., showed a remarkable consistency of 0.1 K in the mean between 5 km and 15 km (Hajj et al. 2004).

In Foelsche et al. (2009) we adopted a different approach and looked at systematic differences between zonal mean climatologies from different satellites for the season SON (Sep-Oct-Nov) 2006. This is a very rigorous test of the consistency, since these differences contain the sampling errors of both climatologies (F3C satellites in final constellation never simultaneously sample the same region of the atmosphere). Nevertheless, the results were very encouraging with larger differences confined to the polar bins, where the sampling was still sparse in the early phase of the F3C mission (with comparatively low orbit altitudes).

In a next step we looked at “double-differences”, where we subtracted the estimated sampling error field from each climatology. We found that seasonal temperature climatologies derived from different F3C satellites agree to within < 0.1 K almost everywhere in the considered domain between 8 km and 35 km altitude. Here we test if these results still hold for JJA 2007 (with F3C satellites in significantly more separated orbits). Figure 4 shows the systematic differences between climatologies derived from Flight Model 2 (FM2) and each of the other F3C satellites. The estimated sampling errors are again subtracted. We note that these double differences contain also the errors in the estimation of the sampling errors for both climatologies.

The systematic differences are again amazingly small (note the 0.1 K contour lines). Differences exceeding 0.1 K are confined to small parts of the domain; most

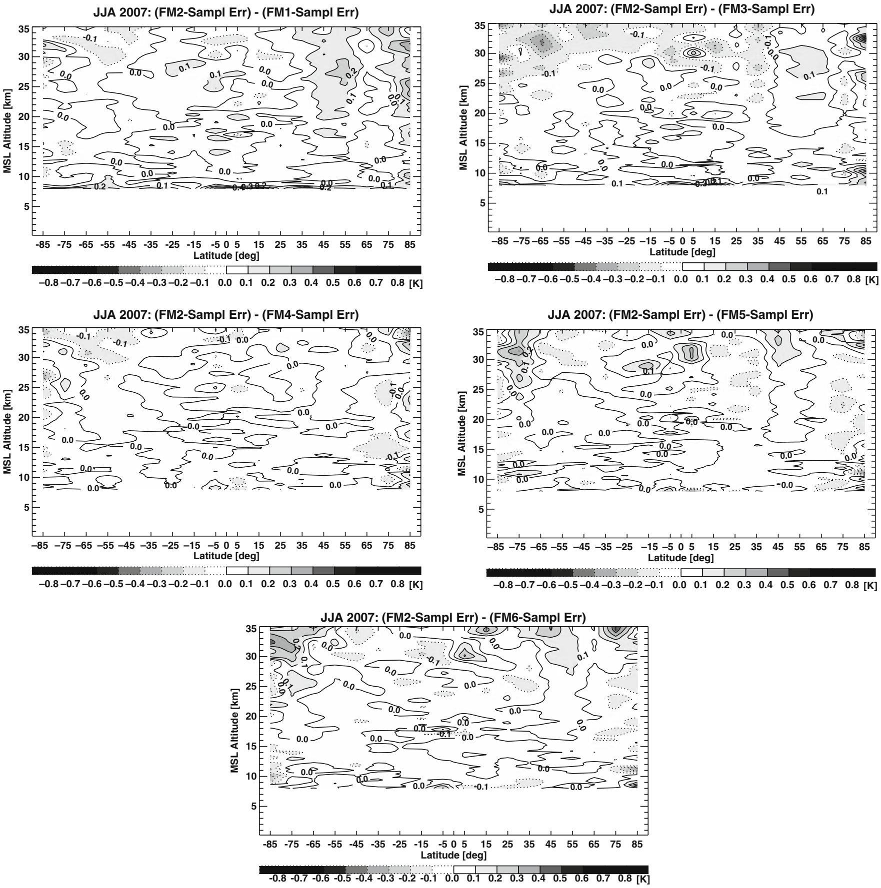

JJA 2007: (FM2-Sampl Err) - (FM1-Sampl Err)

JJA 2007: (FM2-Sampl Err) - (FM3-Sampl Err)

JJA 2007: (FM2-Sampl Err) - (FM4-Sampl Err)

JJA 2007: (FM2-Sampl Err) - (FM5-Sampl Err)

JJA 2007: (FM2-Sampl Err) - (FM6-Sampl Err)

Fig. 4 Systematic differences between JJA 2007 zonal mean, seasonal mean dry temperature climatologies from Formosat-3/COSMIC FM2 and each of the other F3C satellites, with the estimated sampling errors subtracted of them appear above 30 km altitude. Mean differences over the entire domain between 8 km and 35 km altitude are smaller than 0.03 K in any case. The values are: +0.028 K, –0.020 K, –0.014 K, –0.010 K, and –0.003 K, respectively. We note that this consistency is not a proof of absolute accuracy, since there is a possibility of common systematic errors. Nevertheless, we regard the results as very encouraging. These very good agreements show furthermore that the estimation of the sampling error is quite accurate. F3C sampling errors in the polar bins in JJA 2007 (not shown) are considerably smaller than in SON 2006 (see Foelsche et al. 2009) since the higher orbits allow for a better coverage of latitudes beyond 85°.

For SON 2006 we had found a small but systematic difference between CHAMP and F3C (Foelsche et al. 2009). In JJA 2007 (Fig. 5) the situation is very similar. The mean values over the entire domain between 8 km and 35 km altitude are –0.28 K and –0.23 K, respectively, with the largest values above 30 km.

The differences are slightly larger than those found by Ho et al. (2009) for co-located profiles. In the Ho et al. (2009) study, however, phase and orbit data for F3C and CHAMP have both been computed at UCAR, while our present study uses CHAMP phase and orbit data from GFZ, but F3C phase and orbit data from UCAR. We had therefore the suspicion that there might already be differences at phase and orbit data level. Since UCAR computes also CHAMP phase and orbit data we could test this by comparing CHAMP climatologies derived from UCAR and GFZ. The differences are very similar to those in Fig. 5, with a mean systematic difference of –0.29 K for JJA2007 (Fig. 6, left). Differences between F3C and CHAMP/UCAR are therefore much smaller (Fig. 6, right), with a mean value of +0.06 K over the entire domain. Largest (positive) differences are at higher altitudes. This seems reasonable if we assume that ECMWF is indeed somewhat too cold in the stratosphere: The F3C climatologies (which are less influenced by the background) should therefore be slightly warmer than CHAMP (which is closer to the background, since CHAMP data are noisier). The reasons for the small but systematic UCAR-GFZ differences are currently under investigation. Preliminary results indicate that they are stationary to a high degree and that they appear already at bending angle level

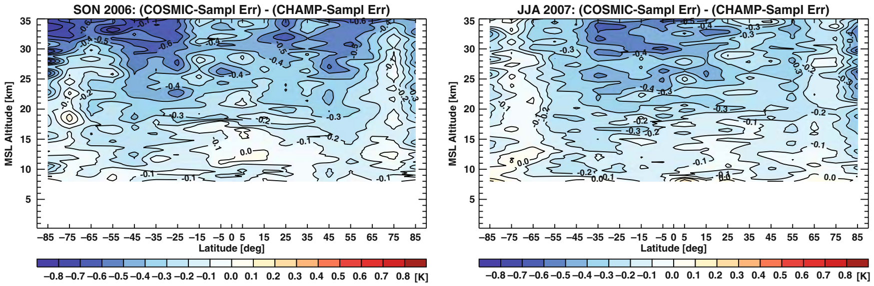

Fig. 5 Systematic differences between zonal mean, seasonal mean dry temperature climatologies from Formosat-3/COSMIC and CHAMP with the estimated sampling errors subtracted: SON 2006 (*left*) and JJA 2007 (*right*)

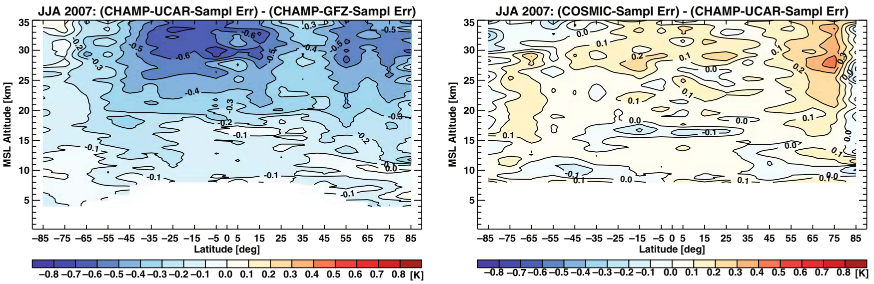

Fig. 6 *Left*: Systematic difference between JJA 2007 zonal mean, seasonal mean dry temperature climatologies from CHAMP based on UCAR and GFZ phase and orbit data, respectively. *Right*: Like the right panel of Fig. 5 but using UCAR phase and orbit data as basis for both Formosat-3/COSMIC and CHAMP climatologies. The estimated sampling errors are again subtracted

(GFZ bending angles being systematically larger than UCAR). Clearly these results highlight the importance of consistent data processing when attempting to build climate records from RO data.

5 Concluding Remarks

It was shown that accurate zonal mean, seasonal mean climatologies between ∼8 km and 30 km altitude can be obtained based on Radio Occultation (RO) profiles. The assimilation of RO data at ECMWF (European Centre for Medium-Range Weather Forecasts) considerably improved operational analyses in regions where the data coverage and/or the vertical resolution and accuracy of RO data is superior to traditional data sources (e.g., in polar regions and at altitudes up to ∼35 km). We analyzed the consistency of seasonal climatologies derived from different satellites. Climatologies from CHAMP and Formosat-3/COSMIC (F3C) agree very well if phase and orbit data from the same processing center are used. Climatologies from different F3C satellites show excellent agreement: After subtraction of the estimated respective sampling errors, altitude- and latitude-resolved seasonal dry temperature climatologies derived from F3C satellites in entirely different orbits agree to within < 0.1 K almost everywhere in the domain between 8 km and 35 km altitude. Mean differences (over the same domain) are smaller than 0.03 K in any case and can be as small as 0.003 K.

Acknowledgements The authors acknowledge GFZ (Potsdam, Germany) for the provision of CHAMP and GRACE RO data, in particular to J. Wickert and T. Schmidt for continuous support. ECMWF (Reading, UK) kindly provided access to their global operational analysis data. UCAR/CDAAC (Boulder, CO, USA) is acknowledged for the provision of Formosat-3/COSMIC and CHAMP data. The work was carried out with financial support from the Austrian Science Fund (FWF) under research grant P18837 (CLIMROCC). AKS was funded from FWF under research grant P18733 (INDICATE). UF received financial support from the Max Kade Foundation (New York, NY, USA) and from UCAR.

References

Anthes RA, Rocken C, Kuo YH (2000) Applications of COSMIC to meteorology and climate. Terr Atmos Oceanic Sci 11(1):115–156

Anthes RA, et al. (2008) The COSMIC/FORMOSAT-3 Mission: Early results. Bull Am Meteorol Soc 89:313–333, doi:10.1175/BAMS-89-3-313

Beyerle G, Heise S, Kaschenz J, König-Langlo G, Reigber C, Schmidt T, Wickert J (2006) Refractivity Biases in GNSS Occultation Data. In: Foelsche et al. 2006a, pp 37–43, doi:10.1007/3-540-34121-8_4

Borsche M, Gobiet A, Steiner AK, Foelsche U, Kirchengast G, Schmidt T, Wickert J (2006) Pre-Operational Retrieval of Radio Occultation Based Climatologies. In: Foelsche et al. 2006a, pp 315–323, doi:10.1007/3-540-34121-8_26

Borsche M, Kirchengast G, Foelsche U (2007) Tropical tropopause climatology as observed with radio occultation measurements from CHAMP compared to ECMWF and NCEP analyses. Geophys Res Lett 34(L03702), doi:10.1029/2006GL027918

Christy JR, Spencer RW (2005) Correcting temperature data sets. Science 310(5750):972–973

von Engeln A (2006) A first test of climate monitoring with radio occultation instruments: Comparing two processing centers. Geophys Res Lett 33(L22705), doi:10.1029/2006GL027767

von Engeln A, Teixeira J, Wickert J, Buehler SA (2005) Using CHAMP radio occultation data to determine the top altitude of the planetary boundary layer. Geophys Res Lett 32(L06815), doi:10.1029/2004GL022168

European Centre for Medium-Range Weather Forecasts (ECMWF) (2004) IFS Documentation CY28rl, Reading, UK

Foelsche U, Kirchengast G, Steiner AK (2003) Global climate monitoring based on CHAMP/GPS radio occultation data. In: First CHAMP Mission Results for Gravity, Magn. and Atm. Studies. Reigber C et al. (eds), Springer, Berlin Heidelberg, pp 397–407

Foelsche U, Kirchengast G, Steiner AK (eds) (2006a) Atmosphere and Climate: Studies by Occultation Methods, Springer, Berlin Heidelberg, 336 pp, doi:10.1007/3-540-34121-8

Foelsche U, Gobiet A, Steiner AK, Borsche M, Wickert J, Schmidt T, Kirchengast G (2006b) Global Climatologies Based on Radio Occultation Data: The CHAMPCLIM Project. In: Foelsche et al. 2006a, pp 303–314, doi:10.1007/3-540-34121-8_25

Foelsche U, Borsche M, Steiner AK, Gobiet G, Pirscher B, Kirchengast G, Wickert J, Schmidt T (2008a) Observing upper troposphere-lower stratosphere climate with radio occultation data from the CHAMP satellite. Clim Dyn 31:49–65, doi:10.1007/s00382-007-0337-7

Foelsche U, Kirchengast G, Steiner AK, Kornblueh L, Manzini E, Bengtsson L (2008b) An observing system simulation experiment for climate monitoring with GNSS radio occultation data: Setup and test bed study. J Geophys Res 113(D11108), doi:10.1029/2007JD009231

Foelsche U, Pirscher B, Borsche M, Kirchengast G, Wickert J (2009) Assessing the climate monitoring utility of radio occultation data: From CHAMP to FORMOSAT-3/COSMIC. Terr Atmos Oceanic Sci 20(1):155–170, doi:10.3319/TAO.2008.01.14.01(F3C)

GCOS (2004) Global Climate Observing System Implementation Plan for the Global Observing System for Climate in Support of UNFCCC. WMO-TD 1219, WMO, Geneva, 136 pp

Gobiet A, Kirchengast G (2004) Advancements of GNSS radio occultation retrieval in the upper stratosphere for optimal climate monitoring utility. J Geophys Res 109(D24110), doi:10.1029/2004JD005117

Gobiet A, Foelsche U, Steiner AK, Borsche M, Kirchengast G, Wickert J (2005) Climatological validation of stratospheric temperatures in ECMWF operational analyses with CHAMP radio occultation data. Geophys Res Lett 32(L12806), doi:10.1029/2005GL022617

Gobiet A, Kirchengast G, Manney GL, Borsche M, Retscher C, Stiller G (2007) Retrieval of temperature profiles from CHAMP for climate monitoring: Intercomparison with Envisat MIPAS and GOMOS and different analyses. Atmos Chem Phys 7:3519–3536

Hajj GA, Kursinski ER, Romans LJ, Bertiger WI, Leroy SS (2002) A technical description of atmospheric sounding by GPS occultation. J Atmos Solar-Terr Phys 64:451–469

Hajj GA, Ao CO, Iijima PA, Kuang D, Kursinski ER, Mannucci AJ, Meehan TK, Romans LJ, de la Torre Juarez M, Yunck TP (2004) CHAMP and SAC-C atmospheric occultation results and intercomparisons. J Geophys Res 109(D06109), doi:10.1029/2003JD003909

Healy SB (2001a) Radio occultation bending angle and impact parameter errors caused by horizontal refractive index gradients in the troposphere: A simulation study. J Geophys Res 106(D11):11875–11889

Healy SB (2001b) Smoothing radio occultation bending angles above 40 km. Ann Geophys 19:459–468

Healy SB (2007) Operational assimilation of GPS radio occultation measurements at ECMWF. ECMWF Newsl 111:6–11

Ho SP, Kuo YH, Zeng Z, Peterson TC (2007) A comparison of lower stratosphere temperature from microwave measurements with CHAMP GPS RO data. Geophys Res Lett 34(L15701), doi:10.1029/2007GL030202

Ho SP, Goldberg M, Kuo YH, Zou CZ, Schreiner W (2009) Calibration of temperature in the lower stratosphere from microwave measurements using COSMIC radio occultation data: Preliminary results. Terr Atmos Oceanic Sci 20(1), doi:10.3319/TAO.2007.12.06.01(F3C)

Karl TR, Hassol SJ, Miller CD, Murray WL (eds) (2006) Temperature trends in the lower atmosphere: Steps for understanding and reconciling differences. Rep by the Climate Change Science Program and the Subcommittee on Global Change Research, Washington DC

Kirchengast G (2004) Occultations for probing atmosphere and climate: Setting the scene. In: Occultations for Probing Atmosphere and Climate, Kirchengast G, Foelsche U, Steiner AK (eds), Springer, Berlin Heidelberg, pp 1–8

Kursinski ER, Hajj GA, Schofield JT, Linfield RP, Hardy KR (1997) Observing Earth's atmosphere with radio occultation measurements using the global positioning system. J Geophys Res 102:23429–23465

Leroy SS, Dykema JA, Anderson JG (2006a) Climate Benchmarking Using GNSS Occultation. In: Foelsche et al. 2006a, pp 287–301, doi:10.1007/3-540-34121-8_24

Leroy SS, Anderson JG, Dykema JA (2006b) Testing climate models using GPS radio occultation: A sensitivity analysis. J Geophys Res 111(D17105), doi:10.1029/2005JD006145

Mears CA, Wentz FJ (2005) The effect of diurnal correction on satellite-derived lower tropospheric temperature. Science 309:1548–1551, doi:10.1126/science.1114772

Pirscher B, Foelsche U, Lackner BC, Kirchengast G (2007) Local time influence in single-satellite radio occultation climatologies from Sun-synchronous and non-Sun-synchronous satellites. J Geophys Res 112(D11119), doi:10.1029/2006JD007934

Ringer MA, Healy SB (2008) Monitoring twenty-first century climate using GPS radio occultation bending angles. Geophys Res Lett 35(L05708), doi:10.1029/2007GL032462

Rocken C, Anthes R, Exner M, Hunt D, Sokolovskiy S, Ware R, Gorbunov M, Schreiner W, Feng D, Herman B, Kuo YH, Zou X (1997) Analysis and validation of GPS/MET data in the neutral atmosphere. J Geophys Res 102(D25):29849–29866

Rocken C, Kuo YH, Schreiner WS, Hunt D, Sokolovskiy S, McCormick C (2000) COSMIC system description. Terr Atmo Oceanic Sci 11(1):21–52

Schmidt T, Heise S, Wickert J, Beyerle G, Reigber C (2005) GPS radio occultation with CHAMP and SAC-C: global monitoring of thermal tropopause parameters. Atmos Chem Phys 5:1473–1488

Schmidt T, Beyerle G, Heise S, Wickert J, Rothacher M (2006) A climatology of multiple tropopauses derived from GPS radio occultations with CHAMP and SAC-C. Geophys Res Lett 33(L04808), doi:10.1029/2005GL024600

Schreiner W, Rocken C, Sokolovskiy S, Syndergaard S, Hunt D (2007) Estimates of the precision of GPS radio occultations from the COSMIC/FORMOSAT-3 mission. Geophys Res Lett 34(L04808), doi:10.1029/2006GL027557

Schrøder T, Leroy S, Stendel M, Kaas E (2003) Validating the microwave sounding unit stratospheric record using GPS occultation. Geophys Res Lett 30(14):1734, doi:10.1029/2003GL017588

Sherwood SC, Lanzante JR, Meyer CL (2005) Radiosonde daytime biases and late-20th century warming. Science 309:1556–1559, doi:10.1126/science.1115640

Sokolovskiy SV (2003) Effect of superrefraction on inversions of radio occultation signals in the lower troposphere. Radio Sci 38(3):1058, doi:10.1029/2002RS002728

Sokolovskiy SV, Kuo YH, Rocken C, Schreiner WS, Hunt D, Anthes RA (2006) Monitoring the atmospheric boundary layer by GPS radio occultation signals recorded in the open-loop mode. Geophys Res Lett 33(12): L12813, doi:10.1029/2006GL025955

Steiner AK, Kirchengast G, Ladreiter HP (1999) Inversion, error analysis, and validation of GPS/MET occultation data. Ann Geophys 17:122–138

Steiner AK, Kirchengast G, Foelsche U, Kornblueh L, Manzini E, Bengtsson L (2001) GNSS occultation sounding for climate monitoring. Phys Chem Earth A 26(3):113–124

Steiner AK, Kirchengast G, Borsche M, Foelsche U, Schoengassner T (2007) A multi-year comparison of lower stratospheric temperatures from CHAMP radio occultation data with MSU/AMSU records. J Geophys Res 112(D22110), doi:10.1029/2006JD008283

Steiner AK, Kirchengast G, Borsche M, Foelsche U (2009) Lower stratospheric temperatures from CHAMP RO compared to MSU/AMSU records: An analysis of error sources. In: Steiner A, Pirscher B, Foelsche U, Kirchengast G (eds) New Horizons in Occultation Research, Springer-Verlag, Berlin Heidelberg, doi:10.1007/978-3-642-00321-9_18

Thorne PW, Parker DE, Tett SFB, Jones PD, McCarthy M, Coleman H, Brohan P (2005) Revisiting radiosonde upper air temperatures from 1958 to 2002. J Geophys Res 110(D18105), doi:10.1029/2004JD005753

Untch A, Miller M, Hortal M, Buizza R, Janssen P (2006) Towards a global meso-scale model: The high-resolution system T799L91 and T399L62 EPS. ECMWF Newsl 108:6–13

Vinnikov KY, Grody NC, Robock A, Stouffer RJ, Jones PD, Goldberg MD (2006) Temperature trends at the surface and in the troposphere. J Geophys Res 111(D03106), doi:10.1029/2005JD006392

Ware R, et al. (1996) GPS Sounding of the atmosphere from low earth orbit: Preliminary results. Bull Am Meteorol Soc 77:19–40

Wickert J, Reigber C, Beyerle G, König R, Marquardt C, Schmidt T, Grunwaldt L, Galas R, Meehan TK, Melbourne WG, Hocke K (2001) Atmosphere sounding by GPS radio occultation: First results from CHAMP. Geophs Res Lett 28(17):3263–3266

Wickert J, Schmidt T, Beyerle G, König R, Reigber C, Jakowski N (2004) The radio occultation experiment aboard CHAMP: Operational data analysis and validation of vertical atmospheric profiles. J Met Soc Japan 82:381–395

Wickert J, Beyerle G, König R, Heise S, Grunwaldt L, Michalak G, Reigber C, Schmidt T (2005) GPS radio occultation with CHAMP and GRACE: A first look at a new and promising satellite configuration for global atmospheric sounding. Ann Geophys 23(3):653–658

Wu BH, Chu V, Chen P, Ting T (2005) FORMOSAT-3/COSMIC science mission update. GPS Solut 9:111–121, doi:10.1007/s10291-005-0140-z

Yuan LL, Anthes RA, Ware RH, Rocken C, Bonner WD, Bevis MG, Businger S (1993) Sensing climate change using the global positioning system. J Geophys Res 98(D8):14925–14937

Yunck TP, Liu CH, Ware R (2000) A history of GPS sounding. Terrestr Atmos Ocean Sciences 11:1–20

Testing Climate Models Using Infrared Spectra and GNSS Radio Occultation

S.S. Leroy, J.A. Dykema, P.J. Gero, and J.G. Anderson

Abstract The Climate Absolute Radiance and Refractivity Observatory will be a climate benchmarking mission intended to include instruments for measuring Earth's atmospheric refractivity by GNSS radio occultation (RO), high spectral resolution thermal infrared spectra emitted from the Earth, and the spectrally resolved reflected shortwave spectrum. Climate benchmarking is necessary to establish a record that can be used to test climate models according to their predictive capability because other attempts at establishing trustworthy timeseries of satellite data have not been particularly successful. We have investigated how GNSS RO measurements and thermal infrared spectra can be used to test models' predictive capability. GNSS RO provides a constraint on the transient sensitivity of the climate system. Infrared radiance spectra can quantify the individual longwave feedbacks of the climate system, including cloud-longwave feedbacks when used in conjunction with GNSS RO. At present, studies are limited to clear sky infrared radiation, so the next research steps should include cloudy sky infrared simulations and reflected shortwave simulations.

1 Introduction

The Decadal Survey of the U.S. National Oceanic and Atmospheric Administration (NOAA) and the U.S. National Aeronautics and Space Administration (NASA) by the U.S. National Research Council (NRC) recommended that NASA deploy a Climate Absolute Radiance and Refractivity Observatory (CLARREO) as one of its four highest priorities. This recommendation came in response to a request from NASA and NOAA to suggest what satellite missions should be flown to form a national climate research program that is responsive to societal demands (National Research Council, Committee on Earth Science and Applications from Space 2007). Society demands data sets deemed trustworthy for trend detection and sufficiently

---

S.S. Leroy (✉)
Harvard School of Engineering and Applied Sciences, Harvard University, Cambridge, MA, USA
e-mail: leroy@huarp.harvard.edu

A. Steiner et al. (eds.), *New Horizons in Occultation Research*,
DOI 10.1007/978-3-642-00321-9_16,

accurate to test climate models according to their predictive capability, and for this reason the U.S. NRC recommended the CLARREO mission to NASA as a top priority. In short, society needs tools that usefully predict future climates depending on its own decisions regarding future economic development and energy production. Those tools are climate models and, pursuant to the scientific paradigm, must be tested empirically.

CLARREO calls for three instruments: a GNSS (global navigation satellite system) occultation instrument, an instrument to measure emitted infrared radiation with high spectral resolution, and an instrument to measure reflected shortwave radiation with high spectral resolution. In order to ensure their data are absolutely accurate, it is required that they are assured traceable to the international standards that define the units of their observables on-board with overall uncertainties sufficient to test climate models (Ohring 2007). It is also required that their sampling patterns be sufficiently dense and uniform so that mission accuracy requirements are met. The optimal configuration for monitoring the emitted infrared spectrum with three satellites has them in perfectly polar orbits (90° inclination) spaced 60° in longitude of ascending node (Kirk-Davidoff et al. 2005). Such a configuration affords robustness in that the bias in annual averages induced by the diurnal cycle would be minimal should one or two satellites fail. Should all three satellites be operational, bias in *seasonal* averages induced by the diurnal cycle would be minimized.

The data types called for by CLARREO were selected because their traceability to international standards is possible. The NRC Decadal Survey's recommendation should answer societal demands, which in this case pertain to testing climate models. In what ways the data types of CLARREO can be used to test climate models according to their predictive capability remains an open question. In testing climate models, the scientific assessments of the Intergovernmental Panel on Climate Change focus much of their efforts in comparing the overall sensitivities of climate models, which is the surface air temperature increase predicted by a climate model when subjected to a prescribed forcing by increased carbon dioxide. Certainly, the sensitivity of the climate system must be modeled correctly, but a trustworthy model must attain the correct sensitivity for the right physical reasons. There are many ways to explain the sensitivity of a climate model (and the actual climate system), and, for the sake of simplicity, we analyze the sensitivity in the language of radiative feedbacks.

2 Radiative Feedbacks

The climate's greenhouse effect comes about because of the presence of well-mixed gases that absorb efficiently in the thermal infrared while the same atmosphere is largely transparent at visible wavelengths where most of the solar forcing occurs. The shortwave radiative forcing occurs largely at the Earth's surface, and the surface cannot easily cool itself by radiating to space in the thermal infrared because of the greenhouse gases present. As a consequence, the surface has to warm more to maintain a radiative balance than it would have without the greenhouse gases present.

It is possible for some elements of the atmosphere to respond to surface temperature change in such a way that radiation from the troposphere is either enhanced or suppressed. When temperature increases and thermal infrared (longwave) radiation from the troposphere is partially suppressed, the action is considered a *positive* radiative feedback; when temperature increases and longwave radiation from the troposphere is enhanced, the action is considered a *negative* radiative feedback.

An injection of anthropogenic greenhouse gases, before anything else happens, has the immediate effect of blocking photons from escaping the troposphere. The amount of radiation flux blocked is called a radiative forcing $\varDelta F_{\mathrm{rad}}$. To first order, the surface responds by increasing its temperature by an amount $\varDelta T^{(1)}$, thus increasing the flux through the tropopause and restoring radiative balance. The statement is

$$\varDelta T^{(1)} = \frac{\varDelta F_{\mathrm{rad}}}{\varGamma} \tag{1}$$

in which $\varGamma \approx 4\varepsilon\sigma T^3$ is the gray-body radiation term for the surface, ε a combination of surface emissivity and the fraction of radiation from the surface that escapes to space, and σ the Stefan-Boltzman constant. The climate system responds dynamically and thermodynamically to such a surface temperature change, and some of those reactions act to enhance radiation to space and some to suppress it. A continuum of such feedbacks exists, a geometric series for surface temperature change results, and the final surface temperature change is

$$\varDelta T = \varDelta F_{\mathrm{rad}} \left(\varGamma - \sum_i \gamma_i^{\mathrm{LW}} - \sum_i \gamma_i^{\mathrm{SW}} \right)^{-1} \tag{2}$$

where the longwave feedback factors γ_i^{LW} and shortwave feedback factors γ_i^{SW} are defined by

$$\begin{aligned} \gamma_i^{\mathrm{LW}} &= \left(\frac{\partial F^{\mathrm{LW}}}{\partial x_i} \right) \frac{\mathrm{d}x_i}{\mathrm{d}T} \\ \gamma_i^{\mathrm{SW}} &= \left(\frac{\partial F^{\mathrm{SW}}}{\partial x_i} \right) \frac{\mathrm{d}x_i}{\mathrm{d}T} \end{aligned} \tag{3}$$

where F^{LW} is the net downward longwave flux at the tropopause, F^{SW} is the net downward shortwave flux at the tropopause, and x_i can be any one of a long list of meteorological, thermodynamic, or constituent properties that can affect longwave or shortwave radiation. A positive feedback has $\gamma > 0$, and a negative feedback has $\gamma < 0$. The largest feedbacks are thought to be the water vapor-longwave feedback, the cloud-shortwave feedback, the upper tropospheric temperature-longwave ("lapse rate") feedback, and the hypothesized aerosol indirect effects in the shortwave. The most uncertain feedbacks are thought to be the cloud-shortwave feedback and the aerosol indirect effect. This calculus of feedbacks has been presented elsewhere (Cess 1976; Wetherald and Manabe 1988) as have reviews about feedbacks implicit in climate models (Held and Soden 2000; Colman 2003; Bony et al. 2006; Soden and Held 2006).

3 Testing Feedbacks with CLARREO

If climate models accurately reproduce climate sensitivity, one way to ascertain whether they do so for the correct physical reasons is to divide climate response according to feedbacks. CLARREO should be capable of doing so because individual feedbacks have distinctive spectral signatures in the thermal infrared and visible wavelengths. GNSS occultation should play an important role because of its insensitivity to clouds: it might resolve the cloud-surface temperature ambiguity inherent to sounding in the thermal infrared. We apply optimal fingerprinting techniques to spectral infrared and microwave refractivity as produced offline by many sophisticated climate models. This should tell us the relative contribution of various data types to testing various climate feedbacks, what accuracy is needed for each data type, and how long we should expect to wait before a satisfactory test can be applied to climate models' predictions.

A feedback can be determined by trend analysis by dividing the trend in outgoing radiation due to a specific thermodynamical variable or constituent concentration by the trend in surface air temperature:

$$\gamma_i^{\mathrm{LW}} = \frac{\mathrm{d}F_i^{\mathrm{LW}}}{\mathrm{d}t} \left(\frac{\mathrm{d}T}{\mathrm{d}t} \right)^{-1} \tag{4}$$

with $\mathrm{d}F_i^{\mathrm{LW}}$ the change in downward radiation at the tropopause due to a change in thermodynamic variable or constituent concentration i. In order to estimate the feedback, one must be able to estimate $\mathrm{d}F_i^{\mathrm{LW}}/\mathrm{d}t$ observationally as well as $\mathrm{d}T/\mathrm{d}t$. Moreover, observations in the thermal infrared allow one to detect radiative forcing by anthropogenic greenhouse gases, ΔF_{rad}. [Presently, an exploration of the possibility of testing climate models has been done only for longwave radiation and not yet for shortwave radiation; hence, we restrict our discussion to the longwave.]

If a variable perturbs the tropopause radiation field, then it has an associated feedback, and because changes in variables lead to unique changes in the infrared spectrum at the tropopause, careful observation of the evolution of the tropopause radiation field should constrain the feedbacks of the climate system. In fact, in most cases individual feedbacks have unique fingerprints in the spectra of outgoing longwave and shortwave radiation. CLARREO, in measuring the outgoing longwave radiation, can uniquely discern the longwave feedbacks because each has a unique signature in the thermal infrared spectrum. How long a timeseries of CLARREO-like data is necessary before climate models' realizations of the climate feedbacks can be tested remains an open question.

In Fig. 1 we show the spectral infrared signatures of tropospheric temperature change, stratospheric temperature change, tropospheric water vapor increase, and

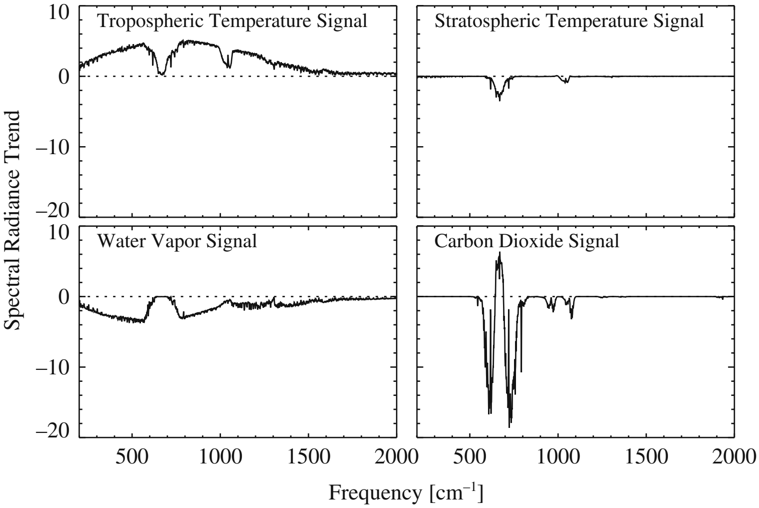

Fig. 1 Spectral infrared signals corresponding to calculus of feedbacks. The tropospheric temperature signal shows how the troposphere cools itself; the carbon dioxide signals shows the spectral fingerprint of radiative forcing by carbon dioxide; the water vapor signal shows the spectral fingerprint of the water vapor-longwave feedback. The units for the radiance trend for all plots in this figure are W cm^{-2} (cm^{-1})$^{-1}$ sr^{-1} decade^{-1}

carbon dioxide increase. Because water vapor inhibits outgoing longwave radiation with time, as can be seen by the sign of the integral of its signal over frequency in Fig. 1, it is associated with a positive longwave feedback. In clear skies, we seek to model the trend in the emitted infrared spectrum as a linear combination of these four signals while allowing for some uncertainty in the modeled shape of these signals. The quality of the posterior fit is determined by comparison of post-fit residuals to the natural variability in the emitted infrared spectrum on interannual time scales. The mathematical technique is just the same as that used in climate signal detection and attribution studies (Allen et al. 2006) with an allowance for signal shape uncertainty (Huntingford et al. 2006). The “model” for the linear trend in the emitted infrared spectrum $\mathrm{d}\mathbf{d}/\mathrm{d}t = \mathrm{d}F_\nu^{\mathrm{LW}}/\mathrm{d}t$ is

$$\frac{\mathrm{d}\mathbf{d}}{\mathrm{d}t} = \sum_i \left(\frac{\mathrm{d}\alpha_i}{\mathrm{d}t}\right) \mathbf{s}_i + \frac{\mathrm{d}}{\mathrm{d}t}\delta\mathbf{n} \tag{5}$$

where the $\mathbf{s}_i$ are the spectral shapes given in Fig. 1, the $\mathrm{d}\alpha_i/\mathrm{d}t$ are scalar estimators of the trends of outgoing longwave radiation associated with individual variables, and the $\delta\mathbf{n}$ are realizations of interannual variability in the tropics (30°S to 30°N) as they would appear in the annual average emitted infrared spectrum. The solution for the trend estimators $\mathrm{d}\alpha_i/\mathrm{d}t$ is given by

$$\frac{\mathrm{d}\alpha}{\mathrm{d}t} = \mathbf{F}^{\mathrm{T}} \frac{\mathrm{d}F_\nu^{\mathrm{LW}}}{\mathrm{d}t} \tag{6}$$

where the columns of the matrix $\mathbf{F}$ are the components of the contravariant basis to the fingerprint basis established by the $\mathbf{s}_i$. As a consequence, $\mathbf{F}^{\mathrm{T}}\mathbf{S} = \mathbf{I}$ where the columns of $\mathbf{S}$ are the $\mathbf{s}_i$, and so we call $\mathbf{F}$ the set of contravariant fingerprints. Consistent with Bayesian inference (Leroy 1998), optimal methods (Bell 1986; North et al. 1995), and a geometric approach (Hasselmann 1997), the contravariant fingerprints are given by

$$\mathbf{F} = \Sigma^{-1}\mathbf{S}(\mathbf{S}^{\mathrm{T}}\Sigma^{-1}\mathbf{S})^{-1} \tag{7}$$

where Σ is a covariance matrix describing the statistics of natural variability and uncertainty in the shapes $\mathbf{s}_i$:

$$\Sigma = \Sigma_{\mathrm{d}\mathbf{n}/\mathrm{d}t} + \Sigma_{\mathbf{S}}. \tag{8}$$

The contributions of natural variability and signal uncertainty must be evaluated differently because of their different natures. Natural variability influences a measured trend in the emitted infrared spectrum simply because any timeseries of a random phenomenon yields a nonzero residual trend. If the covariance of natural variations in the annual average emitted infrared spectrum is $\Sigma_{\delta\mathbf{n}}$, then the residual trend has zero expected mean but an uncertainty of $\Sigma_{\mathrm{d}\mathbf{n}/\mathrm{d}t}$:

$$\Sigma_{\mathrm{d}\mathbf{n}/\mathrm{d}t} = \frac{12\tau}{(N^3 - N)(\mathrm{yr}^3)}\Sigma_{\delta\mathbf{n}} \tag{9}$$

where N is the number of years in the continuous timeseries and $\tau = 1\mathrm{yr}$ for no serial correlation (see Eqs. (6) and (7) in Leroy et al. 2008b). The covariance of natural interannual variability is evaluated using a long control run of a climate model in conjunction with a forward model for the emitted infrared spectrum. On the other hand, the covariance of signal shape uncertainty must be evaluated using a large ensemble of climate models each of which can be used to determine its own set of signal shapes $\mathbf{s}_i$. Because we are interested in trends of spectrally integrated outgoing longwave radiation, for each model used to derive $\mathbf{s}_i$, the signals are normalized such that the spectral integral of $\mathbf{s}_i$ multiplied by π (to account for integration over solid angle) is unity. Then the signal shape uncertainty covariance is

$$\Sigma_{\mathbf{S}} = \sum_{i,j}\left(\frac{\mathrm{d}\alpha_i}{\mathrm{d}t}\right)\left(\frac{\mathrm{d}\alpha_j}{\mathrm{d}t}\right)\langle \mathbf{s}_i\mathbf{s}_j^{\mathrm{T}}\rangle \tag{10}$$

where the $\langle\cdots\rangle$ denotes an ensemble average over a large number of models and the $\mathrm{d}\alpha_i/\mathrm{d}t$ are prior estimates of the trend in outgoing longwave radiation associated with signal i. The contravariant fingerprints are then obtained by substituting the expressions for $\Sigma_{\mathrm{d}\mathbf{n}/\mathrm{d}t}$ and $\Sigma_{\mathbf{S}}$ in Eqs. (9) and (10) into Eq. (8) and in turn into Eq. (7). When the contravariant fingerprints are multiplied by annual average infrared spectral anomalies, the result will be the outgoing longwave radiation (OLR) anomalies associated with the prescribed feedbacks.

Ordinary error estimation (for just one signal **s** instead of multiple signals **S**) dictates that the posterior uncertainty covariance for the OLR trends associated with the feedbacks should be

$$\sigma^2_{\mathrm{d}\alpha/\mathrm{d}t} = \left(\mathbf{s}^{\mathrm{T}} \Sigma^{-1} \mathbf{s}\right)^{-1} \tag{11}$$

but too often prescriptions of natural variability are grossly different from reality. Consequently, a better estimate of the posterior error should be obtained from the data alone. This is done by ordinary linear regression on a detector timeseries $\alpha(t)$ (cf. Eq. (15) below). With the timeseries $\alpha(t)$, the error is determined first by estimating the natural variability in the detectors which is the variance of the $\alpha(t)$ after removal of a best linear fit $\alpha_{\mathrm{fit}}(t)$. The uncertainty in the trend $\mathrm{d}\alpha/\mathrm{d}t$ due to natural variability becomes

$$\sigma^2_{\mathrm{d}\alpha/\mathrm{d}t}\,(\text{natural variability}) = \frac{\sigma^2_{\alpha}}{N(\Delta t)^2} \tag{12}$$

where $(\Delta t)^2 = \sum_{i=1}^{N} (t_i - \bar{t})^2 / N$ is the variance of the coordinate times in the timeseries. The timeseries $\alpha(t)$ contains only variability related to natural variability and no uncertainty due to signal shape uncertainty, so the latter must be added separately. By standard error propagation techniques,

$$\sigma^2_{\mathrm{d}\alpha/\mathrm{d}t}(\text{signal shape}) = \mathbf{F}^{\mathrm{T}} \Sigma_{\mathbf{s}} \mathbf{F} \tag{13}$$

and thus the error in the forecast trend is

$$\sigma^2_{\mathrm{d}\alpha/\mathrm{d}t} = \sigma^2_{\mathrm{d}\alpha/\mathrm{d}t}(\text{natural variability}) + \sigma^2_{\mathrm{d}\alpha/\mathrm{d}t}(\text{signal shape}). \tag{14}$$

If natural variability were correctly prescribed by that used in composing the contravariant fingerprint **F**, then $\sigma^2_{\mathrm{d}\alpha/\mathrm{d}t}(\text{natural variability}) = \mathbf{F}^{\mathrm{T}} \Sigma_{\mathrm{d}\mathbf{n}/\mathrm{d}t} \mathbf{F}$ and the result becomes exactly that in Eq. (11).

To demonstrate the viability of this approach to linear regression, we have computed the contravariant fingerprints **F** using the output of several models of the World Climate Research Programme's (WCRP's) Coupled Model Intercomparison Project (CMIP3) multi-model data set, subjected to SRES-A1B forcing. Case A1B of the Special Report on Emission Scenarios (SRES) predicts radiative forcing of climate in a world of rapid economic growth, rapid technological growth, increasing social interaction, and decelerating population growth (Intergovernmental Pabel on Climate Change (IPCC) 2000). It features approximately 1% yr^{-1} $\mathrm{CO_2}$ increase to $\approx$ 720 ppm and radiative forcing by sulfate aerosols peaking in year $\approx$ 2020. We take annual averages of emitted infrared spectra based on monthly average output and average over the tropics. The signals $\mathbf{s}_i$ are estimated based on the first 50 years of output. We then computed 20 years of emitted infrared spectra from a climate model independent of those used to construct the contravariant basis.

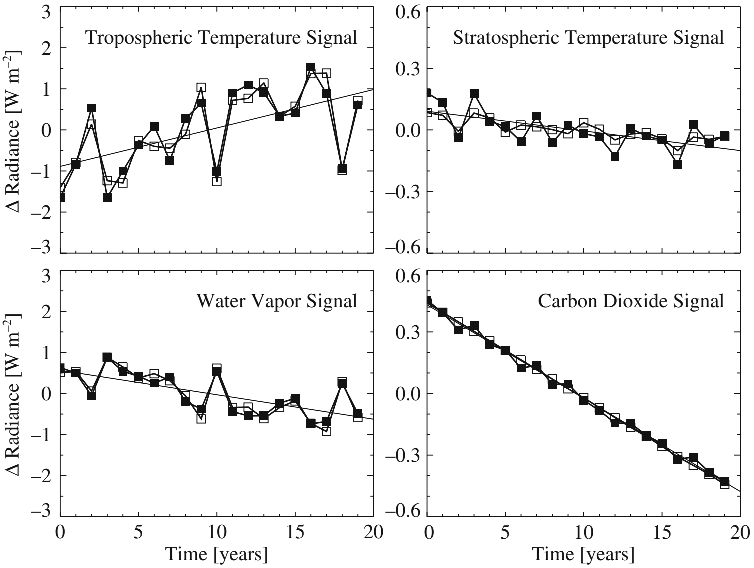

Fig. 2 Detection amplitude timeseries for four signals. The *solid squares* show detection amplitudes for each of four detected signals and the *open squares* show true OLR anomalies for each of the four signals. The thin *solid line* is the best linear fit to the detection amplitudes. The "truth" data set is taken from the first 20 years of output of an SRES-A1B run of GFDL CM2.1

We multiplied the contravariant fingerprints by tropical average, annually averaged emitted infrared spectra from that climate model. The result is a timeseries of detectors $\alpha(t)$:

$$\alpha(t) = \mathbf{F}^{\mathrm{T}}\mathbf{d}(t). \tag{15}$$

The result is shown in Fig. 2. In both the "truth" (open squares) and analysis (solid squares) there is variability from year to year. This variability contributes in large part to the length of time required to elapse before useful climate model testing can take place. In the case of greenhouse forcing by carbon dioxide, it is evident from the small fluctuations associated with interannual variability that direct observation of anthropogenic *radiative forcing* of the climate should be detected and strongly constrained within just a few years. After 5 years of observation, in fact, an estimate of radiative forcing by carbon dioxide with just 20% uncertainty should be obtained. Detection of tropospheric temperature trends (climate response) and longwave suppression by water vapor requires more time because of the large fluctuations associated with interannual variability. After 20 years of observation, an estimate of the water vapor-longwave feedback in the tropics with $\sim$ 50% uncertainty can be obtained by trend analysis.

Figure 2 suggests a different analysis as well. The year to year anomalies of the tropospheric temperature and water vapor signals are strongly anticorrelated. This is related to the simple fact that tropical tropospheric water vapor increases and blocks surface radiation in years when the tropical troposphere is warm following the Clausius-Clapeyron equation. The slope of this correlation then can be used to estimate the water vapor-longwave feedback. In fact, such an *anomaly correlation* analysis can be used to estimate the water vapor-longwave feedback in the tropics with 7% uncertainty in ten years. The uncertainty scales as $(\Delta t)^{-1/2}$ for anomaly correlation analysis whereas the uncertainty scales as $(\Delta t)^{-3/2}$ for trend analysis, with Δt the time baseline of the continuous timeseries of data.

Actual spectral longwave data, though, are dominated by clouds, and thus the use of GNSS radio occultation (RO) is likely to be necessary. Leroy et al. (2006) have shown that the optimal fingerprint of climate change in upper air *dry pressure*—dry pressure is the atmospheric pressure derived from GNSS RO data under the assumption of a completely dry atmosphere—is poleward migration of the mid-latitude jet streams in both the Northern and Southern Hemispheres. In Fig. 3 we show the results of the application of the methodology described by Eqs. (6) through (9) when applied to zonal average, annual average log-dry pressure (instead of infrared spectra F_{ν}^{LW}) as might be obtained from GNSS RO data normalized by the surface air temperature trend $\mathrm{d}T/\mathrm{d}t$.

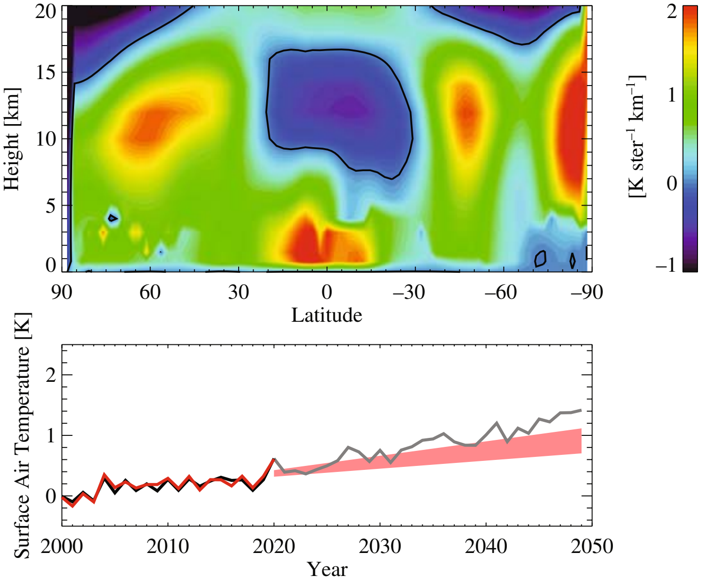

Fig. 3 The *top* plot shows the contravariant fingerprint (**F**) for log-dry pressure as an indicator of surface air temperature trends. The *lower* plot shows the result of the application of this approach using detectors, with a 20-yr timeseries of dry pressure "data" taken from the output of a model not used in the construction of the contravariant fingerprint. The *black curve* shows actual global average annual average surface air temperature, and the *red curve* shows the detectors $\alpha(t)$. The *red-shaded* area from years 2020 to 2050 shows the forecast trend of surface air temperature based on the simulated upper air dry pressure data from 2000 to 2020, and the *gray curve* shows the actual evolution of the surface air temperature

The contravariant fingerprint $\mathbf{F}$ and the detector timeseries $\alpha(t)$ are used to infer past and predict future surface air temperature trends given zonal average, annual average log-dry pressure data from GNSS RO only. The contravariant fingerprint is the map by which one convolves the trends in data to obtain a trend in surface air temperature:

$$\frac{\mathrm{d}T}{\mathrm{d}t} = \left\langle \mathbf{F}, \frac{\mathrm{d}\mathbf{d}}{\mathrm{d}t} \right\rangle = \frac{\mathrm{d}}{\mathrm{d}t} \left\langle \mathbf{F}, \mathbf{d}(t) \right\rangle = \frac{\mathrm{d}}{\mathrm{d}t} \alpha(t) \tag{16}$$

(cf. Eq. 15). The inner product rule in this case is

$$\langle \mathbf{a}, \mathbf{b} \rangle = \int_{-\pi/2}^{\pi/2} 2\pi \; \mathrm{d}(\sin\theta) \int_{0\text{ km}}^{20\text{ km}} \mathrm{d}h \; a\,(\theta, h)\, b\,(\theta, h) \tag{17}$$

where θ is latitude and h is height, the coordinates of the map. The contravariant fingerprint has dimensions of surface air temperature per log-dry pressure per height interval per solid angle interval on the Earth's surface. The intervals are determined by the data grid. The slope of the detector timeseries is used to infer and predict the surface air temperature trend and its related uncertainty.

As can be seen in Fig. 3, when upper air log-dry pressure is used as an indicator of trends in surface air temperature, the fingerprint searches for poleward migration of the mid-latitude jet streams, a tropical contribution that involves subtraction of upper tropospheric temperature trends from lower tropospheric humidity trends, and a possible weakening of the southern stratospheric polar vortex. Poleward migration of the mid-latitude jet streams is the leading indicator of climate change in the tropospheric upper air (Leroy et al. 2006). In this application, the detectors capture the interannual fluctuations of global average surface temperature with accuracy < 0.1 K, meaning GNSS RO can be relied upon to obtain an accurate estimate of the $\mathrm{d}T/\mathrm{d}t$ that is necessary for estimating radiative feedbacks. This is an improvement over the use of *in situ* meteorological stations which are largely restricted to land.

4 Discussion

We have described how monitoring the emitted infrared spectrum and microwave refractivity using GNSS RO can be used to test the forecasting capability of climate models. The infrared spectrum is rich in information relevant to the longwave feedbacks of the climate system and microwave refractivity contains information relevant to the response of the upper air and surface air temperature. Leroy et al. (2008a) showed that a twenty year timeseries of longwave spectral data is expected to provide a 50% uncertain estimate of the water vapor-longwave feedback of the climate system and a 20% uncertain estimate of the longwave forcing by carbon dioxide in 5 years. Anomaly correlation is expected to work well in the tropics on an annual timescale because temperature and humidity are strongly coupled in the tropical troposphere by moist convection. Whether it can be expected to work in the mid- and high latitudes remains an open question, however.

An evaluation of the longwave feedbacks by trend analysis can only be obtained with a corresponding accurate estimate of the trend in global average surface air temperature. Accurate estimation of the global average surface air temperature is expected to be complicated by the evolution of low clouds. Their infrared spectral signatures are very similar, and a small amount of error that might result from this ambiguity would significantly influence an evaluation of the longwave feedbacks, especially a low cloud-longwave feedback. For this reason, microwave refractivity as obtained by GNSS RO has a valuable role to play. Microwave refractivity is mostly insensitive to clouds, and so it can be expected to resolve a low cloud-temperature ambiguity in trends in the emitted infrared spectrum. Leroy et al. (2006) showed that the leading indicator of climate change in upper air dry pressure is poleward migration of the mid-latitude jet streams. Generalized scalar prediction shows that surface air temperature prediction can be obtained by poleward migration of the mid-latitude jet streams as well. The resulting analysis for $\mathrm{d}T/\mathrm{d}t$ is more uncertain than simple measurements of surface air temperature trends because of the influence of natural variability in the upper air, but satellite data does not suffer from the same coverage problems as does *in situ* data.

The future direction in this line of research quite obviously points toward simulations using cloudy outgoing longwave spectra. Clouds are acknowledged to be associated with the most uncertain feedbacks. Only recently have climate models published output relevant to simulating cloudy longwave radiances. Once clouds are included in the simulation of emitted infrared spectra, the surface temperature-low cloud ambiguity is introduced. The surface temperature-low cloud ambiguity in outgoing longwave spectra and the wet-dry ambiguity in microwave refractivity might both be resolved by considering outgoing longwave spectra and microwave refractivity jointly in climate model testing and optimal fingerprinting. Such a joint detection should be accomplished by expanding the proposed data vector to include multiple data types and computing signals and natural variability accordingly.

Finally, the cloud-shortwave feedbacks remain the most uncertain feedbacks implicit in climate models, so an exploration of how climate models can be tested using reflected shortwave (visible) spectra is mandatory for responding to societal demands.

Acknowledgements We acknowledge the modeling groups, the Program for Climate Model Diagnosis and Intercomparison (PCMDI) and the WCRP's Working Group on Coupled Modelling (WGCM) for their roles in making available the WCRP CMIP3 multi-model data set. Support of this data set is provided by the Office of Science, U.S. Department of Energy. This work was supported by grant ATM-0450288 of the U.S. National Science Foundation.

References

Allen M, Gillett N, Kettleborough J, Hegerl G, Schnur R, Stott P, Boer G, Covey C, Delworth T, Jones G, Mitchell J, Barnett T (2006) Quantifying anthropogenic influence on recent near-surface temperature change. Surv Geophys 27:491–544

Bell T (1986) Theory of optimal weighting of data to detect climatic change. J Atmos Sci 43(16):1694–1710

Bony S, Colman R, Kattsov V, Allan R, Bretherton C, Dufresne J, Hall A, Hallegatte S, Holland M, Ingram W, Randall D, Soden B, Tselioudis G, Webb M (2006) How well do we understand and evaluate climate change feedback processes? J Climate 19(15):3445–3482

Cess R (1976) Climate change—Appraisal of atmospheric feedback mechanisms employing zonal climatology. J Atmos Sci 33(10):1831–1843

Colman R (2003) A comparison of climate feedbacks in general circulation models. Climate Dyn 20:865–873, doi:10.1007/s00382-003-0310-z

Hasselmann K (1997) Multi-pattern fingerprint method for detection and attribution of climate change. Climate Dyn 13(9):601–611

Held I, Soden B (2000) Water vapor feedback and global warming. Ann Rev Energy Env 25:441–475

Huntingford C, Stott P, Allen M, Lambert F (2006) Incorporating model uncertainty into attribution of observed temperature change. Geophys Res Lett 33(L05710), doi:10.1029/2005GL024831

Intergovernmental Panel on Climate Change (IPCC) (2000) Special Report on Emissions Scenarios. Cambridge University Press, Cambridge, UK

Kirk-Davidoff D, Goody R, Anderson J (2005) Analysis of sampling errors for climate monitoring satellites. J Climate 18(6):810–822

Leroy S (1998) Detecting climate signals: Some bayesian aspects. J Climate 11(4):640–651

Leroy S, Anderson J, Dykema J (2006) Testing climate models using GPS radio occultation: A sensitivity analysis. J Geophys Res 111(D17105), doi:10.1029/2005JD006145

Leroy S, Anderson J, Dykema J, Goody R (2008a) Testing climate models using thermal infrared spectra. J Climate 21(9):1863–1875, doi:10.1175/2007JCLI2061.1

Leroy S, Anderson J, Ohring G (2008b) Climate signal detection times and constraints on climate benchmark accuracy requirements. J Climate 21(4):841–846

National Research Council, Committee on Earth Science and Applications from Space (2007) Earth Science and Applications from Space: National Imperatives for the Next Decade and Beyond. National Academies Press, Washington, DC

North G, Kim K, Shen S, Hardin J (1995) Detection of forced climate signals: I. Filter theory. J Climate 8(3):401–408

Ohring G (ed) (2007) Achieving Satellite Instrument Calibration for Climate Change. National Oceanographic and Atmospheric Administration, Washington, DC, 155pp

Soden B, Held I (2006) An assessment of climate feedbacks in coupled ocean-atmosphere models. J Climate 19(14):3354–3360

Wetherald R, Manabe S (1988) Cloud feedback processes in a general circulation model. J Atmos Sci 45(8):1397–1415

Construction of Consistent Temperature Records in the Lower Stratosphere Using Global Positioning System Radio Occultation Data and Microwave Sounding Measurements

S.-P. Ho, W. He, and Y.-H. Kuo

Abstract In this study, we use FORMOSAT-3/Constellation Observing System for Meteorology, Ionosphere, and Climate (COSMIC) Global Positioning System (GPS) radio occultation (RO) data to simulate Advanced Microwave Sounding Unit (AMSU) brightness temperatures (Tbs) for the lower stratosphere and compare them to AMSU Tbs from different National Oceanic and Atmospheric Administration (NOAA) missions in July 2007. Our analysis shows that because COSMIC data do not contain orbit drift errors and are not affected by on-orbit heating and cooling of the satellite component, they are very useful to identify the AMSU time/location-dependent biases for different NOAA missions. We also examine the consistency of the calibration coefficients among collocated NOAA AMSU Tb pairs (e.g., NOAA15-NOAA16, NOAA16-NOAA18, and NOAA15-NOAA18) and COSMIC-NOAA pairs. The usefulness of the COSMIC-calibrated AMSU Tbs for calibrating other overlapping AMSU Tbs from different platforms is also examined. These results demonstrate the potential to use both GPS RO and microwave sounding data to construct consistent climate temperature records.

1 Introduction

Accurate temperature trend estimates are crucial to monitor decadal climate variability and to understand climate change forcing mechanisms. To construct consistent climate temperature records, long-term well-calibrated satellite temperature measurements with good temporal and spatial coverage from various missions are needed.

The global all-weather temperature distribution can be obtained from Global Positioning System (GPS) radio occultation (RO) data (Hocke 1997; Feng and

---

S.-P. Ho (✉)
National Center for Atmospheric Research (NCAR) and University Corporation for Atmospheric Research (UCAR), P.O. Box 3000, Boulder, CO, USA
e-mail: spho@ucar.edu

A. Steiner et al. (eds.), *New Horizons in Occultation Research*,
DOI 10.1007/978-3-642-00321-9_17,

Herman 1999). GPS RO can provide high vertical resolution refractivity, which is a function of temperature, water vapor, and pressure. Because the fundamental observable of GPS RO sounding technique, the phase delay, is accomplished via precise measurement of time that is ensured by ultra-stable atomic clocks on the ground, GPS RO data are ideally suited for climate trend detection. The six-satellite FORMOSAT-3/Constellation Observing System for Meteorology, Ionosphere, and Climate (COSMIC) mission (denoted as COSMIC hereafter) was successfully launched in April 2006. COSMIC will provide approximately 2500 GPS RO soundings per day after it is fully deployed, offering more uniform temporal and spatial coverage than seen in previous GPS RO missions (e.g., CHAllenging Minisatellite Payload, CHAMP (Wickert et al. 2004) and Satélite de Aplicaciones Científicas-C, SAC-C (Hajj et al. 2004), both launched in 2000). Even though we have had GPS RO data from CHAMP and SAC-C since 2001 and from COSMIC since 2006, it is still unrealistic to use only seven years of GPS RO data to detect climate trend.

On board the National Oceanic and Atmospheric Administration (NOAA) series of polar-orbiting satellites, the Microwave Sounding Unit (MSU) and the Advanced Microwave Sounding Unit (AMSU) have also provided near all-weather temperature measurements at different atmospheric vertical layers since 1979 and 1998, respectively. Over the past decade, the roughly 30 years of MSU/AMSU measurements have been extensively used for climate temperature trend detection (Christy et al. 2000, 2003; Mears et al. 2003; Vinnikov and Grody 2003; Grody et al. 2004; Vinnikov et al. 2006; Zou et al. 2006). Even though these satellite missions use similar instruments (from NOAA6 to NOAA14 for MSU and from NOAA15 to NOAA18 for AMSU), the equatorial crossing times of the NOAA satellite orbits drift in local time after launch (Fig. 1), which leads to different temporal sampling of the MSU/AMSU measurements for each NOAA satellite. Because the

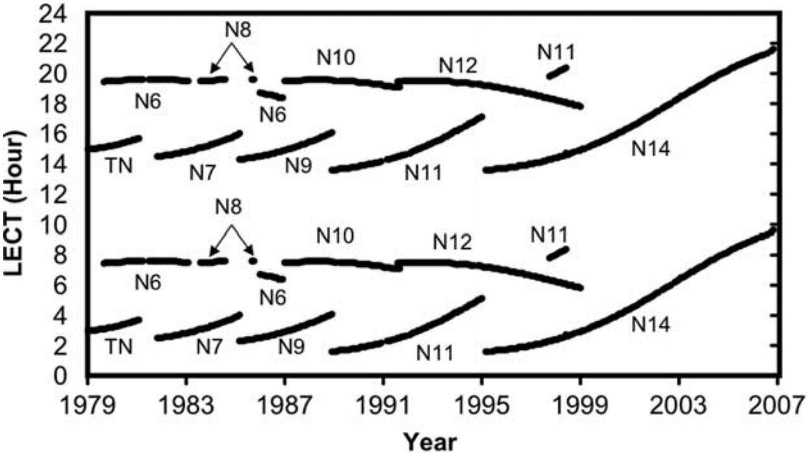

Fig. 1 NOAA satellite orbit drifts with local times after launch from 1978 to 2007. Numbers in the figure represent satellite series from NOAA6 to NOAA14

MSU/AMSU operational calibration coefficients were obtained from pre-launch datasets (Mo et al. 2001), the orbital changes on MSU/AMSU measurements after launch may not be completely accommodated by these calibration coefficients. Different MSU/AMSU missions may contain different measurement biases, which actually vary with times and locations due to on-orbit heating or cooling of the satellite component. This causes great difficulties for climate trend detection. Although different correction methods were proposed by different groups (e.g., Christy et al. 2000; Mears et al. 2003; Grody et al. 2004; Zou et al. 2006), due to lack of an absolute reference, only relative biases are corrected. The temperature trends can still vary as large as 0.1 K/decade when different satellite measurements are used as references (Christy et al. 2003). This leads to extra difficulties for the usage of MSU/AMSU temperature trends for the climate analysis (Christy et al. 2000, 2003; Mears et al. 2003; Grody et al. 2004; Karl et al. 2006; Zou et al. 2006).

The objective of this study is to show the usefulness of GPS RO data to inter-calibrate AMSU brightness temperatures (Tbs) by identifying the orbit-dependent biases for AMSU measurements from different satellite missions and to show the usefulness of the calibrated AMSU Tbs for calibrating other overlapping AMSU Tbs from different platforms. This is to demonstrate that both GPS RO and AMSU/MSU data can be used together to construct consistent climate temperature records. In this study, we use an AMSU fast radiative transfer model to convert COSMIC dry temperature (derived from GPS RO refractivity using the hydrostatic equation and assuming water vapor effect on refractivity is negligible) to synthetic AMSU Tbs for NOAA15, 16, and 18 (N15, N16, and N18), respectively. We focus on the comparison of AMSU temperature in the lower stratosphere (e.g., Tb for AMSU Ch9), where the moisture effect on GPS RO refractivity is negligible. The calibration coefficients (slopes and offsets) among COSMIC synthetic AMSU Tbs and N15, N16, and N18 AMSU Tbs are then constructed. We also construct the calibration coefficients among collocated NOAA AMSU Tb pairs (e.g., N15-N16, N16-N18, and N15-N18). The consistency of the calibration coefficients among COSMIC-NOAA pairs and NOAA-NOAA pairs is examined. We illustrate COSMIC-NOAA and NOAA-NOAA calibration methods in Sect. 2. The comparison results are presented in Sect. 3. We conclude this study in Sect. 4.

2 COSMIC-AMSU and AMSU-AMSU Calibration Methods

In this study, COSMIC RO dry temperature profiles from July 2007 are used to compute the synthetic AMSU Ch9 Tbs. All COSMIC RO dry temperature profiles were downloaded from the UCAR COSMIC Data Analysis and Archive Center (CDAAC)[1]. An AMSU fast forward model from the Cooperative Institute for Meteorological Satellite Studies, CIMSS, $\mathrm{MWF}_{\mathrm{CIMSS}}$ (Hal Woolf, CIMSS, personal communication, 2005) is used to project each COSMIC dry temperature profile into

---

[1] From http://cosmic.cosmic.ucar.edu/cdaac/index.html.

synthetic microwave Tbs. The validation of microwave transmittance of this model is described in Woolf et al. (1999). The atmospheric contribution (weighting function) for AMSU Ch9 ranges mainly from 300–10 hPa and peaks near 110 hPa (not shown). The satellite viewing angle is set to nadir for our calculations. The means of AMSU Tbs for N15, N16, and N18 that are collocated with each COSMIC profile within 15 minutes and 50 km are computed. The COSMIC synthetic AMSU Tbs are used as calibration references to inter-calibrate AMSU Tbs from N15 (Tb_{AMSU_N15}), N16 (Tb_{AMSU_N16}), and N18 (Tb_{AMSU_N18}). Only AMSU pixels with satellite viewing angles ranging from -15° to 15° are included in our collocation procedure. The calibration coefficients (slopes and offsets) for each COSMIC-NOAA AMSU pair are then determined from the best fit for each collocated COSMIC and NOAA AMSU ensemble (see Sect. 3.1). This calibration approach is similar to that of Ho et al. (2007, 2009).

Raw counts and ancillary data for each AMSU pixel including viewing angle, location, and time for July 2007 are downloaded from National Environmental Satellite, Data, and Information Service (NESDIS). The operational calibration coefficients for each NOAA AMSU instrument are also downloaded and are used to convert AMSU raw counts into Tbs. The AMSU Tbs from N15, N16, and N18 within 15 minutes and 50 km are collected (e.g., N15-N16, N16-N18, and N15-N18, respectively). Only AMSU pixels with satellite viewing angles ranging from -15° to 15° are included. The calibration coefficients for each N15-N16, N16-N18, and N15-N18 pair are determined by their best linear fits (see Sect. 3.2).

3 Results

3.1 *Using COSMIC Data to Identify AMSU Biases Over Different Orbits and Locations*

The comparisons between COSMIC-simulated AMSU Ch9 Tbs and collocated AMSU Ch9 Tbs from N15, N16, and N18 within 15 minutes and 50 km are shown in Fig. 2a, b, and c, respectively. The figures depict that COSMIC synthetic AMSU Tbs for N15 (Tb_{COSMIC_N15}), N16 (Tb_{COSMIC_N16}), and N18 (Tb_{COSMIC_N18}) are highly correlated with Tb_{AMSU_N15} (correlation coefficient $= 0.99$), Tb_{AMSU_N16} (correlation coefficient $= 0.99$), and Tb_{AMSU_N18} (correlation coefficient $= 0.99$), respectively, and with small standard deviations to their means of COSMIC-N15 (1.20 K), COSMIC-N16 (1.11 K), and COSMIC-N18 (1.22 K) pairs. This demonstrates the usefulness of COSMIC RO data for inter-calibrating AMSU Tbs, and is consistent with the results of COSMIC RO and AMSU Tbs comparisons for September 2006 (Ho et al. 2009). Because GPS RO data are not affected by orbital change and have no calibration issues, the small differences of the slopes and offsets for COSMIC-N15, COSMIC-N16, and COSMIC-N18 pairs are mainly caused by calibration, orbital drift errors, and measurement anomalies for AMSU Tbs for different missions.

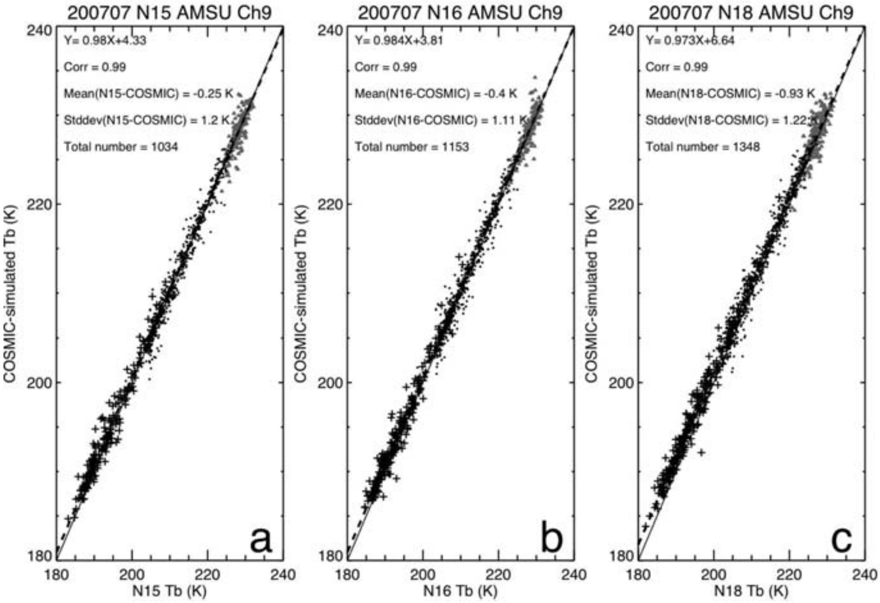

Fig. 2 Comparison of COSMIC-simulated AMSU Ch9 Tbs. (**a**) N15 AMSU Ch9 Tbs, (**b**) N16 AMSU Ch9 Tbs, and (**c**) N18 AMSU Ch9 Tbs for July 2007. Pixels in *gray triangle* are from the 60°N to 90°N zone, pixels in *dark dot* are from the 60°N to 60°S zone, and pixels in *dark cross* are from the 60°S to 90°S zone. The best fit is in *dash line*. Diagonal one-to-one fit is in *solid line*

To further quantify COSMIC-AMSU Tb biases at different locations for different missions, we use different symbols in Fig. 2 to represent COSMIC-NOAA pairs at the 60°N to 90°N zone (in gray triangle), the 60°S to 60°N zone (in dark dot), and the 60°S to 90°S zone (in dark cross) and list the mean AMSU Ch9 Tb biases for N15-COSMIC, N16-COSMIC, and N18-COSMIC pairs over the 60°N to 90°N and the 60°S to 90°S zones in Table 1. It is obvious that the absolute NOAA-COSMIC mean Tb biases are smaller in the Northern Hemisphere and are larger in the Southern Hemisphere. The absolute biases for N18-COSMIC pairs are larger than that for N15-COSMIC and N16-COSMIC pairs (Table 1 and Fig. 2).

Table 1 The mean Tb biases for N15-COSMIC, N16-COSMIC, N18-COSMIC, N15-N16, N16-N18, and N15-N18 pairs over 60°N to 90°N and 60°S to 90°S zones. NOAA-NOAA biases inferred from NOAA-COSMIC are listed in parentheses

	60°N to 90°N	60°S to 90°S
N15-COSMIC	− 0.05 K	− 0.73 K
N16-COSMIC	− 0.22 K	− 0.83 K
N18-COSMIC	− 0.55 K	− 1.50 K
N15-N16	0.03 K (0.17 K)	0.09 K (0.10 K)
N16-N18	0.47 K (0.33 K)	0.57 K (0.67 K)
N15-N18	0.50 K (0.50 K)	0.69 K (0.77 K)

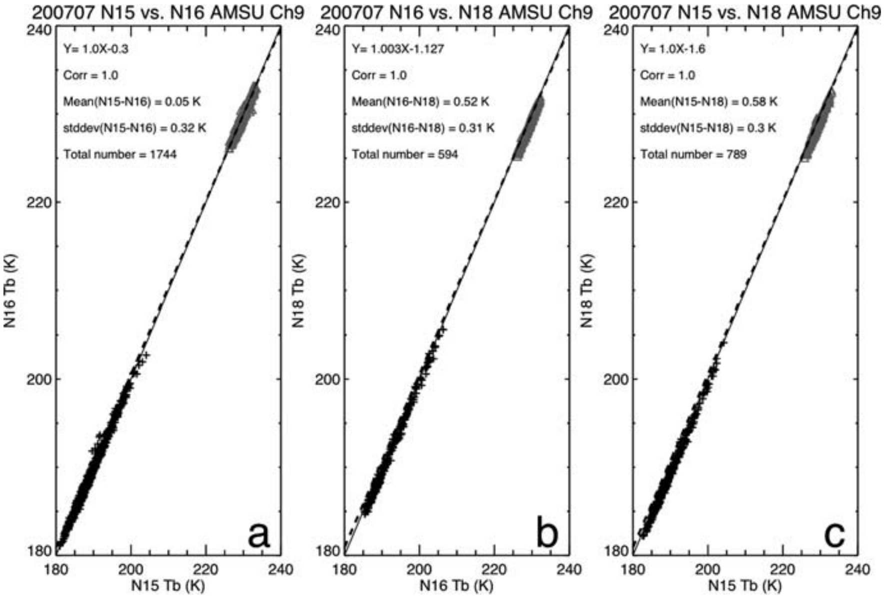

Fig. 3 Comparison of (**a**) N15 AMSU Ch9 Tbs and N16 AMSU Ch9 Tbs, (**b**) N16 AMSU Ch9 Tbs and N18 AMSU Ch9 Tbs, and (**c**) N15 AMSU Ch9 Tbs and N18 AMSU Ch9 Tbs for July 2007. Pixels in *gray triangle* are from the 60°N to 90°N zone, and pixels in *dark cross* are from the 60°S to 90°S zone. The best fit is in *dash line*. Diagonal one-to-one fit is in *solid line*

To see if the NOAA-COSMIC biases are consistent with AMSU inter-satellite biases from different missions, AMSU Ch9 Tbs for N15-N16, N16-N18, and N15-N18 pairs are plotted in Fig. 3a–c, respectively. In Fig. 3, AMSU pairs in the 60°N to 90°N zone and the 60°S to 90°S zone are in gray triangle and in dark cross, respectively. The mean Ch9 Tb biases for N15-N16, N16-N18, and N15-N18 pairs for the 60°N to 90°N and the 60°S to 90°S zones are also listed in Table 1. For NOAA polar satellites, the collocated N15-N16, N16-N18, and N15-N18 pairs within 15 minutes and 50 km all occurred only over polar regions. It is shown in Table 1 that the mean AMSU inter-satellite biases are consistent with those for COSMIC-AMSU pairs where the mean NOAA-COSMIC Tb biases for different missions are all negative. The mean N15-N16, N16-N18, and N15-N18 Tbs at both the 60°S to 90°S and 60°N to 90°N regions can almost always be reproduced using Tb biases of NOAA-COSMIC pairs. For example, the mean N15-N18 Tb bias in the 60°N to 90°N zone (0.5 K) is equal to Tb bias of N15-COSMIC (−0.05 K) minus that of N18-COSMIC (−0.55 K). The reason that some mean N15-N16, N16-N18, and N15-N18 Tbs cannot be exactly reproduced using Tb biases of NOAA-COSMIC pairs (although their Tb differences are small) is mainly due to sample differences among NOAA-COSMIC and NOAA-NOAA pairs.

To find the cause of NOAA-COSMIC Tb biases at the different locations shown in Table 1 and Fig. 2, we plot the binned N15-COSMIC AMSU Ch9 Tb differences for each local time and binned latitude variation for N15 orbit for each local time in Fig. 4. In general, the variation of N15-COSMIC AMSU Tb biases is highly

Fig. 4 Binned N15-COSMIC AMSU Ch9 Tb differences for each local time and binned latitude variation for N15 orbit for each local time. The *gray solid line* is for N15-COSMIC AMSU Ch9 Tb = 0 for different local times

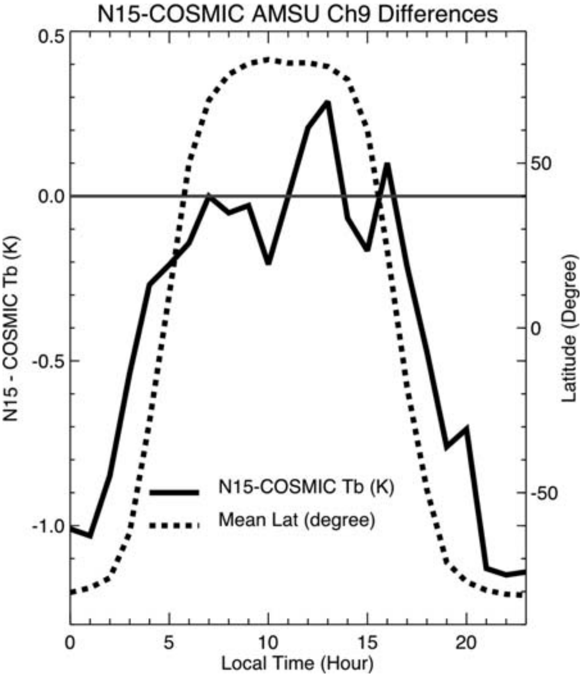

coherent with the N15 orbit change with local time, where N15 satellite may be warmed up during the day and cooled down during the night. It is shown in Fig. 4 that N15-COSMIC Tbs are in general lower during the southern hemispheric winter where N15 is under the shadow of the Earth (solar zenith angle is larger than 80 degrees) and are higher in the Northern Hemisphere (ranges from 7 to 17 local times). Because GPS RO data are not affected by the temperature variation of the satellite component, the mean N15-COSMIC AMSU Tb biases are mainly from AMSU Tb anomalies due to the heating or cooling of the satellite component. Note that because both NOAA satellites are cooled or warmed in the same manner when collocated NOAA pairs are collected, the effect of AMSU temperature anomalies due to satellite heating or cooling is canceled out in AMSU inter-satellite bias comparisons (comparing Figs. 2 and 3). Due to lack of an absolute reference, only relative inter-satellite biases are corrected (absolute AMSU inter-satellite biases are all smaller than that for NOAA-COSMIC pairs), which may lead to uncertainties for climate trend analysis.

3.2 Using the Calibrated AMSU Data to Calibrate Other Overlapped AMSU Measurements

From the previous section, we know the best fit for N16 Tbs and COSMIC data for one particular month (in this case, July 2007, e.g., Fig. 2b), which is

$$\mathrm{Tb}_{\mathrm{COSMIC\_N16}} = 0.984 \cdot \mathrm{Tb}_{\mathrm{AMSU\_N16}} + 3.81, \tag{1}$$

and the best fit for N15-N16 pairs (Fig. 3a) is

$$\mathrm{Tb}_{\mathrm{AMSU\_N16}} = 1.001 \cdot \mathrm{Tb}_{\mathrm{AMSU\_N15}} - 0.3. \tag{2}$$

To use the COSMIC-calibrated N16 Tbs to calibrate N15 Tbs is to construct the calibration coefficients for COSMIC-N15 pairs using Eq. (1) and Eq. (2), and we have

$$\mathrm{Tb}_{\mathrm{COSMIC\_N15\_N16}} = 0.984 \cdot \mathrm{Tb}_{\mathrm{AMSU\_N15}} + 3.51. \tag{3}$$

The robustness of the slope and offset in Eq. (3) can be estimated by comparing $\mathrm{Tb}_{\mathrm{COSMIC\_N15\_N16}}$ to $\mathrm{Tb}_{\mathrm{COSMIC\_N15}}$ constructed from COSMIC-N15 pairs (Fig. 2a), where the best fit for COSMIC-N15 pairs is

$$\mathrm{Tb}_{\mathrm{COSMIC\_N15}} = 0.981 \cdot \mathrm{Tb}_{\mathrm{AMSU\_N15}} + 4.33. \tag{4}$$

By applying $\mathrm{Tb}_{\mathrm{AMSU\_N15}}$ in Fig. 2a to Eqs. (3) and (4), respectively, we have the computed $\mathrm{Tb}_{\mathrm{COSMIC\_N15}}$ and $\mathrm{Tb}_{\mathrm{COSMIC\_N15\_N16}}$ (Fig. 5a). Figure 5a depicts that the correlation coefficient of $\mathrm{Tb}_{\mathrm{COSMIC\_N15\_N16}}$ and $\mathrm{Tb}_{\mathrm{COSMIC\_N15}}$ is equal to 1.0 and

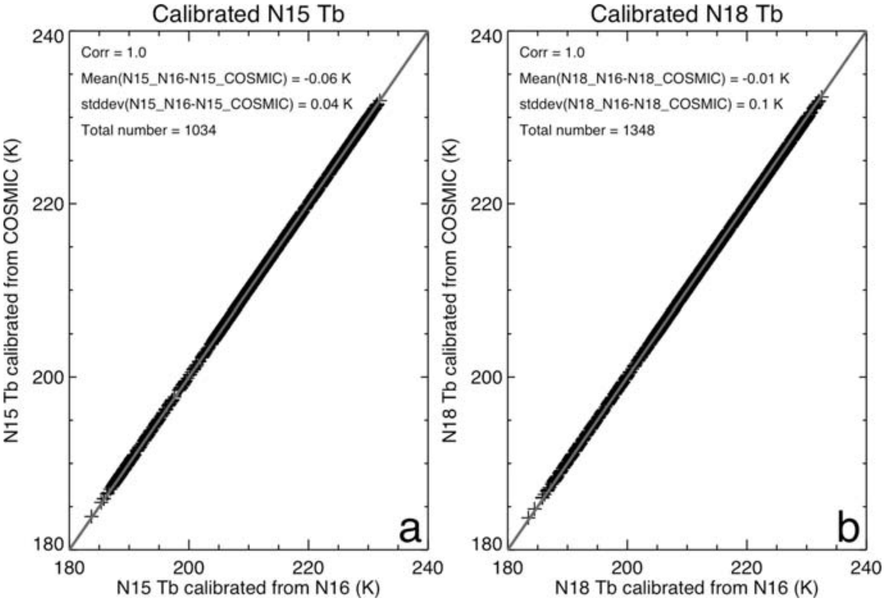

Fig. 5 Comparison of (**a**) COSMIC-calibrated N15 Tbs and N16-calibrated N15 Tbs, and (**b**) COSMIC-calibrated N18 Tbs and N16-calibrated N18 Tbs. The best fit is in *dash line*. Diagonal one-to-one fit is in *gray solid line*

their mean bias is very close to zero (~0.06 K). The very tight fit of Tb_{COSMIC_N15} and $Tb_{COSMIC\_N15\_N16}$ (the standard deviation is about 0.04 K) demonstrates the consistency between the slope and offset (calibration coefficients) found in the N15-COSMIC pairs and those constructed from both N16-COSMIC pairs and N15-N16 pairs. The uncertainty of the N16-calibrated N15 Tbs is about 0.06 K when compared to the COSMIC-calibrated N15 Tbs. Similarly, we can also calibrate N18 Tbs using calibration coefficients for N16-COSMIC (Eq. 1) and N16-N18 pairs from Fig. 3b. The best fit for N16-N18 pairs is

$$Tb_{AMSU\_N18} = 1.003 \cdot Tb_{AMSU\_N16} - 1.127. \tag{5}$$

The calibration coefficients for new COSMIC-N18 pairs reconstructed using Eqs. (1) and (5) are

$$Tb_{COSMIC\_N18\_N16} = 0.981 \cdot Tb_{AMSU\_N18} + 4.91, \tag{6}$$

where the best fit for COSMIC-N18 pairs (Fig. 2c) is

$$Tb_{COSMIC\_N18} = 0.973 \cdot Tb_{AMSU\_N18} + 6.64. \tag{7}$$

$Tb_{COSMIC\_N18\_N16}$ computed from Eq. (6) are plotted together with Tb_{COSMIC_N18} computed from Eq. (7) in Fig. 5b. Figure 5 b shows that the correlation coefficient of $Tb_{COSMIC\_N18\_N16}$ and Tb_{COSMIC_N18} is equal to 1.0 and their mean bias is also very close to zero (~–0.01 K).

4 Conclusions and Future Work

The objective of this study is to demonstrate the potential to use GPS RO and AMSU/MSU data to construct consistent climate temperature records. This is done by using the COSMIC synthetic AMSU Tbs as calibration references to inter-calibrate AMSU Tbs from N15, N16, and N18. Our analysis led to the following conclusions.

1. The COSMIC synthetic AMSU Tbs are highly correlated with AMSU Tbs. The mean Tb biases for AMSU-COSMIC pairs over the 60°N to 90°N zone and the 60°S to 90°S zone are very consistent with the AMSU inter-satellite biases from different missions. The variation of AMSU-COSMIC Tb biases is highly coherent with the NOAA satellite orbit change with local time. AMSU-COSMIC Tb biases are in general lower during the southern hemispheric winter in the night and higher in the Northern Hemisphere in the day. Because COSMIC data, unlike MSU/AMSU data, do not contain orbit drift errors and are not affected by on-orbit heating and cooling of the satellite component, they are very useful to identify the AMSU time/location-dependent biases for different missions. The mean AMSU-COSMIC Tb biases for different NOAA missions are all

negative. This may be due to the inconsistency between the AMSU operational calibration coefficients generated before launch and the orbital changes on AMSU measurements after launch, and/or positive systematic biases introduced from MWF_{CIMSS}. We leave it for a future study.

2. The calibration coefficients found from NOAA-NOAA pairs are also consistent with that of NOAA-COSMIC pairs. For example, we can construct the calibration coefficients for new COSMIC-N15 pairs (AMSU Tb for the newly derived N15 is $Tb_{COSMIC\_N15\_N16}$) using those from COSMIC-N16 and N15-N16 pairs. We assess the robustness of the slope and offset for the new COSMIC-N15 pairs by comparing $Tb_{COSMIC\_N15\_N16}$ to Tb_{COSMIC_N15} which is constructed from COSMIC-N15 pairs. The tight fit of Tb_{COSMIC_N15} and $Tb_{COSMIC\_N15\_N16}$ (the standard deviation is less than 0.1 K) demonstrates the consistency between the slope and offset (calibration coefficients) found in the N15-COSMIC pairs and those constructed using N16-COSMIC pairs and N15-N16 pairs.

Results here demonstrate that although there are only a few years of GPS RO data from both COSMIC and CHAMP that are collocated with AMSU measurements (from 2001 and beyond), we may still be able to use GPS RO data to intercalibrate AMSU/MSU data. The calibrated AMSU/MSU data, in turn, can be used to calibrate other overlapping AMSU/MSU data for those years without GPS RO data (e.g., from 1979 to 2001). In the future, multi-month data from GPS RO and AMSU/MSU data will be used to further quantify the time/location-dependent AMSU/MSU inter-satellite biases. The consistency of the calibration coefficients among collocated NOAA Tb pairs from different missions and COSMIC-NOAA pairs for different seasons of different years will also be examined.

Acknowledgements We would like to thank Mr. Hal Woolf from the Cooperative Institution for Meteorological Satellite Studies for providing the fast AMSU Forward Transfer Algorithm package. We would also like to acknowledge the contributions to this work from members of the COSMIC team at UCAR and members of the satellite operational team at the National Space Organization, Taiwan.

References

Christy JR, Spencer RW, Braswell WD (2000) MSU tropospheric temperatures: Dataset construction and radiosonde comparisons. J Atmos Ocean Tech 17(9):1153–1170

Christy JR, Spencer RW, Norris WB, Braswell WD, Parker DE (2003) Error estimates of version 5.0 of MSU/AMSU bulk atmospheric temperatures. J Atmos Ocean Tech 20(5): 613–629

Feng DD, Herman BM (1999) Remotely sensing the earth's atmosphere using the global positioning system (GPS)—The GPS/MET data analysis. J Atmos Ocean Tech 16(8):989–1002

Grody NC, Vinnikov KY, Goldberg MD, Sullivan JT, Tarpley JD (2004) Calibration of multisatellite observations for climate studies: Microwave Sounding Unit (MSU). J Geophys Res 109(D24104), doi:10.1029/2004JD005079

Hajj GA, Ao CO, Iijima BA, Kuang D, Kursinski ER, Mannucci AJ, Meehan TK, Romans LJ, de la Torre Juarez M, Yunck TP (2004) CHAMP and SAC-C atmospheric occultation results and intercomparisons. J Geophys Res 109(D06109), doi:10.1029/2003JD003909

Ho SP, Kuo YH, Zeng Z, Peterson TC (2007) A comparison of lower stratosphere temperature from microwave measurements with CHAMP GPS RO data. Geophys Res Lett 34(L15701), doi:10.1029/2007GL030202

Ho SP, Goldberg M, Kuo YH, Zou CZ, Schreiner W (2009) Calibration of temperature in the lower stratosphere from microwave measurements using COSMIC radio occultation data: Preliminary results. Terr Atmos Oceanic Sci 20 (1), doi:10.3319/TAO.2007.12.06.01(F3C)

Hocke K (1997) Inversion of GPS meteorology data. Ann Geophys 15:443–450

Karl TR, Hassol SJ, Miller CD, Murray WL (eds) (2006) Temperature trends in the lower atmosphere: Steps for understanding and reconciling differences. A Report by the Climate Change Science Program and the Subcommittee on Global Change Research, Washington, DC

Mears CA, Schabel MC, Wentz FJ (2003) A reanalysis of the MSU channel 2 tropospheric temperature record. J Climate 16(22):3650–3664

Mo T, Goldberg MD, Crosby DS, Cheng Z (2001) Recalibration of the NOAA microwave sounding unit. J Geophys Res 106(D10):10145–10150

Vinnikov KY, Grody NC (2003) Global warming trend of mean tropospheric temperature observed by satellites. Science 302:269–272

Vinnikov KY, Grody NC, Robock A, Stouffer RJ, Jones PD, Goldberg MD (2006) Temperature trends at the surface and in the troposphere. J Geophys Res 111(D03106):1–14, doi:10.1029/2005JD006392

Wickert J, Schmidt T, Beyerle G, König R, Reigber C, Jakowski N (2004) The radio occultation experiment aboard CHAMP: Operational data analysis and validation of vertical atmospheric profiles. J Meteorol Soc Jpn 82(1B):381–395

Woolf HM, van Delst P, Zhang WJ (1999) NOAA-15 HIRS/3 and AMSU transmittance model validation. Tech. rep., Technical Proceedings of the International ATOVS Study Conference, 10th, Boulder, CO

Zou CZ, Goldberg MD, Cheng Z, Grody NC, Sullivan JT, Cao C, Tarple D (2006) Recalibration of microwave sounding unit for climate studies using simultaneous nadir overpasses. J Geophys Res 111(D19114), doi:10.1029/2005JD006798

Lower Stratospheric Temperatures from CHAMP RO Compared to MSU/AMSU Records: An Analysis of Error Sources

A.K. Steiner, G. Kirchengast, M. Borsche, and U. Foelsche

Abstract A comparison of lower stratospheric temperatures (TLS) from (Advanced) Microwave Sounding Unit (MSU/AMSU) records with CHAMP radio occultation (RO) data was performed for September 2001–December 2006. Synthetic TLS temperatures were calculated by applying global weighting functions to monthly RO temperature climatologies and alternatively by applying the RTTOV_8.5 radiative transfer model to the individual CHAMP RO profile data set. The results published by Steiner et al. (2007) showed very good agreement of CHAMP TLS anomalies with MSU records from the University of Alabama in Huntsville (UAH, USA) and from Remote Sensing Systems (RSS, USA) for intra-annual variability. Statistically significant trend differences of UAH and RSS with respect to CHAMP TLS anomalies were found in the tropics (–0.40 K/5 years to –0.42 K/5 years). In this context error sources regarding the retrieval of RO data, the building of climatologies, and the related synthetic MSU computation procedure were analyzed and found to be of minor importance. In the NH extratropics the TLS specific sampling error showed a significant negative trend which is projected globally but tropical trends are small. In total, the contribution of errors from RO was found to be about an order of magnitude smaller than the trend differences and thus insufficient to account for them, especially in the tropical region. Their resolution, currently pursued in a further study, requires either the presence of currently unresolved biases in the MSU records or additional, so far overlooked, sources of error in the RO TLS record. SAC-C, GRACE, and COSMIC TLS temperatures were found to closely match CHAMP temperatures. The results underpin that inter-comparison of independent estimates of the same variable from different instruments is beneficial for the detection of residual weaknesses in otherwise high quality climate records.

A.K. Steiner (✉)
Wegener Center for Climate and Global Change (WegCenter) and Institute for Geophysics, Astrophysics, and Meteorology (IGAM), University of Graz, Austria
e-mail: andi.steiner@uni-graz.at

A. Steiner et al. (eds.), *New Horizons in Occultation Research*,
DOI 10.1007/978-3-642-00321-9_18, © Springer-Verlag Berlin Heidelberg 2009

1 Introduction

Long term upper air temperature records have been established from radiosonde observations (Lanzante et al. 2003; Sherwood et al. 2005; Thorne et al. 2005b) and from satellite observations with the Microwave Sounding Unit (MSU) and the Advanced MSU (AMSU) (Christy et al. 2003; Grody et al. 2004; Christy and Spencer 2005; Mears and Wentz 2005; Vinnikov et al. 2006). These temperature trend series now show convergence toward surface warming estimates and provide a better agreement with climate models (Santer et al. 2005; Karl et al. 2006). Still significant divergence remains in their long-term large-scale mean trends (Seidel et al. 2004; Thorne et al. 2005a). Most likely radiosonde data underestimated tropical mean temperature trends (cooling trend bias) (McCarthy et al. 2008).

In this context the radio occultation (RO) technique offers new possibilities by providing an independent type of high quality observations of the atmosphere. The validation and climatological exploitation of RO data from GPS/MET (Schrøder et al. 2003) and CHAMP (e.g., Schmidt et al. 2004; Gobiet et al. 2005; Borsche et al. 2007) indicated the suitability of RO data for global climate monitoring and modeling (Leroy et al. 2006; Foelsche et al. 2008a, 2009a,b). Steiner et al. (2007) carried out a comparison of CHAMP RO data with MSU/AMSU and equivalent radiosonde data sets and found significant trend differences to MSU/AMSU TLS data in the tropical region which has also been confirmed by Ho et al. (2007). In the current study we analyze in detail respective error sources regarding the retrieval of RO data (potential initialization biases, dry temperature assumption), the building of RO climatologies (sampling error) and the computation procedure of MSU equivalents (static weighting function versus radiative transfer model).

A short description of the respective data sets is given in Sect. 2 and the comparison setup is described in Sect. 3. The results of the study are presented and discussed in Sect. 4. Section 5 summarizes our findings and conclusions and gives a brief outlook to further investigations.

2 Data

Synthetic MSU temperatures were computed from CHAMP RO monthly temperature climatologies and from a few months of complementary RO climatologies from SAC-C, GRACE, and COSMIC, derived at the WegCenter/UniGraz, Austria, as well as from ECMWF analyses. We compared them with MSU temperature records provided by UAH, RSS, and HadAT2 as presented in the Report by the U.S. Climate Change Science Program (CCSP) (Karl et al. 2006) and shown in Fig. 1 to provide context. We focus on the years 2001–2006 and on the upper troposphere/lower stratosphere region (MSU TLS/T4 channel) where CHAMP RO retrievals have the best data quality.

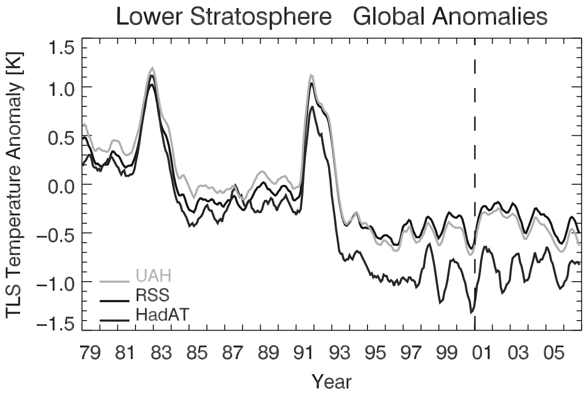

Fig. 1 Global temperature anomalies smoothed with a 7-month moving average filter for the lower stratosphere (TLS) derived from UAH (*light gray*) and RSS (*black*) brightness temperatures and from HadAT2 radiosonde temperatures (*dark gray*) shown for the years 1979–2006. The time period 2001–2006 used in this study for comparison with CHAMP RO data is delimited by dashed vertical lines (Steiner et al. 2007)

2.1 GPS RO Temperature Climatologies

Based on CHAMP RO phase delay and orbit data (version 2 data set) provided by the GFZ Potsdam (Wickert et al. 2004), atmospheric parameters were retrieved at the WegCenter and a record of more than five years of CHAMP RO dry temperature climatologies has been established with the CHAMPCLIM retrieval version 2.3 (CCRv2.3). A description of the CCRv2.3 and the related quality control is given by Borsche et al. (2006) and Gobiet et al. (2007). The construction of climatologies is described by Foelsche et al. (2008b). We used monthly-mean zonal-mean CHAMP dry temperature climatologies at 10° latitude resolution as a function of pressure up to 2.5 hPa (∼40 km) for the time span September 2001–December 2006. An example of a monthly climatology is shown in Fig. 2 (Sect. 3.1). No CHAMP data were available for July 2006 due to satellite problems. In addition, we used RO data from three other satellites as independent "anchor points", i.e., SAC-C for June, July, August (JJA) 2002, GRACE for July 2006, and COSMIC for December 2006. SAC-C (version 2005.3090 data set) and COSMIC (version 1 data set) phase delay and orbit data were provided by the University Corporation of Atmospheric Research/COSMIC Data Analysis and Archival Center (UCAR/CDAAC), Boulder (Rocken et al. 2000; Wu et al. 2005; Schreiner et al. 2007). GRACE phase delay and orbit data (version 2 data set) were provided by GFZ Potsdam (Wickert et al. 2005). The retrieval version CCRv2.3 has been applied to all RO data used in this study ensuring a consistent data set. Possible inhomogeneities which may be introduced due to phase and orbit data stemming from different processing centers are currently under investigation. Regarding synthetic MSU bulk temperatures the implications are estimated to be smaller than the sampling error estimates.

2.2 ECMWF Analyses

The ECMWF produces daily analyses through combination of a short-range forecast with observational data based on four-dimensional variational assimilation (ECMWF 2004). A resolution of T511L60 was used until February 2006, then a major resolution upgrade was introduced on February 1, 2006 by increasing the horizontal resolution to T799 and the vertical resolution to 91 levels (Untch et al. 2006). ECMWF analysis fields are operationally used as reference data in the Weg-Center/UniGraz processing system, at a resolution of T42L60 until February 2006 and of T42L91 since then, at four time layers per day (00 UTC, 06 UTC, 12 UTC, 18 UTC). ECMWF climatologies were produced from the individual analyses at the same resolution as CHAMP climatologies for the same time span.

2.3 MSU/AMSU Brightness Temperatures

MSU as a four channel radiometer provided layer average brightness temperatures for four respective atmospheric layers. Channels 2 and 4 correspond to the temperature in the middle troposphere (TMT) and the lower stratosphere (TLS), respectively. Since 1998 AMSU samples the atmosphere using 20 spectral channels, with channels 5 and 9 closely matching MSU's channels 2 and 4, respectively, ensuring the continuation of the temperature time series (Christy et al. 2003). In parallel, MSU data have been processed through December 2004. AMSU data showed error characteristics indistinguishable from the earlier MSU products justifying the generation of a homogenous MSU/AMSU time series. The bias between AMSU9 and MSU4 was found to be about 0.3 K, which is a value within the range of biases determined amongst the MSUs themselves (Christy et al. 2003). Daily gridpoint ($2.5^\circ \times 2.5^\circ$ bins) noise estimates for TLS are < 0.2 K in the tropics, increasing to 0.3–0.4 K (0.5–0.6 K) in the Northern (Southern) Hemisphere mid-latitudes (http://ghrc.nsstc.nasa.gov/uso/readme/msulimb93.html#1). We used version 5.1 of MSU data produced by UAH. Data were available at http://vortex.nsstc.uah.edu/data/msu for December 1978–December 2006. We used version 2.1 of MSU data produced by RSS and sponsored by the NOAA Climate and Global Change Program. Data were available at www.remss.com for November 1978–December 2006. Monthly-mean brightness temperature anomalies are provided by UAH and RSS on a $2.5^\circ \times 2.5^\circ$ latitude/longitude grid between $\pm 82.5^\circ$ together with 20 year monthly means over 1979–1998.

2.4 HadAT2 Radiosonde Data

HadAT2 temperatures are provided as monthly anomalies with respect to the monthly 1966–1995 climatology from the year 1958 to present (10° longitude by 5° latitude grid on nine pressure levels). A detailed description of the construction of the HadAT2 data set was given by Coleman and Thorne (2005) and by Thorne

Table 1 Characteristics of the original data sets including information on version and horizontal resolution as well as available time period and basic sampling (Steiner et al. 2007)

Data set characteristics

Data set	Version	Horizontal resolution	Time period monthly data	Basic sampling per day globally
CHAMP RO	CCR v2.3	10° zonal means	09/2001–12/2006	~ 150 profiles
SAC-C RO			06/2002–08/2002	~ 150 profiles
GRACE RO			06/2006	~ 150 profiles
COSMIC RO			12/2006	~ 200 profiles/satellite, 2 satellites used
ECMWF	T42L60	10° zonal means	09/2001–01/2006	~ 8 000 grid points, 4 times/day
	T42L91		02/2006–12/2006	
MSU/AMSU	RSS v2.1	2.5° lat × 2.5° lon	11/1978–12/2006	~ 30 000 TLS observations
	UAH v5.1	2.5° lat × 2.5° lon	12/1978–12/2006	
HadAT2 MSU	HadAT2	5° zonal means	01/1958–12/2006	1–2 soundings, 676 stations

et al. (2005b). Standard deviations of global monthly temperature anomalies of radiosonde time-series are about 0.45 K in the stratosphere (Seidel et al. 2004).

Sampling errors become important in the Southern Hemisphere where not all latitude bands are represented and above 100 hPa where there is a significant reduction of measurements. Due to systematic uncertainties (daytime biases) and limitations in the homogenization method trends from HadAT2 are potentially underestimated in the tropical troposphere (McCarthy et al. 2008). This problem may be overcome with new adjusted radiosonde time series (Haimberger 2007; Haimberger et al. 2008) which will be better suited for future climate studies.

Synthetic MSU temperatures based on HadAT2 were available from the Hadley Centre/Met Office, UK, at www.hadobs.org. We used monthly-mean zonal-means at 5° latitude resolution for TLS, which were available for January 1958–December 2006. The data set characteristics are summarized in Table 1.

3 Method

The analysis was performed for monthly and zonal means for four regions, one global region (more precisely quasi-global, 70°S to 70°N), and three sub-regions: tropics (20°S to 20°N), Northern Hemisphere (NH) extratropics (30°N to 70°N) and Southern Hemisphere (SH) extratropics (30°S to 70°S), respectively (see Fig. 2). The comparison was made for the years 2001–2006.

The different data sets were brought to the same basic setup. RO climatologies were provided as 10° zonal means based on averaging of individual RO profiles weighted by the cosine of the latitude (Foelsche et al. 2008b). We note that in case of fewer and irregularly distributed occultations (e.g., GPS/MET) spatial mapping functions might be used in such zonal bands (Schrøder et al. 2003). MSU/AMSU data from UAH and RSS were averaged to 2.5° zonal means. Then weighted averages (weighted by the cosine of the latitude) for the four regions were produced.

Synthetic TLS temperatures were calculated for RO and ECMWF data by applying global weighting functions to zonal-mean monthly-mean temperature climatology profiles and alternatively by applying the RTTOV_8.5 radiative transfer model to the individual profile data set. TLS temperature anomalies were calculated for each data set using the monthly-mean averaged over the years 2002–2005 as reference. The CHAMP averages were used as basis for the computation of the anomaly values of the SAC-C, GRACE, and COSMIC months as well. A detailed description on the calculation procedure is given in Steiner et al. (2007).

3.1 Synthetic MSU Temperatures Using Weighting Functions

The vertical weighting function describes the relative contribution that microwave radiation emitted by a layer in the atmosphere makes to the total intensity measured above the atmosphere on board a satellite. Thus, the brightness temperature for each MSU/AMSU channel corresponds to an average temperature of the atmosphere averaged over that channel's weighting function. For the vertical profile of TLS, 90% of the emissions are generated from the layer between 150 hPa (~12 km) and 20 hPa (~26 km). In the tropics, about 20% of the emissions contributing to TLS originate below the tropopause, here TLS does not exclusively represent stratospheric temperature anomalies (Christy et al. 2003).

RSS provided the weighting functions as instantaneous values at given altitudes whilst UAH provided static mean weighting functions over 5 hPa layers. Both types of weighting functions were converted to CHAMP pressure levels (Fig. 3) and applied to CHAMP temperature climatology profiles. Due to the small differences

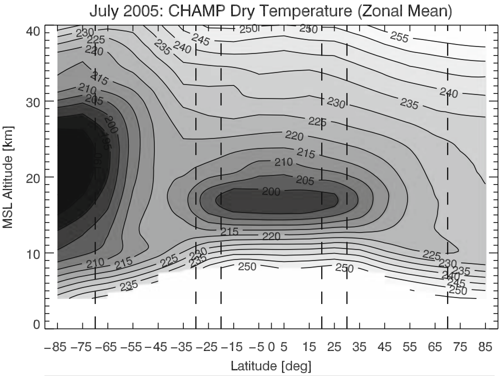

Fig. 2 CHAMP temperature climatology for July 2005, monthly and zonal means for 10° latitude bands on 0.2 km vertical grid. Investigated regions (*dashed*): global (70°S to 70°N), tropics (20°S to 20°N), NH/SH extratropics (30°N to 70°N)/(30°S to 70°S) (Steiner et al. 2007)

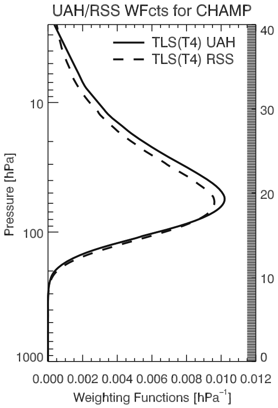

Fig. 3 MSU/AMSU TLS weighting functions from RSS and UAH at CHAMP pressure levels. The respective vertical gridding is indicated on the height axis (*right*)

of the CHAMP TLS temperatures derived with the different weighting functions, the averaged TLS temperature of the two was used for further comparison.

3.2 Synthetic MSU Temperatures Using RTTOVS_8.5

As a validity test we alternatively applied the state-of-the-art RTTOV_8.5 radiative transfer model (Saunders and Brunel 2004; Saunders et al. 2006) to the individual CHAMP RO profile data set for the whole time period under study. The RTTOV_8.5 model was available from the MetOffice (Exeter, UK) at http://www.metoffice.gov.uk/research/interproj/nwpsaf/rtm/. Radiative transfer models account for land/sea differences in surface emissivity and for variations in atmospheric temperature and moisture as a function of space and time. According to Santer et al. (2000) the two methods agree best in the lower stratosphere, since the TLS temperatures are largely insensitive to tropospheric and surface variability. They found trend differences of < 0.01 K/decade globally and < 0.02 K/decade on hemispheric scales arising from the choice of method for computing equivalent MSU temperatures (Santer et al. 2000) which has been confirmed by the results of the current study (see Sect. 4.2).

4 Results and Discussion

4.1 Comparison of TLS Temperatures

Results of the comparison of synthetic CHAMP TLS temperatures to MSU/AMSU records from UAH and RSS as well as to synthetic ECMWF and HadAT2 TLS temperatures are presented in Fig. 4 for the tropical region. SAC-C, GRACE, and COSMIC "anchor point" months are also shown, their TLS temperatures closely match CHAMP temperatures within the sampling error range of < 0.3 K (Fig. 4a). Regarding absolute TLS temperatures (Fig. 4a), ECMWF agrees best with RSS until January 2006, then it closely follows CHAMP due to improvement in ECMWF resolution. Global offsets relative to CHAMP are 0.11 K (± 0.31 K) for UAH and -0.69 K (± 0.16 K) for RSS. These different offsets can be explained by the different reference climatologies provided by UAH and RSS (for the calculation of absolute temperatures) due to different processing, calibration, and merging procedures. A detailed discussion is given in Steiner et al. (2007).

TLS temperature anomalies exhibit overall a very good agreement between UAH, RSS, ECMWF, and CHAMP in all analyzed regions for intra-annual variability (RMS of de-trended anomaly differences of the other data sets to CHAMP < 0.1 K globally, 0.1 K in the tropics, and < 0.25 K in the extratropics). Highest variability of all data sets occurs in the SH extratropics, where especially HadAT2 anomalies exhibit larger RMS differences (about a factor of two; factor of four in the SH extratropics due to sparse data).

Fig. 4 Synthetic TLS temperatures from CHAMP compared to real MSU/AMSU records from UAH (*blue*) and RSS (*red*), as well as HadAT radiosonde (*green*) records and ECMWF (*yellow*) shown for the tropical region. "Anchor point" months from SAC-C, GRACE, and COSMIC are marked with *black dots*. (**a**) Monthly-mean absolute TLS temperatures. (**b**) TLS temperature anomalies with respect to 2002–2005 average seasonal cycle. (**c**) Monthly mean TLS anomaly differences relative to CHAMP

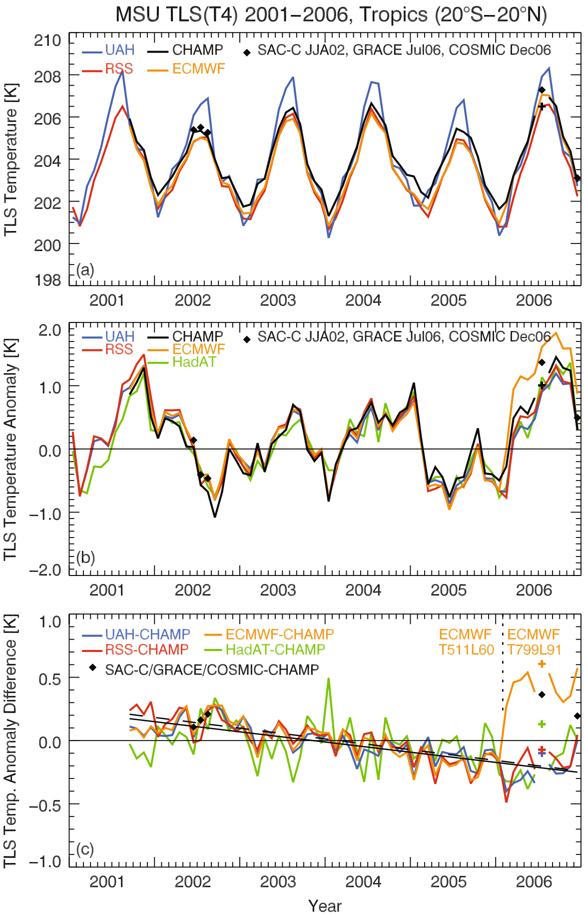

SAC-C, COSMIC, and GRACE show a difference to CHAMP of 0.1–0.2 K, ~0.2 K, and ~0.3 K, respectively, which is consistent with the sampling error of these RO satellites (cf. Pirscher et al. 2007). The close matching of independent RO data from different satellites in very different orbits indicates the consistency and homogeneity of the RO data set.

The anomaly differences of the UAH, RSS, HadAT2, and ECMWF to CHAMP RO are illustrated in Fig. 4c with the multi-year trends of UAH and RSS indicated as trend lines. Regarding multi-year trend differences, HadAT2 shows no appreciable difference from CHAMP trends. UAH and RSS exhibit a statistically significant (at >95% confidence level) cooling trend difference relative to CHAMP globally (–0.30 K/5 years and –0.36 K/5 years), with main contributions from the tropics (–0.40 K/5 years and –0.42 K/5 years), while in the extratropics the trend differences are not significant. The results in the tropics are basically consistent with the findings by Ho et al. (2007) showing values of −0.1 K (−0.2 K) between UAH

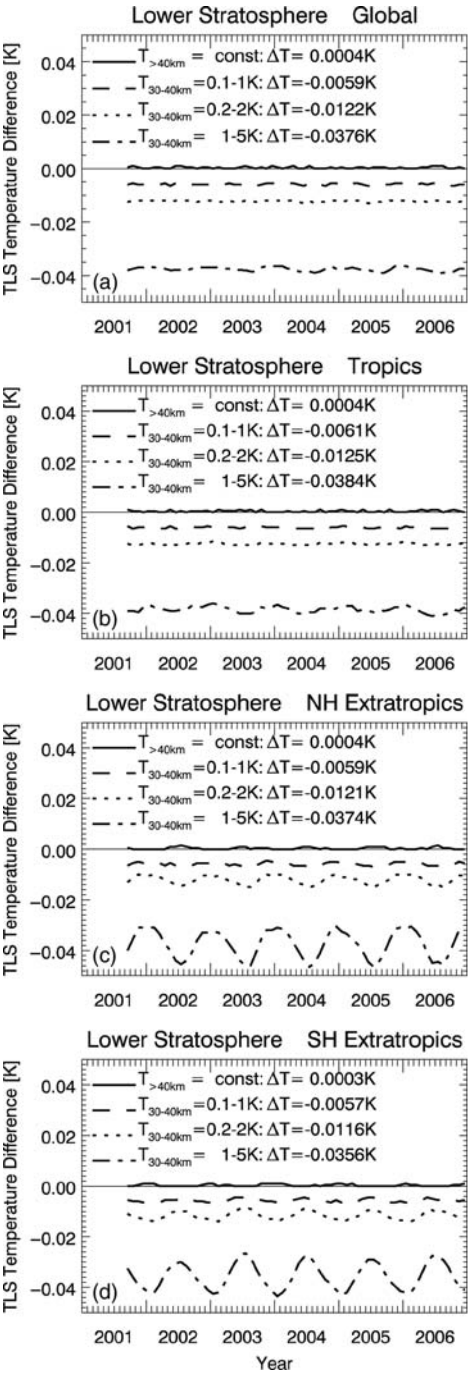

Fig. 5 CHAMP RO initialization bias tests for TLS temperature (perturbed minus unperturbed) for the global region (**a**), the tropics (**b**), NH extratropics (**c**), and SH extratropics (**d**)

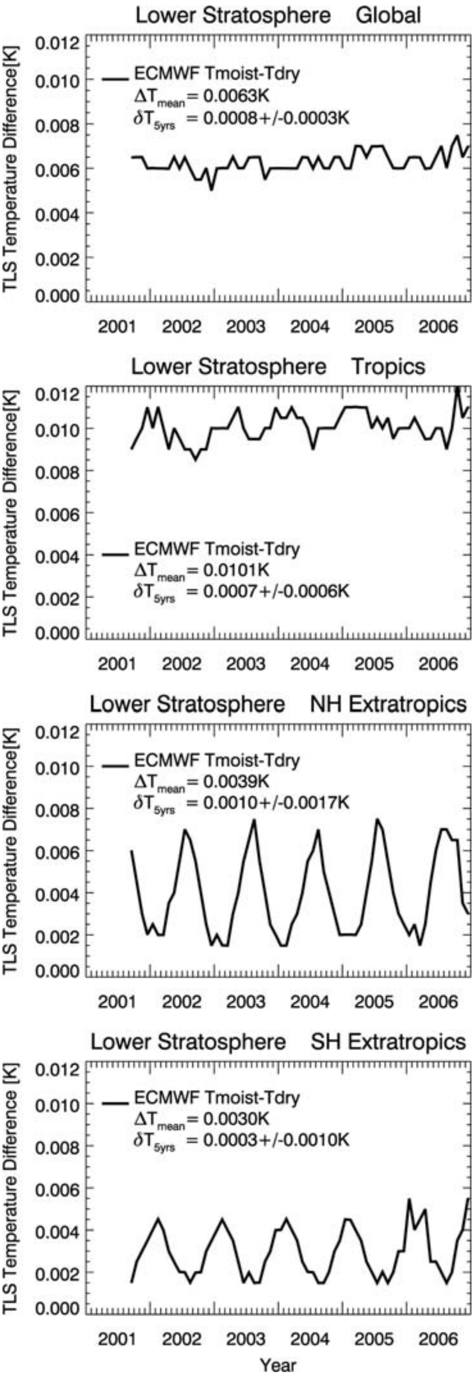

Fig. 6 TLS temperature difference of physical minus dry ECMWF temperature shown for the global region (**a**), the tropics (**b**), NH extratropics (**c**), and SH extratropics (**d**)

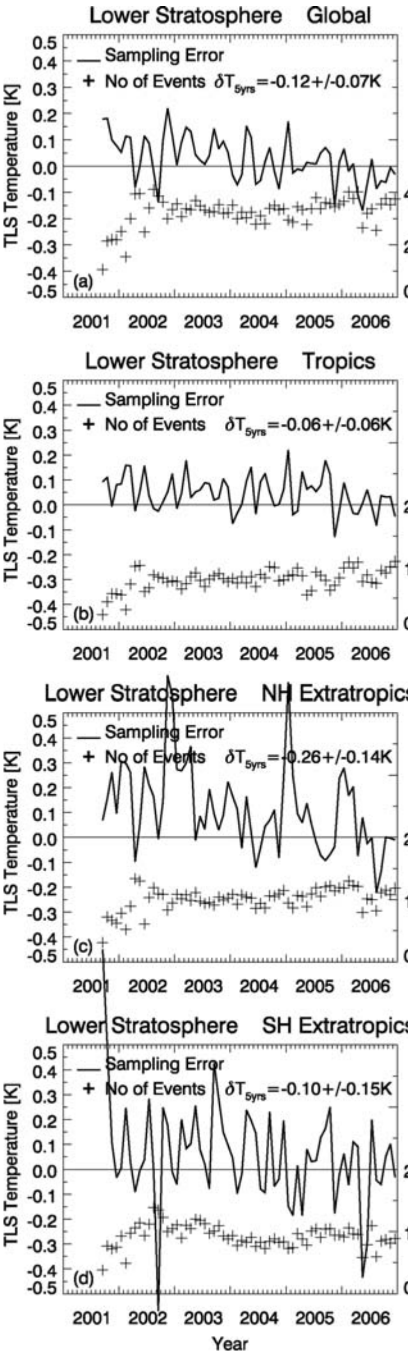

Fig. 7 Sampling error and number of occultations for CHAMP TLS temperature shown for the global region (**a**), the tropics (**b**), NH extratropics (**c**), and the SH extratropics (**d**)

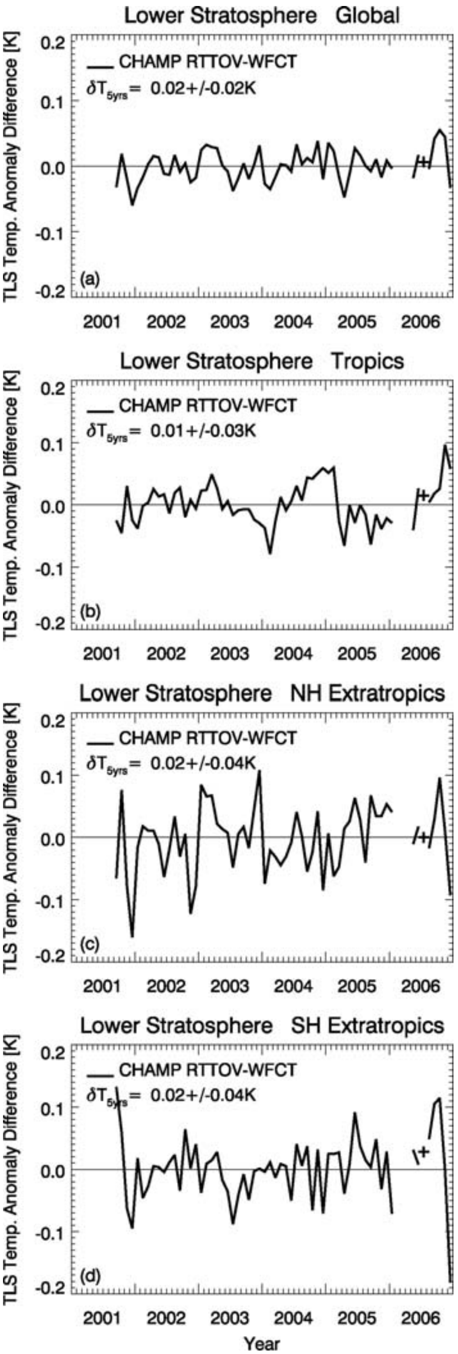

Fig. 8 TLS temperature anomaly difference: using RTTOV_8.5 minus using global weighting functions. No data for Feb–May 2006 due to technical reasons. Regions same as Fig. 7

(RSS) with respect to CHAMP, the lower values can be explained by a different sampling of MSU data and a different investigated time span (June 2001–June 2005).

4.2 Discussion of Error Contributions to RO TLS Data

We investigated error sources regarding the retrieval of RO data (potential initialization biases, dry temperature assumption), the computation of climatologies (sampling error), and the related synthetic TLS computation procedure (weighting function versus radiative transfer model).

Potential Initialization Biases: In the CCRv2.3 retrieval observed bending angle profiles are combined with background bending angle profiles (ECMWF analyses) in a statistically optimal way to minimize residual biases in atmospheric profiles below 35 km. For each observed RO profile, collocated bending angle profiles are computed from the ECMWF analysis field and expanded at up to 120 km using MSISE-90 climatology. This allows the initialization of the hydrostatic integral at very high altitudes (120 km), where the upper-boundary initialization has no effect on the retrieved atmospheric parameters below 40 km. The resulting atmospheric profiles are background-dominated above the stratopause and observation-dominated below 40 km (see Schrøder et al. (2007) on the importance of the stratopause concerning RO initialization). From validation with independent data sets it was found that potential temperature biases are < 0.2 K in the global mean within 10 km–30 km. Latitudinally resolved analyses show observationally constrained biases of < 0.2 K to 0.5 K up to 35 km in most cases, and up to 30 km in any case, even if severely biased (about 10 K or more) a priori information is used in the high altitude initialization of the retrieval (Gobiet et al. 2007). CHAMP biases near 40 km can thus be expected not to exceed about 2 K. The effect of these levels of bias up to 40 km is small in MSU TLS data, due to the small weighting function contributions above 30 km. Perturbation tests are illustrated in Fig. 5 by means of perturbed minus unperturbed TLS temperatures. They showed that biases (or trends in biases over 5 years) linearly increasing from 0.1 K to 1 K or 0.2 K to 2 K from 30 km to 40 km lead to a bias in MSU TLS (or a trend in bias over 5 years) of < 0.006 K or < 0.015 K, respectively. Even an increase from 1 K at 30 km to a 5 K bias at 40 km (or a trend in bias of 5 K over 5 years) would lead to a spurious TLS change of < 0.04 K only.

Dry Temperature Assumption: RO dry temperature profiles are used throughout this study, i.e., the contribution of water vapor to refractivity is neglected. This dry air assumption always holds to < 0.1 K differences between actual physical and dry temperature at altitudes above 8 km in polar winter regimes and above 14 km in the tropics, respectively, with the dry temperature then becoming gradually colder than the actual one deeper into the troposphere as humidity increases (Foelsche et al. 2008b). We investigated this effect on the MSU TLS temperature based on checks with ECMWF analysis data by integrating over dry temperature as well as over physical temperature profiles. The difference in resulting synthetic TLS temperatures is shown in Fig. 6. We found a negligible mean difference (ΔT) over

2002–2006 of < 0.02 K in the tropics, of < 0.01 K globally and in the extratropics, respectively, with a negligible trend of < 0.001 K over the 5 year period. The trend is indicated as $\delta T_{5\ \mathrm{yrs}}$ with the two sigma uncertainty of the trend in Figs. 6, 7, and 8.

Sampling Error: Sampling error characteristics are estimated for CHAMP RO climatologies based on ECMWF analyses (for details see Gobiet et al. 2005; Steiner et al. 2006; Pirscher et al. 2007; Foelsche et al. 2008b). The sampling error for these single-satellite climatologies results from uneven and sparse sampling in space and time. The typical average CHAMP dry temperature sampling error for monthly zonal means in 10°-latitude bands is < 0.3 K in the upper troposphere and lower stratosphere, with the local time component of sampling error being < 0.15 K (Pirscher et al. 2007). For the investigated CHAMP data set the average number of occultation events per month in the regions was 3364 globally, 832 for the tropics, 1044 for the NH extratropics, and 951 for the SH extratropics, respectively. Figure 7 shows the number of events over time as well as the corresponding average monthly sampling error for the TLS temperatures (TLS weighting function applied to the sampling error profile). The 2002–2006 standard deviation of the sampling error was estimated to 0.08 K globally, 0.07 K for the tropics, 0.18 K for the NH extratropics, and 0.17 K for the SH extratropics, respectively. Other than the 10 km–40 km bulk layer estimate of the sampling error (used in Steiner et al. 2007) the TLS specific sampling error interestingly shows a significant trend over 2002–2006 in the NH extratropics (-0.26 K±0.14 K, Fig. 7c) which also projects globally (-0.12 K±0.07 K, Fig. 7a) while tropical trends are small (-0.06 K±0.06 K, Fig. 7b). This transient change in the CHAMP sampling may possibly be due to orbit changes of the CHAMP satellite and to changes in the GPS constellation over the investigated time period, respectively. It may partly relate also to the major resolution upgrade in ECMWF analyses per February 2006 (see Sect. 2.2), however, since 2002–2005 sampling error trends (not shown) are consistently smaller than 2002–2006 ones (e.g., NH extratropics -0.22 K±0.17 K, global -0.07 K±0.08 K, tropics -0.02 K±0.07 K). The present estimates are thus possibly conservative estimates for the "true" sampling error trends. Alternative estimates based on NCEP (National Centers for Environmental Prediction) reanalyses, and a closer look into CHAMP-GPS sampling pattern changes over time, will help in future to understand the estimates in more detail.

TLS Computation Procedure: A further possible error source is the synthetic MSU TLS computation procedure. The difference in absolute TLS brightness temperature between using either the TLS static weighting functions on monthly mean profiles or radiative transfer modeling for the RTTOV channel MSU4 on individual profiles was found on average < 0.2 K (individual maxima of monthly values $\sim$0.3 K) for all four regions used in this study. This is within the MSU4 and AMSU9 bias estimates of Christy et al. (2003). As shown in Fig. 8, the mean differences in TLS anomalies (using RTTOV minus using weighting functions) were found to be 0.002 K±0.02 K globally, 0.003 K±0.03 K in the tropics, and 0.001 K±0.05 K in the NH/SH extratropics. Overall they are < 0.1 K for all four regions, except for a few individual months in the extratropics (still < 0.2 K). The differences do not show any significant drift over 2002–2006 (i.e., < 0.02 K). These results are consistent with those of Santer et al. (2000) that using a radiative transfer model or a suitable global weighting function for computing TLS temperatures yields to a negligible difference in global and large-scale zonal means.

5 Summary, Conclusions, and Outlook

Steiner et al. (2007) carried out a comparison of MSU/AMSU TLS temperatures from UAH and RSS, as well as of HadAT2 and ECMWF synthetic TLS temperatures, with synthetic TLS temperatures derived from CHAMP RO. Synthetic TLS temperatures were calculated by applying global weighting functions to RO temperature climatology profiles and alternatively by applying the RTTOV_8.5 radiative transfer model to the individual CHAMP RO profile data set. The analysis was performed for September 2001–December 2006 for four regions, almost global (70°S to 70°N), tropics (20°S to 20°N), NH extratropics (30°N to 70°N) and SH extratropics (30°S to 70°S). Statistically significant trend differences between UAH and RSS to CHAMP TLS anomalies were found globally (–0.30 K/5 years to –0.36 K/5 years), stemming mainly from the tropics (–0.40 K/5 years to –0.42 K/5 years), whilst in the extratropics these cooling trend differences were not significant.

In this respect known error sources regarding the retrieval of RO data, the building of climatologies, and the related computation procedure of synthetic MSU temperatures were investigated and this study presented a closer analysis of these errors. The analysis yielded estimates of RO trend uncertainty over 5 years of < 0.02 K for potential initialization bias drifts, of < 0.02 K for dry/physical temperature difference, of about -0.1 K for TLS sampling error drift (significantly smaller in the tropics), and of < 0.02 K for weighting function/radiative transfer model uncertainty. The total contribution of these known error sources to the 5-year trend differences is about an order of magnitude smaller than the detected trend differences, and thus insufficient to account for them, especially in the tropical region.

The trend discrepancy is currently investigated in a follow on study and its resolution requires either additional, so far overlooked, sources of error in the RO TLS record or the presence of currently unresolved biases in the MSU records. Future inter-comparison of trends in RO data records of independent processing centers, and trace-back to the international time standard is planned to help quantify potential residual bias drifts.

For example, 2002–2006 RO records of four data centers (GFZ Potsdam, JPL Pasadena, UCAR/CDAAC Boulder, WegCenter Graz) indicated a temperature trend uncertainty amongst the four data sets of < 0.1 K/5 years at 10 km–30 km height in the regions studied here (Ho et al. analysis, B. Ho, UCAR Boulder, pers. communications, 2007). This is again much smaller than the trend differences found relative to MSU.

Furthermore, we found that SAC-C, GRACE, and COSMIC TLS temperatures closely match CHAMP temperatures, indicating the consistency and homogeneity of the RO data series.

The results underpin the benefit of having multiple independent estimates of the same variable from different instruments for detecting residual weaknesses in otherwise high-quality climate records. Continued inter-comparison, and exploiting the traceability of the RO data to the universal time standard (UTC), then enables us to further reduce the uncertainty in the climate records in absolute terms.

Acknowledgements The authors acknowledge GFZ (Potsdam, Germany) for the provision of CHAMP and GRACE RO data and ECMWF (Reading, UK) for access to their global operational analyses data. UCAR/CDAAC (CO, USA) is thanked for the provision of SAC-C and COSMIC data. UAH (AL, USA), RSS (CA, USA), and Hadley Centre/MetOffice (Exeter, UK) are acknowledged for the provision of MSU records. We thank J. Christy (UAH, AL, USA) for the provision of static weighting functions and his complementary helpful comments. We are grateful to H. Coleman (MetOffice/Hadley Centre, Exeter, UK) for her help regarding the HadAT2 data. The authors thank B. Ho (UCAR, Boulder, USA) for valuable discussions on the topic. The work was supported by the Austrian Science Fund (FWF; START Programme Y103-N03, Project INDICATE, P18733-N10, and Project CLIMROCC, P18837-N10). UF received financial support from the Max Kade Foundation (New York, NY, USA) and from UCAR.

References

Borsche M, Gobiet A, Steiner AK, Foelsche U, Kirchengast G, Schmidt T, Wickert J (2006) Pre-operational retrieval of radio occultation based climatologies. In: Foelsche U, Kirchengast G, Steiner AK (eds) Atmosphere and Climate: Studies by Occultation Methods, Springer-Verlag, Berlin Heidelberg New York, pp 315–323, doi:10.1007/3-540-34121-8_26

Borsche M, Kirchengast G, Foelsche U (2007) Tropical tropopause climatology as observed with radio occultation measurements from CHAMP compared to ECMWF and NCEP analyses. Geophys Res Lett 34:L03702, doi:10.1029/2006GL027918

Christy JR, Spencer RW (2005) Correcting temperature data sets. Science 310(5750):972–973

Christy JR, Spencer RW, Norris WB, Braswell WD, Parker DE (2003) Error estimates of version 5.0 of MSU AMSU bulk atmospheric temperatures. J Atmos Ocean Technol 20(5):613–629

Coleman H, Thorne PW (2005) HadAT: An update to 2005 and development of the dataset website. Internal Rep for DEFRA MS-RAND-COO-PROG0407, 11 pp (http://www.hadobs.org)

European Centre for Medium-Range Weather Forecasts (ECMWF) (2004) IFS Documentation CY28rl, Reading, UK

Foelsche U, Kirchengast G, Steiner AK, Kornblueh L, Manzini E, Bengtsson L (2008a) An observing system simulation experiment for climate monitoring with GNSS radio occultation data: Setup and test bed study. J Geophys Res 113:D11108, doi:10.1029/2007JD009231

Foelsche U, Borsche M, Steiner AK, Gobiet G, Pirscher B, Kirchengast G, Wickert J, Schmidt T (2008b) Observing upper troposphere-lower stratosphere climate with radio occultation data from the CHAMP satellite. Clim Dyn 31:49–65, doi:10.1007/s00382-007-0337-7

Foelsche U, Pirscher B, Borsche M, Kirchengast G, Wickert J (2009a) Assessing the climate monitoring utility of radio occultation data: From CHAMP to FORMOSAT-3/COSMIC. Terr Atmos Oceanic Sci 20(1):155–170,doi: 10.3319/TAO.2008.01.14(F3C)

Foelsche U, Pirscher B, Borsche M, Steiner AK, Kirchengast G, Rocken C (2009b) Climatologies based on radio occultation data from CHAMP and Formosat-3/COSMIC. In: Steiner A, Pirscher B, Foelsche U, Kirchengast G (eds) New Horizons in Occultation Research, Springer-Verlag, Berlin Heidelberg, doi:10.1007/978-3-642-00321-9_15

Gobiet A, Foelsche U, Steiner AK, Borsche M, Kirchengast G, Wickert J (2005) Climatological validation of stratospheric temperatures in ECMWF operational analyses with CHAMP radio occultation data. Geophys Res Lett 32:L12806, doi:10.1029/2005GL022617

Gobiet A, Kirchengast G, Manney GL, Borsche M, Retscher C, Stiller G (2007) Retrieval of temperature profiles from CHAMP for climate monitoring: Intercomparison with Envisat MIPAS and GOMOS and different analyses. Atmos Chem Phys 7:3519–3536

Grody NC, Vinnikov KY, Goldberg MD, Sullivan JT, Tarpley JD (2004) Calibration of multisatellite observations for climatic studies: Microwave Sounding Unit (MSU). J Geophys Res 109, D24104, doi:10.1029/2004JD005079

Haimberger L (2007) Homogenization of radiosonde temperature time series using innovation statistics. J Clim 20(7):1377–1403, doi:10.1175/JCLI4050.1

Haimberger L, Tavolato C, Sperka S (2008) Towards elimination of the warm bias in historic radiosonde temperature records – some new results from a comprehensive intercomparison of upper-air data. J Climate 21(18):4587–4606, doi:10.1175/2008JCLI1929.1

Ho SP, Kuo YH, Zeng Z, Peterson TC (2007) A comparison of lower stratosphere temperature from microwave measurements with CHAMP GPS RO data. Geophys Res Lett 34, L15701, doi:10.1029/2007GL030202

Karl TR, Hassol SJ, Miller CD, Murray WL (eds) (2006) Temperature trends in the lower atmosphere: Steps for understanding and reconciling differences. Rep by the Climate Change Science Program and the Subcommittee on Global Change Research, Washington DC

Lanzante JR, Klein SA, Seidel DJ (2003) Temporal homogenization of monthly radiosonde temperature data. Part I: Methodology. J Clim 16(2):224–240

Leroy SS, Dykema JA, Anderson JG (2006) Climate benchmarking using GNSS occultation. In: Foelsche U, Kirchengast G, Steiner AK (eds) Atmosphere and Climate: Studies by Occultation Methods, Springer-Verlag, Berlin Heidelberg, New York, pp 287–301, doi:10.1007/3-540-34121-8_24

McCarthy MP, Titchner HA, Thorne PW, Tett SFB, Haimberger L, Parker DE (2008) Assessing bias and uncertainty in the HadAT-adjusted radiosonde climate record. J Clim 21(4):817–832, doi:10.1175/2007JCLI1733.1

Mears CA, Wentz FJ (2005) The effect of diurnal correction on satellite-derived lower tropospheric temperature. Science 309:1548–1551, doi:10.1126/science.1114772

Pirscher B, Foelsche U, Lackner BC, Kirchengast G (2007) Local time influence in single-satellite radio occultation climatologies from Sun-synchronous and non-Sun-synchronous satellites. J Geophys Res 112:D11119, doi:10.1029/2006JD007934

Rocken C, Kuo YH, Schreiner WS, Hunt D, Sokolovskiy S, McCormick C (2000) COSMIC system description. Terr Atmo Ocean Sci 11(1):21–52

Santer BC, Wigley TML, Boyle JS, Gaffen DJ, Hnilo JJ, Nychka D, Parker DE, Taylor KE (2000) Statistical significance of trends and trend differences in layer-average atmospheric temperature time series. J Geophys Res 105(D6):7337–7356

Santer BD, et al. (2005) Amplification of surface temperature trends and variability in the tropical atmosphere. Science 309:1551–1556, doi:10.1126/science.1114867

Saunders R, Brunel P (2004) RTTOV_8_5 Users guide, NWPSAF-MO-UD-008, EUMETSAT (available at http://www.metoffice.gov.uk/research/interproj/nwpsaf/rtm/rttov8_ug.pdf)

Saunders R et al. (2006) RTTOV-8 – Science and validation report, NWPSAF-MO-TV-007, EUMETSAT. (available at http://www.metoffice.gov.uk/research/interproj/nwpsaf/rtm/rttov8_svr.pdf)

Schmidt T, Wickert J, Beyerle G, Reigber C (2004) Tropical tropopause parameters derived from GPS radio occultation measurements with CHAMP. J Geophys Res 109:D13105, doi:10.1029/2004JD004566

Schreiner W, Rocken C, Sokolovskiy S, Syndergaard S, Hunt D (2007) Estimates of the precision of GPS radio occultations from the COSMIC/FORMOSAT-3 mission. Geophys Res Lett 34:L04808, doi:10.1029/2006GL027557

Schrøder T, Leroy S, Stendel M, Kaas E (2003) Validating the microwave sounding unit stratospheric record using GPS occultation. Geophys Res Lett 30(14):1734, doi:10.1029/2003GL017588

Schrøder TM, Ao CO, de la Torre Juárez M (2007) Sensitivity of GPS occultation to the stratopause height. J Geophys Res 112:D06119, doi:10.1029/2006JD007330

Seidel DJ, et al. (2004) Uncertainty in signals of large-scale climate variations in radiosonde and satellite upper-air temperature datasets. J Clim 17(11):2225–2240

Sherwood SC, Lanzante JR, Meyer CL (2005) Radiosonde daytime biases and late-20th century warming. Science 309:1556–1559

Steiner AK, Löscher A, Kirchengast G (2006) Error characteristics of refractivity profiles retrieved from CHAMP radio occultation data. In: Foelsche U, Kirchengast G, Steiner AK (eds) Atmosphere and Climate: Studies by Occultation Methods, Springer-Verlag, Berlin Heidelberg, New York, pp 27–36

Steiner AK, Kirchengast G, Borsche M, Foelsche U, Schoengassner T (2007) A multi-year comparison of lower stratospheric temperatures from CHAMP radio occultation data with MSU/AMSU records. J Geophys Res 112:D22110, doi:10.1029/2006JD008283

Thorne PW, Parker DE, Christy JR, Mears CA (2005a) Uncertainties in climate trends: Lessons from upper-air temperature records. Bull Am Meteorol Soc 86:1437–1442

Thorne PW, Parker DE, Tett SFB, Jones PD, McCarthy M, Coleman H, Brohan P (2005b) Revisiting radiosonde upper air temperatures from 1958 to 2002. J Geophys Res 110:D18105, doi:10.1029/2004JD005753

Untch A, Miller M, Hortal M, Buizza R, Janssen P (2006) Towards a global meso-scale model: The high-resolution system T799L91 and T399L62 EPS. ECMWF Newsl 108:6–13

Vinnikov KY, Grody NC, Robock A, Stouffer RJ, Jones PD, Goldberg MD (2006) Temperature trends at the surface and in the troposphere. J Geophys Res 111:D03106, doi:10.1029/2005JD006392

Wickert J, Schmidt T, Beyerle G, König R, Reigber C, Jakowski N (2004) The radio occultation experiment aboard CHAMP: Operational data analysis and validation of vertical atmospheric profiles. J Met Soc Jpn 82:381–395

Wickert J, Beyerle G, König R, Heise S, Grunwaldt L, Michalak G, Reigber C, Schmidt T (2005) GPS radio occultation with CHAMP and GRACE: A first look at a new and promising satellite configuration for global atmospheric sounding. Ann Geophys 23(3):653–658

Wu BH, Chu V, Chen P, Ting T (2005) FORMOSAT-3/COSMIC science mission update. GPS solut 9:111–121, doi:10.1007/s10291-005-0140-z

SimVis: An Interactive Visual Field Exploration Tool Applied to Climate Research

F. Ladstädter, A.K. Steiner, B.C. Lackner, G. Kirchengast, P. Muigg, J. Kehrer, and H. Doleisch

Abstract Climate research often deals with large multi-dimensional fields describing the state of the atmosphere. A novel approach to gain information about these large data sets has become feasible only recently using 4D visualization techniques. The *Sim*ulation *Vis*ualization (SimVis) software tool, developed by the VRVis Research Center (Vienna, Austria), uses such techniques to provide access to the data interactively and to explore and analyze large three-dimensional time-dependent fields. Non-trivial visualization approaches are applied to provide a responsive and useful interactive experience for the user. In this study we used SimVis for the investigation of climate research data sets. An ECHAM5 climate model run and the ERA-40 reanalysis data sets were explored, with the ultimate goal to identify parameters and regions reacting most sensitive to climate change, representing robust indicators. The focus lies on the upper troposphere-lower stratosphere (UTLS) region, in view of future applications of the findings to radio occultation (RO) climatologies. First results showing the capability of SimVis to deal with climate data, including trend time series and spatial distributions of RO parameters are presented.

1 Introduction

Since the upper troposphere-lower stratosphere (UTLS) region reacts sensitively to climate change, the variations of its fundamental parameters such as temperature, geopotential height of pressure levels, and refractivity are promising candidates for monitoring the climate. All these key parameters are provided by RO observations with high quality in the UTLS and have high potential for climate analysis and monitoring (e.g., Leroy et al. 2006; Steiner et al. 2007; Foelsche et al. 2008a,b, 2009) and shall be explored to find the most favorable indicators for

---

F. Ladstädter (✉)
Wegener Center for Climate and Global Change (WegCenter) and Institute for Geophysics, Astrophysics, and Meteorology (IGAM), University of Graz, Austria
e-mail: florian.ladstaedter@uni-graz.at

A. Steiner et al. (eds.), *New Horizons in Occultation Research*,
DOI 10.1007/978-3-642-00321-9_19,

monitoring global atmospheric change. Due to the limited time period of available RO data (available on a continuous basis only since September 2001) the parameters are explored in both reanalysis and global climate model (GCM) data first. Climate models such as the ECHAM5 of the Max-Planck-Institute for Meteorology (MPI-M) Hamburg provide long-term climate scenarios and are used over the time frame 1961–2064. Reanalysis data, e.g., the ERA-40 data set of the European Centre for Medium-Range Weather Forecasts (ECMWF), are used from 1961 onwards, with special focus on the time period after 1979 when satellite data were assimilated.

Complementary to classical trend testing methods to find the indicators of choice (Lackner et al. 2009), a novel approach to visually explore the climate data sets is used in this study. The interactive visual analysis tool SimVis (Doleisch et al. 2003; Kehrer 2007) has been developed with special focus on dealing with large data sets, which makes it particularly well applicable to the data fields occurring in climate research. In SimVis, different aspects of the whole data set can be concurrently analyzed in multiple linked views. The sophisticated feature specification tools of SimVis provide a way to interactively select regions of interest (the so-called *features*) in time and space. These techniques are used to gain an overview over all data sets, to easily reveal deficiencies in the data, and to localize regions of trends with high signal-to-noise ratio. No prior knowledge of the fields needs to be presumed, and no subset needs to be preselected, since the data can be explored as a whole at once. Interesting features can be specified while interactively exploring the field. These characteristics can be regarded as the main advantages compared to classical statistical methods.

Section 2 gives a brief description of the data sets used in this study. In Sect. 3 the SimVis software tool is presented and its application to climate data is explained. The results of the data set exploration are shown in Sect. 4, and conclusions are drawn in Sect. 5.

2 Data

The data sets explored are an ECHAM5 Special Report on Emissions Scenarios (SRES) A2 simulation (MPI-M Hamburg, Roeckner et al. (2003)) for the 4th Assessment Report of the Intergovernmental Panel of Climate Change (IPCC AR4) for the time period 1961–2064 and the ERA-40 reanalysis data set (obtained from the ECMWF data server, Simmons and Gibson (2000)) for the time period 1961–2002, respectively. Regarding the ECHAM5 A2 run starting 2001, the ECHAM5 IPCC 20th century run complemented the data before 2001.

The native resolutions were $1.875^\circ \times 1.875^\circ$ on 16 pressure levels for ECHAM5 and $2.5^\circ \times 2.5^\circ$ on 23 pressure levels for ERA-40, respectively. To obtain easy comparability, the data were regridded to a common $2.5^\circ \times 2.5^\circ$ grid in latitude and longitude and to 18 pressure levels ranging from 1000–10 hPa. Due to the limited representation of the 10 hPa level in ECHAM5 (Cordero and de F. Forster 2006), this upper boundary model level is not used in this study, and the highest level effectively interpreted becomes the 20 hPa level for ECHAM5.

In this study we concentrate on seasonal (northern) summer means (JJA), exploring the parameters temperature and refractivity from the ECHAM5 A2 run and geopotential height and temperature from ERA-40, respectively. Decadal averages and trends were generally used, i.e., 1966–2059 effective time span for ECHAM5 and 1966–1997 for ERA-40, respectively.

3 Method

To apply the feature-based visualization technique of SimVis to climate data, additional derived parameters were investigated. In this section the elements and terminology of SimVis are presented, followed by a description of how to apply those key elements to the climate data sets.

3.1 SimVis – The Simulation Visualization Tool

SimVis is a research software framework that was developed for the interactive visualization and analysis of complex (4D, multi-variate) data resulting from computational fluid dynamics (CFD) simulations, e.g., the injection and combustion processes in car engines (Doleisch et al. 2005; Schmidt et al. 2005). The key elements of this software framework such as *interactive feature specification and visualization*, *brushing*, *linked views*, *focus+context visualization*, *derived data*, or different types of *views*, are described in the following.

3.1.1 Feature-Based Visualization and Brushing

SimVis uses a *feature-based visualization* approach. This type of visualization is characterized by the possibility to focus on especially interesting subsets of the data, the so-called *features*. To give to the user the opportunity to interactively select features becomes increasingly important when dealing with larger data sets. In SimVis the user can specify features by a *brushing* mechanism in different views such as scatterplots and histograms. Brushing simply means to select data points directly on the screen (e.g., using the mouse), thus assigning a *degree of interest (DOI)* attribute to each data point. The DOI can be either 0 or 1 in the case of a discrete feature classification. In SimVis also fractional values of the DOI are possible, representing a "fuzzy" selection (Doleisch and Hauser 2002).

In the different views the user can select data attributes (variables) of interest (e.g., the temperature), which either stem directly from the imported data set or are derived attributes (e.g., the temperature trend).

3.1.2 Linked Views

Another important concept is the use of multiple, linked views. Different aspects of the data set are shown in several views side by side. Brushing in one view is immediately propagated to all other views (Doleisch 2004). Thus changing the selection in one of the views is immediately reflected in all other views, using a different coloring scheme for the selected data points. Visualizing different attributes (e.g., climate state variables or diagnostic variables derived from them) in the views easily reveals correlations as well as other distinctive features between the data attributes.

3.1.3 Focus+Context Visualization, 3D View

The 3D view is a core component of the visualization system and allows the user to orientate both in space and time (if time-dependent data is available). SimVis uses a *focus+context (F+C)* visualization (Hauser 2005): according to the DOI value, each data item is either drawn in an emphasized way (being *in focus*) or in a reduced style (e.g., transparent gray in the 3D view). This distinction is consistent through the linking in all views, but plays an especially important role in the 3D view (Fig. 1) . The user can easily distinguish between the relevant data with high degree of interest (colored) and the context (in gray) in which it is located.

3.1.4 Derived Data

In order not to limit the user only to the data attributes (variables) already available in the imported data set itself, SimVis provides the possibility to perform certain mathematical operations on the existing attributes. This concept is very flexible

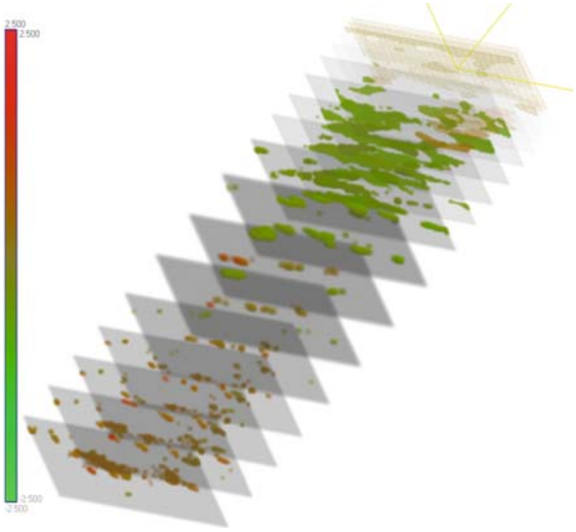

Fig. 1 SimVis 3D view. Shown is the trend in refractivity in the ECHAM5 data set for the year 2044 (seasonal summer means), for all pressure levels ("sheets") from 1000–20 hPa; each "sheet" itself is a latitude-vs.-longitude slice. Data points with high values of the signal-to-noise ratio (see Sect. 3.2) are selected ("in focus") and colored

and easily extendable in the SimVis system. Currently available formulae include, for example, temporal and spatial gradients, data smoothing, elementary algebraic expressions, and normalizations.

3.1.5 Types of Views

There are several types of views available in SimVis, the most important ones being scatterplot, histogram, curve, and 3D view. In scatterplot and histogram views selections can be made via the brushing mechanism explained above. The curve view (Kehrer 2007; Muigg et al. 2008) shows the variation in time of each data point, drawn on top of each other. In this view, advanced brushing mechanisms can be applied, such as selecting all curves going through a certain volume in time and parameter space. The 3D view is a *passive* view (i.e., no selections can be made here) displaying the specified features using F+C visualization. Here, interaction in space and time as well as viewing perspective changes are available.

3.2 SimVis Application to Climate Data

To apply the techniques of feature-based visualization to climate data sets, we need to think about what to consider as features of special interest. The basic parameters available such as temperature, refractivity, and geopotential height have rather well-known dependencies between each other, so additional insight is anticipated mainly from investigating newly derived parameters.

Two derived parameters are considered: The linear trend calculated as a moving 10-years-difference and the signal-to-noise ratio (SNR) defined as the ratio of the trend to the detrended standard deviation. To detect and explore regions sensitive to climate change in time and space, the features of interest are composed of high values for the linear trend while maintaining a high SNR. To obtain these features the following parameters are generated:

- Smoothed Data y^{av}: To generate the linear trend the data y is first smoothed using a moving arithmetic average with an averaging timeframe of 11 years.
- Linear Trend b: The linear trend per year b_i (where i denotes the center year of the current timeframe) is calculated as a moving 10-years difference between the data of year $i+5$ and year $i-5$ (Eq. 1). Due to the exponential character of the refractivity with height, the relative trend (in %) is generated in this case in relation to the first value of the current timeframe (Eq. 2).

$$b_i = \frac{1}{10}(y_{i+5}^{\mathrm{av}} - y_{i-5}^{\mathrm{av}}) \tag{1}$$

$$b_i^{\mathrm{rel}} = \frac{100}{y_{i-5}^{\mathrm{av}}}\frac{1}{10}(y_{i+5}^{\mathrm{av}} - y_{i-5}^{\mathrm{av}}). \tag{2}$$

- Linear Trend Fit Curve y^{FIT}: The trend fit curve for each 11-years timeframe is calculated using the above difference b_i as the slope:

$$y_{ij}^{\mathrm{FIT}} = y_{i-5}^{\mathrm{av}} + [j - (i - 5)]\, b_i, \tag{3}$$

  where i is the center year of the current 11-years timeframe and j runs from $i - 5$ to $i + 5$.

- Detrended Standard Deviation s: The fitted trend curve is removed from the original data y to obtain the detrended standard deviation for the current timeframe:

$$s_i = \left[\frac{1}{11 - 2} \sum_{j=i-5}^{i+5} \left(y_j - y_{ij}^{\mathrm{FIT}} \right)^2 \right]^{\frac{1}{2}}. \tag{4}$$

- Signal-to-Noise Ratio (SNR): Finally, the signal-to-noise ratio is defined as the ratio of the trend to the standard deviation:

$$\mathrm{SNR}_i = \frac{b_i}{s_i}. \tag{5}$$

4 Results

A selection of screenshots showing different aspects of the data using the derived parameters described in Sect. 3.2 (trends/10 years and SNR/10 years, respectively) is presented in Figs. 2 and 3 for the ECHAM5 model and in Figs. 4 and 5 for the ERA-40 reanalysis data, respectively. The color intensity depicts the density of the value in the whole data set. Features selected in several views are depicted in red, features selected only in the current view are shown in blue, and context information in black.

The distribution of the signal-to-noise ratio for each time-step for temperature and refractivity is shown in Fig. 2a and 2d, respectively. Selected are values of the $|\mathrm{SNR}| \geq 1$. This selection is carried out directly in the scatterplot using the brushing mechanism described in Sect. 3.1.1. Any change in this selection (or in any of the subsequently described ones) is immediately propagated into all other views. In Fig. 2b and 2e , the variation of the linear trend (relative trend for the refractivity) over time is shown using the curve view. The additional constraint of selecting high SNR values reflects in the red colored curves. The inversely proportional behavior of temperature and refractivity is clearly observed. Note that the negative temperature (positive refractivity) trend with high significance (high SNR) is prominent over the whole time period, compared to the positive temperature (negative refractivity) trend with high significance only visible in later time periods.

The trend distribution with latitude in Fig. 2c and 2f shows, among other things, that points with high trend values are often also associated with comparably low SNR values (in blue).

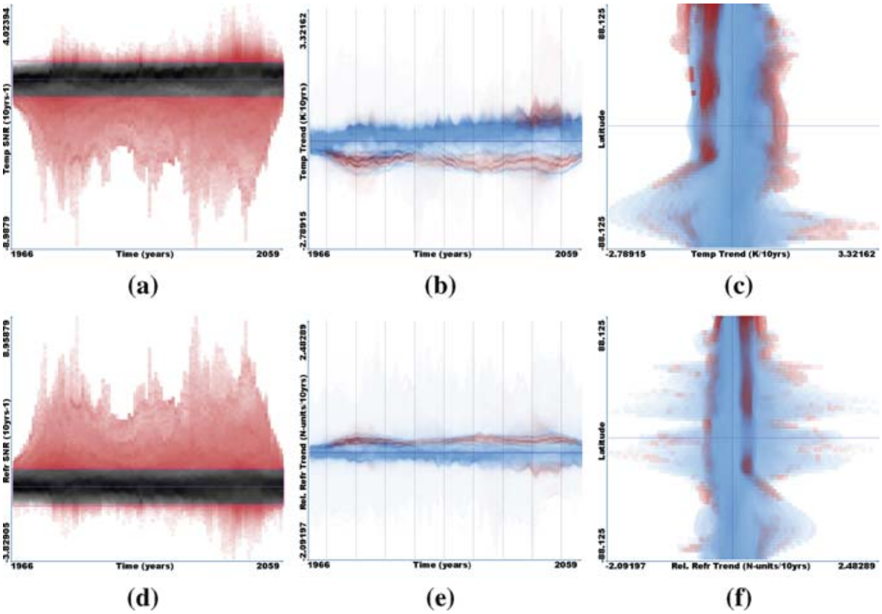

(a) (b) (c)

(d) (e) (f)

Fig. 2 ECHAM5 A2, temperature (in K) in (**a**)–(**c**) and refractivity (in N-units) in (**d**)–(**f**): Selection of high values of SNR in (**a**)/(**d**), the corresponding pattern in the trend variation over time in (**b**)/(**e**), and the trend distribution vs. latitude in (**c**)/(**f**) are depicted. |SNR| ≥ 1 shown in *red*

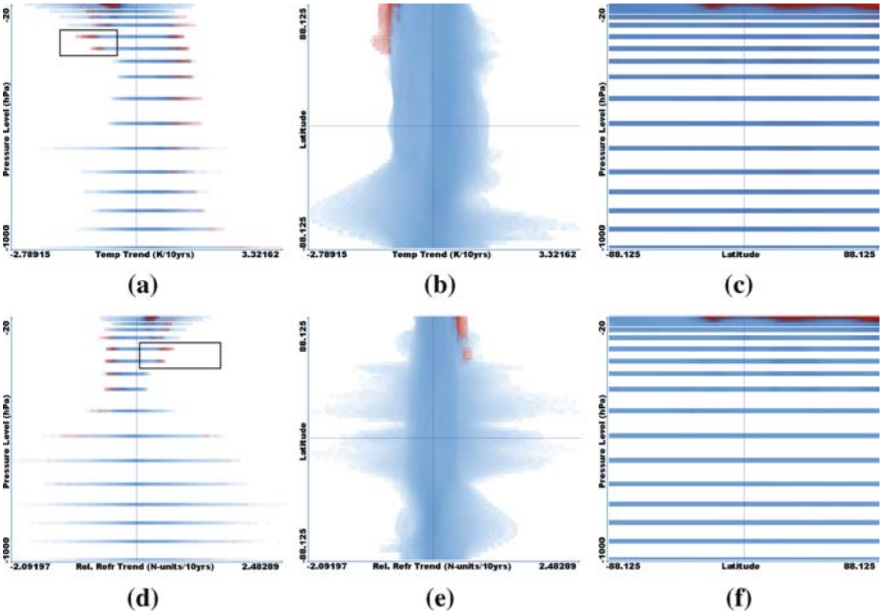

(a) (b) (c)

(d) (e) (f)

Fig. 3 ECHAM5 A2, temperature (in K) represented in (**a**)–(**c**) and refractivity (in N-units) in (**d**)–(**f**): Selection of one specific feature ((**a**)/(**d**), denoted by *rectangle box*) and the corresponding trend distribution versus latitude in (**b**)/(**e**); overview latitude vs. pressure level plot, again without rectangle box selection in (**c**)/(**f**), |SNR| ≥ 1 shown in *red*

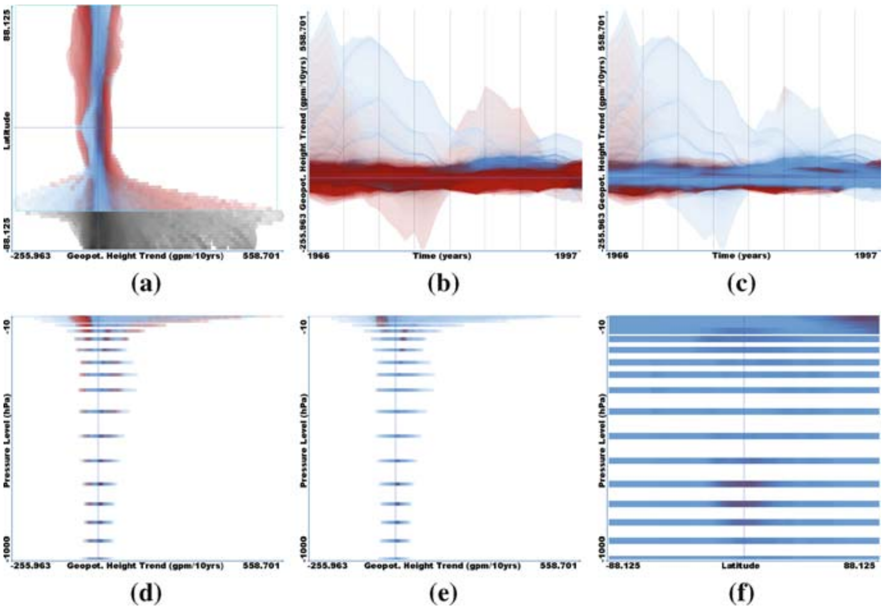

Fig. 4 ERA-40, geopotential height trend (in gpm/10 years): Exclusion of southern high latitudes in *black*, high SNR in *red* in (**a**); resulting trend variation over time, selected latitudes in *red* in (**b**); additional selection of |SNR| $\geq$ 1 in (**c**) and (**d**); additionally restriction to post-1979 time period in (**e**) and (**f**)

The height distribution in Fig. 3a and 3d shows that positive temperature (negative refractivity) trends stem from the troposphere, and that the negative temperature (positive refractivity) trends stem from the upper pressure levels corresponding to the lower stratosphere region, as expected. The SNR-selected data points are marked in red again. Specific selection (rectangle box) is now imposed for negative temperature (positive refractivity) trends at the 150 hPa and 200 hPa levels. With this new selection applied, the red-colored trend distribution with latitude changes from Fig. 2c/2f to what is shown in Fig. 3b/3e. It can be observed that the significant trend features stem only from northern high latitudes, where they are well inside the stratosphere, as expected.

An overview of the spatial distribution of data points with |SNR| $\geq$ 1 (without rectangle box selection) is gained in the plots 3c and f, where pressure levels versus latitude are plotted. Values with high SNR are in particular found at the topmost levels (20–30 hPa) in the ECHAM5 model run, corresponding to robust negative temperature (positive refractivity) trends in the lower stratosphere observable over the whole investigated time period (see Fig. 2b/2e). Note that at low levels with weaker |SNR| $\geq$ 1 presence, the red color dots are effectively "buried" in the predominant blue color dots (visible on the screen, though).

For the ERA-40 reanalysis the distribution of the geopotential height trend with latitude in Fig. 4a (again |SNR| $\geq$ 1 in red) shows high trend variation in southern

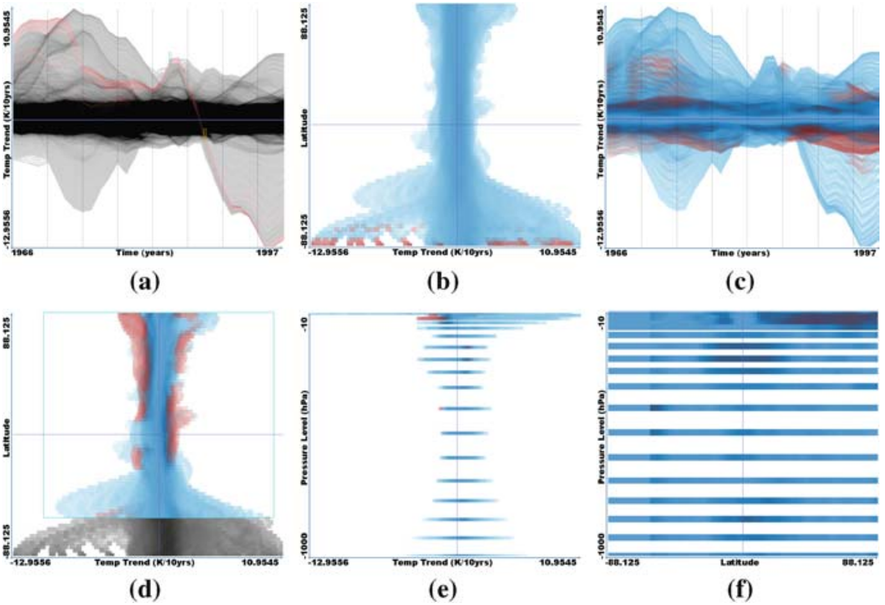

Fig. 5 ERA-40, temperature trend (in K/10 years); selection of a confined trend curve ensemble in *red* in (**a**); corresponding latitude vs. trend distribution in (**b**); exclusion of southern high latitudes and $|\mathrm{SNR}| \geq 1$ values in (**c**); restrict additionally to post-1979 in (**d**)–(**f**)

high latitudes, which is a spurious feature according to Santer et al. (2004). The selection was restricted to data over 90°N to 60°S accordingly. The resulting time variation of the geopotential height trend shown in Fig. 4b (only the latitude selection applies here) now has most outliers removed, with the remaining data points in red. Applying the selection of $|\mathrm{SNR}| \geq 1$ values again further improves the result (Fig. 4c), with some outliers still present in the early years of the data set. The same selections apply for the plot in Fig. 4d, still showing a somewhat ambiguous distribution with pressure levels. Restricting to the post-1979 era when satellite data were assimilated (Uppala et al. 2004) displays a better-contrasted height distribution in Fig. 4e. The pressure levels versus latitude plot (Fig. 4f) is based on all selections described above and presents best SNR for the lower stratosphere at northern high latitudes (negative trends, see Fig. 4e) and the lower tropical troposphere (positive trends, partly up to the lower stratosphere), respectively.

High variation of the ERA-40 temperature trends in time is observed in Fig. 5a. Some of the temperature trend curves showing the highest variation over time are selected in the curve view (red) and analyzed further. The corresponding latitude distribution of the trend in Fig. 5b reveals that it is a spurious feature since it stems from the southern high latitudes. Restricting to 90°N to 60°S and selecting $|\mathrm{SNR}| \geq 1$ (deselecting the curve ensemble before) leads to the trend variation in Fig. 5c. Limiting the time period to the post-1979 era further removes highly variable trends and yields the spatial distributions depicted in Fig. 5d–f. As seen in Fig. 5f, high

SNR (in red) appears in the lower stratosphere region at northern high latitudes for negative trends and in the tropical upper troposphere for positive trends (again, the latter feature is better visible on the screen).

5 Conclusions and Outlook

Using data sets from the ECHAM5 model and the ERA-40 reanalysis we analyzed atmospheric parameters accessible to RO measurements with focus on the UTLS region. We presented the investigation of these large climate data fields using a novel visualization method. The interactive visual field exploration tool SimVis enables the exploration of the whole data set at once and interesting features can be interactively selected by the user.

The utility of this method was demonstrated on the basis of the localization of trends with high SNR in space and in time. Temperature and refractivity from the ECHAM5 model run show robust and sensitive trends in the lower stratosphere region over the whole investigated time period, with considerable contributions from the upper troposphere. Deficiencies in the ERA-40 reanalysis, analyzed in geopotential height and temperature, at southern high latitudes and in early years of the pre-satellite era could be detected. Regions of high SNR reside in the lower stratosphere at northern high latitudes and in the tropical lower troposphere. Ongoing work focuses on the application of the findings to RO observations, the intercomparison of multiple climate model fields, and detailed classical statistical analysis in domains of interest.

Acknowledgements We acknowledge the IPCC climate modeling groups for providing their data for analysis, the Program for Climate Model Diagnosis and Intercomparison (PCMDI) for collecting and archiving the model output, and the JSC/CLIVAR Working Group on Coupled Modelling (WGCM) for organizing the model data analysis activity. The multi-model data archive is supported by the Office of Science, U.S. Department of Energy. This work was funded by the Austrian Science Fund (FWF) Project INDICATE P18733-N10.

References

Cordero EC, de F Forster PM (2006) Stratospheric variability and trends in models used for the IPCC AR4. Atmos Chem Phys 6:5369–5380

Doleisch H (2004) Visual Analysis of Complex Simulation Data using Multiple Heterogenous Views. PhD thesis, Technical University of Vienna, see also http://www.VRVis.at/via/resources/diss-HD/

Doleisch H, Hauser H (2002) Smooth brushing for focus+context visualization of simulation data in 3D. J WSCG 10(1):147–154

Doleisch H, Gasser M, Hauser H (2003) Interactive feature specification for focus+context visualization of complex simulation data. In: VISSYM '03: Proceedings of the symposium on Data visualisation 2003, Grenoble, France, pp 239–248

Doleisch H, Mayer M, Gasser M, Priesching P, Hauser H (2005) Interactive feature specification for simulation data on time-varying grids. In: Proceedings of the Conference Simulation and Visualization (SimVis 2005), Magdeburg, Germany, pp 291–304

Foelsche U, Kirchengast G, Steiner AK, Kornblueh L, Manzini E, Bengtsson L (2008a) An observing system simulation experiment for climate monitoring with GNSS radio occultation data: Setup and test bed study. J Geophys Res 113(D11108), doi:10.1029/2007JD009231

Foelsche U, Borsche M, Steiner AK, Gobiet G, Pirscher B, Kirchengast G, Wickert J, Schmidt T (2008b) Observing upper troposphere-lower stratosphere climate with radio occultation data from the CHAMP satellite. Clim Dyn 31:49–65, doi:10.1007/s00382-007-0337-7

Foelsche U, Pirscher B, Borsche M, Kirchengast G, Wickert J (2009) Assessing the climate monitoring utility of radio occultation data: From CHAMP to FORMOSAT-3/COSMIC. Terr Atmos Oceanic Sci 20(1):155–170, doi:10.3319/TAO.2008.01.14.01(F3C)

Hauser H (2005) Generalizing focus+context visualization. In: Scientific Visualization: The Visual Extraction of Knowledge from Data (Proceedings of the Dagstuhl 2003 Seminar on Scientific Visualization), pp 305–327

Kehrer J (2007) Integrating Interactive Visual Analysis of Large Time Series Data into the SimVis System. Master's thesis, VRVis Research Center, Technical University of Vienna

Lackner BC, Steiner AK, Ladstädter F, Kirchengast G (2009) Trend indicators of atmospheric climate change based on global climate model scenarios. In: Steiner A, Pirscher B, Foelsche U, Kirchengast G (eds) New Horizons in Occultation Research, Springer-Verlag, Berlin Heidelberg, doi:10.1007/978-3-642-00321-9_20

Leroy SS, Dykema JA, Anderson JG (2006) Climate benchmarking using GNSS occultation. In: Foelsche U, Kirchengast G, Steiner AK (eds) Atmosphere and Climate: Studies by Occultation Methods, Springer-Verlag, Berlin, Heidelberg, pp 287–301

Muigg P, Kehrer J, Oeltze S, Piringer H, Doleisch H, Preim B, Hauser H (2008) A four-level focus+context approach to interactive visual analysis of temporal features in large scientific data. IEEE Computer Graphics Forum/Proceedings of EuroVis 2008 27(3):775–782

Roeckner E, Buml G, Bonaventura L, Brokopf R, Esch M, Giorgetta M, Hagemann S, Kirchner I, Kornblueh L, Manzini E, Rhodin A, Schlese U, Schulzweida U, Tompkins A (2003) The atmospheric general circulaton model ECHAM5. Report no. 349, Max-Planck-Insitute for Meteorology, Hamburg, Germany, 127pp

Santer BD, Wigley TML, Simmons AJ, Kållberg PW, Kelly GA, Uppala SM, Ammann C, Boyle JS, Brüggemann W, Doutriaux C, Fiorino M, Mears C, Meehl GA, Sausen R, Taylor KE, Washington WM, Wehner MF, Wentz FJ (2004) Identification of anthropogenic climate change using a second-generation reanalysis. J Geophys Res 109(D21104), doi:10.1029/2004JD005075

Schmidt S, Schögl O, Kirchberger R, Doleisch H, Muigg P, Hauser H, Grabner M, Bornik A, Schmalstieg D (2005) Novel visualization and interaction techniques for gaining insight into fluid dynamics in internal combustion engines. In: Proceedings of the NAFEMS World Congress Conference 2005, Malta

Simmons AJ, Gibson JK (2000) The ERA-40 Project Plan. ERA-40 Project Report Series No. 1, ECMWF, Reading, UK, 62 pp

Steiner AK, Kirchengast G, Borsche M, Foelsche U, Schoengassner T (2007) A multi-year comparison of lower stratospheric temperatures from CHAMP radio occultation data with MSU/AMSU records. J Geophys Res 112(D22110), doi:10.1029/2006JD008283

Uppala S, KÅllberg P, Hernandez A, Saarinen S, Fiorino M, Li X, Onogi K, Sokka N, Andrae U, Da Costa Bechtold V (2004) ERA-40: ECMWF 45-year reanalysis of the global atmosphere and surface conditions 1957–2002. ECMWF Newsletter No. 101-Summer/Autumn 2004, European Centre for Medium-Range Weather Forecasts, Shinfield Park, Reading, Berkshire RG2 9AX, UK

Trend Indicators of Atmospheric Climate Change Based on Global Climate Model Scenarios

B.C. Lackner, A.K. Steiner, F. Ladstädter, and G. Kirchengast

Abstract The upper troposphere-lower stratosphere (UTLS) region is reacting particularly sensitive to climate change and variations of its key parameters are very good candidates for the monitoring and diagnosis of climate change. This study aims at revealing the most promising atmospheric climate change indicators in this region which are accessible by radio occultation (RO) observations. RO based climatologies show the highest data quality in the UTLS. Due to the availability of continuous RO data only since the end of 2001, longer-term climatologies of three representative global climate models were investigated in this respect. We demonstrate that the RO method can valuably contribute to climate monitoring by providing climatologies of a set of atmospheric parameters such as refractivity, geopotential height, and temperature, which differ in sensitivity at different heights and in different regions and cover the UTLS as a whole.

1 Introduction

The vertical thermal structure of the atmosphere reflects a balance between radiative, convective, and dynamical heating and cooling processes of the surface-atmosphere system. In the troposphere radiative processes involving greenhouse gases, aerosols, and clouds dominate together with strong moist convection and dynamical (vertical) motions (e.g., Holton 2004). The latter are weak in the stratosphere where radiative heating and cooling rates due to mainly carbon dioxide, ozone, and water vapor are of importance (e.g., Andrews et al. 1987). Changes in the upper troposphere-lower stratosphere (UTLS) region have strong impact on the Earth's climate system, consequently climate monitoring is in need of long-term stable, self-calibrating, and well height-resolved global data in this region. Up to now, temperature changes are commonly used as climate change benchmarks in trend studies, mostly with

---

B.C. Lackner (✉)
Wegener Center for Climate and Global Change (WegCenter) and Institute for Geophysics, Astrophysics, and Meteorology (IGAM), University of Graz, Austria
e-mail: bettina.lackner@uni-graz.at

A. Steiner et al. (eds.), *New Horizons in Occultation Research*,
DOI 10.1007/978-3-642-00321-9_20, © Springer-Verlag Berlin Heidelberg 2009

focus on surface changes. The establishment of radiosondes in the 1960 s and space borne measurement systems in the late 1970 s enabled the investigation of upper-air temperature (Karl et al. 2006).

Climatologies based on atmospheric profiles retrieved from RO observations allow the monitoring and diagnosis of climate change (Leroy et al. 2006). The RO method provides high quality atmospheric parameters in the UTLS comprising refractivity, pressure, geopotential height, temperature, and in the lower to middle troposphere specific humidity (see e.g. for CHAMP data Wickert et al. 2004; Hajj et al. 2004; Steiner et al. 2006). These parameters are highly relevant to investigate upper tropospheric warming and lower stratospheric cooling in a changing climate.

This study aims at demonstrating the potential of the whole set of RO accessible parameters as climate change indicators in the UTLS region. We define an indicator as a variable, which succeeds best to map the process of anthropogenic climate change in a certain space and time domain. Due to the still limited length of real RO time series (end 2001–2007), we use climate simulations of three representative global circulation models (GCMs). Section 2 gives an overview of the data used within this study and their characteristics. The study design and the trend analysis method as well as the method used to identify the most sensitive parameters and their respective temporal and spatial features is described in Sect. 3. Results are presented in Sect. 4 and discussed with respect to RO in Sect. 5, while in Sect. 6 a summary is given and conclusions are drawn.

2 Data

RO measurements have been continuously available since 2001 only, which can be considered as too short for climatological trend analysis. Thus, the potential of climate monitoring by RO accessible parameters is explored by using simulations of three representative global circulation models of the Intergovernmental Panel on Climate Change (IPCC) Fourth Assessment Report (AR4). The Atmosphere-Ocean GCMs participating in the IPCC model comparison represent the most advanced and comprehensive set of climate simulations so far produced (Cordero and de Forster 2006). We concentrate on the 1961–2060 period employing a concatenation of 20th century and Special Report on Emission Scenarios (SRES) A2 as well as B1 runs of the three GCMs:

- CCSM3 from the National Centers for Environmental Prediction (NCEP) and the National Center for Atmospheric Research (NCAR) (Collins et al. 2006), 5 runs A2, 7 runs B1;
- ECHAM5 from the Max-Planck-Institute for Meteorology in Hamburg (MPI) (Roeckner et al. 2003), 3 runs A2, 3 runs B1;
- HadCM3 from the Hadley Centre for Climate Prediction and Research of the UK-MetOffice (Gordon et al. 2000; Pope et al. 2000), 1 run A2, 1 run B1.

The data are available for download from the WCRP CMIP3[1] multi-model database.[2] The models' climate projections, based upon forcings of varying strengths, form the basis of our knowledge about the anticipated range of possible future climate change. Model results differ depending on the kind of natural and anthropogenic forcings used within the simulations. Besides greenhouse gas forcings, which are prescribed by the A2 and B1 scenarios, the use of ozone forcing plays an essential role for simulating stratospheric temperatures and thus models including ozone forcings should be given preference in stratospheric studies. All selected models use ozone depletion and recovery forcings in their simulations (Roeckner et al. 2005, Jerry Meehl, NCAR/USA, Tim Johns, MetOffice/U.K., Jonathan Gregory, MetOffice/U.K., personal communication, 12/2007), and thus are qualified for our study. Furthermore, the three selected models show different characteristics of internal variation and intensity of circulation (ECHAM5 stronger than CCSM3, HadCM3 in between, cf. Leroy et al. 2006; Meehl et al. 2007). They cover a good range of variability and thus comprise a representative set of GCMs with respect to the whole set of IPCC AR4 models (Reichler and Kim 2008).

The original data, featuring different resolutions (of at least about 2.5° × 2.5°), were regridded to a common 2.5° × 2.5° grid in latitude and longitude. For every seasonal and annual mean we analyzed refractivity (N), geopotential height (Z), temperature (T), and specific humidity (q)—parameters which are provided by RO measurements—on 18 pressure levels ranging from 1000–10 hPa. While Z, T, and q fields are available for download from the WCRP CMIP3 multi-model database, N was derived using the classical Smith-Weintraub formula (Smith and Weintraub 1953).

Even though global-scale climate statistics, such as global mean climatologies of atmospheric parameters, provide in general good indicators for global climate change, regional statistics allow more sophisticated and detailed interpretations.

Thus, a combination of 6 large-scale zonal bands and 30 regions was used (Fig. 1). The zonal bands (marked at the left and right border) range from global mean climatologies over hemispheric means to zonal bands of 30° in latitude. The 30 regions follow the definition in Chapter 11 (Christensen et al. 2007) of the IPCC AR4. They include 22 land regions (solid lines in Fig. 1), 6 regions covering oceanic areas (dotted lines in Fig. 1) and 2 covering the polar caps (ARC, ANT, marked at the right side of Fig. 1), respectively. These IPCC region definitions are similar to those of Giorgi and Francisco (2000). The combination of the 30 IPCC regions and the 6 zonal bands is hereinafter addressed as IPCC+ regions. The regional parameter values were derived for each pressure level from the basic 2.5° × 2.5° grid using area-weighted averaging.

---

[1] World Climate Research Programme's (WCRP's) Working Group on Coupled Modelling (WGCM)

[2] esg.llnl.gov:8080/home/publicHomePage.do, 11/2007

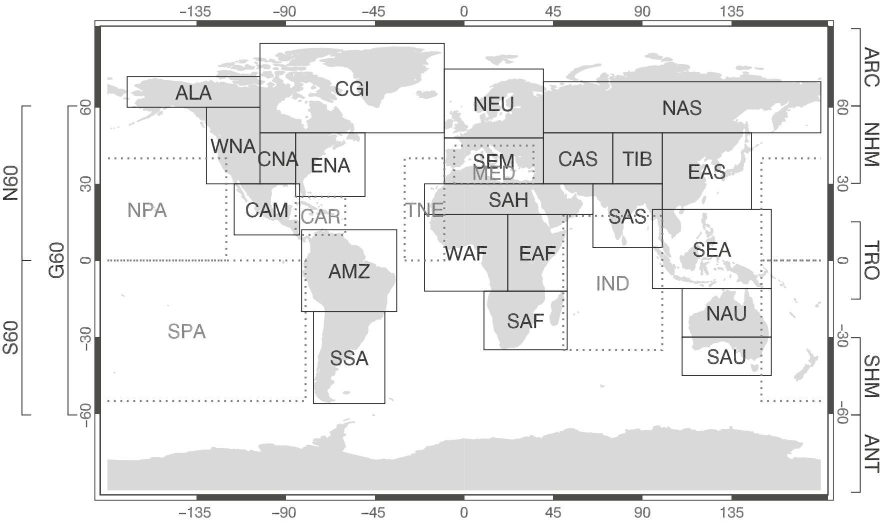

Fig. 1 Large-scale climate regions over land (*solid boxes*) and oceans (*dotted boxes*) based on IPCC (2007) definitions, complemented by global-scale zonal band regions for the tropics, mid-latitudes, and a "non-polar" global region (*marked at both sides*)

3 Method

The aim of the study is to reveal the most promising atmospheric climate change indicators for RO accessible parameters in the UTLS domain for the 36 IPCC+ regions. Altogether 20 different realizations (runs) of A2 and B1 scenarios of the ECHAM5, CCSM3, and HadCM3 were considered (see Sect. 2).

Linear trends (least-square estimates), b, were calculated over 2001–2050 for each pressure level based on anomalies with respect to the 1961–1990 climatological mean. Given the regression line obtained, $\hat{y}(t)$ (Eq. 1), the regression residuals $e(t)$ (Eq. 2) describe the deviations of the observed values $y(t)$ from the regression line:

$$\hat{y}(t) = a + bt \tag{1}$$

$$e(t) = y(t) - \hat{y}(t) \tag{2}$$

The variance of the residuals, s_e^2, is given by

$$s_e^2 = (n-2)^{-1} \sum_i e_i(t)^2, \tag{3}$$

where n is the number of samples (years) in the time series.

The significance of the trends was determined according to Santer et al. (2000) and Wilks (2005), using Students t-test and considering lag-1 autocorrelation (r_1), reducing n to the effective sample size $n_e = n(1 - r_1)/(1 + r_1)$, which was used to determine the critical t-value. The test value t_b is given by the ratio of the trend b itself and the standard error of the trend s_b given by

$$s_b = s_e \left(\sum_i (t_i - \bar{t})^2 \right)^{-1/2} . \tag{4}$$

The coefficient of determination, R^2, was chosen as goodness-of-fit measure. It is the ratio of the sum of squares of deviations of the regression line from the mean value $\bar{y}$ (SSR) and the sum of squares of deviations from the mean value (SST):

$$R^2 = \frac{\mathrm{SSR}}{\mathrm{SST}} = \left(\sum_{i=1}^{N} (\hat{y}_i - \bar{y})^2 \right) \left(\sum_{i=1}^{N} (y_i - \bar{y})^2 \right)^{-1} . \tag{5}$$

Based on the results of the trend analysis, criteria for best trend indicators were formulated as follows:

- for each scenario (A2 or B1) all—or all but one—trends have the same algebraic sign,
- at least 3/4 of all runs (A2 and B1) show a goodness-of-fit of $R^2 \geq 0.5$,
- at least 3/4 of all runs (A2 and B1) show a statistical significance $\geq 90\%$ for the trends.

The criteria were carefully selected to ensure the unveiling of the most robust spatially dependent trend characteristics of all RO accessible parameters in the UTLS region.

4 Results

In a first step we inspected height-resolved time series, which showed that in most regions the climate change signal of the UTLS is even visible by the naked eye. Figure 2 depicts, as an example, time series of geopotential height anomalies for northern hemispheric summer as simulated by one arbitrarily chosen ECHAM5 run for large-scale zonal mean bands. The time period 2001–2050 is highlighted with a frame since it was the basis for subsequent trend analysis (see Sect. 3). The model simulations show a strong signal of a geopotential height increase, reflecting the thermal expansion due to tropospheric temperature rise, through almost the whole UTLS region, typically up to about 20 hPa. The pressure levels of maximum increase depend on the region's latitude: in the tropics, the strongest signal can be found around 50 hPa, in the mid-latitudes around 150–100 hPa and in the Arctic region even below. In the extra-tropics, stratospheric cooling leads to a decrease of geopotential height above around 20 hPa. Signals around and above this height level must be interpreted with caution, since the upper boundary layer of all investigated

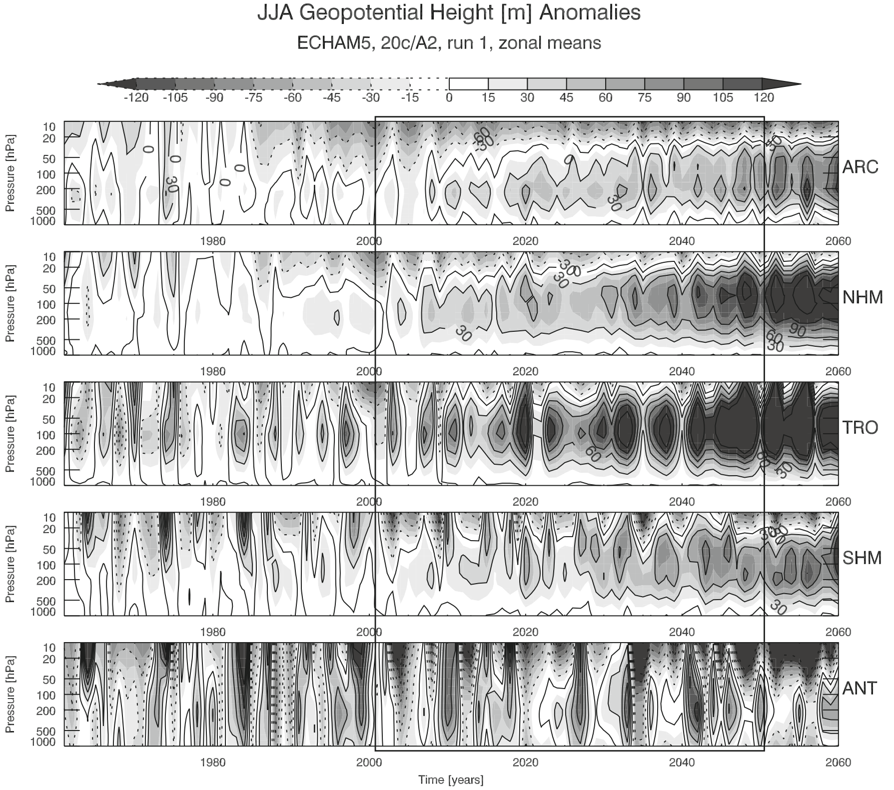

Fig. 2 Time evolution (20th century combined with SRES A2) of ECHAM5 seasonal mean JJA geopotential height profiles in five zonal IPCC+ regional bands (from IPCC Arctic region/ARC via the northern mid-latitudes/NHM, the tropics/TRO, and southern mid-latitudes/SHM to the IPCC Antarctic region/ANT). The time period 2001–2050, which forms the basis for the trend analysis, is highlighted with a frame

models is 10 hPa, yielding probably untrustworthy results there (Cordero and de Forster 2006). At higher latitudes, the year to year variations in the strength of the polar vortex cover a possible climate change signal and thus polar regions are not suitable for this kind of climate change tracing during the hemispheric winter, as shown for Antarctica (Fig. 2, bottom panel). The atmospheric parameters N, T, and q (not shown) also exhibit strong climate signals during the first part of the 21th century.

For most regions, the trends of the model runs agree quite well in magnitude and direction (Fig. 3, left, shows an example), a fact that deserves great importance for qualifying as best trend indicators (see Sect. 3). The trend signal of various runs of an individual model shows generally similar vertical peculiarities. Large discrepancies occur for trends at high latitudes in the winter hemisphere, as shown for Alaska in Fig. 3, right panel: above about 100 hPa, CCSM3 has a tendency towards pronounced negative temperature trends, ECHAM5 to rather positive

Fig. 3 Temperature trends for two selected regions (60°N–60°S and Alaska) of ECHAM5 seasonal mean DJF temperatures

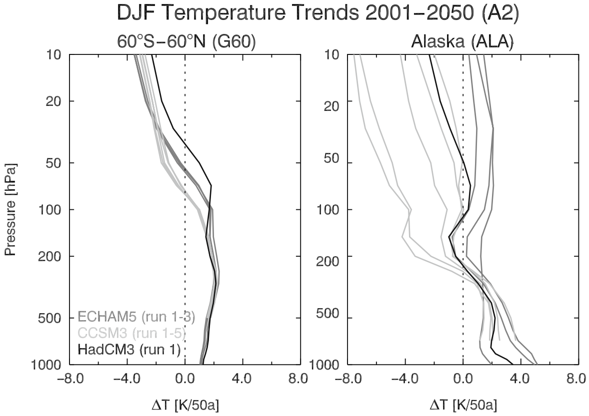

trends. Such discrepancies lead to an exclusion of those regions as trend indicators, due to the criteria defined.

Besides the consistent direction of trends across the ensemble of model runs, trend significance and goodness-of-fit determine the identification of best trend indicators. Figure 4 illustrates these quantities for refractivity in fall as an example.

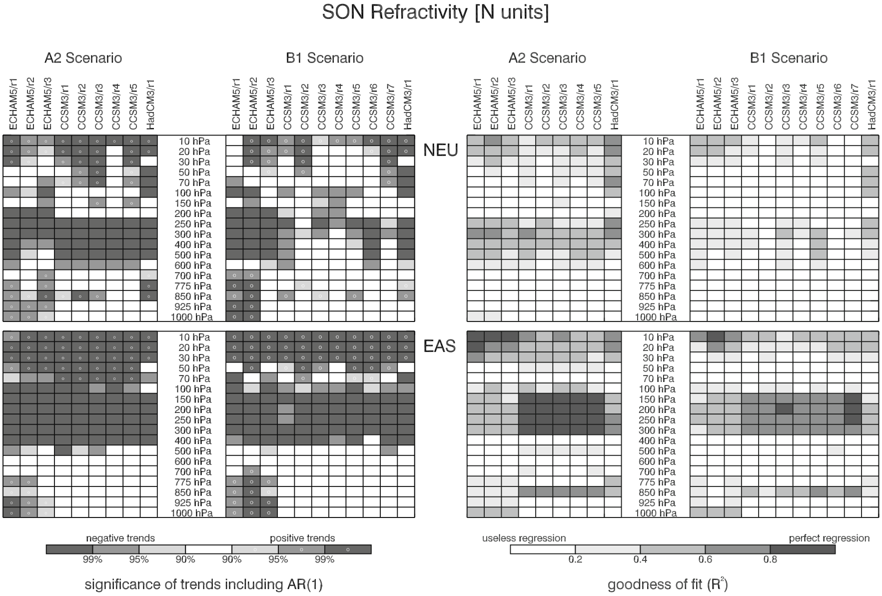

Fig. 4 Trend significances (*left*) and goodness-of-fit (*right*) in northern Europe (NEU, *top*) and eastern Asia (EAS, *bottom*) for SON refractivity. The results of all model runs (*columns* in the plots) at all pressure levels (*rows* of the plots) are presented. In the left hand side plots, *dark gray* cells indicate significances greater than 99%, *medium gray* 95–99%, and *light gray* 90–95%, respectively. A positive sign of the trend is marked by a circle spot in the cell

Most regions show high significances of trends at selected height ranges. The significances plots (Fig. 4, left) give for each parameter a good overview of regions and height ranges that are particularly sensitive to climate change. However, goodness-of-fit turned out to be the limiting factor for the assessment of best trend indicators. Figure 4 (right) presents the respective values for R^2. The shading is chosen in a way that dark boxes indicate better fits. Best fits agree mostly quite well with high significances of the trends, but regions which are dominated by a higher variability—which leads to a worse ratio between the total variance in the data and the variance explained by the regression and thus to a worse goodness-of-fit value—are sorted out. As shown with the direction of trends (see Fig. 3), these regions are mainly found at high latitudes of the winter hemisphere.

In the last step of the study, the results of the trend analysis were merged according to the criteria defined in Sect. 3, allowing the identification of geographical regions and height domains qualified for best trend indicators. Figure 5 presents a summary of the trend study's results. For each RO accessible parameter, one example season is shown. Within each plot, one box represents one pressure level (the rows) of one region (the columns). If the criteria defined are fulfilled, the box is colored. The gray shading indicates the significance level of the detected trends, the circle spot marks the positive trend direction (increase).

5 Discussion with Respect to RO

Generally, the retrieval of RO parameters starts with phase delay measurements and satellite orbit parameters. In the Wegener Center processing scheme a priori information is only involved at the stage of the bending angle initialization via statistical optimization (Gobiet and Kirchengast 2004; Borsche et al. 2006; Foelsche et al. 2008; Gobiet et al. 2007), leading to refractivity, geopotential height, and—by means of the hydrostatic equation—to pressure. Temperature is derived assuming a dry atmosphere, which is valid for upper tropospheric/lower stratospheric levels (e.g., Foelsche et al. 2008). In the mid- to lower troposphere the moist-dry ambiguity inherent in refractivity can only be resolved by means of background information, such as tropospheric temperature and surface pressure (e.g., short range forecast data from numerical weather prediction), for the retrieval of humidity (Kursinski and Hajj 2001). Thus, RO data yield good temperature results in the UTLS, while specific humidity only should be interpreted in the lower and middle troposphere and bearing in mind that background information is included.

Regarding RO data, we thus only consider results above 400 hPa for refractivity, geopotential height, and dry temperature, but for the sake of completeness, we also show the lower levels in Fig. 5. The focus of RO climatologies still lies on large-scale zonal means, but recent satellite missions such as COSMIC (Anthes et al. 2008) will provide an increasingly insight also into regional analysis due to a better spatial coverage by occultation events in consequence of a whole constellation of satellites in orbit.

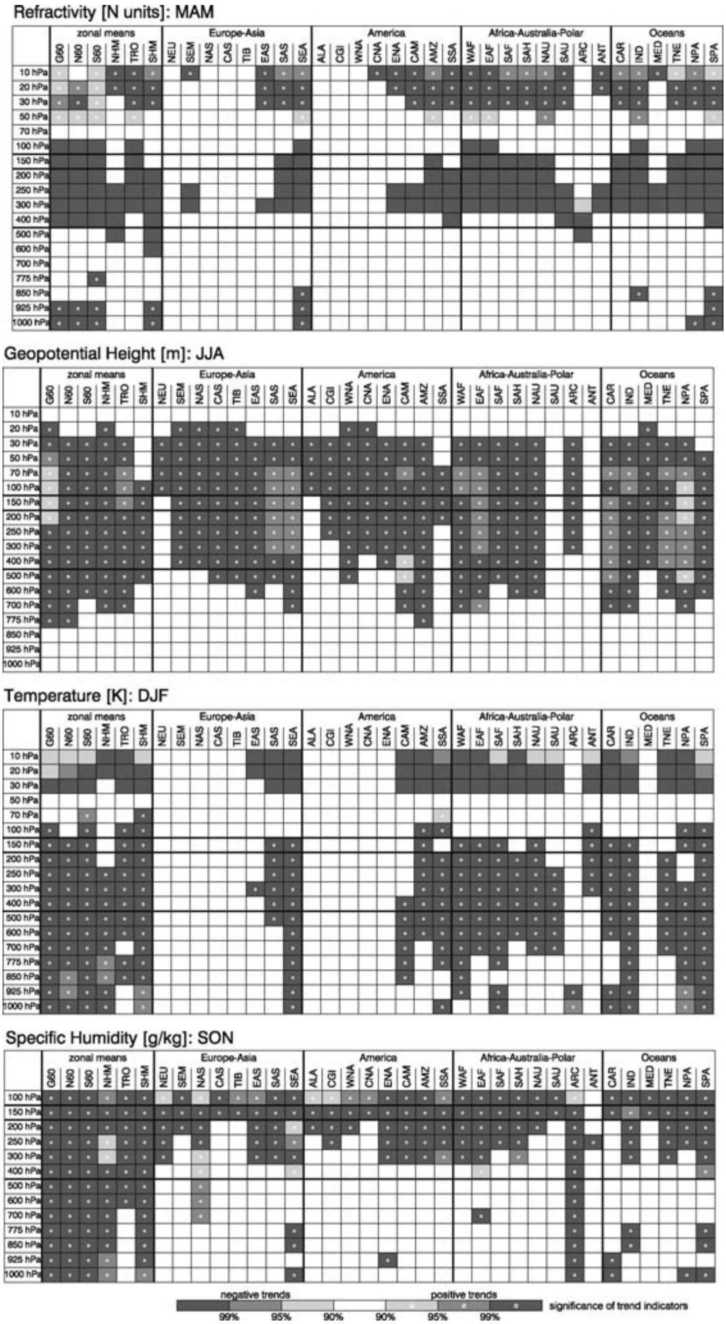

Fig. 5 Regions (*columns*) and pressure levels (*rows*) of best trend indicators, shown for suitable seasons and all RO accessible parameters investigated in this study. The significance level of the trends is indicated by the *shading* (dark for high significances), a positive trend is marked by a circle

The most pristine RO parameter closest to bending angle (on the applicability of the latter for climate change detection see Ringer and Healy 2008), refractivity, shown for MAM, is approximately inversely proportional to temperature and a suitable trend indicator between 300 hPa and 100 hPa and between 30 hPa and 10 hPa throughout all seasons and large-scale zonal bands. For (late) winter (DJF and MAM) continental regions in mid and high latitudes of the Northern Hemisphere, the defined criteria for trend indicators are not fulfilled, due to higher variability and thus worse goodness-of-fit values in these regions.

Geopotential height of pressure levels (shown for JJA) can be interpreted as an integrated tropospheric bulk temperature and allows to define the UTLS from about 400 hPa to 20 hPa in almost all—not only large-scale zonal bands—regions as trend indicator area. Similar to temperature, northern hemispheric continental winter regions are excluded from being indicator regions, while for JJA only the southernmost regions (SSA, SAU, and ANT) do not comply with our trend indicator definition.

Thus, refractivity and geopotential height already suffice to cover the whole UTLS with RO accessible trend indicators.

Nevertheless, temperature is the most commonly used and interpreted parameter in climate science. RO temperature trends are generally best represented in the UT (about 400–100 hPa) and LS (about 30–10 hPa). In northern hemispheric winter (DJF, see Fig. 5), the continental regions of the mid and high latitudes again disqualify as trend indicators due to worse goodness-of-fit values as a consequence of higher atmospheric variability.

Specific humidity was only investigated up to 100 hPa since stratospheric water vapor concentrations are not accessible by RO. The emphasize of RO accessible specific humidity is, as specified above, on lower and middle tropospheric levels (up to 300 hPa). There, zonal means (except in the tropics above 700 hPa, which show larger variations) and the Arctic region are good indicators in SON (shown in Fig. 5) and all other seasons; individual IPCC regions generally show too much variability below 300 hPa.

Overall, the GCMs show similar trend pattern in spring and autumn, but the strongest signals are generally found in northern hemispheric summer, when internal variation is less than in other seasons.

6 Summary and Conclusions

The potential of RO accessible trend indicators was demonstrated by means of climate simulations of three representative IPCC AR4 models (ECHAM5, CCSM3, HadCM3). The model simulations, investigated for the years 1961–2060 show a strong climate change signal in height regions depending on the respective physical processes governing the individual parameters.

Based on suitable criteria—including direction of trends, trend significances, and goodness-of-fit—the RO accessible parameters allow the identification of geographical regions and height domains qualified for best trend indicators. Spring and autumn show similar trend patterns, but clearest results in GCM simulations are found in the summer season.

- *Refractivity* is a suitable trend indicator between 300 hPa and 100 hPa as well as between 30 hPa and 10 hPa.
- *Geopotential height*, together with refractivity the most pristine RO parameter, is a suitable trend indicator in a wide height domain (400–20 hPa), which is partly not covered by the other parameters.
- *Temperature* trends are best represented in the UT (400–100 hPa) and LS (30–10 hPa), except over continental regions of winter hemispheric mid and high latitudes.
- *Specific humidity* shows best results for zonal means and the Arctic region for all seasons in the lower troposphere where RO data are well sensitive to humidity.

For the UTLS—our RO focus region—refractivity and geopotential height alone are adequate trend indicators. Temperature can be used as additional indicator especially in the upper troposphere. Together, the RO accessible parameters can provide a dataset for the UTLS region fulfilling the needs of climate monitoring and diagnosis for long-term stable, self-calibrated, and well height-resolved global data.

Acknowledgements We acknowledge the modeling groups, the Program for Climate Model Diagnosis and Intercomparison (PCMDI) and the WCRP's Working Group on Coupled Modelling (WGCM) for their roles in making available the WCRP CMIP3 multi-model dataset. Support of this dataset is provided by the Office of Science, U.S. Department of Energy. This work was funded by the Austrian Science Fund (FWF) Project INDICATE P18733-N10.

References

Andrews DG, Holton JR, Leovy CB (1987) Middle Atmosphere Dynamics. Academic Press, New York

Anthes RA, Bernhardt PA, Chen Y, Cucurull L, Dymond KF, Ector D, Healy SB, Ho SP, Hunt DC, Kuo YH, Liu H, Manning K, McCormick C, Meehan TK, Randel WJ, Rocken C, Schreiner WS, Sokolovskiy SV, Syndergaard S, Thompson DC, Trenberth KE, Wee TK, Yen NL, Zeng Z (2008) The COSMIC/FORMOSAT-3 mission: Early results. Bull Am Meteorol Soc 89: 313–333, doi:10.1175/BAMS-89-3-313

Borsche M, Gobiet A, Steiner AK, Foelsche U, Kirchengast G, Schmidt T, Wickert J (2006) Pre-operational retrieval of radio occultation based climatologies. In: Foelsche U, Kirchengast G, Steiner AK (eds) Atmosphere and Climate: Studies by Occultation Methods, Springer-Verlag, Berlin Heidelberg New York, pp 315–323, doi:10.1007/3-540-34121-8-26

Christensen JH, Hewitson B, Busuioc A, Chen A, Gao X, Held I, Jones R, Kolli RK, Kwon WT, Laprise R, Magaña Rueda V, Mearns L, Menéndez CG, Räisänen J, Rinke A, Sarr A, Whetton P (2007) Regional climate projections. In: Solomon S, Qin D, Manning M, Chen Z, Marquis M, Averyt KB, Tignor M, Miller HL (eds) Climate Change 2007: The Physical Science Basis. Contribution of Working Group I to the Fourth Assessment Report of the Intergovernmental Panel on Climate Change, Cambridge University Press, Cambridge, United Kingdom and New York, NY, USA, pp 847–940

Collins WD, Bitz CM, Blackmon ML, Bonan GB, Bretherton CS, Carton JA, Chang P, Doney SC, Hack JJ, Henderson TB, Kiehl JT, Large WG, McKenna DS, Santer BD, Smith RD (2006) The community climate system model version 3 (CCSM3). J Climate 19(11): 2122–2143

Cordero EC, de Forster PM (2006) Stratospheric variability and trends in models used for the IPCC AR4. Atmos Chem Phys 6(12):5369–5380

Foelsche U, Borsche M, Steiner AK, Gobiet G, Pirscher B, Kirchengast G, Wickert J, Schmidt T (2008) Observing upper troposphere-lower stratosphere climate with radio occultation data from the CHAMP satellite. Clim Dyn 31:49–65, doi:10.1007/s00382-007-0337-7

Giorgi F, Francisco R (2000) Uncertainties in regional climate change prediction: a regional analysis of ensembles simulations with the HadCM2 coupled AOGCM. Clim Dyn 16:169–182

Gobiet A, Kirchengast G (2004) Advancements of Global Navigation Satellite System radio occultation retrieval in the upper stratosphere for optimal climate monitoring utility. J Geophys Res 109(D24110), doi:10.1029/2004JD005117

Gobiet A, Kirchengast G, Manney GL, Borsche M, Retscher C, Stiller G (2007) Retrieval of temperature profiles from CHAMP for climate monitoring: intercomparison with Envisat MIPAS and GOMOS and different atmospheric analyses. Atmos Chem Phys 7:3519–3536

Gordon C, Cooper C, Senior CA, Banks HT, Gregory JM, Johns TC, Mitchell JFB, Wood RA (2000) The simulation of SST, sea ice extents and ocean heat transports in a version of the Hadley Centre coupled model without flux adjustments. Clim Dyn 16:147–168

Hajj GA, Ao CO, Iijima BA, Kuang D, Kursinski ER, Mannucci AJ, Meehan TK, Romans LJ, de la Torre Juarez M, Yunck TP (2004) CHAMP and SAC-C atmospheric occultation results and intercomparisons. J Geophys Res 109(D06109), doi:10.1029/2003JD003909

Holton JR (2004) An Introduction to Dynamic Meteorology, International Geophysics, vol 88, 4th edn, Academic Press, New York

Karl TR, Hassol SJ, Miller CD, Murray WL (2006) Temperature Trends in the Lower Atmosphere: Steps for Understanding and Reconciling Differences. A Report by the Climate Change Science Program and the Subcommittee on Global Change Research,Washington, DC

Kursinski ER, Hajj GA (2001) A comparison of water vapor derived from GPS occultations and global weather analyses. J Geophys Res 106(D1):1113–1138, doi:10.1029/2000JD900421

Leroy SS, Anderson JG, Dykema JA (2006) Testing climate models using GPS radio occultation: A sensitivity analysis. J Geophys Res 111(D17105), doi:10.1029/2005JD006145

Meehl GA, Covey C, Delworth T, Latif M, McAvaney B, Mitchell JFB, Stouffer RJ, Taylor KE (2007) The WCRP CMIP32 multimodel dataset: A new era in climate change research. Bull Am Meteorol Soc doi:10.1175/BAMS-88-9-1383

Pope VD, Gallani ML, Rowntree PR, Stratton RA (2000) The impact of new physical parameterizations in the Hadley Centre climate model: HadAM3. Clim Dyn 16:123–146

Reichler T, Kim J (2008) How well do coupled models simulate today's climate? Bull Am Meteorol Soc 89:303–311

Ringer MA, Healy SB (2008) Monitoring twenty-first century climate using GPS radio occultation bending angles. Geophys Res Lett 35(L05708), doi:10.1029/2007GL032462

Roeckner E, Bäuml G, Bonaventura L, Brokopf R, Esch M, Giorgetta M, Hagemann S, Kirchner I, Kornblueh L, Manzini E, Rhodin A, Schlese U, Schulzweida U, Tompkins A (2003) The Atmospheric General Circulaton Model ECHAM5. Report No. 349, Max-Planck-Institute for Meteorology, Hamburg, Germany, 127 pp

Roeckner E, Jungclaus J, Mikolajewicz U, Hagemann S (2005) Model Information of Potential Use to the IPCC Lead Authors and the AR4: ECHAM5˙MPI-OM. available from www-pcmdi.llnl.gov/ipcc/model_documentation/ipcc_model_documentation.php

Santer BD, Wigley TML, Boyle JS, Gaffen DJ, Hnilo JJ, Nychka D, Parker DE, Taylor KE (2000) Statistical significance of trends and trend differences in layer-average atmospheric temperature time series. J Geophys Res 105(D6):7337–7356

Smith EK, Weintraub S (1953) The constants in the equation for atmospheric refractive index at radio frequencies. Proc IRE 41:1035–1037

Steiner AK, Löscher A, Kirchengast G (2006) Error characteristics of refractivity profiles retrieved from CHAMP radio occultation data. In: Foelsche U, Kirchengast G, Steiner AK (eds) Atmosphere and Climate: Studies by Occultation Methods, Springer-Verlag, Berlin Heidelberg, New York, pp 27–36

Wickert J, Schmidt T, Beyerle G, König R, Reigber C, Jakowski N (2004) The radio occultation experiment aboard CHAMP: Operational data analysis and validation of vertical atmospheric profiles. J Meteorol Soc Jpn 82:381–395

Wilks DS (2005) Statistical Methods in the Atmospheric Sciences: An Introduction (International Geophysics). Academic Press Inc, New York

Part V
Future Occultation Missions

ROSA – The Italian Radio Occultation Mission Onboard the Indian OCEANSAT-2 Satellite

F. Vespe, G. Perona, V. De Cosmo, M. Petitta, M. Materassi, N. Tartaglione, A. Zin, R. Notarpietro, C. Benedetto, S. Casotto, A. Speranza, and A. Sutera

Abstract Within the next October 2008 the Indian satellite OCEANSAT-2 will be launched. This satellite is a follow-on mission to the first one which had a scatterometer and an Ocean Color Monitoring (OCM) instrument onboard both devoted to ocean investigation and applications (prediction of cyclone trajectory, fishery, coastal zone mapping, etc.). For the second mission the Italian Radio Occultation GPS receiver (ROSA) devoted to atmospheric investigation will be added to the two payloads. The ROSA payload was designed and developed for the retrieval of atmospheric pressure, temperature, and humidity profiles. Its performance and specifications will be described in the present paper. The Italian Space Agency (ASI) has promoted the ROSA receiver development to strengthen scientific activities as well as to provide end-user applications. In conclusion the paper highlights the radio occultation related activities in Italy targeted on the next OCEANSAT-2 space mission hosting the ROSA receiver.

1 Introduction

OCEANSAT-2 is an Indian space mission, which will be launched tentatively at the end of 2008. It is the follow on to the first one and has the same payload: A scatterometer and the Ocean Color Monitoring (OCM) instrument. The scatterometer consists of a parabola antenna of 1 m diameter, which works at a frequency of 13.5 GHz (Ku-band) suitable for measuring sea surface wind velocity (both magnitude and direction). Two off-axis feeds in its focal plane define two pencil beams (inner and outer), which measure the back scatter coefficient σ_0. They have in turn a footprint of about 42 km × 30 km and 57 km × 35 km. The usable swath coverage is 1400 km. The inner beam operates in HH polarization, the outer beam in VV polarization. The OCM instrument is a multispectral optical camera (8 channels),

F. Vespe (✉)
Agenzia Spaziale Italiana-Centro di Geodesia Spaziale, 75100 Matera, Italy
e-mail: francesco.vespe@asi.it

A. Steiner et al. (eds.), *New Horizons in Occultation Research*,
DOI 10.1007/978-3-642-00321-9_21,

that operates with narrow spectral bands in the visible and near infrared bands. It provides ocean color data with a revisiting time of two days with a circular footprint 360 m wide. The second Indian mission main objective is just to assure continuity of operational data services of the first one while promoting new applications in the area of ocean studies including prediction of cyclone trajectory, fishery, and coastal zone mapping. In October 2005 a Memorandum of Understanding (hereafter MoU) was signed between the Italian Space Agency (ASI) and the Indian Research Space Organization (ISRO). In that MoU it was decided to put the ROSA GPS receiver onboard the OCEANSAT-2 satellite. Furthermore, ASI offered the possibility to download the OCEANSAT-2 scatterometer data at the Matera ASI station where a ground facility suitable to serve current and future space missions like ERS and ENVISAT (ESA), ALOS (JAXA Japanese mission), RADARSAT (Canadian), SAC-D (Argentinian) is going to be realized.

Finally, the third item of the agreement was the promotion of a close cooperation between Italy and India for the development of scientific activities and collaborations for the data exploitation of each payload.

Thus in view of the opportunities to fly ROSA on the Indian satellite as well as on other international space missions (the Argentina's Aquarius/SAC-D) or national ones (SABRINA) ASI's policy plans to cover not only the activities related to the payload but also provide tools for the full exploitation of data on an operational and scientific basis. In parallel to the activities to accommodate the receiver onboard OCEANSAT-2, a program for developing tools suitable for ROSA data processing was undertaken in which research institutions, as well as small companies are involved. Thus in the next sections an overview of all these activities, which will be performed under the ASI umbrella will be given. In Sect. 2 the receiver is described and its accommodation on the satellite will be sketched. The specifications, the requirements, and the philosophy of the software we are going to develop will be outlined in Sect. 3. The scientific activities of the partners will be described in Sect. 4. Finally, some remarks and conclusions will be drawn in the last part of the paper.

2 The ROSA Receiver

The ASI is very active in the field of GPS Radio Occultation (hereafter GPS RO) since several years. The milestones of such developments were the manufacturing of a LAGRANGE GPS receiver devoted to LEO-POD and navigation applications flown onboard the Argentinian SAC-C mission, the development and the manufacturing of the proto flight model receiver ROSA and, finally, the accommodation of ROSA on OCEANSAT-2. The ROSA development is currently carried out by THALES-Alenia. In Fig. 1 the receiver with the antennas is sketched.

Thus GPS signals are acquired through multiple antennas: A zenith antenna is used for navigation purpose and for Precise Orbit Determination (POD), two sounding antennas, pointing toward velocity and anti-velocity satellite vectors are used for Earth limb rising-setting occultation observations for scientific purposes. The

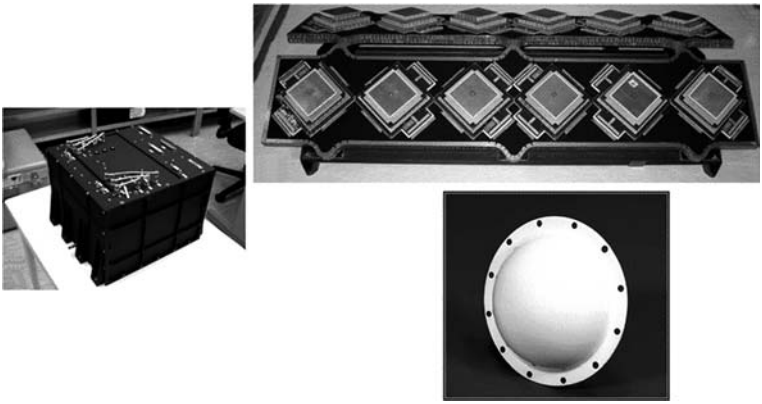

Fig. 1 The receiver is shown on the *left hand side*. The antenna devoted to radio occultation to be placed on the spacecraft facing the velocity and the anti-velocity directions is sketched *right top*, while the figure *right bottom* shows the hemispheric antenna devoted to navigation

Navigation module is able to track up to 8 satellites on both L1 and L2 frequencies while the radio occultation module is able to track simultaneously up to 3 occulting satellites. Anyway, the main specifications of the instrument are summarized in Table 1. The performance of the instrument shall guarantee the capability to retrieve atmospheric profiles with a vertical resolution of $\approx$0.3 km in the lower troposphere. One only of the two RO antennas can be installed on OCEANSAT-2. It will point along the velocity direction. Thus the receiver will catch only RO of rising GPS satellites (the angular velocity of LEO (Low Earth Orbit) satellites indeed is faster than GPS satellites) and the number of RO events is halved as well. In Fig. 2 the global distribution of the RO events is shown.

Table 1 Requirements and specifications, which ROSA is supposed to fulfill

Requirement	Impact on the instrument configuration
To perform accurate positioning	Hemispherical coverage antenna: ±75° around zenith
To maximize the number of occultations per satellite	Both GPS and GLONASS tracking, rising and setting.
	Antennae for occultation: ±45° fore and aft.
	16 dual-frequency channels, arbitrary allocations to GNSS satellites.
Sounding penetration: down to surface	Antenna with high gain and low tracking threshold.
	High sampling rate and open loop mode for sounding the lower troposphere.
	High performance codeless tracking scheme in the receiver signal processor.
To limit resources	Weight $<$ 25 kg
	Volume $<$ 20 L + antennae
	Power $<$ 60 W

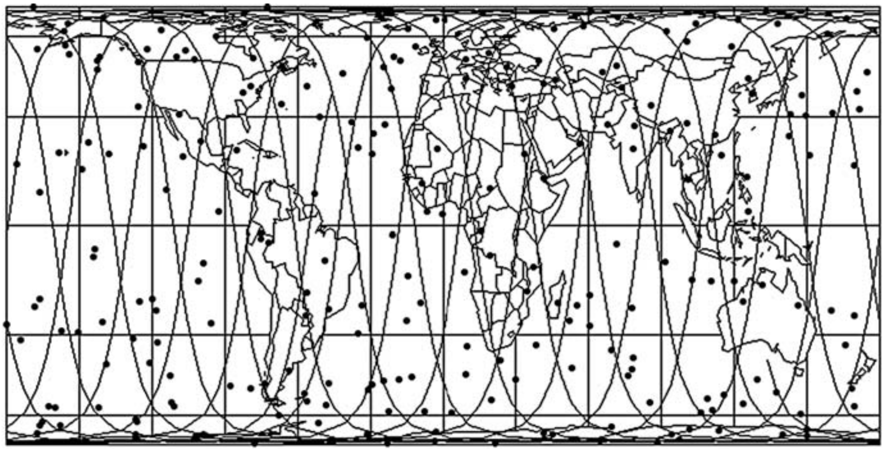

Fig. 2 The global distribution of RO events with an antenna pointing in the velocity direction

The main problem to face are the disturbances induced by the other instruments on the RO observations. Such disturbances can have an impact on the measurements of the phase and amplitudes of the GPS signal caught by the antenna. In Fig. 3 the shape of the satellite and the position of the RO antenna are depicted. A severe disturbance is the multipath mainly due to the scatterometer antenna and the solar panels.

Thus a simulation has been performed just to understand the impact of multipath on the phase and amplitude measurements of the GPS signal. The simulation has been performed by rotating in turn the panel and the scatterometer antenna fixing

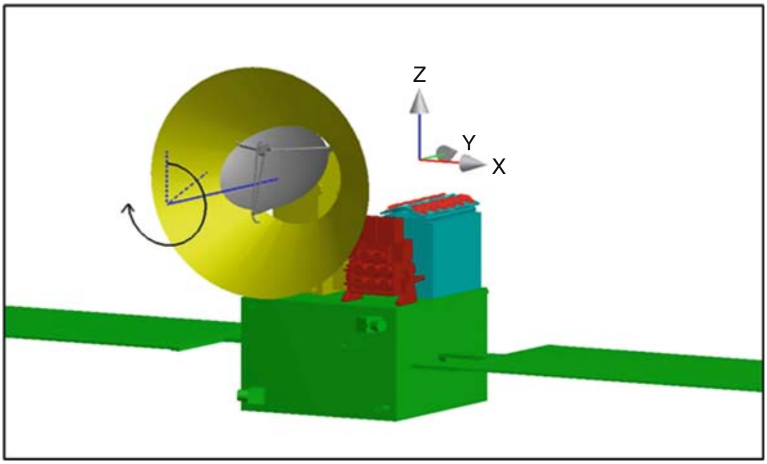

Fig. 3 The arrangement of the antenna on the spacecraft and the other payloads

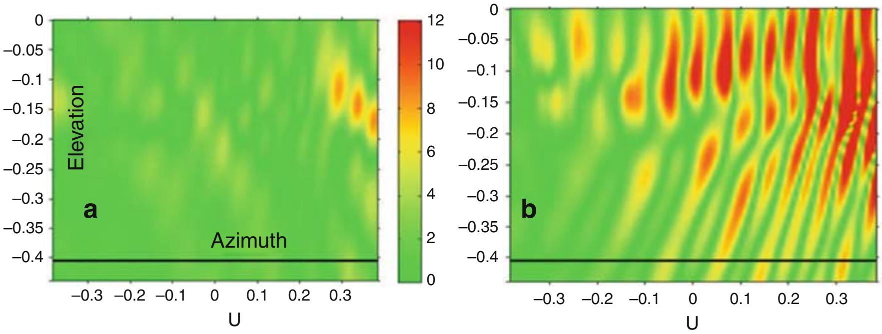

Fig. 4 The figures are the multipath diagrams of two different configurations of the GPS antenna. In (**a**) the antenna is tilted 15° in azimuth (i.e., the angle between the velocity vector and the antenna pointing direction) but not in (**b**). The horizontal axis is the azimuth position of the transmitted source (GPS); while the vertical is its elevation. In both selected cases the attitudes of the scatterometer antenna and the solar panel are the same

them in 4 positions (16 different configurations) both with GPS antenna placed as it is shown in Fig. 3 or tilted 15° (32 diagrams). In Fig. 4 some diagrams are shown presenting a selection of the most favorable positions of the GPS antenna.

From Fig. 4 the azimuth tilting of about 15° of the antenna minimizes in a no-negligible way the multipath effects of the satellite, which induces an uncertainty of up to 12°. The drawback of the proposed solution is the reduction of the number of occultations that will be observed, but only few tens of events are missed. Therefore we deem as the best solution the antenna position tilted 15° in azimuth with respect to the velocity direction.

3 Software Development

In parallel to the ROSA receiver project, ASI has started the development of software devoted to GPS RO data processing as well. The objective of such a project is manifold. First of all, ASI is planning to cover every step of the processing chain from data acquisition to the provision of products and applications suitable for the user community covering scientific as well as social aspects. Secondly, we plan to create a national scientific community, which will work on respective topics and be able to promote a fully exploitation of GPS RO as well as develop state of the art algorithms relevant for atmospheric physics, meteorology, and climatology. Furthermore, ASI aims to meet the strategic challenge of making GPS RO a tool suitable for operational meteorology as well as for proper global change monitoring. Finally, for the development of such tool we will use innovative computing solutions like for example the GRID computing (hereafter GC) approach.

GC computing, according to Foster and Kesselman (1998), is a strategy to develop services and standard protocols for sharing computing and archiving facilities, which are kept hidden from the users. The GC extends the electric power grid approach to computing, i.e., you can connect to the network by simply plug in. The current development of the GC will be helpful in sharing computing power, data exchange archive, and dissemination services etc.

The software consists basically of two modules. The first one is devoted to the Precise Orbit Determination (hereafter POD) of LEO: SoftWare for OCEANSAT-2 Orbit Determination (SWORD). A version of SWORD is already running. It adopts a dynamical approach of POD, i.e., it models all the possible conservative perturbations acting on an Earth's satellite like static part of gravity field, Earth and ocean tides, *n*-body interactions as well as non-gravitational like Earth's albedo, solar radiation pressure, atmospheric drag, thermal drag due to Sun heating, and infrared radiation sent forth by Earth etc. The mathematical and statistic algorithms applied in SWORD are well described in Tapley (1989). Although the dynamical approach is suitable to perform subtle orbit analysis in the field of space geodesy it could turn out unpractical for operational applications. Thus for operational meteorology applications we would need to estimate the orbits in near real time (with a time lag < 1 h and an accuracy < 50 cm at least). The orbit solutions given by the dynamical approach need more time than the kinematic one. Thus we plan to enhance the current version of SWORD with kinematic algorithms in view of its application in operational meteorology. For this purpose we need to construct single and double differences with ground GPS network observations.

The second module is just the data processing chain of GPS RO from the excess shift Doppler (level 1) to the production of pressure, temperature, and water vapor profiles (level 3). In view of the OCEANSAT-2 space mission the project plans to issue a first release of the software with reliable algorithms implemented. This first release, named basic in Table 2, has the purpose to cover the processing chain of GPS RO data in the first phase of the OCEANSAT-2 mission. On the other hand, the new algorithms developed in the GC environment, after proved reliability, will be implemented in the data processing tool. Table 2 summarizes the main features of the software.

Concerning the computation of the bending angle as a function of the impact parameter (step a) we apply in the first release the method of geometric optics; while in the final version we are confident to implement the method of physical optics processing the wave field by a Fourier integral operator associated with the canonical transform (Gorbunov 2002) as well as other variations of radio-holographic techniques (Hocke et al. 1999; Sokolovskiy 2001; Beyerle et al. 2003). These subtle algorithms are needed because the principles of geometric optics do not work properly for the low layers of the troposphere over equatorial zones where irregularities are not negligible. The GPS receiver will track in open loop mode when the GPS signal crosses the lowest layers of the atmosphere. So, we have to get ready to process this new kind of data (step b). Another challenging activity concerns the retrieval of humidity profiles (step e). We plan to implement indeed the iterative algorithms proposed by Gorbunov ana Sokolovskiy (1993) as well as the 1DVAR approach (Healy and Eyre 2000). Particularly intriguing will be the implementation of new algorithms, which will try to avoid the use of external information (de la Torre Juàrez

Table 2 The table summarizes the processing chain of the software. The basic column describes briefly the main algorithms, which will be part of the first release of the software; while in the final column the main algorithms we plan to implement in the next release are pointed out

	Basic	Final
a. L1 and L2 bending angle vs. impact parameter profiles	Geom. opt. methods	Canonical Transform (CT), Full Spectrum Inversion (FSI) (physical opt.)
b. Ionosphere free bending angle vs. impact parameter profiles	Std technique needed both L1 and L2	Tomography and use of open loop data
c. Stratospheric initialization of ionosphere-free bending angle vs. impact parameter profiles	through global climatology	through local climatology
d. Dry air vertical atmospheric parameters	Abel integral, hydrostatic equation	Boundary Profile eValuation (BPVα), (see Vespe and Persia 2006)
e. Water vapor and vertical atmosphere parameters	through climatological models	Numerical Weather Prediction (NWP) or stand alone techniques (BPWn), (see Vespe et al. 2004), 1DVAR
f. Electron density vertical profiles	Onion peeling	Tomography

and Nilsson 2003; Vespe et al.2004; Vespe and Persia 2006. Before including these algorithms in the processing chain we need to extensively test and validate them.

4 Scientific Activities

Scientific activities not strictly relevant for the development of the data processing chain but based on GPS RO data, are encouraged and funded in the fields of climatology, operational meteorology, space weather, and space geodesy. We are going to describe some activities for which we have already preliminary results.

4.1 Space Geodesy

In the last decade the launch of several satellites able to probe the atmosphere with the GPS RO technique like GPS/MET, SAC-C, CHAMP, GRACE, Formosat-3/COSMIC, TerraSAR-X, MetOp-A etc., have made available a huge amount of data. These data currently are used to reconstruct the mapping function (hereafter MF). The MF is helpful to assess in a proper way the atmosphere delay, which disturbs the estimated coordinates of ground GPS station. The tropospheric delay is given by the following relationship: $\mathrm{ZTD} \cdot m(E)$ where ZTD stands for the zenith total delay, which is estimated together with the coordinates. The MF has the form

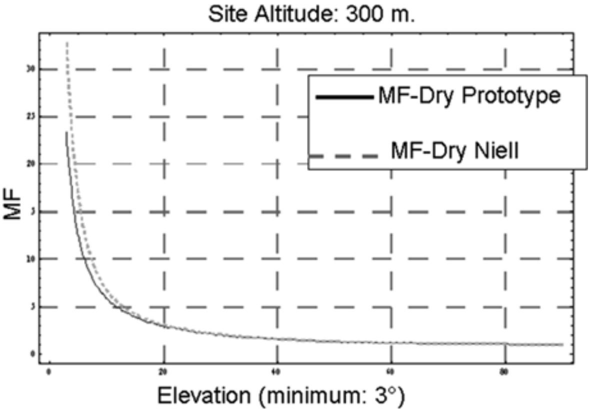

Fig. 5 The *solid line* represents the MF derived from GPS RO data while the *dotted gray line* is the Niell MF. The plot is achieved for a site altitude of 300 m

$$m(E) = \frac{1+\frac{a}{1+\frac{b}{1+c}}}{\sin(E)+\frac{a}{\sin(E)+\frac{b}{\sin(E)+c}}} + \left(\frac{1}{\sin(E)} - \frac{1+\frac{a_h}{1+\frac{b_h}{1+c_h}}}{\sin(E)+\frac{a_h}{\sin(E)+\frac{b_h}{\sin(E)+c_h}}}\right)h. \quad (1)$$

E stands for the elevation angle of the GPS satellite from the horizon. The coefficients a, b, c are indeed functions of latitude and height of the site of which we want to compute the coordinates and the day of the year. Niell (1996) used the same MF estimating the coefficients by using atmospheric profiles retrieved with balloons. We are re-computing these coefficients using the profiles coming from the GPS RO space missions. In Fig. 5 the MF derived from GPS RO data is compared with Niell one.

The next step will be the validation of our MF. For this purpose we will implement it in BERNESE software to estimate the coordinates of the nodes of a GPS ground network. Then the results will be validated against the same solutions achieved applying different MFs (namely Niell). The job is currently performed by the INNOVA company, which is part of the ROSA project.

4.2 Climate

In the context of ROSA research the University of Camerino proposes an approach to use GPS RO data to study gravity waves and clear air turbulence. In order to perform this study we have to exploit the vertical resolution of the radio occultation signal. The target of the present study is the Mediterranean region, where sources of gravity waves are present because of the existing complex orography. The analysis will be performed on data coming from different radio occultation sources such as the Formosat-3/COSMIC, CHAMP, and ROSA missions. Gravity waves observed at scales within the resolving power of RO can be generated by various dynamical “unbalance” processes, typically interactions of atmospheric flows with mountains, and/or adiabatic processes and propagation in the troposphere. Atmospheric gravity waves are currently treated by applying only a statistical approach. An outstanding example is the so called wave-drag introduced a couple of decades ago in the global models (see Pulido and Thuburn 2005).

The Mediterranean area is rich of potential sources of gravity waves for the obvious reason of being surrounded by high and steep mountains and dominated by a thermal source like the Mediterranean Sea. It has long been suspected that gravity and gravity-inertia waves can play a deterministic role in the local Mediterranean dynamics, in particular during the occurrence of frontal precipitations in the area. If we consider the wave oscillations as small perturbations of the "background profile" (computed for example by using a filter at 8 km), the normalized temperature fluctuation can be assumed to follow a gravity wave dynamics dictated by the background Brunt-Väisälä frequency.

In order to study some gravity wave climatologies, we adopt the point of view of Smith et al. (1987) concerning velocity fluctuations successively extended by Allen and Vincent (1995) to temperature fluctuations. The analysis accounts for some limitations of radio occultation measurements, such as the real resolution of the observation given by the size of the Fresnel diameter (e.g., Hinson and Magalhaes 1991). If we would not consider this real resolution, phenomena appearing as gravity waves could instead be related to sub-Fresnel scale noise (Marquardt and Healy 2005).

4.3 Space Weather

The contribution to the project of the National Research Council of Italy (CNR) based in Florence (i.e., from the Complex System Institute, ISC, and the Applied Physics Institute "Nello Carrara", IFAC) is a study on the role of Total Electron Content (hereafter TEC) data from a LEO satellite in space weather. Note that both RO data and navigational data are included in the study of TEC data from LEO satellites. This study plans to cover three tasks: A quantitative assessment of how processing TEC data from a LEO improves the retrieval of ionospheric profiles via stochastic inversion techniques (SIT); a study of how the navigational TEC data from a LEO satellite may be used to monitor the space weather; a study of the fine structure of the ionosphere by analyzing the fine structure of the RO data. Since real TEC data from the ROSA receiver will be available only in the future, currently our investigations are carried out on data from other LEOs (CHAMP and Formosat-3/COSMIC), assuming it will be sensible to apply these achievements to ROSA data. The study on the retrieval of ionospheric vertical profiles via a SIT consists of assessing the improvement brought by involving RO data, optimizing the inversion parameters in the SIT with RO and studying the assimilation of GPS, ROSA, and ionosonde data (this last item could lead to real time inversion). The profiles $N_e(h)$ retrieved via SIT will be compared with independent measurements of related quantities, e.g., from ionosondes. TEC data used will be those from the GPS network and CHAMP, while ionosonde data will come from the Space Physics Interactive Data

Resource (SPIDR) website and the European Digital Upper Atmosphere Server network (DIAS). Real data from ROSA will be used as soon as available.

The purpose of our second research line is the assessment of the possibility of monitoring the response of the geospace to heliophysical events by using the navigational data from GPS receivers onboard a LEO, giving information about the topside part of the ionosphere and the plasmasphere. In this framework we are going to build a dynamical picture of Sun-geospace interaction, working mainly on "historical" data series as those from the TOPEX mission. Then, these findings will be applied to the already existing LEO data base (CHAMP and Formosat-3/COSMIC), and then to the real data from ROSA. Ionospheric irregularities are studied analyzing the RO data from LEOs at a time scale as small as possible, and sensible. With a suitably high sampling frequency (e.g., 50 Hz for the GPS ground receivers) it would be possible to detect very small scale structures inducing radio scintillation, which may not be the case of ROSA. However, the present investigation is focused on the development of suitable data analysis tools to process non-stationary signals with a rich multi-scale structure, as those due to the "intermittent" nature of the plasma distribution that generates them. The tool chosen is the wavelet analysis. Investigating the small scale structure of the ionospheric medium by analyzing RO data from a LEO will be useful for two purposes: On the one hand one might make a comparison between the radio scintillations of mainly ionospheric origin (from ground GPS receivers) and that of mainly low-ionospheric or tropospheric origin (the RO data from a LEO), on the other hand, even if the sampling time of the LEO data would not be enough for scintillation studies, however the wavelet analysis of RO data will render it possible to understand the vertical distribution of the ionosphere irregularities.

5 Conclusions and Remarks

The Italian Space Agency has put a lot of effort and energy in developing hardware and software tools devoted to GNSS RO in the last decade. Currently its strategy is to cover all the steps of the processing chain from data acquisition down to end-user products and applications. It is acquainted with the possibilities that in the next decade the exploitation of the GNSS technique could boost dramatically research and operations in the field of climate and meteorology. ASI indeed wants to join the current international efforts aiming to make GNSS RO reliable and relevant for atmospheric remote sensing applications. The objective can be pursued using the large number of space missions currently devoted to GPS RO: CHAMP, GRACE, Formosat-3/COSMIC, MetOp, TerraSAR-X. ASI currently does not plan to have an own space mission devoted to RO where to embark ROSA receiver. Thus ASI is asking for installing it as an added payload on other international space missions just like the Indian OCEANSAT-2 and next Argentinian SAC-D. The main drawback of this approach, however, is that ROSA sometimes does not find a proper allocation on the satellite. The two high gain antennas indeed are quite big and they must be mounted only facing in turn the velocity and anti-velocity direction. Thus often there is no room to place the GPS RO antennas in a proper position. For this purpose ASI team is conceiving a space mission of dozen of mini-satellites fully devoted to GPS RO like Formosat-3/COSMIC. On the other hand ASI is strongly interested to use ROSA also in bistatic mode, i.e., able to catch the GPS signal reflected by the water surfaces. For this purpose the development of a next release of the software ROSA devoted to this kind of applications is planned as well as for the treatment of GPS RO from sub-orbital platforms.

References

Allen S, Vincent R (1995) Gravity waves activity in the lower atmosphere: Seasonal and latitudinal variations. J Geophys Res 100:1327–1350

Beyerle G, Gorbunov ME, Ao CO (2003) Simulation studies of GPS radio occultation measurements. Radio Sci 38(5):1084, doi:10.1029/2002RS002800

Foster I, Kesselman C (eds) (1998) The Grid: Blueprint for a New Computing Infrastructure. Morgan Kaufmann, San Fransisco

Gorbunov ME (2002) Canonical transform method for processing radio occultation data in the lower troposphere. Radio Sci 37(5):1076–1085

Gorbunov ME, Sokolovskiy SV (1993) Remote Sensing of Refractivity from Space for Global Observations of Atmospheric Parameters. Tech. Rep. 119, Max Planck Institute for Meteorology, Germany

Healy GA, Eyre J (2000) Retrieving temperature, water vapor and surface pressure information from refractive index profiles derived by radio occultations: A simulation study. Q J R Meteorol Soc 126:1661–1683

Hinson D, Magalhaes J (1991) Equatorial waves in the stratosphere of Uranus. Icarus 94:64–91

Hocke K, Pavelyev AG, Yakovliev OI, Barthes L, Jakowski N (1999) Radio occultation data analysis by the radioholography method. I Atmos Terr Phys 61:1169–1177

Marquardt C, Healy CS (2005) Measurement noise and stratospheric gravity wave characteristics obtained from GPS occultation data. J Meteorol Soc Jpn 83:417–428

Niell AE (1996) Global mapping functions for the atmosphere delay at radio wavelengths. J Geophys Res 101:3228–3246

Pulido M, Thuburn J (2005) Gravity wave drag estimation from global analyses using variational data assimilation principles. I: Theory and implementation. Q J R Meteorol Soc 131(609):1821–1840

Smith SA, Fritts DC, VanZandt TE (1987) Evidence for a saturated spectrum of atmospheric gravity waves. J Atmos Sci 44:1404–1410

Sokolovskiy SV (2001) Modeling and inverting radio occultation signals in the moist troposphere. Radio Sci 36(3):441–458

Tapley BD (1989) Fundamentals of orbit determination. In Theory of Satellite Geodesy and Gravity Field Determination. Springer Verlag, Berlin

de la Torre Juárez M, Nilsson M (2003) On the detection of water vapor profiles and thin moisture layers from atmospheric radio occultations. J Geophys Res 108(D9):4276, doi:10.1029/2002JD002880

Vespe F, Persia T (2006) Derivation of the water vapor content from the GNSS radio occultations observations. J Atmos Ocean Technol 23(7):936–943

Vespe F, Benedetto C, Pacione R (2004) The use of refractivity retrieved by radio occultation technique for the derivation of atmospheric water vapor content. Phys Chem Earth 29:257–266

Radio Occultation Mission in Korea Multi-Purpose Satellite KOMPSAT-5

S. Cho, J. Chung, J. Park, J. Yoon, Y. Chun, and S. Lee

Abstract The first occultation mission in the Korean space program, KOMPSAT-5, is scheduled for launch in 2010. KOMPSAT-5 will have a dual frequency GPS receiver to generate precision orbit determination data and occultation data. The KOMPSAT-5 spacecraft and the characteristics of its occultation payload are described in this paper. An occultation processing system developed by KASI is also introduced.

1 Introduction

Recently, GPS radio occultation is one of the most active GPS and low Earth orbit satellite application. After the launch of COSMIC program, the area of utilization of GPS radio occultation has been expanded. Although, the amount of occultation data increases steadily and the occultation data are provided in near real-time, the demand of practical application of occultation requires more dense global coverage and real time data provision. Many new space missions that include GPS radio occultation instruments are planned and will be launched in the near future. One of them is the KOMPSAT-5 (KOrea Multi-Purpose SATellite-5) program. The KOMPSAT-5 carries a space-borne dual frequency GPS receiver and generates POD (Precision Orbit Determination) data and GPS radio occultation data. The KOMPSAT-5 program is the first space program with GPS occultation instrument in Korea and is expected to contribute to the global occultation observations. KASI (Korea Astronomy and Space Science Institute) is in charge of the development of a dual frequency GPS receiver and also an occultation science program for the KOMPSAT-5 mission. In this paper, we introduce the KOMPSAT-5 program and its payload for the GPS occultation mission. The occultation mission of KOMPSAT-5 and the occultation processing system currently being developed by KASI are also discussed.

S. Cho (✉)
Korea Astronomy and Space Science Institute, Daejeon, Korea
e-mail: skcho@kasi.re.kr

A. Steiner et al. (eds.), *New Horizons in Occultation Research*,
DOI 10.1007/978-3-642-00321-9_22, © Springer-Verlag Berlin Heidelberg 2009

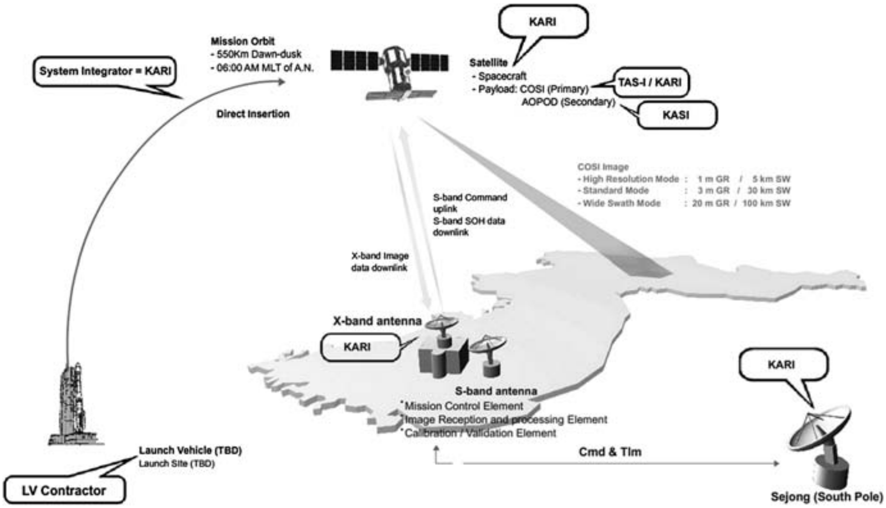

Fig. 1 KOMPSAT-5 program architecture

2 KOMPSAT-5

The KOMPSAT program is a government funded space program which was started in the mid 90's. The first satellite of the KOMPSAT program was launched in 1999 and the second satellite was launched in 2006. Currently, KOMPSAT-3 and KOMPSAT-5 are under development at the same time.

KOMPSAT-5 is in the critical design phase and scheduled to be launched in 2010. The main mission of KOMPSAT-5 is observing the Earth by using a Synthetic Aperture Radar (SAR). In Fig. 1, the KOMPSAT-5 program architecture is described (Lee 2007). In order to satisfy the orbit determination accuracy requirements, Atmosphere Occultation and Precision Orbit Determination (AOPOD) system is used. The AOPOD system consists of a dual frequency GPS receiver and a Laser Retro Reflector Array (LRRA). The dual frequency GPS receiver generates precision orbit determination data and GPS radio occultation data. The LRRA is used for POD validation of KOMPSAT-5.

3 AOPOD System

3.1 IGOR Receiver and GPS Antennas

The Integrated GPS and Occultation Receiver (IGOR) is manufactured by Broad Reach Engineering and is based on the heritage of the JPL (Jet Propulsion Laboratory) Black Jack receiver. Since KOMPSAT-5 uses 1553B bus as a main interface, the KOMPSAT-5 IGOR has been modified to include a 1553B interface. An internal solid state recorder (SSR) was added in the IGOR for storing receiver output data during the mission. Since KOMPSAT-5 carries a SAR device, IGOR uses four external filters between each of the GPS antennas and IGOR in order to avoid interferences from the SAR devices. Figure 2 shows an engineering model of the KOMPSAT-5 IGOR receiver. One of the filter/preamp assemblies is on the top of the receiver frame. The KOMPSAT-5 IGOR has two POD antennas and two occultation antennas. Figure 3 shows the KOMPSAT-5 POD and occultation antennas. The POD antenna is a patch type omnidirectional antenna attached on the $-Z$ plane of the KOMPSAT-5.The occultation antenna is a patched array type antenna to optimize the performance for an occultation science. The occultation antennas are installed in the velocity and anti-velocity direction for observing rising and setting occultations. The normal operation mode of KOMPSAT-5 is a 33.7° tilted right looking mode. For the occultation antennas, the tilt angle is compensated by using appropriate brackets. Figures 4 and 5 show the configuration of the KOMPSAT-5 POD and occultation antennas, respectively. Table 1 summarizes the characteristics of the KOMPSAT-5 IGOR.

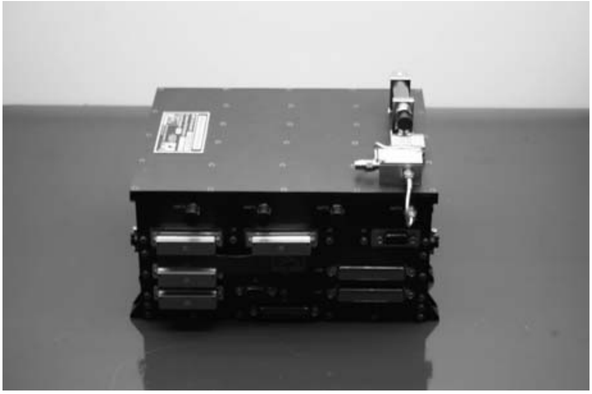

Fig. 2 KOMPSAT-5 IGOR engineering model

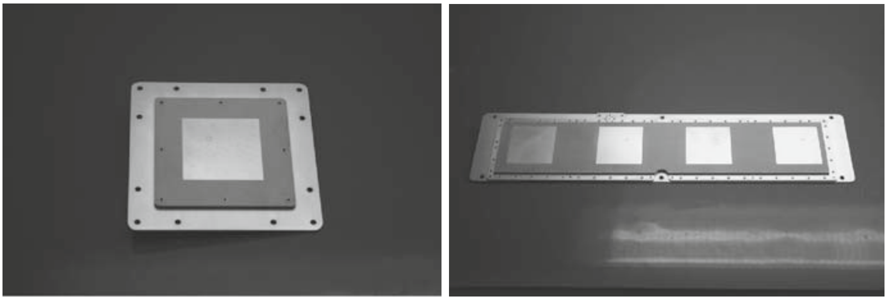

Fig. 3 KOMPSAT-5: POD antenna (*left*) and occultation antenna (*right*)

Fig. 4 Location of the KOMPSAT-5 POD antennas

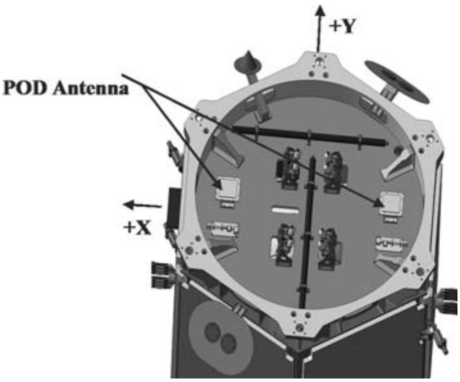

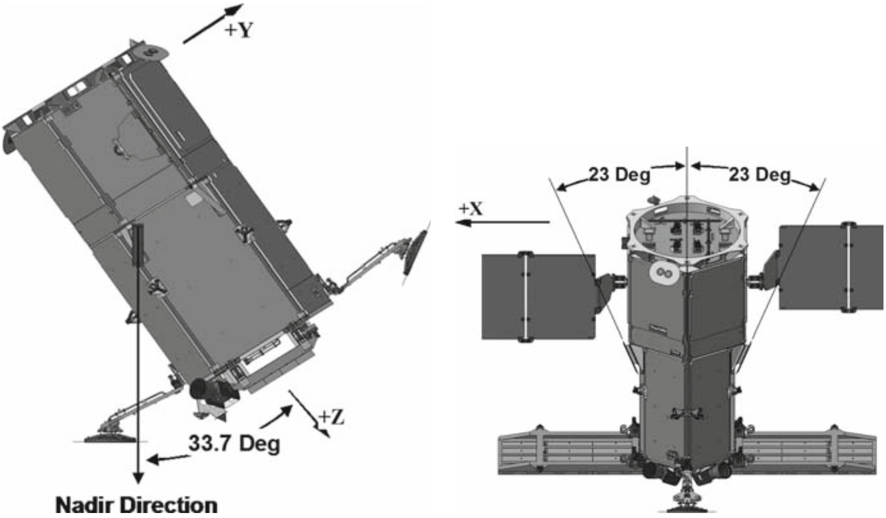

Fig. 5 Configuration of the KOMPSAT-5 occultation antennas

Table 1 KOMPSAT-5 IGOR characteristics

KOMPSAT-5 IGOR	Specification
Internal memory	128 MB solid state recorder
Bus interface	MIL-STD 1553B bus/RS422
POD antenna	Two patch type antennas
Occultation antenna	Two patched array antennas
External signal filter	Four Filter/Preamp assemblies
RF port	Four RF ports, 12 channels per port

3.2 Laser Retro Reflector Array

A Laser Retro Reflector Array (LRRA) will be used for POD validation of KOMPSAT-5. The KOMPSAT-5 LRRA developed by GFZ (GeoForschungsZentrum) is shown in Fig. 6. The KOMPSAT-5 LRRA has four cube corner prisms mounted in a compact frame. A bracket will be used to compensate the tilt angle of the spacecraft and ensuring a better field of view. Figure 7 shows the configuration of the LRRA.

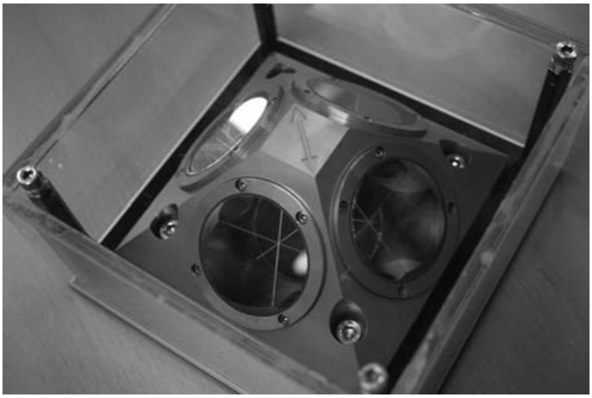

Fig. 6 KOMPSAT-5 laser retro reflector array

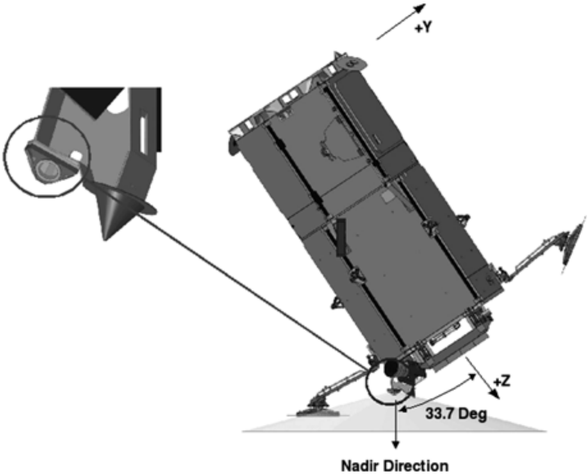

Fig. 7 Location of the KOMPSAT-5 laser retro reflector array

Table 2 KOMPSAT-5 orbital elements

Orbital elements	Mean values
Semi-Major Axis (km)	6928.114
Eccentricity	0.00107
Inclination (deg)	97.60
R.A of Ascending Node (deg)	339.73
Argument of Perigee (deg)	90.0
Mean Anomaly (deg)	270.0

4 Occultation Characteristics

4.1 Mission Orbit

The mission orbit of KOMPSAT-5 is a Sun-synchronous dawn-dusk circular orbit with an average altitude of 550 km which provides about 14.5 revolutions per day. In Table 2, the KOMPSAT-5 orbital elements are listed for the reference.

4.2 Occultation Characteristics

For KOMPSAT-5, the occultation mission is a secondary mission. The KOMPSAT-5 has two occultation antennas for rising and setting occultations observations. Simulations of the KOMPSAT-5 mission are provided by using EGOPS (End-to-end GNSS Occultation Performance Simulator) (Kirchengast et al. 2002). It has been shown that KOMPSAT-5 may observe more than 500 occultation events per day in normal conditions. Figure 8 shows all occultation events for one day of simulation for KOMPSAT-5. The data from two POD antennas are utilized together with occultation data. The observed occultation data will be stored in the Solid State Recorder (SSR) and collected by the spacecraft's 1553B bus interface. The data downlink to the ground station is via S-band telemetry.

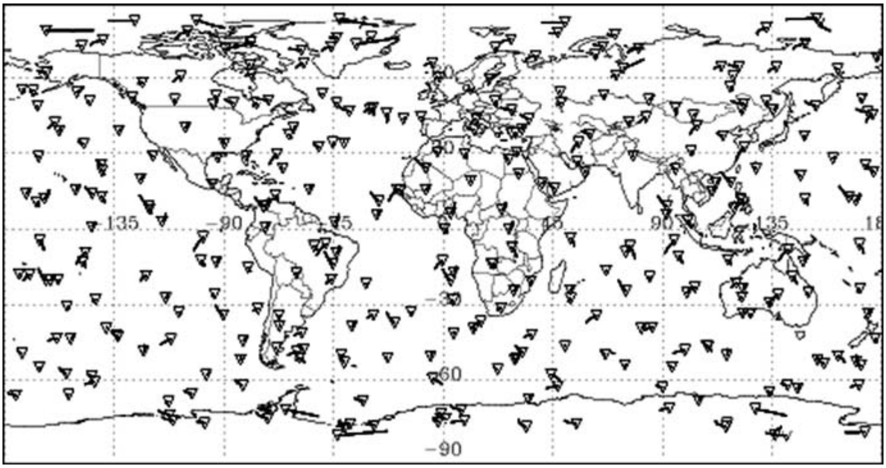

Fig. 8 Sample of one day occultation simulation of KOMPSAT-5

5 Occultation Data Processing System

KASI is in charge of the scientific research using KOMPSAT-5 occultation data. The scientific data of KOMPSAT-5 will be released to the public. KASI plans to release raw data and processed data. KASI is developing KROPS (KASI Radio Occultation Processing System) for processing the GPS radio occultation data and generating atmospheric profiles. Figure 9 describes the external interface of KROPS. In Fig. 9,

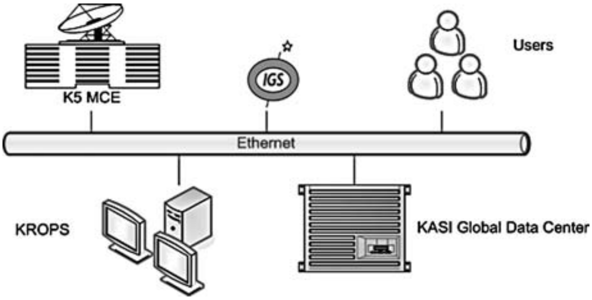

Fig. 9 KROPS external interfaces

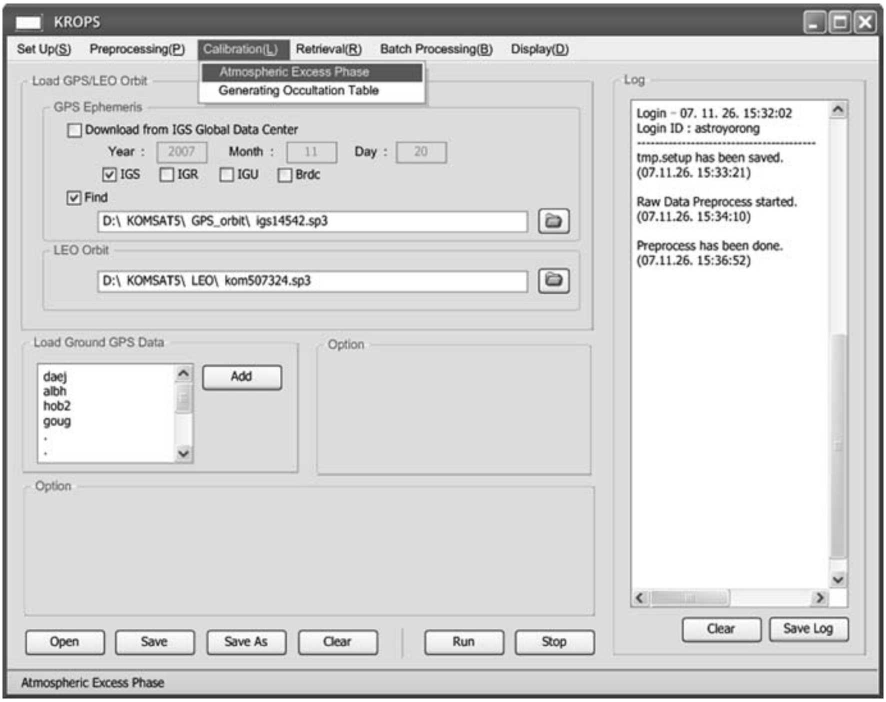

☐ Download from IGS Global Data Center
Year : 2007 Month : 11 Day : 20
☑ IGS ☐ IGR ☐ IGU ☐ Brdc
☑ Find
D:\ KOMSAT5\ GPS_orbit\ igs14542.sp3

D:\ KOMSAT5\ LEO\ kom507324.sp3

daej
albh
hob2
goug
.
.

```
Login - 07. 11. 26. 15:32:02
Login ID : astroyorong
----------------------------------------
tmp.setup has been saved.
(07.11.26. 15:33:21)

Raw Data Preprocess started.
(07.11.26. 15:34:10)

Preprocess has been done.
(07.11.26. 15:36:52)
```

Atmospheric Excess Phase

Fig. 10 KROPS main window

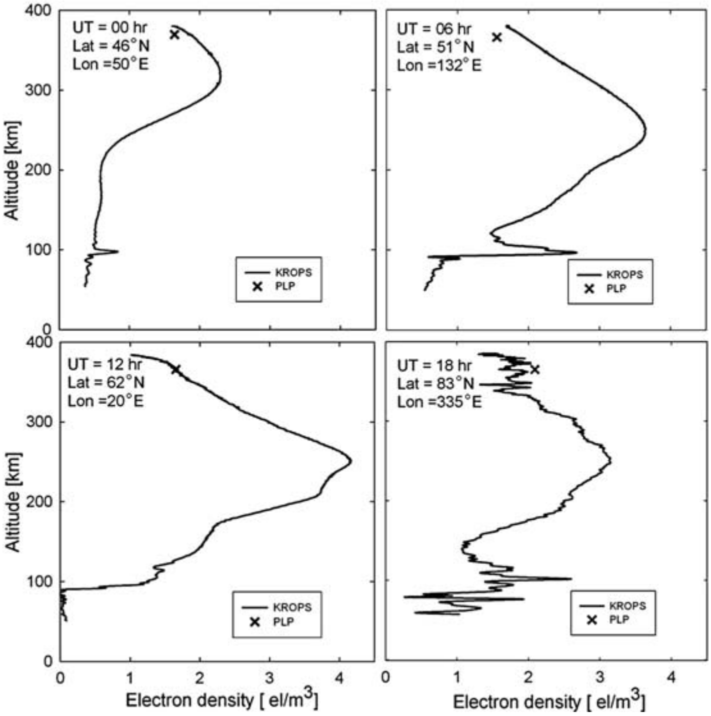

Fig. 11 Preliminary results of KROPS

K5 MCE is the KOMPSAT-5 Mission Control Element, which receives the occultation and POD data from the spacecraft. KASI operates also the IGS (International GNSS Service) Global Data Center (GDC). The occultation data will be archived in the KASI GDC and then released to public users.

A Linux-based PC workstation is used as a platform for KROPS. Figure 10 shows the user interface of KROPS. The algorithm implemented in KROPS has been tested by using data from CHAMP and COSMIC. In Fig. 11, preliminary results of processing CHAMP data from June 20, 2004 with KROPS are shown. The comparison data are from the PLP (Planar Langmuir Probe) of CHAMP (Lee et al. 2007).

6 Summary and Conclusions

Currently, KOMPSAT-5 is in a detailed design phase. KASI is in charge of developing of the AOPOD system, which includes a dual frequency GPS receiver and a laser retro reflector. A dual frequency GPS receiver will be used for generation of POD data and occultation science data. For processing the occultation data, KASI is developing KROPS. The first version of KROPS will be released by the end of year 2008.

Since KOMPSAT-5 has only one ground station, KOMPSAT-5 contacts the ground station twice a day. The occultation data from KOMPSAT-5 will be released only twice a day. The limitation of S-band telemetry downlink rate of KOMPSAT-5 restricts the amount of occultation data, which can be downloaded to the ground station. Current estimation of maximum amount of occultation data is 30 MB/day. In addition to this limitation, due to the location of the occultation antennas on the KOMPSAT-5, multi-path problems and field of view limitations are expected.

References

Kirchengast G, Fritzer J, Ramsauer J (2002) End-to-end GNSS Occultation Performance Simulator Version 4 (EGOPS4) Software User Manual. Tech. Rep. 3, IGAM/UG Technical Report for ESA/ESTEC, Institute for Geophysics, Astrophysics, and Meteorology, Univ of Graz, Austria

Lee S (2007) Introduction of KOMPSAT-5 Program. 1st AOPOD Workshop 2007, Jeju Island, Korea

Lee W, Chung J, Cho S, Park J, Cho J, Yoon J, Lee J, Chun Y, Lee S (2007) Retrieval of electron density profile for KOMPSAT-5 GPS radio occultation data processing system. J Astron Space Sci 24(4):297–308

The Contribution of PROBA2-LYRA Occultations to Earth Atmosphere Composition Analysis

M. Dominique, D. Gillotay, D. Fussen, F. Vanhellemont, J.F. Hochedez, and W. Schmutz

Abstract LYRA is a solar EUV/VUV radiometer that will embark in early 2009 on-board the PROBA2 mission. Its heliosynchronous orbit generates brief eclipses, during which we intend to study the vertical distribution of the global extinction coefficient, using the solar occultation method. We also consider the potential of our approach in retrieving the thermospheric N_2, O, O_2 and mesospheric O_2 and O_3 densities from the extinction coefficient. A forward model of the atmosphere transmittance is presented. This model includes the ability to incorporate the inhomogeneities of solar emission over the Sun's surface to enhance the vertical resolution in the results. The chosen inversion method is provided as well, and tested with simulated data.

1 Introduction

LYRA, the Lyman-Alpha Radiometer, is a solar EUV/VUV (extreme ultraviolet/vacuum ultraviolet) radiometer (Hochedez et al. 2006) that will embark in early 2009 on-board PROBA2, the Project for On-Board Autonomy 2, an ESA (the European Space Agency) micro-mission. It will monitor the solar flux in four passbands relevant to solar physics and space weather. LYRA has been designed by the Royal Observatory of Belgium (ROB), with Dr. J.-F. Hochedez as principal investigator, and built by the Physikalisch-Meteorologisches Observatorium, Davos (PMOD), with Dr. W. Schmutz as lead co-investigator. LYRA benefited from additional important contributions from its international partnership: CSL, Liege and IMOMEC, Diepenbeek both in Belgium, MPS, Lindau, Germany, and NIMS, Tsukuba, Japan.

The four LYRA passbands are:

- Lyman-Alpha (Ly): 115–125 nm
- Herzberg continuum (Hz): 200–220 nm

M. Dominique (✉)
Royal Observatory of Belgium; Belgian Institute for Space Aeronomy, Brussels, Belgium
e-mail: marie.dominique@oma.be

A. Steiner et al. (eds.), *New Horizons in Occultation Research*,
DOI 10.1007/978-3-642-00321-9_23, © Springer-Verlag Berlin Heidelberg 2009

- Aluminium filter (Al): 17–80 nm
- Zirconium filter (Zr): 1–20 nm

LYRA will benefit from pioneering wide bandgap detectors based on diamond. These sensors make the instrument radiation hard and solarblind: They minimize the use of additional filters needed to block the unwanted visible light but also attenuate seriously the desired UV radiation. This enhances the detector's effective area, and therefore increases the accuracy, the acquisition frequency, or an optimal combination of both. The PROBA2 heliosynchronous orbit generates brief eclipses three months per year. Our main purpose is to see whether those eclipses may be used to study the high atmosphere composition by the solar occultation method. Chemical species addressed are thermospheric N_2, O, O_2 and mesospheric O_2 and O_3 in the winter hemisphere. LYRA's high acquisition frequency (up to 100 Hz) and signal-to-noise ratio enable a very favorable vertical sampling, which is unfortunately counterbalanced by the extent and inhomogeneity of the solar source. For example, for a punctual light source, we would expect an altitude resolution of 3 km for a 1 Hz acquisition cadence, while the limitation introduced by the Sun extension is $\simeq$25 km. In this paper, we present the forward modeling and the chosen inversion method. The latter takes the above hurdles into account by dividing the Sun surface into parcels and analyzing the contribution of each parcel independently. We analyze the potential offered by this method and illustrate it with our first results, obtained from simulated data.

2 Forward Model of the Atmosphere Transmittance

Extinction of the solar emission by the atmosphere at a given wavelength λ is deduced from the well-known Beer-Lambert (or Bouguer) law:

$$I(\lambda) = I_0(\lambda)\exp\{-\tau(\lambda)\} \tag{1}$$

where $I_0(\lambda)$ is the solar spectral irradiance at wavelength λ, $I(\lambda)$ is the solar spectral irradiance after absorption by the atmosphere, and $\tau(\lambda)$, the optical thickness, which is defined by

$$\begin{aligned}\tau(\lambda) &= \int_0^L \sum_{i=0}^{N} n_i(z(s))\sigma_i(\lambda)\mathrm{d}s \\ &= \int_0^L \gamma(\lambda, z(s))\mathrm{d}s\end{aligned} \tag{2}$$

Here,

- N is the number of active atmospheric constituents,
- the integration is performed over the optical path (with L, the distance between the Sun and the satellite measured along this path).
- $n_i(z(s))$ is the density of the atmospheric constituent i at altitude $z(s)$,

- $\sigma_i(\lambda)$ is the absorption cross-section of constituent i at wavelength λ,
- $\gamma(\lambda, z(s))$ is the extinction coefficient.

Note that, in Eq. (2), only absorption takes part in the extinction process. The contribution of molecular scattering has been neglected so far. The impact of such an approximation is still under investigation. It is foreseen to introduce it later in the model for the channels for which it is relevant.

LYRA is a full-Sun radiometer. Due to the wide angular size of the Sun (30 arcmin), the optical path is highly dependent on the emitting zone of its surface. At the nearest point to the Earth's surface (the so-called tangential point), rays emitted by the different zones of the Sun's surface span over approximately 25 km (Fussen et al. 1997, 2001), which would drastically limit the vertical resolution of our retrieval, if not taken into account in the modeling. The measured atmospheric transmittance, defined as the ratio of the irradiance after absorption to the unattenuated irradiance, observed in the LYRA channel c, may be modeled by

$$T_c(r_\perp) = \frac{\int_0^\infty \mathrm{d}\lambda F_c(\lambda) \int_0^{\theta_{\max}} \mathrm{d}\theta \sin(\theta)\cos(\theta+\xi) \int_0^{2\pi} \mathrm{d}\varphi \exp(-\tau(\lambda,\theta,\varphi)) I_0(\lambda,\theta,\varphi)}{\int_0^\infty \mathrm{d}\lambda F_c(\lambda) \int_0^{\theta_{\max}} \mathrm{d}\theta \sin(\theta)\cos(\theta+\xi) \int_0^{2\pi} \mathrm{d}\varphi I_0(\lambda,\theta,\varphi)} \tag{3}$$

where

- $r_\perp$ is the tangential radius,
- θ, φ, and ξ are illustrated in Fig. 1. Parameters θ and φ identify the emitting zone of Sun surface,
- F_c is the instrumental response in channel c.

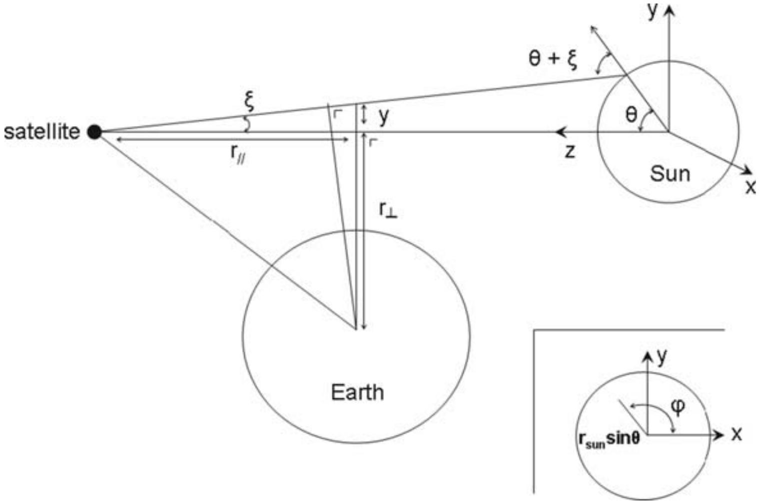

Fig. 1 Geometrical representation of the occultation configuration

Since the Sun radius (r_{Sun}) is tiny compared to the Sun – detector distance d_{SD}, we can neglect ξ and replace $\theta_{\max}$ by $\frac{\pi}{2}$. As a startpoint, let us also consider a revolution symmetry on I with respect to φ, which is a rather crude approximation in which the major emission spatial variability would come from the limb darkening or limb brightening, depending on the considered wavelength. This approximation will be given up later without too many difficulties.

Then, following Lumpe et al. (1991), we will apply the variables substitution:

$$\begin{cases} \mu = \cos(\theta) \\ y = \beta \sin(\theta)\sin(\varphi). \end{cases} \tag{4}$$

We obtain

$$T_c(r_\perp) = \frac{2\int_0^\infty \mathrm{d}\lambda\, F_c(\lambda) \int_{-\beta}^{\beta} \mathrm{d}y \int_0^b \mathrm{d}\mu \frac{\mu}{\beta\sqrt{b^2-\mu^2}} \exp\left[-\tau(\lambda, z_\perp + y)\right] I_0(\lambda, y, \mu)}{2\int_0^\infty \mathrm{d}\lambda\, F_c(\lambda) \int_{-\beta}^{\beta} \mathrm{d}y \int_0^b \mathrm{d}\mu \frac{\mu}{\beta\sqrt{b^2-\mu^2}} I_0(\lambda, y, \mu)} \tag{5}$$

with $\beta = r_{\mathrm{Sun}} r_{//}/d_{\mathrm{SD}}$, $b = (1 - y^2/\beta^2)^{1/2}$, and $z_\perp = r_\perp - r_{\mathrm{E}}$ is the tangential altitude of rays emitted by the Sun center.

A further approximation is made by separating the spectral and spatial components of the non-attenuated irradiance $I_0(\lambda, y, \mu) = I_1(\lambda) I_2(y, \mu)$ and by introducing $\sigma^\star_{i,c}$, the averaged absorption cross-section of component i on the wavelength range of channel c. From this, we define $\tau^\star_c$ by:

$$\begin{aligned} \tau^\star_c(z_\perp + y) &= \int_0^{L(z_\perp + y)} \sum_{i=0}^{N_c} n_i(z(s)) \sigma^\star_{i,c} \mathrm{d}s \\ &= \int_0^{L(z_\perp + y)} \gamma^\star_c(z) \mathrm{d}s \end{aligned} \tag{6}$$

and

$$\begin{aligned} T_c(r_\perp) &= \frac{\left(\int_0^\infty \mathrm{d}\lambda\, F_c(\lambda) I_1(\lambda)\right) \cdot \left(\int_{-\beta}^{\beta} \mathrm{d}y\, \exp\left[-\tau^\star_c(z_\perp + y)\right] \int_0^b \mathrm{d}\mu \frac{\mu I_2(y,\mu)}{\beta\sqrt{b^2-\mu^2}}\right)}{\left(\int_0^\infty \mathrm{d}\lambda\, F_c(\lambda) I_1(\lambda)\right) \cdot \left(\int_{-\beta}^{\beta} \mathrm{d}y \int_0^b \mathrm{d}\mu \frac{\mu I_2(y,\mu)}{\beta\sqrt{b^2-\mu^2}}\right)} \\ &= \frac{\int_{-\beta}^{\beta} \mathrm{d}y\, \exp\left[-\tau^\star_c(z_\perp + y)\right] \int_0^b \mathrm{d}\mu \frac{\mu I_2(y,\mu)}{\beta\sqrt{b^2-\mu^2}}}{\int_{-\beta}^{\beta} \mathrm{d}y \int_0^b \mathrm{d}\mu \frac{\mu I_2(y,\mu)}{\beta\sqrt{b^2-\mu^2}}} \\ &= \frac{\int_{-\beta}^{\beta} \mathrm{d}y\, \exp\left[-\int_0^{L(z_\perp + y)} \sum_{i=0}^{N_c} n_i(z(s)) \sigma^\star_{i,c} \mathrm{d}s\right] \int_0^b \mathrm{d}\mu \frac{\mu I_2(y,\mu)}{\beta\sqrt{b^2-\mu^2}}}{\int_{-\beta}^{\beta} \mathrm{d}y \int_0^b \mathrm{d}\mu \frac{\mu I_2(y,\mu)}{\beta\sqrt{b^2-\mu^2}}}. \end{aligned} \tag{7}$$

Note that the occultation process is only a few minutes long. This highlights one last hypothesis we implicitly made: we have considered, in the model above, that solar emission undergoes no change during the whole process.

3 Retrieval Process

The retrieval is performed in two steps. First, we use the above Eq. (7) to retrieve, for each channel, the distribution of the extinction coefficient $\gamma_c^\star(z)$ as a function of the altitude z. This step is performed by using the Levenberg-Marquardt algorithm (see Press et al. 1992) to minimize the merit function defined by Eq. (8):

$$\sum_{i=1}^{M}\left(\frac{T_i^{\text{measured}} - T_i^{\text{modeled}}}{\eta_i}\right)^2 \tag{8}$$

where M is the number of measurements and η_i is the estimated measurement error.

The second step consists in separating, for each altitude z, the contribution of the active atmospheric components to the total extinction coefficient by solving the system:

$$\begin{cases} \gamma_{c1}^\star(z) = \sum_{i=0}^{N_{c1}} n_i(z)\sigma_{i,c1}^\star \\ \gamma_{c2}^\star(z) = \sum_{i=0}^{N_{c2}} n_i(z)\sigma_{i,c2}^\star \\ \gamma_{c3}^\star(z) = \sum_{i=0}^{N_{c3}} n_i(z)\sigma_{i,c3}^\star \\ \gamma_{c4}^\star(z) = \sum_{i=0}^{N_{c4}} n_i(z)\sigma_{i,c4}^\star \end{cases} \tag{9}$$

To validate our procedure, we have built a batch of simulated data based on the MSISE-90 model (Hedin 1991) for the atmospheric constituents vertical distributions and on the Science softCon database (Nölle et al. 2005) for their respective cross-sections (once again, scattering was neglected). The absorption cross-section variations with the temperature have been neglected so far. Their introduction in the model is to be considered in the future.

The component distributions and cross-sections were introduced in the forward model together with a chosen spatial profile of solar irradiance to estimate the atmospheric transmittance for a given set of tangential point altitudes. The vertical sampling was 2 km. A random noise of 10^{-4} order of magnitude for Zr channel and 10^{-5} elsewhere was added to the attenuated and unattenuated signals (i.e., the numerator and denominator of Eq. (7)). This amount of noise is representative of what we expect with LYRA for acquisition cadences of the order of 1 Hz.

In a first attempt, we have postulated that $I_2(y, \mu)$ is constant all over the solar disk. A second step would involve introducing the limb brightening for Al and Zr channels (see e.g., Warren et al. 2001) and a limb darkening for Hz channel (see e.g., Bonnet and Blamont 1968; Samain 1979). The solar emission radial variation for the Ly channel is still subject to discussion and should be carefully evaluated. This will be part of a future paper. Our final objective is to use a more realistic model, taking into account the quiet Sun regions, active regions, and coronal holes as well. The spatial distribution of these regions would be determined using information from imaging telescopes such as SWAP (Sun Watcher with APS detectors and image Processing), also on-board PROBA2.

Afterwards, we have used the noisy simulated data as input of the retrieval process and compared the output with the initial simulated values.

4 Results

Results of the extinction coefficient retrieval are provided in Figs. 2, 3, 4, and 5. For each channel, we have processed five batches of randomly noisy data. The vertical distributions of the extinction coefficient retrieved (plain lines) are compared to the initial data (dot-dash lines). Results for Zr channel suffer from a higher level of noise (10^{-4} instead of 10^{-5}).

For each LYRA channel, we have then determined the active components by comparing their contribution to the total extinction (see Table 1)).

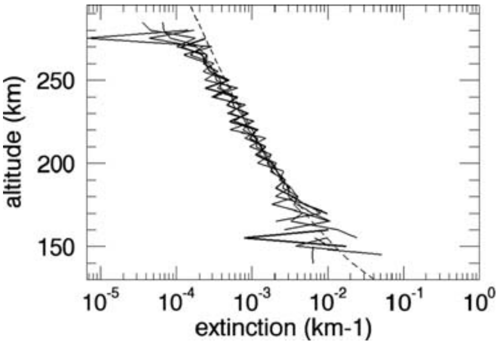

Fig. 2 Extinction coefficient retrieved for Zr channel as a function of altitude from noisy simulated data

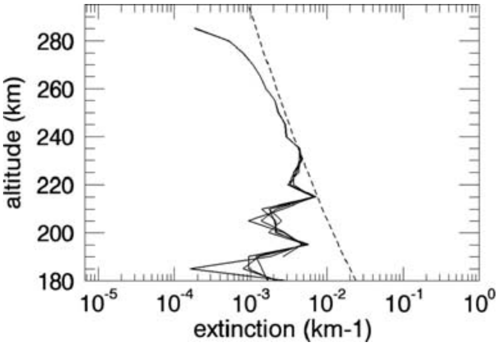

Fig. 3 Extinction coefficient retrieved for Al channel as a function of altitude from noisy simulated data

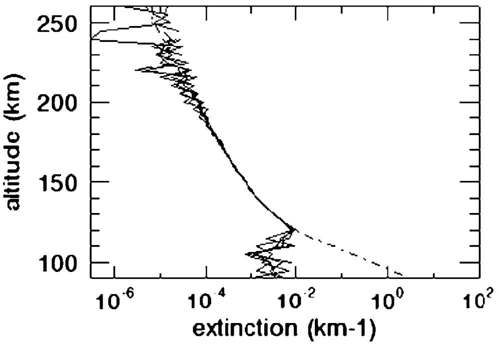

Fig. 4 Extinction coefficient retrieved for Ly channel as a function of altitude from noisy simulated data

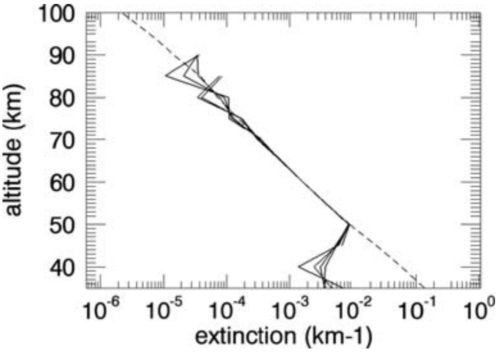

Fig. 5 Extinction coefficient retrieved for Hz channel as a function of altitude from noisy simulated data

Table 1 Active components in each Lyra channel

Channel	Active components	Altitude range (in km)
Zr	O, O_2, N_2	154 – 292
Al	O, O_2, S_2	225 – 320
Ly	O_2	116 – 189
Hz	O_2, O_3	45 – 74

In an ideal world, the extinction coefficient could have been retrieved over the same range of altitudes for all the channels. This would have meant that Eq. (9) is a well-determined system with four equations and four unknowns. But this is unfortunately not the case. In each channel, the extinction coefficient has proven to be retrievable over a range of optical thicknesses varying from 0.1 to 10. This limitation is induced by the Levenberg-Marquardt algorithm and could maybe be improved to a limited extend by using a priori constraints. Nevertheless, regions where the optical thickness is not between 0.1 and 10 are regions where the attenuation is either very small, either so high that nearly no signal is detected. Such regions will always be affected by a significant error. Depending on the channel, the retrieved interval of optical thicknesses corresponds to very different ranges of altitudes (the altitudes corresponding to optical thicknesses from 0.1 to 10 are provided in Table 1). The above system is therefore under-determined and will not be auto-sufficient to separate the densities of constituents. Nevertheless the fact that we could retrieve the extinction coefficient distribution is considered as a positive result in itself.

5 Conclusion

We have implemented a method to retrieve the extinction coefficient distribution as a function of altitude from LYRA data, and we wish to use the results to analyze the respective contributions of O, O_2, O_3, and N_2 to this extinction. This method has been submitted to some simplifying hypotheses (spectral average of the absorption cross-sections over each LYRA channel, uniformity of the solar emission) and tested on simulated noisy data. The extinction coefficient distribution as a function of altitude could be retrieved. We may then consider to extract the respective contributions of each active atmospheric component, but this would require the addition of external information.

Acknowledgments Funding of M. Dominique and J.-F. Hochedez by the Belgian Federal Science Policy Office (BELSPO) through the ESA/PRODEX programme is hereby appreciatively acknowledged. LYRA is a project of the Centre Spatial de Liege, the Physikalisch-Meteorologisches Observatorium Davos, and the Royal Observatory of Belgium. The authors acknowledge the contribution of the whole LYRA consortium and the anonymous referees for their review.

References

Bonnet RM, Blamont JE (1968) Limb-darkening observations between 1800 and 2900 Å. Solar Phys 3(1):64–81

Fussen D, Arijs E, Nevejans D, Leclere F (1997) Tomography of the Earth's atmosphere by space-borne ORA radiometer: Spatial inversion algorithm. J Geophys Res 102: 4357–4365

Fussen D, Vanhellemont F, Bingen C (2001) Remote sensing of the Earth's atmosphere by the spaceborne Occultation Radiometer, ORA: Final inversion algorithm. Appl Opt 40(6):941–948

Hedin AE (1991) Extension of the MSIS thermosphere model into the middle and lower atmosphere. J Geophys Res 96:1159–1172

Hochedez JF, Schmutz W, Stockman Y, Schühle U, BenMoussa A, Koller S, Haenen K, Berghmans D, Defise JM, Halain JP, Theissen A, Delouille V, Slemzin VA, Gillotay D, Fussen D, Dominique M, Vanhellemont F, McMullin D, Kretzschmar M, Mitrofanov AV, Nicula B, Wauters L, Roth H, Rozanov E, Rüedi I, Wehrli C, Soltani A, Amano H, Van der Linden R, Zhukov AN, Clette F, Koizumi S, Mortet V, Remes Z, Petersen R, Nesládek M, D'Olieslaeger M, Roggen J, Rochus P (2006) LYRA: A solar UV radiometer on Proba2. Adv Space Res 37:303–312

Lumpe JD, Chang CS, Strickland DJ (1991) Atmospheric constituent density profiles from full disk solar occultation experiments. J Quant Spectrosc Radiat Transf 46(6):483–506

Nölle A, Pätzold F, Pätzold S, Meller R, Moortgat GK, Röth EP, Ruhnke R, Keller-Rudek H (2005) UV-Vis Spectra of Atmospheric Constituents. www.science-softcon.de, science-softCon

Press WH, Teukolsky SA, Vetterling WT, Flannery BP (1992) Numerical Recipes in C: The Art of Scientific Computing, 2nd edn. Cambridge University Press, Cambridge

Samain D (1979) Solar continuum data on absolute intensities, center to limb variations and Laplace inversion between 1400 and 2100 Å. Astron Astrophys 74:225–228

Warren HP, Mariska JT, Lean J (2001) A new model of solar EUV irradiance variability: 1. Model formulation. J Geophys Res 106(A8):15745–15757

The Active Temperature, Ozone and Moisture Microwave Spectrometer (ATOMMS)

E.R. Kursinski, D. Ward, A. Otarola, R. Frehlich, C. Groppi, S. Albanna, M. Shein, W. Bertiger, H. Pickett, and M. Ross

Abstract The Active Temperature, Ozone and Moisture Microwave Spectrometer (ATOMMS) is designed to observe Earth's climate. It extends and overcomes several limitations of the GPS radio occultation capabilities by simultaneously measuring atmospheric bending and absorption at frequencies approximately 10 and 100 times higher than GPS. This paper summarizes several important conceptual improvements to ATOMMS made since OPAC-1 including deriving the hydrostatic upper boundary condition directly from the ATOMMS observations, our much improved understanding of the impact of turbulence and its mitigation, and a new approach to deriving atmospheric profiles in the presence of inhomogeneous liquid water clouds. ATOMMS performance significantly exceeds that of radiometric sounders in terms of precision and vertical resolution and degrades only slightly in the presence of clouds and it does so independently of models. Our aircraft-to-aircraft occultation demonstration of ATOMMS performance will begin in 2009 representing a major step towards an orbiting observing system.

1 Introduction

The Active Temperature, Ozone and Moisture Microwave Spectrometer (ATOMMS) is a natural extension of the GPS radio occultation (RO) concept that uses at least two frequency bands approximately 10 and 100 times higher than GPS frequencies to probe the 22 GHz and 183 GHz water lines and 184 GHz and 195 GHz ozone lines. A third band between 500 GHz and 600 GHz would also be quite useful for profiling H_2O and its isotopes and initializing the hydrostatic integral.

Serious work on the ATOMMS concept began in 1998 as the Atmospheric Moisture and Ocean Reflection Experiment (AMORE) (which included the 22 GHz

---

E.R. Kursinski (✉)
Institute of Atmospheric Physics, University of Arizona, Tucson, Arizona, USA
e-mail: kursinski@atmo.arizona.edu

A. Steiner et al. (eds.), *New Horizons in Occultation Research*,
DOI 10.1007/978-3-642-00321-9_24, © Springer-Verlag Berlin Heidelberg 2009

portion of the ATOMMS occultation concept) was proposed to NASA as an Earth System Science Pathfinder (ESSP) mission. While AMORE was technically too immature for selection, the same year NASA did fund the Atmospheric Temperature, Ozone and Moisture Sounder (ATOMS), a joint effort between the University of Arizona and JPL that included both the 22 GHz and 183–195 GHz occultation concepts via its Instrument Incubator Program (IIP). AMORE and ATOMS also triggered parallel research and proposal efforts in Europe such as ACE+ and ACCURATE. In the US, the National Science Foundation (NSF) has funded the ongoing development and refinement of the ATOMMS concept since 2001 including funding in 2007 the ATOMMS aircraft to aircraft occultation demonstration that is summarized at the end of this paper. We also note the Mars Atmospheric Climate Observatory (MACO) mission concept that is focused on the Martian hydrological cycle using water occultation observations at 183 GHz supplemented by other observations. MACO was developed with seed funding from NASA in 2000 for the Mars Scout opportunity in 2002 (Kursinski et al. 2004b). While it was not selected for a Phase A study for the second Mars Scout opportunity in 2006 because it was viewed as too high risk, MACO has been recognized as a revolutionary concept for quantitatively determining the Martian hydrological cycle and climate and will hopefully become a real mission in the future.

ATOMMS is designed to address key open questions about climate such as, “Is the upper troposphere warming faster than the lower troposphere and the surface”, “Where is the transition between tropospheric warming and stratospheric cooling”, and the closely related question: “How are lapse rates adjusting to the changes in vertical heating and dynamical feedbacks associated with climate change”.

ATOMMS has a niche in the upper troposphere/lower stratosphere (UTLS) regime where water vapor and ozone are very important radiatively. Our ability to measure vertically resolved water vapor in the upper troposphere under all sky conditions has been close to nil. Existing observational techniques have very different types of uncertainties, errors, and resolutions and the comparisons have not agreed very well, problems that can be resolved by ATOMMS. ATOMMS can answer fundamental open questions on basic behavior and trends in the UTLS regime.

In this context, it is important to note that the problem of deriving of atmospheric temperature and constituent profiles from satellite measurements of radiance emitted by the atmosphere and surface is mathematically ill-posed (e.g., Huang et al. 2002) A continuum of profiles exists that are consistent with the radiance measurements and selecting a “unique” profile from this continuum requires imposing additional constraints and assumptions that have their own implicit climatology. From the standpoint of determining unambiguously how our climate is changing and evaluating model realism and predictive skill, this situation is quite poor because the imposed climatological assumptions imbedded in the “unique” profile solutions are inseparable from true climatological behavior.

Analyses produced by Numerical Weather Prediction (NWP) centers are quite powerful. However, in a climate context, the analyses are inherently ambiguous because they suffer from the same problem in that the analyzed state estimate is based in part on atmospheric models that contain unknown errors. In terms of evaluating and improving climate model realism and accuracy, which is a critical goal of climate change research, analyses are incestuous because they are not independent of the quantity, the model, which is being assessed. With this in mind, an overarching goal of ATOMMS has been to create an observing system capable of estimating several key climate state variables and determine how the climate system is truly evolving, *independently of atmospheric models*.

ATOMMS was conceived to overcome the wet-dry ambiguity that limits direct interpretation of the GPS RO refractivity profiles in the warmer ($>$ 240 K) regions of the troposphere because the wet and dry contributions to refractivity cannot be separated using refractivity measurements alone. By measuring both bending and absorption along each occultation signal path, each ATOMMS occultation provides sufficient information to resolve the wet-dry ambiguity and *simultaneously* determine temperature, pressure, and moisture directly from the observations themselves.

Based on our assessment described below, ATOMMS will profile water vapor, temperature, and pressure from near the surface to the mesopause and ozone through the middle atmosphere down into the upper troposphere. It will do so in both clear and cloudy conditions to provide the first unbiased characterization of the troposphere. With the proper choice of frequencies, it will also determine water isotopes and winds in the middle atmosphere (Kursinski et al. 2004a). Occultations are extremely well suited for observing certain scales of behavior and ATOMMS will determine telltale signature of processes that must be represented accurately in models. ATOMMS' four orders of magnitude lower sensitivity to the ionosphere vs. GPS means the ATOMMS profiles are essentially insensitive to the solar and diurnal cycles in the ionosphere (unlike GPS) and will extend to the mesopause or higher depending on the choice of signal frequencies as discussed below. ATOMMS will also determine any subtle systematic GPS RO ionospheric errors over the solar and diurnal cycles.

ATOMMS will measure behavior at important scales of variability including in and below clouds thus avoiding biases that result for sensors that are incapable of probing below clouds. ATOMMS will monitor trends and variability and separate behavior in the free troposphere from that in the planetary boundary layer (PBL). The ATOMMS information will be used to understand the processes controlling moisture in troposphere and stratosphere and coupling to clouds and precipitation and in general improve physical model representations for future weather and climate predictions.

In this paper, we summarize several important aspects of ATOMMS that have evolved significantly since OPAC-1. We have developed a new approach to the hydrostatic upper boundary condition derived directly from the ATOMMS observations. Our understanding of the impact of the effects of turbulence and how to mitigate them has improved dramatically since OPAC-1. We also summarize a new approach that we have developed to derive atmospheric profiles in the presence of inhomogeneous liquid water. We conclude with a summary of our planned ATOMMS aircraft-aircraft occultation demonstration that represents a major step towards an orbiting ATOMMS observing system.

2 High Altitude Initialization of the Hydrostatic and Abel Integrals

As mentioned, ATOMMS can probe to much higher altitudes than GPS because its much higher frequencies reduce ionospheric sensitivity by orders of magnitude. As a result, unlike GPS RO, ATOMMS can make measurements that directly constrain the upper boundary conditions for the Abelian bending angle and hydrostatic integrals and achieve independence from models and climatologies through the middle atmosphere.

2.1 Constraining the Abel Bending Angle Integral

In the middle atmosphere where water concentrations are low, radio occultations profile temperature, pressure, and density by determining density versus altitude and combining that with a boundary condition on the hydrostatic integral. Density is derived from refractivity which is derived from bending angle derived in turn from the atmospheric Doppler shift. Maximizing the upper altitude of the bending angle profile requires minimizing errors in the atmospheric Doppler profile. Minimization is achieved via a combination of much higher frequencies to reduce ionospheric sensitivity, use of excellent reference oscillators in combination with GPS to further calibrate the oscillator errors, maximizing the signal-to-noise ratio (SNR) and very accurate reconstruction of the orbits.

A key question is at what altitude in an occultation does observational noise become sufficiently smaller than the atmospheric Doppler signature that accurate profiling of the atmosphere can begin. Frequency variations of a 10^{-13} ultra stable oscillator (USO) are approximately 10 times less than the atmospheric Doppler near 85 km altitude (Kursinski et al. 1997). GPS measurements made during the occultations can be used to estimate and remove USO frequency variations at time scales of several seconds or longer (limited by the GPS SNR). Such an error reduction can extend a low vertical resolution bending angle profile higher by a scale height or more and extend the Abel integral that derives refractivity. Conceivably, if every ATOMMS instrument in orbit were to radiate occultation signals such that occultation signals travel in both directions, the USO errors can be cancelled as is done on GRACE (e.g., Dunn et al.2003). This approach will be used in the ATOMMS aircraft to aircraft occultation demonstration.

Orbital inaccuracy is an important source of error. To be 10% of the atmospheric Doppler at 85 km, the velocity error along the occultation path direction must be 0.03 mm/s or less. A beauty of the occultations is that any slowly varying error such as that due to a bias in the orbital velocity will be evident as a non-zero signal frequency (after orbital motion has been removed) at altitudes above the detectable atmosphere. Any such non-zero frequency and slow variation above the detectable atmosphere can be fitted and extrapolated down through altitudes where the atmosphere is detectable to reduce the errors due to orbit and other sources below those of the reference oscillator. Such an approach has been used in planetary occultations where the orbit reconstructions are less accurate.

We estimate that ATOMMS will derive accurate, high vertical resolution bending angle profiles to at least 80 km altitude, approximately consistent with Kursinski et al. (2002).

2.2 Hydrostatic Integral Constraint

A conceptual innovation we have come to realize is that measurements of absorption lineshape can provide the boundary condition for the hydrostatic integral at very high altitudes. Kursinski et al. (2002) showed that temperature accuracies of 1 K can be achieved up to 40 km altitude using just the ATOMMS observations themselves and no *external* information for the hydrostatic constraint. This is achieved by combining the refractivity profile, hydrostatic equilibrium, and the pressure and temperature constraints imbedded in the profile of the 183 GHz line shape. We have come to realize that sub-Kelvin performance can be extended to much higher altitudes with accurate measurements of the Doppler broadened line shape at higher altitudes that yield a direct estimate of temperature. This temperature constraint in combination with density (derived from bending angle) yields pressure and therefore constrains the hydrostatic integral. The approximate altitudes at which the Doppler linewidth is 10 times that of the collisional linewidth are 80 km, 77 km, and 70 km for 118 GHz (O_2), 183 GHz (H_2O), and 557 GHz (H_2O), respectively.

The strength of the 183 GHz line combined with ppm middle atmospheric water vapor mixing ratios is not sufficient for the 183 GHz observations to accurately determine the 183 GHz linewidth at 77 km altitude. The 50–60 GHz and 118 GHz O_2 lines can provide this hydrostatic constraint. Wu et al. (2003) have demonstrated that temperatures can be derived from emission in the 50–60 GHz O_2 band with accuracies of approximately 8 K and 15 K at 80 km and 90 km altitude, respectively. From a climate perspective, the complication is the O_2 lines result from magnetic dipoles and are therefore sensitive to the Earth's magnetic field and Zeeman splitting complicating and likely limiting the ultimate accuracy of the retrieval.

The best approach may be to probe the very strong 557 GHz water line and profile water vapor to much higher altitudes than is possible with the 183 GHz line. Furthermore, observations between 500 GHz and 600 GHz can accurately profile water isotopes in the middle atmosphere as well as provide information to cross-compare with the 183 GHz water results. Sensitivity to the ionosphere at 557 GHz is an order of magnitude smaller than that at 183 GHz. Occultation SNRs can be higher at 557 GHz because of higher antenna gain. The wind induced Doppler shift of the 557 GHz line is also 3 times larger (although the pressure induced line shift is 4 times larger, the uncertainties of which may limit the accuracy of wind estimates). The Doppler linewidth is 3 times larger so the Doppler linewidth dominates the collisional width at lower altitudes. Figure 1 shows the approximate accuracy of temperature versus altitude derived from including occultation measurements of the

Fig. 1 The temperature error versus altitude in the upper middle atmosphere and lower thermosphere, representative of a typical ATOMMS profile. Temperature has been derived combining density from occultation-derived profiles of refractivity and the Doppler width of the 557 GHz water line in combination with the hydrostatic integral

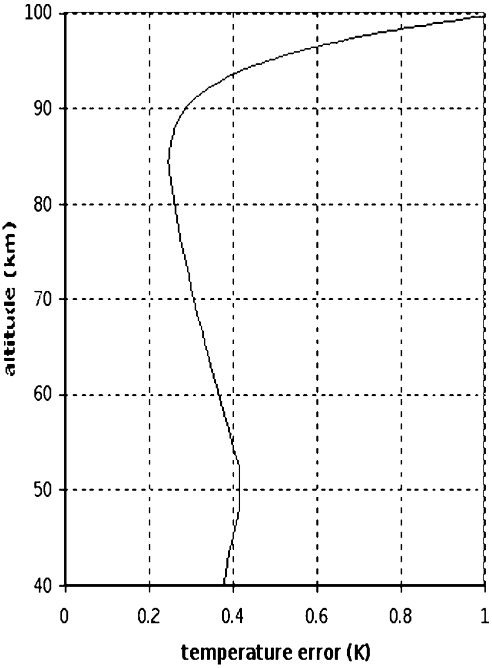

557 GHz linewidth. We note that since the accuracy will depend on the accuracy of the spectroscopy, ATOMMS should sample the line with at least one more tone than that the number required for the temperature and wind retrievals in order to provide information needed to assess and refine the spectroscopy.

3 Assessing the Impact of Turbulence on ATOMMS Observations and Retrievals

The potential importance of turbulence to ATOMMS was identified in a talk at OPAC-1 (Feng et al. 2002). Propagation of electromagnetic signals through a turbulent refractive medium creates interference through diffraction that produces phase and amplitude scintillations. From the standpoint of measuring the absorption signatures of atmospheric water vapor and ozone, turbulent amplitude scintillations are a noise source. For those interested in turbulence, ATOMMS is a planetary-scale microwave scintillometer that will provide an unprecedented global turbulence monitor.

We summarize our findings concerning the impact of amplitude scintillations due to turbulence on the ATOMMS measurements. The differential opacity measurement approach used by ATOMMS and described by Kursinski et al. (2002) is key to controlling the impact of turbulence.

3.1 Simulation Results for Variations in the Refractive Index

To evaluate the effects of 3-D turbulent variations in the refractive index, we have used a method suggested by R. Frehlich at NCAR and set up a numerical occultation signal propagation simulator using a simple Cartesian geometry with a plane wave source on one side of a box filled with turbulence. Microwave signals are propagated through the box, and then through an additional 3000 km of vacuum to approximate the signal propagation measured by a satellite in an Earth occultation geometry. We have specified the turbulent spectrum as 3-D, homogeneous von Karman turbulence with an inner scale of 10 cm and an outer scale of 500 m, and a magnitude of the turbulence defined by the refractive index structure parameter, C_n^2. Besides testing the effectiveness of amplitude ratioing on the directly measured signal amplitudes, we have also considered how 1-D back-propagation (the simplest form of diffraction correction) together with vertical smoothing can reduce amplitude scintillations.

Figure 2 shows two examples of scintillation simulations results. The left hand figure is representative of wet turbulence contributions in the mid-troposphere near the 22 GHz water line. The turbulent magnitude was specified by setting the real refractive index structure parameter, C_n^2, equal to 10^{-16} (Jursa 1985). The right hand panel is representative of dry turbulence contributions in the upper troposphere near the 183 GHz water line, where a typical value for the dry-real refractive index structure parameter of $C_n^2 = 10^{-17}$ has been used (Jursa 1985). The amplitude variations are caused by diffraction, since no absorption is included in the simulations, i.e., the imaginary part of the refractive index is zero. The standard deviations of the single frequency raw amplitude variations (before applying a 1-D back propagation and smoothing) are roughly 7–8% for both the 22 GHz and 183 GHz simulations. The combination of 1-D back propagation and smoothing reduces the raw single

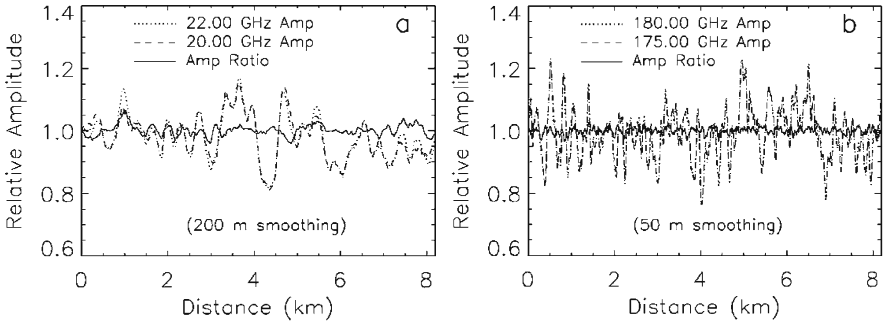

Fig. 2 Simulation of the impact of turbulent variations in the refractive index on occultation amplitudes. (**a**) Tropospheric conditions ($C_n^2 = 10^{-16}$) at frequencies near the 22 GHz water line after applying 1-D back propagation and 200 m smoothing. (**b**) Upper tropospheric jet stream conditions ($C_n^2 = 10^{-17}$) at frequencies near the 183 GHz water line after applying 1-D back propagation and 50 m smoothing. Relative means that an amplitude of unity would be measured in the absence of turbulence. In both cases, the amplitude standard deviation for individual frequencies is ~7–8%, and the standard deviation of the amplitude ratio is ~1–2%

channel standard deviations by roughly a factor of 2. Note that for both the 22 GHz and 183 GHz regions, the smoothing is over a scale similar to the diameter of the first Fresnel zone. Therefore, there is little loss in resolution or information content associated with this smoothing.

The results indicate how the ratioing approach will reduce the impact of turbulence at frequencies near the 22 GHz and 183 GHz water absorption lines. Although the raw amplitude scintillations are comparable in the two panels (since shorter wavelengths are more affected by turbulence), the closer fractional separation of the calibrations tones near 183 GHz yields better cancellation of the turbulence effects after ratioing.

To understand the optimal separation between signal frequencies, we did many simulations with different frequency separations and turbulence realizations to reveal the statistical behavior shown in Fig. 3. Figure 3 shows that the amplitude errors can be reduced significantly by a combination of amplitude ratioing, vertical smoothing, and 1-D back propagation. For the simulated conditions, the single frequency 22 GHz amplitude variations without vertical smoothing are about 13% and about 8% after applying 200 m vertical smoothing. Thus amplitude ratioing can effectively reduce the retrieval errors caused by turbulence. Based on these results, two trade-offs in the ATOMMS system are apparent. First, the amplitude diffraction error decreases as the frequency separation between signal pairs decreases. However, as the frequency separation decreases, the differential absorption signature, due to the difference between the water vapor absorption at the two frequencies, also decreases. Secondly, the standard trade-off exists between the retrieved vertical resolution and the level of vertical smoothing required to satisfactorily reduce measurement fluctuations.

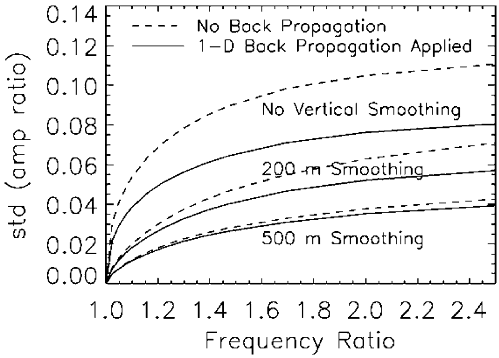

Fig. 3 Standard deviation of the error in measuring amplitude ratios due to turbulence for the atmospheric conditions specified in Fig. 2. The base frequency is 22 GHz and frequency ratio refers to base frequency divided by the second frequency. Three pairs of curves are shown, upper curves drawn with *dashed lines* indicating no 1-D back propagation applied and lower curves drawn with *solid lines* indicating 1-D back propagation applied. The three pairs of curves correspond to no vertical smoothing applied to the amplitude ratio, 200 m vertical smoothing applied, and 500 m vertical smoothing applied

3.2 Determining the Wet Refractive Index Structure Parameter, C_{nw}^2

The relation between the refractivity of air at radio frequencies and atmospheric variables is given in Eq. (1) from Rüeger (2002) where N is total atmospheric refractivity, N_{d} and N_{w}, respectively the first term and the second term (which is within the brackets) in Eq. (1), are the contributions of the dry gas and water vapor components of the atmosphere, P_{d} is dry partial pressure in hPa, T is temperature in K, e is partial pressure of water vapor in hPa, and the constants are those of the "best average" case. The constant for the dry component of refractivity assumes a $\mathrm{CO_2}$ mixing ratio of 375 ppm.

$$N = N_{\mathrm{d}} + N_{\mathrm{w}} = 77.6890\frac{P_{\mathrm{d}}}{T} + \left(71.2952\frac{e}{T} + 375463\frac{e}{T^2}\right) \tag{1}$$

The impact of dry turbulence has received much attention in the literature due in particular to its impact on astronomy. The wet refractivity term has received less attention and is only relevant at microwave frequencies slow enough to respond to the motion of the permanent dipole of the water molecule. Since scintillations at ATOMMS frequencies are dominated by wet rather than dry turbulence over much of the troposphere, we have developed a parameterization of wet turbulence described in Otarola (2008).

At radio frequencies, in the warmer regions of the troposphere, the fluctuations in the refractive index tend to depend more on humidity fluctuations and less on temperature fluctuations (e.g., Coulman and Vernin 1991). The structure constant of the air index of refraction fluctuations, C_n^2, is the variance of the difference in index of refraction variations at points separated by one meter. C_n^2 can be written as shown in Eq. (2). This is possible under the assumption that the power spectral density of the dry, wet, and cross terms share similar spectral characteristics with the only exception being the power level. Equation (2) is similar to that found in the works of Wesely (1976) and Coulman (1985) except that it is written in terms of the structure constants associated with the dry and wet components of air refractivity, $C_{n\mathrm{d}}^2$ and $C_{n\mathrm{w}}^2$, respectively, and the covariance of the variations in the dry and wet components of the air refractive index, $C_{n\mathrm{d},n\mathrm{w}}$.

$$C_n^2 = C_{n\mathrm{d}}^2 + 2C_{n\mathrm{d},n\mathrm{w}} + C_{n\mathrm{w}}^2 \tag{2}$$

Therefore, the strength of the turbulence, $C_n^2 L$, where L is the path length through the atmosphere depends on fluctuations in both the dry and wet components of the air index of refraction, $C_{n\mathrm{d}}^2$ and $C_{n\mathrm{w}}^2$. While the literature includes some empirical formulations for the determination of the $C_{n\mathrm{d}}^2$ structure constant as a function of altitude (e.g., Fenn et al. 1985), little information is available about how to estimate the contribution to the turbulence strength from fluctuations in humidity. Combining our analysis of aircraft observations of temperature, pressure, and humidity at various altitudes levels in the atmosphere with a theoretical framework, we have derived a relationship between the wet component of the index of refraction structure constant and the mean wet refractivity that is given in Eq. (3) (Otarola 2008).

$$C_{n\mathrm{w}}^2 = 8 \times 10^{-18} \langle N_\mathrm{w} \rangle^2 \tag{3}$$

The procedure we have developed to model and account for the effects that turbulent variations in real refractivity will have on ATOMMS retrieval system performance is outlined here. Under the condition of weak turbulence (weak scintillations), the appropriate equation for computing the expected amplitude variations for a signal propagating through a turbulent medium is given by Eq. (4) (Frehlich and Ochs 1990),

$$\left\langle \left[\ln\left(\frac{A}{A_0}\right) \right]^2 \right\rangle = 0.56 k^{7/6} \int_0^L C_n^2(x) \left[x - \frac{x^2}{L} \right]^{5/6} \mathrm{d}x \tag{4}$$

where A is the amplitude that is varying due to scintillations, A_0 is the mean amplitude of the signal, k is the signal wavenumber, C_n^2 is the refractive index structure parameter, L is the total distance from transmitter to receiver, and the integration proceeds along the propagation direction, specified here as the x direction. In order to utilize this equation, one must specify values for C_n^2 along the propagation path. As mentioned above, for microwave signals, the atmospheric refractivity depends on both the dry air density (dry part) and water vapor density (wet part). Turbulent variations in both components will result in amplitude scintillations on our signals. Figure 4a shows a representative profile of the dry part and two realizations of the wet parameterization for Mid-Latitude Summer (MLS) and Arctic Winter (ArW) conditions, respectively. Figure 4b shows simulated profiles of the turbulent amplitude fluctuations for 20 GHz signals using the C_n^2 profiles in Fig. 4a and

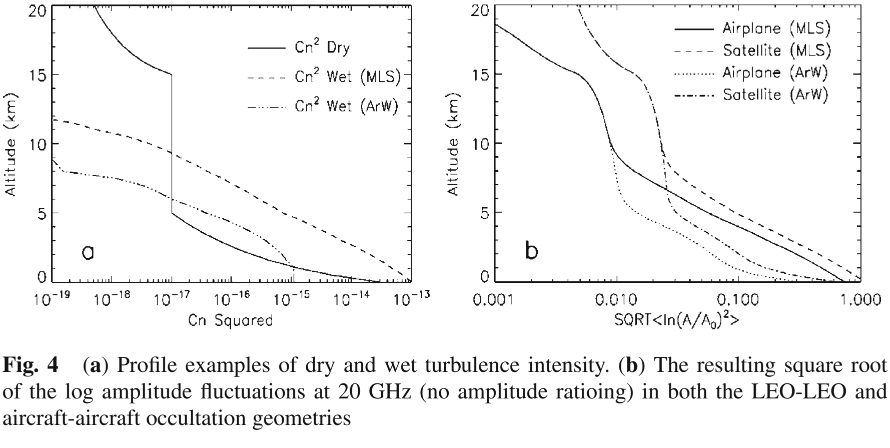

Fig. 4 (**a**) Profile examples of dry and wet turbulence intensity. (**b**) The resulting square root of the log amplitude fluctuations at 20 GHz (no amplitude ratioing) in both the LEO-LEO and aircraft-aircraft occultation geometries

Eq. (4). As Fig. 4b shows, we estimate, based on Eq. (4), that turbulent scintillations measured during the high altitude aircraft-to-aircraft occultations will be a factor of 2–3 smaller than those of the LEO-LEO occultations due to the shorter aircraft-to-aircraft path length. The amplitude scintillation fluctuations will be reduced significantly with amplitude ratioing as indicated in Fig. 2.

Because ATOMMS utilizes calibration tones to mitigate unwanted instrumental and atmospheric effects, a key quantity is the difference between optical depths measured at two (or more) frequencies, defined as $\Delta\tau = \tau(f_1) - \tau(f_2)$, rather than the optical depth at a single frequency, $\tau(f_1)$. The optical depth difference is proportional to the logarithm of the ratio of the two signal amplitudes. Therefore, the appropriate quantity for retrieval error estimation is the residual uncertainty in the amplitude ratios, rather than the amplitude uncertainty at an individual frequency.

3.3 Comparison with Turbulence Estimates of Gorbunov and Kirchengast (2007)

Gorbunov and Kirchengast (2007) (GK07) performed 2-D occultation simulations to assess the effects of turbulence near 22 GHz. Our Cartesian turbulence simulations are less realistic in that the turbulence effects are not imbedded in a full occultation retrieval simulation. This is adequate if the process is linear. On the other hand, our simulations are more realistic than GK07 in that they include the turbulence effects of all 3 dimensions. This is important because a limitation of occultation diffraction correction schemes is that they are 2-D, designed for cylindrical atmospheres with no variation in the dimension orthogonal to the occultation plane. Clearly there are turbulent variations in that dimension that must be considered. Our approach has the advantage of being much faster computationally, allowing us to simulate a large number of cases to yield the smooth statistical behavior evident in Fig. 3 in order to parameterize the turbulent errors for inclusion in our error covariance studies.

We can compare GK07 and our estimates of turbulence errors. In GK07 Fig. 6, the differential transmission error using frequencies of 9.7 GHz and 17.25 GHz in the 5–8 km altitude interval at low latitudes is ~0.05 dB or 1% for anisotropy coefficients of ≥ 4. Our turbulence parameterization estimates indicate that for typical mid-latitude summer conditions, the fractional amplitude error at 22 GHz measured at 6.5 km altitude is approximately 6% (see Fig. 4b). From Fig. 2 (where the fractional amplitude error at 22 GHz is 13%), the fractional error in the amplitude ratio for a frequency ratio of 1.8 is 5%. So, based on our findings regarding how turbulence errors scale, the fractional error in the ratio of the 9.7 GHz and 17.25 GHz amplitudes under low latitude conditions near 6.5 km altitude will be $2\% = 6\%\,(5/13)(17.25/22)^{0.35}$. This is equivalent to the "differential transmission error" as defined by GK07. So our estimate of the differential transmission error for low latitude, mid-tropospheric conditions is approximately twice that of GK07. Interestingly our approach, which is simpler, actually predicts larger errors.

The similarity of these two error estimates is promising as it suggests that despite the very different approaches used to simulate the effects of turbulence, the levels of turbulent noise behavior being approximated are somewhat realistic. A better understanding and reconciliation of the differences between the two error estimate approaches clearly warrants more attention. Our understanding will improve and uncertainties will decrease dramatically with the aircraft to aircraft occultations which will directly measure the real impact of turbulence on ATOMMS occultation measurements and retrievals.

4 Simulated Retrieval Errors (Clear Sky)

Figure 5 shows the computed errors in the retrieved temperature and water vapor pressure for six Lowtran atmospheres under clear-sky conditions. The simulations include the following sources of uncertainty: uncertainty in the near vertical profile of refractivity is set based on refractivity errors estimated for GPS/MET by Kursinski et al. (1995, 1997), instrumental measurement errors in difference optical depths for frequency pairs are based on Kursinski et al. (2002), and uncertainty in determining the difference optical depths due to amplitude scintillations resulting from turbulent variations in the real part of the atmospheric index of refraction. The latter source of uncertainty accounts for both the dry (non-water vapor) as well as the wet (water vapor) contribution to turbulent variations in the refractivity. Extending upward in altitude, the standard deviation of the temperature error remains below

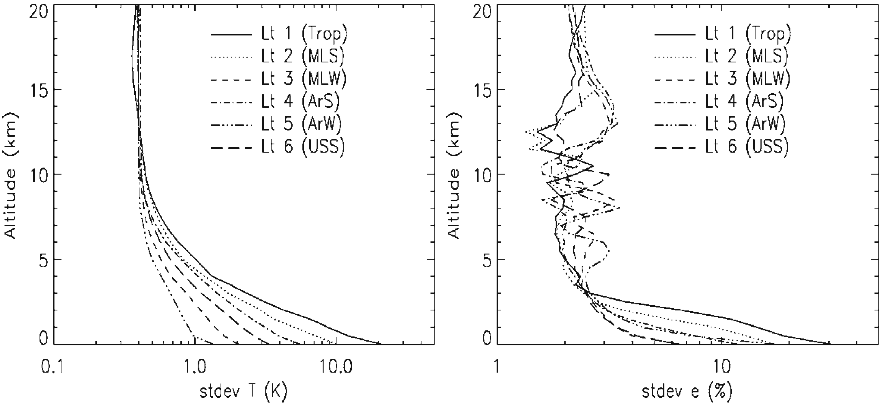

Fig. 5 Computed standard deviation of the error in the retrievals of temperature (*left panel*), expressed in Kelvin and water vapor partial pressure (*right panel*), expressed in percent, using simulated ATOMMS observations for the six labeled Lowtran atmospheres (Trop = tropical; MLS = mid-latitude summer; MLW = mid-latitude winter; ArS = Arctic summer; ArW = Arctic winter; USS = U.S. Standard)

1 K and the standard deviation of the water vapor error remains below 2% up to at least 60 km (not shown).

It is only at the lowest altitudes, below about 5 km, where we begin to see the retrieval errors increase significantly. There are several related reasons for this that are associated with the increase in air pressure and water vapor content as the ground surface is approached. As the water vapor content increases, the absorption optical depth becomes large which necessitates using occultation tone frequencies farther below the 22 GHz line center. Because of collisional line broadening, the difference in the optical depths at our closely spaced frequency pairs becomes smaller (the absorption line shape broadens), which reduces the information content of the measurements. At the same time, the orthogonality between the refractivity information and the absorption information for separating water vapor from temperature decreases as the amount of water vapor increases (Kursinski et al. 2002). On top of these, turbulent fluctuations in refractivity generally increase as the surface is approached which increase the error in the measured amplitudes and derived optical depths. Thus, the ability to produce accurate retrievals at low altitudes is limited by effects related to the mean amount of water vapor. For example, for the dry arctic winter case, temperature errors of less than 1 K are estimated to extend essentially right down to the surface, whereas for the tropical atmosphere, temperature errors become larger than 1 K below about 5 km in altitude. Errors in water vapor retrievals are approximately 2–3% above 3 km altitude and increase to 6–30% at the surface for arctic winter and tropical conditions, respectively.

5 An Approach for Retrievals in the Presence of Inhomogeneous Liquid Water Clouds

We have developed a new conceptual approach for isolating and removing the effects of inhomogeneous liquid water clouds that are potentially a limiting error source for ATOMMS. Previous approaches such as Kursinski et al. (2004a) have assumed that liquid water is distributed spherically symmetrically, clearly a poor approximation given the clumpy and inhomogeneous distribution of clouds.

Our approach is conceptually analogous to the method of isolating and removing ice clouds described in Kursinski et al. (2002). Ice clouds cause scattering but no absorption and the scattering dependence on frequency is weak. Therefore the extinction effect is reduced substantially by ratioing the signal amplitudes at similar frequencies, largely eliminating the effect of ice clouds prior to the unraveling of the onion skin via the Abel transform or equivalent retrieval process. A strength of this elimination approach is its lack of sensitivity to the horizontal distribution of the ice clouds.

Our desire has been to develop a similar approach for isolating and removing the effects of liquid water clouds. Frequencies near 183 GHz will not be used to measure absorption when liquid water clouds are present because the absorption of liquid water is too large at these frequencies. At low band frequencies (near 22 GHz), scattering can be neglected and the problem is one of separating cloud liquid water absorption from that due to water vapor and dry air. The liquid water absorption spectrum is more complex than that due to scattering by ice both in terms of spectral shape and its dependence on temperature. Because cloud droplet sizes fall in the Rayleigh regime with respect to the low band wavelengths, absorption due to liquid water will depend primarily on liquid water path rather than droplet size distribution. Because the spatial distribution of clouds can be very inhomogeneous, the frequency dependent cloud absorption signature must be isolated and removed from the slant-path absorption measurements before passing them through the Abel transform or equivalent. Not doing so may result in the inhomogeneous distribution of clouds producing some rather poor water vapor retrieval results.

We have developed a species separation inversion routine capable of handling inhomogeneous cloudiness that we will briefly outline here. A manuscript describing this strategy in more detail is in preparation. The inversion routine begins with amplitude calibration measurements taken above the atmosphere and proceeds downward toward the surface. Above the troposphere, we assume there are no clouds and we can readily separate the dry air absorption from water vapor absorption and thus retrieve temperature and water vapor content. As the inversion routine moves down into the troposphere, for each set of measured optical depth difference pairs at a given tangent altitude, we determine whether or not the spectral absorption signature can be satisfactorily explained by a combination of water vapor and dry air absorption. If not, then the algorithm attempts to fit the residual optical depth differences with cloud absorption. We have found that the spectral shape and magnitude of liquid water absorption at the low band frequencies, although somewhat uncertain, depends mainly on the cloud liquid water path and cloud temperature. Figure 6

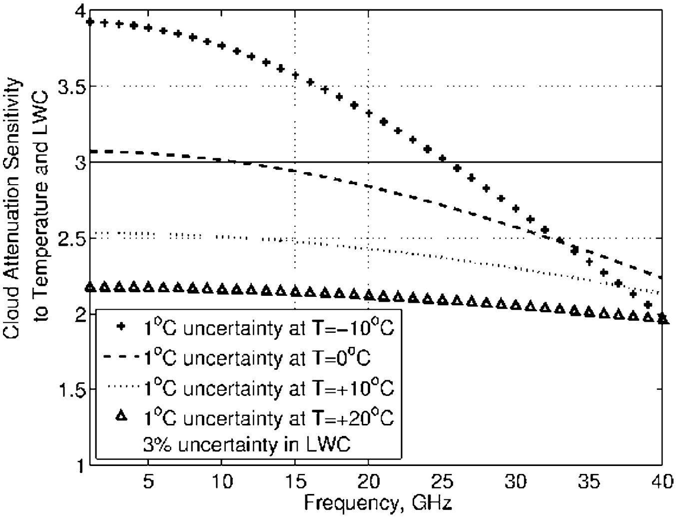

Fig. 6 Fractional change (expressed in percentage) in the absorption spectrum of liquid water clouds for 1 K changes in cloud temperature and a 3% change in liquid water content (LWC). Based on the liquid water dielectric model of Otarola (2007)

shows the fractional changes, in percentage, expected in the cloud absorption spectrum resulting from changes in cloud temperature and in cloud liquid water content (LWC). The dissimilar changes in spectra clearly indicate that changes due to cloud temperature cannot be accurately represented by changes in LWC, particularly at colder temperatures. Thus, if our retrieval algorithm detects the presence of clouds along an occultation path, an estimate is made for two "fitting" parameters: cloud liquid water path and effective cloud temperature. Importantly, no presumption of spherical symmetry is invoked for clouds. The estimate for cloud absorption is removed from each occultation path before making the final species retrievals for temperature and water vapor, which assume local spherical symmetry.

Preliminary simulations have shown that we can separate cloud absorption optical depth from the optical depths due to water vapor and dry air based on differences in their absorption as a function of frequency. The presence of clouds generally results in somewhat larger errors in the retrievals of water vapor and temperature. Based on our latest simulations, we expect to retrieve water vapor, temperature, and pressure in cloudy conditions with accuracies within a factor of two of water vapor retrievals in clear air, consistent with the prediction of Kursinski et al. (2002). Two examples showing the effects of clouds on the retrievals of temperature and water vapor are shown in Figs. 7 and 8. In general, the errors in the retrievals of temperature and water vapor increase from the altitude of the cloud downward. This is expected because occultation observations corresponding to lower tangent altitudes can still pass through clouds located at higher altitudes.

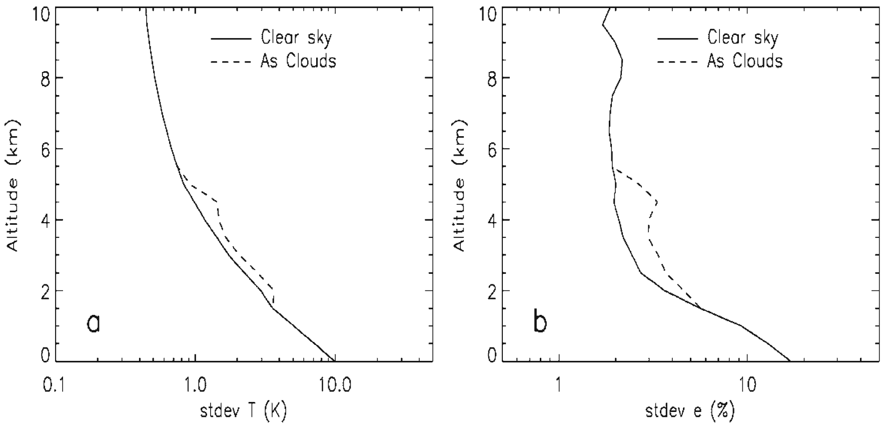

Fig. 7 Computed standard deviation of the errors in the retrievals of (**a**) temperature and (**b**) water vapor pressure using simulated ATOMMS observations. The background atmosphere is the Lowtran 2 mid-latitude summer profile. *Solid lines* are for clear sky conditions, while the *dashed lines* were computed after placing a broken deck of altostratus clouds between 4.5 km and 5.5 km altitude. The cloud field is highly non-symmetric about the local tangent point. Cloud elements have liquid water contents of 0.3 g m^{-3}

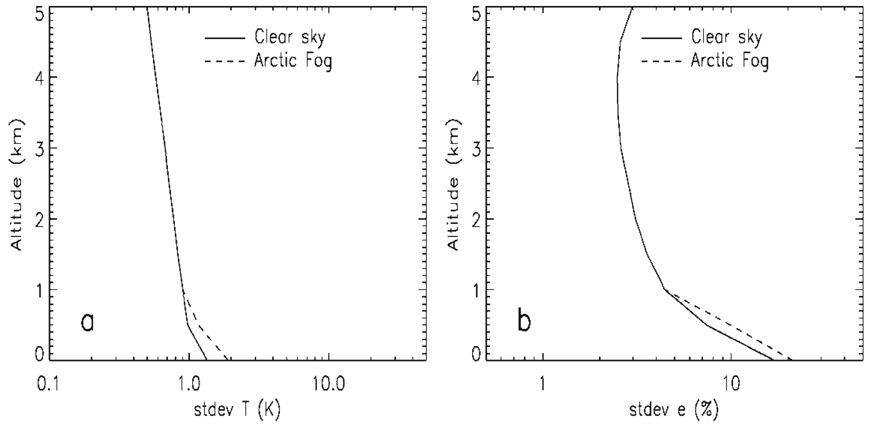

Fig. 8 Same as Fig. 7 except the background atmosphere is the Lowtran 5 Arctic Winter. For the inhomogeneous Arctic fog case, a cloud with liquid water content of 0.15 g m^{-3} extends from ground level to 1.0 km above ground

The ability to estimate two additional parameters, cloud liquid water path and effective cloud temperature, along each occultation path, requires sampling the spectrum with a sufficient number of frequencies to separate the liquid water, water vapor, and dry air spectra using the slant optical depths. Beside the refractivity information derived from the phase measurements and the hydrostatic constraint, we require absorption information from at least four frequencies to isolate liquid water clouds from water vapor and unwanted variations from the instrument and turbulence.

If our error estimates prove representative as we expect, then the accuracy (as opposed to precision) of ATOMMS will be limited ultimately by the knowledge of spectroscopy. To quantify and reduce spectroscopic uncertainty, we believe it is crucial that ATOMMS observes at least one additional frequency, bringing the minimum number to five. For this reason, the aircraft version of ATOMMS has 8 frequencies near 22 GHz and we now refer to the technique as an “Active Spectrometer”. In general, it is very important that ATOMMS probes with a number of tones that provide sufficient information to ensure that ATOMMS observations do *not* yield an underdetermined retrieval problem (at least under the local spherical symmetry constraint).

6 ATOMMS Aircraft to Aircraft Occultation Demonstration

In spring 2009, we will begin to demonstrate the ATOMMS occultation concept using two high-altitude NASA WB-57F aircraft as substitutes for the eventual orbiting platforms. Development of the ATOMMS aircraft instrument and the analysis of the measurements are funded by NSF. NASA is providing the aircraft time. The two aircraft will fly toward one another at approximately 19 km altitude, thus creating a rising occultation that will profile the atmosphere from 0 km to 19 km altitude. This range is sufficient to demonstrate most of the key features of ATOMMS including accurate retrievals in the presence of ice and liquid water clouds and characterization of the impact of turbulence. The low transmit power of the ATOMMS instrument requires high gain antennas and precise pointing. The two WB-57F aircraft that we will use for the demonstration have been fitted with precise pointing noses (see Fig. 9) for imaging material falling from the Space Shuttle at launch. The shuttle imaging system in the noses will be replaced by our ATOMMS instrumentation.

Validation, a key part of the demonstration, is challenging because ATOMMS is a state of the art remote sensing system with the ability to penetrate clouds and extremely high vertical resolution but somewhat coarse horizontal resolution. At least one of the aircraft-to-aircraft occultation demonstrations is planned over the Atmospheric Radiation Measurement Program (ARM) site in Oklahoma to utilize the instrumentation there. To the extent possible, the plane of the occultation will be aligned with the prevailing wind direction so that the ground profile observations provide information about the vertical and horizontal structure in the same plane as the occultation measurements. A key aspect of the assessment of the retrievals will be cross comparison of the 22 GHz and 183 GHz water vapor retrievals within a 2 km altitude interval in the troposphere where both sets of profiles will be very accurate.

Fig. 9 WB-57F aircraft with WAVES nose cone. The large mirror is about the size of the 30 cm aperture of the ATOMMS instrument. (Figure provided courtesy of M. Ross)

We also note that the possibility of including ACCURATE (Kirchengast et al. 2008) in these aircraft to aircraft demonstrations was discussed at OPAC-3. We hope that an aircraft-compatible version of the near-IR portion of ACCURATE can be developed and proceed sufficiently quickly in Europe that at least one of the ATOMMS aircraft to aircraft occultation demonstrations can include the near-IR portion of ACCURATE to demonstrate and assess its capabilities as well.

Acknowledgements This work was supported by NSF ATM grants, 0139511, 0551448, 0723239, and 0739506.

References

Coulman CE (1985) Fundamental and applied aspects of astronomical seeing. Ann Rev Astron Astrophys 23:19–57, doi:10.1146/annurev.aa.23.090185.000315

Coulman CE, Vernin J (1991) Significance of anisotropy and the outer scale of turbulence for optical and radio seeing. J Appl Opt 30:118–126

Dunn C, Bertiger W, Bar-Sever Y, Bettadpur S, Desai S, Franklin G, Haines B, Kruizinga G, Kuang D, Meehan T, Nandi S, Nguyen D, Rogstad T, Romans L, Thomas J, Tien J, Watkins M, Wu S (2003) Instrument of GRACE: GPS augments gravity measurements. GPS World 14(2):16–28

Feng D, Marathay A, Herman B, Beran M (2002) Propagation limitations on the active microwave occultation remote sensing. 1st International Workshop on Occultations for Probing Atmosphere and Climate (OPAC-1), Sept 16–20, 2002, Graz, Austria, abstract at http://www.uni-graz.at/opac1/ ≫ Scientific Programme ≫ Fri, Sep 20

Fenn RW, et al. (1985) Optical and infrared properties of the atmosphere. In: Jursa AS (ed) Handbook of Geophysics and the Space Environment, US Air Force Laboratory, chap. 18

Frehlich R, Ochs GR (1990) Effects of saturation on the optical scintillometer. Appl Opt 29:548–553

Gorbunov ME, Kirchengast G (2007) Fluctuations of radio occultation signals in X/K band in the presence of anisotropic turbulence and differential transmission retrieval performance. Radio Sci 42(RS4025), doi:10.1029/2006RS003544

Huang B, Smith WL, Huang HL, Woolf HM (2002) Comparison of linear forms of the radiative transfer equation with analytic Jacobians. Appl Opt 41(21):4209–4219

Jursa AS (ed) (1985) Handbook of Geophysics and the Space Environment. Air Force Geophys. Lab., Bedford, Mass

Kirchengast G, Schweitzer S, Ladstädter F (2008) ACCURATE–observing greenhouse gases, isotopes, wind, and thermodynamic variables by combined MW radio and IR laser occultation. 3rd International Workshop on Occultations for Probing Atmosphere and Climate (OPAC-3), Sept 17–21, 2008, Graz, Austria, presentation at http://www.uni-graz.at/opac3/ ≫ Scientific Programme ≫ Thu, Sep 20

Kursinski ER, Hajj GA, Hardy KR, Romans LJ, Schofield JT (1995) Observing tropospheric water vapor by radio occultation using the global positioning system. Geophys Res Lett 22(17):2365–2368

Kursinski ER, Hajj GA, Schofield JT, Linfield RP, Hardy KR (1997) Observing Earth's atmosphere with radio occultation measurements using the global positioning system. J Geophys Res 102(D19):23, 429–423, 465

Kursinski ER, Syndergaard S, Flittner D, Feng D, Hajj G, Herman B, Ward D, Yunck T (2002) A microwave occultation observing system optimized to characterize atmospheric water, temperature, and geopotential via absorption. J Atmos Ocean Technol 19(12):1897–1914

Kursinski ER, Feng D, Flittner D, Hajj G, Herman B, Romberg F, Syndergaard S, Ward D, Yunck T (2004a) An active microwave limb sounder for profiling water vapor, ozone, temperature, geopotential, clouds, isotopes and stratospheric winds. In: Kirchengast G, Foelsche U, Steiner

AK (eds) Occultations for Probing the Atmosphere and Climate, Springer, Berlin Heidelberg, pp 173–188

Kursinski ER, et al. (2004b) The Mars Atmospheric Constellation Observatory (MACO) concept. In: Kirchengast G, Foelsche U, Steiner AK (eds) Occultations for Probing the Atmosphere and Climate, Springer, Berlin Heidelberg, pp 393–405

Otarola A (2007) The Complex Permittivity of Pure Liquid Water from Microwave Frequencies up to 1.5 THz. Master's thesis, Dept. Atmospheric Sciences, University of Arizona, Tucson, Arizona

Otarola AC (2008) The Effects of Turbulence in an Absorbing Atmosphere on the Propagation of Microwave Signals Used in an Active Sounding System. PhD thesis, Dept. Atmospheric Sciences, University of Arizona, Tucson, Arizona

Rüeger JM (2002) Refractive Index Formulae for Radio Waves. JS28 Integration of Techniques and Corrections to Achieve Accurate Engineering, FIG XXII International Congress, Washington, D.C., USA, April 19–26

Wesely ML (1976) Combined effect of temperature and humidity fluctuations on refractive index. J Appl Meteorol 15:43–49

Wu DL, Read WG, Shippony Z, Leblanc T, Duck TJ, Ortland DA, Sica RJ, Argall PS, Oberheide J, Hauchecorne A, Keckhut P, She CY, Krueger DA (2003) Mesospheric temperature from UARS MLS: Retrieval and validation. J Atmos Sol Terr Phys 65(2):245–267

Author Index

A. Steiner et al. (eds.), *New Horizons in Occultation Research*,
DOI 10.1007/978-3-642-00321-9_BM2,